Hiroaki Katsuragi

Physics of Soft Impact and Cratering



Lecture Notes in Physics

Volume 910

Founding Editors

W. Beiglböck

J. Ehlers

K. Hepp

H. Weidenmüller

Editorial Board

M. Bartelmann, Heidelberg, Germany

B.-G. Englert, Singapore, Singapore

P. Hänggi, Augsburg, Germany

M. Hjorth-Jensen, Oslo, Norway

R.A.L. Jones, Sheffield, UK

M. Lewenstein, Barcelona, Spain

H. von Löhneysen, Karlsruhe, Germany

J.-M. Raimond, Paris, France

A. Rubio, Donostia, San Sebastian, Spain

M. Salmhofer, Heidelberg, Germany

S. Theisen, Potsdam, Germany

D. Vollhardt, Augsburg, Germany

J.D. Wells, Ann Arbor, USA

G.P. Zank, Huntsville, USA

The Lecture Notes in Physics

The series Lecture Notes in Physics (LNP), founded in 1969, reports new developments in physics research and teaching-quickly and informally, but with a high quality and the explicit aim to summarize and communicate current knowledge in an accessible way. Books published in this series are conceived as bridging material between advanced graduate textbooks and the forefront of research and to serve three purposes:

- to be a compact and modern up-to-date source of reference on a well-defined topic
- to serve as an accessible introduction to the field to postgraduate students and nonspecialist researchers from related areas
- to be a source of advanced teaching material for specialized seminars, courses and schools

Both monographs and multi-author volumes will be considered for publication. Edited volumes should, however, consist of a very limited number of contributions only. Proceedings will not be considered for LNP.

Volumes published in LNP are disseminated both in print and in electronic formats, the electronic archive being available at springerlink.com. The series content is indexed, abstracted and referenced by many abstracting and information services, bibliographic networks, subscription agencies, library networks, and consortia.

Proposals should be sent to a member of the Editorial Board, or directly to the managing editor at Springer:

Christian Caron Springer Heidelberg Physics Editorial Department I Tiergartenstrasse 17 69121 Heidelberg/Germany christian.caron@springer.com

More information about this series at http://www.springer.com/series/5304

Hiroaki Katsuragi

Physics of Soft Impact and Cratering



Hiroaki Katsuragi Department of Earth and Environmental Sciences Nagoya University Nagoya, Japan

ISSN 0075-8450 ISSN 1616-6361 (electronic) Lecture Notes in Physics ISBN 978-4-431-55647-3 ISBN 978-4-431-55648-0 (eBook) DOI 10.1007/978-4-431-55648-0

Library of Congress Control Number: 2015943249

Springer Tokyo Heidelberg New York Dordrecht London

© Springer Japan 2016

This work is subject to copyright. All rights are reserved by the Publisher, whether the whole or part of the material is concerned, specifically the rights of translation, reprinting, reuse of illustrations, recitation, broadcasting, reproduction on microfilms or in any other physical way, and transmission or information storage and retrieval, electronic adaptation, computer software, or by similar or dissimilar methodology now known or hereafter developed.

The use of general descriptive names, registered names, trademarks, service marks, etc. in this publication does not imply, even in the absence of a specific statement, that such names are exempt from the relevant protective laws and regulations and therefore free for general use.

The publisher, the authors and the editors are safe to assume that the advice and information in this book are believed to be true and accurate at the date of publication. Neither the publisher nor the authors or the editors give a warranty, express or implied, with respect to the material contained herein or for any errors or omissions that may have been made.

Printed on acid-free paper

Springer Japan KK is part of Springer Science+Business Media (www.springer.com)

Preface

The subject of this book, soft impact, concerns impact on soft materials such as gases, liquids, granular matter, and their mixtures. In particular, impacts on granular matter are the main focus of this book. The wide range of granular matter relates to earth and planetary problems as well as phenomena in our everyday lives. The motivation for writing this book originated from this common term between soft matter physics and earth and planetary science. Because the study of soft impact remains in its infancy, it is difficult to provide a systematic introduction to soft impact on the basis of a rigorous theoretical framework. Therefore, in this book, various experimental results are introduced instead of a well-defined theory, which is why this work was recklessly written by an inexperienced experimentalist. Any mistake or bias in the content is because of a deficiency in my ability. A catalog of various experimental results and their implications is provided in this book. While many experimental studies on soft impact have been published recently, the consistency among these studies has not been discussed in depth. The simple purpose of this book is to sort through these experimental results and clarify our current understanding of soft impact phenomena. The fundamentals of continuum mechanics and dimensional analysis are necessary bases for a proper understanding of the physics of soft impact; thus, these fundamentals are described first. Then, physics of soft impact and cratering are discussed on the basis of these fundamentals. The content in each chapter is deeply related to that in other chapters. Many equations and concepts are cross-referenced among them. The purpose of this book is to provide a connecting point between granular physics and planetary phenomena; however, both fields are too profound to be covered completely. Comprehensive reviews of both fields are undoubtedly beyond my ability. Therefore, the specific topic, soft impact, is the particular focus of this book.

Throughout this book, intuitive explanation has priority over rigorous theoretical explanation because physical intuition is the most important aspect of dimensional analysis and scaling. For the derivations of equations, I have attempted to provide sufficient details to avoid losing the essence of computational procedures. However, in some places, only the guidelines of the computations have been provided in the

vi Preface

footnotes because their details are beyond the scope of this book. Readers can skip these details without losing the main story. Although it was difficult to implement a self-contained style, I have taken care to ensure that highly expert knowledge is not required to read this book, the content of which is based on materials used in a graduate course. The intended readers of this book are, therefore, graduate students who are interested in soft matter physics or earth and planetary science. Knowledge of elementary mechanics is required and fundamental knowledge of continuum mechanics and contact mechanics is helpful to read the content. The first three chapters provide basic concepts and methodologies. To use this book in a graduate course, these chapters should be reviewed in the first half of a semester. Then, in the next half, some topics picked up from the following chapters should be covered depending on the interest. Chapter 4 discusses the drag force of soft impact. Chapters 5 and 6 deal with the impact cratering. Chapter 7 introduces various topics relating to soft impact and planetary problems. For those who want to study a topic further or obtain a more theoretical background, pointers for further reading are provided in the summary sections. Additionally, the list of references is useful to locate the original source for each result. Particularly for experimental studies, the obtained results might depend on the details of the experimental conditions. Thus, specific parameters and experimental conditions are provided in the text as much as possible. However, reading the original papers might be necessary in some cases.

I would like to acknowledge many people who supported the writing of this book. I began the study of granular impact with Doug Durian at the University of Pennsylvania about 10 years ago. I have learned many things from him concerning granular physics and experimental techniques. This collaboration resulted in the origin of this book. Fruitful discussions with colleagues in the earth and planetary physics group at Nagoya University (Sei-ichiro Watanabe, Sin-iti Sirono, Tomokatsu Morota, Muneyoshi Furumoto, and Hiroyuki Kumagai) are another origin. These discussions were very helpful in the development of the idea of relations among soft impacts and planetary phenomena. Furthermore, I am grateful to the many friends who have kindly permitted my reuse of their original figures. Thanks to their brilliant works, the physics of soft impact has progressed. I am also indebted to many friends and colleagues who have discussed various things about soft impact phenomena. Additionally, I would like to thank the graduate students who have collaborated with me. Although it is difficult to list all the names of collaborators and friends here, I truly appreciate all their courtesies and kindness. Finally, I must express my gratitude to my family, Natsu, Asuka, and Yamato. Their cheerfulness has always been a source of energy in the course of writing, which took over 2 years. Actually, this work was beyond my ability alone and would not have been possible without their support.

The study of soft impact remains a growing field. I hope that great breakthroughs in both soft matter physics and planetary science will be made hereafter through further investigations of soft impact.

Contents

1	Introduction References 1				
2	Scaling and Dimensional Analysis				
	2.1		and Dimensions	13	
2.2 Force, Stress, and Strain			, Stress, and Strain	14	
			e Definitions of Viscosity and Elasticity	20	
	2.4	Conservation Laws			
		2.4.1	Mass Conservation	23	
		2.4.2	Linear Momentum Conservation and		
			Navier-Stokes Equation	24	
		2.4.3	Energy Conservation	25	
	2.5	Dime	nsional Analysis	27	
		2.5.1	Nondimensionalization of the Governing Equation	27	
		2.5.2	Π -Groups	29	
		2.5.3	Dimensional Analysis of Blast Wave Front Propagation	32	
		2.5.4	Scaling of Contact Mechanics	35	
	2.6	Fluid	Drag Force	37	
		2.6.1	Viscous Drag	37	
		2.6.2	Inertial Drag and Drag Coefficient	39	
		2.6.3	Terminal Velocity and Stokes Number	40	
		2.6.4	Virtual Mass	42	
		2.6.5	Fluid Impact Drag Force	42	
		2.6.6	Epstein Drag	45	
		2.6.7	General Form of the Drag Force	46	
	2.7			48	
	2.8	Similarity Law and Modeling		53	
		2.8.1	Geometric Similarity	55	
		2.8.2	Kinematic Similarity	55	
		2.8.3	Dynamical Similarity	56	

viii Contents

		2.8.4	Modeling of Geological Phenomena	58
		2.8.5	Dimensional Dependence of Body and Surface Forces	59
	2.9	Summ	nary	60
	Refer	ences		61
3	Cons	titutive	Laws	63
•	3.1		elasticity	63
	3.2		city and Nonlinear Flow	66
	3.3		lex Moduli	67
	3.4		and, Attenuating Oscillation, and Restitution Coefficient	68
	3.5		port Phenomena	71
		3.5.1	Diffusion	72
		3.5.2	Advection	76
		3.5.3	Comparison of Diffusion and Advection	76
	3.6	Frictio	on	78
		3.6.1	Coulomb Friction and Angle of Repose	78
		3.6.2	Rate- and State-Dependent Friction	80
		3.6.3	Inertial Number and Granular Friction	81
	3.7	Static	Structure of Granular Matter	84
		3.7.1	Janssen Effect	84
		3.7.2	Stress Dip	87
		3.7.3	Dynamic Janssen Effect	87
	3.8		ct Force Distribution in a Static Granular Structure	89
	3.9	Fluidi	zed Granular Matter	91
		3.9.1	Granular Convection and Undulations	92
		3.9.2	Interstitial Air, Room Temperature, and Gravity	94
		3.9.3	Granular Temperature	95
		3.9.4	Brazil Nut Effect and Segregation	96
	3.10	Summ	nary	100
	Refer	ences		101
4	Soft 1	Drag Fo	orce	105
-	4.1		lar Impact Drag Force	105
		4.1.1	Simple Scaling Approach	106
		4.1.2	Controversy over Granular Impact Drag Force Models	109
		4.1.3	Unified Drag Force Model	110
		4.1.4	Material Dependence of the Drag Force Model	117
		4.1.5	Direct Force Measurement	119
		4.1.6	Inertial and Viscous Drag Forces for the Granular Impact	121
		4.1.7	Various Effects in the Granular Impact Drag Force	125
		4.1.8	Oblique Impact	133
	4.2		ılar Slow Drag Force	136
		4.2.1	Granular Vertical Slow Drag	136
		4.2.2	Granular Horizontal Slow Drag	142
		4.2.3	Swimming in Sand	146
		4.2.4	Drag Force in a Vibrated Granular Bed	147

Contents ix

	4.3	Drag I	Forces of Other Soft Materials	149
		4.3.1	Viscoelastic Fluid Drag	149
		4.3.2	Viscoplastic Fluid Drag	151
		4.3.3	Dense Suspension Drag	151
	4.4	Summ	nary	153
	Refer	ences		154
5	Morr	hodyna	amics of Planetary Impact Craters	157
	5.1	-	fication of Craters	157
	5.2	Popula	ation of Craters	163
	5.3		anics of Planetary Impact Cratering	168
		5.3.1	Contact and Compression	168
		5.3.2	Excavation	172
		5.3.3	Ejecta Deposition	173
		5.3.4	Modification	174
		5.3.5	Degradation	176
	5.4	Acous	stic Fluidization and Seismic Shaking Induced	
			pact	176
		5.4.1	Acoustic Fluidization	177
		5.4.2	Global Seismic Shaking	179
	5.5	Scalin	g for Planetary Impact Cratering	184
		5.5.1	Crater Volume Scaling	184
		5.5.2	Ejecta Scaling	190
		5.5.3	Oblique Impact Scaling	194
		5.5.4	Porous Target Impact Scaling	195
		5.5.5	Viscosity Scaling	197
	5.6		nary	198
				199
6		_	Cratering	203
	6.1	-	I Impact Cratering	203
		6.1.1	Geometric Energy Balance of Liquid Impact Cratering	204
	()	6.1.2	Cavity Growth Dynamics of Liquid Impact Cratering	207
	6.2		lar Impact Cratering	210
		6.2.1	Scaling of Granular Impact Craters	211
	6.2	6.2.2	Ejecta Splashing	214
	6.3		t-Induced Granular Jet Formation	217
	6.4		lar-Granular Impact Cratering	221
		6.4.1	Impact Deformation of a Mud Ball	221
		6.4.2	Crater Morphology by Granular-Granular Impact	223
		6.4.3	Interaction of Multiple Impactors	226
	6.5		et-Granular Impact Cratering	228
		6.5.1	Droplet Deformation by an Impact on a Solid Wall	
		6.5.2	Crater Morphology by Droplet-Granular Impact	232

x Contents

	6.6	Instab	ility of Soft Impact Cratering Rim	242	
		6.6.1	Impact Reynolds Number Scaling	243	
		6.6.2	Rayleigh-Taylor Instability	244	
		6.6.3	Instability-Based Scaling and Splashing Parameter	247	
		6.6.4	Instability in Various Cratering and Impact Phenomena	250	
	6.7	Wet G	ranular Impact Cratering	253	
	6.8	Fluid	Flow Impact Cratering	255	
	6.9	Summ	nary	257	
	Refe	rences		258	
7	Grains and Dust Dynamics				
	7.1		mpact of Dust Aggregates	261	
		7.1.1	Relative (Impact) Velocity of Dust Aggregates	262	
		7.1.2	Dust Growth	268	
		7.1.3	Static Structure of Dust Aggregates	270	
		7.1.4	Restructuring and Fragmentation of Dust Aggregates	271	
		7.1.5	Experiments of Dust Aggregate Collisions	274	
		7.1.6	Soft Impact of Dust Aggregates	275	
	7.2	Regol	ith Grains	278	
		7.2.1	Regolith Formation by Impacts	279	
		7.2.2	Compaction by Thermal Cycling	281	
		7.2.3	Thermal Conduction and Thermal Inertia	282	
		7.2.4	Regolith Migration	283	
		7.2.5	Regolith Convection	285	
		7.2.6	Wind Transport of Regolith	289	
	7.3	Summ	nary	294	
	Refe		*	295	
8	Pers	pectives		297	
T	dov			202	
ш	utx			.วบ.ว	

Chapter 1 Introduction

Ever since Galileo Galilei observed that the lunar surface is rough, continuous efforts have been devoted to understanding the reason for this roughness. Today, we have access to the detailed structure of the surface terrain of the moon, as shown in Fig. 1.1. A lot of circular structures called craters appear almost all over the surface: these pits are evidence of ancient impacts. Numerous astronomical objects have impacted the moon and have left craters. Astronomical impacts have been one of the most important and ubiquitous processes since the formation of the solar system. Thus, an in-depth understanding of impact cratering is a necessary key to shedding light on the history of the solar system. However, a fundamental understanding of this concept remains in development mainly because the physical basis for impact phenomena remains in its infancy. Moreover, the actual planetaryrelated phenomena are very complex processes. Therefore, various approaches in addition to the physics of impact would also be necessary to fully explain the entire phenomenology of planetary impacts. The physics of impact is only a part of these various approaches. Nevertheless, many unsolved problems remain even in the very fundamental physics of impact.

Impact mechanics itself is an exciting problem for soft matter physics and may relate to biological and industrial phenomena as well. Human skin is a typical soft matter, suggesting that we experience soft impact when we grab something by hand. Everyone knows that running over beach sand is much more difficult than walking on a paved road. In many industrial fields, soft matter is handled in various production processes. The aim of this book is to connect and unify the understanding of various impact phenomena from the planetary scale to the everyday-life scale using the scaling method.

Among the many intriguing issues concerning impact phenomena, we focus specifically on the nature of *soft impact* in this book. "Soft impact" means the impact of soft materials such as granular matter and liquid droplets. Because such soft materials can be easily deformed, low-velocity impact is sufficient to reveal the dynamics. Soft impact is relevant to both soft matter mechanics and planetary-scale

1

2 1 Introduction

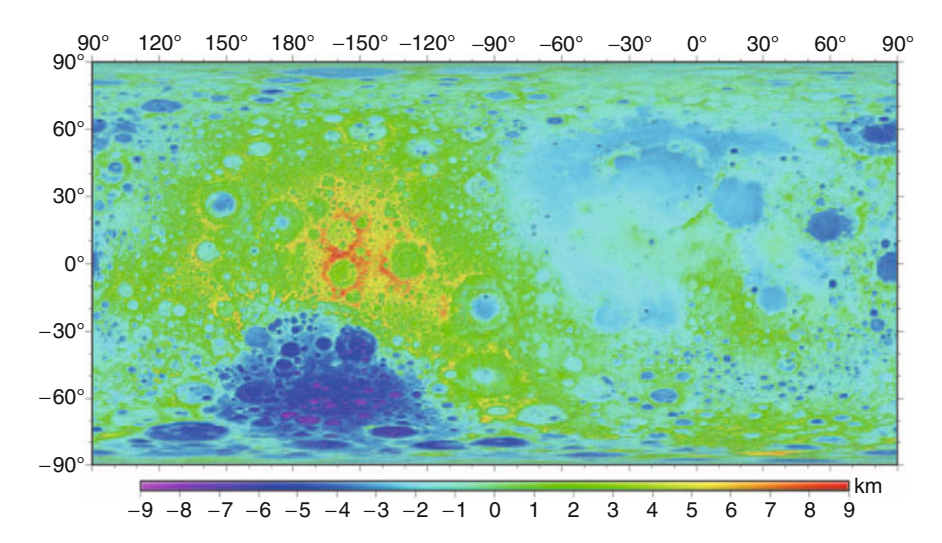


Fig. 1.1 Lunar surface elevation map based on SELENE (Kaguya) data. Numerous craters appear as circular pits, which are considered to be remnants of the impacts

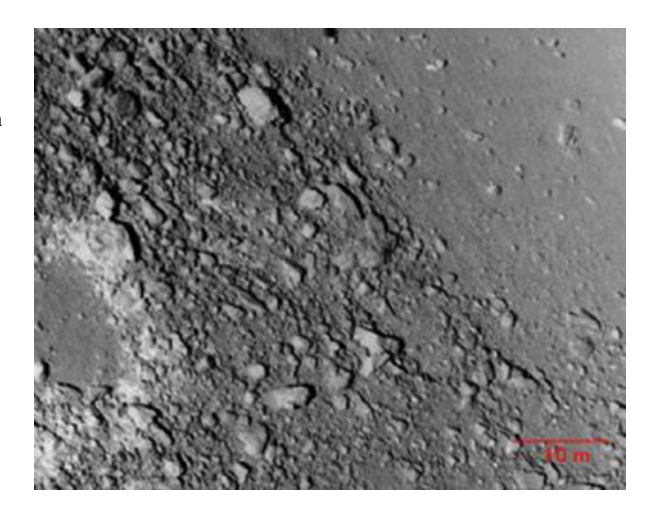
phenomena. You may feel that the scale of our everyday-life and planetary-scale phenomena are quite different. However, some relations among soft and planetary impacts have been noted by recent investigations. Of course, we must be very careful when comparing small-scale and large-scale phenomena. The fundamental methodology and its application to various-scale impact phenomena are discussed in this book.

As already mentioned, the impact has to be understood as an important elementary factor to solve the history of the solar system. Thus, planetary scientists have long studied impact cratering and associated geomorphology [1, 2]. However, most of their attention has been focused on the high-velocity impact on a rock or other hard materials. Although the possible effect of viscoplasticity has been briefly discussed in Ref. [1], explaining the detailed relation between planetary cratering dynamics and soft impact is difficult. Since the beginning of the twenty-first century, fundamental studies of soft impacts have been extensively conducted in the field of soft matter physics. Although the physics of high-velocity and low-velocity impacts differ, these impacts may share a certain aspect of cratering dynamics. In fact, various planetary crater shapes can be mimicked by low-velocity granular impact experiments.

Granular impact has been studied thoroughly in recent years. These experiments have revealed what happens in a collision between a solid projectile and a granular bed. For example, a phenomenological form of the granular drag force has been developed on the basis of experimental results. Granular drag force is one of the main topics discussed in this book. Crater morphology due to granular impact is also intensively discussed in this book.

1 Introduction 3

Fig. 1.2 Close-up view of the surface of the asteroid Itokawa (vicinity of Komaba crater) (The image was taken by the Hayabusa. (C)JAXA)



Granular matter is a very important constituent of the Earth, planets, and asteroids. In Fig. 1.2, a close-up view of the asteroid Itokawa taken by the explorer Hayabusa is presented. The surface of Itokawa appears to be covered with many boulders and small grains called regolith. Usual terrestrial planets are known to be covered with regolith. Regolith possesses a rough irregular shape and polydispersity similar to sand grains on the Earth but is quite different in terms of composition and formation process. Itokawa's surface is covered with an enormous amount of centimeter- or sub-centimeter-sized regolith as well as meter-sized boulders (Fig. 1.2). The grain size of regolith on Itokawa is close to that on Earth. In contrast, the gravitational force on Itokawa is very weak, approximately 10^{-5} of that on the Earth. Thus, the granular dynamics under the microgravity condition is a key to reveal the surface processes occurring on Itokawa or other small planetary surfaces that consist of regolith. Even though it is not very easy to attain the microgravity condition, the sub-centimeter-sized grains are ubiquitous on the Earth. Therefore, we should first evaluate granular physics with sub-centimeter-sized grains under Earth's gravity, namely under the gravitational acceleration of 9.8 m/s². Then, the effect of microgravity can be properly evaluated. To date, we are still in the process of developing granular physics on Earth. In the meantime, various interesting findings, which might also be relevant to planetary science, have been reported in the recent granular physics literature.

Granular matter The physics of granular matter is one of the most important topics throughout this book. As mentioned above, granular matter can be a key factor

¹The strength of *bulk* granular matter is considerably weaker than that of usual rocks. Thus, granular impact usually models the gravity-dominant regime rather than the strength-dominant regime. Gravity is most likely essential even in the microgravity condition. Under a microgravity environment, the cohesive force among grains could be crucial.

4 1 Introduction

in various planetary-related phenomena. Soft impact is a specific topic in which the physics of granular matter plays an essential role in describing the intrinsic feature of the phenomena.

What is granular matter? How can we define it? Granular matter is usually defined by a collection of macroscopic rigid and dissipative grains. Dissipation includes inelastic collision and friction. These dissipative effects are relevant only when grains are in contact with each other. In addition, the grain size should be sufficiently large to consider the gravity-dominant regime rather than thermodynamic regime. This definition of granular matter is the simplest and minimal definition. Most granular characteristics can be reproduced, at least qualitatively, by this simply defined minimal granular-matter model. Spherical glass beads are often used as a typical granular matter in various experiments. Because almost all numerical simulations also use spherical particles, glass beads are advantageous to compare the experimental results with numerical results. Note that, however, actual regolith and natural sand have irregular shapes. The size distribution of grains must also be considered to model the natural granular behavior. Additionally, the effects of interstitial fluid and cohesion are not negligible in some experimental conditions. Moreover, elastic (or plastic) deformations of grains must be considered to explain realistic granular behavior. One of the major difficulties involved in the modeling of granular behavior is that these complex factors sometimes play crucial roles and significantly affect granular behaviors. Whilst a simpler model is better for a physical explanation, we must keep these issues in mind to discuss the application of granular physics to natural regolith behaviors. All we can do is use a step-bystep approach. At first, the principal effects of gravity and dissipation should be revealed using the behaviors of macro-grains.² Then, various complex effects can be contemplated as additional factors using careful experiments, simulations, and theoretical modeling. In fact, recent studies on granular matter consider complex effects such as deformation, size dispersion, and friction. However, its application to planetary-scale phenomena remains deficient.

The next problem is how to characterize the granular matter using physics. We usually discriminate three states of matter: gas, liquid, and solid. Although each grain composing granular matter is solid, bulk granular matter can behave like gas, liquid, and solid. Fluid mechanics (hydrodynamics) was established to characterize the behaviors of gases and liquids, whereas elastic mechanics allows us to evaluate the deformability, strength, and other properties of a solid. Connecting these two characteristics (fluid viscosity and solid elasticity), we can even define the viscoelastic property. All the aforementioned frameworks are applicable only to continua, i.e., these frameworks represent continuum mechanics. There might be an effective continuum mechanics for granular matter when the number of grains is sufficiently large. Therefore, the assumption of continuum (bulk) granular matter is one possible strategy to approach granular physics. This strategy is more or

²The grain diameter should be greater than the sub-millimeter scale to neglect surface effect under the Earth gravity.

1 Introduction 5

less phenomenological. However, the granular matter can be characterized only by several governing equations and relevant arguments if this strategy succeeds. Moreover, this approach is useful to analyze experimental results in which the measurable quantities are limited in many cases. Of course, granular matter is inherently discrete; it must not be a perfect continuum. From a theoretical viewpoint, macroscopic phenomenological mechanics should be linked to the microscopic grains dynamics.³ Unfortunately, we are still developing phenomenological granular mechanics. The microscopic theories are also still inadequate.⁴ Nevertheless, considerable key developments in granular physics have been achieved in recent decades [3–7].

In this book, impact and planetary-related experimental results are particularly emphasized. The scales of these topics are sufficiently large to assume continuum-like granular matter. Thus, the phenomenological approach is often utilized to understand the intrinsic physical process.

Fluid and granular instability Granular matter is notorious in industrial fields for its counterintuitive behavior. These counterintuitive behaviors result in various difficulties in production processes, including clogging, segregation, and shear banding. In addition to these phenomena, beautiful pattern formations have been observed in various granular experiments. For instance, a rotating drum filled with two different types of grains exhibits banding segregation [7–9] and flower-like patterns [4, 10]. A stratification structure has also been observed in granular heaping and avalanching [11–13]. These peculiar phenomena are fascinating enough to attract physicists. The unified explanation of this variety of intriguing phenomena by a simple framework is the ultimate goal of granular physics. One possible step toward this goal is the comparison of granular phenomenology with viscous, elastic, or viscoplastic mechanics.

Because flowing granular matter is capable of inducing various pattern formations similar to fluids, granular flow dynamics could be compared with fluid mechanics. Fluid motion is frequently characterized by its instabilities [14]. Thus, a comparison based on instability might be helpful in highlighting the similarities and differences between fluids and granular matter. Some representative fluid instabilities are briefly listed below.

• Rayleigh-Taylor instability: When a large-density fluid layer is placed onto a small-density fluid layer, the state is unstable because of gravity. The overturn of this unstable structure is initiated by a fingering structure whose characteristic length scale is determined by fluid properties. This type of instability is called Rayleigh-Taylor instability and relates even to the remnant structure of a supernova [15]. An intuitive explanation of the Rayleigh-Taylor instability is given in Sect. 6.6.2.

³For equilibrium thermodynamics, statistical mechanics successfully plays this role.

⁴Kinetic theory has contributed to describe dilute granular gas dynamics.

6 1 Introduction

• Rayleigh-Plateau instability: A free-falling fluid stream is unstable because of surface tension. The stream finally splits into droplets to minimize the surface area. This instability is called Rayleigh-Plateau instability.

- **Viscous fingering instability**: When a less viscous fluid is injected into a more viscous fluid layer confined in a quasi-two-dimensional cell (Hele-Shaw cell), viscous fingering instability occurs. This instability results in a fractal pattern formation in an isotropic situation because of the Laplace growth.
- **Kelvin-Helmholtz instability**: An interface of two fluids of different densities and velocities undergoes instability called Kelvin-Helmholtz instability, which is a parallel shear flow instability that produces a vortex sheet structure. The vortex structure can sometimes be observed even in cloud shapes.
- **Taylor vortex instability**: A rotating flow also exhibits a peculiar instability. Fluids sheared by concentric rotating cylinders form a vortex structure called a Taylor vortex, which is a type of three-dimensional instability.
- **Faraday wave instability**: A vibrated fluid layer produces surface wave patterns on its surface. This pattern formation is called Faraday wave instability.

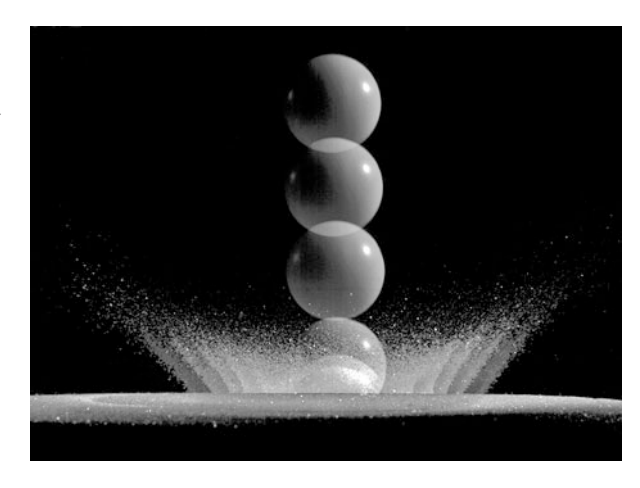
All these instabilities had been considered to be characteristic features of a fluid. However, recent granular experiments overrode the idiosyncrasy of the fluid instabilities. Surprisingly, all the abovementioned instabilities can be mimicked by granular matter. Experiments have demonstrated the granular analogues of the Rayleigh-Taylor [16], Rayleigh-Plateau [17, 18], viscous fingering [19], Kelvin-Helmholtz [20], Taylor vortex [21], and Faraday wave [22, 23] instabilities. In fact, these instabilities are not exactly the same as fluid instabilities, and the similarity is rather limited in its appearance. The specific origin of each granular instability is different from the corresponding fluid instability. Merely because the granular matter can produce various behaviors, some of these behaviors might only look similar to fluid instabilities.

Although each investigation on granular instability is quite interesting, the instability-based classification of fluid and granular matter is not so easy. Phenomenologically, granular matter can induce various instabilities that are very similar to fluid instabilities. However, the mechanisms of these instabilities are not identical to those of fluids; this leads to a slightly confusing situation and represents a difficulty in the study of granular matter. Can we say that granular matter really behaves like a fluid? The answer is partially "yes" and partially "no." The created patterns or instabilities by various granular experiments might not be sufficient to classify granular matter and fluid. Because the instability-based pattern formations are extremely beautiful and fascinating, they have attracted the attention of many physicists. These detailed studies certainly reveal very crucial properties of granular matter. However, an instability-based study is not a unique way to understand granular properties. We apply another simple strategy to study granular matter.

Impact drag force The simplest way to examine an unknown object is probably by mechanical probing. Consider a situation in which you are in front of an unknown object. What is the first thing you should do? The simplest thing to do first is "careful observations from various angles." Then, as a next step, one might push the

1 Introduction 7

Fig. 1.3 Granular impact example. The motion of a solid sphere impacting a glass-bead bed is captured by a high-speed camera. Granular splashing is observed in addition to the deceleration of the sphere



material and observe the response. This mechanical probing method corresponds to one of the most primitive methods in physical research. Mechanical probing can be regarded as a sort of drag force measurement that will determine the mechanical characteristics of an unknown object. Quantitatively, the force resisting penetration should be measured; then, the measured data should be analyzed with penetrating velocity and depth to obtain the typical drag force characterization. For instance, a series of high-speed video images of a stone striking onto a sand bed allows us to quantify the impact drag force using Newton's second law of motion. In Fig. 1.3, an example of the motion of a solid sphere impacting a glass-bead bed is shown. Assuming continuum-like mechanics, the corresponding granular drag force may be written by a concise equation. In addition, standard drag force theory has been established in fluid mechanics. Thus, a comparison of the drag force equations is presumably helpful to classify fluid and granular matter. Moreover, the drag force can characterize not only granular matter and fluid but also other soft matter such as viscoelastic materials. Therefore, drag force characterization can be employed as a fundamental tool to classify a wide range of soft matter. Drag force characterization is one of the main topics in this book with a particular focus on low-velocity impact phenomena. While the basic drag force equation will be simple, the various factors such as the cohesive force may affect this equation. We consider, however, that these factors would be minor compared with dominant effects such as momentum transfer. Although we have not yet completely understood these additional (minor) effects, the state-of-the-art granular impact drag force will be reviewed in this book. The impacts of other soft matter and some related topics are also discussed to provide an overview of the generality of the soft matter drag force law.

Impact cratering In an appropriate impact energy regime, the impact inevitably leaves a crater on the target surface. The morphology of impact cratering on a soft matter target is another main topic of this book. The cratering morphology provides useful information for understanding planetary phenomena as well as basic granular physics. As observed in Fig. 1.1, the surface of the moon is covered with

8 1 Introduction

vast amounts of craters. Their size-frequency distribution, spatial distribution, and morphology are meaningful keys to studying the history of the solar system [1]. From the viewpoint of soft impact mechanics, various experiments that can make a collection of crater shapes will be discussed in this book. For example, the liquid-droplet-impact phenomenon is a gold mine of interesting crater shapes. In addition to the final crater shape, transient splashing and jetting caused by the impact are also informative to discuss the granular physics and planetary surface processes. A typical ejecta splashing structure formed by a granular impact can be observed in Fig. 1.3.

Similarity law, dimensional analysis It should be noted that laboratory experiments of soft impact cannot be directly applied to the space environment. In the space environment, the situation is very different from the laboratory in terms of atmospheric pressure, temperature, and gravity. A high-velocity impact experiment in a low-temperature vacuum chamber under microgravity condition must be performed to directly reproduce the impact occurring in space. Furthermore, a geological-scale (huge) impactor and target are necessary for a complete reproduction, which is certainly impossible. To overcome this difficulty, the similarity law is usually considered.⁵

The similarity law enables us to scale down massive phenomena to a laboratory scale on the basis of the concept of dimensional analysis. Dimensional analysis is particularly powerful and has been used in fluid mechanics. Using an appropriate normalization, one can obtain a dimensionless form of the equation of motion of a fluid. Then, the relevant dimensionless numbers are naturally derived. These dimensionless numbers are important parameters to characterize the considered fluid phenomena. More systematically, the number of independent dimensionless numbers can be calculated for a specific system considered using dimensional analysis. Dimensional analysis is applicable to not only fluids but also general physical systems. Recently, the method of dimensional analysis has been widely applied to the evaluation of geological-scale impacts. Using the similarity law, the size of geological-scale phenomena can be reduced to a laboratory scale. The similarity law guarantees that the system behaves similarly as long as the relevant dimensionless number is identical. In other words, dimensional analysis is very useful to obtain the scaling law. Once the scaling law is obtained by the laboratory experiments, the law can be extrapolated to larger or smaller scales as long as the governing physics is unchanged. Thus, we can estimate the order of various physical quantities using the scaling. This approach is most likely the only way to speculate what happens in geological-scale phenomena by utilizing laboratoryscale experiments, particularly because the available information on geological

⁵Another possible way to study such large-scale and extreme-environment phenomena is the theoretical or numerical approach. Because the focus of this book is primarily experimental studies, the similarity law is mainly considered.

1 Introduction 9

or astronomical phenomena is usually very limited. Order estimates based on dimensional analysis are convenient to discuss the phenomena with very limited information.

Using dimensional analysis and the corresponding scaling relation, essential physics governing a phenomenon can be deduced in most cases. The scaling method is also utilized to obtain physical intuition about the phenomenon. The concept of the similarity law is very useful in various fields of science and engineering. However, note that dimensional analysis is not almighty; in particular, empirically obtained scaling laws have to be carefully applied. Thus, this book will first introduce the basics of scaling and dimensional analysis. These methods will be used everywhere in the remainder of this book. In particular, the characterization of planetary craters by dimensional analysis is intensively reviewed in this book. This framework is very insightful for discussing planetary-scale impact cratering. Dimensional analysis and scaling are also helpful for laboratory-scale impact phenomena.

Constitutive laws Because the macroscopic continuum-like behaviors of granular matter are mainly considered in this book, some constitutive laws are important elements in the physical considerations. Constitutive laws describe the macroscopic relations among properties such as stress, deformation, flow, friction, rebound, and attenuation. Because these properties must originate from the integration of microscopic dynamics, such details are omitted in this book. Namely, only some important constitutive laws are selected and introduced. Additionally, advective and diffusive transports and some specific constitutive laws for granular matter are introduced. These constitutive laws correspond to the background knowledge for analyses and interpretations of the following various soft impact phenomena.

Related topics There are some other impact-related interesting phenomena. Here we briefly introduce the topics that we will discuss in this book. Planetary-scale impact causes seismic shaking as well as cratering and works to erase the crater shape. Thus, impact cratering is not a simple process. The model for this type of seismic shaking is also discussed in this book. Impacts of fluffy dust aggregates, which are constructed by sub-micron monomers, are very important processes to form planetesimals. Numerical simulations are very powerful to analyze such a small-scale phenomenon. Thus, both the numerical and experimental results are discussed for this topic. Regolith migration induced by impact or wind transport is another interesting impact-related phenomenon. We must determine the origin of regolith formation and how the regolith grains are moved by the impact-induced seismic shaking and surface wind, to interpret various planetary surface morphologies. Moreover, the convection of regolith may be triggered by impact. These special topics relate to both soft impact physics and planetary science.

Summary In summary, soft impact dynamics will be discussed to reveal fundamental physics and relate this information to geological or planetary phenomena. Granular matter is specifically focused on as an important constituent of geological or planetary phenomena. The specific topics discussed in this book are (i) impact drag force and (ii) impact cratering. Granular matter is regarded as a type of continua

10 1 Introduction

to develop phenomenological models. Dimensional analysis and scaling will be used to determine the essential physics of these phenomena. This book will review and discuss the recent experimental results of various impact-related phenomena. From the theoretical viewpoint, we will not address microscopic details in more depth than constitutive laws. To investigate the theoretical points of granular matter in detail, there are some appropriate textbooks available [24–28]. However, the readers of this book do not have to be familiar with these theories of granular matter. Basic knowledge of continuum mechanics will be useful to understand the content.

Organization of the book This book is organized as follows. In the next chapter (Chap. 2), the minimal fundamentals necessary to understand soft impact are introduced. The basics of dimensional analysis are mainly covered in this chapter. Furthermore, the basic framework of the drag force model is discussed in this chapter, which will be instructive for understanding the essence of the scaling theory. Next, in Chap. 3, useful constitutive laws are briefly explained. The constitutive laws introduced in this chapter provide a firm basis for understanding physics of soft impact and cratering. The similarity and difference between granular matter and fluids are also highlighted in this chapter. Additionally, the representative features of granular matter are introduced. Those who are already familiar with fluid and granular mechanics can skip these two chapters. In Chap. 4, impact drag force is intensively discussed; recent experimental results are reviewed, and a unified understanding is introduced. Various effects such as container wall, packing fraction, and interstitial fluid are also discussed in terms of the impact drag force. Some other related phenomena, e.g., slow penetration and viscoelastic impact, are also reviewed in this chapter. Then, planetary impact cratering is described in Chap. 5. In this chapter, crater morphology, mechanics, and their dimensional analysis method are reviewed. In Chap. 6, after reviewing the basic scaling theory of the impact cavity formation in fluid, some recent experimental results on soft impact cratering are presented. Transient phenomena such as jetting and splashing are discussed in addition to the final crater shape. In Chap. 7, the impact of fluffy dust aggregate and transport of regolith grains will be discussed. Finally, perspectives on the relation between soft impact and planetary or geological science are presented in Chap. 8.

The primary points discussed in this book are summarized in the list below.

- Scaling and dimensional analysis (Chap. 2): The basic methodology used in this book is introduced.
- Fundamentals of constitutive laws (Chap. 3): Phenomenological description and characteristic (counterintuitive) laws relevant to continuum and granular matters are reviewed.
- **Impact drag force** (Chap. 4): The focus of this chapter is granular impact drag force. Some related phenomena are also reviewed briefly.
- Impact cratering morphology (Chap. 5): The morphological classification and the scaling of planetary impact cratering are discussed. Seismic shaking, shock propagation, and Π -groups scaling for planetary impact cratering are also reviewed.

References 11

• **Soft impact cratering** (Chap. 6): Various crater shapes formed by soft impacts are discussed. Jetting, ejecta splashing, and more complex structures are introduced on the basis of experimental results.

• Relation between soft matter and earth and planetary science (Chap. 7): The possible applications of soft matter physics to planetary or geological phenomena are discussed. In particular, the collisional growth of dust aggregates and regolith migration dynamics are the main focus.

Primarily, experimental results and related intuitive explanation through dimensional thoughts are discussed throughout this book.

References

- 1. H.J. Melosh, *Impact Cratering* (Oxford University Press, New York, 1989)
- G.R. Osinski, E. Pierazzo (eds.), Impact Cratering: Processes and Products (Wiley-Blackwell, Hoboken, 2013)
- 3. H.M. Jaeger, S.R. Nagel, R.P. Behringer, Rev. Mod. Phys. 68, 1259 (1996)
- 4. J.M. Ottino, D.V. Khakhar, Annu. Rev. Fluid Mech. 32, 55 (2000)
- 5. I.S. Aranson, L.S. Tsimring, Rev. Mod. Phys. 78, 641 (2006)
- 6. S. Luding, Nonlinearity 22, R101 (2009)
- 7. G. Seiden, P.J. Thomas, Rev. Mod. Phys. 83, 1323 (2011)
- 8. H. Caps, R. Michel, N. Lecocq, N. Vandewalle, Physica A 326, 313 (2003)
- 9. S. Inagaki, K. Yoshikawa, Phys. Rev. Lett. 105, 118001 (2010)
- 10. I. Zuriguel, J. Gray, J. Peixinho, T. Mullin, Phys. Rev. E 73, 061302 (2006)
- 11. H.A. Makse, S. Havlin, P.R. King, H.E. Stanley, Nature **386**, 379 (1997)
- 12. H.A. Makse, R.C. Ball, H.E. Stanley, S. Warr, Phys. Rev. E 58, 3357 (1998)
- 13. M. Shimokawa, S. Ohta, Phys. Rev. E 77, 011305 (2008)
- S. Chandrasekhar, Hydrodynamic and Hydromagnetic Stability (Oxford University Press, New York, 1961)
- 15. J.J. Hester, Annu. Rev. Astron. Astrophys. 46, 127 (2008)
- J.L. Vinningland, O. Johnsen, E.G. Flekkøy, R. Toussaint, K.J. Måløy, Phys. Rev. Lett. 99, 048001 (2007)
- J.R. Royer, D.J. Evans, Q.G. Loreto Oyarte, E. Kapit, M.E. Möbius, S.R. Waitukaitis, H.M. Jaeger, Nature 459, 1110 (2009)
- 18. G. Prado, Y. Amarouchene, H. Kellay, Phys. Rev. Lett. 106, 198001 (2011)
- 19. X. Cheng, L. Xu, A. Patterson, H.M. Jaeger, S.R. Nagel, Nat. Phys. 4, 234 (2008)
- 20. D.J. Goldfarb, B.J. Glasser, T. Shinbrot, Nature 415, 302 (2002)
- 21. S.L. Conway, T. Shinbrot, B.J. Glasser, Nature 431, 433 (2004)
- 22. F. Melo, P.B. Umbanhowar, H.L. Swinney, Phys. Rev. Lett. **75**, 3838 (1995)
- 23. P.B. Umbanhowar, F. Melo, H.L. Swinney, Nature **382**, 793 (1996)
- R.M. Nedderman, Statistics and Kinematics of Granular Materials (Cambridge University Press, New York, 1992)
- N.V. Brilliantov, T. Pöschel, Kinetic Theory of Granular Gases (Oxford University Press, New York, 2004)
- 26. A. Mehta, Granular Physics (Cambridge University Press, Cambridge, 2007)
- 27. K.K. Rao, P.R. Nott, An Introduction to Granular Flow (Cambridge University Press, Cambridge, 2008)
- B. Andreotti, Y. Forterre, O. Pouliquen, Granular Media (Cambridge University Press, Cambridge, 2013)

Chapter 2 Scaling and Dimensional Analysis

The fundamental concepts necessary to understand *soft impact* will be presented in this and the next chapter. First, definitions of unit, dimension, stress, and strain are introduced. Then, the basic ideas of scaling and dimensional analysis are briefly explained on the basis of fundamental continuum mechanics. After reviewing the elementary theory of the fluid drag force, a list of meaningful dimensionless numbers is provided. Finally, the concept of the similarity law, which is important in the design and analysis of the experimental system, is described. In the next chapter, constitutive laws of soft matter particularly for granular matter are intensively discussed. Because this and the next chapters concern fundamentals, those who already have a good understanding of continuum mechanics and granular matter do not need to read these chapters. Note that, however, many equations derived in these chapters will be used in the subsequent chapters.

2.1 Units and Dimensions

We must first define the unit and dimension. In any physical experiment, some physical quantities must be measured and related quantitatively to find the governing physical law. For the quantification, the measured quantities must be compared with the standard units, e.g., 1 kg for mass, 1 m for length, and 1 s for time. These three units (kg, m, s) are independent of each other and indispensable to the mechanical characterization of motion and dynamics of objects. Such a set of fundamental units is called a system of units. Namely, the units kg, m, and s are the fundamental units comprising a system of units for the mechanical characterization. Other units defined by combinations of fundamental units are called derived units. For instance, the unit of velocity is a derived unit because it can be composed of the units of length and time as m/s. The specific value of a measured physical quantity depends on the set of units used in the quantification, e.g., 1 m/s = 3.6 km/h. The necessary

number of fundamental units constructing the system of units depends on the physical system under consideration. The system of units must involve a sufficient number of units to derive all the other units necessary for the physical characterization of the system. In the above example, three units are selected, assuming a purely mechanical system. When a thermal effect is indispensable, temperature should be involved in the system of units. For electromagnetic phenomena, electric charge should also be considered. Because most of the discussions in this book concern purely mechanical cases, three mechanical units (e.g., (kg, m, s)) are generally used to compose the system of units.

The dimension does not depend on the system of units. Whatever the system of units used, the unit of velocity is defined by the unit of length divided by time. To clearly focus on this dimensional relation, we can use fundamental dimensions instead of corresponding fundamental units. The following conventional notations of dimensions are generally used in dimensional analysis [1]. The dimensions of mass, length, and time are denoted by M, L, and T, respectively, i.e., the system of units (kg, m, s) corresponds to the set of fundamental dimensions (M, L, T). The dimension of an arbitrary quantity is written as $[\cdot]$, for instance, [velocity] = [length]/[time] = L/T. Fundamental dimensions are certainly independent of each other because the corresponding fundamental units are independent.

As mentioned before, any physical quantity is measured by comparison with the corresponding standard. This rule is a simple proportional quantification rule. For example, 20 m corresponds to 20 times longer than a specific standard unit of 1 m. Because of this simple linearity and the arbitrariness of the selection of the system of units, the dimension of any physical quantity can be expressed by the product of power-law monomials of fundamental dimensions [2]. Nonlinear expressions such as cosine and exponential do not appear in the dimensions of any physical quantity. Thus, the dimensional analysis can be discussed using linear equations of powers of the fundamental dimensions, as explained later in Sect. 2.5.

In general, it makes no sense to add different dimensional quantities, e.g., the length of an object plus its mass is quite a meaningless computation. We can add, subtract, compare or equate quantities of the same dimension; this requirement is called dimensional homogeneity.

2.2 Force, Stress, and Strain

For the study of soft matter mechanics, definitions of force, stress, strain, and strain rate are first necessary. Force can be defined by the motion of a mass point or a rigid body as

$$F = ma, (2.1)$$

where F, m, and a are the force, mass and acceleration, respectively. This equation, Newton's equation of motion, is probably the most famous physical equation.

The bold symbols indicate vector quantities. While the mass is inherently a scalar quantity, the force and acceleration are vector quantities. If the motion is purely one-dimensional, the scalar version of Eq. (2.1) is sufficient to describe the relation among the force, mass, and acceleration. However, real space is not onedimensional; it is three-dimensional. Thus, a vector notation is required to express the direction of the force and acceleration. In three-dimensional space, a vector comprising three independent components is necessary to describe a directional quantity such as force: $\mathbf{F} = (F_i, F_j, F_k)$ and $|\mathbf{F}| = \sqrt{F_i^2 + F_j^2 + F_k^2}$, where i, j, k are three independent directions of the space. By considering a symmetric, isotropic, or low-dimensional motion, it is sometimes possible to simplify the physical relation such that the relation consists only of the scalar quantities. While we will provide an overview of the general vector and tensor notations in this chapter, we will mainly focus on such simpler cases from the next chapter. Such a simplification is advantageous for an intuitive understanding of the dimensional analysis. From Eq. (2.1), the dimension of force is computed as [force] = [mass] \cdot [acceleration] = ML/T^2 .

It should be noted that the force can cause deformation or flow as well as the motion described by Eq. (2.1). Therefore, the forces should be classified in terms of their roles. There are certain types of forces. The first one is called *body force* and acts on the mass through Newton's equation (Eq. (2.1)) as (body force) = (mass) × (acceleration). The second one is the *surface force* acting on the surface, (surface force) = (stress) × (surface area). That is, stress is defined by (force)/(surface area) at the limit of the infinitesimal surface area. Body force determines the motion of the centroid, and surface force can also induce deformation and flow. Because the stress is defined by force divided by area, its dimension is [stress] = [force]/[area] = M/LT^2 .

The difference among the scalar, vector, and tensor should be recognized with regard to force, stress, and strain. Body force can be written in a vector expression. In fact, the directions of force and acceleration completely agree in Eq. (2.1). In contrast, the surface force acts on a surface. Their directions are independent which implies that there are two independent directions: normal to the surface and the direction of the applied force. Consequently, stress and deformation must be second rank tensors for their full descriptions. Furthermore, the direction of the resultant deformation or flow does not necessarily coincide with the stress direction. Thus, higher rank tensors are actually required for the complete calculation of continuum mechanics. However, here we introduce only some elementary expressions of stress and strain tensors.

An example of the stress tensor notation in a small volume unit cell, $dx_i dx_j dx_k$, is schematically shown in Fig. 2.1. On each surface of the unit cell, the directions of stress tensors in equilibrium are indicated by arrows. The stress tensor σ_{ij} has $9 = 3 \times 3$ components in three-dimensional space (x_i, x_j, x_k) . Because the stress field is nonuniform in general, σ_{ij} is a function of position. When the size of the unit cell is sufficiently small, we can assume a linear approximation,

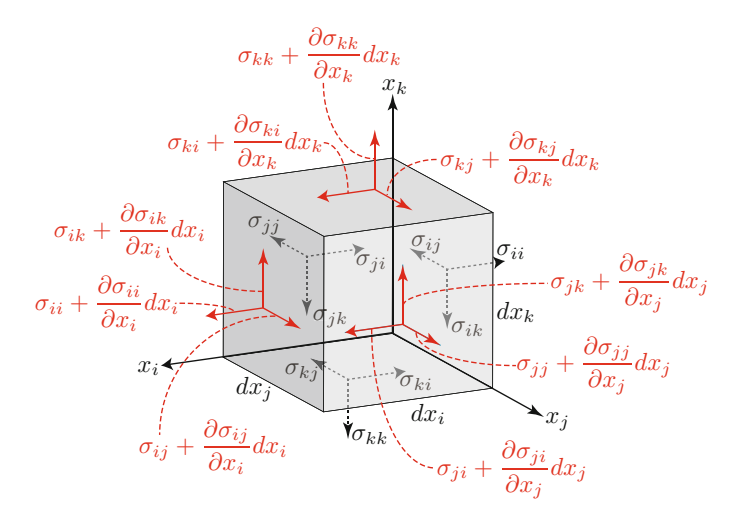


Fig. 2.1 Stress tensor in Cartesian coordinate system (x_i, x_j, x_k) . A stress component σ_{ij} represents the stress value acting on the surface whose normal direction is x_i and its loading direction is x_j . The coordinate system on each surface denotes the direction of stress components in equilibrium with a linear approximation of Eq. (2.2)

$$\sigma_{ij}(x_i + dx_i) = \sigma_{ij}(x_i) + \frac{\partial \sigma_{ij}}{\partial x_i} dx_i. \tag{2.2}$$

Next, we consider the equilibrium condition in this unit cell. Equilibrium demands that the total forces vanish in the unit cell. Let us consider the force balance in the x_i direction. Then, the total force balance in the x_i direction including both the body and surface forces is written as

$$\left(\sigma_{ii} + \frac{\partial \sigma_{ii}}{\partial x_{i}} dx_{i}\right) dx_{j} dx_{k} - \sigma_{ii} dx_{j} dx_{k} + \left(\sigma_{ji} + \frac{\partial \sigma_{ji}}{\partial x_{j}} dx_{j}\right) dx_{k} dx_{i} - \sigma_{ji} dx_{k} dx_{i}
+ \left(\sigma_{ki} + \frac{\partial \sigma_{ki}}{\partial x_{k}} dx_{k}\right) dx_{i} dx_{j} - \sigma_{ki} dx_{i} dx_{j} + \rho a_{i} dx_{i} dx_{j} dx_{k} = 0.$$
(2.3)

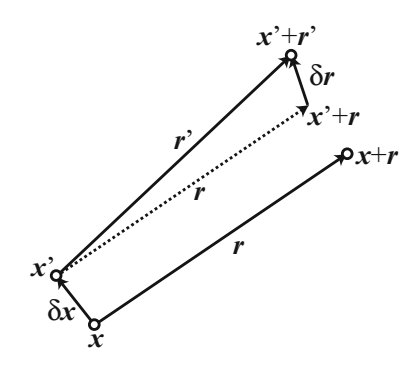
Here, ρ and a_i are the density and acceleration due to the body force in the x_i direction, respectively. Dividing Eq. (2.3) by $dx_i dx_i dx_k$, we obtain

$$\sum_{j} \frac{\partial \sigma_{ji}}{\partial x_j} + \rho a_i = 0. \tag{2.4}$$

This is a general equilibrium condition of the unit cell in the x_i direction. A similar calculation of the torque balance leads to a simple relation,

$$\sigma_{ij} = \sigma_{ji}. \tag{2.5}$$

Fig. 2.2 Schematic image of deformation $\delta r = r' - r$. Two points x and x' are supposed to be in a continuum. These points are moved to x + r and x' + r' because of the deformation δr and bulk motion r



This relation indicates that σ_{ij} is a symmetric tensor. Therefore, the number of truly independent components in the torque-balanced stress tensor is actually six because of this symmetry. Symmetric tensors can be diagonalized by the appropriate rotation of the coordinate system. The eigenvectors and eigenvalues of the stress tensor correspond to the principal axes and extreme values of the stresses, respectively.

The strain (and strain rate) must be defined by a tensor to describe deformation (and flow) in three-dimensional space. To quantify the deformation, let us consider two points in a continuum, x and x'. These two points are supposed to be close and related by a small distance vector, $\delta x = x' - x$. When the point x moves to x + r for some reason, the point x' should also be moved. If the continuum is a rotationless rigid body, x' has to be moved to the position x' + r. Otherwise, a finite deformation vector δr must be added to x' + r because of the deformation. A schematic image of this deformation is presented in Fig. 2.2. Assuming δx and δr are sufficiently small, these parameters are related by neglecting the higher order terms as

$$\delta r_i = \sum_i \frac{\partial r_i}{\partial x_j} \delta x_j. \tag{2.6}$$

Defining the deformation gradient (strain) tensor D by $\delta r = D\delta x$, the tensor component D_{ij} can be written as $D_{ij} = \partial r_i/\partial x_j$. The on-diagonal components D_{ii} , D_{jj} , and D_{kk} relate to the elongation or contraction in each direction. Furthermore, the off-diagonal component D_{ij} can be decomposed into a symmetric part γ_{ij} and an antisymmetric part h_{ij} as

$$D_{ij} = \gamma_{ij} + h_{ij}, \tag{2.7}$$

$$\gamma_{ij} = \frac{1}{2} \left(D_{ij} + D_{ji} \right) = \frac{1}{2} \left(\frac{\partial r_i}{\partial x_j} + \frac{\partial r_j}{\partial x_i} \right), \tag{2.8}$$

$$h_{ij} = \frac{1}{2} \left(D_{ij} - D_{ji} \right) = \frac{1}{2} \left(\frac{\partial r_i}{\partial x_j} - \frac{\partial r_j}{\partial x_i} \right). \tag{2.9}$$

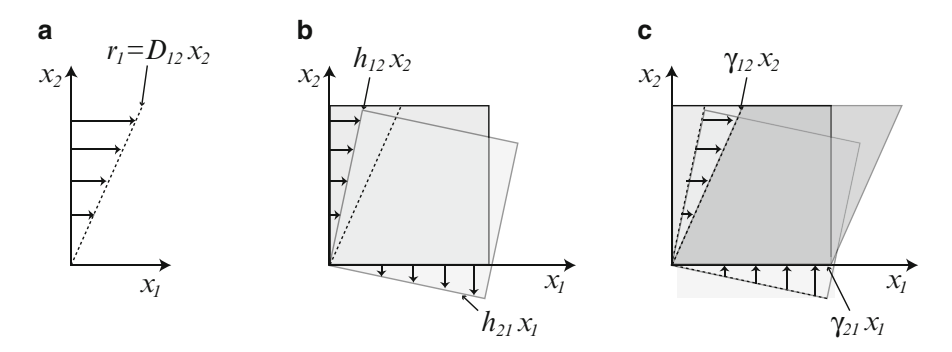


Fig. 2.3 Decomposition of a simple shear into antisymmetric and symmetric deformations in twodimensional case. (a) Simple shear deformation $r_1 = D_{12}x_2$ is written by $r_1 = (h_{12} + \gamma_{12})x_2$ with $h_{12} = -h_{21} = \gamma_{12} = \gamma_{21} = D_{12}/2$, i.e., $D_{21} = 0$ in this simple shear. Considering an incompressible case $D_{11} + D_{22} = \text{const.}$, (b) a square box is rotated by the antisymmetric component, and (c) the box is sheared by the symmetric component. Finally, a parallelogram whose area is the same as the initial square is formed as a result of the simple shear

This decomposition has a physical meaning. These components satisfy the relations, $\gamma_{ij} = \gamma_{ji}$ and $h_{ij} = -h_{ji}$. Actually, the antisymmetric part h_{ij} relates to rotational motion, and the symmetric part γ_{ii} relates to shear deformation; thus, γ_{ii} is defined as shear strain. A schematic illustration of the relation among simple shear, antisymmetric deformation, and symmetric deformation in the two-dimensional case is shown in Fig. 2.3. Because h_{ij} is antisymmetric ($h_{ij} = -h_{ji}$), it corresponds to the rotational motion without any net deformation, as observed in Fig. 2.3b. The initial square is rotated by h_{ii} . In contrast, the symmetric component $\gamma_{ii} = \gamma_{ii}$ represents the shearing deformation, as shown in Fig. 2.3c. Namely, we can trace a deformation from a square to a parallelogram by the sum of a rotation due to the antisymmetric deformation (Fig. 2.3b) and a shearing due to the symmetric deformation (Fig. 2.3c). The simple shear (Fig. 2.3a) can be decomposed into these two components under the constant volume ($\sum_i D_{ii} = \text{const.}$) constraint. To discuss the general deformation, the shear strain γ_{ij} is usually more important than the rotational strain h_{ii} because the shear deformation relates to a net deformation. From Eq. (2.8), strain is evidently dimensionless; [strain] = [length]/[length] = 1.

For the strain rate, a similar calculation can be applied to the velocity u instead of the deformation r. Then, the shear strain rate tensor $\dot{\gamma}_{ij}$ is written as

$$\dot{\gamma}_{ij} = \frac{1}{2} \left(\frac{\partial u_i}{\partial x_j} + \frac{\partial u_j}{\partial x_i} \right). \tag{2.10}$$

Therefore, the dimension of the shear strain rate is the inverse of time, [strain rate] = $[velocity]/[length] = T^{-1}$.

Strain and strain rate are related to stress by constitutive laws. For instance, a general form of linear constitutive relation between stress and strain is written as

$$\sigma_{ij} = \sum_{k} \sum_{l} c_{ijkl} \gamma_{kl}, \qquad (2.11)$$

where c_{ijkl} is a fourth rank elastic constant tensor with $81 = 3^4$ components in principle. However, the number of independent components in an isotropically elastic material in equilibrium can be reduced because of symmetry and isotropy. Concretely, there are two truly independent directions even in an isotropic medium: normal and tangential. Thus, the elastic constant tensor for an isotropic medium can be written as

$$c_{ijkl} = \lambda_L \delta_{ij} \delta_{kl} + \mu_L \left(\delta_{ik} \delta_{jl} + \delta_{il} \delta_{jk} \right), \tag{2.12}$$

where λ_L and μ_L are Lame's elastic constants. δ_{ij} is Kronecker's delta; δ_{ij} is 1 if i = j, otherwise 0. Substituting Eq. (2.12) into Eq. (2.11), a constitutive relation,

$$\sigma_{ij} = \lambda_L \sum_{k} \gamma_{kk} \delta_{ij} + 2\mu_L \gamma_{ij}, \qquad (2.13)$$

is obtained. This relation is a general description of the linear elastic constitutive law for isotropic media in equilibrium. This constitutive relation is called Hooke's law.

A similar constitutive law enables us to model the viscosity. For viscous fluid flow, the stress and strain rate tensors should be related as

$$\sigma_{ij} = -p\delta_{ij} + \sum_{k} \sum_{l} g_{ijkl} \dot{\gamma}_{kl}, \qquad (2.14)$$

where the pressure p is necessary to represent the hydrostatic stress balance. For isotropic viscous fluids, g_{ijkl} can be written by two constants ζ and η ,

$$g_{ijkl} = \zeta \delta_{ij} \delta_{kl} + \eta \left(\delta_{ik} \delta_{jl} + \delta_{il} \delta_{jk} \right). \tag{2.15}$$

Then, Eq. (2.14) can be rewritten as

$$\sigma_{ij} = \left(-p + \zeta \sum_{k} \dot{\gamma}_{kk}\right) \delta_{ij} + 2\eta \dot{\gamma}_{ij}. \tag{2.16}$$

The trace of the tensor σ_{ij} becomes $\sum_i \sigma_{ii} = 3(-p + \xi \sum_k \dot{\gamma}_{kk})$, where $\xi = \zeta + 2\eta/3$. Usually, $\zeta = -2\eta/3$ is assumed. Namely, ζ is defined such that all the normal stress components are effectively involved in p. Equation (2.16) is a general form of the isotropic viscous constitutive law in equilibrium.

In this section, we have overviewed the basics of stress, strain, strain rate, and their tensor notations. The aim of this book is not a mathematically complete description of continuum mechanics. The definitions of stress, strain, and strain rate

explained thus far are sufficient (maybe too much) to read the following content. Thus, we will not discuss further details of tensor algebra. See, e.g., Refs. [3–5] for more details. In the next section, we will simplify the notations and use scalar forms by considering isotropic cases and simple setups. Such simplified situations are helpful in understanding dimensional analysis and scaling. Specifically, we use a simple scalar strain defined by the deformation length scale δr normalized to the original representative length scale l, $\gamma = \delta r/l$. Additionally, the strain rate is simply defined as $\dot{\gamma} = d\gamma/dt = (d\delta r/dt)/l$, where t denotes time. In the remainder of this book, dimensional analysis or order estimate will be mainly discussed on the basis of various experimental observations of soft matter impacts. Therefore, simple constitutive laws expressed by scalar quantities are usually discussed which indicates that we mainly focus on isotropic materials and simple geometry with the appropriate coordinate system. Most of the soft matter that we consider in this book is isotropic. The isotropic approximation is applicable to random structures such as grain networks in granular matter. Therefore, bulk granular matter can be regarded as a type of isotropic media. For anisotropic media such as crystalline solid and liquid crystals, the tensor expression is intrinsically important.

2.3 Simple Definitions of Viscosity and Elasticity

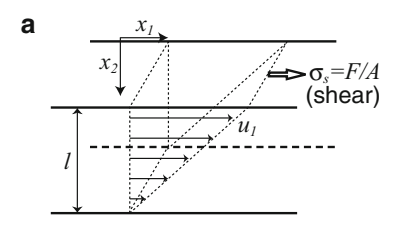
As introduced in the previous section, the most fundamental constitutive laws for the flow and deformation of isotropic continuous media are linear viscosity and elasticity. Here we simplify these laws using an intuitive approach to consider the scalar-based constitutive laws. In this section, the viscous law is first redefined. Then, some of the simplified elastic constitutive laws are introduced. The intuitive approach is helpful to understand the physical essence and define the measurable quantities.

Viscosity Shear viscosity¹ η is defined by the relation between shear stress and shear strain rate. Let us consider a simple shear (Figs. 2.3 and 2.4a) to simplify the relation such that it is written by scalar quantities. As shown in Fig. 2.4a, shear stress σ_s is defined by a stress applied to a plane: the shear force F along the x_1 direction divided by a planar area A. Because of this shear stress, flow with a velocity profile $u_1(x_2)$ is induced, where the direction of the x_2 axis is perpendicular to the shear direction x_1 . By defining the shear strain rate by $\dot{\gamma} = du_1/dx_2$, the simplified viscous constitutive law is written as

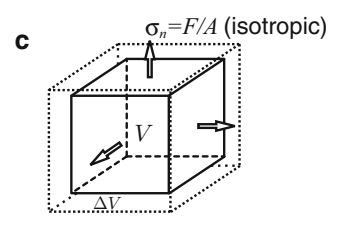
$$\sigma_s = \eta \dot{\gamma}. \tag{2.17}$$

¹The word *viscosity* indicates dynamic viscosity. Kinematic viscosity is defined by η/ρ . η defined in Eq. (2.17) is essentially the same as that introduced in Eq. (2.16).

Fig. 2.4 Schematic illustration of shear, tensile. and isotropic constitutive laws. Plane (simple) shear, longitudinal tensile, and isotropic geometries are shown in (a), (b), and (c), respectively. Newtonian fluids hold $\sigma_s = \eta(du_1/dx_2) =$ $\eta u_1/l = \eta \dot{\gamma}$. Elastic solids satisfy a simple linear relation, $\sigma_e = E\Delta l/l$. The volume strain $(\Delta V/V)$ and isotropic normal stress (pressure) are related by the bulk modulus as $\sigma_n = K(\Delta V/V) = -\Delta p$







Here we neglect the normal stress to focus on the shear effect. The stress tensor notation including on-diagonal components (pressure) corresponds to Eq. (2.16) and will be rewritten in Eq. (2.29). Note that the definition of the simple shear strain rate $\dot{\gamma}$ is slightly different from the shear strain rate tensor $\dot{\gamma}_{ii}$ (simple shear vs. pure shear). By the definition of $\dot{\gamma}_{ii} = (1/2)(\partial u_1/\partial x_2 + \partial u_2/\partial x_1)$, the corresponding constitutive law can be written as $\sigma_{ii} = 2\eta \dot{\gamma}_{ii}$. In either case, both definitions result in an identical η value. It is often assumed that η is independent of the flow state. This assumption is reasonable for most gases and liquids in the low Reynolds number regime (see Sect. 2.5.1 for the definition of the Reynolds number). Such constant- η fluids are called Newtonian fluids. In Newtonian fluids, the velocity profiles $u_1(x_2)$ must be linear as shown in Fig. 2.4a, and its slope corresponds to the viscosity. This linear shear viscosity is one of the simplest constitutive laws in continuum mechanics. In the sense of linear relation, both gas and liquid can be Newtonian fluids; however, the temperature dependence of η is quite different between a gas and a liquid. This discrepancy originates from the different microscopic origins of viscosity. Then, one might think that the viscosities of gas and liquid have to be discussed separately. However, microscopic details should be neglected in the spirit of a constitutive law. Regardless of its origin, a viscous fluid satisfying Eq. (2.17) is called a Newtonian fluid. In general, constitutive laws are macroscopic and empirical relations.

The inviscid and incompressible fluid is called a perfect fluid. In the perfect fluid, shear stress does not exist even in the flowing state.

Elasticity For elastic solids, stress balances with the strain rather than the strain rate because elastic solids cannot flow. That is, the stress is supported by the elastic deformation, i.e., strain. The corresponding constitutive law is written as

$$\sigma_{\rm s} = G\gamma, \tag{2.18}$$

where G is the elastic shear modulus (or stiffness). For the complete description of the general relation between stress and strain, the relation must be expressed in tensors as mentioned in the previous section. However, here, we consider its scalar version for brevity's sake. In the definition of shear viscosity, we have considered a simple shear as shown in Fig. 2.4a. By considering the relation between the shear stress σ_s and the shear strain γ instead of the shear strain rate $\dot{\gamma}$, Eq. (2.18) is simply obtained. The shear modulus G is identical to Lame's elastic constant μ_L (Eq. (2.13)).

There are some other elastic moduli. The value of the elastic modulus depends on the loading and deformation conditions. When the longitudinal stress σ_e is applied to the specimen, the Young's modulus E characterizes the elasticity as

$$\sigma_e = E \frac{\Delta l}{l},\tag{2.19}$$

where the longitudinal strain $\Delta l/l$ is the ratio between the longitudinal deformation length Δl and the original length l (Fig. 2.4b). This linear relation of longitudinal stress and strain (Eq. (2.19)) originates from Hooke's law.

As observed in Fig. 2.4b, contraction (or elongation) to the orthogonal direction $\Delta D/D$ should be considered in addition to longitudinal strain for an accurate estimate. Here D and ΔD are the original transverse length scale and its small deformation associated with the longitudinal deformation Δl . In this case, Poisson's ratio v_p is defined as

$$v_p = -\frac{\Delta D/D}{\Delta l/l}. (2.20)$$

Note that Δl and ΔD usually take an opposite sign to make ν_p positive, which implies that the elongation in the longitudinal direction usually results in contraction in the orthogonal direction and vice versa. If the volume is conserved, $D^2 l = (D-\Delta D)^2(l+\Delta l)$ is held. Then, neglecting higher order terms of small deformation, $\nu_p = 1/2$ is obtained. For most solid materials, $\nu_p \simeq 0.3$. For isotropic materials, E and ν_p can be written by λ_L and μ_L . Using tensor notation, Eqs. (2.19) and (2.20) can be written as $\sigma_e = p = E\gamma_{11}$ and $\nu_p = -\gamma_{22}/\gamma_{11}$. Using the constitutive law (Eq. (2.13)), the loading condition is expressed by $p = \lambda_L(\gamma_{11} + \gamma_{22} + \gamma_{33}) + 2\mu_L\gamma_{11}$ and $0 = \lambda_L(\gamma_{11} + \gamma_{22} + \gamma_{33}) + 2\mu_L\gamma_{22} = \lambda_L(\gamma_{11} + \gamma_{22} + \gamma_{33}) + 2\mu_L\gamma_{33}$. Then, we obtain the relations $E = \mu_L(3\lambda_L + 2\mu_L)/(\lambda_L + \mu_L)$ and $\nu_p = \lambda_L/2(\lambda_L + \mu_L)$.

When the stress σ_n is applied normally to all the surfaces of an isotropic medium, a volume change is induced. The bulk modulus K is the ratio between the normal

2.4 Conservation Laws 23

stress and the volume strain, which is defined by the volume change ΔV divided by the initial volume V (Fig. 2.4c):

$$\sigma_n = K \frac{\Delta V}{V} = -\Delta p. \tag{2.21}$$

In isotropic materials, the bulk modulus K can be related to λ_L and μ_L again. Using the relations $\Delta V/V = \gamma_{11} + \gamma_{22} + \gamma_{33}$ and $-\Delta p = \lambda_L(\Delta V/V) + 2\mu_L\gamma_{ii}$ (i = 1, 2, 3), K can be rewritten as $K = (3\lambda_L + 2\mu_L)/3$.

It is well known that a rubber band behaves like a spring; it exhibits stiffness and a restoring force. Rubber band elasticity can be described by Hooke's law, at least in the small strain regime. However, the specific origins of Hooke's law are completely different among elastic solids and rubber bands. In the former, the enthalpy-based force of a crystalline solid results in the restoring force, while the entropy-based force is the main origin of the restoring force in the latter. This difference can be confirmed by the temperature dependence of the elastic modulus. This different temperature dependence is similar to the different temperature dependence of η between a gas and a liquid. Hooke's law is valid for both an elastic solid and a rubber band as a useful mechanical constitutive law. If we are also interested in thermodynamic properties, they have to be distinguished.

Note that Eqs. (2.17), (2.18), (2.19), and (2.21) are linear. These equations are valid only in a small $\dot{\gamma}$ or γ regime. In a large $\dot{\gamma}$ or γ regime, the constitutive laws become nonlinear. Some of the nonlinear constitutive laws will be introduced in Chap. 3. Currently, the linear constitutive laws are sufficient to discuss the scaling and dimensional analysis in the following sections of this chapter.

2.4 Conservation Laws

Conservation laws are important relations in conservative systems. Usual continua such as elastic solids or viscous fluids obey each corresponding governing equation that satisfies the conservation laws. Here three conservation laws of fluids—mass conservation, linear momentum conservation, and energy conservation—are introduced. The famous Navier-Stokes equation is derived using the linear momentum conservation law. In the next section, the Navier-Stokes equation will be used to learn dimensional analysis. From the energy conservation, Bernoulli's principle, which relates the drag force to the lift force acting onto an object moving in a fluid, is obtained.

2.4.1 Mass Conservation

The first conservation law explained is mass conservation. Let us consider a macroscopic fluid unit called a *fluid particle* that has density ρ and moving velocity u. Then, the mass conservation law is written as

$$\frac{d}{dt} \int_{V} \rho dV + \int_{S} \rho \boldsymbol{u} \cdot \boldsymbol{n} dS = 0, \qquad (2.22)$$

where $\int_V dV$ and $\int_S dS$, denote volume and surface integrations, respectively, and the surface S encloses a volume V. \boldsymbol{n} is the unit normal vector of the surface S. The first term represents the density variation with time t, and the second term corresponds to the net inflow (or outflow) to the volume V through its surface S. The surface integral can be transformed to the volume integral by Gauss' theorem, $\int_V \nabla \cdot \psi dV = \int_S \psi \cdot \boldsymbol{n} dS$, where ψ can be a tensor, vector, or scalar of any dimension. Additionally, the currently considered volume V is arbitrary as long as it is macroscopic. Therefore, $\int_V f(\boldsymbol{u}) dV = 0$ is equivalent to $f(\boldsymbol{u}) = 0$. Then, the derivative notation of the mass conservation is written as

$$\frac{\partial \rho}{\partial t} + \nabla \cdot (\rho \mathbf{u}) = 0, \tag{2.23}$$

or equivalently,

$$\frac{D\rho}{Dt} + \rho \nabla \cdot \boldsymbol{u} = 0, \tag{2.24}$$

where the operator D/Dt is

$$\frac{D}{Dt} = \frac{\partial}{\partial t} + \boldsymbol{u} \cdot \nabla. \tag{2.25}$$

The operator ∇ is a vector differentiation defined by $\nabla = \sum_{i=1}^{3} e_i (\partial/\partial x_i)$ for a three-dimensional Cartesian coordinate system (x_1, x_2, x_3) , where e_i is a unit vector of each orthogonal direction. Equation (2.23) is called the equation of continuity, and its physical meaning will be discussed again in Sect. 3.5 in terms of transport phenomena.

The expression using the operator D/Dt is called the Lagrange derivative or convective derivative. The first term on the right-hand side of Eq. (2.25), $\partial/\partial t$, corresponds to the fixed point observation that is called the Eulerian derivative. The second term represents the advective contribution by the flow of velocity u.

For an incompressible fluid ($\rho = \text{const. i.e.}$, $D\rho/Dt = 0$), the mass conservation is simply written as

$$\nabla \cdot \boldsymbol{u} = 0. \tag{2.26}$$

2.4.2 Linear Momentum Conservation and Navier-Stokes Equation

The Navier-Stokes equation, which is the most basic fluid governing equation, can be derived using linear momentum conservation and the constitutive law. The linear momentum conservation for a viscous fluid is 2.4 Conservation Laws 25

$$\frac{d}{dt} \int_{V} \rho u dV = \int_{S} \sigma n dS + \int_{V} \rho a dV, \qquad (2.27)$$

where σ and \boldsymbol{a} are respectively the stress tensor applied to the surface S and the acceleration due to the body force exerted on a fluid particle of volume V that is bounded by the surface S. The left-hand side of Eq. (2.27) represents the temporal variation in the linear momentum. The first term on the right-hand side is the momentum change by the surface force (stress) and the second term originates from the body force contribution. If any stress is not applied to the surface, Eq. (2.27) is equivalent to Eq. (2.1), in which only the body force is considered. Using Gauss' theorem again, Eq. (2.27) is rewritten as

$$\rho \frac{D\mathbf{u}}{Dt} = \nabla \sigma + \rho \mathbf{a}. \tag{2.28}$$

This is a simple form of linear momentum conservation in a viscous fluid particle. For an incompressible ($\rho = \text{const.}$) Newtonian fluid ($\eta = \text{const.}$), the stress tensor σ_{ii} is written as

$$\sigma_{ij} = -p\delta_{ij} + \eta \left(\frac{\partial u_i}{\partial x_i} + \frac{\partial u_j}{\partial x_i} \right). \tag{2.29}$$

This is the Cartesian notation of the constitutive law of an incompressible Newtonian fluid (simplified from Eq. (2.16)). Substituting Eq. (2.29) into Eq. (2.28) and using a little tensor algebra, the Navier-Stokes equation for incompressible Newtonian fluid is determined to be

$$\rho \frac{D\mathbf{u}}{Dt} = -\nabla p + \eta \nabla^2 \mathbf{u} + \rho \mathbf{a}. \tag{2.30}$$

Here Eq. (2.26) is used to simplify the viscosity-dependent term. For more details concerning the derivation of Eq. (2.30), see, e.g., Refs. [3–5]. For inviscid fluid flow, the second term on the right-hand side can be dropped. The equation without the viscous term is called the Euler equation.

2.4.3 Energy Conservation

By similar consideration, energy conservation can be discussed in incompressible viscous fluids. Let $e_{\rm int}$ be the internal energy of the fluid per unit mass that is dimensionally equivalent to stress. Then, the energy conservation law can be written by the first principle of thermodynamics as

$$\rho \frac{D}{Dt} \left(\frac{1}{2} |\mathbf{u}|^2 + e_{\text{int}} \right) = \nabla \cdot (\sigma \mathbf{u}) + \rho \mathbf{a} \cdot \mathbf{u} - \nabla \cdot \mathbf{q}, \tag{2.31}$$

where $|\cdot|$ denotes the norm of the vector and $\nabla \cdot \boldsymbol{q}$ represents the thermal energy transfer rate per unit volume (local heat flux). The left-hand side represents the Lagrange derivative of total (kinetic + internal) energy. On the right-hand side, the first term corresponds to the work performed by the surface force per unit volume, the second term denotes the work performed by the body force per unit volume, and the last term comes from the thermal energy flux.

Note that the fluid viscosity induces dissipation. Forming a scalar product from the linear momentum conservation by multiplying u to Eq. (2.28), one can obtain a relation,

$$\rho \frac{D}{Dt} \left(\frac{1}{2} |\mathbf{u}|^2 \right) = \rho \frac{D\mathbf{u}}{Dt} \cdot \mathbf{u} = (\nabla \sigma) \cdot \mathbf{u} + \rho \mathbf{a} \cdot \mathbf{u}. \tag{2.32}$$

Substituting Eq. (2.32) into Eq. (2.31), the relation

$$\rho \frac{De_{\text{int}}}{Dt} = \nabla \cdot (\sigma u) - (\nabla \sigma) \cdot u - \nabla \cdot q \tag{2.33}$$

is obtained. The tensor component from the first and second terms on the right-hand side is computed as [6]

$$\frac{\partial}{\partial x_i} \left(\sigma_{ij} u_j \right) - \frac{\partial \sigma_{ij}}{\partial x_i} u_j = \sigma_{ij} \frac{\partial u_j}{\partial x_i}. \tag{2.34}$$

Thus, these terms relate to the shear stress and strain rate, i.e., viscosity. From Eqs. (2.33) and (2.34), one can recognize that the shear viscosity is coupled with internal energy and local heat flux. The stress applied to the viscous fluid cannot be completely transformed into the linear momentum of the fluid. Therefore, the viscosity induces the dissipation. Note that, however, the elasticity conserves the energy. Thus, the constitutive laws of viscosity and elasticity are qualitatively different.

Considering the simple situation of inviscid flows, Bernoulli's principle is derived from the conservation laws. Viscosity, associated heat flux, and internal energy are negligible in an inviscid flow; therefore, we should consider Eq. (2.32). Because we neglect the viscosity that relates to the shear stress, the remaining relevant stress is only the pressure. Then, the first term on the right-hand side of Eq. (2.32) can be simplified as the time derivative of pressure; -Dp/Dt. Here, note that the dimension of $(\nabla \sigma) \cdot \boldsymbol{u}$ is equivalent to the temporal derivation of stress. For the second (body force) term, the simplest form of energy per unit volume is hydrostatic pressure $\sim -\rho gz$, where z is the height difference along the direction of gravity. Thus, the body force term can be written as $-D(\rho gz)/Dt(=-\rho g(Dz/Dt))$. According to the conservation law, the sum of kinetic energy per unit volume, pressure, and hydrostatic pressure is independent of time, $(D/Dt)(\rho u^2/2 + p + \rho gz) = 0$. Finally, a simple expression of the conservation law along the stream line (by Lagrangian viewpoint) is obtained as

$$\frac{1}{2}\rho u^2 + p + \rho gz = \text{const.} \tag{2.35}$$

This relation is called Bernoulli's principle. When the dynamic pressure (also known as ram pressure) $\rho u^2/2$ increases, the static pressure p decreases. Then, the lift force can be induced using Eq. (2.35) if u is not uniform (i.e., asymmetric) around an object.

There are some other conservation laws, including that for angular momentum. These laws are also essential ingredients in continuum mechanics. However, we are not going to describe further details of the conservation laws. Instead, we proceed to the next topic: dimensional analysis, which is the central concept throughout this book.

2.5 Dimensional Analysis

In this section, the dimensional analysis method is introduced in detail. Dimensional analysis is the central methodology in this book. There are two systematic approaches to obtain the relevant dimensionless numbers. One approach is based on the nondimensionalization of the governing equation, and the other approach is the Π -groups method. The former is better if we know the specific form of the governing equation, whereas the latter is more general and systematic. However, some arbitrariness remains in the analysis. The advantage of the latter method is generality; this approach is applicable even if the governing equation of the system is completely unknown. An intuitive way to discuss the scaling relation is also introduced in this section as a possible third approach in dimensional analysis. This method is powerful if the appropriate balance law is considered to derive meaningful scaling, and its essence is similar to that of dimensional analysis.

2.5.1 Nondimensionalization of the Governing Equation

If we know the governing equation of the system, we can directly perform the dimensional analysis. Let us begin with the Navier-Stokes equation derived in the previous section. Here we consider an incompressible fluid without body forces $(\rho a = 0)$. Then, from Eqs. (2.30) and (2.25), the governing equation is written as

$$\rho \left[\frac{\partial \mathbf{u}}{\partial t} + (\mathbf{u} \cdot \nabla) \mathbf{u} \right] = -\nabla p + \eta \nabla^2 \mathbf{u}. \tag{2.36}$$

All the quantities and operators in Eq. (2.36) have their own units. For instance, velocity has a unit of (length)/(time), namely, m/s in the SI unit system. A unit such as m/s is an artificial rule to measure a physical quantity. As discussed in Sect. 2.1, the governing physical law must be free from such an artificial rule. Of course,

Eq. (2.36) must also be dimensionally homogeneous. Therefore, Eq. (2.36) can be nondimensionalized using dimensionless quantities

$$x_i^* = \frac{x_i}{l}, \quad t^* = \frac{t}{t_o}, \quad u^* = \frac{u}{U}, \quad \text{and} \quad p^* = \frac{p}{\rho U^2},$$
 (2.37)

where l, t_o , and U are representative values of length, time, and norm of velocity (speed), respectively. Using these dimensionless quantities, Eq. (2.36) is rewritten as

$$\rho \left[\frac{\partial U \boldsymbol{u}^*}{\partial t_o t^*} + \left(U \boldsymbol{u}^* \cdot \frac{\nabla^*}{l} \right) U \boldsymbol{u}^* \right] = -\frac{\nabla^*}{l} \rho U^2 p^* + \eta \frac{\nabla^{*2}}{l^2} U \boldsymbol{u}^*, \tag{2.38}$$

where $\nabla^* = l\nabla$ is a dimensionless operator corresponding to ∇ . Multiplying a factor $l/\rho U^2$ by Eq. (2.38), the dimensionless form of Eq. (2.36) can be obtained as

$$\left[\frac{l}{Ut_o}\right]\frac{\partial \boldsymbol{u}^*}{\partial t^*} + (\boldsymbol{u}^* \cdot \nabla^*)\boldsymbol{u}^* = -\nabla^* p^* + \left[\frac{\eta}{\rho Ul}\right]\nabla^{*2}\boldsymbol{u}^*. \tag{2.39}$$

In Eq. (2.39), we can find two important parameters

$$S_t = \frac{l}{Ut_o},\tag{2.40}$$

$$R_e = \frac{\rho Ul}{\eta}.\tag{2.41}$$

 S_t and R_e are called the Strouhal number and the Reynolds number, respectively. Clearly, these quantities are dimensionless because of the dimensional homogeneity: $[S_t] = [R_e] = 1$. Because these values are dimensionless, they are independent of unit systems such as SI and cgs. This indicates that inherent parameters for the behavior of incompressible viscous fluid are S_t and R_e . In other words, the dynamical behaviors of two systems obeying Eq. (2.39) with the same S_t and R_e are completely similar, even if the representative length or time scales are quite different between these two systems. This similarity law enables us to perform contracted model experiments. The concept of this similarity law will be discussed later in Sect. 2.8.

As long as the equation is sound—a physically meaningful equation must be dimensionally homogeneous as discussed in Sect. 2.1—it can be nondimensionalized using an appropriate normalization. As demonstrated above for the Navier-Stokes equation example, one can obtain the dimensionless form of the governing equation by the proper normalization. Only identification of representative quantities is required for the normalizations. Using the dimensionless equation, the relevant dimensionless numbers are directly deducible. However, for most soft matter, governing equations have not yet been established. For such complex physical systems, how can we approach the essential physics? Dimensional analysis using the Π -groups method provides a systematic way to approach the physical system without a well-defined governing equation.

2.5.2 Π-Groups

In this subsection, we consider a situation in which the governing equation is unknown. Even in such a circumstance, there is a systematic approach called the Π -groups method that allows us to derive relevant dimensionless numbers. To consider the general case, let us assume the presence of a certain function f of n relevant quantities Q_1, Q_2, \ldots, Q_n . The function f satisfies

$$f(Q_1, Q_2, \dots, Q_n) = 0.$$
 (2.42)

In this stage, these quantities are not necessarily independent of each other, which suggests that Eq. (2.42) can be simplified. In other words, the number of truly relevant and independent quantities can be smaller than n. The Π -groups method allows us to determine the number of independent dimensionless numbers. The function f corresponds to the governing equation of the system under consideration. Although knowing the specific form of the equation is not necessary, it has to be dimensionally homogeneous. As demonstrated by the example of the Navier-Stokes equation, a dimensionally homogeneous equation can be rewritten in a fully dimensionless form. Because all the dimensions must be expressed by power-law monomials of fundamental dimensions, a relevant dimensionless number can be produced using a set of exponents (a_1, a_2, \ldots, a_n) such as

$$\left[Q_1^{a_1}Q_2^{a_2}\cdots Q_n^{a_n}\right] = 1. (2.43)$$

In general, there are plural sets of the exponents $(a_1, a_2, ..., a_n)$ that satisfy Eq. (2.43). Let m be the number of independent dimensionless numbers, and Π_i be the i-th dimensionless number. Then, Π_i can be written as

$$\Pi_i = Q_1^{a_{1i}} Q_2^{a_{2i}} \cdots Q_n^{a_{ni}}, \tag{2.44}$$

where the set of exponents $(a_{1i}, a_{2i}, \dots, a_{ni})$ satisfies Eq. (2.43) $(1 \le i \le m)$. Using Π_i , Eq. (2.42) is simply rewritten by a certain function ϕ as

$$\phi(\Pi_1, \Pi_2, \dots, \Pi_i, \dots, \Pi_m) = 0. \tag{2.45}$$

Buckingham has demonstrated that the number m is determined by the number of fundamental dimensions k as m = n - k [7]. This relation is called the Buckingham Π theorem. The number of fundamental dimensions k depends on the considered system. If the system is purely mechanical and free from thermal and electromagnetic phenomena, k is 3, e.g., mass M, length L, and time T. Although we can select other three independent dimensions for the set of fundamental dimensions, the set (M, L, T) is usually employed for dimensional analysis because the dimensions M, L, and T are familiar to us and directly measurable in many experiments. If thermal and electromagnetic effects are involved, temperature and

electric charge should be added to the set of independent quantities. Then, the number of fundamental dimensions k also increases. In any case, Eq. (2.45) is equivalent to the relation

$$\Pi_i = \psi(\Pi_1, \dots, \Pi_{i-1}, \Pi_{i+1}, \dots, \Pi_m),$$
(2.46)

where ψ corresponds to the solution form for Π_i of Eq. (2.45). Using this form, one can construct the scaling relation. Usually, Π_i is selected to include the physical quantity that we would like to know. Since Buckingham proposed the Π theorem [7, 8], this systematic method of dimensional analysis has been used in various fields of science and engineering [2, 9, 10].

Here let us reconsider the incompressible viscous fluid dynamics. Suppose that we only know the relevant quantities of the phenomena without any governing equation, although we actually know the Navier-Stokes equation. A specific problem (e.g., turbulent flow in pipes or a period of pendulum motion) is usually considered as a subject for the dimensional analysis. However, here we think about an abstract situation. Possibly relevant quantities of incompressible viscous fluid motion are the density ρ , representative speed U, length scale l, timescale t_o , pressure p, and viscosity η ; n=6. The fundamental dimensions are mass M, length L, and time T; k=3. Thus, there are n-k=6-3=3 independent dimensionless numbers in the system. To obtain relevant dimensionless numbers, we should construct a dimension table as shown in Table 2.1. Because the density ρ has a dimension of [mass]/[volume], [ρ] is ML^{-3} . All the other quantities can also be written by the product of some powers of M, L, T: [U] = LT^{-1} , [I] = L, [I_o] = T, [I_o] = [force]/[area] = I_o H I_o T I_o 1. These powers are listed in Table 2.1.

On the other hand, the *i*-th dimensionless number Π_i is generally expressed using Eq. (2.44) as

$$\Pi_i = \rho^{a_{1i}} U^{a_{2i}} l^{a_{3i}} r_o^{a_{4i}} \rho^{a_{5i}} \eta^{a_{6i}}. \tag{2.47}$$

From Eqs. (2.43) and (2.47) and Table 2.1, the powers have to satisfy the following simultaneous equations,

$$a_{1i} + a_{5i} + a_{6i} = 0,$$
 (2.48)

$$-3a_{1i} + a_{2i} + a_{3i} - a_{5i} - a_{6i} = 0, (2.49)$$

$$-a_{2i} + a_{4i} - 2a_{5i} - a_{6i} = 0. (2.50)$$

Table 2.1 Dimension table for the relevant variables for incompressible viscous fluid motion

	[ho]	[U]	[l]	$[t_o]$	[<i>p</i>]	[η]
М	1	0	0	0	1	1
L	-3	1	1	0	-1	-1
Т	0	-1	0	1	-2	-1

Equations (2.48), (2.49), and (2.50) originate from the nondimensionalization of M, L, and T, respectively. Now, we have 6(=n) variables and 3(=k) equations. Thus, we can reduce the number of independent variables to 3(=n-k). This is the simple essence of the Buckingham Π theorem. For instance, these equations are rewritten as

$$a_{1i} = -a_{5i} - a_{6i}, (2.51)$$

$$a_{2i} = a_{4i} - 2a_{5i} - a_{6i}, (2.52)$$

$$a_{3i} = -a_{4i} - a_{6i}. (2.53)$$

Then, we can compute (a_{1i}, a_{2i}, a_{3i}) from (a_{4i}, a_{5i}, a_{6i}) . Defining Π_1 by $(a_{41}, a_{51}, a_{61}) = (1, 0, 0)$, we obtain $(a_{11}, a_{21}, a_{31}) = (0, 1, -1)$, which results in

$$\Pi_1 = \frac{t_o U}{l} = S_t^{-1}. (2.54)$$

Similarly, Π_2 and Π_3 are respectively obtained by $(a_{42}, a_{52}, a_{62}) = (0, 1, 0)$ and $(a_{43}, a_{53}, a_{63}) = (0, 0, 1)$ as,

$$\Pi_2 = \frac{p}{\rho U^2},\tag{2.55}$$

and

$$\Pi_3 = \frac{\eta}{\rho U l} = R_e^{-1}. \tag{2.56}$$

Here we reproduce the dimensionless numbers in Eqs. (2.37) and (2.39) as a Π -group (Π_1 , Π_2 , Π_3). If we are interested in the pressure p, we finally obtain a simple relation using Eq. (2.46):

$$\frac{p}{\rho U^2} = \psi(S_t, R_e). \tag{2.57}$$

The specific form of the governing equation is necessary to obtain the actual functional form of ψ . It is impossible to derive the complete physical relation only by the dimensional analysis. In many cases, the power-law form is used to approximate the relation among dimensionless numbers because the power-law form is scale-invariant. Of course, if we know the governing equation, the specific form can be obtained similar to Eq. (2.39).

Table 2.2 Partially nondimensionalized dimension table transformed from Table 2.1

	$[\rho/\rho]$	[U]	[l]	$[t_o]$	$[p/\rho]$	$[\eta/ ho]$
М	0	0	0	0	0	0
L	0	1	1	0	2	2
Т	0	-1	0	1	-2	-1

Table 2.3 Fully nondimensionalized dimension table transformed from Table 2.2

	[ho/ ho]	[U/U]	[l/l]	$[t_o U/l]$	$[p/\rho U^2]$	$[\eta/\rho Ul]$
М	0	0	0	0	0	0
L	0	0	0	0	0	0
Т	0	0	0	0	0	0

 η/ρ should be normalized to l or l^2 to eliminate the length dimension L. Finally, the temporal dimension T can be eliminated by the normalization using a representative timescale l/U. Then, we obtain Table 2.3. From Table 2.3, one can readily find three fundamental quantities ρ , U, and l, as well as three dimensionless numbers, $\Pi_1 = t_o U/l$, $\Pi_2 = p/\rho U^2$, and $\Pi_3 = \eta/\rho Ul$. This result suggests that the set of dimensions ($[\rho]$, [U], [l]) can be used to construct a set of fundamental dimensions instead of (M, L, T).

In the Π -groups method, arbitrariness persists in the reduction procedure of dimensional variables. We must select an appropriate set of quantities to form relevant dimensionless numbers for each problem of interest. For example, a set of $\Pi_1' = \rho l^2 p/\eta^2$, $\Pi_2' = U \eta/lp$, and $\Pi_3' = t_o p/\eta$ also composes a complete set of dimensionless numbers for the incompressible viscous fluid flow. Both sets, (Π_1, Π_2, Π_3) and (Π_1', Π_2', Π_3') , are equally valid in terms of dimensional analysis. We must judge which set is better by considering the underlying physics for each problem.

In this section, systematic methods of dimensional analysis have been introduced. Further reduction of relevant dimensionless numbers might be possible if some of the numbers are invariant and not independent [11]. This generalization works well when there are many relevant quantities, and some of the quantities are invariant. A more intuitive approach to dimensional analysis and scaling is exemplified by contact mechanics in Sect. 2.5.4. Prior to that, a historically famous example of blast wave analysis is described in the next subsection to demonstrate the efficacy of the dimensional analysis method.

2.5.3 Dimensional Analysis of Blast Wave Front Propagation

A high-energy explosion is somewhat similar to a high-velocity impact because both events leave a crater. Such high energy phenomena are often understood using dimensional analysis. Taylor has estimated the explosive energy essentially using dimensional analysis [12, 13]. Here let us examine its concept to see the significance of the dimensional analysis.

Fig. 2.5 Schematic image of the blast wave front propagation

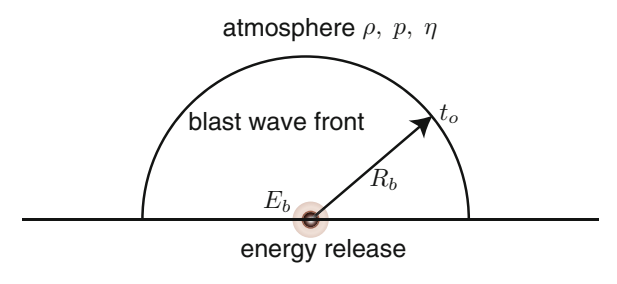


Table 2.4 Dimension table for the blast wave propagation

	$[E_b]$	$[R_b]$	$[t_o]$	[ρ]	[p]	[η]
М	1	0	0	1	1	1
L	2	1	0	-3	-1	-1
Т	-2	0	1	0	-2	-1

In the intermediate stage of explosion, the blast wave front propagates hemispherically to the atmosphere (Fig. 2.5). The relevant physical quantities in this stage are the released energy E_b , the radius of the blast wave front R_b , atmospheric density ρ , its pressure p, its viscosity η , and timescale t_o . The dimension table for this problem is shown in Table 2.4. Using Table 2.4, three possibly relevant dimensionless numbers can be derived because the number of independent dimensionless numbers m is computed as m = n - k = 6 - 3. For instance, the following three dimensionless numbers might be useful,

$$\Pi_1 = \frac{\rho R_b^5}{E_b t_o^2},\tag{2.58}$$

$$\Pi_2 = \frac{pR_b^3}{E_b},$$
(2.59)

$$\Pi_3 = \frac{\eta R_b^3}{E_b t_o}. (2.60)$$

 Π_1 , Π_2 , and Π_3 can be related by the form of Eq. (2.46) as

$$\frac{\rho R_b^5}{E_b t_o^2} = \psi \left(\frac{p R_b^3}{E_b}, \frac{\eta R_b^3}{E_b t_o} \right). \tag{2.61}$$

The relation of Eq. (2.61) is obtained routinely using the Π -groups method. We need additional deeper physical considerations to extract useful insight from the set of (Π_1, Π_2, Π_3) . Π_2 represents the balance between the atmospheric pressure p and the released energy per unit volume E_b/R_b^3 . The pressure released by the explosion must be considerably larger than p; therefore, Π_2 might be less important. Π_3 represents the ratio between the viscous stress η/t_o and the energy density E_b/R_b^3 . However, atmospheric viscosity is most likely too weak to decelerate the blast wave front, which suggests that Π_3 might also be less important. For Π_1 , it denotes the balance

between the kinetic energy of the blast wave front $\rho R_b^3 (R_b/t_o)^2$ and the released energy E_b (or $\rho (R_b/t_o)^2$ vs. E_b/R_b^3). Because the blast wave front actually expands against the atmospheric inertia, this balance is likely the principal factor to estimate the explosion scale. Therefore, one can guess that Π_1 is much more crucial than Π_2 and Π_3 . Using these considerations, it is plausible to assume that Π_2 and Π_3 are irrelevant and negligible. In other words, Π_2 and Π_3 are extremely small constants in the current phenomenon. Hence, $\psi(\Pi_2, \Pi_3)$ can be roughly assumed to be constant on the order of magnitude of unity² in the intermediate stage of the explosion, then Eq. (2.61) is simplified as

$$\frac{\rho R_b^5}{E_b t_o^2} \simeq 1. \tag{2.62}$$

Finally, the scaling between the blast wave front radius R_b and timescale t_o is obtained as

$$R_b \simeq \left(\frac{E_b}{\rho}\right)^{1/5} t_o^{2/5}.\tag{2.63}$$

The validity of this scaling relation was actually confirmed by photographs of real atomic explosion [13]. Moreover, Taylor computed the numerical factor of the scaling relation utilizing the adiabatic index (the ratio of the specific heats). The computed numerical prefactor for Eq. (2.63) was somewhat close to unity, which indicates that the estimate of the released energy by Eq. (2.63) is reasonable. The estimated energy was indeed very accurate. This blast wave analysis is a famous successful example of the method of dimensional analysis.

A rough order estimate is useful for evaluating the principal factors in the physical system. In real explosions observed in Ref. [13], the order of magnitude of each quantity could be roughly estimated as $E_b=10^{14}\,\mathrm{J}$, $R_b=10^2\,\mathrm{m}$, $t_o=10^{-2}\,\mathrm{s}$, $\rho=10^0\,\mathrm{kg/m^3}$, $p=10^5\,\mathrm{Pa}$, and $\eta=10^{-5}\,\mathrm{Pa}\cdot\mathrm{s}$. Using these values, the order of magnitude of each Π_i can be computed as $\Pi_1=1$, $\Pi_2=10^{-3}$, and $\Pi_3=10^{-11}$. These estimates indicate that the kinetic energy of propagating blast wave front dominates the dynamics, and the viscosity effect is minor, being eleven orders of magnitude smaller. The atmospheric pressure effect is considerably stronger than the viscosity effect, although this effect is much less important than the blast wave kinetic energy (inertia). By assuming $U=R_b/t$ and $l=R_b$ in Eq. (2.60), Π_3 becomes the same as R_e^{-1} (Eq. (2.41)). Because $\Pi_3=R_e^{-1}\simeq 10^{-11}$ is very small, the blast wave motion is in the very high $R_e(\simeq 10^{11})$ regime. We can reconfirm that Π_1 is more important than Π_2 and Π_3 from this order estimate. Such order comparisons of dimensionless numbers are sometimes helpful in speculating about

²This assumption is the extremely important to reach the reasonable scaling. If the energy released by explosion is mainly transmitted to the blast wave kinetic energy, these energies should be of the same order of magnitude. Therefore, Π_1 should have an order of magnitude of 10^0 .

the principal physical mechanisms. However, dimensional analysis is not perfect. This approach does not work well if all the relevant parameters are not involved. Even when it works well, in general, numerical factors cannot be determined solely by dimensional analysis.

2.5.4 Scaling of Contact Mechanics

There is another approach to scaling and dimensional analysis. The balance laws of energy, force, momentum, among others, can be used to obtain physically meaningful scaling laws. Because this method is based on the physically relevant balance laws, the scaling relation obtained using this method is intuitively comprehensive in terms of the governing physical mechanism. In this subsection, an example of the scaling relation that is deduced by a simple energy balance is briefly introduced.

Elastic deformation of a contacting spherical grain is discussed as a typical example of the useful application of the scaling concept. The physical essence of this phenomenon can be understood by a simple scaling analysis. For a completely quantitative analysis, an exact calculation that demands a complicated calculation is necessary. Here we discuss the scaling relation of contact mechanics to highlight the efficacy of the intuitive dimensional thought.

Let us consider an elastic sphere contacting a rigid floor with the normal loading force F. Young's modulus of the sphere is denoted as E and its initial radius is written as R. Then, because of the elasticity, small but finite deformation must be observed as schematically illustrated in Fig. 2.6. The elastic deformation δ and the radius of the contact circle a are related as $a \sim (R\delta)^{1/2}$ using Pythagorean theorem and the assumption of $R \gg \delta$. This assumption implies that we focus on the linear elastic regime. Hence, the discussion in this subsection is only valid for the linear elastic regime. Considering an energy balance, we obtain the relation



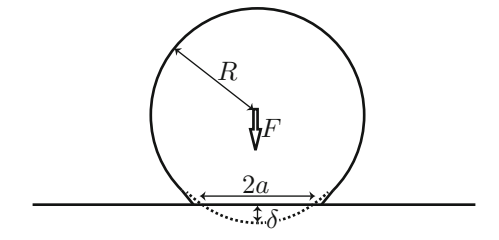


Fig. 2.6 Elastic contact deformation of a sphere due to the normal loading force F. The radius of the initial elastic sphere is R. The deformation displacement is δ , and the radius of the contact circle is a. While the deformation is exaggerated in the figure, the considered deformation is very small, $\delta \ll R$

The left-hand side of this equation represents the stored energy of elastic deformation, (elastic modulus) \times (strain) \times (area) \times (displacement). The right-hand side corresponds to the work performed by the loading, (force) \times (displacement). The symbol \sim indicates the scaling (proportional) relation between the same dimensional quantities neglecting a numerical factor.³ Equation (2.64) is simplified as

$$a \sim \left(\frac{FR}{E}\right)^{1/3}.\tag{2.65}$$

Using the relation $a \sim (R\delta)^{1/2}$, Eq. (2.65) can be rewritten as

$$F \sim ER^{1/2}\delta^{3/2}$$
. (2.66)

Equation (2.66) expresses a nontrivial relation between force and deformation. Although one might expect $F \propto \delta$ by the linear elasticity, Eq. (2.66) implies a nonlinear relation $F \propto \delta^{3/2}$. Note that only the linear elastic constitutive law is used to deduce the relation. This nonlinear contact force law is called the Hertz law. The complete stress calculation including a numerical prefactor can be found in Ref. [14]. The Hertz law is now very famous and used in many particulate computations. Of course, Eq. (2.66) is dimensionally sound because the dimension of force comprises the product of the elastic modulus and square of length (area). Key points to derive Eq. (2.66) are assumptions of (i) tiny displacement $\delta \ll R$ and (ii) definition of strain by (a/R) for the deformation of the sphere. Then, we can estimate how elasticity, size, and applied force affect the deformation of the sphere using a simple energy balance, as discussed thus far.

When the sphere is sufficiently small, surface tension γ_c plays an essential role in the contact mechanics (see Sect. 2.8.5 for the size dependence of the dominant force.) The dimension of γ_c is [force]/[length] = [energy]/[area] = MT⁻². In the small grain's contact mechanics, the deformation is determined by the balance between elasticity and surface tension effect. Thus, the work by normal load $F\delta$ in Eq. (2.64) is replaced by the surface energy gain due to the contact, $\sim \gamma_c a^2$. Then, Eq. (2.64) is rewritten as

$$E\left(\frac{a}{R}\right)a^2\delta \sim \gamma_c a^2. \tag{2.67}$$

Using a relation $a \sim (R\delta)^{1/2}$, we finally obtain the scaling relations,

$$a \sim \left(\frac{\gamma_c}{F}\right)^{1/3} R^{2/3}, \qquad \delta \sim \left(\frac{\gamma_c}{F}\right)^{2/3} R^{1/3}.$$
 (2.68)

³This notation is used in the remainder of this book. The symbol \simeq represents an approximate equality, and the symbol \propto denotes the proportional relation of different dimensional quantities.

Using Eq. (2.68), we can evaluate how the deformations a and δ are scaled by the sphere radius R and mechanical property (length scale) γ_c/E . This relation between the surface energy and elastic deformation was first considered by Johnson, Kendall, and Roberts [15], and the result is called JKR theory. Here we have only derived the scaling relations of JKR theory. The detailed computations of the contact mechanics are described in Ref. [14]. The validity of the JKR theory has also been confirmed by the experiment [16].

All the abovementioned calculations are only based on energy balance scaling. Scaling analysis based on dimensional thought is often useful to understand the intrinsic physics of the considered phenomenon. Balances of energy, force, stress, among others are usually used to discuss the scaling relation. The scaling concept is particularly practical for soft matter physics such as polymers [17] and capillary-related phenomena [18]. While the scaling concept is very helpful to find the essential physical mechanism, the proper vision is necessary to draw appropriate scaling relations avoiding an incorrect evaluation.

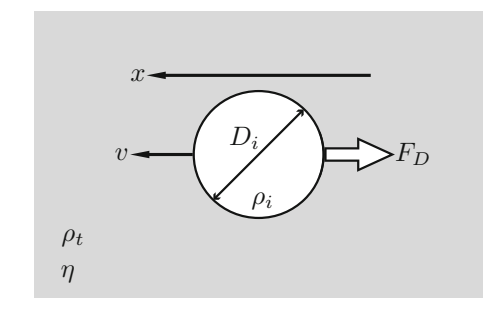
2.6 Fluid Drag Force

Fluid drag force is an illustrative example of the relation of dimensional analysis and the specific equation of motion. The fluid drag force has long been studied because this force relates to aeronautical and marine engineering as well as our daily life. Dimensionless numbers crucial for the drag force can be explained on the basis of the equation of motion. Furthermore, the impact drag force is discussed in addition to the steady drag force. The drag force is a key element of this book. The physics of the fluid drag force will be compared with granular impact drag force later in Chap. 4. In this section, the basic theory of the fluid drag force is introduced.

2.6.1 Viscous Drag

The starting point to discuss fluid drag is a general relation for a viscous fluid, Eq. (2.57). Because the pressure and viscosity are possible sources of the drag force, this equation is worth considering. Equation (2.57) demonstrates that the pressure of an incompressible viscous fluid is a function of S_t , R_e , and ρU^2 . For the sake of simplicity, we consider a steady drag state for now, i.e., the state does not vary with time. Then, a representative timescale is irrelevant. Therefore, the effect of S_t becomes negligible. The most important dimensionless number for the steady-state drag is R_e , which is regarded as $\rho U^2/(\eta U/l)$. The numerator is the inertial stress that also appears in the normalization of the pressure as $p/\rho U^2$, and the denominator is the viscous stress. Thus, this number represents the ratio between inertial and viscous effects. In the low R_e regime, the flow state is dominated by the viscous effect. In contrast, the inertial effect governs the flow state in the high R_e regime, leading to turbulent flow. R_e is an indicator of the dominating physical effects.

Fig. 2.7 Drag force F_D exerted on a rigid sphere (density ρ_i and diameter D_i) moving with velocity v in a quiescent fluid of density ρ_t and viscosity η



First, we focus on the drag force in the low R_e regime ($R_e \ll 1$). In this regime, the drag force exerted on a moving rigid sphere in a quiescent fluid is dominated by the viscous drag force rather than the inertial drag force. Namely, the dimensionless number $p/\rho U^2$ is irrelevant in this regime. Let us consider a sphere moving with velocity (speed) v in an infinitely spreading viscous fluid of viscosity η in the low R_e regime (Fig. 2.7). The corresponding viscous drag force F_{η} is written using Stokes' law as 4 [4, 19]

$$F_{\eta} = 3\pi D_i \eta v, \tag{2.69}$$

where D_i is the diameter of the sphere. The point of Eq. (2.69) is a linear relation between F_{η} and v. Additionally, F_{η} is also proportional to D_i . The form of Eq. (2.69) can be dimensionally understood as $F_{\eta} \sim D_i \eta v$ (or $F_{\eta}/D_i^2 \sim \eta v/D_i$). According to Eq. (2.69), the impulse made by Stokes drag (viscous drag) during time $dt = D_i/v$ is written as $F_{\eta}dt = 3\pi D_i^2 \eta$. This relation implies that Stokes drag consumes the momentum of the dragged sphere to produce a cylindrical shear field with diameter $3D_i$ and length D_i . That is, the territorial length scale of the Stokes drag corresponds to $D_i = (3D_i - D_i)/2$. This result is natural because D_i is a unique length scale

⁴The derivation of this form is not so simple. Some tips for the vector analysis in spherical coordinate and a fundamental knowledge of fluid mechanics are necessary for the calculation. While the details of the derivation are skipped here, an outline is briefly provided below. For the Stokes dynamics, the solution called *Stokeslet* which satisfies $\nabla p = \eta \nabla^2 u$ and Eq. (2.26) is useful. In spherical coordinates (r, θ, ϕ) , the stream function φ of the Stokeslet obeys the equation, $\mathcal{E}^2 \varphi = 0$, where $\mathcal{E} = (\partial^2/\partial r^2) + (\sin \theta/r^2)(\partial/\partial \theta)[(1/\sin \theta)(\partial/\partial \theta)]$. Here θ corresponds to the zenith angle from the flow (z) axis. The stream function φ is related to the velocity components u_r and u_θ as $u_r = (1/r^2 \sin \theta)(\partial \varphi/\partial \theta)$ and $u_\theta = (-1/r \sin \theta)(\partial \varphi/\partial r)$. Considering the boundary conditions $\varphi(r=R_i)=0$, $(\partial \varphi/\partial r)(r=R_i)=0$ (no slip on the surface of the spherical object in radius R_i) and $\varphi(r \to \infty) = (1/2)vr^2 \sin^2 \theta$ (uniform flow of velocity v along z axis), the solution for $\mathcal{E}^2 \varphi = 0$ is obtained by assuming the variable separation form $\varphi = f(r) \sin^2 \theta$ as $\varphi = (1/2 - 3R_i/4r + R_i^3/4r^3)vr^2\sin^2\theta$. Then, the velocity components are written as $u_r = (1 - 3R_i/2r + R_i^3/2r^3)v\cos\theta$ and $u_\theta = -(1 - 3R_i/4r - R_i^3/4r^3)v\sin\theta$. The shearoriginated drag force F_s is computed by $F_s = \int_s \eta \dot{\gamma}_{r\theta} \sin \theta ds$, where s is the small surface unit of the object and $\dot{\gamma}_{r\theta} = r(\partial/\partial r)(u_{\theta}/r) + (1/r)(\partial u_r/\partial \theta)$ is the shear strain rate. The normal drag force F_n can be computed by $\int_s 2\eta (\partial u_r/\partial r) \cos \theta ds$ at $r = R_i$. Finally, F_η can be computed from $F_{\eta} = F_s + F_n$ and $D_i = 2R_i$.

relevant to this phenomenon. Note that this relation is valid only for a Newtonian fluid, in which the shear strain rate is proportional to the shear stress. Thus, the shear strain rate is dimensionally expressed as v/D_i , i.e., $\dot{\gamma}^{-1} = dt = D_i/v$.

2.6.2 Inertial Drag and Drag Coefficient

Next, the drag force exerted on a moving sphere in the high R_e regime ($R_e \gg 1$) is considered. In this regime, the momentum transfer between the sphere and fluid plays an important role. Thus, the sphere density ρ_i and the fluid density ρ_t are necessary information to calculate the drag force. A small volume of the sphere that sweeps within the infinitesimal duration dt is written as $(\pi/4)D_i^2vdt$. The momentum transferred from the sphere to the fluid during dt is computed as $\rho_t \cdot (\pi/4)D_i^2vdt \cdot v$. Meanwhile, the sphere's momentum loss by the infinitesimal deceleration dv (absolute value) is calculated as $\rho_i \cdot (\pi/6)D_i^3 \cdot dv$. These two momenta should be balanced: $\rho_t(\pi/4)D_i^2v^2dt = \rho_i(\pi/6)D_i^3dv$. Then, the inertial drag force F_i is finally obtained as

$$F_{i} = \rho_{i} \frac{\pi}{6} D_{i}^{3} \frac{dv}{dt} = \rho_{t} \frac{\pi}{4} D_{i}^{2} v^{2}. \tag{2.70}$$

The inertial drag force depends on the squared velocity v^2 and the intersectional area of the sphere $(\pi/4)D_i^2$. This velocity dependence is quite distinct from the viscous drag form.

Because the inertial drag is based on the momentum transfer, it is applicable to general drag phenomena including the impact drag of various materials. To evaluate the strength of the general drag force F_D , the drag coefficient C_D is defined as

$$C_D = \frac{F_D/A}{\rho_t v^2/2},$$
 (2.71)

where A is the area of intersection; thus, $A = \pi D_i^2/4$ for a sphere. C_D is a dimensionless ratio of the drag stress and inertial stress.⁵ Equation (2.71) for a sphere is rewritten as

$$F_D = \frac{C_D}{2} \frac{\pi}{4} \rho_t D_i^2 v^2 = \frac{C_D}{2} F_i. \tag{2.72}$$

Using the general drag force F_D , the basic equation of motion for the drag force exerted on a sphere of mass $m_i = \rho_i(\pi/6)D_i^3$ is certainly expressed by the equation of motion (Eq. (2.1)) as

⁵Using usual notations of representative quantities ($v=U, D_i=l$, and $\rho_t=\rho$), Eq. (2.71) becomes $C_D \sim F_D/\rho U^2 l^2$ by omitting a numerical factor.

$$m_i \frac{dv}{dt} = -F_D. (2.73)$$

Note that the negative sign in Eq. (2.73) originates from the fact that the drag force acts against the motion. In other words, a positive F_D results in deceleration (negative dv/dt). Namely, F_D denotes the absolute value of the drag force. The situation discussed in this subsection is schematically illustrated in Fig. 2.7.

In principle, the drag coefficient C_D can be computed using Eq. (2.71) for any R_e flow, as long as D_i , ρ_t , v, and F_D are measurable. As mentioned before, viscous drag dominates the entire drag force in the low R_e regime. If C_D satisfies $C_D = 24\eta/\rho_t v D_i$, the drag force becomes $F_D = F_\eta$. Assuming $D_i = l$ and v = U in Eq. (2.41), C_D in this case is written as

$$C_D = \frac{24}{R_e}. (2.74)$$

Note that this relation is held only in the low R_e regime ($R_e \ll 1$). Thus, C_D is considerably greater than unity in this viscous regime. If the momentum transfer is a principal origin of F_D , C_D should be almost on the order of magnitude of unity. The actual relation between C_D and R_e for the moving sphere is as follows [2, 4, 19]. At $R_e \ge 1$, C_D keeps decreasing until $R_e \simeq 10^2$. Then, C_D is roughly constant in the high R_e regime ($10^3 \le R_e \le 10^5$). In this regime, the value of C_D is slightly less than unity. Therefore, the inertial drag is almost dominant in this regime. In the very high R_e regime ($R_e > 10^5$), C_D exhibits a sudden decrease due to the turbulence of the boundary layer.

The drag coefficient is a useful indicator to characterize the strength of the drag force. Although only the spherical shape has been considered in this subsection, in general, C_D strongly depends on the shape of the object. For airplane or ship designs, a lower value of C_D is better for efficiency. Therefore, the shape dependence of C_D is one of the main concerns in fluid engineering.

2.6.3 Terminal Velocity and Stokes Number

As a simple practice problem, here we consider the terminal velocity of a sinking sphere into a viscous fluid under gravitational acceleration g. The one-dimensional motion along the vertical direction is considered. Then, the equation of motion is written with instantaneous sphere velocity v as

$$m_i \frac{dv}{dt} = -F_D + m_i g - m_i g \left(\frac{\rho_t}{\rho_i}\right). \tag{2.75}$$

⁶ All other drag force forms used in this section (F_{η}, F_i) , and F_E are also written using their absolute values. Hence the motion's direction is considered as a positive direction (Fig. 2.7).

The last term of the right-hand side comes from a buoyancy effect. The vertically downward direction is set to the positive direction. Because the terminal velocity is a steady-state velocity, the left-hand side of Eq. (2.75) has to be zero at the terminal velocity. Substituting the viscous drag force F_{η} into F_D of Eq. (2.75), the viscous terminal velocity v_{η} is calculated as

$$v_{\eta} = \frac{(\rho_i - \rho_t)}{18} \frac{gD_i^2}{\eta}.$$
 (2.76)

The form on Eq. (2.76) can be evaluated dimensionally. The gravitational force F_g is written as $(F_g = m_i g \sim \rho_i D_i^3 g)$, and the viscous drag force satisfies $F_\eta \sim \eta D_i v_\eta$ (Eq. (2.69)). Therefore, from the dimensional viewpoint, the terminal velocity is computed from the balance $F_g \sim F_\eta$ as $v_\eta \sim \rho_i g D_i^2 / \eta$ (for $\rho_i \gg \rho_t$, i.e., $\rho_i - \rho_t \simeq \rho_i$). This form is indeed dimensionally the same as Eq. (2.76). For the general drag case, Eq. (2.72) should be substituted into Eq. (2.75). Then, the general terminal velocity v_t is calculated as

$$v_t = \sqrt{\left(\frac{\rho_i - \rho_t}{\rho_t}\right) \frac{4gD_i}{3C_D}}. (2.77)$$

Similar to the viscous drag case, Eq. (2.77) can be verified dimensionally. The form of the gravitational force is the same as before, $\rho_i D_i^3 g$, which, in turn, balances with $F_D \sim \rho_t C_D D_i^2 v_t^2$. Consequently, the terminal velocity is given as $v_t \sim \sqrt{\rho_i g D_i / \rho_t C_D}$. Moreover, because ρ_i / ρ_t and C_D are dimensionless, the dimension of v_t is basically determined by $\sqrt{g D_i}$. Substituting Eq. (2.74) into Eq. (2.77), the viscous terminal velocity (Eq. (2.76)) is certainly recovered.

Here a dimensionless number S_{tk} called the Stokes number is introduced using Eq. (2.76). Consider a situation $\rho_i \gg \rho_t$, and replace v_η with $S_{tk}U$ (U is a representative absolute value of velocity). Then, using a representative length scale l instead of g as $g = U^2/l$, Eq. (2.76) can be written as

$$S_{tk} = \frac{\rho_i U D_i^2}{18\eta l}. (2.78)$$

 S_{tk} represents the ratio of the sphere's inertia to the fluid viscosity. Therefore, the degree of relative motion between the sphere and fluid can be evaluated by S_{tk} . In the high S_{tk} regime ($S_{tk} \gg 1$), the sphere cannot follow the fluid flow because of its own inertia. The sphere and the fluid move almost independently in this regime. In contrast, a sphere will follow the streamline of the fluid flow in the low $S_{tk} (\ll 1)$ regime. S_{tk} can be used to characterize the fidelity of tracer particles in fluid flow

⁷This form is understandable by considering a centrifugal acceleration.

measurements. The low S_{tk} condition is necessary to experimentally measure the fluid flow by the image analysis of motions of particles dispersed in a fluid flow.

The viscous braking time (stopping time) t_b can be computed by the simple equation of motion, $m_i(dv/dt) = -F_{\eta}$. By solving this equation, one can obtain $v = v_0 \exp(-t/t_b)$ with

$$t_b = \frac{\rho_i D_i^2}{18\eta},\tag{2.79}$$

where v_0 denotes the initial velocity. Therefore, S_{tk} is written as

$$S_{tk} = \frac{t_b}{l/U}. (2.80)$$

In general, S_{tk} can be regarded as a ratio between the viscous braking time t_b and the characteristic flow timescale l/U. The braking time can be simply calculated using $t_b = m_i |v/F_D|$. Equation (2.79) is also readily obtained by this relation. The braking time represents a characteristic timescale of the drag force.

2.6.4 Virtual Mass

In Eq. (2.73), only the motion of the sphere of mass m_i is considered. To accelerate (or decelerate) a sphere in a fluid pool, the surrounding fluid must also be accelerated (or decelerated). Thus, the drag force F_D affects the change of the net momentum including the surrounding fluid, $(m + m_{\text{virt}})dv/dt$. Then, Eq. (2.73) is rewritten as

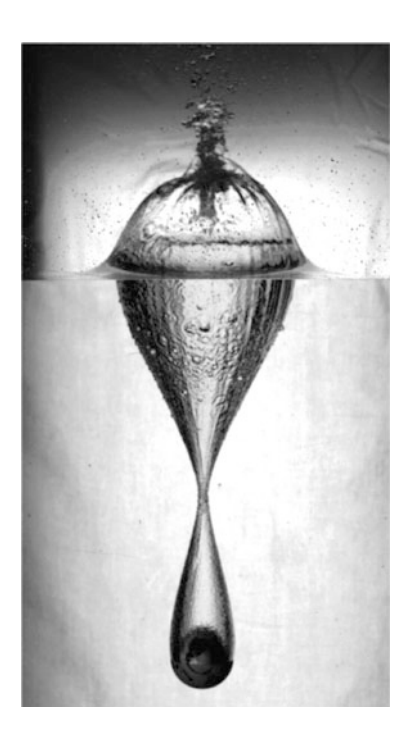
$$(m_i + m_{\text{virt}})\frac{dv}{dt} = -F_D, \tag{2.81}$$

where m_{virt} is called virtual mass (or added mass or apparent mass). The effect of virtual mass is common in fluid drag force. However, its specific value depends on various conditions. It is not easy to systematically predict the value of the virtual mass. The value is often determined by fitting to experimental data.

2.6.5 Fluid Impact Drag Force

The viscous and inertial drag forces discussed thus far are based on steady drag without any boundary. For the *impact* on a target surface, the effect of the boundary surface is not negligible. At the surface, the impactor feels the sudden resistance force mainly because of the density difference; this density difference causes inertial drag. Thus, in the classic study of a solid sphere's impact on water, the inertial drag

Fig. 2.8 Impact cavity formation induced by $D_i = 57.2$ mm billiard ball impact into a water pool with $v_0 = 5.95$ m/s. Both the surface and deep closures can be clearly observed (Reproduced with permission from Ref. [22])



was the main focus [20]. When a steel sphere strikes the surface of water, cavities are usually formed (Fig. 2.8). In Fig. 2.8, one can observe two cavity closures: (i) a closure of splash on the surface (surface closure) and (ii) a closure of the cavity produced in the fluid target (deep closure). Dimensional analysis by Gilbarg and Anderson revealed the relation between the surface and deep closure times [21]. In this cavity formation regime, the drag force is well-described by the inertial drag. Equation (2.70), which is the equation of motion of inertial drag, can be simplified as $dv/dt = -(3/2)(\rho_t/\rho_i)(v^2/D_i)$. By integrating this equation, a simple relation for v(t) is obtained as

$$\frac{1}{v(t)} - \frac{1}{v_0} = \left(\frac{3}{2D_i} \frac{\rho_t}{\rho_i}\right) t. \tag{2.82}$$

To test the validity of this form, the impact experiment was performed with steel spheres ($D_i = 0.635 - 3.81$ mm) impacting on a water pool with impact velocity $v_0 = 7.62 - 63.4$ m/s [20]. As a result, Eq. (2.82) was approximately satisfied and the drag coefficient C_D for the impact can be scaled as

$$C_D \sim \frac{\rho_t v_0}{\eta} \frac{v_0}{\sqrt{g/D_i}}.$$
 (2.83)

This relation has a typical form of the dimensional analysis. All the relevant parameters are related by the power-law form to form a dimensionless relation. Although the theoretically confirmed derivation of Eq. (2.83) has not been obtained, it can be understood by the dimensional concept. Specifically, the right-hand side of Eq. (2.83) can be regarded as R_e . While D_i (the impactor's diameter) is usually employed for the characteristic length scale of R_e , here we use a particular length scale, $l = U/\sqrt{g/D_i}$, to consider the gravitational effect. Substituting this l, $\rho = \rho_t$, and $U = v_0$ into Eq. (2.41), we obtain the right-hand side of Eq. (2.83) as a type of R_e . Note that Eq. (2.83) is an empirical relation and holds only for the impact drag. For the steady-state drag, C_D is inversely proportional to R_e (in the low R_e ; Eq. (2.74)) or almost independent of R_e (at high R_e regime).

The dynamics of a disk impacting a water pool was measured by Glasheen and McMahon [23]. Using much more accurate data than Ref. [20], these researchers quantified the virtual mass and drag coefficient. To compute the virtual mass, sudden velocity drop directly after the instant of impact was used. Concretely, the impact velocity v_0 is decelerated down to $v_{\rm dec}$ within a very short timescale ($\simeq 1$ ms [23]). This sudden velocity drop presumably originates from the momentum transfer from the impactor to the surrounding water; $m_{\rm virt}v_{\rm dec} \simeq m_i(v_0-v_{\rm dec})$. Thus, the virtual mass can be estimated as

$$m_{\text{virt}} = \frac{v_0 - v_{\text{dec}}}{v_{\text{dec}}} m_i. \tag{2.84}$$

After this initial impact pulse, the drag force is dominated by the cavity created by the impact. In this regime, the drag force is an increasing function of time. If we assume the modified drag coefficient C_D^* using

$$F_D = C_D^* D_i^2 \left(\frac{1}{2} \rho_t v^2 + \rho_t g z \right), \tag{2.85}$$

 $C_D^*(\simeq 0.7)$ becomes constant in their experiment [23], which indicates that the drag force is affected by the hydrostatic pressure as well as inertia. The closure time of deep cavity $T_{\rm close}$ was also measured and characterized as

$$T_{\rm close} \simeq \sqrt{\frac{D_i}{g}}.$$
 (2.86)

Equation (2.86) indicates that the deep cavity closure time is independent of the impact velocity. This result contrasts with the drag force itself, which strongly depends on the impact velocity.

Using the impact drag force and the cavity closure time, the mechanism of Basilisk lizards running on water was discussed in Ref. [24]. In principle, people can run on water by utilizing the same mechanism. That is, we can run on water if the cadence is faster than the cavity closure timescale. According to Ref. [24], a person of $m_i = 80 \,\mathrm{kg}$ (with effective feet radius $R_i = 0.1 \,\mathrm{m}$, step period $T_{\mathrm{step}} = 0.25 \,\mathrm{s}$, and

a half length of leg $l_{\rm leg}=0.5\,{\rm m}$) must stroke the water surface downwards at almost $v=30\,{\rm m/s}$, to run on water. Unfortunately, this velocity is beyond the ability of a usual human. The cavity formation and its closure are very important processes for fluid impact. Furthermore, ambient pressure affects fluid impact dynamics [21, 25]. The jet formation induced by the cavity closure, particularly in the granular target case, will be discussed later (Sect. 6.3).

2.6.6 Epstein Drag

In highly rarefied gas, the mean free path of gas molecules $\lambda_{\rm mfp}$ becomes large. Then, the simple continuum mechanics discussed thus far cannot be applied to calculate the drag force. When $\lambda_{\rm mfp}$ is much larger than D_i , the integral of individual impacts among the dragged object and molecules (free molecule flow) determines the drag force. In such a situation, the mean speed of gas molecules $\langle u_t \rangle$ is a key quantity. Assuming ideal gas behavior, $\langle u_t \rangle$ is computed from the Maxwell-Boltzmann distribution and is written as (see e.g., [26])

$$\langle u_t \rangle = \sqrt{\frac{8k_BT}{\pi m_m}},\tag{2.87}$$

where k_B , T, and m_m are Boltzmann constant $k_B \simeq 1.38 \times 10^{-23}$ J/K, the temperature, and the mass of gas molecules, respectively. The same setup—a rigid sphere of mass m_i and diameter D_i moving with velocity v in the quiescent (without any systematic flow) rarefied gas of density ρ_t —is considered again. Assuming an elastic (energy conservative) collision between the object and molecules, the momentum transfer between them can be computed as

$$m_i dv = 4\pi \left(\frac{D_i}{2}\right)^2 v dt \cdot \frac{\langle u_t \rangle}{3} \rho_t. \tag{2.88}$$

The first factor on the right-hand side represents the volume swept by the object during dt, and the second factor comes from the elastic collision of isotropic gas motion in three-dimensional space. From Eq. (2.88), the drag force exerted on the object in highly-rarefied gas is computed as [27]

$$F_E = \delta_E \frac{\pi}{3} D_i^2 \rho_t \langle u_t \rangle v, \qquad (2.89)$$

⁸This velocity can roughly be estimated by the impulse balance, $m_i g T_{\text{step}} = 0.5 \rho_t v^2 \pi R_i^2 l_{\text{leg}} / v$.

⁹This equation dimensionally represents a simple relation, $m_m \langle u_t \rangle^2 \sim k_B T$. More precisely, this relation can be computed by $\langle u_t \rangle = (m_m/2\pi k_B T)^{2/3} \int_0^\infty u_t \exp(-m_m u_t^2/2k_B T) 4\pi u_t^2 du_t$.

where δ_E is a certain efficiency factor. The Epstein drag F_E is proportional to v and D_i^2 . Its D_i dependence is different from viscous drag. Note that the average gas speed $\langle u_t \rangle$ is independent of v and is determined mainly by temperature as written in Eq. (2.87). Therefore, F_E is also different from the inertial drag F_i defined in Eq. (2.70). The braking time for the Epstein drag t_b is computed using the relation $t_b = m_i |v/F_E|$ (see Sect. 2.6.3) and Eq. (2.89) as

$$t_b = \frac{1}{2\delta_E} \frac{\rho_i}{\rho_t} \frac{D_i}{\langle u_t \rangle}.$$
 (2.90)

The Epstein drag is relevant when $\lambda_{\rm mfp}/D_i \gg 1$ and $v \ll \langle u_t \rangle$. The dimensionless number

$$K_n = \frac{\lambda_{\text{mfp}}}{D} \tag{2.91}$$

is called the Knudsen number. In general, $K_n \ll 1$ must be satisfied to neglect molecular dynamics in the drag force evaluation. At the other limit $K_n \gg 1$, molecular-level mechanics must be considered as discussed in this subsection. Because the main interest of this book is focused on continuum-level mechanics, a small K_n regime is usually assumed. In Sect. 7.1, Epstein drag is used to discuss the drag force acting on dust aggregates in space.

2.6.7 General Form of the Drag Force

In general, the drag force equation can contain a constant term as well as inertial and viscous (or Epstein) terms. The general form of the drag force equation can be written as

$$m_i \frac{dv}{dt} = -\alpha_d v^2 - \beta_d v - \gamma_d, \qquad (2.92)$$

where α_d , β_d , and γ_d are (usually positive) parameters characterizing inertial, viscous (or Epstein), and constant (static) drag forces, respectively. Note that these coefficients have different dimensions. Let us consider the impact situation, in which the impactor has its initial impact velocity v_0 and finally comes to rest when the initial kinetic energy $m_i v_0^2/2$ is transferred or dissipated by the drag force. Then, the total moving distance for the impactor from the impact point to its cessation point, x_{tot} , can be computed from Eq. (2.92). The form of x_{tot} depends on the type of drag force model, as described below.

When $\alpha_d = \beta_d = 0$ and $\gamma_d \neq 0$, only the constant drag force is relevant. This drag force model is called the Robins-Euler drag model. In this case, the total moving distance x_{tot} is calculated as $x_{\text{tot}} = m_i v_0^2 / 2 \gamma_d$ by the simple energy balance between the initial kinetic energy $m_i v_0^2 / 2$ and the work performed against the constant drag force $\gamma_d x_{\text{tot}}$.

If only the inertial drag is irrelevant ($\alpha_d = 0$ and $\beta_d \gamma_d \neq 0$), the drag force comprises the viscous and constant terms. This type of drag force model is called the Bingham drag model. In the Bingham drag model, the velocity and total moving distance can be analytically computed by the variable transformation of $\hat{v}_1 = (\beta_d v + \gamma_d)/m_i$, and thus, $d\hat{v}_1 = (\beta_d/m_i)dv$. The equation simplified by this variable transformation is written as $d\hat{v}_1/dt = -(\beta_d/m_i)\hat{v}_1$. From this equation, the velocity as a function of time is computed as

$$v(t) = \left(v_0 + \frac{\gamma_d}{\beta_d}\right) \exp\left(-\frac{\beta_d}{m_i}t\right) - \frac{\gamma_d}{\beta_d}.$$
 (2.93)

The total moving distance x_{tot} can be calculated by integrating Eq. (2.93) until the velocity vanishes. The stopping time $t_{\text{stop}} = (m_i/\beta_d) \ln[(\beta_d v_0 + \gamma_d)/\gamma_d]$ is obtained from the relation $v(t_{\text{stop}}) = 0$. Then, one obtains a form of x_{tot} with an initial condition of $x(t=0) = x_0$ of

$$x_{\text{tot}} = \int_{0}^{t_{\text{stop}}} v(t)dt = \left[x_0 - \frac{m_i}{\beta_d} \left(v_0 + \frac{\gamma_d}{\beta_d} \right) \exp\left(-\frac{\beta_d}{m_i} t \right) - \frac{\gamma_d}{\beta_d} t \right]_{0}^{t_{\text{stop}}}$$

$$= \frac{m_i}{\beta_d^2} \left[\beta_d v_0 - \gamma_d \ln\left(1 + \frac{\beta_d v_0}{\gamma_d}\right) \right]. \tag{2.94}$$

The Poncelet drag model corresponds to the case of $\beta_d = 0$ (and $\alpha_d \gamma_d \neq 0$). For the Poncelet drag model, the velocity can be computed as a function of the moving distance, v(x). Specifically, the equation is linearized by the transformation of variable, $\hat{v}_2 = \alpha_d v^2 + \gamma_d$ and thus, $d\hat{v}_2 = 2\alpha_d v dv$. The linearized equation is written as $d\hat{v}_2/dx = -(2\alpha_d/m_i)\hat{v}_2$. This differential equation can be readily solved and the velocity v(x) is finally calculated as

$$v(x) = \sqrt{\left(v_0^2 + \frac{\gamma_d}{\alpha_d}\right)} \exp\left(-\frac{2\alpha_d}{m_i}x\right) - \frac{\gamma_d}{\alpha_d}.$$
 (2.95)

Using the criterion of $v(x_{tot}) = 0$, x_{tot} is computed as

$$x_{\text{tot}} = \frac{m_i}{2\alpha_d} \ln\left(1 + \frac{\alpha_d v_0^2}{\gamma_d}\right). \tag{2.96}$$

The general case $(\alpha_d \beta_d \gamma_d \neq 0)$ can be evaluated by completing the square for Eq. (2.92) as follows:

$$m_i \frac{dv}{dt} = -\left[\alpha_d \left(v + \frac{\beta_d}{2\alpha_d}\right)^2 - \frac{\beta_d^2 - 4\alpha_d \gamma_d}{4\alpha_d}\right]. \tag{2.97}$$

Then, the general drag force model is reduced to the Poncelet drag model. Specific forms of the velocity and moving distance for the general model can be found in Ref. [28].

In Ref. [29], these forms were compared with the dynamics of a high-velocity (typically $v_0 \sim 10^2$ m/s) impact of a solid impactor to a sand bed. They observed that the inertial drag is dominant in the high-velocity impact. Actually, even in low-velocity impact, the inertial drag plays an important role in the granular impact. Thus, the Poncelet drag model will be modified to explain the low-velocity dynamics of a solid impact on a loose granular bed, as will be discussed later in Sect. 4.1.3.

2.7 Dimensionless Numbers

Some of the relevant dimensionless numbers for soft impact mechanics will be listed in this section. General notations (e.g., l, t_o , and ρ for the characteristic length, time, and density) are used in the definitions of dimensionless numbers. Specific values for these quantities depend on the system. For instance, two kinds of density values, ρ_i and ρ_t , were introduced to discuss the drag force exerted on a moving sphere (ρ_i) in a quiescent fluid (ρ_t) in the previous section. For granular matter, the grain material (true) density ρ_g is used in addition to the bulk granular density which corresponds to the general density ρ in the fluid case. Most of the dimensionless numbers introduced in this section are relevant to fluids and granular matter.

Froude number The role of gravity is not negligible, particularly in geological systems. The inertial drag force equation (Eq. (2.70)) is scale invariant because of the absence of the gravity effect. Under a scaling transformation by a constant factor α_o ($D_i' = \alpha_o D_i$, $t' = \alpha_o t$, $v' = v (= d\alpha_o l/d\alpha_o t)$, $\rho_i' = \rho_i$, and $\rho_t' = \rho_t$), the form of Eq. (2.70) is unchanged. In such a system, when the length scale D_i and l are scaled up by the factor α_o and the densities are fixed, the timescale t is elongated by the factor α_o ; this is a type of similarity law. In Eq. (2.75), in contrast, this scale invariance is violated by gravity. The gravity brings symmetry breaking to the system. The value of g introduces a characteristic time, length, or velocity to the system as well as its direction, which may affect the drag behavior in general.

To estimate the effect of gravity compared with the inertial effect, the Froude number F_r is defined by the ratio between the inertia and gravity ¹⁰:

$$F_r = \frac{U^2}{gl}. (2.98)$$

 $^{^{10}}F_r$ is sometimes defined as $F_r = U/\sqrt{gl}$.

For geological phenomena, the role of gravity is quite crucial. Moreover, g is not a constant for general planetary phenomena but varies depending on the size of planets, asteroids or other astronomical objects. Thus, F_r is an important dimensionless number in geological and planetary impact phenomena. This parameter represents the ratio of inertial stress ρU^2 and hydrostatic gravitational pressure ρgl .

Weber number For small-scale phenomena, the surface tension (or capillary force) must be considered [18]. In Sect. 2.5.4, the surface tension was, in fact, very important to compute the elastic deformation of small grains. The upper limit of the length scale for capillary-driven phenomena is derived from the ratio between surface tension and gravity. The capillary length λ_c , which corresponds to the upper limit, is defined as¹¹

$$\lambda_c = \sqrt{\frac{\gamma_c}{\rho g}}. (2.99)$$

Almost all liquids exhibit a surface tension on the order of $\gamma_c \simeq 10^{-2}\,\text{N/m}$ and density on the order of $\rho \simeq 10^3\,\text{kg/m}^3$. Therefore, on the surface of the Earth $(g \simeq 9.8 \simeq 10^1\,\text{m/s}^2)$, the order of λ_c for most liquids is $\mathcal{O}(10^0)\,\text{mm}$. Therefore, capillary-related phenomena on the Earth are limited to the length of at most a few millimeters.

The surface tension tends to straighten the curved interface to minimize the surface energy. Thus, the capillary pressure by the surface tension depends on the curvature of the curved interface. The pressure due to this effect is called the Laplace pressure which is written as [18]

$$\Delta p = \gamma_c \left(\frac{1}{R_1} + \frac{1}{R_2} \right). \tag{2.100}$$

Here Δp , R_1 , and R_2 are the pressure difference across the interface and two principal radii of curvatures of the interface, respectively. For example, the fluid bubble pressure can be estimated using Eq. (2.100). The pressure difference for a spherical bubble of radius R_b is 12 $\Delta p = 2\gamma_c/R_b$.

As discussed thus far, dimensionless numbers are useful in characterizing the force or stress balance. To make a dimensionless number relevant to capillary pressure, the inertial stress ρU^2 is divided by the Laplace pressure Δp . Then, a ratio called the Weber number is obtained:

$$W_e = \frac{\rho U^2 l}{\gamma_c}. (2.101)$$

¹¹This form comes from the stress balance, $\rho g \lambda_c = \gamma_c / \lambda_c$.

¹²This relation can also be derived by the simple linear approximation of the energy balance per infinitesimal radius variation of the bubble dR_b , $\Delta p 4\pi R_b^2 dR_b \simeq 4\pi [(R_b + dR_b)^2 - R_b^2] \gamma_c$.

Here we assume a representative length scale as $l = R_1 R_2/(R_1 + R_2)$. In general, the low W_e regime is governed by the capillary (Laplace) pressure, while the high W_e regime is dominated by the inertia. W_e plays a crucial role particularly in the case of droplet impact discussed in Sect. 6.5.

Capillary number To evaluate the competition between viscous and capillary forces, the capillary number C_a is defined as the ratio W_e/R_e ,

$$C_a = \frac{\eta U}{\gamma_c}. (2.102)$$

In the large C_a regime, viscosity dominates the behavior, and capillary effect is negligible. If ηU is too large, C_a is no longer the relevant dimensionless number. In such a situation, the capillary effect becomes completely negligible, and another dimensionless value, such as R_e , becomes essential.

Ohnesorge number The capillary number is not a unique one to compare the surface tension and viscosity. When the density effect is more important than the velocity effect, a dimensionless number called the Ohnesorge number O_h defined by $\sqrt{W_e}/R_e$ can be used. The specific form of O_h is written as

$$O_h = \frac{\eta}{\sqrt{\rho l \gamma_c}}. (2.103)$$

According to Eq. (2.103), the small O_h regime is primarily governed by the capillary effect, whereas the large O_h regime is dominated by viscosity. However, note that the capillary-dominant length scale is limited up to the capillary length λ_c . If the characteristic length scale l is considerably greater than λ_c , the system is governed by the gravity effect rather than the capillary effect as long as the gravity is relevant.

Bond number To discuss the ratio between the gravity and capillary force, the Bond number B_o is convenient. B_o can be derived from the definition of the capillary length λ_c (Eq. (2.99)). Defining B_o as the ratio between the representative length scale and capillary length as $B_o = l^2/\lambda_c^2$, B_o is written as

$$B_o = \frac{\rho g \ell^2}{\gamma_c}. (2.104)$$

In the large B_o regime, gravity dominates the behavior.

Mach number When the motion of the fluid is sufficiently slow, the incompressible assumption holds well. However, the compressibility cannot be negligible in the high-speed regime. To evaluate the flow state, a ratio between the representative speed U and the bulk speed of sound C_s is introduced as the Mach number:

$$M_a = \frac{U}{C_s}. (2.105)$$

For simple gas, C_s is approximately expressed as $C_s \simeq \sqrt{p/\rho}$. For $M_a > 0.3$, fluid compressibility has to be considered because the flow speed becomes comparable to the wave propagation speed.

Deborah number In general, a motion is induced by a force. However, the force can be relaxed by relaxation mechanisms such as viscosity. Therefore, the ratio of relaxation and motion timescales governs the behaviors resulting from their competition. The Deborah number D_e is defined by the ratio of these timescales:

$$D_e = \frac{t_{\text{relax}}}{l/U},\tag{2.106}$$

where t_{relax} is the relaxation timescale. In the large $D_e(\gg 1)$ regime, the relaxation effect is negligible, i.e., the motion speed is considerably faster than the relaxation rate. In contrast, the relaxation dominates the behavior in the regime of $D_e \ll 1$ because the relaxation timescale is sufficiently short to relax the system during its motion. The form of D_e is identical to the Strouhal number S_t (Eq. (2.40)). Furthermore, the Stokes number S_{tk} can be regarded as a type of D_e . In S_{tk} , the viscous braking time t_b corresponds to the relaxation timescale (see Eqs. (2.79) and (2.80)).

Péclet number Next, the competition among diffusion and advection is considered. The dimension of kinematic viscosity is $[\eta/\rho] = L^2T^{-1}$, which indicates that the kinematic viscosity is a type of diffusion coefficient, K_d (see Eq. (3.23) for the definition of K_d). Then, the Péclet number P_e is defined by replacing η/ρ with K_d in R_e^{-1} :

$$P_e = \frac{Ul}{K_d}. (2.107)$$

The Péclet number represents the ratio between the advective transport rate and the diffusive transport rate, in terms of transport phenomena. Details of diffusion and advection will be discussed later in Sect. 3.5.

Atwood number Density ratio is sometimes a very useful dimensionless number. For instance, the density ratio ρ_i/ρ_t is an essential factor in Eq. (2.90). Density ratio also plays a crucial role in granular impact analyses (see, e.g., Eqs. (4.25) and (6.58)). Furthermore, a different type of dimensionless density ratio, the Atwood number, is important to compute the hydrodynamic instability induced by density difference (e.g., Rayleigh-Taylor instability discussed in Sect. 6.6.2). The Atwood number A_t is defined as

$$A_t = \frac{\rho_h - \rho_l}{\rho_h + \rho_l},\tag{2.108}$$

where ρ_h and ρ_l indicate the densities of heavier-weight and lighter-weight components, respectively.

Thus far, dimensionless numbers relevant to fluids have been introduced. From now on, dimensionless numbers relating to granular matter will be introduced.

Packing fraction Packing fraction ϕ is an important dimensionless quantity characterizing the granular packing state and is defined by the ratio of the volume of packed grains V_g to the total volume of that space V_t :

$$\phi = \frac{V_g}{V_e}.\tag{2.109}$$

Packing fraction is related to the porosity (or void fraction) ϵ as

$$\epsilon = 1 - \phi. \tag{2.110}$$

The packing fraction is sometimes called the volume fraction, filling factor, packing factor, or solid fraction. The term solid fraction is often used for a mixture of grains and liquid.

Bagnold number If grains are dispersed and sheared in a viscous fluid having viscosity η , the granular flow is classified by the ratio between granular inertia and fluid viscosity. To calculate the balance, Bagnold introduced a dimensionless number called the Bagnold number B_a [30, 31]:

$$B_a = \frac{\rho_g D_g^2 \lambda_B \dot{\gamma}}{n},\tag{2.111}$$

where ρ_g , D_g , and $\dot{\gamma}$ are the density of grains, diameter of grains, and shear strain rate, respectively. The linear concentration λ_B is defined as

$$\lambda_B = \frac{1}{(\phi_0/\phi)^{1/3} - 1},\tag{2.112}$$

where ϕ and ϕ_0 are the solid fraction and its maximum value, respectively. In the low B_a regime ($B_a < 40$), viscosity dominates the flow, while the inertia governs the flow in the high B_a regime ($B_a > 450$). In the intermediate regime, there is a mix. The form of B_a is actually very similar to S_{tk} (Eq. (2.78)) if we assume $\rho_g = \rho_i$, $D_g = D_i = l$, and $D_g \dot{\gamma} = U$. While S_{tk} represents the balance between a single grain's inertia and the surrounding fluid viscosity, B_a characterizes the balance in a sheared dense grains system.

Shields number Next, the mixture of grains and fluid under gravity is considered. When the grain density ρ_g is larger than the fluid density ρ , grains deposit upon the bottom because of gravity. If there is a fluid flow of velocity U above the sediment of grains, grains could be blown. The ratio between the strengths of sedimentation and blowing is characterized by the Shields number, S_h . S_h is defined by the shear stress acting on the sediment surface, $\sigma = \rho U^2$, as a function of the gravitational stress, $(\rho_g - \rho)gl$:

$$S_h = \frac{\rho}{\rho_g - \rho} \frac{U^2}{gD_g},\tag{2.113}$$

where D_g is the characteristic grain size. Using S_h , the competition among fluid flow and the grains' gravity can be evaluated.

Inertial number Even for sheared dry granular matter, there is an important dimensionless number. In the simple shear condition, there are some relevant physical quantities: the mean shear strain rate $\dot{\gamma}$, grain diameter D_g , confining pressure p, and material true density ρ_g . Using these quantities, a dimensionless number called the inertial number I is defined as [32, 33]

$$I = \frac{\dot{\gamma} D_g}{\sqrt{p/\rho_g}}. (2.114)$$

This dimensionless number represents the relative importance of shearing inertia and confining pressure. The inertial number I can be regarded as a ratio of two characteristic timescales, $\dot{\gamma}^{-1}$ and $D_g/\sqrt{p/\rho_g}$. The former corresponds to a macroscopic shear timescale, and the latter is a microscopic rearrangement timescale of the grains structure under the confining pressure p. The inertial number actually corresponds to the square root of the Savage number [34] or Coulomb number [35].

Summary of dimensionless numbers Various dimensionless numbers have been introduced in this chapter. These dimensionless numbers are useful for characterizing the state of fluid and granular matter. Important dimensionless numbers discussed in this chapter are summarized in Table 2.5. Some of these numbers were obtained by nondimensionalizations of the governing equation or the drag force equation. Others were derived from the balance laws of energy, force, or stress. While the dimensionless numbers can be systematically calculated using nondimensionalization or Π -groups method, physical considerations have mainly been used to define them, particularly in this section.

To characterize soft impact phenomena, the impact velocity v_0 and impactor's diameter D_i are usually used for U and l in these dimensionless numbers. In some dimensionless numbers, D_i or D_g is already used to clearly indicate the size of the considered solid object: a sphere or constitutive grains.

2.8 Similarity Law and Modeling

As demonstrated above, the method of dimensional analysis is very useful to deduce the relevant physical mechanisms for the phenomenon of interest. Dimensionless numbers can be useful indicators for various physical effects. We have already observed the efficacy of scaling and dimensional analysis. However, this is not

Table 2.5 Dimensionless numbers relevant to fluid-, drag-, impact-, and granular-related phenomena. To apply impact phenomena, impact velocity v_0 is usually used as representative velocity (speed) U. In some dimensionless numbers, the solid sphere's diameter D_i and its density ρ_i , or the grain's diameter D_g and its density ρ_g are employed as representative quantities instead of the general notations, l and ρ

Name	Form	Physical meaning	Equation
Strouhal number	$S_t = \frac{l}{Ut_o}$	Characteristic length vs. motion length	(2.40)
Reynolds number	$R_e = \frac{\rho U l}{\eta}$	Inertia vs. viscosity	(2.41)
Drag coefficient	$C_D = \frac{F_D/A}{\rho v^2/2}$	Drag vs. inertia	(2.71)
Stokes number	$S_{tk} = \frac{t_b U}{l}$	Braking time vs. flow timescale	(2.80)
Knudsen number	$K_n = \frac{\lambda_{\mathrm{mfp}}}{l}$	Mean free path vs. representative length	(2.91)
Froude number	$F_r = \frac{U^2}{gl}$	Inertia vs. gravity	(2.98)
Weber number	$W_e = \frac{\rho U^2 l}{\gamma_c}$	Inertia vs. capillarity	(2.101)
Capillary number	$C_a = \frac{\eta U}{\gamma_c}$	Viscosity vs. capillarity	(2.102)
Ohnesorge number	$O_h = \frac{\eta}{\sqrt{\rho l \gamma_c}}$	Viscosity vs. capillarity	(2.103)
Bond number	$B_o = \frac{\rho g l^2}{\gamma_c}$	Capillarity vs. gravity	(2.104)
Mach number	$M_a = \frac{U}{C_s}$	Flow velocity vs. speed of sound	(2.105)
Deborah number	$D_e = \frac{t_{\rm relax}}{l/U}$	Relaxation time vs. motion time	(2.106)
Péclet number	$P_e = \frac{Ul}{K_d}$	Advection vs. diffusion	(2.107)
Atwood number	$A_t = \frac{\rho_h - \rho_l}{\rho_h + \rho_l}$	Density difference vs. total density	(2.108)
Packing fraction	$\phi = rac{V_g}{V_t}$	Grains volume vs. total volume	(2.109)
Bagnold number	$B_a = \frac{\rho_g D_g^2 \lambda_B \dot{\gamma}}{\eta}$	Grains inertia vs. viscous drag force	(2.111)
Shields number	$S_h = \frac{\rho}{\rho_g - \rho} \frac{U^2}{g D_g}$	Fluid flow vs. grain gravity	(2.113)
Inertial number	$I = \frac{\dot{\gamma} D_g}{\sqrt{p/\rho_g}}$	Shearing inertia vs. confining pressure	(2.114)

the end of the story of dimensional analysis. Dimensional analysis provides fundamentals to the concept of similarity law or similar modeling [36]. In general, geological and astronomical phenomena occur during extremely long timescales and on very large length scales. To investigate such phenomena by experimental studies, we must create a small-scale mimic called a *model*. In the small-scale model, we expect that the underlying physics is similar to the original phenomena. However, this assumption is not sufficient for the reduced modeling. The concept of similarity law must be contemplated to properly model the original phenomena (prototype). In this section, the fundamentals of similarity law and similar modeling are discussed.

2.8.1 Geometric Similarity

The term *similarity* usually indicates a geometrical term. Two bodies are geometrically similar when all the corresponding lengths are equally proportional and all the correspondent angles are identical. This type of simple similarity is called *geometric similarity*. Let l_m be a length in the model and l_p be a corresponding length in the (original) prototype. Then, the geometric similarity is written as

$$\frac{l_m}{l_p} = \text{const.} {(2.115)}$$

The constant corresponds to a homothetic ratio and must be identical for all the corresponding length scales. The constant in Eq. (2.115) is also called a model ratio of length in terms of physical similarity law. In addition to Eq. (2.115), the correspondent angles of the model θ_m and the prototype θ_p have to be identical everywhere in the model and prototype:

$$\theta_m = \theta_p. \tag{2.116}$$

This equality of angles is an obvious requirement for geometric similarity.

2.8.2 Kinematic Similarity

When two geometrically similar bodies move or deform, *kinematic similarity* must also be considered. The time required to move or deform in the model must be equally proportional to that in the prototype. Thus the kinematic similarity is expressed as

$$\frac{t_m}{t_p} = \text{const.} \tag{2.117}$$

Here t_m and t_p are the times required to move or deform in the model and prototype, respectively. The constant in Eq. (2.117) is called a model ratio of time. Of course, geometric similarity (Eqs. (2.115) and (2.116)) is also supposed to be satisfied during the motion or deformation in the kinematic similarity.

2.8.3 Dynamical Similarity

What is the next similarity? Thus far, the similarities of shape and motion (or deformation) of two bodies (model and prototype) have been discussed. Specifically, two types of similarities based on the length and time have been considered: geometric and kinematic similarities. Then, one might expect the similarity of mass as a next step because there are three fundamental dimensions in mechanics: L, T, and M. To consider the similarity of mass, mass distributions between the model and prototype must be equally proportional everywhere in the model and prototype, similar to the geometric and kinematic similarities. The similarity is written as

$$\frac{m_m}{m_p} = \text{const.}, \tag{2.118}$$

where m_m and m_p denote the masses of small corresponding parts in the model and prototype, respectively. The constant in Eq. (2.118) is called a model ratio of mass. Because we are interested in distributions of mass of corresponding small parts, the masses m_m and m_p can be replaced by corresponding distributions of densities, ρ_m and ρ_p .

If all these three similarities are fulfilled, are the model and prototype completely similar? Unfortunately, the answer is "No." We have to re-examine the force and constitutive laws. The similarity of force is indispensable to complete *dynamical similarity* because the force is the origin of motion and deformation. Dynamical similarity can be written as

$$\frac{|F_m|}{|F_p|} = \text{const.},\tag{2.119}$$

where F_m and F_p are the corresponding forces in the model and prototype, respectively. The constant in Eq. (2.119) is called a model ratio of force. In addition to Eq. (2.119), the direction of the correspondent force vectors must be identical between the model and prototype, i.e., Eq. (2.116) is required for the force as well as geometry.

If these similarities are completely preserved, two similar bodies behave similarly in terms of the mechanics. However, it is difficult to completely satisfy all the similarities. For example, experiments performed on the surface of the Earth are strongly constrained by the gravitational acceleration ($g = 9.8 \text{ m/s}^2$), which cannot be easily varied. This constraint results in the fixed model ratio of force (constant in

Eq. (2.119)) for the modeling of phenomena occurring on the Earth:

$$\frac{|F_m|}{|F_p|} = \frac{m_m g}{m_p g} = \frac{m_m a_m}{m_p a_p},\tag{2.120}$$

where a_m and a_p are the absolute values of acceleration in the model and prototype, respectively.¹³ From Eq. (2.120), a simple relation $a_m/a_p = 1$ is obtained. Because the model ratio of acceleration is written as $a_m/a_p \sim (l_m/l_p)(t_m/t_p)^{-2}$, Eq. (2.120) can be simplified to

$$1 = \frac{l_m}{l_p} \left(\frac{t_m}{t_p}\right)^{-2}. (2.121)$$

Equation (2.121) indicates that the model ratios of length and time cannot be independently varied to satisfy the dynamical similarity law under the constant gravitational acceleration condition.

To avoid this difficulty, only the principal force balance is usually considered, instead of the complete similarity. For instance, the gravitational force is negligible for the fast viscous flow perpendicular to gravity. Under this situation, the equivalence of the model ratio of force is written as

$$\frac{|F_m|}{|F_p|} = \frac{m_m a_m}{m_p a_p} = \frac{\eta_m U_m l_m}{\eta_p U_p l_p},\tag{2.122}$$

where η_m , U_m , η_p , and U_p are the absolute values of the model viscosity, model velocity, prototype viscosity, and prototype velocity, respectively. The directional agreement of acceleration and velocity between the model and prototype (Eq. (2.116)) is certainly assumed here again. Equation (2.122) includes inertial and viscous forces as principal forces. The viscous force is evaluated by the constitutive law of Eq. (2.17) as $F \sim \sigma_s l^2 \sim \eta (U/l) l^2 \sim \eta Ul$. Using the relations $m_x \sim \rho_x l_x^3$ and $a_x \sim U_x^2/l_x$, (x = m or p), Eq. (2.122) is transformed into

$$\frac{\rho_m U_m l_m}{\eta_m} = \frac{\rho_p U_p l_p}{\eta_p}. (2.123)$$

Each term in Eq. (2.123) has the same form as R_e (Eq. (2.41)). This result suggests that R_e must be identical if the model and prototype are dynamically similar in terms of inertia and viscosity balance. As discussed in the previous section, some dimensionless numbers can be expressed by the force (or stress) ratios. To satisfy the dynamical similarity of the considered force balance, the corresponding dimensionless number must be identical. The appropriate dimensionless number

¹³The same direction of acceleration vectors in the model and prototype is surely assumed. This similarity is also assumed later in Eqs. (2.122) and (2.124).

must be selected as an indicator for the adequate modeling. Conversely, as long as the selected dimensionless number is the same, two different systems are said to be dynamically similar in terms of the focused force balance.

The dimensionless numbers listed in Table 2.5 can be classified using the similarity law. The packing fraction ϕ represents a geometric similarity because this parameter only concerns the volume ratio. Additionally, an identical ϕ indicates statistical similarity because the structure of granular matter is basically random. Exact geometric similarity cannot be held for random structures. All other dimensionless numbers represent each corresponding dynamical similarity. Some can also be regarded as kinematic dimensionless numbers because they only include kinematic variables; maybe it is meaningless to strictly classify kinematic and dynamic dimensionless numbers. In general, at least one of the dynamical similarities must be satisfied to construct a physically similar model. Ideally, all the dynamical similarities should be satisfied for exact similar modeling.

2.8.4 Modeling of Geological Phenomena

Using the similarity law, we can construct a proper model for geologically large-scale and long-time phenomena. Historically, the experiment for the salt dome structure is a famous example of similar modeling. A salt dome diapir structure is created when a lightweight salt layer is covered with a heavy sedimentary rock layer. Nettletin performed an experiment with viscous fluids to model the salt dome structure [37]. Specifically, a heavy syrup layer was placed on a lightweight oil layer. Then, this gravitationally unstable structure induced a diapir structure similar to salt domes. Because a long time $(6\times10^7~{\rm year}\simeq2\times10^{15}~{\rm s}~[38])$ is required to form a real salt dome structure, the effect of inertia is negligible. In addition, it is assumed that the competition between gravitational (buoyant) force and viscous force is essential to describe the deformation. Then, the relevant force ratio composed by gravitational force and viscous force is expressed as

$$\frac{|\mathbf{F}_m|}{|\mathbf{F}_p|} = \frac{m_m g}{m_p g} = \frac{\eta_m l_m^2 t_m^{-1}}{\eta_p l_p^2 t_n^{-1}}.$$
 (2.124)

This equation is rewritten as

$$\frac{\eta_m}{\eta_p} = \frac{\rho_m}{\rho_p} \frac{l_m}{l_p} \frac{t_m}{t_p}.$$
 (2.125)

If we use a usual viscous liquid in the model, its density is on the same order as that of sedimentary rock, $\rho_m/\rho_p \simeq 1$. Both densities are on the order of 10^3 kg/m³. The size ratio between the model and original salt dome is approximately $l_m/l_p \simeq 0.1$ m/1 km= 10^{-4} . Using a viscous liquid of viscosity $\eta_m = 10$ Pa·s, the time required to make a salt dome structure in the model was measured to be 10^3 s

(\simeq 17 min). Substituting these values into Eq. (2.125), the actual viscosity of the sedimentary rock (rock salt) can be computed as $\eta_p \simeq 10^{17} \, \text{Pa·s}$. The viscosity ratio is $\eta_m/\eta_p \simeq 10^{-16}$ and the value of $\rho_m l_m t_m/\rho_p l_p t_p$ is also $\simeq 10^{-16}$. In this case, the value of the dimensionless number $\rho_x t_x l_x/\eta_x$ (x=m or p) is 10^5 both for the model and prototype.

In many cases, small-scale and short-time model experiments for geological phenomena must be carried out with extremely soft materials to satisfy the proper dynamical similarity. In other words, we can mimic the large-scale and long-time behavior of hard matter using very soft materials. Soft-matter experiments have great potential applicability to geological-scale phenomena [39–41]. Thus, sandbox modeling is utilized to simulate natural tectonic phenomena. Loose granular matter is much weaker than rock, which is actually an advantage for similar modeling.

2.8.5 Dimensional Dependence of Body and Surface Forces

As mentioned in Sect. 2.2, the difference between body and surface forces should be recognized to discuss the mechanical behavior of soft matter. Moreover, the surface tension is proportional to length, (surface tension force) = (surface tension) \times (length of curve). Equation (2.119) implies that all the corresponding forces must be equally proportional between the model and prototype, which is a strong constraint for the modeling by similarity law. Here we should be careful about the dimensional dependence of the forces. The forces have different dependences on the length scale l. Assuming a uniform object, the body force is proportional to l^3 , and the surface force is proportional to l^2 . Thus, their ratio is

$$\frac{\text{(body force)}}{\text{(surface force)}} \propto \frac{l^3}{l^2} = l. \tag{2.126}$$

This relation indicates that the body force decays faster than the surface force when the size of the forced object becomes small. In other words, the body or surface force is dominant in large or small objects, respectively. Representative body forces are gravity and inertia, and representative surface forces originate from pressure and shear stress. In general, the surface force becomes less important for a large object.

Furthermore, surface tension is proportional to *l*. Thus, this effect dominates considerably smaller phenomena than body and surface forces. The ratio between the body force and surface tension force is written as

$$\frac{\text{(body force)}}{\text{(surface tension force)}} \propto \frac{l^3}{l} = l^2. \tag{2.127}$$

The surface tension effect is limited to a very small scale, which explains why the length scale of capillary-related phenomena under gravity is limited to the capillary length (Eq. (2.99)). These size dependences of the dominant forces could

be the origin of the complexity of granular behavior. Dominant inter-granular forces crossover depending on the size and shape of grains.

The energies by these forces can be dimensionally estimated as

$$E_{\rm body} \sim \rho a l^4,$$
 (2.128)

$$E_{\rm surf} \sim \sigma l^3,$$
 (2.129)

$$E_{\rm tension} \sim \gamma_c l^2,$$
 (2.130)

where E_{body} , E_{surf} , and E_{tension} are the energies expressed by the body force, surface force, and surface tension, respectively. From Eq. (2.129), one can realize that stress σ can be regarded as energy density. Additionally, Eq. (2.130) implies that the surface tension γ_c corresponds to the surface energy per unit area.

We have assumed that the material properties such as density ρ , elastic moduli G and E, viscosity η , and surface tension γ_c are constant. This assumption is reasonable in many cases. If these values vary significantly depending on the length scale l, the simple dimensional considerations discussed above fail to hold, which is a limitation of the dimensional consideration. Even in such a situation, if the material properties are scaled by the size, the dimensional analysis method remains applicable.

2.9 Summary

The basic concept and fundamental tools necessary to read the remainder of this book were introduced in this chapter. First, stress, strain, strain rate, and their relations were briefly explained. After discussing the simplest constitutive laws (linear viscosity and elasticity), the Navier-Stokes equation was derived from the linear momentum conservation law. Then, the dimensional analysis method was overviewed on the basis of nondimensionalization of the governing equation. The Π -groups method and other physical considerations were also used to demonstrate the usefulness of the dimensional analysis. To prepare for the discussion of soft impact drag force (Chap. 4), the conventional theory of the fluid drag force model was also reviewed. Next, the various dimensionless numbers that are relevant to the characterization of soft impact mechanics and cratering were summarized as listed in Table 2.5. Finally, the ideas of similar modeling and similarity law were discussed. All the topics discussed in this chapter will be foundations for the understanding of soft impact phenomena. We are now almost ready to proceed. Those who wish to study further can read some textbooks on continuum mechanics [3–5] and scaling (dimensional analysis) [2, 10]. In the next chapter, some advanced constitutive relations will be introduced, in addition to some interesting phenomenologies of complex granular behaviors. These phenomenologies are also powerful and necessary for a physical understanding of the soft impact phenomena.

References 61

References

- 1. J.C. Maxwell, Proc. Lond. Math. Soc. 3, 257 (1871)
- 2. G.I. Barenblatt, Scaling (Cambridge University Press, Cambridge, 2003)
- 3. Y. Fung, A First Course in Continuum Mechanics, 3rd edn. (Prentice Hall, New Jersey, 1993)
- 4. P.K. Kundu, I.M. Cohen, D.R. Dowling, Fluid Mechanics, 5th edn. (Academic, Waltham, 2011)
- P. Oswald, Rheophysics: The Deformation and Flow of Matter (Cambridge University Press, Cambridge, 2009)
- K.K. Rao, P.R. Nott, An Introduction to Granular Flow (Cambridge University Press, Cambridge, 2008)
- 7. E. Buckingham, Phys. Rev. 4, 345 (1914)
- 8. E. Buckingham, Nature **96**, 396 (1915)
- 9. D. Bolster, R.E. Hershberger, R.J. Donnelly, Phys. Today 64, 42 (2011)
- 10. J.C. Gibbings, *Dimensional Analysis* (Springer, London, 2011)
- 11. A.A. Sonin, PNAS 101, 8525 (2004)
- 12. G. Taylor, Proc. R. Soc. A 201, 159 (1950)
- 13. G. Taylor, Proc. R. Soc. A 201, 175 (1950)
- 14. K.L. Johnson, *Contact Mechanics* (Cambridge University Press, Cambridge, 1985)
- 15. K.L. Johnson, K. Kendall, A.D. Roberts, Proc. R. Soc. A 324, 301 (1971)
- 16. M.K. Chaudhury, G.M. Whitesides, Langmuir 7, 1013 (1991)
- 17. P. de Gennes, Scaling Concepts in Polymer Physics (Cornell University Press, Ithaca, 1979)
- P. de Gennes, F. Brochard-Wyart, D. Quéré, Capillarity and Wetting Phenomena Drops, Bubbles, Pearls, Waves (Springer, New York, 2004)
- 19. L.D. Landau, E.M. Lifshitz, Fluid Mechanics (Pergamon, London, 1960)
- 20. A. May, J.C. Woodhull, J. Appl. Phys. 19, 1109 (1948)
- 21. D. Gilbarg, R.A. Anderson, J. Appl. Phys. 19, 127 (1948)
- 22. T.T. Truscott, A.H. Techet, J. Fluid Mech. **625**, 135 (2009)
- 23. J.W. Glasheen, T.A. McMahon, Phys. Fluids 8, 2078 (1996)
- 24. J.W. Glasheen, T.A. McMahon, Nature **380**, 340 (1996)
- 25. A. May, J.C. Woodhull, J. Appl. Phys. 21, 1285 (1950)
- 26. W.G.V. Rosser, An Introduction to Statistical Physics (Wiley, New York, 1982)
- 27. P.S. Epstein, Phys. Rev. 23, 710 (1924)
- 28. W.A. Allen, E.B. Mayfield, H.L. Morrison, J. Appl. Phys. 28, 370 (1957)
- 29. W.A. Allen, E.B. Mayfield, H.L. Morrison, J. Appl. Phys. 28, 1331 (1957)
- 30. R.A. Bagnold, Proc. R. Soc. A 225, 49 (1954)
- 31. C.S. Campbell, M.L. Hunt, R. Zenit, C.E. Brennen, J. Fluid Mech. 452, 1 (2002)
- 32. GDR MiDi, Eur. Phys. J. E 14, 341 (2004)
- 33. F. da Cruz, S. Emam, M. Prochnow, J.N. Roux, F.m.c. Chevoir, Phys. Rev. E 72, 021309 (2005)
- 34. S.B. Savage, K. Hutter, J. Fluid Mech. 199, 177 (1989)
- 35. C. Ancey, P. Coussot, P. Evesque, J. Rheol. 43, 1673 (1999)
- 36. M.K. Hubbert, Bull. Geol. Soc. Am. 48, 1459 (1937)
- 37. L.L. Nettleton, Bull. Geol. Soc. Am. 18, 1175 (1934)
- 38. D.C. Barton, Bull. Geol. Soc. Am. 17, 1025 (1933)
- 39. M.K. Hubbert, Bull. Geol. Soc. Am. **62**, 356 (1951)
- 40. P. Cobbold, L. Castro, Tectonophys. **301**, 1 (1999)
- 41. Y. Yamada, Y. Yamashita, Y. Yamamoto, Tectonophys. 484, 156 (2010)

Chapter 3 Constitutive Laws

Constitutive laws describe the relation among macroscopic quantities such as stress, strain, and strain rate. Although most of the constitutive laws for complex soft matter are empirically introduced, they are useful to quantitatively evaluate the deformation and flow states of soft matter. In this chapter, some classic constitutive laws such as viscoelasticity and viscoplasticity are first explained. Rebound and its restitution coefficient are explained using a simple viscoelastic oscillation. Then, models of transport phenomena such as diffusion and advection are briefly reviewed. After describing frictional constitutive laws, peculiar characteristics of granular matter are presented in terms of constitutive laws. The indefiniteness of the frictional property makes understanding static granular behaviors very difficult. Most of these discussions and characteristics are relevant to the analysis of granular-related soft impact phenomena.

3.1 Viscoelasticity

Viscoelasticity refers to a combination of viscosity and elasticity. Linear viscosity and elasticity were already introduced in Sects. 2.2 and 2.3. Many natural materials, however, cannot be purely described by linear constitutive laws. Natural materials often exhibit complex nonlinear rheological behaviors. To characterize complex rheological behaviors, viscosity and elasticity can be coupled. Viscous behavior is modeled by a dashpot element, which satisfies the viscous constitutive law $\sigma = \eta \dot{\gamma}$, where σ , η and $\dot{\gamma}$ are stress, viscosity, and strain rate, respectively (Eq. (2.17)). Linear elasticity is modeled by a spring element, which satisfies the simplified version of Eq. (2.18), $\sigma = G\gamma$. Using these elements, viscosity and elasticity can be merged as viscoelasticity.

There are two classic models of viscoelasticity: the Maxwell model and the Kelvin-Voigt model. Schematic illustrations of these models are presented in

Fig. 3.1 Schematic illustrations of classic viscoelastic models. (a) The Maxwell model consists of a series connection of a dashpot and spring. (b) The Kelvin-Voigt model consists of parallel connection of these elements

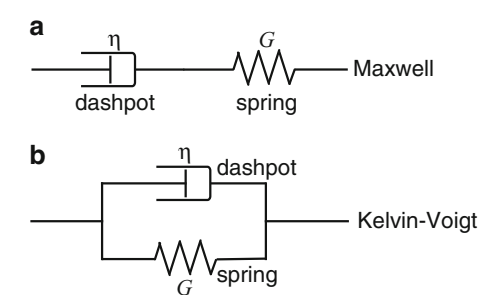


Fig. 3.1. The former is defined by a series connection of a dashpot and a spring (Fig. 3.1a), and the latter corresponds to their parallel connection (Fig. 3.1b). In the Maxwell model, the stress applied to the dashpot element σ_{η} and that applied to the spring element σ_{G} are identical because of the action-reaction law. In contrast, the strain of the dashpot element γ_{η} and that of the spring element γ_{G} are not common but are distributed simply because they are connected in series. Namely, the conditions are written as $\sigma_{M} = \sigma_{\eta} = \sigma_{G}$ and $\gamma_{M} = \gamma_{\eta} + \gamma_{G}$, where σ_{M} and γ_{M} are the exerted stress and associated strain of the entire Maxwell model, respectively. Using the linear elastic and viscous constitutive laws, the governing equation for the Maxwell model can be written as

$$\frac{d\gamma_M}{dt^*} = \frac{d\sigma_M^*}{dt^*} + \left(\frac{Gt_o}{\eta}\right)\sigma_M^*,\tag{3.1}$$

where $t^* = t/t_o$ and $\sigma_M^* = \sigma_M/G$ are the nondimensionalized time normalized to the characteristic timescale t_o and the stress normalized to the elastic modulus G, respectively. Internal stress relaxation can be modeled by solving Eq. (3.1) with boundary conditions $\sigma_M(t=0) = \sigma_0 = G\gamma_M(t=0)$ and $d\gamma_M/dt = 0$. These conditions correspond to a suddenly applied constant strain γ_M , which initially induces an internal stress $G\gamma_M$. The internal stress is first stored in a spring element, and then, it is gradually dissipated by a viscous dashpot element. Using this procedure, the internal stress relaxation is observed as a simple exponential function:

$$\sigma_M^* = \frac{\sigma_0}{G} \exp\left(-\frac{Gt_o}{\eta}t^*\right). \tag{3.2}$$

Similarly, the governing equation for the Kelvin-Voigt model is derived. In the Kelvin-Voigt model, stress is distributed and strain is common among a dashpot and a spring. Thus, the entire stress σ_V and strain γ_V for the Kelvin-Voigt model satisfy the relations $\sigma_V = \sigma_\eta + \sigma_G$ and $\gamma_V = \gamma_\eta = \gamma_G$. Using a similar computation as for the Maxwell model case, the governing equation of the Kelvin-Voigt model is obtained as

3.1 Viscoelasticity 65

$$\frac{d\gamma_V}{dt^*} = \sigma_V^* - \left(\frac{Gt_o}{\eta}\right)\gamma_V. \tag{3.3}$$

For the Kelvin-Voigt model, the stress is normalized as $\sigma_V^* = \sigma_V/(\eta/t_o)$. A creep motion can be designed using this model. Solving Eq. (3.3) with boundary conditions $\sigma_V = \sigma_0$ (a constant independent of time) and $\gamma_V(t=0) = 0$, the creep motion is computed as

$$\gamma_V = \frac{\sigma_0}{G} \left[1 - \exp\left(-\frac{Gt_0}{\eta}t^*\right) \right]. \tag{3.4}$$

Using this boundary condition, the stress is applied suddenly and maintained constant. Then, the applied stress induces viscous (creep) motion in the early stage. After that, the strain gradually increases and is finally saturated at the asymptotic value σ_0/G resulting from the elastic support by a spring element.

The ratio of the elastic modulus and viscosity introduces a characteristic timescale. In the nondimensionalization of the Maxwell model, stress σ_M is normalized to G because the initially applied stress is mainly supported by a spring element at the early stage. In the nondimensionalization of the Kelvin-Voigt model, the stress σ_V is normalized to η/t_o because the initial stress is principally supported by a dashpot element. Actually, both normalizations result in the exponential relaxations for the Maxwell model (Eq. (3.2)) and Kelvin-Voigt model (Eq. (3.4)); the normalization factor is rather arbitrary. From these similar exponential relaxation forms, a characteristic timescale in the simple viscoelastic systems is deduced as

$$t_M = \frac{\eta}{G},\tag{3.5}$$

where t_M is called the viscoelastic relaxation time (or Maxwell time). Using this relaxation timescale, the Deborah number (Eq. (2.106)) for the viscoelastic system is written as

$$D_e = \frac{\eta}{G} \frac{U}{I},\tag{3.6}$$

where U and l are the representative speed and length scale, respectively. In the Maxwell model, the elasticity dominates the dynamics at the timescale shorter than t_M . The elasticity represents a memory of the initial shape, i.e., the memory of the initial shape is partly maintained by the elasticity in a short time regime. This memory effect corresponds to the energy conservation. In contrast, viscosity dominates the dynamics of the Maxwell model at the longer time regime, $t > t_M$. The viscous dashpot element dissipates energy in this longer time regime. Thus, the Maxwell model finally dissipates the energy through the viscosity of the dashpot element. In this sense, the Maxwell model can be considered a viscoelastic fluid at the long time limit that can flow slowly and relax the initial stress at the long time limit. Furthermore, the memory of the initial shape is finally lost. In contrast, the

Kelvin-Voigt model might be regarded as a sort of viscoelastic solid at the long time limit. Its dynamics is dominated by viscosity at a short time, $t < t_M$, but behaves elastically at a long time, $t > t_M$. The applied stress is supported by a spring element at the long time limit. The applied stress is finally balanced with the elasticity of the spring element. Note that the viscosity also dissipates the energy in the Kelvin-Voigt model. In the short time range $t < t_M$, furthermore, the Maxwell and Kelvin-Voigt models show elastic and viscous responses, respectively. t_M is the switching timescale from elastic to viscous (Maxwell) or from viscous to elastic (Kelvin-Voigt).

The Maxwell and Kelvin-Voigt models are the most fundamental viscoelastic models. Using various combinations of elementary units (Hooke's spring and viscous dashpot), advanced rheological models have been proposed to explain complex viscoelastic behaviors. Examples include Burgers model, Jeffrey model, and generalized Maxwell model. For further study of such various rheological models, Ref. [1] is a good textbook.

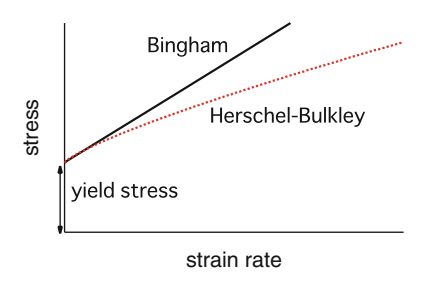
3.2 Plasticity and Nonlinear Flow

Plasticity can also be modeled by a simple constitutive law. The classic viscoelastic models can explain a certain class of viscoelasticity but are not almighty. The Maxwell model behaves like a fluid because it finally flows and relaxes the internal stress approximately at the timescale t_M . This behavior indicates that the Maxwell model exhibits plastic deformation or flow. This model finally obliterates the memory of the initial shape. There is no any limitation of deformation in the Maxwell model, which appears natural because usual viscous fluids also have no limitation of deformation. In contrast, the Kelvin-Voigt model exhibits a solid-like response to the applied stress at a long time regime, $t > t_M$. All the stress must be finally supported by the elasticity. Thus, this model recovers the initial shape when the applied stress is removed. While the model maintains a perfect memory, the recovery requires a finite time approximately t_M . Additionally, the energy is dissipated by viscosity during the creep motion and its recovery to the initial shape. In this creep motion, no limitation of the elastic deformation is employed again. However, this assumption is slightly strange because every solid-like object has its strength as a limit of elastic deformation. When the applied stress exceeds a certain limit, the stress cannot be supported by elasticity and the material starts to fracture and flow. This plastic property can be considered using the yield stress Y_s . The simplest plastic constitutive law is the Bingham model. If the applied stress is less than Y_s , the behavior is similar to an elastic solid. Once the applied stress exceeds Y_s , the object starts to flow. The Bingham model assumes the simple linear viscous law (Eq. (2.17)) in the flow regime, which is a type of typical viscoplastic behavior.

¹If the elastic behavior below Y_s is focused, the word elastoplasticity is used.

3.3 Complex Moduli 67

Fig. 3.2 Viscoplastic constitutive laws. The *solid line* and *dotted curve* correspond to the Bingham model and Herschel-Bulkley model, respectively. Both models consist of the yield stress and linear or nonlinear viscosity



In classic viscoelastic models, the timescale t_M is a separator between elastic and viscous regimes. Similarly, the yield stress Y_s partitions the elastic and plastic regimes in a viscoplastic model. Furthermore, if the nonlinear relation between the stress and strain rate is considered in the flow regime, the constitutive law called the Herschel-Bulkley model is written as

$$\sigma = Y_s + k\dot{\gamma}^n,\tag{3.7}$$

where k and n are parameters characterizing the flow. When n is unity, Eq. (3.7) corresponds to the Bingham model. Usually, the exponent n is in the range of $0 < n \le 1$ [1]. The viscoplastic constitutive laws are schematically illustrated in Fig. 3.2.

3.3 Complex Moduli

Next, we consider dynamic rheology. In the above discussion, idealized very simple models were considered. Although the constancy of t_M is assumed both in the Maxwell and Kelvin-Voigt models, the relaxation timescale t_M is not a constant in general. To extend the framework of rheological characterizations, the steady-state dynamic rheological characterization is frequently employed. Let us consider a simple sinusoidal strain with amplitude γ_0 and angular frequency $\omega(=2\pi f,$ where f is the frequency) as

$$\gamma = \gamma_0 \exp(i\omega t), \tag{3.8}$$

where *i* is the imaginary unit. In the dynamic steady-state regime, stress σ and strain γ can be related as

$$\sigma(t) = G^*(\omega)\gamma(t),\tag{3.9}$$

where G^* is the complex modulus that is decomposed as

$$G^* = G' + iG'', (3.10)$$

in which G' and G'' are the storage modulus and loss modulus, respectively. The former represents the in-phase elastic response, and the latter represents the in-quadratic-advance viscous response. In this notation, σ is written as

$$\sigma = \sigma_0 \exp(i\omega t + \delta_l), \tag{3.11}$$

where σ_0 is the stress amplitude and δ_l is the loss angle. δ_l relates to G' and G'' as

$$G' = \frac{\sigma_0}{\gamma_0} \cos \delta_l,\tag{3.12}$$

$$G'' = \frac{\sigma_0}{\gamma_0} \sin \delta_l. \tag{3.13}$$

When the loss angle δ_l is zero, the corresponding rheological behavior is a purely elastic and conservative. In contrast, when $\delta_l = \pi/2$, purely viscous (dissipative) response is observed. These two end-member effects are mixed in general viscoelastic materials. In the dynamic steady state, the aforementioned rheometrical method is very powerful and widely used to characterize various soft matter. Note that the elementary constitutive laws are assumed to be linear ($\sigma = G'\gamma$ and $\sigma = G''\dot{\gamma}$) for each ω . The relation among σ_0 , γ_0 , and δ_l depends on ω . Because $2\pi\omega^{-1}$ corresponds to a characteristic timescale of the stress-strain relation, the relations such as Eqs. (3.12) and (3.13) denote the relative importance of viscosity and elasticity at the timescale $2\pi\omega^{-1}$. The analysis of the steady response to sinusoidaloscillation input is very compatible because the derivative of the sinusoidal function can be simply expressed by the phase shift, $d\sin(\omega t)/dt = \omega\sin(\omega t + \pi/2)$. Thus, this type of dynamical rheometry becomes the standard approach to characterize the dynamic property at steady states. In contrast, the very transient dynamics of the impact is the main focus of this book. The impact drag force is also useful to characterize the behavior of soft matter, as discussed in the following chapters.

3.4 Rebound, Attenuating Oscillation, and Restitution Coefficient

Rebound, resulting from an impact, is a very fundamental phenomenon particularly in the case of solid impacts. The restitution coefficient is used to characterize the state of rebound. The normal restitution coefficient ϵ_r is defined as

$$\epsilon_r = -\frac{\mathbf{v'} \cdot \mathbf{n}}{\mathbf{v} \cdot \mathbf{n}},\tag{3.14}$$

where v, v', and n are the velocity before impact, velocity after impact, and normal vector of the impact, respectively. Usually, the direction of the velocity after the impact becomes opposite to that before the impact, which indicates that ϵ_r is

usually positive. If $\epsilon_r = 1$, the kinetic energy is conserved, and this collision is called an elastic collision. In general, ϵ_r is less than unity because of the energy dissipation. This dissipative rebound is called an inelastic collision. Thus, ϵ_r should be in the range $0 \le \epsilon_r \le 1$. Moreover, ϵ_r is considered a material-dependent constant. These assumptions work well as a first-order approximation; however, the actual ϵ_r depends on various factors such as the impact velocity, angle, and impactor's size. For example, ϵ_r is scaled by the impact velocity \mathbf{v} as $\epsilon_r \propto |\mathbf{v}|^{1/4}$ by considering plastic deformation [2]. Furthermore, ϵ_r can exceed unity by an oblique impact of a solid ball on an elastic plate [3, 4]. In this case, translational momentum is transferred to the normal direction by the oblique impact. Thus, the energy conservation law is not broken by this pseudo kinetic energy gain. Note that ϵ_r in Eq. (3.14) is defined only by the normal component. A collision with $\epsilon_r > 1$, called super rebound, has also been observed in nanocluster collisions [5, 6]. In nano collisions, thermal energy is sometimes transformed into translational kinetic energy, although such an abnormal energy transfer rarely occurs. Negative ϵ_r can also be observed in a nanocluster oblique impact [7]. In general, the restitution coefficient is a very complex function comprising various parameters such as impact velocity and adhesion force [8, 9]. Nevertheless, ϵ_r is usually assumed to be constant in many cases for the sake of simplicity.

The restitution coefficient of an inelastic collision can be modeled by viscous damping in a simple viscoelastic impact. Let us consider the one-dimensional viscoelastic equation of motion for a deformable body of mass m_i and length scale D_i :

$$m_i \frac{d^2x}{dt^2} = -kx - \eta D_i \frac{dx}{dt},\tag{3.15}$$

where t, x, k, and η correspond to the time, deformation, effective spring constant, and effective viscosity, respectively. This equation of motion is similar to the Kelvin-Voigt viscoelastic model, and this linear ordinary differential equation (ODE) can be easily solved as²

$$x = x_0 \exp\left[\left(-\frac{\eta D_i t}{2m_i}\right) + i\left(\frac{t\sqrt{4m_i k - \eta^2 D_i^2}}{2m_i}\right)\right],\tag{3.16}$$

with an initial condition $x(t = 0) = x_0$. In this model, a dissipative spring behavior is assumed to model the viscoelastic rebound. Concretely, we assume that the impact and rebound occur at t = 0 and at its half cycle of oscillation, respectively. When $4m_ik < \eta^2 D_i^2$, the system becomes overdamped, i.e., no rebound occurs. Otherwise,

²The easiest way is to assume the form $x = x_0 \exp(\lambda_x t)$. By substituting this form into Eq. (3.15) and selecting a relevant solution, one can obtain Eq. (3.16).

the rebound occurs at a half cycle of oscillation, $t\sqrt{4m_ik - \eta^2D_i^2}/2m_i = \pi$. Because Eq. (3.16) describes simple exponential decay, the corresponding velocity v = dx/dt also obeys the exponential decay with the same decay rate. Therefore, by considering Eq. (3.14), ϵ_r of this viscoelastic rebound is written as

$$\epsilon_r = \exp\left(-\frac{\pi \eta D_i}{\sqrt{4m_i k - \eta^2 D_i^2}}\right). \tag{3.17}$$

When the impact is inviscid ($\eta = 0$), an elastic collision ($\epsilon_r = 1$) is recovered. This simple relation between the restitution coefficient and viscous damping is frequently used to evaluate or define ϵ_r in numerical simulations of granular matter such as the discrete element method (DEM). DEM is one of the most famous and widely employed granular computation methods [10]. In actual DEM simulations, some other effects (e.g., tangential friction) are also considered.

Dissipation by the inelastic collision plays a crucial role, particularly in dilute granular gas. In dense granular flow or deformation, friction is more important. Because we will focus on the dense regime in the following chapters, frictional constitutive laws will be discussed in more detail in Sect. 3.6.

Equation (3.15) presents the general form of attenuating oscillations. We can define a dimensionless dissipation rate by the nondimensionalization of Eq. (3.15). By introducing representative and dimensionless values for time and deformation as $t = t_0 t^*$ and $x = x_0 x^*$, respectively, Eq. (3.15) can be nondimensionalized as

$$\frac{d^2x^*}{dt^{*2}} - -t_o^2 \frac{k}{m_i} x^* - t_o \frac{\eta D_i}{m_i} \frac{dx^*}{dt^*}.$$
 (3.18)

As a characteristic timescale, here we employ a period of harmonic oscillation $t_o = \sqrt{m_i/k}$. Substituting this value into Eq. (3.18), the simplest version of the dimensionless equation of attenuating oscillation is obtained:

$$\frac{d^2x^*}{dt^{*2}} = -x^* - \frac{\eta D_i}{\sqrt{m_i k}} \frac{dx^*}{dt^*}.$$
 (3.19)

Thus, the most important dimensionless parameter for attenuating oscillation can be defined as

$$\frac{1}{Q} = \frac{\eta D_i}{\sqrt{m_i k}}. (3.20)$$

Q is called the quality factor. The reciprocal of quality factor Q^{-1} indicates the dimensionless attenuation (dissipation) rate per oscillation's unit time, $\sqrt{m_i/k}$ (= $T_p/2\pi$, where T_p is the period of harmonic oscillation). Because Q^{-1} is an indicator

of the attenuation rate, large Q indicates small attenuation, and vice versa. If $4m_i k \gg \eta^2 D_i^2$, Eq. (3.17) can be approximated by $\epsilon_r \simeq \exp(\pi/2Q)$.

3.5 Transport Phenomena

Transport phenomena are ubiquitous in nature. Although achieving a microscopic understanding of transport phenomena is not so easy, the phenomenological modeling of transport is relatively comprehensible in terms of constitutive relations. In this section, we focus on diffusion and advection, and their fundamentals are briefly introduced.

We have already derived the equation for transport phenomena. We must return to the Navier-Stokes equation of the incompressible Newtonian fluid. By neglecting the body force and pressure gradient terms in Eq. (2.30), one can obtain a simple equation:

$$\frac{\partial \mathbf{u}}{\partial t} = -(\mathbf{u} \cdot \nabla)\mathbf{u} + \frac{\eta}{\rho} \nabla^2 \mathbf{u}. \tag{3.21}$$

This equation is called the advection-diffusion equation. Although this form was derived on the basis of the conservation law in Sect. 2.4, it can also be understood by another basis. In this section, each term in Eq. (3.21) is re-examined from the viewpoint of transport phenomena. The first and second terms on the right-hand side correspond to advection and diffusion, respectively. This equation actually models momentum transport in an incompressible fluid both by advection and lateral diffusion.

Transport phenomena are generally modeled by the following flux equation:

$$J_i = \sum_j K_{ij} L_j, \tag{3.22}$$

where J_i , K_{ij} , and L_j correspond to the flux of the *i*-th component, transport coefficients, and *j*-th driving force of the transport under consideration. In general, some transport fluxes and driving forces are coupled by Eq. (3.22), and the number of fluxes *i* and driving forces *j* is not necessarily determined a priori. For the sake of brevity, however, here we consider the case of $K_{ij} = \delta_{ij}K_t$, where δ_{ij} is Kronecker's delta. Additionally, we assume that K_t is a constant. Then, Eq. (3.22) is simplified to a simple linear transport relation among the flux J, driving force L, and transport coefficient K_t as $J = K_t L$.

3.5.1 Diffusion

To consider diffusion transport, a gradient-dependent driving force should be assumed. Let us consider a transport of general physical quantity Ψ and assume that its driving force L is expressed by its spatial gradient, $\nabla \Psi$. Then, the flux of Ψ is written as

$$\boldsymbol{J} = K_d \nabla \Psi, \tag{3.23}$$

where K_d is a transport coefficient. This type of gradient-driven transport phenomena is ubiquitous in nature, e.g., Ψ can be the temperature (Fourier's law), fluid momentum (Newtonian viscosity), material density (Fick's law), or electrostatic potential (Ohm's law). If the flux J is spatially uniform as $K_d \nabla \Psi = \text{const.}$, a steady flow of Ψ is achieved, and Ψ becomes independent of time everywhere. However, when J is spatially inhomogeneous, the spacial distribution of Ψ varies with time depending on the profile of $\nabla \Psi$.

To examine the flux balance, the one-dimensional case is first considered. The temporal variation of Ψ in a small range between x and x + dx, Ψdx , is induced because of the difference of the inflow J and outflow $J + (\partial J/\partial x)dx$ (Fig. 3.3). Thus, the temporal variation of Ψdx is written as

$$\frac{\partial \Psi}{\partial t}dx + J - \left(J + \frac{\partial J}{\partial x}dx\right) = 0. \tag{3.24}$$

By expanding this calculation to three-dimensional space, one can obtain a relation

$$\frac{\partial \Psi}{\partial t} = \nabla \cdot \boldsymbol{J}.\tag{3.25}$$

This equation represents the most fundamental law in the modeling of transport phenomena and is called the equation of continuity. Note that this equation is held both for diffusion and advection. Gauss' theorem used in Sect. 2.4 actually corresponds to the integral form of this equation. Substituting Eq. (3.23) into Eq. (3.25), the diffusion equation is obtained as

$$J(x) \xrightarrow{\partial \psi} dx \qquad J(x) + \frac{\partial J(x)}{\partial x} dx$$

$$\downarrow \qquad \qquad \downarrow \qquad \qquad \qquad \downarrow \qquad \qquad \qquad \downarrow \qquad$$

Fig. 3.3 Schematic image of the transport of quantity $\Psi(x,t)$ in a one-dimensional space. If J(x,t) is not spatially uniform, a local increase or decrease of $\Psi(x,t)dx$ is produced by the gradient of the flux. The balance law is denoted in Eqs. (3.24) and (3.25)

$$\frac{\partial \Psi}{\partial t} = K_d \nabla^2 \Psi. \tag{3.26}$$

Here we assume that K_d (called the diffusion coefficient (or diffusivity)) is constant. The dimension of K_d is $[K_d] = L^2T^{-1}$.

The diffusion equation is readily nondimensionalized. By introducing representative values for each quantity as $\Psi = \Psi_o \Psi^*$, $t = t_o t^*$, and $\nabla = l^{-1} \nabla^*$, Eq. (3.26) is nondimensionalized as

$$\frac{\partial \Psi^*}{\partial t^*} = \frac{K_d}{l^2/t_o} \nabla^{*2} \Psi^*. \tag{3.27}$$

Thus, the important dimensionless value for the diffusion is $K_d t_o/l^2$. This dimensionless number represents the rate of diffusive transport, and this value should be a constant in the uniform diffusional field. Then, a simple form of the spreading distance l during t_o is obtained as

$$l \sim \sqrt{K_d t_o},$$
 (3.28)

which is a general relation held in diffusion transport. More generally, the relation $l \propto t_o^{\alpha_d}$ is frequently observed in various natural transport phenomena. When $\alpha_d > 1/2$, the phenomenon is called super-diffusion, and the transport with $\alpha_d < 1/2$ is called sub-diffusion.

Diffusion and random walk Diffusion transport can be regarded as a collection of independent random walks. Let us consider many random walkers distributed in a one-dimensional space. The number density of random walkers at position x and time t is denoted by $\Psi(x,t)$. All the random walkers are supposed to be independent and move back and forth with equal probability. We define that the random walkers move distance $|\Delta x|$ during a short time Δt . Then, the expected number density of random walkers $\Psi(x,t)$ obeys the following relation:

$$\Psi(x, t + \Delta t) - \Psi(x, t) = \frac{1}{2}\Psi(x + \Delta x, t) + \frac{1}{2}\Psi(x - \Delta x, t) - \Psi(x, t).$$
 (3.29)

The left-hand side indicates the increase or decrease in the number density of random walkers during Δt at position x. The first and second terms on the right-hand side correspond to the inflow of random walkers from the positions $x \pm \Delta x$, and the last term expresses the outflow by the random walk. Using a Taylor expansion, Eq. (3.29) can be rewritten as

$$\frac{\partial \Psi}{\partial t} \Delta t + \mathcal{O}((\Delta t)^2) = \frac{1}{2} \frac{\partial^2 \Psi}{\partial x^2} (\Delta x)^2 + \mathcal{O}((\Delta x)^4). \tag{3.30}$$

Neglecting the higher-order terms $\mathcal{O}((\Delta t)^2)$ and $\mathcal{O}((\Delta x)^4)$, one can obtain the one-dimensional diffusion equation with a diffusion coefficient $K_d = (\Delta x)^2/2\Delta t$,

which is certainly consistent with Eq. (3.28). This result indicates that diffusion can occur by superimposing a large number of independent random walks. The above calculation can be easily expanded to two- or three-dimensional space.

Solutions of the diffusion equation We can solve the one-dimensional diffusion equation with infinite or semi-infinite boundary conditions [11]. To simplify the diffusion equation on the basis of Eq. (3.28), we employ a dimensionless variable $\xi = x/2 \sqrt{K_d t}$. Then, $\partial \Psi / \partial t$ is written as

$$\frac{\partial \Psi}{\partial t} = \frac{d\Psi}{d\xi} \frac{\partial \xi}{\partial t} = \frac{d\Psi}{d\xi} \left(-\frac{\xi}{2t} \right). \tag{3.31}$$

A similar chain rule for differentiation can be applied to the spatial derivative. Thus, the diffusion term is rewritten as

$$\frac{\partial^2 \Psi}{\partial x^2} = \frac{\partial}{\partial x} \left(\frac{d\Psi}{d\xi} \frac{\partial \xi}{\partial x} \right) = \frac{1}{2\sqrt{K_d t}} \frac{d^2 \Psi}{d\xi^2} \frac{\partial \xi}{\partial x} = \frac{1}{4K_d t} \frac{d^2 \Psi}{d\xi^2}.$$
 (3.32)

By introducing a variable $\phi = d\Psi/d\xi$, the diffusion equation is finally cast into a first-order ODE as

$$-\xi\phi = \frac{1}{2}\frac{d\phi}{d\xi}.\tag{3.33}$$

This equation can be immediately integrated as $-\xi^2 = \ln \phi - \ln c_o$, where c_o is an integral constant. This relation is transformed into

$$\phi = \frac{d\Psi}{d\xi} = c_o \exp(-\xi^2). \tag{3.34}$$

Considering the Gaussian integral formula, $\int_0^\infty \exp(-x^2) dx = \sqrt{\pi}/2$, a solution for the diffusion equation is computed as

$$\Psi = \frac{2c_o}{\sqrt{\pi}} \int_0^{\xi} \exp(-\xi'^2) d\xi' = c_o \text{erf}(\xi).$$
 (3.35)

The integral function $erf(\xi)$ is called the error function of ξ . Finally, the diffusion in one-dimensional semi-infinite space can be described by a simple form:

$$\Psi = \Psi_0 \operatorname{erf}\left(\frac{x}{2\sqrt{K_d t}}\right). \tag{3.36}$$

This form corresponds to a solution under the initial condition $\Psi(t=0) = \Psi_0$ (independent of x) and the boundary conditions $\Psi(x=0) = 0$ and $\Psi(x=\infty) = \Psi_0$ at t > 0 and $x \ge 0$.

More generally, $\Psi(x, t)$ for the space-dependent initial condition can be written as

$$\Psi = \frac{1}{2\sqrt{\pi K_d t}} \int_{-\infty}^{\infty} \Psi_0(x') \exp\left[-\frac{(x - x')^2}{4K_d t}\right] dx'.$$
 (3.37)

To obtain a simple solution example, here we introduce the delta function $\delta(x)$ which satisfies $\int_{-\infty}^{\infty} \delta(x) dx = 1$, $\delta(x) = 0$ at $x \neq 0$, and $\delta(0) = \infty$. By substituting $\Psi_0(x') = \delta(x')$ into Eq. (3.37), a solution of the one-dimensional diffusion equation can be expressed by the Gaussian distribution form

$$\Psi = \frac{1}{2\sqrt{\pi K_d t}} \exp\left(-\frac{x^2}{4K_d t}\right). \tag{3.38}$$

One can easily verify that Eq. (3.38) satisfies the diffusion equation. This solution typically exhibits diffusive propagation from a point source to an infinite space. The profiles of the black-solid and blue-dotted curves in Fig. 3.4 were obtained using Eq. (3.38). The details of Fig. 3.4 will be discussed later in Sect. 3.5.3.

There are some other solutions of the one-dimensional diffusion equation. For instance, a spatially attenuating oscillatory and traveling-wave solution of the diffusion equation is written as

$$\Psi = \Psi_0 \exp(-k_n x) \sin(\omega_n t - k_n x), \tag{3.39}$$

$$k_n = \sqrt{\frac{\omega_n}{2K_d}},\tag{3.40}$$

where ω_n and k_n are the angular frequency and wavenumber, respectively. This attenuating traveling wave can be a solution of the diffusion equation. In this case, the wave number depends on the frequency and diffusion coefficient. Another example, a temporally attenuating solution, can be described as

$$\Psi = \Psi_0 \exp(-K_d k_n^2 t) \sin(k_n x), \tag{3.41}$$

$$k_n = \frac{n\pi}{I},\tag{3.42}$$

where n is a natural number. It is easy to verify that these solutions satisfy the onedimensional diffusion equation. The complex profile of $\Psi(x,t)$ can be expressed by a linear combination of Eqs. (3.39) and (3.41) (of various n) with the help of a Fourier series expansion (the principle of superposition). To use the trigonometric solution of Eq. (3.41), the system size l must be finite to define the wavenumber k_n , in contrast to the solution of Eqs. (3.36), (3.37) and (3.38) in which a semi-infinite boundary condition is assumed.

3.5.2 Advection

Advection is another representative transport phenomenon that is quite different from diffusion. In the last subsection, the gradient of the physical quantity was considered for the driving force of diffusion transport. For advective transport, however, the driving force must be directly proportional to the amount of the physical quantity itself. Namely, the flux is written as

$$J = C_{\Psi}\Psi,\tag{3.43}$$

where C_{Ψ} is a constant. Its dimension is $[C_{\Psi}] = \mathsf{LT}^{-1}$. Using a similar calculation as that used for the diffusion case, we obtain a simple equation:

$$\frac{\partial \Psi}{\partial t} = C_{\Psi} \nabla \Psi. \tag{3.44}$$

This equation is the advection equation. The advection equation is nondimensionalized as

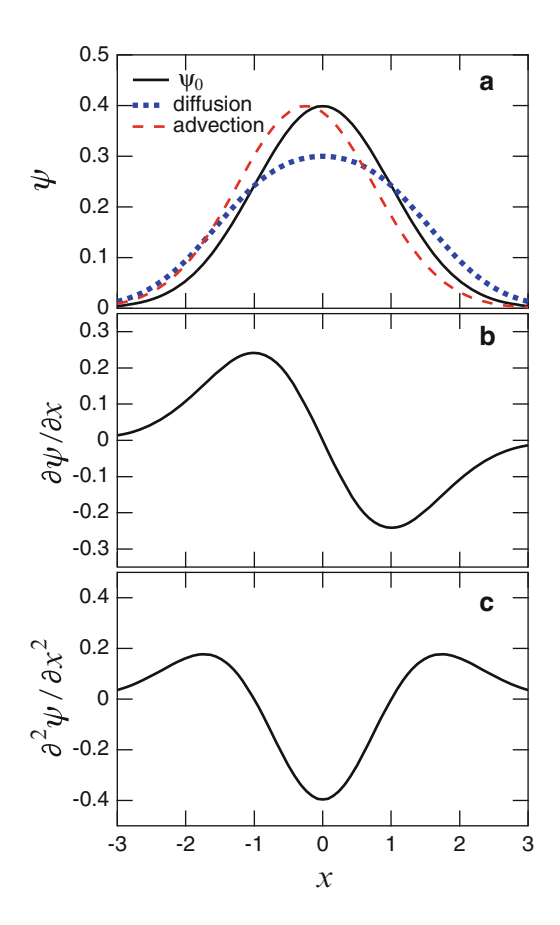
$$\frac{\partial \Psi^*}{\partial t^*} = \frac{C_{\Psi}}{l/t_o} \nabla^* \Psi^*. \tag{3.45}$$

From this nondimensionalized advection equation, it is apparent that the dimensionless number $C_{\Psi}t_o/l$ is a unique quantity to characterize advective transport. The existence of this dimensionless number indicates that $l \sim C_{\Psi}t_o$, i.e., C_{Ψ} corresponds to the drift velocity of advection.

3.5.3 Comparison of Diffusion and Advection

The difference between diffusion and advection can be demonstrated by considering the temporal development of a bump structure. Let us consider the one-dimensional diffusion and advection of an initial bump structure Ψ_0 represented by the black solid curve in Fig. 3.4a. The difference between diffusion and advection is only the order of spatial differentiation. In Fig. 3.4b, c, the first- and second-order spatial derivatives of the initial bump structure are shown, respectively. In addition, the blue dotted curve in Fig. 3.4a represents the diffusion by $\Psi_0 + K_d t_o (\partial^2 \Psi / \partial x^2)$ with $K_d t_o = 1/4$. The flattening tendency of the bump structure due to the diffusional relaxation is clearly confirmed. In fact, these bumps exhibit the Gaussian form. Thus, this diffusive variation in the profile can be understood by different-time snapshots of Eq. (3.38). Steady-state diffusion is achieved by $0 = \frac{\partial^2 \Psi}{\partial x^2}$. The solution of this equation is a constant flux state that is attained when the gradient of Ψ is identical everywhere in x. Thus, the straight line $(\frac{\partial \Psi}{\partial x} = \text{const.})$ is the steady-state solution of the one-dimensional diffusion-based relaxation.

Fig. 3.4 Temporal development of the initial bump structure by diffusion and advection. The black solid curve in (a) represents the initial profile Ψ_0 . The first-order derivative of $\Psi_0(x)$ is presented in (b), and the second-order derivative is presented in (c). The blue dotted curve in (a) indicates $\Psi_0 + K_d t_o (\partial^2 \Psi / \partial x^2)$ which corresponds to diffusion. Because the Ψ_0 in this figure is actually the Gaussian form, these two profiles can be expressed by Eq. (3.38) at different times. The red dashed curve in (a) represents the advection by $\Psi_0 + C_{\Psi} t_o(\partial \Psi/\partial x).$ $K_d t_o = 1/4$ and $C_{\Psi} t_o = 1/4$ are used (in arbitrary units)



Moreover, the horizontal flat state ($\Psi=$ const.) is a steady state if no asymmetry is assumed in the system. In contrast, the advection results in a drift of the bump. In Fig. 3.4a, the profile of $\Psi_0 + C_{\Psi}t_o(\partial\Psi/\partial x)$ is represented by the red dashed curve, where $C_{\Psi}t_o = 1/4$ is used. The drift motion of the bump structure can be confirmed between the black solid and red dashed curves in Fig. 3.4a. As mentioned before, C_{Ψ} corresponds to the traveling rate of advection. Namely, a solution of the advection equation can be written in the form of $\Psi(x,t) = f(x-C_{\Psi}t)$, where $\Psi_0 = \Psi(x,0) = f(x)$ is the initial condition. This traveling wave solution models the propagation of Ψ in one direction with velocity C_{Ψ} , which is the advection phenomenon. Note that the term $(u \cdot \nabla)u$ represents the advection in the Navier-Stokes equation because velocity (momentum per unit mass) transport is considered; $\Psi = C_{\Psi} = u$ in this case.

In general, diffusion and advection coexist such as in Eq. (3.21). In this situation, the strength of diffusion and advection can be compared using the Péclet number (Eq. (2.107))

$$P_e = \frac{C_{\Psi}l}{K_L},\tag{3.46}$$

where l is the representative length scale in the system under consideration. When $P_e \gg 1$, advection is dominant. Furthermore, the other limit, $P_e \ll 1$, corresponds to the diffusion-dominant regime.

We have assumed that transport coefficients such as K_d and C_{Ψ} are constant. These specific values depend on the materials and conditions employed. Moreover, these values may depend on space and time. In the analyses of geological or planetary-scale phenomena, it is difficult to fully consider such complexities in these phenomena because the available information is very limited. Moreover, the model should be as simple as possible. Thus, constant transport coefficients are usually used. Transport phenomena are also very important fundamental processes in the chemical engineering field. Several additional details are required to solve engineering problems. We neglect these difficult points for simplicity's sake. Furthermore, we do not discuss the microscopic mechanics of transport phenomena. In this sense, the diffusion and advection equations are constitutive relations, which explains why transport phenomena are introduced here as a type of constitutive law. This phenomenological approach is a standard methodology in this book.

3.6 Friction

The friction law is also an important constitutive law for general soft matter and geophysical phenomena. The origins of a certain class of earthquakes are slips of faults. Thus, the frictional constitutive law is very important for its dynamics. Although usually expressed by a very simple law, the actual frictional behaviors are very complex. Friction works only at the interface between different or same materials. This behavior contrasts with elasticity and viscosity, which instead characterize deformation and flow, respectively, in a continuous medium.

3.6.1 Coulomb Friction and Angle of Repose

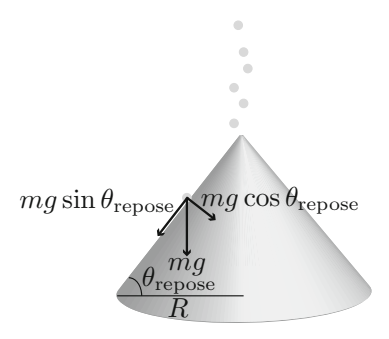
Let us begin with the simplest frictional constitutive law: Coulomb friction. As long as the static friction coefficient μ_0 satisfies the condition

$$\sigma_s \le \mu_0 p, \tag{3.47}$$

the interface never slips. Here σ_s is the shear stress and p is the normal stress at the interface. The slip occurs when σ_s exceeds $\mu_0 p$. This condition is called the Coulomb failure criterion. Friction is an essential factor in the static granular network structure. Microscopically, the granular network structure is supported by the friction at the grains' contacts. The macroscopic friction property of bulk granular matter is not necessarily the same as the microscopic friction property.

3.6 Friction 79

Fig. 3.5 Schematic image of the angle of repose θ_{repose} . A small mass unit m is stable as long as the shear force does not exceed the friction force. The angle of repose shows bistability before and after the angle's relaxation by an avalanche



Here we focus on the bulk frictional property. For bulk granular matter, the friction coefficient $\mu_f \simeq \mu_0$ can be estimated by the angle of repose θ_{repose} as

$$\mu_f = \tan \theta_{\text{repose}}.\tag{3.48}$$

This relation is obtained from the stress balance at the surface of the granular slope. Here we consider a small mass part (particle) m on the surface of a granular pile of inclination angle θ . The shear force acting on this mass unit is $mg \sin \theta$, and the normal force is $mg \cos \theta$. At the critical angle θ_{repose} , the relation $mg \sin \theta_{\text{repose}} = \mu_f mg \cos \theta_{\text{repose}}$ must be satisfied (Fig. 3.5). Equation (3.48) corresponds to this critical relation. The angle of repose is analogous to the internal friction angle θ_i and is measured by a shear test. In the shear test, the shear stress σ_s and confining pressure p at the yielding state are related by [12]

$$\sigma_{\rm s} = p \tan \theta_i + C_c, \tag{3.49}$$

where C_c is the coefficient of cohesion. The value of the angle of repose is very similar to the internal friction angle. However, note that the angle of repose depends on the measuring method and boundary conditions [13].

More generally, μ_f is not a constant. Once slip occurs at the interface, the shear and normal stresses are related by another friction coefficient called the dynamic friction coefficient. This coefficient is usually slightly smaller than the static friction coefficient. For the dynamic friction coefficient μ_d , the inequality in (3.47) becomes the equation

$$\sigma_s = \mu_d p. \tag{3.50}$$

Accordingly, the angle of repose is bistable. If sand grains are slowly poured above the sand heap, the sand grains pile up until the heap angle θ reaches the critical angle θ_m . The critical angle θ_m is called the maximum stable angle. When the heap angle exceeds θ_m , an avalanche occurs on the surface, which relaxes the heap gradient and finally halts. This angle that finally achieves a stable heap and is usually defined as $\theta_{\rm repose}$ is slightly less than the maximum stable angle θ_m .

According to Eq. (3.48), $\tan \theta_m$ and $\tan \theta_{\rm repose}$ roughly correspond to the static and dynamic friction coefficients, respectively. Thus, the relations $\mu_0 = \tan \theta_m$ and $\mu_d = \tan \theta_{\rm repose}$ are more appropriate definition. Nonetheless, the definition of the angle of repose (Eq. (3.48)) is generally used because the measurement of $\theta_{\rm repose}$ is easier than θ_m . When a heap consisting of grains with diameter D_g is formed on a dish of radius R, the difference between these two angles $\delta_\theta = \theta_m - \theta_{\rm repose}$ is negligible under the condition

$$D_{\sigma} > R\delta_{\theta}. \tag{3.51}$$

For large grains satisfying condition (3.51), the addition of a grain causes an increase in angle D_g/R , which is larger than δ_θ . This effect implies that δ_θ cannot be resolved under such a condition; therefore, two angles θ_m and $\theta_{\rm repose}$ degenerate. The condition (3.51) is consistent with experimental results [14]. Typical values are $\delta_\theta \simeq 2^\circ$ and $R \simeq 30 D_g$. In the case of a large granular heap $(R > 30 D_g)$, bistability becomes important. This bistability is a possible source of the history-dependent complex behaviors of granular matter.

3.6.2 Rate- and State-Dependent Friction

Although the Coulomb friction law is simple and convenient to estimate the friction effect, the actual friction is considerably more complex. In fact, the friction coefficient depends on various factors such as the waiting time, slip velocity, and interface roughness. It is not easy to involve all these factors in the macroscopic constitutive law. Perhaps the implication of all these factors is too much. We do not need a complete but complicated constitutive law. What we need here is a useful and simple constitutive law for the friction even if the law is based on empirical results. A well-known frictional constitutive law is rate- and state-dependent friction (RSF) [15]:

$$\mu_f(u) = \mu_f(u_0) + \alpha_u \log \frac{u}{u_0},$$
(3.52)

where u, u_0 , and α_u are the slip velocity, reference velocity, and dimensionless constant, respectively. This constitutive law for the dynamic (steady state) friction has been confirmed by various experiments and widely used to discuss earthquake dynamics³ [16].

While Coulomb friction and RSF are commonly used in a wide range of phenomena, their capabilities are limited. For example, when the slip velocity is

³More precisely, the RSF law is written as $\mu_f(u, \theta') = \mu_f(u_0) + \alpha_u' \log(u/u_0) - \beta_u \log(l/\theta'u_0)$, where θ' is the time-dependent state variable and l is a characteristic length scale. At steady state, Eq. (3.52) is obtained ($\alpha_u = \alpha_u' - \beta_u$) by assuming $\theta' = l/u$.

3.6 Friction 81

decreased to a very slow rate, the mode of motion transitions from continuous slip to unstable stick-slip motion. In the granular stick-slip phenomenon, the friction coefficient is no longer a unique function of the slip velocity [17, 18]. The relation between the friction coefficient and instantaneous slip velocity becomes a loop. This behavior implies that the friction coefficient depends not only on the instantaneous slip velocity but also on the history of motion and degree of fluidization. The relation among the loop of friction coefficient, RSF law, and bistability of the angle of repose has not yet been clarified. The laws are rather independent empirical laws, and their relation must be an important key to understanding the complex nature of friction and granular matter.

In general, it has been considered that the friction does not depend on the apparent contact area and is only a proportional function of the loading pressure (stress). Because of this property, Coulomb's criterion can be written in the form of an inequality of stresses (3.47). This simple proportionality is called Amontons' law. However, numerical and theoretical investigations revealed that Amontons' law can be macroscopically broken in the slip of an elastic body. The friction coefficient decreases as the loading pressure or system size increases [19]. This breakdown of Amontons' law originates from the precursor slips due to the elasticity of a sliding object. The actual frictional behavior is much more difficult than the frictional behavior considered.

3.6.3 Inertial Number and Granular Friction

Granular friction behavior in a quasi-static state is much more complicated than that in a flowing state. Friction is crucial to characterize dense granular flows because the dissipation in a dense granular matter is dominated by friction. In contrast, for dilute granular systems, the inelastic collision will be a principal source of dissipation. The inertial number I (Eq. (2.114)) can be used to characterize the regime of granular flow. According to Ref. [20], granular flows are classified into three regimes: the quasi-static regime ($I \le 10^{-2}$), the intermediate dense flow regime ($10^{-2} \le I \le 0.2$), and the collisional regime ($0.2 \le I$). In the collisional regime, the kinetic theory is primarily applicable, and inelastic collision is essential for dissipation. In the quasi-static regime, granular flow becomes unstable, and stick-slip motion is observed. In the intermediate dense flow regime, empirical constitutive laws have been proposed [21, 22]. This regime is actually the most understandable case with respect to friction because a simple constitutive law is applicable. Using the inertial number I, Pouliquen et al. obtained an empirical constitutive law of friction in the intermediate dense flow regime:

$$\mu_f(I) = \mu_0 + \frac{\mu_s - \mu_0}{I_0/I + 1},$$
(3.53)

where I_0 is a constant, μ_0 is the minimum value of the friction coefficient at the low I limit ($I \rightarrow 0$), and μ_s is an asymptotic friction coefficient for large I ($I \rightarrow \infty$). Although Eq. (3.53) is mainly validated in the dense flow regime, this equation is empirically applicable to a wider I regime. Once the parameters are calibrated by a particular geometry (e.g., plane shear), the estimated I_0 , μ_0 , and μ_s can be used for various flow geometries such as chute flow and heap flow. Assuming that Eq. (3.50) is attained in the flow state, ⁴ rheological relations can be computed using Eq. (3.53). Representative values for glass beads are obtained as $I_0 = 0.3$, $\mu_0 = \tan 21^\circ$, and $\mu_s = \tan 33^\circ$ [22].

They also obtained an empirical relation for the packing fraction in the intermediate dense flow regime:

$$\phi(I) = \phi_{\text{max}} - b_I I, \tag{3.54}$$

where b_I is a parameter determined by $b_I = \phi_{\text{max}} - \phi_{\text{min}}$. Here ϕ_{max} and ϕ_{min} are the maximum and minimum packing fractions in the intermediate dense flow regime, respectively. Equations (3.53) and (3.54) were empirically obtained. Nevertheless, these constitutive laws are able to explain various granular flows including full three-dimensional flows [21, 22].

In a two-dimensional granular simulation, a linear relation between μ_f and I was also observed [20]. The obtained constitutive law was $\mu_f = \mu_0 + a_I I$, where a_I is a dimensionless constant. This linear constitutive law has a similar form as the Bingham model (see Sect. 3.2). In fact, μ_0 is related to the yield stress through the confining pressure p as $Y_s = \mu_0 p$, and I is proportional to the strain rate $\dot{\gamma}$ (Eq. (2.114)). Furthermore, Herschel-Bulkley-like nonlinear behavior was observed in a numerical simulation of three-dimensional sheared granular matter [23]. The generalized relations are

$$\mu_f(I) = \mu_0 + a_I I^{n_1}, \tag{3.55}$$

and

$$\phi(I) = \phi_{\text{max}} - b_I I^{n_2}. \tag{3.56}$$

The exponents obtained by the simulation were $n_1 = 0.28 \pm 0.05$ and $n_2 = 0.56 \pm 0.02$ [23]. The value of μ_0 depends on the friction of the individual grains. Because the value of n_1 is smaller than unity, Eq. (3.55) may appear similar to the RSF (Eq. (3.52)). Moreover, Eq. (3.53) is also a convex function of *I*. These equations are qualitatively similar. In Fig. 3.6, the curves of Eqs. (3.53) and (3.55) are presented. To obtain a curve similar to Eq. (3.53), $\mu_0 = 0.25$ is used for

⁴This equality assumption is probably the most important assumption in making the friction problem solvable. The quasi-static regime does not necessarily satisfy this assumption, which explains why the quasi-static regime is much more difficult than the intermediate flow regime.

3.6 Friction 83

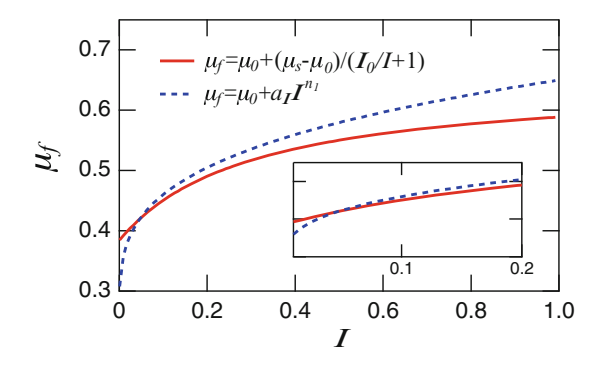


Fig. 3.6 Relations between friction coefficient μ_f and inertial number *I*. The *solid curve* corresponds to Eq. (3.53) with $I_0=0.3$, $\mu_0=\tan 21^\circ$, and $\mu_s=\tan 33^\circ$. This curve is based on the experimental result of glass beads [22]. The *dotted curve* represents Eq. (3.55) with $\mu_0=0.25$, $a_I=0.5$, and $n_1=0.28$. This curve is based on numerical results [23]. The *inset* shows an intermediate dense flow regime $(10^{-2} \le I \le 0.2)$

Eq. (3.55). Then, these two curves are very similar particularly in the dense flow regime (the inset of Fig. 3.6). Because Eq. (3.55) was determined on the basis of a numerical simulation, the considered range of I is wider than the experimentally obtained Eq. (3.53) [21–23].

Using Eqs. (2.114), (3.55), and (3.50), a general form of the frictional constitutive law is obtained as

$$\sigma_s = \mu_0 p + a_I (D_g \sqrt{\rho_g})^{n_1} p^{1 - \frac{n_1}{2}} \dot{\gamma}^{n_1}. \tag{3.57}$$

If the relation is linear $(n_1 = 1)$, granular viscosity can be computed as

$$\eta = a_I \sqrt{\rho_g p D_g^2}. (3.58)$$

Substituting Eq. (3.58), $\rho = \rho_g$ (grain density), U = u (slip velocity), and $l = D_g$ (grain diameter) into Eq. (2.41), the effective Reynolds number is defined by

$$R_e = u \sqrt{\frac{\rho_g}{p}}. (3.59)$$

Here the numerical factor a_I is neglected. This dimensionless number was utilized to characterize the flash weakening of sheared granular matter [24]. The inertial number is recovered if we consider $u = \dot{\gamma} D_g$ in Eq. (3.59). Thus, the inertial number can be regarded as an analog of the Reynolds number for a sheared dense granular flow. Note that the applicability of the linear constitutive law is limited in actual granular behaviors. Furthermore, the microscopic friction coefficient among grains is not involved in the definition of the inertial number I.

How does this macroscopic frictional constitutive law relate to the microscopic dissipations originating from inter-grain friction and inelastic collision? Microscopic friction coefficient indirectly affects macroscopic friction. In the linear regime, the angular distribution of the normal forces among grains is modified by microscopic friction [20]. In the general form of Eq. (3.55), it has been shown that the microscopic friction affects μ_0 and that the inelastic collision affects the I dependence [25]. Namely, the former (the relation between the microscopic friction and μ_0) corresponds to the tangential component of dissipation, and the latter (the relation between the inelastic collision and I dependence) originates from the normal component of dissipation. By combining the RSF form and inertial number dependence, a unified form, $\mu_f = \mu_0 - \alpha_I \log I + a_I I$, was also proposed [26].

The form of Eq. (3.59) is somewhat similar to the Mach number (Eq. (2.105)), which represents the relative importance of the incompressibility of the fluid: $R_e \sim I \sim Ma$ for $\dot{\gamma}$ -proportional dense granular flows. In the small Mach number regime, a fluid can be regarded as incompressible. For sheared granular matter, Eq. (3.59) may represent the degree of dilatancy rather than incompressibility. The dilatancy is not negligible in the large I regime. More detailed characterization, particularly of the nonlinearity, is an important future problem. If a small amount of water is added to a granular bed, the frictional property is drastically affected. Specifically, the friction can be reduced by water [27]. Detailed characterization of the frictional behavior of wet granular matter is also a crucial issue for future work.

3.7 Static Structure of Granular Matter

Granular behavior in the static or quasi-static regime is much more complicated than that in the flow regime. Therefore, the frictional constitutive laws in the flow regime were mainly discussed in the previous section. This property contrasts with that of usual fluids. Static fluid is much easier to analyze than flowing (dynamic) fluid. In a quiescent fluid, there is no shear stress. All the stress components are normal stress, i.e., pressure. Because of this simplicity, Pascal's and Archimedes' principles hold, which is not true for granular matter (or other complex fluids). The difficulty presented by the static granular structure will be discussed in this section. The most famous constitutive law for static granular matter is the Janssen effect. Pressure saturation in a granular column supported by a side wall can be discussed using the Janssen effect [28, 29].

3.7.1 Janssen Effect

Let us consider the pressure of a granular column in a cylindrical container, as illustrated in Fig. 3.7a. The depth z is measured downward from the top surface

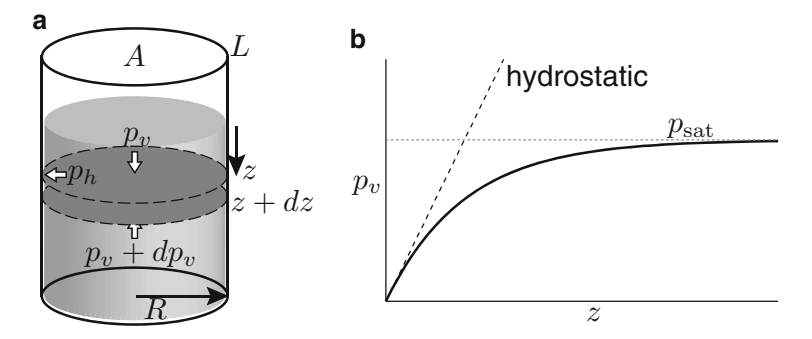


Fig. 3.7 Janssen model of granular pressure measured at the container wall. (a) Schematic image of a granular column in a cylindrical container. (b) A qualitative form of $p_v(z)$ obtained by the Janssen constitutive relation, $p_h = \kappa p_v$

of the column. In general, the granular internal forces are scattered randomly by complex force chain structures. Examples of visualized granular force chains are presented in Figs. 3.10 and 4.10. Due to this force scattering, a part of the vertical stress originating from self-gravity is supported by the side wall friction as well as the bottom wall. To consider the force scattering, Janssen employed a simple constitutive relation between the vertical pressure p_v and horizontal pressure p_h

$$p_h = \kappa p_v, \tag{3.60}$$

where κ is a parameter ranging from $0 \le \kappa \le 1$. The scattered horizontal pressure p_h acts as a normal stress on a side wall and results in the frictional support, $\mu_w p_h$, where μ_w is a (Coulomb) friction coefficient among grains and a side wall. Considering a slice between z and z + dz (intersectional area of A and perimeter length of L), the vertical force balance is written as

$$Adp_v = \rho g A dz - \mu_w p_h L dz, \qquad (3.61)$$

where ρ is the bulk granular density. Substituting Eq. (3.60) to Eq. (3.61), the equation can be rewritten in differential equation form

$$\frac{dp_v}{dz} + \frac{\mu_w \kappa L}{A} p_v = \rho g. \tag{3.62}$$

This differential equation is transformed by multiplying by a factor $\exp(\mu_w \kappa Lz/A)$ such that it can be solvable as

$$\frac{d}{dz}\left[p_v \exp\left(\frac{\mu_w \kappa L}{A}z\right)\right] = \rho g \exp\left(\frac{\mu_w \kappa L}{A}z\right). \tag{3.63}$$

By integrating Eq. (3.63) and using the boundary condition $p_v(z=0)=0$, we finally obtain

$$p_v = \frac{\rho g R}{2\mu_w \kappa} \left[1 - \exp\left(-\frac{2\mu_w \kappa}{R}z\right) \right]. \tag{3.64}$$

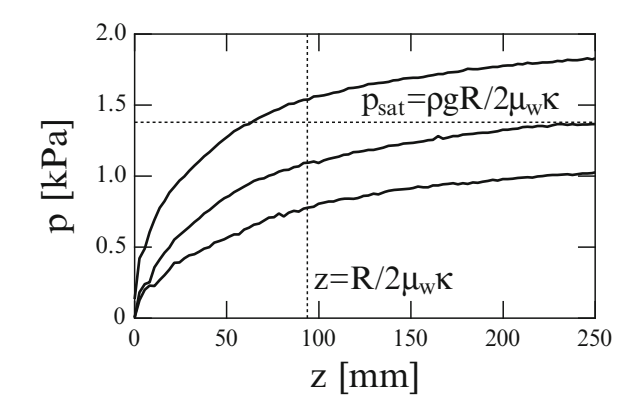
Here the relation $A/L = \pi R^2/2\pi R = R/2$ (R is the radius of the container) is used. In small $z(\ll R/2\mu_w\kappa)$ region, a simple hydrostatic relation, $p_v = \rho gz$, is obtained by the Taylor expansion of Eq. (3.64). However, p_v is saturated in the deep region toward an asymptotic value:

$$p_{\text{sat}} = \frac{\rho g R}{2\mu_{\text{w}}\kappa}.$$
 (3.65)

Roughly speaking, p_v saturates to $p_{\text{sat}} \simeq 2\rho gR$ at its characteristic depth $z \simeq 2R$ because μ_w and κ are usually close to 1/2. The specific functional form of $p_v(z)$ is shown in Fig. 3.7b.

The Janssen effect can be confirmed by a simple experiment. An example data set of the measured granular pressure at the container's bottom is shown in Fig. 3.8. In the experiment, a cylindrical container of $R=37.5\,\mathrm{mm}$ was filled with glass beads of diameter 0.8 mm. The glass beads were poured by a granular supplier with a constant rate of 1.8 g/s. During the sedimentation, the pressure at the bottom was measured by a pressure sensor. Then, the relation between the pressure at the bottom and the column height was obtained as indicated in Fig. 3.8. In this experiment, the known parameters were $\rho=1.5\times10^3\,\mathrm{kg/m^3}$ and $\mu_w\simeq0.4~(=\tan22^\circ;$ the wall friction is approximated by the internal friction). Assuming $\kappa=0.5$, we obtain $p_{\mathrm{sat}}=1.4\,\mathrm{kPa}$. This value is represented by the horizontal dashed line in Fig. 3.8. The corresponding characteristic length scale is also shown as the vertical dashed line in Fig. 3.8. The three solid data curves represent independent experimental runs under identical experimental condition. All the curves exhibit a similar exponential-like saturation trend, as predicted by the Janssen model. Moreover, the predicted p_{sat}

Fig. 3.8 Experimental data of granular pressure at the bottom of a cylindrical container. The *horizontal* dashed line corresponds to $p_{\text{sat}} = \rho g R/2 \mu_w \kappa$ with $\mu_w \kappa = 0.2$, and the *vertical* dashed line denotes the corresponding characteristic length scale



roughly agrees with the experimentally obtained value; however, the reproducibility is not very good. Poor reproducibility is one of the main difficulties in the study of granular behavior. In fact, it is notorious, particularly in industrial fields. The actual value of p_{sat} strongly depends on the history of sedimentation. Once a local structure is fixed by a particular sedimentation history, it is difficult to reorganize the structure during the sedimentation process. This history-dependent grain network structure determines how the force is scattered by the force chains. Therefore the static granular behavior exhibits history dependence and poor reproducibility.

3.7.2 Stress Dip

In a static granular pile, the curious stress dip structure can also be observed. When the sand pile is made by glass beads dropped from a small outlet of the funnel, the resultant stress (pressure) distribution at the bottom wall show a certain dip right beneath the apex of the sand pile. If there is no redirection of the force, the gravitational force acts only in the vertical direction. Then, the bottom wall pressure should be written by the hydrostatic pressure. The actual granular heap does not exhibit this simple behavior. Therefore, the stress dip structure is clear evidence of the force redirection. The force redirection tendency is qualitatively consistent with the Janssen effect. In addition, complex history dependence is observed in the stress dip phenomenon. The appearance of the stress dip actually depends on the preparation of the deposit. When a sand pile is prepared by uniform sedimentation through a sieve, the stress dip is not observed [30, 31]. This experimental result clearly demonstrates the strong history dependence of granular piling and the resultant stress structure. Moreover, the stress dip structure depends on the shape of the grains. Zuriguel et al. measured the stress distributions of a two-dimensional sandpile using photoelastic circular or elliptic cylinders [32]. These researchers observed that the stress dip was significantly enhanced when elliptic grains were used. The effect of the preferred alignment in elliptic cylinders is a possible origin of the enhanced stress dip.

3.7.3 Dynamic Janssen Effect

As discussed thus far, the granular static state is considerably more complex than its flowing state. This tendency is also true for the Janssen effect. As shown in Fig. 3.8, the static granular pressure does not exhibit good reproducibility. However, the pressure recovers reproducibility in a slightly dynamic state. Vanel et al. developed a reproducible approach to test the Janssen effect [33, 34]. These researchers simply poured grains into a tube. Prior to pouring the grains, a solid piston was inserted into the bottom part of the tube such that the piston did not touch the tube wall. The piston was attached to a spring beneath the piston. Thus, the kinetic energy

of dropped grains during the filling was partly stored by the spring, and the piston slowly moved downward because of the mass of the grains. This slow but finite motion is particularly important to create a sliding limit state, which is the basic assumption of theoretical models such as the Janssen effect. Then, the apparent mass $M_{\rm app}$ was measured by an electronic scale placed below the piston. $M_{\rm app}$ corresponds to the product of the bottom wall pressure and the area, $M_{\rm app} = pA$. Using this system, the researchers obtained very reproducible $M_{\rm app}$.

Bertho et al. demonstrated that dynamic reproducibility can be observed more directly by moving a tube wall [35]. While their experimental setup was similar to the previous one [33], the tube was positively moved upward after the sedimentation of grains. The obtained behavior of $M_{\rm app}$ as a function of time is shown in Fig. 3.9. Each curve in Fig. 3.9 represents individual experimental realization. In regime 1 of Fig. 3.9, $M_{\rm app}$ exhibits various values similar to those in Fig. 3.8. This regime corresponds to the period directly after the sedimentation. Thus, such a wide variation in $M_{\rm app}$ is natural for granular piling. Regime 2 of Fig. 3.9 represents the period during the upward motion of the tube wall. One can observe a sudden data collapse to the master curve of $M_{\rm app}$ in this regime. After the wall stop, $M_{\rm app}$ distributes again as shown in regime 3 of Fig. 3.9. However, its variance is significantly reduced compared with that of the initial state (regime 1). This experimental result clearly demonstrates the importance of the dynamic effect in obtaining reproducible granular behavior.

The granular discharge rate from a wedge orifice at the bottom of a container is almost independent of the granular amount remaining in it. This behavior contrasts with that of usual fluids, in which the discharge rate depends on the height of the fluid layer remaining in the container because of the hydrostatic pressure. The

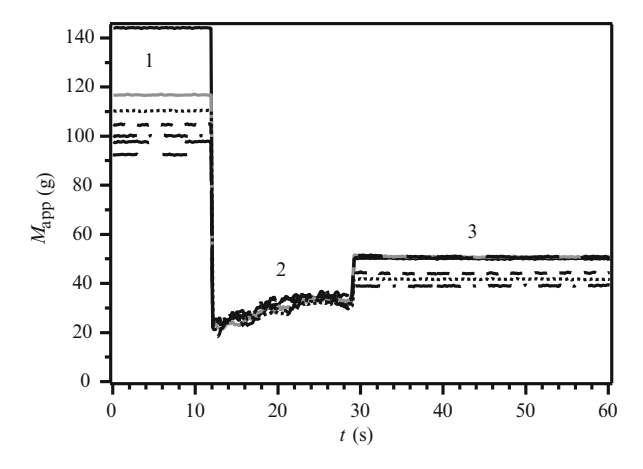


Fig. 3.9 Apparent mass M_{app} of the granular packing as a function of time. Regimes 1, 2, and 3 correspond to the duration of right after the sedimentation, the tube upward motion (with 4 mm/s), and after the tube cessation, respectively. The data collapse can be observed only in regime 2 (Reprinted with permission from Ref. [35]. Copyright 2003 by American Physical Society)

discharge rate is proportional to the square root of the layer's height (Torricelli's law). Because of the Janssen effect, the granular pressure in the container is saturated. It has been considered that pressure saturation causes the constant discharge rate of the granular flow. This effect is supposed to enable hourglasses to be good clocks. However, an experimental study demonstrated that the constant discharge rate is actually independent of the Janssen effect [36]. Moreover, the side wall geometry can also affect the pressure saturation [37]. The situation is slightly confusing. The Janssen model is useful to estimate the granular pressure in a container. Nonetheless, its effect has not yet been fully understood.

3.8 Contact Force Distribution in a Static Granular Structure

Microscopic contact forces among grains must be measured to understand the difficulty of static granular constitutive laws. All the inter-grain contact forces must satisfy the criterion (3.47) to maintain a static grain network structure. Note that criterion (3.47) is not an equation but an inequality. Moreover, the granular network structure has numerous contact points, which indicates that the granular internal stress structure is expressed by simultaneous inequalities. We are unable to solve such an indefinite problem, which is one of the most difficult points in the physics of granular matter. Due to the indefiniteness, the internal stress structure in static granular matter cannot be solved solely by the geometrical information. Therefore, it is impossible to completely quantify the internal stress state using a grain network structure itself; this strongly depends on the history of structuring. In the Janssen model, the stress redirection parameter κ is introduced and the friction balance (equality) is assumed on the side wall. This model works well qualitatively; however, the reproducibility is insufficient as long as the static state is considered.

To overcome this problem, intergranular contact forces have been quantified by an experiment with photoelastic disks. An image of stress structure visualized by photoelastic disks is presented in Fig. 3.10a. In Fig. 3.10a, photoelastic disks are simply piled up in a two-dimensional vertical Hele-Shaw cell. Thus, only their own weights are exerted on the disks. One can observe the heterogeneous granular stress structure characterized by so-called force chains. Using image analysis, stress applied to each disk can be computed from the fringe patterns. Solving the full inverse photoelastic problem for each disk, both normal and tangential contact forces can be computed [38, 39]. Then, using the computed results, the fringe patterns can be reproduced. A comparison between the experimental and computed results is presented in Fig. 3.10. The left image (Fig. 3.10a) shows the experimental result and the right image (Fig. 3.10b) shows the corresponding computed result.

This force chain structure is qualitatively similar to the case of isotropic compression [38]. Both the surface force and body force result in similar force chain structures in static granular matter. The only difference is their depth dependences.

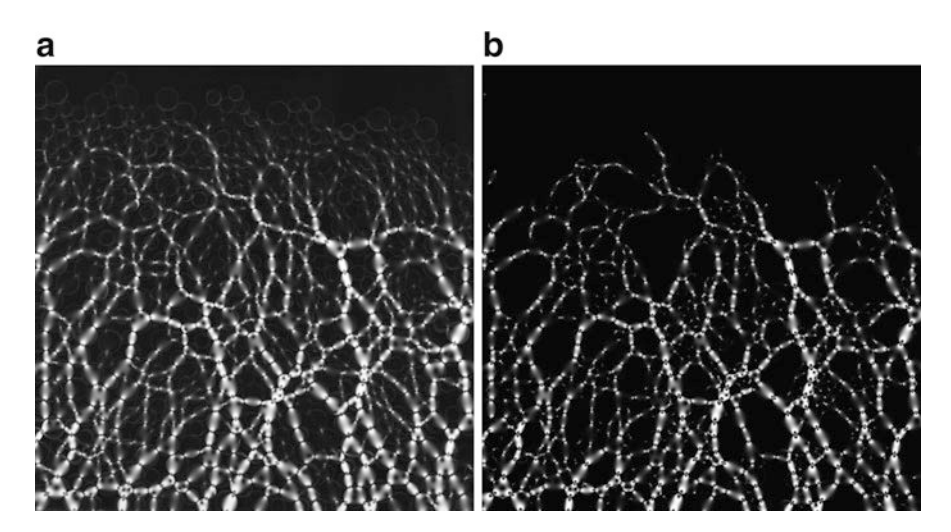


Fig. 3.10 Photoelastic characterization of inter-grain contact forces. Each image corresponds to (a) the experimental result and (b) the corresponding computed result of the method developed by Refs. [38, 39]. The photoelastic disks are piled up in a two-dimensional cell. Self-gravity (body force) mainly forms the force chain network

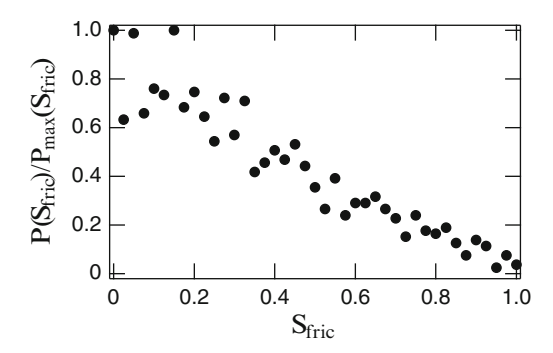
Because the force chains shown in Fig. 3.10a are produced by their own weights, the deeper region consists of the highly stressed (brighter) disks because of the hydrostatic effect.

The frictional state at each contact can be characterized by the photoelastic image. To characterize the frictional state, the variable $S_{\rm fric}$, which indicates the state of frictional support in the force chain network, is introduced [38]. $S_{\rm fric}$ is defined by the normal component F_n and the tangential component F_t of the contact force at each contact point as

$$S_{\text{fric}} = \frac{F_t}{\mu_0 F_n}. (3.66)$$

Thus, $S_{\rm fric}=1$ corresponds to the critical state at which the friction force balances with the tangential force. In other words, $S_{\rm fric}=1$ is equivalent to the equality case of the criterion (3.47). The variable $S_{\rm fric}$ indicates how far a contact force is from the Coulomb failure criterion. In Fig. 3.11, the normalized probability distribution $P(S_{\rm fric})/P_{\rm max}(S_{\rm fric})$ computed from Fig. 3.10b is shown, where $P_{\rm max}(S_{\rm fric})$ is the maximum value of the probability distribution $P(S_{\rm fric})$. The experimental result suggests that most of the contacts are far below the Coulomb failure criterion. Thus, we can conclude that the static granular structure is far below the critical state. Contacts with small $S_{\rm fric}$ are dominant in the static granular matter. This striking feature of the granular contact force distribution was first observed in sheared or isotropically compressed photoelastic disk experiments [38]. Furthermore, a

Fig. 3.11 Distribution of the normalized variable $S_{\rm fric}$ (defined by Eq. (3.66)) is shown. The data are computed from the image shown in Fig. 3.10



similar trend was confirmed by numerical simulations [40, 41]. We must link this microscopic contact force distribution to the macroscopic constitutive laws such as friction, Janssen, or maybe to more general laws. This is the most important and difficult point to build granular physics in the static regime.

The size-frequency distribution of the contact force exhibits an exponential form in sheared or isotropically compressed experiments [38]. Additionally, the same tendency can be observed in the own-weight loading (body force) case. The contact force characteristics and its distribution are almost independent of the loading conditions: surface force or body force. Furthermore, the exponential tail of the force distribution on the container wall has also been reported in granular packing experiments [42, 43].

Localization of the force chain restructuring might also be important in characterizing the granular behavior. In a granular avalanche flow, a clear correlation between the avalanche size and localization of force chain restructuring has been observed [44]. The spatial distribution and localization of the force chain is crucial in addition to its size-frequency distribution.

3.9 Fluidized Granular Matter

When granular matter is agitated by air flow or vibration, another class of granular behavior occurs. Such fluidized granular matter is in a sort of dynamic state. Therefore, its behavior should be simpler and more comprehensive than that in the static state. In fluidized granular matter, the friction remains important in general and, overall, fluid-like behaviors can be observed. Nevertheless, fluidized granular matter also exhibits some counterintuitive phenomena such as convection, segregation, and pattern formations. A brief review of these characteristic features of fluidized granular matter will be presented in this section.

In the fully fluidized granular bed, the steady-state dynamic rheometry discussed in Sect. 3.3 can be applied [45]. In the study, some empirical relations among complex moduli and angular frequency ω were experimentally observed. However, their

physical meanings have not yet been well understood. Instead, granular convection and segregation are particularly featured in this section. Granular convection and segregation are often induced by the mechanical vibration of a granular bed in a container vessel. The key elementary processes include dynamic friction, free fall, reorganization of grain network, and impacts among grains and (bottom or side) wall.

3.9.1 Granular Convection and Undulations

One of the most striking phenomena in fluidized granular matter is convective motion. If the granular column is vertically vibrated under gravity, convection occurs. Granular convection was initially recognized and analyzed by a heap structure induced by convection [46, 47]. The inclined surface structure of a vibrated granular bed was first observed by Faraday [48]. To quantitatively characterize vibration strength, a dimensionless acceleration Γ is usually employed. Γ is defined as

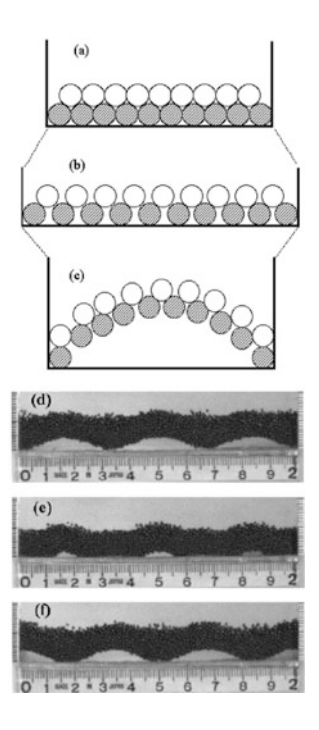
$$\Gamma = \frac{(2\pi f)^2 A_0}{g},\tag{3.67}$$

where A_0 is the amplitude of the vibration, f is the frequency, and g is the gravitational acceleration. The numerator corresponds to the maximum acceleration of the vibration, a_0 . If we assume a simple sinusoidal vibration, the acceleration becomes $a = (d/dt^2)A_0\sin(2\pi ft)$. Because granular convection is induced by the vibration against gravity, Γ must be relevant to characterize the convective motion. When Γ exceeds unity, the granular matter experiences free-fall duration in each vibration cycle. In principle, grains can move easily in the free-fall duration. Thus, global convective motions become possible in the regime of $\Gamma > 1$.

Granular convection is characterized by some distinct features. The onset of granular convection occurs slightly above $\Gamma=1$ [46, 47, 49–51]. Moreover, the structure of convection rolls varies as Γ increases [52]. According to both experiments [53, 54] and numerical simulations [49], the convective motion is limited to shallow regions of the vibrated granular bed. The convective velocity exhibits exponential decay as a function of depth, resulting in a frozen zone in a deep region. The existence of this frozen zone in a deep region is a peculiar feature of granular convection.

To analyze the vibrated granular bed, an inelastic bouncing ball model (IBBM) has been proposed [55, 56]. Because the vibrated granular behavior is similar to that of a perfectly inelastic body, its bulk behavior can be modeled by an inelastic ball on a vibrating base. When the instantaneous downward acceleration of the base exceeds *g*, the granular bed begins to levitate. The flight time of the levitation can be computed by IBBM, which roughly explains the period-doubling nature of

Fig. 3.12 Undulations in a vibrated granular bed. (a)–(c) Schematic diagram of the arch-like structure formed by a horizontal dilation is presented. (d-f) Experimentally obtained undulations at different phases are shown in (d) $t^* = 0$, (e) $t^* = 0.48$, and (f) $t^* = 1.12$, where $t^* = tf$ and f is the vibration frequency (Reprinted with permission from Ref. [62]. Copyright 2005 by American Physical Society)



the vibrated granular bed [57]. Free-fall flight time is an increasing function of Γ and coincides with the vibration period at 5 $\Gamma_{pd} = \sqrt{\pi^2 + 1}$. At this Γ_{pd} , the flight time undergoes saddle-node bifurcation causing period-doubling [58]. Further explanation of the terminologies of nonlinear dynamics such as period-doubling and bifurcation, can be found in textbooks such as [59, 60].

Spatial pattern formation is also induced in the vibrated granular bed. The vibrated granular bed is horizontally dilated by the impact on the bottom wall during each vibration cycle. Due to this horizontal dilation, undulations are observed under a certain condition [61–63]. In Fig. 3.12, experimentally observed granular undulations and a schematic understanding are shown. One can observe the archlike structure in the pictures of the experiment (Fig. 3.12d–f). This undulation structure is explained by the buckling due to the horizontal dilation as observed in Fig. 3.12a–c.

⁵When a ball is put on a sinusoidally vibrating base by the acceleration $a = -\Gamma g \sin(\omega t)$, the ball detaches from the base at time $t_d = (1/\omega) \arcsin(1/\Gamma)$. Here $\omega = 2\pi f$ is the angular frequency. By considering free fall of the ball, a relation for the impact time t_0 between the ball and base can be computed as $1 + \omega t_0 \sqrt{\Gamma^2 - 1} - (\omega t_0)^2/2 = \cos(\omega t_0) + \sqrt{\Gamma^2 - 1} \sin(\omega t_0)$. Specifically, $\Gamma_{pd} = \sqrt{\pi^2 + 1}$ is obtained by substituting $\omega t_0 = 2\pi$ into this equation.

3.9.2 Interstitial Air, Room Temperature, and Gravity

Interstitial air pressure plays a role in granular convection when the constituent grain diameter is less than 1 mm [50]. The effect of air drag becomes crucial when the grains are small because air drag is a force applied to surface and gravitational (and inertial) force is a body force (see Sects. 2.2 and 2.8.5). In general, the air drag effect is almost negligible as long as the grain diameter and density are sufficiently large. In contrast, the interstitial air effect dominates the behavior in the small-grain system. Here let us estimate the interstitial air effect using Stokes' law (Eq. (2.69)). By considering the force balance between the viscous drag force and the gravitational force applied to a grain with diameter D_g (= D_i) and density ρ_g , we obtain a dimensionless number

$$R_{\eta g} = \frac{3\pi \eta v D_g}{(\pi/6)\rho_g D_o^3 g} = \frac{18\eta v}{\rho_g g D_o^2}.$$
 (3.68)

 $R_{\eta g}$ is actually equivalent to S_{tk}^{-1} by considering the gravitational force as an origin of inertia (see Eq. (2.78)). Moreover, the form of Eq. (3.68) can directly be derived from the form of the viscous terminal velocity, Eq. (2.76). To evaluate the balance, here we use typical values of air viscosity $\eta=2\times 10^{-5}\,\mathrm{Pa}\cdot\mathrm{s}$, grain density $\rho_g\simeq 2\times 10^3\,\mathrm{kg/m^3}$, gravitational acceleration $g\simeq 9.8\,\mathrm{m/s^2}$, convective velocity $v\simeq 5\,\mathrm{mm/s}$ [51], and grain diameter $D_g=1\,\mathrm{mm}$. Then, the ratio becomes $R_{\eta g}\simeq 10^{-4}$, which indicates that gravity dominates the dynamics. Because $R_{\eta g}$ is inversely proportional to D_g^2 , $R_{\eta g}$ becomes 10^{-2} for the $D_g=0.1\,\mathrm{mm}$ case. This small $R_{\eta g}$ implies that the gravitational force still dominates the dynamics. However, the air drag level becomes several percent of the gravitational force. Moreover, the buoyancy force reduces the net gravitational force exerted on the grains. Therefore, grains on the order of $D_g=10^{-1}\,\mathrm{mm}$ may be affected by the interstitial air drag force. For grains with $D_g=10^{-2}\,\mathrm{mm}$, the air drag and gravity are comparable.

In classical Rayleigh-Benard convection, heat is transported by convection (see e.g., [64]). Thus, the temperature gradient is very important to characterize the convective motion. For the vibrated granular matter, however, ambient temperature is usually irrelevant. The effect of temperature can also be estimated by a dimensionless number, which represents the ratio between the thermal energy k_BT and gravitational potential energy $\rho(\pi/6)D_g^3gD_g$,

$$R_{Tg} = \frac{6k_BT}{\pi \rho_g g D_g^4},\tag{3.69}$$

where $k_B (= 1.38 \times 10^{-23} \text{ J/K})$ and T are Boltzmann constant and the temperature, respectively. Substituting T = 300 K (room temperature), $D_g = 1 \text{ mm}$, $\rho_g = 2 \times 10^3 \text{ kg/m}^3$, and $g \simeq 9.8 \text{ m/s}^2$ into Eq. (3.69), R_{Tg} is estimated to be $R_{Tg} \simeq 10^{-12}$. Therefore, we can conclude that room temperature is quite irrelevant for usual

granular convection.⁶ Obviously, the temperature gradient is not a driving force of granular convection. Although the structures of convective rolls are somewhat similar between granular and Rayleigh-Benard convections [52], their physical origins are completely different. For a vibrated granular bed, various effects may affect the onset and structure of the convective motion. For example, the container wall effect is an important factor [65] in addition to the interstitial air effect.

3.9.3 Granular Temperature

Because both $R_{\eta g}$ and R_{Tg} are very small, the gravitational force dominates the dynamics of the fluidized granular matter composed of large grains ($D_g > 10^{-1}$ mm). For such macroscopic granular matter, what is the driving force of granular convection? Agitation by mechanical vibration is undoubtedly the source of convective motion. Thus, the dimensionless vibration strength Γ can naturally be a relevant dimensionless parameter. Therefore, the structure of granular convection has been characterized by Γ . Pak and Behringer proposed another candidate for a strength parameter for the granular vibration called the shaking strength or shaking parameter, as described in [66],

$$S_{\Gamma} = \frac{(2\pi f A_0)^2}{g D_g}. (3.70)$$

 S_{Γ} is a product of two dimensionless numbers, Γ and A_0/D_g . In other words, S_{Γ} is a modified version of Γ to involve the grain diameter D_g as a relevant length scale in the dimensionless number. S_{Γ} can be regarded as the ratio of kinetic energy and gravitational potential energy per grain mass. The former is most likely proportional to the kinetic energy of the sinusoidally $(A_0 \sin(2\pi ft))$ vibrated base plate, which is expressed as $(1/2)v_{\rm base}^2 \sim (1/2)(2\pi fA_0)^2\cos^2(2\pi ft)$, where $v_{\rm base}$ is the velocity of the vibrating base. The latter is evaluated by gD_g . S_{Γ} is defined by the ratio of these two factors, $(2\pi fA_0)^2$ and gD_g . Thus, S_{Γ} represents a type of energy balance, while Γ denotes a balance of body forces. In other words, Γ and S_{Γ} are the dimensionless numbers based on acceleration or velocity, respectively. S_{Γ} is particularly important for a strongly shaken granular bed [63, 67, 68]. Granular convection can be observed both in weakly ($\Gamma \simeq 3$) and strongly ($\Gamma \simeq 50$) agitated granular beds. In the strongly agitated case, various characteristic behaviors can be observed by a systematically controlled experiment [63], e.g., granular bouncing,

⁶Here we do not use any peculiar property of the vibration in the definition of R_{Tg} . Thus, the ambient temperature is irrelevant for general macroscopic granular behavior. At room temperature (T = 300 K), $R_{Tg} \simeq 1$ is attained by tiny grains having diameter $D_g = 1 \mu \text{m}$. This diameter scale corresponds to the range of typical colloid particles.

granular Leidenfrost, 7 undulations, and granular gas states. For the strongly vibrated granular matter, the onset of granular convection can be understood by an intrinsic instability characterized by S_{Γ} rather than boundary effect [68].

For general fluidized granular matter, the averaged fluctuation of the kinetic energy per grain can be used as the granular temperature:

$$\frac{3}{2}T_g = \frac{1}{2}\langle m_g \delta v^2 \rangle,\tag{3.71}$$

where m_g is the grain mass, δv is the velocity fluctuation, and $\langle \cdot \rangle$ denotes the average. This temperature form is analogous to the molecular gas temperature. Sometimes, the square of velocity fluctuation is simply used as a specific granular temperature:

$$\hat{T}_g \sim \langle \delta v^2 \rangle.$$
 (3.72)

The dimension of \hat{T}_g is the energy per unit mass. If we assume $v_{\rm base} \sim \delta v$ in the vibrated granular matter, S_{Γ} is regarded as the ratio of granular temperature and gravitational potential. In general, T_g is relevant for dilute isotropic granular gas. Thus, S_{Γ} is useful to analyze the abovementioned strongly shaken granular bed because it is close to a gas state. The granular temperature T_g is also frequently used in the dense regime because we do not have any other appropriate indicator better than T_g to characterize the global activity of granular matter. This term actually works well to characterize the dense granular flow as well [69].

3.9.4 Brazil Nut Effect and Segregation

The granular size segregation induced by a vertical vibration is called the Brazil nut effect (BNE). When the polydispersity of a vibrated granular bed is not sufficiently large, convective motion dominates the phenomenon. If large grains are involved in the system, notable segregation occurs. Larger grains rise up to the surface of the bed. For the BNE, the grain size difference is usually much more important than the density difference. This tendency is somewhat unexpected because the density difference is the most important factor for the fluid segregation induced by gravity. Additionally, it is easy to produce the BNE by manual shaking of a granular mixture. Thus, the BNE is a good demonstration to dramatically show the complex nature of granular matter, particularly to the general public. Larger grains can rise up in a vibrated granular bed even if the larger grains are denser than the small grains. This phenomenon is unstable in terms of gravitational potential energy, which suggests that the state caused by the BNE may correspond to a metastable state. As discussed

⁷The classical Leidenfrost effect is water droplet levitation on a hot plate due to its own vapor.

later, Eq. (3.75) denotes the condition to attain the metastable state. This metastable state will be broken by extremely dense grains. The sinking of larger and much denser grains is called the reverse Brazil nut effect (RBNE).⁸

The physical mechanism of the BNE remains unsolved and controversial. One possible idea is the transport by granular convection induced by the vibration. As discussed in Sect. 3.9.1, the granular convection is usually observed in the state $\Gamma > 1$. Then, larger grains can be carried by the convective flow. Once large grains are carried to the surface of the bed, they cannot sink again into the bed. At the side wall, large grains cannot follow the convective flow due to the friction. This type of BNE can be easily observed in a granular vibration experiment.

Another idea to explain the BNE is the competition between condensation and percolation [70, 71]. Hong et al. assumed that the vibrated granular bed is fluidized at a certain granular temperature, $T_{gc} \propto m_g g D_g$, for monodisperse grains with diameter D_g and mass m_g . Considering a binary mixture of large and small grains, partially fluidized state can be achieved by tuning the granular temperature. Let m_l and m_s be the masses of large and small grains and D_l and D_s be the diameters of large and small grains, respectively. Then, the fluidization temperature ratio for large and small grains, $T_{gc}(l)/T_{gc}(s)$, is written as

$$\frac{T_{gc}(l)}{T_{gc}(s)} = \frac{m_l g D_l}{m_s g D_s}. (3.73)$$

When the granular temperature T_g is tuned in the range of $T_{gc}(s) < T_g < T_{gc}(l)$, small grains are fluidized and large grains are still condensed. Because of this heterogeneous temperature structure, the BNE is observed in this regime due to the relative motion among large and small grains during a vibration cycle. Specifically, a void opened by condensed large grains motion will be rapidly filled by the percolation of small fluidized grains [70, 72]. Because this percolation effect can be quantified by the grain volume ($\sim D_g^3$), competition between condensation and percolation is expressed as

$$\frac{T_{gc}(l)}{T_{gc}(s)} = \frac{m_l D_l}{m_s D_s} \sim \left(\frac{D_l}{D_s}\right)^3. \tag{3.74}$$

The crossover from the BNE to the RBNE occurs in the balance of Eq. (3.74). Using densities of large grains ρ_l and small grains ρ_s , we finally obtain the phase boundary condition as

$$\frac{D_s}{D_l} \sim \frac{\rho_l}{\rho_s}.\tag{3.75}$$

⁸This naming is slightly odd because the RBNE is a rather natural phenomenon compared with the ordinary BNE, with respect to the gravitational potential.

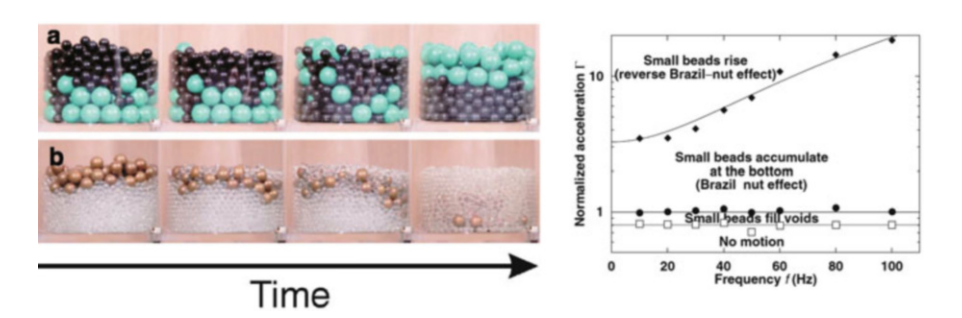


Fig. 3.13 Temporal evolution of **(a)** Brazil nut effect (BNE) and **(b)** reverse Brazil nut effect (RBNE). The *right panel* shows the phase diagram of the BNE and the RBNE for a binary mixture of 4-mm-diameter glass beads and 10-mm-diameter polyurethane spheres (Reprinted with permission from Ref. [75]. Copyright 2003 by American Physical Society)

The BNE should be observed in the regime of $D_s/D_l > \alpha_r(\rho_l/\rho_s)$, whereas the RBNE occurs at $D_s/D_l < \alpha_r(\rho_l/\rho_s)$, where α_r is some constant. According to a numerical simulation, Hong et al. demonstrated the possibility of the crossover from the BNE to the RBNE under this condition [71]. The aforementioned discussion has assumed that the granular temperature is homogeneous among large and small grains. However, the actual vibrated granular bed presumably has a granular temperature gradient. Thus, it is not easy to reproduce the RBNE in experiments [73, 74].

Breu et al. experimentally confirmed the crossover from the BNE to the RBNE for the first time [75] (Fig. 3.13). Their experimental result is basically consistent with the condensation vs. percolation scenario. However, they also observed that the crossover condition depends on the vibration strength (Γ) and frequency (f)(Fig. 3.13). The segregation in the condensation vs. percolation scenario does not explicitly involve the gravitational effect; it is canceled out, as observed in Eq. (3.73). To consider the gravity effect explicitly, granular gas theory has also been used to explain the crossover from the BNE to the RBNE [76]. In that framework, segregation occurs because of the competition between gravity and entropy rather than that between condensation and percolation. Although the framework allows us to understand the crossover in terms of conventional thermodynamics, the condensation process in a vibrated granular bed is not recognized [77]. Another model based on the free energy theory is described in Ref. [78]; however, the vibration strength was not explicitly considered in that theory. All these theories have succeeded in elaborating each possible mechanism for the BNE and the RBNE. However, it is unclear whether the effects can be unified.

Systematic numerical simulations with soft particles have revealed the Γ -dependent boundary between the BNE and the RBNE [79]. According to the numerical result, the boundary is written as

$$\frac{D_l}{D_s} = 1 + \alpha_r(\Gamma) \left(\frac{\rho_l}{\rho_s} - 1 \right), \tag{3.76}$$

where $\alpha_r(\Gamma)$ is a coefficient depending on Γ . Note that the Γ dependence is included in this form. Additionally, the qualitative trend of the relation between the density and size ratios is different from Eq. (3.75).

Moreover, the BNE might be affected by various other effects: buoyancy [80, 81], interstitial air [82], and intergranular friction (and their aging) [83]. The segregation is not limited in the vertical direction, e.g., horizontal segregation was also observed in a numerical simulation [84]. For wet granular matter, the segregation is affected by the liquid content and its viscosity. Therefore, the segregation behavior becomes complex in a vibrated wet granular bed [85]. Using the form of S_{tk} (Eq. (2.78)), the characteristic length of grain motion in a viscous fluid (Stokes regime) can be estimated as $l \simeq \rho_g U D_g^2 / 18 \eta$, which indicates that the grain's characteristic traveling distance depends on the grain size as $l \sim R_e D_g$. The density and size dependences of the BNE-RBNE crossover are related, as described in Eqs. (3.75) or (3.76). The size dependence of the crossover condition might be modified by the viscosity-dependent length $l \sim R_e D_g$. This viscosity-related effect could be a source of segregation [72]; however, it is difficult to explain the entire wet granular segregation solely by this effect.

If the granular bed is completely fluidized by the horizontal vibration of side walls, granular buoyancy is experimentally observed [86]. The granular buoyancy effect has been proposed by the numerical simulation of the BNE [80, 81]. Huerta et al. performed a horizontal vibration experiment with a vibrated side wall [86]. Note that only the side wall is vibrated in this experiment; the entire container is not shaken. In contrast, the entire container is usually shaken in vertical vibration experiments. This horizontal vibration condition suppresses the convective flow and aims to eliminate the convective flow effect for the origin of buoyant force. In this experiment, they observed the buoyant force exerted on an intruding object. The experimental result indicated that the buoyant force simply obeys Archimedes' principle, which means that the granular matter behaves like a fluid, in terms of buoyancy in the fully fluidized state.

Many more intriguing phenomena have been observed in fluidized granular matter. Sheared granular matter can also cause granular convection and segregation [72, 87–89]. In densely packed sheared granular matter, confining pressure plays a role in characterizing the segregation [89]. Granular matter can be fluidized by air flow through the bed as well [90–93]. In a vertically vibrated granular bed, soft impact between a container wall and a granular bed must occur and play a role. Therefore, we focused mainly on the mechanically driven vibrated granular bed in this section. The similarities and differences between vibrated, sheared, and aerated granular matter are not yet very clear. Furthermore, the reverse buoyancy effect, in which heavy but similar sized grains rise and lightweight grains sink in a vibrated granular bed, has been reported [94]. To understand this reverse buoyancy, it appears that the inertia of the grains is important. The inertia must be a key to discuss the fidelity of large grains to the convective flow of fluidized small grains (see the discussion near Eq. (2.78) for fidelity evaluation).

As discussed thus far, various factors might affect granular convection and segregation. Perhaps, a unified understanding by simple parameters such as Γ , the

100 3 Constitutive Laws

density ratio, and the size ratio might be intrinsically impossible. Case analysis may be necessary for each condition. Possible ideas for the principal reasons of granular convection and segregation can be listed as follows:

- grain-wall friction
- · intergranular friction
- percolation vs. condensation
- · interstitial fluid
- · buoyancy

The BNE, RBNE, buoyancy, and reverse buoyancy can be produced by tuning these factors and the boundary conditions. Although all these factors are crucial when considering the origin of granular convection and segregation, it is difficult to classify and separate them at this point. This complexity is an origin of various counterintuitive phenomena observed in granular matter. Some of these factors are also important for the granular impact study as discussed in Chap. 4. For the granular impact case, these effects are discussed in some experiments.

3.10 Summary

In this chapter, the fundamental constitutive laws for general continua and elementary properties of granular matter were briefly introduced. Classic viscoelastic and viscoplastic models and the dynamic rheological measurement method were first introduced. Specifically, the explained classic models included the Maxwell, Kelvin-Voigt, Bingham, and Herschel-Bulkley models. After discussing the rebound and restitution coefficient, the very basics of transport phenomena models such as diffusion and advection were introduced. Then, studies of the frictional constitutive laws were reviewed. Rate- and state-dependent friction (RSF) and the friction laws based on the inertial number were particularly featured. The difficulty of static granular investigation was highlighted through the Janssen effect and contact force distributions. The indefiniteness of friction and history dependence of granular deposits are the principal reasons for poor reproducibility in static granular phenomena. Fluidized granular matter was also discussed. Convection and segregation were focused on through characterizations by dimensionless numbers. Granular segregation is affected by various factors such as grain size, density, wall friction, and interstitial fluid. Parameter-dependent complex behaviors are typical characteristics of granular matter. Similar complexity will be reconfirmed for granular impact mechanics in the next chapter.

Of course, the review of granular physics is not exhausted in this chapter. Topics not discussed in this chapter include kinetic theory for granular gas, various contact mechanics such as capillary bridge, and classic stress balance theories in soil mechanics such as Mohr's circle. For further reading, there are many textbooks on the physics of granular matter [12, 95–100]. An in-depth review of macroscopic

References 101

constitutive laws and scaling analysis for dense granular matter was provided in this chapter. We are ready to continue our investigation of impact dynamics and related planetary issues. These topics are discussed in subsequent chapters.

References

- P. Oswald, Rheophysics: The Deformation and Flow of Matter (Cambridge University Press, Cambridge, 2009)
- 2. K.L. Johnson, Contact Mechanics (Cambridge University Press, Cambridge, 1985)
- 3. M.Y. Louge, M.E. Adams, Phys. Rev. E 65, 021303 (2002)
- 4. H. Kuninaka, H. Hayakawa, Phys. Rev. Lett. 93, 154301 (2004)
- 5. H. Kuninaka, H. Hayakawa, Phys. Rev. E **79**, 031309 (2009)
- 6. H. Kuninaka, H. Hayakawa, Phys. Rev. E 86, 051302 (2012)
- 7. K. Saitoh, A. Bodrova, H. Hayakawa, N.V. Brilliantov, Phys. Rev. Lett. 105, 238001 (2010)
- 8. N.V. Brilliantov, F. Spahn, J.M. Hertzsch, T. Pöschel, Phys. Rev. E 53, 5382 (1996)
- 9. N.V. Brilliantov, N. Albers, F. Spahn, T. Pöschel, Phys. Rev. E **76**, 051302 (2007)
- 10. P.A. Cundall, O.D.L. Strack, Géotechnique 29, 47 (1979)
- J.D. Pelletier, Quantitative Modeling of Earth Surface Processes (Cambridge University Press, Cambridge, 2008)
- 12. R.M. Nedderman, Statistics and Kinematics of Granular Materials (Cambridge University Press, New York, 1992)
- H. Sakaguchi, A. Murakami, T. Hasegawa, T. Igarashi, J. Geotech. Eng. Proc. JSCE 511/III-30, 221 (1995)
- 14. S.R. Nagel, Rev. Mod. Phys. 64, 321 (1992)
- 15. C. Marone, Annu. Rev. Earth Planet. Sci. 26, 643 (1998)
- H. Kawamura, T. Hatano, N. Kato, S. Biswas, B.K. Chakrabarti, Rev. Mod. Phys. 84, 839 (2012)
- 17. S. Nasuno, A. Kudrolli, J.P. Gollub, Phys. Rev. Lett. **79**, 949 (1997)
- 18. S. Nasuno, A. Kudrolli, A. Bak, J.P. Gollub, Phys. Rev. E 58, 2161 (1998)
- 19. M. Otsuki, H. Matsukawa, Sci. Rep. 3, 1586 (2013)
- F. da Cruz, S. Emam, M. Prochnow, J.N. Roux, F.m.c. Chevoir, Phys. Rev. E 72, 021309 (2005)
- 21. P. Jop, Y. Forterre, O. Pouliguen, Nature **441**, 727 (2006)
- 22. O. Pouliquen, C. Cassar, P. Jop, Y. Forterre, M. Nicolas, J. Stat. Mech. P07020 (2006)
- 23. T. Hatano, Phys. Rev. E **75**, 060301 (2007)
- 24. O. Kuwano, T. Hatano, Geophys. Res. Lett. 38, L17305 (2011)
- 25. T. Hatano, O. Kuwano, Pure Appl. Geophys. **170**, 3 (2013)
- 26. O. Kuwano, R. Ando, T. Hatano, Geophys. Res. Lett. 40, 1295 (2013)
- A. Fall, B. Weber, M. Pakpour, N. Lenoir, N. Shahidzadeh, J. Fiscina, C. Wagner, D. Bonn, Phys. Rev. Lett. 112, 175502 (2014)
- 28. H.A. Janssen, Z. Ver. Dtsh. Ing. 39, 1045 (1895)
- 29. M. Sperl, Granul. Matter 8, 59 (2006)
- 30. T. Jotaki, R. Moriyama, J. Soc. Powder Tech. Jpn. 14, 609 (1977) (in Japanese)
- 31. L. Vanel, D. Howell, D. Clark, R.P. Behringer, E. Clément, Phys. Rev. E 60, R5040 (1999)
- 32. I. Zuriguel, T. Mullin, J.M. Rotter, Phys. Rev. Lett. 98, 028001 (2007)
- 33. L. Vanel, E. Clément, Eur. Phys. J. B 11, 525 (1999)
- L. Vanel, P. Claudin, J.P. Bouchaud, M.E. Cates, E. Clément, J.P. Wittmer, Phys. Rev. Lett. 84, 1439 (2000)
- 35. Y. Bertho, F. Giorgiutti-Dauphiné, J.P. Hulin, Phys. Rev. Lett. 90, 144301 (2003)

102 3 Constitutive Laws

 M.A. Aguirre, J.G. Grande, A. Calvo, L.A. Pugnaloni, J.C. Géminard, Phys. Rev. Lett. 104, 238002 (2010)

- 37. M.Y. Karim, E.I. Corwin, Phys. Rev. Lett. 112, 188001 (2014)
- 38. T.S. Majmudar, R.P. Behringer, Nature 435, 1079 (2005)
- 39. J.G. Puckett, K.E. Daniels, Phys. Rev. Lett. 110, 058001 (2013)
- 40. L.E. Silbert, G.S. Grest, J.W. Landry, Phys. Rev. E 66, 061303 (2002)
- 41. J.W. Landry, G.S. Grest, L.E. Silbert, S.J. Plimpton, Phys. Rev. E 67, 041303 (2003)
- 42. C.h. Liu, S.R. Nagel, D.A. Schecter, S.N. Coppersmith, S. Majumdar, O. Narayan, T.A. Witten, Science 269, 513 (1995)
- 43. D.M. Mueth, H.M. Jaeger, S.R. Nagel, Phys. Rev. E 57, 3164 (1998)
- 44. N. Yoshioka, H. Sakaguchi, Adv. Geophys. 13, 281 (2007)
- 45. A. Barois-Cazenave, P. Marchal, V. Falk, L. Choplin, Powder Tech. 103, 58 (1999)
- 46. C. Laroche, S. Douady, S. Fauve, J. Phys. Fr. 50, 699 (1989)
- 47. P. Evesque, J. Rajchenbach, Phys. Rev. Lett. **62**, 44 (1989)
- 48. M. Faraday, Phil. Trans. R. Soc. 121, 299 (1831)
- 49. Y.h. Taguchi, Phys. Rev. Lett. 69, 1367 (1992)
- 50. H.K. Pak, E. Van Doorn, R.P. Behringer, Phys. Rev. Lett. 74, 4643 (1995)
- 51. A. Garcimartín, D. Maza, J.L. Ilquimiche, I. Zuriguel, Phys. Rev. E 65, 031303 (2002)
- 52. K.M. Aoki, T. Akiyama, Y. Maki, T. Watanabe, Phys. Rev. E 54, 874 (1996)
- E.E. Ehrichs, H.M. Jaeger, G.S. Karczmar, J.B. Knight, V.Y. Kuperman, S.R. Nagel, Science 267, 1632 (1995)
- J.B. Knight, E.E. Ehrichs, V.Y. Kuperman, J.K. Flint, H.M. Jaeger, S.R. Nagel, Phys. Rev. E 54, 5726 (1996)
- 55. P. Pierański, J. Phys. Fr. 44, 573 (1983)
- 56. A. Mehta, J.M. Luck, Phys. Rev. Lett. 65, 393 (1990)
- 57. J. Pastor, D. Maza, I. Zuriguel, A. Garcimartín, J.F. Boudet, Physica D 232, 128 (2007)
- 58. P. Holmes, J. Sound Vib. 84, 173 (1982)
- J.M.T. Thompson, H.B. Stewart, Nonlinear Dynamics and Chaos, 2nd edn. (Wiley, New York, 2002)
- D.L. Turcotte, Fractals and Chaos in Geology and Geophysics, 2nd edn. (Cambridge University Press, Cambridge, 1997)
- 61. S. Douady, S. Fauve, C. Laroche, EPL (Europhys. Lett.) 8, 621 (1989)
- 62. O. Sano, Phys. Rev. E 72, 051302 (2005)
- P. Eshuis, K. van der Weele, D. van der Meer, R. Bos, D. Lohse, Phys. Fluids 19, 123301 (2007)
- 64. P.K. Kundu, I.M. Cohen, D.R. Dowling, *Fluid Mechanics*, 5th edn. (Academic, Waltham, 2011)
- 65. M. Bourzutschky, J. Miller, Phys. Rev. Lett. 74, 2216 (1995)
- 66. H.K. Pak, R.P. Behringer, Phys. Rev. Lett. 71, 1832 (1993)
- 67. P. Eshuis, K. van der Weele, D. van der Meer, D. Lohse, Phys. Rev. Lett. 95, 258001 (2005)
- P. Eshuis, D. van der Meer, M. Alam, H.J. van Gerner, K. van der Weele, D. Lohse, Phys. Rev. Lett. 104, 038001 (2010)
- 69. K. Saitoh, H. Hayakawa, Phys. Rev. E 75, 021302 (2007)
- 70. A. Rosato, K.J. Strandburg, F. Prinz, R.H. Swendsen, Phys. Rev. Lett. 58, 1038 (1987)
- 71. D.C. Hong, P.V. Quinn, S. Luding, Phys. Rev. Lett. 86, 3423 (2001)
- 72. J. Williams, Powder Tech. **15**, 245 (1976)
- G.A. Canul-Chay, P.A. Belmont, Y. Nahmad-Molinari, J.C. Ruiz-Suárez, Phys. Rev. Lett. 89, 189601 (2002)
- 74. P.V. Quinn, D.C. Hong, S. Luding, Phys. Rev. Lett. 89, 189602 (2002)
- 75. A.P.J. Breu, H.M. Ensner, C.A. Kruelle, I. Rehberg, Phys. Rev. Lett. 90, 014302 (2003)
- 76. H. Walliser, Phys. Rev. Lett. 89, 189603 (2002)
- 77. P.V. Quinn, D.C. Hong, S. Luding, Phys. Rev. Lett. **89**, 189604 (2002)
- 78. J.A. Both, D.C. Hong, Phys. Rev. Lett. 88, 124301 (2002)

References 103

 M.P. Ciamarra, M.D.D. Vizia, A. Fierro, M. Tarzia, A. Coniglio, M. Nicodemi, Phys. Rev. Lett. 96, 058001 (2006)

- 80. N. Shishodia, C.R. Wassgren, Phys. Rev. Lett. 87, 084302 (2001)
- 81. N. Shishodia, C.R. Wassgren, Phys. Rev. Lett. 88, 109901 (2002)
- 82. M.A. Naylor, M.R. Swift, P.J. King, Phys. Rev. E 68, 012301 (2003)
- 83. S. Ulrich, M. Schröter, H.L. Swinney, Phys. Rev. E 76, 042301 (2007)
- 84. D.A. Sanders, M.R. Swift, R.M. Bowley, P.J. King, Phys. Rev. Lett. 93, 208002 (2004)
- 85. C.C. Liao, S.S. Hsiau, T.H. Tsai, C.H. Tai, Chem. Eng. Sci. 65, 1109 (2010)
- 86. D.A. Huerta, V. Sosa, M.C. Vargas, J.C. Ruiz-Suárez, Phys. Rev. E 72, 031307 (2005)
- 87. J.M. Ottino, D.V. Khakhar, Annu. Rev. Fluid Mech. 32, 55 (2000)
- 88. R. Khosropour, J. Zirinsky, H.K. Pak, R.P. Behringer, Phys. Rev. E 56, 4467 (1997)
- 89. L.A. Golick, K.E. Daniels, Phys. Rev. E 80, 042301 (2009)
- 90. W. Losert, L. Bocquet, T.C. Lubensky, J.P. Gollub, Phys. Rev. Lett. 85, 1428 (2000)
- 91. T.A. Brzinski III, D.J. Durian, Soft Matter 6, 3038 (2010)
- 92. G. Bruni, D. Barletta, M. Poletto, P. Lettieri, Chem. Eng. Sci. 62, 397 (2007)
- 93. I. Tomasetta, D. Barletta, P. Lettieri, M. Poletto, Chem. Eng. Sci. 69, 373 (2012)
- 94. T. Shinbrot, F.J. Muzzio, Phys. Rev. Lett. 81, 4365 (1998)
- N.V. Brilliantov, T. Pöschel, Kinetic Theory of Granular Gases (Oxford University Press, New York, 2004)
- 96. J. Duran, Sands, Powders, and Grains: An Introduction to the Physics of Granular Materials (Springer, New York, 2000)
- 97. A. Mehta, *Granular Physics* (Cambridge University Press, Cambridge, 2007)
- 98. I.S. Aranson, L.S. Tsimring, Granular Patterns (Oxford University Press, Oxford, 2009)
- 99. K.K. Rao, P.R. Nott, An Introduction to Granular Flow (Cambridge University Press, Cambridge, 2008)
- 100. B. Andreotti, Y. Forterre, O. Pouliquen, *Granular Media* (Cambridge University Press, Cambridge, 2013)

Chapter 4 Soft Drag Force

When a steel ball is dropped into a water pool, it will continue to sink with a terminal velocity. If the ball is dropped onto a sandbox, it usually stops suddenly in the vicinity of the surface. How can we classify these two cases in terms of physics? To answer this question, the impact drag force must be a key factor. The general drag force models introduced in Sect. 2.6.7 should be improved to explain soft matter impact dynamics. In this chapter, recent studies of soft matter impact drag force are reviewed. In particular, the granular impact drag force is intensively discussed through a comparison with the fluid drag force.

4.1 Granular Impact Drag Force

The impact drag force by a granular target must be different from simple viscous or inertial drag. This problem is not trivial. In this section, the granular impact drag force model is discussed on the basis of low-velocity impact experiments and simulations (impact velocity is less than 10 m/s). In low-velocity impact, the disruption of constitutive grains does not matter. The stress caused by the impact is considerably smaller than the strength of the grains. Hence, only the motion of the grains is important. Because of this simplicity, low-velocity impact is moderate to investigate the physics of granular matter.

The impact drag force by dry noncohesive granular matter is focused on in this section. In almost all discussions in this section, grains with diameters $D_g > 0.1$ mm are assumed. As discussed in Sect. 3.9.2, the interstitial air effect is negligible in this D_g regime. Thus, the target granular bed is regarded as simple noncohesive dry granular matter. We first discuss the impact drag force using this ideal granular matter. The impact situation and notations used are illustrated in Fig. 4.1. Initially, the vertical impact is considered. While we are still on the way to revealing the vertical drag force model, some studies on the oblique impact will be briefly

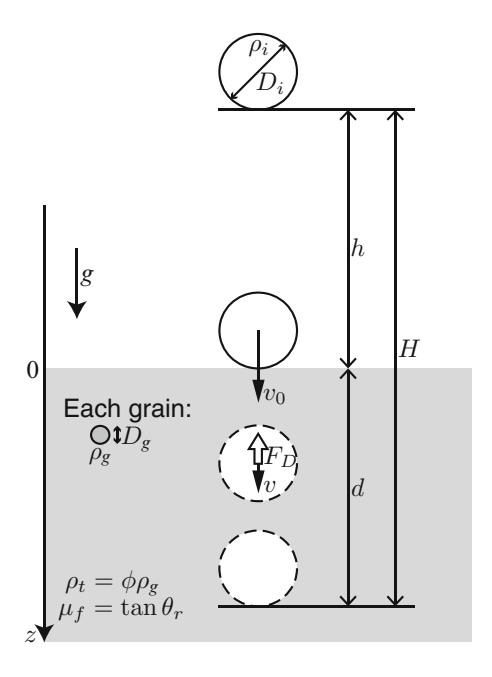


Fig. 4.1 Schematic drawing of the setup of the granular impact. A rigid solid sphere of diameter D_i and density ρ_i is dropped from a free-fall height h. The impact velocity is $v_0 = \sqrt{2gh}$. The vertical position z is measured at the bottom of the impactor. The zero penetration depth (z=0) is defined by the initial surface level of the target bed. The impactor penetrates into a target granular bed whose bulk density is $\rho_t = \phi \rho_g$ and whose internal friction is μ_f . For brevity, we use $\mu_f = \tan \theta_{\rm repose}$. Here ρ_g , ϕ , and $\theta_{\rm repose}$ are the grain density, packing fraction, and angle of repose of the target granular matter, respectively. The grain diameter is written as D_g . The drag force F_D is a function of the instantaneous impactor's velocity v and depth z. The final penetration depth is denoted as d, and the total drop distance is defined as H = h + d

reviewed in the final part of this section (Sect. 4.1.8). We restrict ourselves within the larger (and rigid) impactor case; $D_i/D_g \gg 1$. Then, the target granular bed can be regarded as a continuum, and the drag force equation will be one-dimensional as long as the vertical impact is considered. Additionally, a spherical impactor is usually employed in the studies reviewed in this section. Some complex effects such as the confined wall, packing fraction, and interstitial fluid will be discussed in the later part (Sect. 4.1.7).

4.1.1 Simple Scaling Approach

A clear crater is left on a granular target surface after the impact of a solid sphere. The first step to approach the granular impact drag might be an observation of the crater left on the target surface. In contrast, in a fluid target, a crater or cavity formed by the impact is immediately relaxed. For the granular target, the yield

stress and plastic deformation allow the crater to sustain its form. This difference is one of the most important differences between fluid and granular impacts. For the granular impact, therefore, the resultant crater shape is the first clue to impact dynamics. Scaling analysis is useful to discuss primitive data such as the crater depth or diameter. Scaling laws for crater morphology were first introduced in 1950 by Lampson using the explosive (high-energy) cratering data [1, 2]. Recent experiments of low-velocity granular impacts are roughly consistent with the scaling laws [3–7].

The proposed scaling laws are based on a simple energy balance. If the plastic deformation of the target dominates the cratering process, the impact kinetic energy E_{kei} is consumed to form a crater $Y_t V_c \sim Y_t D_{\text{cra}}^3$, where Y_t , V_c , and D_{cra} are the bulk strength¹, crater's volume, and representative dimension of the crater, e.g., depth or diameter, respectively. Then, the crater dimension is scaled as

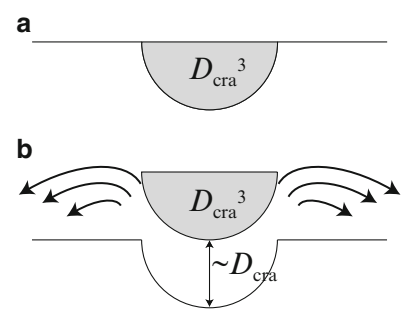
$$D_{\rm cra} \propto E_{\rm kei}^{1/3}.\tag{4.1}$$

However, if the ejection is the most important process, $E_{\rm kei}$ is translated to the gravitational potential energy to lift the crater volume $V_c \sim D_{\rm cra}^3$ to height $D_{\rm cra}$, $E_{\rm kei} \propto V_c D_{\rm cra}$. Then, the scaling is written as

$$D_{\rm cra} \propto E_{\rm kei}^{1/4}.\tag{4.2}$$

Schematic images of these scaling laws are presented in Fig. 4.2. These relations can also be obtained using the systematic dimensional analysis (see Sects. 5.5.1 and 6.1.1 for details). Large nuclear (explosive) craters exhibit intermediate scaling, $D_{\rm cra} \propto E_{\rm kei}^{1/3.4}$ [1]. These scaling relations are based on the energy balance. If the effect of momentum is considered, the scaling exponent could be reduced. For instance, $D_{\rm cra} \propto (v_0^2)^{1/7}$ is obtained by the momentum-based scaling, Eq. (5.58) with the exponent $\mu = 1/3$ (see Sect. 5.5 for details). Moreover, the crater's diameter

Fig. 4.2 Outlines of two scaling laws for crater dimension. (a) Energy balance between the impact kinetic energy and the plastic deformation is essential (Eq. (4.1)). (b) The impact kinetic energy is scaled by the ejection potential energy (Eq. (4.2))



¹The strength has a stress dimension which corresponds to the energy density to exceed the elastic limit (Eq. (2.129)).

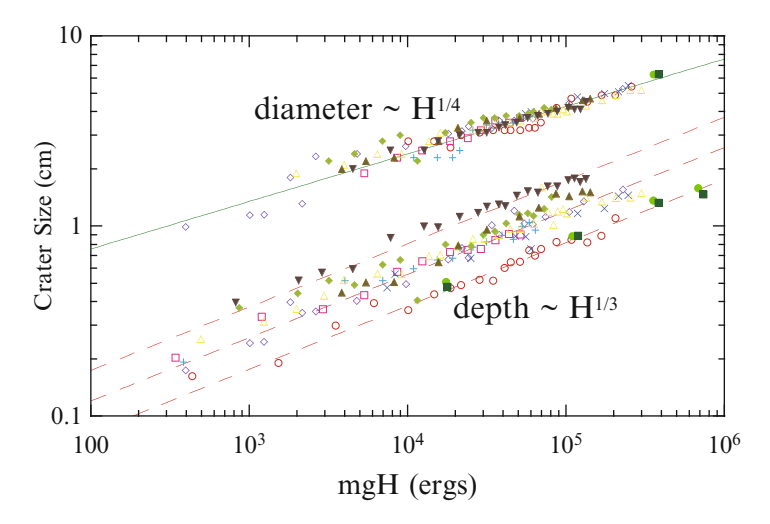


Fig. 4.3 Scaling laws for granular impact crater's diameter and depth. Various spheres of $D_i = 15.2-38.2$ mm and glass beads of $D_g = 0.2$ mm were used in the experiment. The different marks indicate different experimental conditions (Reprinted with permission from Ref. [3]. Copyright 2003 by American Physical Society)

and depth are proportional to each other in planetary craters. Thus, the selection of a representative length scale (diameter or depth) does not affect the scaling analysis.

The validity of this scaling has been examined in low-velocity granular impact experiments [3, 5–7]. In the experiments, a rigid sphere was released from a certain free-fall height h and the sphere struck a granular target (Fig. 4.1). Then, the crater's dimensions were measured. Equation (4.1) was confirmed for the final penetration depth of the impactor, $d \propto E_{\rm kei}^{1/3}$ [3, 7]. Note that the penetration depth d is close to but slightly different from the crater depth. For the crater diameter D_c , the experimental results indicated that D_c obeys Eq. (4.2), $D_c \propto E_{\rm kei}^{1/4}$ [3, 6]. These direction-dependent scaling laws contrast with the actual planetary craters, in which the diameter and depth are scaled identically. The actual experimental data in Ref. [3] are presented in Fig. 4.3. In Ref. [3], the total drop height H = h + d is used instead of the impact velocity $v_0 = \sqrt{2gh}$, to estimate the released potential energy. The obtained scaling is written as

$$\frac{d}{d_0} = \left(\frac{H}{d_0}\right)^{1/3},\tag{4.3}$$

where d_0 is the final penetration depth for h = 0 ($v_0 = 0$), i.e., the bottom of the sphere just touches the surface of the granular target before its release.

The scaling laws appear to work well for observations and experiments. However, there has not been any direct evidence for the physical pictures shown in Fig. 4.2. The drag force law should be revealed to determine the true origin of the scaling law.

4.1.2 Controversy over Granular Impact Drag Force Models

The final penetration depth d is a key quantity to discuss the impact drag force. The impactor's kinetic energy is dissipated during the penetration. To explain the scaling of Eq. (4.3), a drag force scaling² $F_D \propto z^{\alpha_s} v^{(4-2\alpha_s)/3}$, which is consistent with the form of Eq. (4.3), was experimentally tested [8], where z is the instantaneous penetration depth of the impactor, and α_s is an arbitrary number $(0 \le \alpha_s \le 2)$. However, this drag force model could not explain the experimental data [8]. Instead, the inertial drag was employed in Refs. [8, 9].

Quasi-two-dimensional experiments and numerical simulations have also been used to investigate granular impact dynamics [10]. Impact dynamics is decomposed into three stages: impact, penetration, and collapse. The penetration stage dominates the drag force dynamics in the low-velocity granular impact. During the penetration stage, both the experimental and numerical results indicated that the stopping time, t_{stop} , is almost constant regardless of the impact velocity v_0 , where t_{stop} is defined as the time duration from the impact moment (t=0) to the impactor's cessation ($t=t_{\text{stop}}$). This constant t_{stop} indicates that the deceleration a=dv/dt is determined only by v_0 because the average behavior of a is simply expressed by $a \simeq -v_0/t_{\text{stop}}$. Thus, the drag force can be written as $F_D \propto v_0$ in this case. A similar constant t_{stop} feature has been reported in Refs. [11–13].

Another research group has focused on the Bingham model behavior of granular matter. The Bingham model is characterized by the existence of yield stress (Sect. 3.2). When the applied shear stress is less than the yield stress, the Bingham model behaves like an elastic material. If the applied stress exceeds the yield stress, the Bingham model starts to flow. The shear strain rate is linearly related to the shear stress in the flow regime. To evaluate the effective viscosity and yield stress from the granular impact data, de Bruyn et al. investigated the relation between d and v_0 [14]. These researchers confirmed the linear relation $d = d_0 + \alpha_1 v_0$ (Fig. 4.4), where d_0 and α_1 are fitting parameters. This result is consistent with the form of a Binghamtype drag force, $F_D = F_0 + C_\eta v$. Here F_0 is a constant drag force originating from the yield stress, and C_η is a parameter related to the viscosity. However, their fitting result shows negative d_0 in dense granular target cases (Fig. 4.4). The negative d_0 (final penetration depth for $v_0 = 0$) is evidently unphysical.

Using highly loose granular matter called "quicksand," zero impact velocity $(v_0 = 0)$ penetration, d_0 , was studied extensively. Lohse et al. examined the impactor mass m_i dependence of d_0 using the quicksand target [15]. These researchers observed a simple proportional relation, $d_0 \propto m_i$. To explain the experimental result, they assumed a depth-proportional drag force, $F_D = kz$, where k is a constant. A somewhat similar depth-proportional drag force model has also been discussed in Ref. [16]. This drag force model is related to the Coulomb friction.

²This scaling form can be made by combining two extreme cases. One case is computed by energy balance; $F_D \propto z^{\alpha_s} d \propto H \propto d^3$ and $z \sim d$, i.e., $\alpha_s = 2$. The other case is obtained by another energy balance $F_D \propto v^{\beta_s} d \propto d^3$ and $d \propto H^{1/3} \propto v^{2/3}$, i.e., $\beta_s = 4/3$.

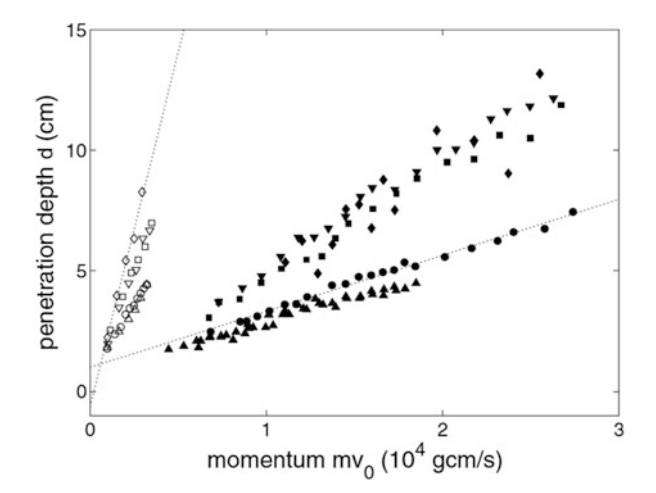


Fig. 4.4 Relation between the final penetration depth and impact momentum. Steel spheres with $D_i = 12.4$ or 25.4 mm and glass beads with $D_g = 0.045$ –0.3 mm were used. The different marks indicate different experimental conditions. Even though the linear relation can be confirmed, this relation results in negative d_0 (steeper dashed line) for dense granular targets (Copyright 2004 Canadian Science Publishing. Reproduced with permission [14])

The Coulomb friction force F_C is written as $F_C = \mu_f p A$, where μ_f , p, and A are the frictional coefficient, pressure at the sphere's surface and contacting area, respectively. Assuming that μ_f and A are constant, F_C is proportional to p. If the granular pressure in the container can be written by the hydrostatic³ one, the pressure is proportional to the depth, $p \propto z$. Consequently, F_C is simply proportional to z.

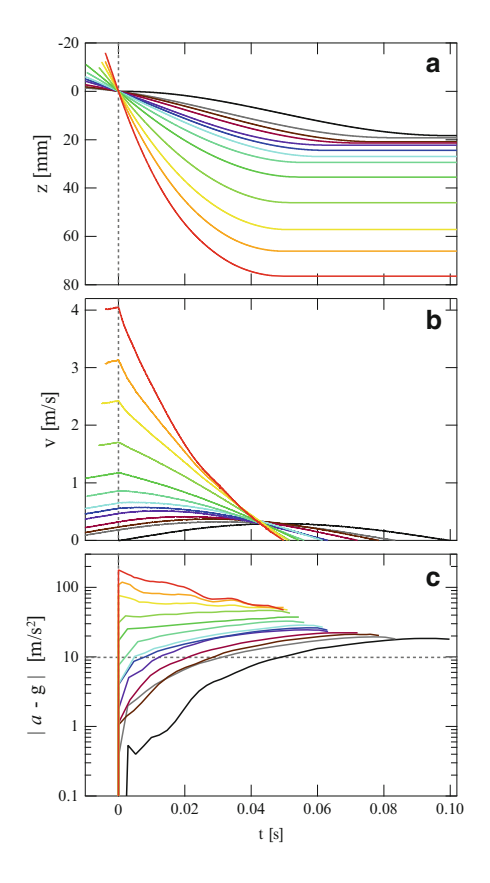
All the aforementioned experimental results have their own drag force models. However, they have looked rather disparate. It has been difficult to find a consensus concerning the granular impact drag force. This controversy still exists; however, a possible unification of these results is discussed in the next subsection.

4.1.3 Unified Drag Force Model

To obtain a unified drag force model, a careful and accurate experiment is indispensable. To meet this requirement, an accurate velocimetry method was developed and applied to the impactor [17]. The method attains a 100 nm spatial resolution and

³In general, the pressure of confined granular column becomes saturated due to the Janssen effect mentioned in Sect. 3.7.1. However, the pressure can be approximated by the hydrostatic pressure in the shallow regime. The word *hydrostatic* is used to indicate the *lithostatic* (or soil pressure) situation in granular matter as well. Namely, the words hydrostatic pressure, lithostatic pressure, and soil pressure are not distinguished in this book.

Fig. 4.5 Instantaneous (a) penetration depth, (b) velocity, and (c) acceleration of a steel sphere ($D_i = 25.4 \text{ mm}$ and $\rho_i = 8.07 \times 10^3 \text{ kg/m}^3$) impacting a glass-bead bed ($D_g = 0.3 \text{ mm}$, $\rho_t = 1.52 \times 10^3 \text{ kg/m}^3$, and $\theta_{\text{repose}} = 24^\circ$) with various impact velocities (Data from Ref. [17])



a 20 μ s temporal resolution. In the experiment, a steel sphere with $D_i=25.4\,\mathrm{mm}$ was dropped to make a free-fall impact onto a glass-bead bed with $D_g\simeq0.3\,\mathrm{mm}$. The impactor's velocity was measured accurately using the developed velocimetry method. The density of the steel sphere was $\rho_i=8.07\times10^3\,\mathrm{kg/m^3}$. The glass-bead target possessed a bulk density of $\rho_t=1.52\times10^3\,\mathrm{kg/m^3}$ and an angle of repose of $\theta_{\mathrm{repose}}=24^\circ$. Under this experimental condition, the glass-bead target can be regarded as noncohesive granular matter. In Fig. 4.5, the experimentally obtained data of z, v, and a for various v_0 are displayed. The moment of impact corresponds to t=0. At $t=t_{\mathrm{stop}}$, the acceleration data have finite values (Fig. 4.5c), which suggests that the impactor cessation is discontinuous in terms of acceleration. A similar tendency has been confirmed in other experiments (e.g., Fig. 4.9). This sudden stop originates from frictional support.

As a unified drag force model, a combination of inertial drag and frictional drag was employed. That is, the equation of motion of the impacting sphere is written in accordance with Newton's second law as follows [17]

$$m_i \frac{d^2 z}{dt^2} = m_i g - \frac{m_i}{d_1} v^2 - kz, \tag{4.4}$$

where d_1 is some characteristic length scale. Additionally, d_1 is supposed to be independent of z, and k is assumed to be independent of v = dz/dt. Similar inertial-dominant drag force models have been proposed in Refs. [8, 9]. Moreover, the inertial drag has been considered for ballistic penetration analyses [18]. Equation (4.4) also corresponds to a modified version of the Poncelet drag model (Sect. 2.6.7). In Eq. (4.4), the constant drag force term in the Poncelet drag model is replaced by the depth-dependent term.

Although Eq. (4.4) is very simple, it was not derived from microscopic first principles. Actually, it was first obtained based on experimental results. Because this equation of motion is the most important element in this section, we trace the details of the derivation process of Eq. (4.4) in the following. If Eq. (4.4) is appropriate to describe the granular impact drag force, the fundamental relation between acceleration a = dv/dt and velocity v must be quadratic. Equation (4.4) can be transformed to

$$a - g = -\frac{v^2}{d_1} - \frac{k}{m_i} z. {(4.5)}$$

The parameters z, v, and a were experimentally measured as functions of time t for various v_0 (Fig. 4.5). From these raw time series data, a-g and v at some fixed depths z_i are extracted. The relation between the extracted a-g and v is shown in Fig. 4.6a. As expected, the quadratic relation can be confirmed, which provides strong evidence of the inertial drag force of the granular impact. In addition, the net acceleration minus the inertial contribution, $a-g+v^2/d_1$ for all v_0 is shown as a function of z in Fig. 4.6b. This component corresponds to the frictional drag in Eq. (4.4). In Fig. 4.6b, a linear relation in $a-g+v^2/d_1$ vs. z can be clearly confirmed. These results are fully consistent with Eqs. (4.4) and (4.5).

From these data, two characteristic parameters $1/d_1$ and k/m_i can be estimated by the relations,

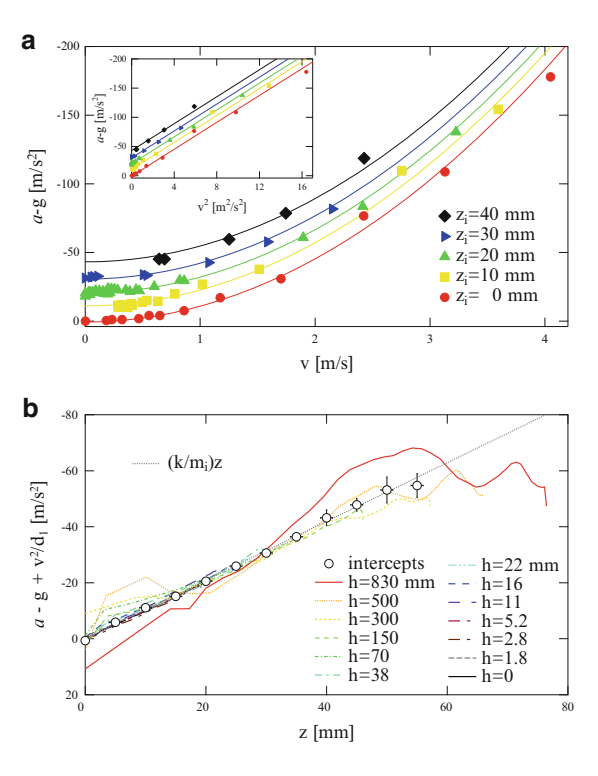
$$\frac{\partial(a-g)}{\partial(v^2)} = -\frac{1}{d_1},\tag{4.6}$$

and

$$\frac{\partial(a-g)}{\partial z} = -\frac{k}{m_i}. (4.7)$$

A constant drag force term, which is independent both of v^2 and z, is not necessary in Eq. (4.4). In the inset of Fig. 4.6a, a-g vs. v^2 is displayed. The parallel linearity in this plot suggests that $1/d_1$ is truly constant and independent of z. The value obtained by the fitting is $d_1 = 87 \pm 7$ mm. For the frictional drag force, k/m_i is independent of v. Thus, the data in Fig. 4.6b show a good data collapse to the simple proportional relation. From the slope of the data in Fig. 4.6b, k/m_i is estimated to be $1040 \pm 40 \, \mathrm{s}^{-2}$. The evaluation and material property dependence of d_1 and k/m_i will be discussed later in this section.

Fig. 4.6 (a) Net acceleration vs. velocity at some fixed depths and (b) frictional drag force as a function of z. The data used in this figure are the same as those used in Fig. 4.5. The *inset* of (a) shows a-g vs. v^2 , and the main plot shows a-g vs. v. Both clearly show the existence of the inertial drag. The linear depth-dependent frictional drag can be confirmed in (b) (Data from Ref. [17])



The validity of the drag force model of Eq. (4.4) has been demonstrated by the above analysis. Then, how about the compatibility of the model with the previously reported empirical laws? In Ref. [17], the experimental results shown in Fig. 4.5 were compared with these empirical laws. In Fig. 4.7, the comparisons of the data and empirical laws are plotted. The scaling $d \propto H^{1/3}$ [3] and $d = d_0 + \alpha_1 v_0$ [14] are shown as solid lines in Fig. 4.7a, b, respectively. It is apparent that the data fit both the empirical laws. Note that all the data shown in Fig. 4.7 come from the same experiment. For $v_0 = 0$, the linear Coulomb-friction-like behavior is confirmed (Fig. 4.7c). This linear trend is consistent with the previously reported empirical law of Ref. [15]. Moreover, t_{stop} becomes almost constant ($\simeq 0.051 \,\text{s}$) in the regime of $v_0 > 1 \,\text{m/s}$ (Fig. 4.7d). This constant t_{stop} character is consistent with previous experiments and simulations [10–13]. The value of $t_{\text{stop}} = 0.051 \,\text{s}$ can be derived from the characteristic timescale of the system [17]:

$$t_{\text{stop}} \simeq \sqrt{\frac{D_i}{g}}.$$
 (4.8)

This t_{stop} can be understood by the inertial drag $(D_i^2 v^2 \sim D_i^3 g)$ and $t_{\text{stop}} \sim D_i/v$. More precise measurements of the stopping time by various impactors and targets have revealed a scaling of $t_{\text{stop}} \sim (\rho_i/\rho_t)^{1/4} \sqrt{D_i/g}$ [12]. Based on the numerical

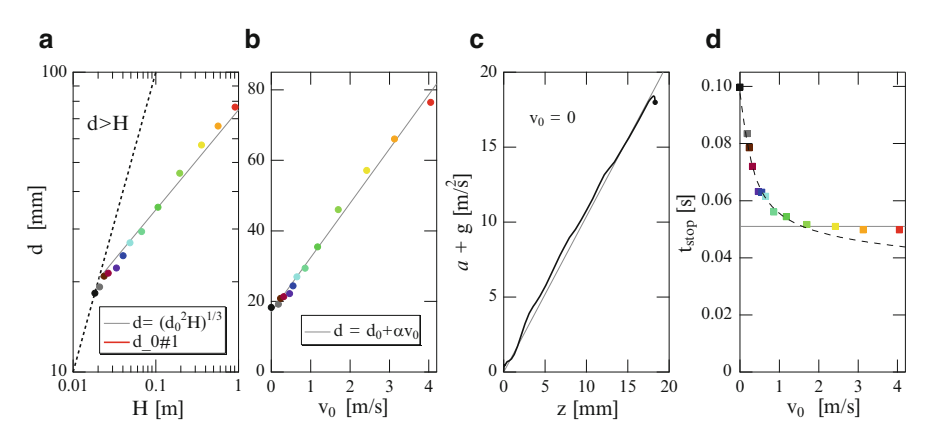


Fig. 4.7 Compatibility of Eq. (4.4) with empirical laws, (a) $d \propto H^{1/3}$, (b) $d = d_0 + \alpha_1 v_0$, (c) $F_D \propto z$ for $v_0 = 0$, and (d) constant t_{stop} . In (a), (b), and (d), data points correspond to experimental results and *solid lines* represent the corresponding empirical laws. In (c), a - g vs. z for $v_0 = 0$ is shown as the *black curve*. The *dashed curve* in (d) was computed using the time at which the velocity reached zero in the numerical integration of Eq. (4.4). The *gray* level in (d) corresponds to $t_{\text{stop}} = 0.51$ s (Data from Ref. [17])

simulation in Ref. [13], the $(\rho_i/\rho_t)^{1/2}$ dependence of t_{stop} was also reported. Because the factor $(\rho_i/\rho_t)^{1/4}$ or $(\rho_i/\rho_t)^{1/2}$ is not so large (at least within the same order in the current experimental condition, $\rho_i/\rho_t \simeq 5.3$), these forms are still roughly consistent with the result of Ref. [17]. The aforementioned results suggest that Eq. (4.4) is completely consistent with the empirical laws [3, 6, 10, 14, 15]. Recall that these empirical laws have looked disparate as discussed before. It can be considered that the empirical laws are approximate scaling or limiting behaviors of Eq. (4.4).

In Eq. (4.4), the inertial and frictional drag terms correspond to fluid-like and solid-like behaviors of granular matter, respectively. That is, the dual nature of granular matter is manifested by Eq. (4.4). The unified drag force model is plausible in terms of this duality as well.

Because Eq. (4.4) has a simple form, it can be analytically solved but only in v-z space [8, 19]. To solve the equation, we consider an energy form. The kinetic energy of the impactor, $E_{\rm kei}$, is denoted as

$$E_{\rm kei} = \frac{1}{2} m_i v^2. (4.9)$$

Then, the left-hand side of Eq. (4.4) is expressed by E_{kei} as

$$\frac{dE_{\text{kei}}}{dz} = m_i v \frac{dv}{dz} = m_i \frac{dv}{dt}.$$
 (4.10)

Here Eq. (4.4) is generalized as

$$m_i \frac{d^2 z}{dt^2} = m_i g - \frac{m_i}{d_1} v^2 - f(z), \tag{4.11}$$

where the depth-dependent force is rewritten by the general form f(z). Using Eq. (4.10), the generalized drag force equation is written as

$$\frac{dE_{\text{kei}}}{dz} = m_i g - \frac{2}{d_1(z)} E_{\text{kei}} - f(z). \tag{4.12}$$

In this general notation, $d_1(z)$ can depend on z. This linear ordinary differential equation is formally solved as [19]

$$E_{\text{kei}}(z) = K_p(z) \left(K_0 + \phi_p(z) \right),$$
 (4.13)

where $K_0 = m_i v_0^2 / 2$ is the kinetic energy at the moment of impact (initial condition). $K_p(z)$ is written as

$$K_p(z) = \exp\left(-\int_0^z \frac{2}{d_1(z')} dz'\right),$$
 (4.14)

and $\phi_p(z)$ is

$$\phi_p(z) = \int_0^z \frac{m_i g - f(z')}{K_p(z')} dz'. \tag{4.15}$$

This formal solution corresponds to a type of energy transfer form. One can easily verify that Eqs. (4.13), (4.14), and (4.15) satisfy Eq. (4.12). Then, the velocity v(z) is obtained by Eq. (4.9) as

$$v(z) = \left[\frac{2}{m_i} K_p(z) \left(K_0 + \phi_p(z) \right) \right]^{1/2}. \tag{4.16}$$

Assuming that d_1 is constant, $K_p(z)$ is computed as

$$K_p(z) = \exp\left(-\frac{2z}{d_1}\right). \tag{4.17}$$

Furthermore, $\phi_p(z)$ can be calculated with the simple assumption f(z) = kz (constant k):

$$\phi_p(z) = \int_0^z \exp\left(\frac{2z'}{d_1}\right) \left(m_i g - k z'\right) dz'$$

$$= \left[\exp\left(\frac{2z}{d_1}\right) - 1\right] \left[\frac{m_i g d_1}{2} + \frac{k d_1^2}{4}\right] - \frac{k z d_1}{2} \exp\left(\frac{2z}{d_1}\right). \tag{4.18}$$

Substituting Eqs. (4.17) and (4.18) into Eq. (4.16), we finally obtain the specific form of v(z) as

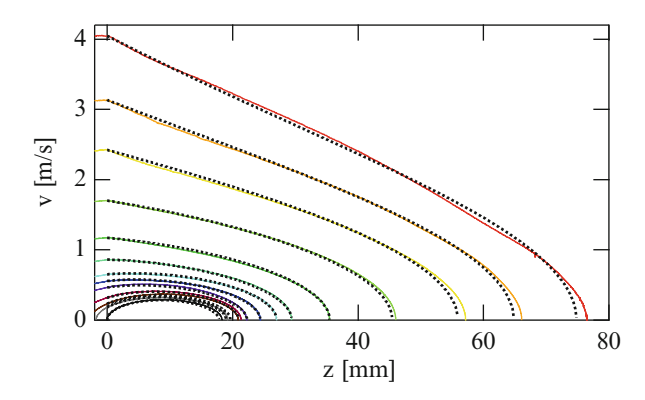


Fig. 4.8 Experimental data and analytic solutions of v(z). The *solid* and *dotted curves* correspond to experimental data and analytic solutions, respectively. The data used in this plot are same as those in Figs. 4.5 and 4.6. Although we can confirm the excellent agreement, this analytic solution cannot perfectly fit the very shallow penetration data (not shown here) by fixed d_1 and k [20]

$$v(z) = \left[v_0^2 e^{-\frac{2z}{d_1}} - \frac{kd_1 z}{m_i} + \left(1 - e^{-\frac{2z}{d_1}} \right) \left(g d_1 + \frac{kd_1^2}{2m_i} \right) \right]^{1/2}. \tag{4.19}$$

A comparison of the analytic solutions and the experimental data is presented in Fig. 4.8. The solutions and experimental data show an excellent agreement by constant d_1 and k. However, there is a limit of applicability of this drag force law. d_1 and k are not constant for a very shallow impact case [20] (not shown in Fig. 4.8). For such an impact, the impact drag force might be slightly different. The analytic solution for very shallow impacts tends to overestimate the penetration depth. It might be a shape effect of the impactor or some other complex rheological effect of granular matter. Furthermore, it might be caused by the force-chain-structure difference between prefluidized and fluidized granular target [21].

The physical meanings of the values of d_1 and k in Eq. (4.4) can be discussed by comparing the values with the momentum transfer and Coulomb friction. The experimentally obtained value of $1/d_1 = 11 \, (\text{m}^{-1})$ is comparable to $\rho_t/\rho_i D_i \simeq 4.9 \, (\text{m}^{-1})$, which implies the consistency of the momentum transfer form, $(m_i/d_1)v^2 \sim \rho_t D_i^2 v^2$. However, the order of magnitude of the frictional drag term is not so consistent. If we assume Coulomb friction and hydrostatic pressure, k will satisfy $k = C_k \mu_f \rho_t g D_i^2$. Here C_k is a dimensionless constant. In the experiment, ρ_t , D_i , and μ_f are $1.52 \times 10^3 \, \text{kg/m}^3$, 25.4 mm, and 0.45, respectively. Substituting these experimental conditions, $C_k = 80$ is obtained. This C_k value is much larger than unity, which indicates that the granular frictional drag is much larger than the values expected from ordinary Coulomb friction. The main reason for this large frictional drag is most likely the abnormal pressure in granular penetration, which may be considerably greater than hydrostatic or Janssen pressure.

From the viewpoint of rheological modeling, Eq. (4.4) qualitatively resembles the Kelvin-Voigt model. Stresses by inertial and frictional contributions are simply combined while the penetration depth and velocity are common in the system. However, Eq. (4.4) is quite different from Eq. (3.3). Granular targets cannot store

elastic energy in general. The granular drag force consists of a velocity-squared-proportional momentum transfer term and depth-proportional frictional force. At the moment of impact, inertial drag dominates the entire drag force. The momentum is transferred from the impactor to the target granular medium. As the impactor penetrates into the target, velocity decreases drastically because of the inertial drag, and the frictional drag becomes crucial in the late and deep stage. Once the inertia of the impactor is balanced with frictional drag, the impactor is immediately arrested.

The frictional drag force term is formally similar to the elastic force. However, the frictional drag cannot store the elastic energy; it is rather plastic and dissipative. Although the granular drag force has fluid-like and solid-like responses, these responses are different from the conventional viscoelastic one. The kinetic energy of the impactor is transferred to ejecta and dissipated by internal friction. The energy dissipation and partition were estimated numerically in Ref. [22]. Equation (4.4) becomes meaningless once v=0 is reached. In other words, the rebound after v=0 computed by Eq. (4.4) cannot be clearly observed in the experiment. There is no elastic contribution in the granular impact drag force.

Because the usual frictional drag acts tangentially at the interface, one might expect a shear component for the frictional term. However, Brzinski et al. experimentally demonstrated that the frictional drag acts normal to the surface of the impactor [23]. Moreover, in the experiment, the air flow through the target granular bed with its speed U_{air} during the impact was used to reduce the gravitational loading effect. They observed that the frictional drag force kz vanishes at a certain air flow speed $U_{air} = U_c$. According to the experimental result, the reduced frictional drag force can be computed by multiplying kz by a reduction factor $1 - U_{air}/U_c$. The origin of the large frictional drag force may be intermittent force chains emitted at the impact surface, which act in the roughly normal direction of the surface (e.g., Fig. 4.10).

A drag force model that is essentially similar to Eq. (4.4) has been proposed by Boguslavskii et al. [24, 25]. These researchers considered the higher order terms and the cross terms of v^2 and z and approximately computed the final penetration depth and other related quantities. Using the model, the experimental results of relatively deep granular impact penetrations can be evaluated. For deep penetrations, two peaks appear in the a(z) profile. The first peak, called the dynamic peak, originates from the inertial drag, and the second peak, called the static peak, corresponds to the frictional drag. Even in shallow penetrations, we can observe the sudden decrease in acceleration that roughly corresponds to the second peak (Fig. 4.5c). Another modeling of the drag force equation has been studied based on a general inverse formulation [26, 27]. However, this modeling is based on some arbitrariness in the selection of the model.

4.1.4 Material Dependence of the Drag Force Model

Two quantities d_1 and k are essential parameters of the granular impact drag force. Although the value of k/m_i is too large compared with the simple assumption,

Eq. (4.4) appears to be phenomenologically sound. In the above analysis, these two values were computed by the fitting to the experimental data taken by a steel sphere impactor and glass-bead target. The natural next question is how do the parameters d_1 and k depend on material properties such as the impactor's diameter D_i , density ρ_i , and target density ρ_t ? To verify the material dependence of the parameters, systematic experiments were performed for various impactors and targets [20]. For each experimental condition, d_1 and k were computed by data fitting.

From the experimental data, a simple relation for the inertial drag,

$$\frac{d_1}{D_i} = \frac{0.25}{\mu_f} \frac{\rho_i}{\rho_t},\tag{4.20}$$

is obtained. This scaling form is basically understandable by the momentum transfer from the impactor to the target, $(\rho_i D_i^3/d_1)v^2 \sim \rho_t D_i^2 v^2$, (Sect. 2.6.2). While the μ_f dependence is unclear a priori, $d_1 \sim \mu_f^{-1}$ is empirically obtained from the experimental data. If we consider the virtual mass, d_1 depends on μ_f as $d_1 \propto 1/(1+\alpha_{d1}\mu_f)$. The advantage of this form is its convergence in the frictionless limit ($\mu_f \rightarrow 0$). In experiments, it is difficult to vary μ_f in a wide range. Thus, we cannot conclude which one is better by using the current experimental result. On the basis of residual errors, the scaling form (Eq. (4.20)) is slightly better than the virtual mass form [20].

Next, scaling for the frictional drag is considered. The following relation should hold if the Coulomb friction and hydrostatic pressure are used for the origin of the frictional drag $(kz/m_i \sim \mu_f \rho_t gz D_i^2/\rho_i D_i^3)$:

$$\frac{kD_i}{\mu_f m_i g} \sim \frac{\rho_t}{\rho_i}.\tag{4.21}$$

However, this scaling cannot explain the experimental data. Instead, the empirical scaling,

$$\frac{kD_i}{\mu_f m_i g} = 12 \left(\frac{\rho_t}{\rho_i}\right)^{1/2},\tag{4.22}$$

fits the data well. The curious scaling exponent 1/2 can be derived on the assumption of the geometric mean of the density for the frictional drag force, $(\rho_i\rho_t)^{1/2}d^2z/dt^2 \sim \rho_t gz/D_i$. In Ref. [15], the virtual mass was considered to explain the frictional drag. This virtual mass effect corresponds to the arithmetic mean of densities. However, the geometric mean is better than the arithmetic mean in explaining the general frictional drag force, at least for the experimental data set in Ref. [20]. Moreover, the value of k is increased by pre-shear straining [28]. There might be some other parameters relevant to describe the behavior of k.

The inertial drag in the granular impact is very similar to the fluid inertial drag. Material-dependent scaling is consistent with the conventional momentum transfer theory. The order of the inertial drag force is also reasonable. However, the frictional drag force exhibits complex behavior such as nontrivial scaling.

Moreover, as mentioned in the previous subsection, the order of the frictional drag is approximately one order of magnitude greater than the simple assumption of the Coulomb friction and hydrostatic pressure. To uncover the physics of the granular frictional drag force, more detailed studies are needed. For now, two dimensionless numbers d_1/D_i and kD_i/m_ig are the most important quantities to characterize the granular impact drag force.

The drag force equation can be evaluated by dimensional analysis. Substituting Eqs. (4.20) and (4.22) into Eq. (4.5), the drag force is nondimensionalized as

$$\frac{a}{g} - 1 = -4\mu_f \frac{\rho_t}{\rho_i} \frac{v^2}{gD_i} - 12\mu_f \left(\frac{\rho_t}{\rho_i}\right)^{1/2} \left(\frac{z}{D_i}\right). \tag{4.23}$$

Then, we find three important dimensionless quantities: a/g, $(\mu_f \rho_t/\rho_i)(v^2/gD_i)$, and $\mu_f(\rho_t/\rho_i)^{1/2}(z/D_i)$. In terms of Π -groups, there are 8 relevant quantities: $a, v, z, g, D_i, \rho_i, \rho_i$, and μ_f . Because there are three fundamental dimensions: M, L, and T, five independent dimensionless numbers can be obtained. In this case, the simplest set of dimensionless numbers is obtained as

$$\Pi_1 = \frac{a}{g}, \quad \Pi_2 = \frac{v^2}{gD_i}, \quad \Pi_3 = \frac{z}{D_i}, \quad \Pi_4 = \frac{\rho_t}{\rho_i}, \quad \Pi_5 = \mu_f.$$
(4.24)

Here Π_2 corresponds to the Froude number. Then, the three important dimensionless numbers discussed above are expressed as Π_1 , $\Pi_2\Pi_4\Pi_5$, and $\Pi_3\Pi_4^{1/2}\Pi_5$. Comparing the inertial and frictional dimensionless numbers, one can obtain a characteristic dimensionless number D_r as

$$D_r = \frac{\Pi_2 \Pi_4 \Pi_5}{\Pi_3 \Pi_4^{1/2} \Pi_5} = \frac{v^2}{gz} \left(\frac{\rho_t}{\rho_i}\right)^{1/2}.$$
 (4.25)

When D_r is very large, inertial drag dominates the granular drag force. In contrast, the frictional drag becomes predominant in the very small D_r regime.

Using the granular target bed fluidized by air flow of speed U_{air} , the frictional drag force was measured to be $\simeq 30(1-U_{air}/U_c)\mu_f\rho_r gzA$, where U_c is the critical air speed above which the frictional drag vanishes [23]. This form rather indicates the simple linear relation, Eq. (4.21). Then, D_r becomes equivalent to $F_r(=\Pi_2)$. The degree of target fluidization due to both the impact and the aeration cannot be estimated directly. In particular, the impact results in both fluidization and compaction simultaneously by shearing (tangential) and normal loading, respectively.

4.1.5 Direct Force Measurement

Some intriguing characteristics of the granular impact were observed by a direct force measurement. Goldman and Umbanhowar directly measured the acceleration of the impactor using an accelerometer [12]. In Fig. 4.9, examples of a/g vs. t for

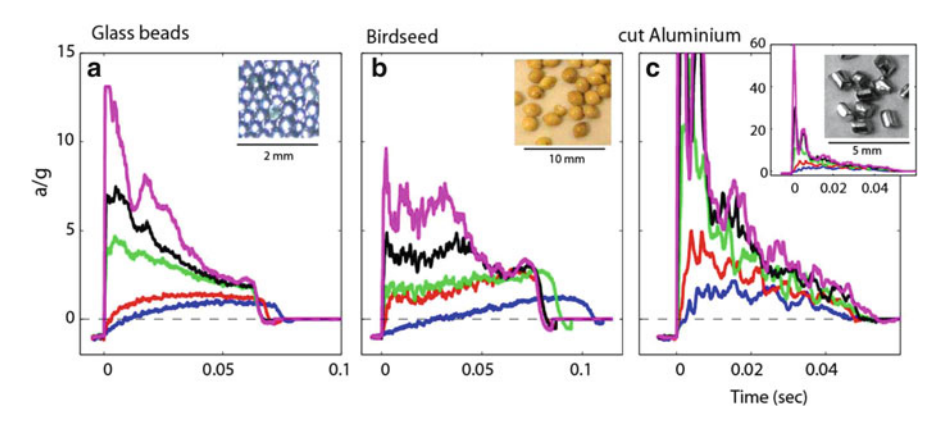


Fig. 4.9 Normalized acceleration a/g for various target grains and the impact velocities. The impactor is a bronze sphere $(D_i = 38 \text{ mm} \text{ and } m_i = 0.2 \text{ kg})$. Photos of target grains are shown in the *insets* of each panel (Reprinted with permission from Ref. [12]. Copyright 2008 by American Physical Society)

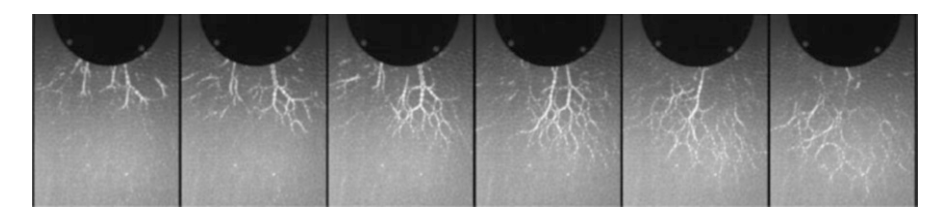


Fig. 4.10 Propagation of the force chain pulses created by the impact (Reprinted with permission from Ref. [30]. Copyright 2012 by American Physical Society)

various target grains are displayed. To understand the drag force law of Eq. (4.4), the target granular matter must be a sort of continua. Thus, Eq. (4.4) can only describe the average behavior. However, the real acceleration data exhibit complex behaviors, as observed in Fig. 4.9. The fluctuation of a/g strongly depends on the shape of the grains. The size ratio between the impactor and grains D_i/D_g also appears to be important for the fluctuation. An extremely large fluctuation was observed for angulated cut-aluminium-grain target (Fig. 4.9c). This fluctuation might have originated from the intermittency of force chain networks created by the impact [29].

Using a photoelastic imaging technique, Clark et al. studied the particle dynamics of granular impact [30]. They carried out a quasi-two-dimensional impact experiment and used a high-speed camera to capture the force chain dynamics and clearly observed the force chain propagation immediately after the impact. The propagations of the force chains occurred very intermittently. Example snapshots are presented in Fig. 4.10. The authors discussed the relation between the force chain pulse propagation and the drag force fluctuation. Consequently, it was revealed that the drag force fluctuation has a nearly exponential probability distribution. In

addition, the drag force fluctuation exhibited a clear correlation with the force chain propagation [30], which indicates that the drag force fluctuation is intrinsic for the granular impact. This fluctuation is caused by the force chain pulse propagation. In other words, the origins of the fluctuation are the inherent discreteness and random packing structure of the target granular bed. This force chain pulse propagation is significant in the case of stiffer target grains. When the target grains are soft, a dense force structure that propagates with a well-defined front can be observed [31].

Another characteristic feature in Fig. 4.9 is the abrupt cessation observed in the glass bead and birdseed cases. The acceleration data a/g show a sudden decrease in the final stage. This finite jump in a/g presumably originates from the frictional drag. During the final stage of deceleration, frictional drag dominates the entire deceleration because the velocity v is very small. The large z (for frictional drag) and the small v (for inertial drag) inevitably result in a sudden stop. A similar jump (abrupt cessation) can also be confirmed in Fig. 4.5c. Directly before the impactor ceases, a micro rebound (small pit of a/g) can also be observed in Fig. 4.9. Similar rebound has been reported in another experiment (Supplementary Information of [17]) and in two-dimensional numerical simulations [13, 32]. Although the micro rebound may be a symptom of granular elasticity, further studies are required to confirm its origin.

In Ref. [12], Goldman and Umbanhowar also observed the viscous drag force (linear relation between drag force and velocity) for relatively high-velocity impacts, which is counterintuitive because the viscosity is dominant in the low-velocity (low R_e) regime for ordinary fluids. Viscosity-like behavior was also observed in another experiment of the granular impact with a relatively high-velocity impact ($v_0 \simeq 70\,\text{m/s}$) [33]. The experimental result and corresponding numerical simulation suggest that there is a velocity-proportional component of the drag force. Although this problem might only be a square completion problem (Eq. (2.97)), further investigations are necessary to reveal the origin of this viscous-like drag force of the granular impact. Possible physical meanings of the velocity-proportional viscous-like drag will be discussed in the next subsection.

4.1.6 Inertial and Viscous Drag Forces for the Granular Impact

Inertial drag by Bagnold scaling In Eq. (4.4), a viscous drag term is not present. However, as mentioned above, Refs. [12, 14, 33] have proposed the viscous drag force for the relatively high impact velocity regime. In ordinary viscous fluids, the viscous effect dominates the drag force in the low R_e regime. In contrast, R_e cannot be defined for granular matter because its viscosity is not well defined. The reason for this difficulty in the treatment of viscosity for granular matter is discussed in this subsection.

From the viewpoint of dimensional analysis, the shear stress σ_s in sheared dry granular matter is expressed by

$$\sigma_s \sim \frac{m_g}{D_g} \dot{\gamma}^2,\tag{4.26}$$

where m_g and $\dot{\gamma}$ are the granular mass and shear strain rate, respectively. Because only $\dot{\gamma}^{-1}$ involves a relevant timescale in the sheared granular system, Eq. (4.26) is a unique dimensional solution to form a stress dimension [34–36]. Equation (4.26) was derived first by Bagnold [34] and is called the Bagnold scaling. Although Eq. (4.26) is derived for collisional (sparse) granular gas, dense granular flow also satisfies the equation [37, 38], which is natural as long as Eq. (4.26) is a unique dimensional solution for the sheared granular matter. Here the granular viscosity η is calculated using its definition $\eta = \sigma_s/\dot{\gamma}$ as

$$\eta = \frac{\sigma_s}{\dot{\gamma}} \sim \frac{m_g}{D_g} \dot{\gamma}. \tag{4.27}$$

The relation of Eq. (4.27) indicates that the granular viscosity itself is proportional to the shear strain rate $\dot{\gamma}$. For the impact phenomena, the main source of the shear strain rate is the penetrating velocity v. Thus, v and $\dot{\gamma}$ are related as $v \sim D_i \dot{\gamma}$. Using this relation, Eq. (4.27) is written as $\eta \sim (m_g/D_g D_i)v$; the viscosity is proportional to the velocity. That is, the viscous drag force is proportional to v^2 , similar to the inertial drag. Therefore, the viscous and inertial drag forces are not distinguishable for the granular impact. Furthermore, the stress applied to the impactor from each single grain, σ_g , is calculated from Eq. (4.26) as

$$\sigma_g \sim \rho_g \left(\frac{D_g}{D_i}\right)^2 v^2.$$
 (4.28)

Here the relations $m_g \sim \rho_g D_g^3$ and $v \sim D_i \dot{\gamma}$ are used. The total inertial drag force would be the sum of Eq. (4.28) for all related grains. Dimensionally, the stress can be regarded as a momentum transfer per unit time in a unit area. In fact, Bagnold also considered the momentum transfer to derive the Bagnold scaling. As long as $\dot{\gamma}^{-1}$ is a unique timescale in the system, the entire drag force must be proportional to $\dot{\gamma}^2$ (or equivalently v^2). The linear v dependence of the drag force cannot be observed in such systems. In fact, the v^2 -proportional drag force has been observed ubiquitously in many granular systems [39–42]. Furthermore, a microscopic collision model for the granular drag force, which is proposed based on momentum transfer among the impactor and clusters of grains connected by force chains, reproduces the v^2 -proportional drag force very well [43]. Thanks to the microscopic model, the shape dependence and rotational mode of the drag force can also be explained from the viewpoint of collisions of the impactor and grains.

Granular-temperature-based viscosity Random grain motion might add another timescale to the granular system. In the above discussion, only the timescale $\dot{\gamma}^{-1}$ determined the drag force form, particularly for the velocity dependence. Here we consider another possible timescale that may be relevant to the granular viscosity. Using kinetic theory, the granular temperature \hat{T}_g is related to the shear stress [36,

44]. \hat{T}_g is defined by the grain velocity fluctuation, $\hat{T}_g \sim \langle \delta v_i^2 \rangle = \langle (v_i - \langle v_i \rangle)^2 \rangle$ (Eq. (3.72)). Here $\langle \cdots \rangle$ represents the average overall grains (j is an integer; grain index). Because \hat{T}_g involves a timescale of velocity fluctuation, the relation $\eta \propto$ $\hat{T}_g^{1/2}$ is dimensionally possible. If \hat{T}_g is independent of $\dot{\gamma}$, η can also be independent of $\dot{\gamma}$. Because the viscosity is regarded as a diffusion of the momentum density, the viscosity presumably depends on the temperature. In fact, usual fluids exhibit temperature-dependent viscosity. The viscosity of a gas is an increasing function of temperature, as $\eta \propto T^{1/2}$. This temperature dependence can be understood by the kinetic theory (e.g., Eq. (4.49)). Contrary to the kinetic theory, liquid viscosity is a decreasing function of temperature. The mechanism of viscosity is different between a gas and a liquid. Moreover, the granular viscosity is different from both of them. In an experiment of granular avalanches, the relations $\langle \delta v_i \rangle \sim \langle v_i \rangle$ and $\langle \delta v_i \rangle \sim \sqrt{\langle v_i \rangle}$ were observed for slow ($\langle v_i \rangle \leq 30$ mm/s) and fast ($\langle v_i \rangle > 30$ mm/s) regimes, respectively [45]. The former recovers $\eta \propto v$, which is consistent with the impact drag force model and Bagnold scaling. However, the latter yields another scaling $\eta \propto v^{1/2}$; then, the inertial drag force is proportional to $v^{3/2}$. Indeed, $v^{3/2}$ -dependent drag was observed in a numerical simulation in a relatively lowvelocity (v < 7 m/s) regime [46]. However, this tendency ($v^{3/2}$ dependence in the slow impact velocity regime) is qualitatively opposite to the finding of the avalanche experiment. Detailed characterization of the granular impact using \hat{T}_g is a prevailing crucial future problem. The granular temperature during very slow penetration will be discussed later (Fig. 4.16).

Gravity-based viscosity If gravity is considered, another timescale is introduced by the gravitational acceleration g. To estimate the gravity effect, the ratio F_r to R_e is calculated from Eqs. (2.41) and (2.98) as

$$\frac{F_r}{R_e} = \frac{\eta U}{\rho g l^2}. (4.29)$$

This is a dimensionless number representing the ratio between the viscous and gravitational stresses. Using this form, the characteristic viscosity at a certain state of F_r/R_e is written as

$$\eta \sim \frac{\rho g l^2}{U} = \frac{\rho g l}{\dot{\gamma}},\tag{4.30}$$

where $\dot{\gamma} = U/l$ is assumed. For the granular impact, the target granular density ρ_t corresponds to ρ , and the impactor's diameter D_i corresponds to l. Then, Eq. (4.30) implies that the gravitational pressure $\rho_t g D_i$ produces the viscous stress. That gravitational pressure is perhaps inappropriate for the granular impact phenomena in the large $F_r(\gg 1)$ regime. The instantaneous inertial drag should be governed by the momentum transfer rather than the gravitational (hydrostatic) pressure.

Even so, it is imaginable to consider the relation between gravity- and velocity-dependent drag forces, particularly in the small F_r regime. The gravity effect was

actually considered when discussing granular viscosity in Refs. [12, 14]. If we use $\rho = \rho_t$, $l = D_i$, and $U = \sqrt{gD_i}$, Eq. (4.30) becomes

$$\eta \sim \rho_t g^{1/2} D_i^{3/2}. \tag{4.31}$$

This viscosity form is similar to Eq. (3.58) if we employ the gravitational (hydrostatic) pressure and impactor's diameter as the pressure and length scale, respectively. In Ref. [12], however, $\eta \propto \rho_t g^{1/2} D_i^{5/2}$ was reported; the D_i dependence is different. Moreover, $\eta \sim (\rho_i \rho_t)^{1/2} g^{1/2} D_i^{3/2}$ was derived in Ref. [14]. This form is also slightly different from Eq. (4.31). In Ref. [14], the elastic energy transfer was considered and the geometric mean density form was obtained.

As mentioned in the previous subsection, the granular viscous drag is dominant in the relatively high-velocity impact regime. Perhaps this tendency originates from fluidization of the granular matter. The high-velocity penetration might fluidize the surrounding granular layer; then, the granular temperature \hat{T}_g increases. In such a high \hat{T}_g regime, η might be determined by $\hat{T}_g^{1/2}$ rather than v. Note that, however, the experiment with an aerated granular bed, in which \hat{T}_g is most likely relevant, is consistent with a v^2 -dependent inertial-like drag force [41]. In the aerated granular bed, the fluidization is homogeneously induced, while the impact results in a very local fluidization. This localization might affect the scaling. Such a fluidization effect might be an essential factor to understand the form of granular drag force. The physical origin of the effective granular viscosity remains under debate.

Granular jet When a granular jet (stream of grains) hits a rod vertically, granular sheet flow such as a water-bell structure [47] can be developed [48]. The opening angle of the granular sheet depends on the diameter ratio between the jet and the target rod. If the jet diameter is sufficiently large, one can observe the cone structure. In contrast, when the jet diameter is small, the granular jet deflects at a right angle and a plane sheet normal to the jet is produced. Although the granular jet behavior is very similar to liquid behavior, the surface tension cannot contribute to its dynamics in the granular jet. Moreover, the granular jet behavior is close to perfect fluid behavior, in which there is no viscous effect. To determine the granular jet rheology, a three-dimensional numerical simulation of the granular jet impact was performed [49]. According to the numerical result, although both the measured shear stress and shear strain rate are very small, the usual viscosity is observed in the granular jet. Only because the shear stress is considerably less than the normal stress, the granular jet behavior appears similar to that of a perfect fluid. The dynamics is almost dominated by the normal component even for a water-belllike cone structure. Although the relatively high-speed granular jet is not a perfect fluid, the corresponding shear stress is almost negligible. This result is qualitatively similar to the vertical granular impact characterization [23], in which the linear shear viscosity effect is usually negligible.

Inertial drag scaling To demonstrate the importance of the inertial drag in the granular impact, the relation between $|(a_0 - g)/g|$ and v_0^2/gd_1 is shown in Fig. 4.11.

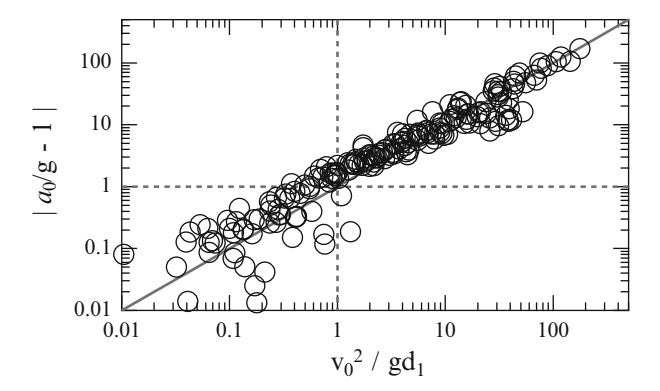


Fig. 4.11 Normalized net drag force at the impact moment, $|a_0/g - 1|$ vs. v_0^2/gd_1 , for various impactors and targets

Here a_0 corresponds to the acceleration at z=0. The data shown in this plot are obtained from the experiment with various impactors and targets [20]. One can confirm a data collapse to the relation

$$\frac{a_0}{g} - 1 = -\frac{v_0^2}{gd_1}. (4.32)$$

Because the frictional drag is absent at z=0, we can purely evaluate the inertial drag using Fig. 4.11 and Eq. (4.32). To make the plot shown in Fig. 4.11, Eq. (4.20) is actually used to calculate d_1 . Considering Eqs. (2.98) and (4.20), Eq. (4.32) can be rewritten as $a_0/g - 1 = -(4\mu_f \rho_t/\rho_i)F_r \sim \Pi_2\Pi_4\Pi_5$ in Eq. (4.24) at t=0). Thus, the dimensionless number $(\rho_t/\rho_i)F_r$ is probably the most important parameter to characterize the granular inertial drag force.

4.1.7 Various Effects in the Granular Impact Drag Force

In the previous subsections, the target granular bed has primarily been considered as a type of continua. Furthermore, the phenomenological impact drag force law has been derived based on the experimental and numerical results. For the sake

⁴Because z=0 is defined by the fitting of v(t) in the analyses of the experimental data (not by the direct image analysis of the bottom of the impactor sphere) [17], it might be slightly different from the exact point at which the bottom of the impactor reaches the surface of the target granular bed (Fig. 4.1). The depth z=0 (t=0) corresponds to an effective starting point of the deceleration by the impact. Of course, the depth must be close to the actual z=0. The data in Fig. 4.11 slightly deviates from the scaling of Eq. (4.32) at $v_0^2/gd_1 < 1$. This deviation might concern the accuracy limit of the z=0 identification.

of simplicity, complex effects such as the container's wall, packing fraction, and interstitial fluid, have been neglected thus far. Such effects sometimes play crucial roles in the dynamics of granular matter. In this subsection, some results concerning how such effects affect the granular impact dynamics will be introduced.

Wall effect The effect of the container's wall has been studied in Refs. [50–52]. The studies in Refs. [50, 51] demonstrated that the effects of a bottom wall and a one-sided lateral wall are not very significant. The confining wall (container size) effect is more complex than the one-sided wall effect [51]. The scaling of d is affected by the confining wall effect [51]. According to Ref. [52], the confining wall can either increase or decrease the penetration depth d depending on v_0 . These results are briefly reviewed in the following discussion.

To examine the bottom wall effect, a solid sphere was dropped onto granular beds with various thickness [50, 51]. The thickness dependence of the final penetration depth d was measured to quantify the wall effect. Both studies reported that d is rarely affected by the bottom wall until the impactor reaches very close to the bottom wall (\sim a few millimeters). In Ref. [50], even the effective attraction force was observed for low-velocity impact onto a thin granular bed.

To examine the one-sided lateral wall effect, the impactor was dropped to an off-center-point of a sufficiently large container filled with glass beads ($D_{\rm con}=190\,{\rm mm}$) [50]. Here $D_{\rm con}$ is the inner diameter of the tube container. The main control parameter was the initial gap between the impactor and the wall. The researchers observed that the impactor experiences repulsion from the wall during the penetration. The strength of the repulsion depends on the impactor's size as well as the gap distance. Because of this repulsion, the impactor penetrates obliquely (toward the center of the container) into the target bed. Because the impact kinetic energy is dissipated during the net impactor's motion, the final vertical penetration depth d decreases for this oblique penetration.

The interaction of two impactors was also investigated [50]. In the experiment, two identical spheres were impacted simultaneously onto the target, with an initial gap width between the impactors, G_d . The horizontal displacement toward the repulsive direction ξ_d and the final vertical penetration depth d were measured for various G_d . The results suggested that d is independent of G_d , whereas ξ_d increases with decreasing G_d . The normalized horizontal displacement ξ_d/d is written as $\xi_d/d = 0.12 \exp(-G_d/G_0)$ with a characteristic length scale $G_0 = 7$ mm [50]. Because G_0 is considerably smaller than the impactor's diameter $(G_0/D_i \simeq 0.03)$, the repulsive effect is very limited. G_0 roughly corresponds to $20D_g$.

The container's size must be varied to investigate the confining wall effect directly. In Ref. [51], the diameter of the container $D_{\rm con}$ and that of the spherical impactor D_i were varied in the ranges $24 \le D_{\rm con} \le 190$ mm and $5 \le D_i \le 40$ mm, respectively. The sphere was dropped onto the center of the target container (filled with $D_g = 0.3$ –0.4 mm glass beads), and the final penetration depth d was measured to quantify the confining lateral wall effect. The authors assumed a power law form of d by extending Eq. (4.3) as $d/D_i = A_c(\rho_i/\rho_t)^{\beta_c}(H/D_i)^{\alpha_c}$, where A_c , α_c , and β_c are fitting parameters. $A_c = 0.37 \pm 0.01$, $\alpha_c = 0.40 \pm 0.04$, and $\beta_c =$

 0.61 ± 0.02 were obtained for the largest container $D_{\rm con} = 190$ mm, in which the wall effect is negligible. By decreasing $D_{\rm con}$, both A_c and α_c exponentially decrease. Specifically, the authors observed that $\alpha_c = 0.4[1 - \exp(-(D_{\rm con} - D_i)/0.8D_i)]$ and $A_c = 0.37[1 - \exp(-D_{\rm con}/0.7D_i)]$. According to their experimental results, when $D_{\rm con}$ is greater than $5D_i$, α_c and A_c are almost saturated. For a narrow container with $D_{\rm con} < 5D_i$, d decreases because of the wall-supported drag.

The confining container size effect is actually slightly more complex. The abovementioned studies were based on the measurement of the final penetration depth d and the horizontal displacement ξ_d . In Ref. [52], time-resolved impact dynamics was acquired and discussed to examine the confining wall effect. In the experiment, a steel sphere ($D_i = 16 \text{ mm}$) was dropped onto a sand bed ($D_g = 0.02$ – $0.06 \,\mathrm{mm}$). The result clarified that the narrow container can increase d (deeper penetration) for the low-velocity impact $(v_0 \sim 6\sqrt{gD_i})$. However, the narrow container results in a decrease in d (shallower penetration) for the high-velocity impact $(v_0 \sim 19 \sqrt{gD_i})$, which is a slightly confusing result. What is happening in the drag force? To resolve this confusion, the drag force parameters m_i/d_1 and k in Eq. (4.4) were estimated in the analysis of the experimental result. Then, m_i/d_1 and k exhibited opposite dependencies on the container size: m_i/d_1 increases whereas k decreases as the container size D_{con} decreases. In the low v_0 regime, the frictional drag kz dominates the dynamics such that the narrower container decreases the drag force. This behavior results in a deeper penetration in the low v_0 and small $D_{\rm con}$ regime. In contrast, the inertial drag dominates the drag force in the high v_0 regime, which indicates that the narrower container causes a larger drag force that results in the reduction in d. A narrower container can result in either smaller or larger d depending on v_0 . The noticeable difference between Refs. [51] and [52] is the grain shape and size. While spherical glass beads of $D_g = 0.3-0.4 \,\mathrm{mm}$ were used in Ref. [51], nonspherical slightly polydisperse sand grains of $D_g = 0.02$ -0.06 mm were used in Ref. [52]. This difference might be the reason for the partly contradicting behaviors in these results.

The infinite penetration of an impactor due to the Janssen effect can also be observed experimentally [53]. Pacheco-Vázquez et al. performed the penetration experiment using a long silo (6 m in height) filled with very light-weight polystyrene beads ($\rho_t \simeq 14\,\mathrm{kg/m^3}$). If the intruder's mass was heavier than the critical mass m_c , infinite penetration with a terminal velocity was observed. To explain this experimental result, the Janssen effect was considered for the depth-dependent frictional drag. Specifically, they assumed the form of the depth-dependent drag force f(z) as

$$f(z) = k\lambda_J (1 - e^{-z/\lambda_J}), \tag{4.33}$$

where λ_J is a characteristic length scale due to the Janssen effect that value is close to the container's diameter (Sect. 3.7.1). Then, the frictional drag is saturated near $z = \lambda_J$, and the terminal velocity is attained by the balance among gravity $m_i g$, inertial drag $m_i v^2/d_1$, and frictional drag $k\lambda_J$. The terminal velocity v_t is calculated by substituting $d^2z/dt^2 = 0$ and $f(z) = k\lambda_J$ into Eq. (4.11):

$$v_t = \sqrt{\frac{d_1(m_i g - k\lambda_J)}{m_i}}. (4.34)$$

Thus, the critical intruder mass is $m_c = k\lambda_J/g$. The experimentally obtained $m_c \simeq 86\,\mathrm{g}$ was consistent with this estimate. Using very light-weight grains, fluid-like infinite penetration with a terminal velocity v_t can be observed in the granular penetration.

Using the same light-weight grain pack, a penetration experiment under reduced gravity was also performed [54]. The granular impact dynamics was measured in a falling bucket whose falling velocity was reduced by a counter-weight. By varying the counter-weight mass, the effective gravity $g_{\rm eff}$ was controlled. Such an experimental system is called an Atwood machine.⁵ The researchers focused on the zero initial velocity impact, $v_0 = 0$. In this experiment, the penetration timescale was observed to be scaled by $g_{\rm eff}^{-1/2}$, as expected (Eq. (4.8)). In contrast, the measured penetration depth was independent of $g_{\rm eff}$. This result can be explained by assuming $k \propto g_{\rm eff}$ based on Eq. (4.22) and neglecting the inertial drag effect. Then, the equation of motion can be written as $m_i d^2 z / dt^2 = m_i g_{\rm eff} (1 - f'(z))$, where $f'(z) = f(z)/m_i g_{\rm eff}$ is independent of v. Using a relation $d^2 z / dt^2 = v dv / dz$ (Eq. (4.10)), this equation can be integrated with respect to z as

$$\frac{1}{2}v^2 = g_{\text{eff}} \int_0^z \left(1 - f'(z')\right) dz'. \tag{4.35}$$

Here the initial condition $v_0 = 0$ at z = 0 is used. At z = d, the velocity should vanish. Thus, the right-hand side of Eq. (4.35) must be zero at $^6z = d$. This criterion (v = 0) in Eq. (4.35) does not depend on $g_{\rm eff}$ because the integral in Eq. (4.35) is free from $g_{\rm eff}$, i.e., all the terms on the right-hand side are proportional to $g_{\rm eff}$. The relation $t_{\rm stop} \propto g_{\rm eff}^{-1/2}$ can also be obtained from Eq. (4.35) $(v^2 \propto g_{\rm eff})$ and assuming $t_{\rm stop} \propto v^{-1}$.

Packing fraction effect The target granular bed is actually compressed or dilated by the impact depending on the initial packing fraction ϕ_0 and the impact velocity v_0 . A change in the packing fraction can be considered as a change in the target bulk density $\rho_t (= \phi \rho_g)$. Thus, the effect of ϕ may be effectively included in Eqs. (4.20) and (4.22) through ρ_t dependence. In this case, the drag force form of Eq. (4.4) is robust and unchanged; however, this is not the case. The granular impact drag force behaves in a more complicated manner than we expect.

Umbanhowar and Goldman controlled the initial packing fraction of the target granular bed in the range $0.57 < \phi_0 < 0.63$. Then, a steel sphere ($D_i = 3.96$ mm) was impinged on the target granular bed ($D_g = 0.3$ mm glass beads), and its

⁵The effective acceleration is reduced by a factor of the Atwood number (Eq. (2.108)) when the two bodies' volumes are identical.

⁶The trivial solution v = 0 at d = 0 is ignored here.

acceleration was measured [55]. They observed that the drag force was significantly affected by ϕ_0 . If ϕ_0 is tuned to $\phi_c = 0.59$ (the critical packing state), the packing fraction does not change after the impact. When $\phi_0 < \phi_c$, a compaction occurs as a result of the impact and a dilation occurs when $\phi_0 > \phi_c$. The experimental result also revealed that d is a decreasing function of the change of the packing fraction, $\phi_f - \phi_0$, where ϕ_f indicates the final packing fraction after the impact. Although this trend is qualitatively consistent with the ρ_t dependence (Eqs. (4.4) and (4.20)), the experimental data for $\phi_0 \neq \phi_c$ cannot be fitted by the drag force model of Eq. (4.4). Typically, the inertial drag force coefficient $1/d_1$ depends on z and even becomes negative in a deep region; it is evidently unphysical. They reported that the frictional drag is also affected by ϕ_0 . Thus, Eq. (4.4) should not be simply applied to the case of $\phi_0 \neq \phi_c$. In the experiments of Refs. [17, 20], $\phi_0 = 0.59$ is achieved by the air fluidization of the target granular bed before each impact.

In an experiment of slow penetration, phase-transition-like behavior of the shear resistance has been observed [56]. In the experiment, a thin rod (6.3 mm in diameter) was slowly penetrated into a glass-bead bed ($D_g \sim 0.27 \, \mathrm{mm}$), and the resistance force was measured. A clear crossover of the resistance force was observed near $\phi = 0.6$. This ϕ -sensitive nature of the granular bed might be a reason for the strong ϕ dependence of the impact drag force.

If the drag force is measured in a bulk granular layer, the effect of jamming [57, 58] (random solidification) must be considered [59]. In the free-fall impact of an impactor on a granular bed, grains on the surface expand significantly, and ejecta splashing is induced. However, this type of deformation is inhibited when the granular layer is completely confined in a box. In this confined situation, grains cannot expand such as by splashing because of the limited free space. In general, the granular packing fraction cannot exceed a certain value ϕ_I above which the solidification of the granular packing (called jamming) occurs.⁷ Takehara and Okumura considered that the origin of v^2 -dependent inertial drag is the collision between an intruder and a cluster of grains in the confined granular system [42, 59]. These researchers assumed that in the two-dimensional case, the size of the cluster of grains is scaled as $D_g D_i l_{clu}$, where D_g , D_i , and l_{clu} are the grain diameter, intruder's diameter, and characteristic length scale, respectively. By systematically varying the initial packing fraction ϕ_0 , they measured the two-dimensional granular drag force at steady state, i.e., the drag velocity v is fixed, and the corresponding granular drag force is measured in a two-dimensional bulk granular layer that is confined by walls. Then, the measured drag force F_D shows a divergence, $F_D \propto (\phi_J - \phi_0)^{-1/2}$. This divergent drag force corresponds to the critical growth of the length scale, $l_{\rm clu} \sim (\phi_J \phi_0)^{-1/2}D_i$ [59]. In the cluster collision model, the inertial drag term (momentum transfer per unit time) can be obtained from the product of the collision frequency $D_i v/D_g^2$ and the momentum of the dragged cluster $\rho_t D_g D_i l_{\text{clu}} v$ as $(l_{\text{clu}}/D_g) \rho_t D_i^2 v^2$. Therefore, the dimensionless factor $l_{\rm clu}/D_g \sim (\phi_J - \phi_0)^{-1/2} D_i/D_g$ determines the drag force in the vicinity of ϕ_J . Note that the driving and boundary conditions for

⁷If the constituent grains are soft, $\phi > \phi_I$ can be attained by the compressive external loading.

this experiment are different from those in the impact case. Although the physics of jamming is a very intriguing problem and many papers concerning the jamming transition have been published, the details are beyond the focus of this book.

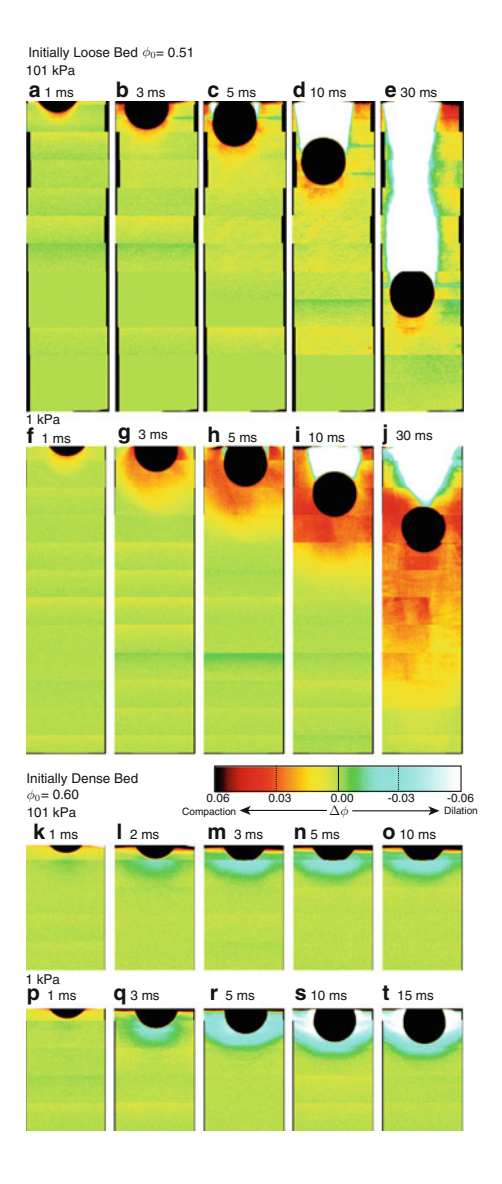
Interstitial air effect Granular impact dynamics is affected by interstitial air if the granular target consists of small grains ($D_g < 0.1 \,\mathrm{mm}$). The interstitial air effect is not negligible for such small grains [60]. In general, interstitial air causes air drag against granular motion. Additionally, the air drag is a source of dissipation. Nonetheless, some experimental results have demonstrated that interstitial air can increase the final penetration depth d [61–63]. More precisely, d can also be decreased by the interstitial air effect under some experimental conditions. The value of d actually depends on both the interstitial air and packing fraction.

Royer et al. performed a granular impact experiment under various ambient pressure (1–101 kPa) and initial packing fraction (0.51 $< \phi_0 <$ 0.61) [63]. A steel sphere with $D_i = 12 \,\mathrm{mm}$ and boron carbide grains with $D_g = 0.05 \pm 0.01 \,\mathrm{mm}$ were used in the experiment. The researchers captured the impactor motion using high-speed X-ray imaging. Using the obtained images, they also quantified the local compaction or dilation of the target granular bed. Some results are presented in Fig. 4.12. For an initially loose target with $\phi_0 = 0.51$ (Fig. 4.12a-j), local compaction occurs after the impact. The degree of local compaction is considerably larger under the vacuum condition (1 kPa) than under the atmospheric condition (101 kPa). In contrast, the initially dense target ($\phi_0 = 0.60$) mainly causes local dilation (Fig. 4.12k–t). The dilation occurs more significantly in the vacuum condition than in the atmospheric condition. Therefore, they concluded that the interstitial air resists the change in the local packing fraction. For an initially loose (or dense) target granular bed, compaction (or dilation) is induced by the impact. This compaction (or dilation) results in an increase (or decrease) in the drag force (see Eqs. (4.4), (4.20), and (4.22)); compaction (or dilation) means an increase (or decrease) in ρ_t . Therefore, the interstitial air can increase (or decrease) d for the initially loose (or dense) target, respectively. The crossover packing fraction between compaction and dilation was reported as $\phi_c \simeq 0.58$ in this experiment. At this crossover packing fraction, d is almost independent of the ambient pressure. Note that the interstitial air is crucial only for fine grains ($D_g < 0.1$ mm). For fine grains, both the interstitial air and the packing fraction effects are important. The electrostatic effect might also be important for dry and fine grains. However, no systematic studies have been performed on the electrostatic effect of granular impact.

The interstitial air also affects the jet formation created by the collapse of the void opened by the impact [60, 64]. The jet formation is discussed later in Sect. 6.3.

Interstitial liquid effect If the interstitial fluid is liquid (not gas), the impact behavior becomes completely different. In Ref. [65], a wet granular bed was employed as a target. The glass beads ($D_g = 0.52 \, \mathrm{mm}$) and water were mixed in various ratios. The mixtures included pendular, funicular, and capillary states [66]. The saturation parameter S_{at} , which is the main parameter used to characterize the liquid content, is defined as

Fig. 4.12 Composite X-ray images of the granular impact. The local packing fraction variation $\Delta \phi = \phi - \phi_0$ is shown in addition to the impactor (black circle) motion. One can confirm the deeper penetration in the cases of low initial packing fraction under atmospheric pressure (101 kPa) or high initial packing fraction under vacuum condition (1 kPa) (Reprinted with permission from Ref. [63])



$$S_{at} = \frac{V_{\text{liq}}}{V_{\text{liq}} + V_{\text{air}}},\tag{4.36}$$

where $V_{\rm liq}$ and $V_{\rm air}$ are the liquid and air-void volumes, respectively. A steel sphere ($D_i=20\,{\rm mm}$) was dropped onto the mixed target bed. According to the experimental result, d_0 (the final penetration depth by $v_0=0$) for the wet target is always less than that of the dry target. In contrast, for large v_0 impact, the final penetration depth d is greater in the wet target than in the dry target. Moreover, the maximum value of d is attained at $S_{at}\simeq 5-10\,\%$. The depth scaling for

•				
Effect	d+	d-	Experimental condition	Ref.
Small container size D_{con}	$(\text{low } v_0)$	(high v_0)	$D_{\rm con} < 5D_i$	[51, 52]
Initial packing fraction ϕ_0	$ \phi_0 < \phi_c $	$ \phi_0>\phi_c $	$\phi_c \simeq 0.58 - 0.59$	[55, 63]
Interstitial air	$(\phi_0 < \phi_c)$	$(\phi_0 > \phi_c)$	$1-101 \text{ kPa}, D_g < 0.1 \text{ mm}$	[63]
Interstitial liquid	(high v_0)	$(\text{low } v_0)$	$0 < S_{at} < 93 \%$	[65]

Table 4.1 Various effects on the final penetration depth d in granular impact. d+ indicates the increasing of d and d- indicates the decreasing of d by each effect

the wet granular target was obtained as $d \propto H^{0.55}$ or $\propto H^{0.45}$, depending on the target preparation methods. Note that the power is clearly greater than 1/3 (dry granular case) (Eq. (4.3)). Wet grains are cohesive because of the capillary bridge force. The capillary bridge force will resist the dilation of the bed. However, the lubrication effect is also present because of the liquid content. The competition between cohesion and lubrication might be a key factor to understand the complex behavior of wet granular impact. More detailed studies are necessary to discuss this competition effect. Furthermore, in the liquid saturated case, 1/3 scaling is recovered [67]. The situation is very complex.

Summary of various effects for the granular impact drag force As discussed in this subsection, the granular impact drag force is noticeably affected by various effects. Using these effects, we can either reduce or enhance the drag force. However, the drag force response to each effect is neither obvious nor trivial and instead works as if it were magic with sand. Here we summarize the qualitative results produced by the various effects (also see Table 4.1).

- Proximity of the bottom wall: almost negligible until the impactor is very close to the bottom (approximately a few mm)
- Proximity of the one-sided lateral wall: oblique penetration by the effective repulsion
- Proximity of the confining lateral wall: increasing (or decreasing) d at low (or high) v_0
- Interaction of two impactors: repulsion decaying exponentially by initial gap width (decay length scale is approximately 7 mm for d = 0.3 mm brass beads)
- Pressure saturation by the Janssen effect: infinite penetration by the heavy intruder $(m_i \ge m_c)$
- Initial packing fraction: decreasing (or increasing) d at high (or low) ϕ_0
- Interstitial air: decreasing (or increasing) d at high (or low) ϕ_0 compared with vacuum condition
- Interstitial liquid: decreasing (or increasing) d at low (or high) v_0 compared with interstitial gas condition

We have focused mainly on the vertical one-dimensional motion of the impactor. For a small size ratio of D_i/D_g , the lateral motion's fluctuation is not negligible. In such a case, the dynamics will be different, and the fluctuation of the drag force plays an essential role. The detailed study in this regime is open to future investigation.

The grains' adhesive effect has also been investigated recently using a numerical simulation [68]. However, its effect is limited and only slightly affects the impactor's motion.

4.1.8 Oblique Impact

Thus far, only the vertical impact has been emphasized. If the impact occurs obliquely, its dynamics might be affected by the inclination angle. In general, planetary-scale impact events occur obliquely. While the vertical impact must be first clarified, the oblique impact should be studied next to discuss practical impacts in nature. There are a few investigations that concern the oblique impact between a solid impactor and a granular bed. In this subsection, these studies are briefly reviewed.

Using a two-dimensional numerical simulation, Wang et al. studied the drag force model for oblique impact [69]. The notations of the directions and angles in oblique impacts are shown in Fig. 4.13. Using the numerical simulation, the researchers observed that Eq. (4.4) is simply applicable in the vertical direction of the oblique impact. The drag force in the horizontal direction was also modeled by the sum of the inertial and frictional drag forces. Then, the drag force components in two directions (*z*: vertical; *x*: horizontal) are written as

$$F_x = -\operatorname{sgn}(v_x) \left[c_x v_x^2 + k_x z \right], \tag{4.37}$$

$$F_z = m_i g - c_z v_z^2 - k_z z. (4.38)$$

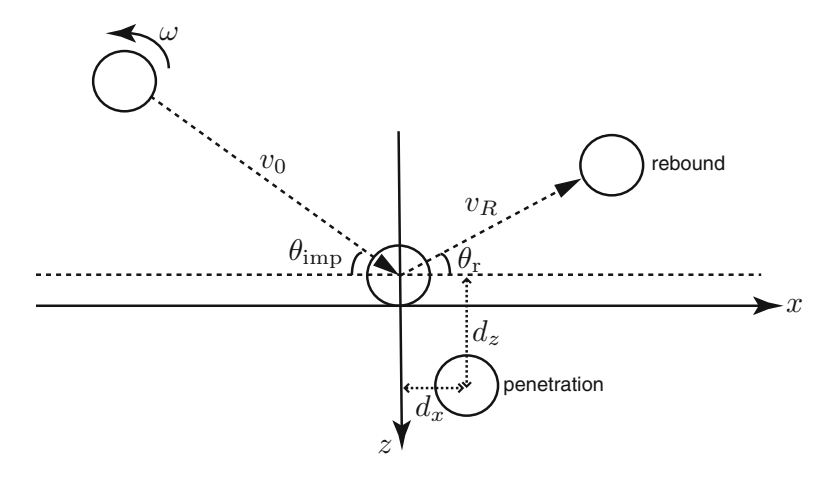


Fig. 4.13 Definitions of directions, angles, and rotation of the impactor in an oblique impact. The vertical impact corresponds to $\theta_{\rm imp} = 90^{\circ}$. Because of the experimental limitation, the rebounding angle $\theta_{\rm r}$ is usually defined in the measured x-z plane. The projected velocity and corresponding rebounding angle are used in the three-dimensional case

The form of F_z is identical to that of Eq. (4.4), and F_x also consists of the same drag force components: inertial and frictional. Note that F_x acts in the opposite direction of the horizontal velocity v_x (sgn(·) is the sign function). Here c_x , c_z , k_x , and k_z are parameters depending on the impact angle as well as the impactor's and target's properties. This drag force form is valid in a relatively large impact angle regime, $\theta_{\rm imp} \geq 30^\circ$. When the impact angle $\theta_{\rm imp}$ is lower than 30°, the drag force becomes complicated and a simple description using Eqs. (4.37) and (4.38) becomes impossible.

The stopping time t_{stop} shows a qualitative difference across the critical impact angle $\theta_{\text{imp}} = 30^{\circ}$. In the large impact angle regime ($\theta_{\text{imp}} \geq 30^{\circ}$), t_{stop} is a decreasing function of the impact velocity v_0 and asymptotically approaches the characteristic time scale, $t_{\text{stop}} \simeq \sqrt{D_i/g}$. This tendency is similar to the vertical impact (Fig. 4.7d). In contrast, t_{stop} becomes an increasing function of v_0 in the low impact angle regime ($\theta_{\text{imp}} < 30^{\circ}$). At the critical angle ($\theta_{\text{imp}} = 30^{\circ}$), t_{stop} is almost a constant. This result indicates that the role of inertial drag, which causes immediate deceleration, is less important in the low impact angle regime. The typical timescale $\sqrt{D_i/g}$ corresponds to the deceleration timescale due to the inertial drag (Eq. (4.8)).

It is not clear whether this critical angle $\theta_{imp} = 30^{\circ}$ is universal. In Ref. [70], the ricochet angle for oblique granular impact was experimentally measured. According to the results of the three-dimensional experiment, the ricochet angle θ_{rc} is written as

$$\theta_{\rm rc} = 210^{\circ} \left(\frac{\rho_t}{\rho_i}\right)^{1/2} \left(\frac{D_g}{D_i}\right)^{2/3}.$$
 (4.39)

This angle is almost independent of the impact velocity. When $\theta_{imp} \geq \theta_{rc}$, penetration occurs. In the low impact angle regime ($\theta_{imp} < \theta_{rc}$), the ricochet should be observed. Equation (4.39) cannot be applied for $\theta_{rc} > 90^{\circ}$. To test the consistency among Refs. [69] and [70], the corresponding θ_{rc} for Ref. [69] can be estimated using Eq. (4.39) obtained in Ref. [70]. The estimated value is $\theta_{rc} = 42^{\circ}$. However, the penetration is observed in the numerical simulation of smaller angle $\theta_{imp} < 42^{\circ}$ [69]. This difference might originate from the different dimensionality (two- or three-dimensional) of the abovementioned systems or the large experimental uncertainty [70].

The oblique granular impact plays a key role in the aeolian grain transport process. It is apparent that oblique impacts dominate almost all the impact processes in the natural aeolian transport of sand grains. An understanding of aeolian transport is necessary to discuss sand dune morphology and its formation event. A very basic framework of aeolian (wind) transport of sand grains will be discussed later in Sect. 7.2.6. The sand dune structure can be observed on the surface of Mars as well as on the Earth (see, e.g., Fig. 7.10). Because Mars has an atmosphere, aeolian transport can induce the sand dune structure. To discuss the grain transport on sand dunes, the oblique impact among comparative size grains must be investigated. Simple oblique impact experiments, in which an impactor grain is identical to

grains of the target bed (i.e., $D_g = D_i$ and $\rho_i = \rho_t$), were performed both in two dimensions [71–74] and in three dimensions [75]. The recent three-dimensional experiment [75] reveals that the directional restitution coefficient $\epsilon_{R0} = v_R/v_0$ and its vertical component $\epsilon_{z0} = v_{Rz}/v_0$ are independent of v_0 and empirically written as

$$\epsilon_{R0} = A_R - B_R \sin \theta_{\rm imp},\tag{4.40}$$

$$\epsilon_{z0} = \frac{A_{Rz}}{\sin \theta_{\rm imp}} - B_{Rz},\tag{4.41}$$

where v_R is the rebound speed and v_{Rz} is its z component. Experimentally determined values of these parameters are $A_R = 0.87$, $B_R = 0.72$, $A_{Rz} = 0.03$, and $B_{Rz} = 0.15$ [75]. Incorporating these relations, the rebound angle θ_r is computed from the relation $\epsilon_{z0}v_0 \sin\theta_{imp} = v_R \sin\theta_r$ as

$$\sin \theta_{\rm r} = \frac{\epsilon_{z0}}{\epsilon_{R0}} \sin \theta_{\rm imp} = \frac{A_{Rz} - B_{Rz} \sin \theta_{\rm imp}}{A_R - B_R \sin \theta_{\rm imp}}.$$
 (4.42)

Using this definition, ϵ_{z0} can exceed unity (approximately 1.5 [75]). Because $\epsilon_{R0} < 1$ is always satisfied, large ϵ_{z0} does not mean a violation of energy conservation. Large ϵ_{z0} indicates that the horizontal momentum of the impactor is transferred to the vertical direction by the oblique impact, similar to Refs. [76, 77] (see also Sect. 3.4). Note that the definitions of ϵ_{R0} and ϵ_{z0} are different from the normal restitution coefficient ϵ_r , defined in Eq. (3.14). This anisotropic momentum transfer might be crucial in the aeolian transport of sand grains.

The ejected grain velocity $v_{\rm ej}$ was measured in the same grain's oblique impact experiment and can be roughly scaled by v_0 as

$$\frac{\langle v_{\rm ej} \rangle}{\sqrt{gD_i}} \sim \left(\frac{v_0}{\sqrt{gD_i}}\right)^{1/4}.$$
 (4.43)

The value is almost independent of θ_{imp} . The number of ejected (splashed) grains n_{ej} was also measured in the experiment. The experimentally obtained scaling relation for n_{ej} is [75]

$$\langle n_{\rm ej} \rangle \sim \left(1 - \langle \epsilon_{R0}^2 \rangle \right) \left(\frac{v_0}{\sqrt{gD_i}} \right)^{3/2}.$$
 (4.44)

These scaling behaviors can be modeled using a single chain model [78, 79]. That is, the aforementioned properties can be reproduced by the accumulation of binary collisions in the force chain structure.

The effect of the impactor's rotation has also been investigated using a twodimensional numerical simulation [80]. For the oblique impact, the impactor's rotation with angular velocity ω affects the penetration of each direction, d_x and d_z . See Fig. 4.13 for the definitions of ω , d_x , and d_z . The maximal value of d_z (the

greatest penetration depth) is actually achieved at $\omega=0$. Namely, the impactor's rotation decreases the vertical penetration depth. The horizontal penetration d_x can either increase or decrease depending on the direction of the rotation, i.e., the sign of ω . When ω is positive and $0^{\circ} < \theta_{\rm imp} < 90^{\circ}$ (back spin), d_x will decrease, and vice versa.

The study of oblique impact has not been sufficient to reveal the entire behavior. Both the experimental and numerical investigations are still deficient. Because natural impacts are dominated by oblique impacts, much more detailed studies are necessary steps for the future.

4.2 Granular Slow Drag Force

As discussed above, the granular impact drag force can be decomposed into two parts: the inertial drag and the frictional drag. In a viscous fluid, the drag force is dominated by the viscous drag in the low R_e regime and by the inertial drag in the high R_e regime. Although we do not know the form of R_e for granular matter, the slow penetration drag could correspond to drag in the low R_e regime. Furthermore, a quasi-static regime can be observed by studying the slow drag force. The slow penetration drag is experimentally measurable, and it would be helpful to elucidate the physics of the granular drag force. In this section, we will discuss the studies of granular slow drag, both in vertical and horizontal directions.

4.2.1 Granular Vertical Slow Drag

First, an overview of the vertical slow penetration drag is provided. A standard experimental setup to measure the slow granular vertical drag force is shown in Fig. 4.14. In the system, a solid intruder is slowly plunged into a granular column, and its penetration resistance force (slow drag force) is measured. Then, the relation between the drag force F_D and the penetration depth z is analyzed. In this system, the regime of slow-penetration rate is usually emphasized. In this slow regime, the viscous-like drag force may be detected or only the frictional drag kz may be observed. As discussed in Sect. 4.1.3, the value of the frictional drag kz is considerably greater than the expected value estimated by the hydrostatic pressure and Coulomb friction. The study of the slow penetration drag force might also provide clues for this puzzle.

One of the simplest and most meaningful experiments on granular vertical slow penetration was carried out by Stone et al. [81, 82]. These researchers used a pack

⁸The dimensionless number D_r defined by Eq. (4.25) might correspond to R_e for the granular impact drag phenomenon.

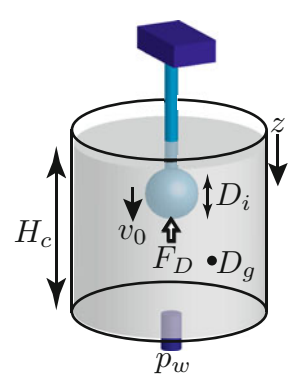


Fig. 4.14 Schematic illustration of the slow vertical drag experiment. A penetrator with diameter D_i is slowly (with velocity v_0) plunged into a granular column (height H_c) that consists of grains with diameter D_g . The drag force is denoted as F_D . In this figure, the penetrator has a spherical shape. However, its shape is arbitrary in general experiments. The transmitted bottom wall pressure p_w was also measured in some experiments

of glass beads and a horizontal disk penetrator. The measured slow drag force was simply proportional to the penetration depth z in a shallow regime, similar to a frictional component of the impact drag force, kz. The drag force is independent of the penetration velocity. Thus, the slow drag force can be categorized in a quasistatic state rather than a viscous state. In a deep-penetration regime, the drag force tends to be saturated, most likely due to the Janssen effect. The measured drag force value in this experiment is approximately one order of magnitude greater than the simple hydrostatic pressure expectation, similar to the impact drag observation. Although this problem was not discussed in Refs. [81, 82], we can roughly compare the slow drag force and hydrostatic-based frictional drag force in some plots of Refs. [81, 82]. While its physical meaning is still not well understood, the slow drag behavior is roughly consistent with the impact drag with respect to *very large* depth-dependent drag. In this sense, it may be inappropriate to conclude that the origin of the kz drag force is the Coulomb friction and hydrostatic pressure.

The most important finding in Refs. [81, 82] is the exponential growth of the slow penetration drag force in the vicinity of the container's bottom. They defined the drag force increase $\Delta F_D = F_D - F_{bulk}$, where F_{bulk} represents the bulk linear drag force component. Then, ΔF_D exponentially grows as

$$\Delta F_D \propto \exp\left(\frac{H_c - z}{\lambda_b}\right),$$
 (4.45)

where H_c is the depth of the bottom wall (column height) and λ_b is a characteristic length scale. Using systematic experiments, Stone et al. observed the relation $\lambda_b \propto \sqrt{F_{bulk}(H_c)/D_i}$. From the dimensional viewpoint, $\lambda_b \sim \sqrt{F_{bulk}(H_c)/\rho_t g D_i}$ was proposed for the characteristic length scale of the slow granular drag near the bottom.

The slow penetration drag force is slightly curved in the F_D vs. z plot. As a first-order approximation, the slow penetration drag can be modeled by a linear function of z. In some experiments, however, the depth-dependent granular slow drag was analyzed with a power law form,

$$F_D \propto z^{\alpha_F}$$
. (4.46)

The power law exponent α_F ranges from 1 to 1.5 depending on the experimental conditions [83–86]. In particular, the container's horizontal dimension, intruder's size, and its shape affect the value of α_F . In a wide container, α_F is close to unity [82] whereas a narrow container results in large α_F . This finding implies that the lateral wall affects the slow penetration drag. By means of the Janssen effect, the pressure would be saturated in a deep region because of the lateral wall support. However, the side wall enhances the drag force for the slow penetration. The force chain structures connecting the intruder and side wall might cause the resistance to the shearing by slow penetration, which might result in the enhancement of the slow drag force in narrow containers. That is, the force chain structure might be responsible for this large absolute value of the slow drag. Meanwhile, the frictional drag appears to act normally to the intruder [23]. The shear contribution in the granular drag force remains controversial. In these experiments, the absolute value of the drag force is approximately one order of magnitude greater than the hydrostatically expected value, again even in this nonlinear regime. In Ref. [83], the slow drag force against a sphere's withdrawing was also measured. The order of the withdrawing drag force is close to the hydrostatic expectation, which is natural because the large force chain structures toward the lateral wall are rarely established in the withdrawal process in a relatively shallow regime as long as the top boundary is a free surface (i.e., no additional loading to the top surface). Then, only the hydrostatic component dominates the resistance force.

Using highly confined ($\sim 10^1$ MPa) polydisperse and rough shaped grains, the drag force exerted on a slowly moved cylinder was experimentally measured [87]. The measured granular bulk density linearly depends on the pressure in the range 10–40 MPa. In this regime, the slow drag force is simply proportional to the bulk density or, equivalently, to the confining pressure. When the confining pressure is increased, the grain contact forces as well as density can be exaggerated. It is not clear which parameter (the confining pressure, density, or contact force) is the most essential for the slow drag. In general, these parameters are related to each other.

The origin of nonlinear slow drag force was examined by the relation between the slow drag force and the transmitted wall pressure [85, 86]. In the experiment, the pressure increase at the wall $\Delta p_w = p_w(z) - p_w(0)$ was measured and linked to the drag force F_D exerted on the sphere of diameter D_i as $F_D/(\sigma_\alpha D_i^2) \sim (D_i/D_g)^{1-\alpha_p}(z/D_g)^{\alpha_p}$ and $\Delta p_w/\sigma_\beta \sim (H_c/D_g)^{1-\beta_p}(F_D/(\sigma_\alpha D_i^2))^{\beta_p}$, where H_c , σ_α , σ_β , α_p , and β_p are the column height, unit stress for the drag, unit stress for the wall pressure, drag force scaling exponent, and pressure transmission scaling exponent, respectively. In this experiment, the top surface was open to air; namely, a free top surface boundary condition was employed. As mentioned above, the scaling

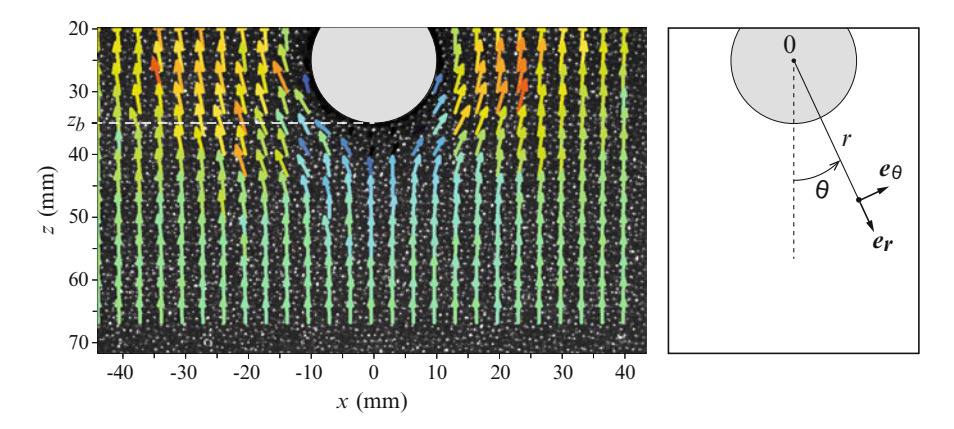


Fig. 4.15 The *left panel* shows an example image of the instantaneous granular flow field around a penetrating cylinder disk with diameter $D_i = 20$ mm. The penetration velocity is $v_0 = 50$ mm/s, and the glass-bead diameter is $D_g = 1$ mm. The *right panel* shows the notations used in the analysis. e_r and e_θ are the unit vectors to the radial and angular directions, respectively (Reprinted with permission from Ref. [89]. Copyright 2013 by American Physical Society)

exponents α_p and β_p could depend on the container's and intruder's sizes [88]. The experimentally obtained values for α_p and β_p are greater than or equal to unity. Considering the force balance, large exponents indicate that the force chain network grows nonlinearly. Perhaps, stress localization, such as a stress dip structure (Sect. 3.7.2), is responsible for this abnormal pressure. Otherwise, it is difficult to satisfy the force balance condition in this pressure growth model. The nonlinear pressure growth cannot continue due to the force balance unless the relating wall area increases. Considering that the withdrawal drag can be explained by the simple hydrostatic pressure, the side wall effect would be a crucial parameter to characterize the nonlinear drag force behavior. The important hallmarks in these nonlinear stress transmission laws are the grain contact number dependencies: $(D_i/D_g)^{1-\alpha_p}$ and $(H_c/D_g)^{1-\beta_p}$. These factors represent the number of grains around the penetrating sphere and those in the column's vertical direction, respectively. In general, the grain contacts are responsible for the nonlinearity and dissipation of the granular matter. Thus, these effectively relevant grain (contact) numbers can affect the nonlinearity. If the linear relations are assumed to be $\alpha_p = \beta_p = 1$, these grain number dependencies are eliminated. Although this measurement phenomenologically links the slow drag force nonlinearity to graincontact discreteness, the microscopic foundation of this relation remains unsolved.

The relation between the drag force and flow field around a penetrating object was also experimentally analyzed [89–91]. Seguin et al. measured the two-dimensional granular flow field using the particle image velocimetry (PIV) method [92]. An example of the measured velocity field and the notation of the cylindrical coordinate used are shown in Fig. 4.15. These researchers plunged a cylinder disk into a quasi-two-dimensional glass-bead pack with a slow

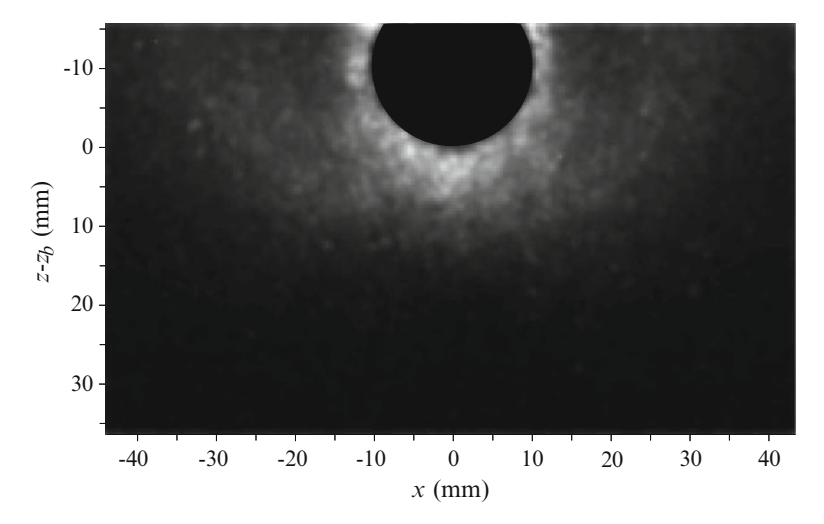


Fig. 4.16 Granular temperature for the penetration of a disk intruder ($D_i = 20 \,\mathrm{mm}$ and $v_0 = 10 \,\mathrm{mm/s}$) into a packing of glass beads with diameter $D_g = 1 \,\mathrm{mm}$. In this figure, z_b corresponds to the bottom of the intruder. The *gray* level indicates the local granular temperature. The *bright region* corresponds to high granular temperature (Reprinted with permission from Ref. [89]. Copyright 2013 by American Physical Society)

penetration velocity v_0 . The drag force and associated granular flow velocity fields were measured, and their relations were discussed using the granular temperature [89, 91]. The flow velocity field $v(r, \theta)$ can be expressed as

$$\frac{\mathbf{v}(r,\theta)}{v_0} = A_r \mathbf{e}_r \cos \theta + A_\theta \mathbf{e}_\theta \sin \theta. \tag{4.47}$$

Experimentally obtained parameters A_r and A_θ indicated that the granular flow associated with the penetration is irrotational and almost incompressible because their forms satisfy $\nabla \cdot \boldsymbol{v}(r,\theta) = 0$ [89]. Furthermore, they confirmed that the slow drag force is independent of v_0 . To explain the constant drag force, they measured the granular temperature $\hat{T}_g = \langle (\boldsymbol{v} - \langle \boldsymbol{v} \rangle_t)^2 \rangle_t$. The measured granular temperature map is presented in Fig. 4.16. The hot (high \hat{T}_g) region is localized in the vicinity of the penetrating sphere. In fact, \hat{T}_g is almost a constant \hat{T}_{g0} in the vicinity of $r-(D_i/2) \leq 4D_g$. Then, \hat{T}_g decays exponentially as $\hat{T}_g \propto \exp(-r/r_0)$ with a characteristic length scale r_0 . In addition, a simple relation $\hat{T}_{g0} \sim v_0^2(D_g/D_i)$ was obtained by the systematic experiment. According to the granular kinetic theory [91, 93], the granular pressure p_g and effective granular viscosity η_g are written as

$$p_g \sim \rho_t \hat{T}_g, \tag{4.48}$$

$$\eta_g \sim \rho_t D_g \sqrt{\hat{T}_g},$$
(4.49)

Because the granular temperature \hat{T}_g is proportional to the squared velocity, Eq. (4.48) implies that the granular pressure p_g originates from the dynamic pressure of the granular random motions. Combining Eqs. (4.48) and (4.49), we obtain the granular viscosity per controlled pressure as $\eta_g \sim p_g D_g / \sqrt{\hat{T}_g}$. Substituting an experimentally obtained relation $\hat{T}_{g0} \sim v_0^2 (D_g/D_i)$ into η_g , the viscosity around the penetrator can be written as

$$\eta_{g0} \sim \frac{p_g \sqrt{D_g D_i}}{v_0}.\tag{4.50}$$

As η_{g0} is inversely proportional to v_0 , the resultant viscous drag force becomes independent of v_0 , $F_\eta \sim \eta_{g0} D_i v_0 \sim p_g D_i^2 \sqrt{D_g/D_i}$. Thus, the granular slow drag force is determined by p_g and appears quasi-static (v_0 -independent). This result contrasts with the fact that gas viscosity is independent of its pressure. While the D_i^2 dependence of the drag force reminds us of the inertial and Epstein drag forces (Eqs. (2.70) and (2.89)), the velocity independence is inconsistent. Note that the momentum-transfer-based granular viscosity is proportional to the velocity (Sect. 4.1.6). Moreover, Eq. (4.49) is consistent with $\eta \propto T_g^{1/2}$ (Sect. 4.1.6) and, hence, the v^2 -dependent inertial drag force. Rather, the constant slow drag could originate from the structure of the narrow region near the intruder that exhibits the shear banding. The shearing induces the localized high-temperature region and results in the normal drag force via the granular pressure defined by Eq. (4.48). This condition (normally applied drag force) is consistent with the result of Ref. [23].

A key assumption in the derivation of Eq. (4.50) is the selection of the main control parameter p_g and its temperature dependence (Eq. (4.48)). It is difficult to maintain the relation of Eq. (4.48) into the region far away from the intruder. This relation is valid only in the vicinity of the penetrator, where $\hat{T}_g = \hat{T}_{g0}$. Moreover, it is not apparent why the kinetic granular theory can be applied to the dense slow granular flow regime. \hat{T}_g is almost negligible in the immobile grains region because Eq. (4.48) can be regarded as a type of dynamic pressure: density times squared velocity (granular temperature). There might be another static source of p_g even in such a quiescent region. In the two-dimensional relatively high-velocity drag experiment, the mobile region around the penetrator expands to $r \sim D_i$ [42], which contrasts with the slow drag, where the mobile region (shear banding) is limited to a few grain diameters. For granular slow drag, the localized high (granular) temperature zone introduces a rate-independent and quasi-static penetration drag force. The absolute pressure value and its depth dependence are affected by the side wall boundary condition.

The cavity formation in two-dimensional granular slow drag was also studied experimentally [94]. The area of the opened deep cavity strongly depends on the initial packing fraction. In looser packing, the larger cavity is opened after the passing of the dragged object. Simultaneously, the fluctuation of the drag force grows as the packing fraction increases. These signals might be related to the

jamming transition at a certain packing fraction value. The divergence of the drag force due to the jamming was already discussed in Sect. 4.1.7.

4.2.2 Granular Horizontal Slow Drag

The horizontal drag force might be simpler than the vertical penetration drag force. If the object is placed at a fixed depth and slowly dragged in the horizontal direction, the constant drag force can be observed. Because the penetration depth is fixed, one can purely focus on the drag force component of the fixed hydrostatic (or Janssen) pressure. Typical experimental setups of the horizontal drag are shown in Fig. 4.17. In this subsection, the granular horizontal drag force and related topics are briefly reviewed.

Albert et al. measured the horizontal slow drag force exerted on a vertical cylinder [95]. The cylinder was vertically extended to a depth *z* at an off-centered position of a bucket of glass beads. Then, the bucket of glass beads was rotated very slowly, and the drag force was measured (Fig. 4.17a). Whereas the raw drag force data look unsteady, the averaged drag force shows a simple relation [95]:

$$F_D \sim \rho_t g D_i z^2, \tag{4.51}$$

where D_i corresponds to the diameter of the buried cylinder. The proportional constant omitted in Eq. (4.51) slightly depends on D_i/D_g (size ratio between the cylinder and grains); however, the value is always on the order of unity (10°). The right-hand side of Eq. (4.51) is rewritten as $\rho_t gz \cdot D_i z$. Then, the drag force can be interpreted solely by the hydrostatic pressure in contrast to the vertical case, in which the drag is much greater than the hydrostatic expectation.

The effect of the shape of the dragged object was also examined [99]. Various shaped objects were attached at the tip of the rod, and the drag force exerted on the

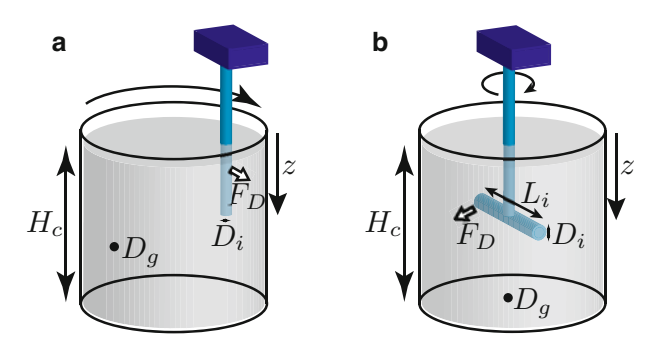


Fig. 4.17 Horizontal granular drag force measurement systems. (**a**) A vertical cylinder is buried in a rotating bucket [95–98]. In Ref. [99], a discrete object attached at the bottom tip of the vertical rod was used instead of the bare vertical cylinder. (**b**) A horizontal cylinder is rotated in a fixed bucket [41, 100]

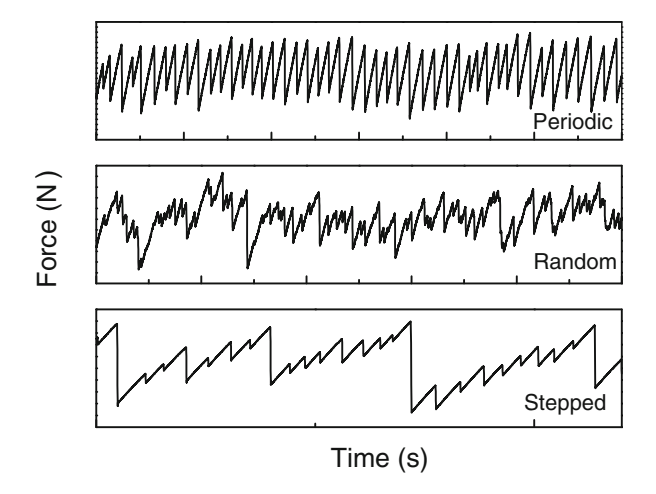


Fig. 4.18 Fluctuations of slow horizontal drag forces. The drag force exerted on the horizontally moving vertical cylinder inserted in a granular bed was measured (Fig. 4.17a). The transition among these states depends on the insertion depth and the grain's and cylinder's dimensions. Typically, the transition from the periodic state to the stepped state occurs via the random state as the insertion depth increases (Reprinted with permission from Ref. [97]. Copyright 2001 by American Physical Society)

object was measured. In sharp contrast to the fluid drag case, the granular horizontal slow drag force was almost independent of the shape. Instead, F_D exhibited a nonlinear dependence on z. The simple hydrostatic form predicts the drag force $F_D \sim \rho_t g z A$, where A is the intersectional area of the dragged object. As mentioned above, Eq. (4.51) obeys this form. However, the nonlinear relation of $F_D \propto \rho_t g A z^{\alpha_F}$ ($\alpha_F > 1$) was observed when a discrete object was attached. This nonlinearity is presumably related to the nonlinear depth-dependent vertical drag force, Eq. (4.46). That is, the side wall effect must be taken into account when a discrete object is dragged. Equation (4.51) is valid only for the simple vertical cylinder without a discrete object at its tip.

Even in a simple vertical cylinder's drag, the fluctuation of F_D exhibits nontrivial behaviors [96, 97]. In Fig. 4.18, three distinct behaviors of the drag force fluctuation are displayed. If the buried depth z and grain size D_g are sufficiently small ($z < 100 \, \mathrm{mm}$ and $D_g \leq 1.1 \, \mathrm{mm}$), the drag force fluctuation becomes periodic (Fig. 4.18 top). For large grains ($D_g > 1.1 \, \mathrm{mm}$), random fluctuation is observed (Fig. 4.18 middle). Finally, the stepped fluctuation (Fig. 4.18 bottom) can be observed in the deeply penetrated regime ($z > 140 \, \mathrm{mm}$). The scattered force chains and the finite size effect (side wall effect) might cause the transitions among those states [96, 97]. The power spectra of the slow drag force fluctuations P(f) (f is frequency) show the power law tail of $P(f) \sim f^{-2}$. This f^{-2} spectrum indicates simple behavior such as random walks (Brownian motion). A similar f^{-2} spectrum was observed in two-dimensional sheared granular matter [101].

Using a similar experimental system, the effect of gravity was evaluated [98]. A bucket of glass beads was filled with an aqueous solution of lithium heteropolytungstate (LST) which has a controllable high density. The high-density interstitial fluid causes a buoyant force and effectively reduces the gravitational effect. By the systematic experiment, a linear relation between the drag force and the effective gravitational acceleration was observed, which indicates that Eq. (4.51) is also robustly held in the reduced gravity environment. Note that, however, the depth dependence of the drag force applied to the discrete object exhibits a nonlinear depth dependence, as described before. This tendency cannot be explained by the simple hydrostatic pressure caused by the gravity g.

The horizontal drag force can also be measured using a horizontally rotated cylinder in a granular bed. The torque needed to spin the horizontally placed cylinder was measured and related to the rotational motion (Fig. 4.17b). Then, the relation between the drag force and deformation or its rate can be characterized. This spin drag force was measured both in an aerated [41] and a quiescent [100] granular bed. Although the drag force in an aerated granular bed was consistent with the impact drag (Eq. (4.4)), the drag force in a quiescent granular bed exhibited a slightly strange behavior. Guillard et al. measured the drag force exerted on a rotating cylinder with diameter D_i and length L_i in a glass-bead bed with bulk density ρ_t . They observed that the drag force, F_D^{half} linearly depends on the penetration depth z during the first half rotation. In contrast, after the first half rotation, this depth dependence is eliminated. The drag force after the first half rotation approaches an asymptotic constant value F_D^{∞} that is independent of z. The obtained drag force laws are written as

$$F_D^{\text{half}} \simeq 15 D_i L_i \rho_t gz,$$
 (4.52)

$$F_D^{\infty} \simeq D_i L_i \rho_t g L_i f_F \left(\frac{L_i}{D_i}\right),$$
 (4.53)

where $f_F(L_i/D_i)$ is a function whose value is close to 10 for the large aspect ratio (L_i/D_i) case. Equation (4.52) is qualitatively understood by the drag force based on the hydrostatic pressure in terms of the linear z dependence. The numerical prefactor 15 in Eq. (4.52) is an order of magnitude greater than unity again. Such a large prefactor has actually been observed both in aerated granular spin drag and quiescent granular vertical impact drag. Moreover, the asymptotic drag force F_D^{∞} is very peculiar. Equation (4.53) does not depend on the penetration depth or the container's size. If the constant drag force originates from the pressure saturation due to the Janssen effect, the container's size must determine the asymptotic value. Nonetheless, F_D^{∞} does not depend on the container's size, which indicates that the constant F_D^{∞} is not a result of Janssen's pressure screening. Rather, the pressure is screened by the cylinder itself. Perhaps, this phenomenon is a manifestation of the history dependence of the granular behavior. By the first half rotation, a path for the cylinder is opened by optimizing the local granular network structures. Then, the constant drag force F_D^{∞} is achieved. To erase the history dependence, some dynamic effects, such as aeration or vibration, are needed. Otherwise, history dependence

results in a constant F_D^{∞} that is independent of z and the container's size. Indeed, the formation of arches that screen the hydrostatic pressure was confirmed by the corresponding numerical simulation [102].

To date, the free-surface deformation due to the granular horizontal drag has been neglected. As long as the vertical impact drag or slow (quasi-static) horizontal drag is considered, the effect of surface deformation is negligible in terms of the drag force equation. Of course, ejecta splashing is observed in the granular impact experiment. The splashing is a result of momentum transfer from the impactor to the granular target. However, its detail does not affect the form of the drag force equation. Can we then always ignore the surface deformation? The answer is no. Gravish et al. experimentally demonstrated the coupling of the surface deformation and the drag force [103]. They plowed a granular bed by dragging a vertical plate horizontally. During the plow, the drag force and surface deformation were measured. In this experiment, the most important parameter was the initial packing fraction ϕ_0 , which ranged from 0579 to 0.619. The bulk drag force was roughly proportional to ϕ_0 , which is natural because ϕ_0 represents the bulk density of the plowed granular matter. They also observed the ϕ_0 -dependent bifurcation of the drag force. The drag force is approximately constant in the low ϕ_0 regime, $\phi_0 < \phi_c$, where $\phi_c = 0.603$. However, the drag force becomes periodic in the high ϕ_0 regime, $\phi_0 \ge \phi_c$. This bifurcation is related to the surface deformation. In the low $\phi_0(<\phi_c)$ regime, the surface deformation is smooth and continuous and produces a constant drag force. When ϕ_0 is greater than ϕ_c , the surface deformation accumulates and results in periodic radial upwellings that cause a periodic drag force. As already mentioned, in the cylinder drag experiment [97], the drag force fluctuation shows a bifurcation from the periodic state to the stepped state depending on the experimental conditions (Fig. 4.18). However, it is not clear whether the periodicities of the cylinder drag and the plate drag originate from identical origins.

Drag-induced lift was also observed in the granular horizontal drag experiment [104]. For incompressible fluid, the drag can be coupled with the pressure through Bernoulli's principle (Eq. (2.35)). Therefore, the drag force can be related to the lift force in aerodynamics. For incompressible fluid flow, the effect of the dynamic pressure is not significant in the low R_e regime. Thus, the lift force is also very small in low R_e flow. Nonetheless, the granular lift force can be observed even in the slow drag regime. The lift force applied to the horizontally dragged object in a granular bed originates from the shape effect of the dragged object. Note that, however, the lift force is induced even for the symmetric sphere drag. This result might be simply understood by the depth-dependent hydrostatic pressure. By integrating the applied stress on the differential surface area on the dragged object, the net drag and lift forces are calculable using numerical simulations [104]. The numerical simulations revealed the complicated shape dependence of the granular lift force exerted on the dragged object [105, 106]. The lift force is coupled with a detachment of the granular flow, which is related to the shock wave structure. A Bernoulli-like effect in granular matter can be observed when multiple impactors penetrate a very light-weight granular bed [107]. Cooperative impactors' motion due to such a granular-hydro interaction will be introduced later in Sect. 6.4.3.

4.2.3 Swimming in Sand

Proper understanding of the drag and lift forces may provide an approach for efficient swimming in sand. Swimming in sand is evidently much more difficult than swimming in fluid. Is it possible to swim in sand in principle? Sandfish lizards are known for their special ability of moving in dry sand. Maladen et al. analyzed how sandfish lizards swim in sand using X-ray imaging [108]. They observed that sandfish lizards do not use their limbs for propulsion. Instead, undulating motion plays an important role. The swimming speed of the center of mass v is related to the undulation frequency $f_{\rm un}$ and its wavelength $\lambda_{\rm un}$ as $v/\lambda_{\rm un} = H_{\rm un}f_{\rm un}$, where $H_{\rm un}$ is the dimensionless wave efficiency. For sandfish lizards, $H_{\rm un} \simeq 0.5$ was obtained [108]. Organisms moving in low R_e fluid and organisms undulating along the solid surface exhibit $H_{\rm un} \simeq 0.25$ and 0.8-09, respectively. The wave efficiency of sandfish lizards is intermediate between those in fluids and solids. On the basis of these fundamental aspects, a snakelike robot that can swim in a granular bed was developed [109]. The swimming efficiency depends on the friction between the body surface and grains whereas the efficiency is almost independent of the grain-grain friction.

Another simple strategy to propel an object in sand was considered by numerical simulation. An artificial two-dimensional sand swimmer was proposed by Shimada et al. [110]. Specifically, a push-me-pull-you mechanism, which was originally proposed for swimming at low R_e flow [111], was employed as a candidate for an efficient sand swimmer. The system comprises two disks that can expand and contract that are connected by a thin (virtual) wire of length L (Fig. 4.19). The diameter of the anterior disk D_A , that of the posterior disk D_p , and their distance L are controllable variables. A stroke of the swimmer consists of four cycles. In the initial state (t = 0), $D_p (= D_p^+)$ is greater than $D_A (= D_A^-)$ and the wire length is short $L(=L^{-})$, as observed in Fig. 4.19. Then, the wire is linearly expanded to $L = L^{+}$ during the period T. In this cycle, the posterior disk is anchored by friction; thus, the anterior disk is effectively pushed by the posterior disk. After that, D_A is reduced to D_A^- , and D_p is expanded to D_p^+ , (t = 2T). Then, the posterior disk is pulled by shortening the wire length to $L = L^{-}$ (t = 3T). Finally, the initial state (t=0) is recovered by expanding D_p to D_p^+ and contracting D_A to D_A^- in the final cycle (t = 4T). This swimmer primarily utilizes the friction for propulsion. During the swimming, energy is consumed by frictional resistance against the expansioncontraction and push-pull processes. The relations among the propulsion efficiency and the other parameters (timescale T, length scales L^* (= $L^+ - L^- > 0$), D_A^* $(=D_A^+ - D_A^- > 0)$, and $D_p^* (=D_p^+ - D_p^- > 0)$) are not trivial problems. Shimada et al. evaluated the efficiency of this swimmer using numerical simulations. They defined the efficiency of the swimmer as $E_f = \delta x \rho A g / W$, where δx , ρ , A, and Ware the propulsion distance, density of disks, area of disks, and work performed by the swimmer, respectively. A snapshot of swimming is shown in the bottom part of Fig. 4.19. They observed that the efficiency of the swimmer shows a peak at some frequency when the environmental granular bed is confined by a constant load at the top surface. Because of the confinement, the top surface of the granular bed is

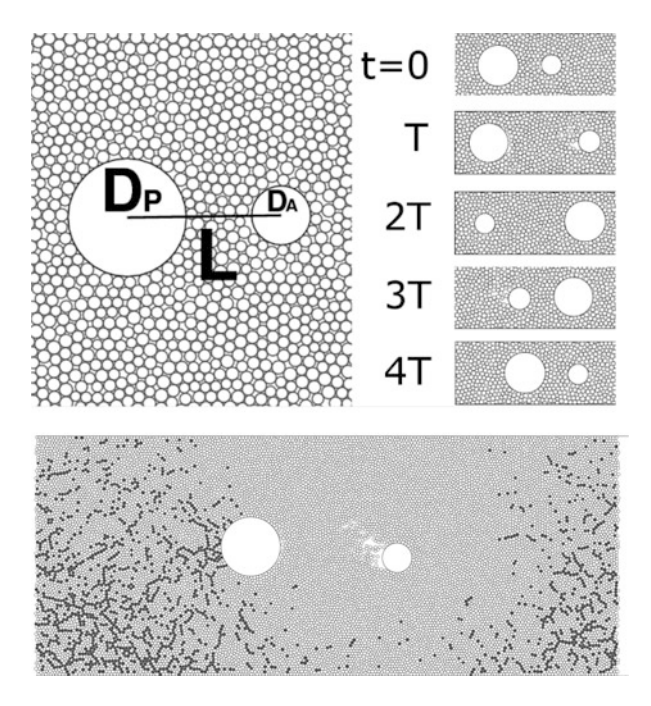


Fig. 4.19 Geometric setup and cycles of the sand swimmer. The *upper right panels* show a series of deformations at the end of each cycle (Reprinted with permission from Ref. [110]. Copyright 2009 by American Physical Society) Below the cycles diagram, a snapshot image of the granular swimmer is shown. *Dark grains* indicate that the grains experience many collisions per unit time (Courtesy of Takashi Shimada)

not a free surface. The most effective frequency is determined by two timescales. The first timescale is that of motion which is related to the fluidization of the granular bed. The second timescale is that of gravitational relaxation. For the anchor (larger) disk, the consolidated surrounding granular structure is preferred to make an effective propulsion. However, the fluidized state is better to push or pull the smaller disk. Therefore, the swimming efficiency is affected by the balance between these timescales that are compensating with each other. The degree of consolidation or fluidization is determined by the rate of motions or, equivalently, the frequency of the system. Therefore, an optimal frequency exists to swim in granular matter.

4.2.4 Drag Force in a Vibrated Granular Bed

The next problem discussed in this subsection is the drag force in a vibrated granular bed. As discussed in Sect. 3.9, the granular bed can be fluidized by vibration. In the vibrated granular bed, convection may induce the segregation of grains. While the segregation mechanism itself is an intriguing problem, here we focus only on the

drag force in a vibrated granular bed. Therefore, the frictional property of the slow drag in a vibrated granular bed, in which the convection is carefully inhibited, is particularly discussed. Using a two-dimensional granular bed vibrated by arrayed oscillators, the frictional drag force applied to an intruder of diameter $D_i = 20 \,\mathrm{mm}$ was experimentally measured [112]. The arrayed oscillators were placed at the bottom, and they consisted of disks with $D_g = 4$ or 5 mm. In this experiment, the arrayed oscillators were employed to suppress the convective motion in the bed. Then, the simple descent dynamics of the large (and dense) intruder can be observed by placing an intruder on it. Specifically, when the denser intruder with density ρ_i is placed on this vibrated granular bed of bulk density ρ_t , the intruder sinks into the bed. This descent phenomenon resembles the reverse Brazil nut effect (RBNE). Note that any additional loading is not applied to the intruder. Only the constant gravitational force is applied. Thus, this experiment corresponds to the stress-controlled measurement of the vertical slow drag. In contrast, all the other vertical slow drag experiments discussed in Sect. 4.2.1 were rate-controlled; the penetration rate was fixed. Under the typical vibration condition ($f = 20 \,\mathrm{Hz}$ and the root-mean-squared acceleration is 2g), the descent velocity is less than 1 mm/s. This velocity regime most likely corresponds to the slow (rate-independent) drag regime. To understand the descent dynamics, the effective friction can be estimated by the balance between the gravitational force $(\rho_i - \rho_t)gD_i^3$ and frictional force $\mu_{\rm eff}\rho_t g D_i^2 z$ as

$$\mu_{\text{eff}} \sim \frac{\rho_i - \rho_t}{\rho_t} \frac{D_i}{z}.$$
 (4.54)

The form of Eq. (4.54) can be primarily understood by the combination of the buoyant force, hydrostatic pressure, and Coulomb friction. As mentioned before, the drag force in such a slow motion should be independent of velocity. However, the weak velocity dependence of $\mu_{\rm eff}$ was reported in this system. $\mu_{\rm eff}$ was scaled by the normalized vertical velocity $\langle v_z \rangle / \sqrt{gz}$ as [112]

$$\mu_{\text{eff}} = \left(\frac{\langle v_z \rangle}{\sqrt{gz}}\right)^{0.37}.\tag{4.55}$$

This velocity dependence is neither inertial ($\sim v^2$) nor viscous ($\sim v$). This form is somehow similar to the frictional constitutive law for a sheared granular layer (Eq. (3.55)).

The granular drag force exerted on a moving thin wire in bulk granular matter is affected by a very weak level vibration [113]. As discussed previously (Sect. 3.9.4), the granular matter can be fluidized and exhibits Archimedes' principle of the buoyant force when vibrated strongly enough without enhancing the granular convection [114]. Even if the applied vibration is very weak, the granular drag force is affected by it; this effect is called sonofluidization. Various types of frictional drag forces were observed in the sonofluidized granular experiment. First, under the no-vibration condition, the drag force exerted on a wire exhibits

the rate- and state-dependent frictional (RSF) drag (Eq. (3.52)). Next, the drag force becomes linear rate-dependent friction in the low-velocity regime with an appropriate sonofulidization. Finally, the effective friction approaches zero at low velocity and maximal sonofluidization. Thus, the granular matter can asymptotically attain the fully fluidized state even with a weak vibration.⁹

4.3 Drag Forces of Other Soft Materials

The drag force is, in principle, measurable for various soft materials such as viscoelastic, elastoplastic, viscoplastic, and even more complex media. The drag force by a viscous fluid or granular matter has been intensively discussed thus far in this book. In this section, the drag force and related rheology of other soft materials are briefly introduced.

4.3.1 Viscoelastic Fluid Drag

The impact dynamics of viscoelastic micellar fluid was experimentally investigated [115]. They dropped a solid sphere $(9.53 \le D_i \le 25.4 \,\mathrm{mm}, 1.35 \times 10^3 \le \rho_i \le 7.97 \times 10^3 \,\mathrm{kg/m^3})$ onto a viscoelastic micellar fluid from free-fall heights in the range $5 \le h \le 1270 \,\mathrm{mm}$. Because of the elasticity of the micellar fluid, the solid sphere was rebounded. The maximum penetration depth z_p and the rebound height h_R were measured and characterized by the relevant parameters. The target viscoelastic micellar fluid is an aqueous solution of wormlike surfactant micelles that exhibits shear thinning behavior and its rheological properties (elastic shear modulus, viscosity, and relaxation time) are $G = 22 \,\mathrm{Pa}$, $\eta = 43 \,\mathrm{Pa}\cdot\mathrm{s}$, and $t_{\mathrm{relax}} = 2 \,\mathrm{s}$ at the zero shear limit, respectively [115, 116].

To characterize the maximum penetration depth z_p , the Froude number $F_r = v_0^2/gD_i$ and a dimensionless number $\Lambda = (\rho_i - \rho_t)gD_i/G$ were used in this study. Λ represents the ratio between gravity (buoyancy) and elasticity. A simple scaling for z_p was obtained as

$$\frac{z_p}{D_i} \sim (F_r \Lambda)^{1/3} \sim \left(\frac{(\rho_i - \rho_t)v_0^2}{G}\right)^{1/3}.$$
(4.56)

The scaling variable,

$$F_r \Lambda = \frac{(\rho_i - \rho_t) v_0^2}{G},\tag{4.57}$$

⁹The maximal sonofluidization remains very weak compared with usual mechanical vibration discussed in Sect. 3.9.

is called the elastic Froude number. Although the 1/3 power-law scaling is somewhat similar to that for the granular impact (Eq. (4.3)) and ejecta potential scaling (Fig. 4.2a), they are not completely identical. In particular, the role of elasticity is considerably less important for the granular impact. That is why the *elastic* Froude number is used in Eq. (4.56) instead of the bare Froude number. Furthermore, for a viscoelastic material, viscosity must be considered to describe its behavior. To consider the viscosity effect, the Deborah number $D_e = t_{\text{relax}}(v_0/D_i)$ is employed. Because the relaxation time in a viscoelastic material corresponds to the ratio of viscosity and elastic modulus (Eq. (3.5) and $t_{\text{relax}} = t_M$), D_e can represent the balance between the viscous stress and elastic stress as $D_e = \eta v_0 D_i/GD_i^2$. Assuming the Maxwell model energy balance, Eq. (4.56) can be modified as [115]

$$\frac{z_p}{D_i} \sim (F_r \Lambda)^{1/3} \left(\frac{1 + D_e^2}{D_e^2}\right)^{1/3}.$$
(4.58)

This relation corresponds to the energy balance $(\rho_i - \rho_t)D_i^3v_0^2 \sim G\gamma^2z_p^3$. Here the squared strain γ^2 is approximated by $(t_Mv_0/D_i)^2/[1+(t_Mv_0/D_i)]^2$, where t_M is the Maxwell time (Eq. (3.5)). In the $D_e \gg 1$ limit, Eq. (4.56) is recovered; however, the rebound height h_R does not show any systematic trend. The data of h_R is highly scattered around its mean value ($h_R \simeq 25$ mm) independent of the impact velocity v_0 .

These researchers also studied the surface texture on the cavity formed by the impact [115]. In the low v_0 regime, the cavity shape is rather smooth. As v_0 increases, the cavity becomes bulbous in shape. When v_0 exceeds a critical value, the cavity surface shape varies to a rough surface texture. From the experimental observation, this transition occurs near $D_e \simeq 400$ –700, depending on Λ [115].

The concepts of viscous drag and terminal velocity (Sect. 2.6) have been modified and applied to the viscoelastic case to explain the viscosity of some viscoelastic fluids [117]. However, it is difficult to fully reproduce the behaviors of highly viscoelastic drag force using a simple viscous terminal velocity model. Obviously, the terminal-velocity-based method is limited in the steady-state measurement. Thus, the dynamics of impact and rebound cannot be described along the line of simple steady-state viscosity. The main reason for viscoelastic rebound is its elasticity. Because of the elastic contribution, transient behaviors can also be observed in a viscoelastic penetration. For instance, transient oscillations were observed in the sedimentation of a sphere [118]. Moreover, a similar oscillation was observed in a bubble rising through a viscoelastic fluid [119]. Actually, even the steady (not transient) oscillation of a sphere falling in a viscoelastic fluid was observed in the experiments [120, 121]. For the wormlike micellar fluid case, the oscillatory motion is caused by the formation and breaking of flow-induced structure [121]. The ideas of flow-induced structure and its breaking qualitatively resemble those of drag-induced wedge formation and its breaking observed in the granular plow experiment [103] (Sect. 4.2.2). Both result in periodic motions, which are the typical behaviors in complex soft matter drag.

4.3.2 Viscoplastic Fluid Drag

A viscoplastic fluid obeying the Herschel-Bulkley model (Eq. (3.7)) was also used as a target of the solid sphere's impact experiment [122]. Because the viscoplastic fluid has a finite yield stress, it can sustain an impact crater shape when the stress is relaxed under the level of the yield stress. Therefore, the impact crater can remain and will not be completely relaxed. The resultant crater morphology will be discussed later at the end of Sect. 6.1. In Ref. [122], the impact drag force was not measured. The shape of the remaining crater, cavity pinch-off, and jetting of the viscoplastic impact were emphasized instead. The drag force by a viscoplastic target has not yet been understood. The drag force measurement and its relation to the resultant crater morphology for a viscoplastic target are interesting issues to be discussed in the future.

4.3.3 Dense Suspension Drag

Dense granular suspensions also exhibit intriguing phenomena due to impact. Dense suspensions of micrometer-sized grains can be deformed easily by slow forces. However, these suspensions are drastically hardened by rapid forces. This particular property of dense suspensions results in dynamic solidification by an impact. Waitukaitis and Jaeger investigated the dynamic jamming front propagation occurring in this sudden hardening induced by an impact [123]. To quantify this phenomenon, they used various methods: high-speed video imaging, embedded acceleration measurement, and X-ray imaging. In the experiment, a cylindrical rod with mass m_i was dropped vertically into a cornflour suspension, with the impact velocity in the range $0.2 < v_0 < 2$ m/s. Then, a jamming front seed was nucleated by grains at the impact point. This jamming front propagates in the suspension almost one-dimensionally. The jamming front propagation velocity $v_{\rm front}$ can be roughly described as

$$v_{\text{front}} = v_0 \frac{D_g}{\delta_g},\tag{4.59}$$

where D_g and δ_g are the grain size and interstitial gap length (average gap length among grains), respectively. A solid plug is produced by the nearly one-dimensional propagation of the jamming front. The length of this solid plug grows with time and causes a large drag force against the impact. The measured drag force can be explained by the idea of virtual mass. The virtual mass $m_{\rm virt}$ considered in this study is proportional to the square of the penetration depth. Utilizing this virtual mass, the measured kinematic data set of the impactor rod (a, v, z) can be fully reproduced by the simple model

$$(m_i + m_{\text{virt}})\frac{dv}{dt} = m_i g - \frac{dm_{\text{virt}}}{dt}v. \tag{4.60}$$

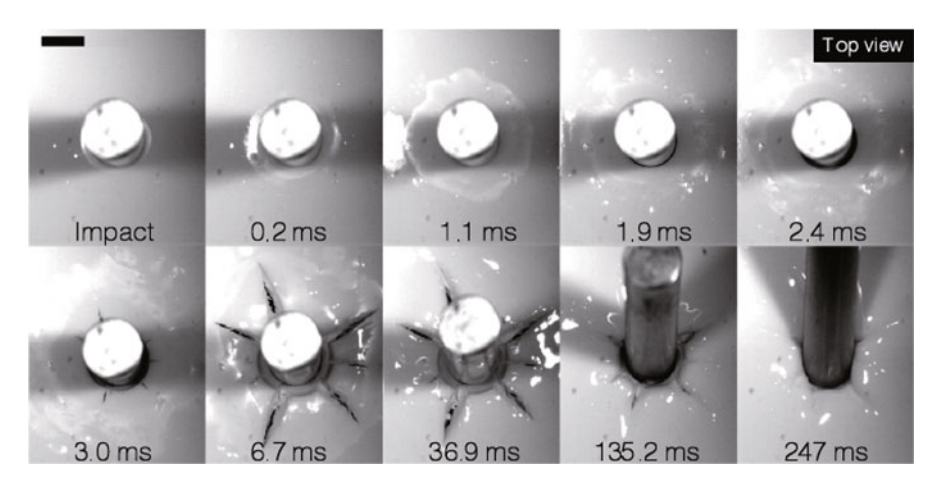


Fig. 4.20 Time sequence of the crack formation due to the free-fall impact of a rod onto a dense suspension layer. The target is a cornstarch suspension, and the impactor is a tungsten carbide rod. Its free-fall height is 770 mm. The scale bar corresponds to 10 mm (Reprinted with permission from Ref. [124]. Copyright 2013 by American Physical Society)

The propagation of the jamming front is a key to the very strong resistance force against the rapid forcing.

This simple model is novel one. Usually, the strong resistance to rapid forcing has been explained by the suspension's dilatant effect against the shear. The volume of the wet granular system must expand to attain the shear deformation. This dilation is not so easy for a dense suspension, in general. Thus, a large resistance force is produced. The jamming front propagation scenario explained above is slightly different from this conventional idea. The compression by the impact and associated jamming wave propagation play essential roles for the thickening of the suspension. Similar one-dimensional chain-like collisions were used to explain dry granular oblique impact [75] (Sect. 4.1.8).

There is certainly a limit to the impact-induced thickening of a dense suspension. When the impact inertia is extremely large, the suspension responds similar to a brittle solid; that is, fracturing occurs. To demonstrate the brittle fracturing in a dense suspension, the experiment of the vertical rod impact was performed with a thin target layer of a dense suspension [124]. Clear crack growth was observed, as shown in Fig. 4.20. According to Ref. [124], the number and length of cracks mainly depend on the thickness of the target suspension. If the suspension layer is too thick, it is difficult to solidify the entire layer because the jamming wave front propagates with a finite velocity of Eq. (4.59). In a thick layer, the suspension is relaxed by the viscosity before the entire solidification by the jamming front's arrival to the bottom. Crack formation occurs only in a solidified (brittle) state. The target specimen must be solidified by the impact itself before its fracturing. Therefore, a thinner layer is better for producing a crack. The number of cracks is inversely proportional to the thickness of the target suspension layer and diminishes in a sufficiently thick suspension layer [124].

4.4 Summary 153

Dense suspensions behave like solids or liquids depending on the loading conditions. For the vertical impact case, a simple one-dimensional model such as Eq. (4.60) is sufficient to understand the basics of the drag force and the related solidification. In the viscoelastic target impact, an oscillatory behavior was also observed, as discussed in Sect. 4.3.1. Oscillatory behaviors can also be observed in dense suspensions [125]. A phenomenological model to reproduce the oscillatory behavior of dense suspensions was proposed [126, 127]. The idea of this model is slightly different from that of the model involving jamming front propagation. Specifically, the exponential divergence of the shear viscosity depending on a certain state variable is assumed in the model of Ref. [126, 127] in contrast to the onedimensional (normal) jamming wave model described by Eq. (4.60) [123]. In the former, the lateral momentum transfer due to the viscosity is the main effect. In the latter, the jamming front propagation dominates the dynamics. In either case, a representative timescale of the lateral momentum transfer or the jamming front propagation is comparative with the characteristic (relaxation) timescale of the dynamics. Thus, their competition causes some unexpected phenomena such as oscillation and fracturing. In a usual viscoelastic fluid (Maxwell) model, a crossover between elastic and viscous behaviors occurs at the relaxation timescale. i.e., Maxwell time (Eq. (3.5)). In contrast, the applied shear stress or normal loading determines the behavior in dense suspensions. According to another numerical simulation, the frictional contact among grains in a suspension is essential for the abrupt hardening (discontinuous shear thickening) in dense suspensions [128, 129]. The model successfully reproduces general behaviors of the discontinuous shear thickening. There are other models to describe the shear thickening behavior [130–132]. The rheological characterization of dense suspension remains a matter of debate.

4.4 Summary

Various impact (and slow) drag forces produced by soft matter targets were reviewed throughout this chapter. In particular, the granular drag force by the vertical impact of a solid sphere was emphasized, and a simple unified drag force model was derived on the basis of experimental results. Many other experimental results on granular drag force were overviewed, and their complex behaviors were understood in terms of scaling and dimensional thought. Because of the rich phenomenology, a completely unified understanding of granular impact drag force has not yet been achieved. Systematic and unified understandings of these diverse results are still insufficient to clarify the entire granular impact dynamics. Alternatively, many experimental results were merely introduced and summarized in this chapter. Then, the slow granular drag force was emphasized, and some interesting topics such as granular swimming were also discussed. After reviewing slow granular drag mechanics, drag forces in complex fluids such as viscoelastic, viscoplastic and dense suspensions were also discussed. Up to this point, the fundamental physical concept of the drag force by soft matter impact has been discussed along the line of

continuous mechanics formulae. We have focused on fundamental physics rather than application to actual planetary impact phenomena. Starting from the next chapter, the physics and morphology of actual impact cratering on a planetary scale and some related fundamental physical processes will be mainly discussed.

References

- 1. H.J. Melosh, *Impact Cratering* (Oxford University Press, New York, 1989)
- 2. J.C. Amato, R.E. Williams, Am. J. Phys. 66, 141 (1998)
- 3. J.S. Uehara, M.A. Ambroso, R.P. Ojha, D.J. Durian, Phys. Rev. Lett. 90, 194301 (2003)
- 4. J.S. Uehara, M.A. Ambroso, R.P. Ojha, D.J. Durian, Phys. Rev. Lett. 91, 149902 (2003)
- 5. K.A. Newhall, D.J. Durian, Phys. Rev. E 68, 060301 (2003)
- 6. A.M. Walsh, K.E. Holloway, P. Habdas, J.R. de Bruyn, Phys. Rev. Lett. 91, 104301 (2003)
- 7. M.A. Ambroso, C.R. Santore, A.R. Abate, D.J. Durian, Phys. Rev. E 71, 051305 (2005)
- 8. M.A. Ambroso, R.D. Kamien, D.J. Durian, Phys. Rev. E 72, 041305 (2005)
- L.S. Tsimring, D. Volfson, in *Powders and Grains 2005*, ed. by R. Garcia-Rojo, H.J. Herrmann, S. McNamara (Balkema, Rotterdam, 2005), pp. 1215–1218
- M. Pica Ciamarra, A.H. Lara, A.T. Lee, D.I. Goldman, I. Vishik, H.L. Swinney, Phys. Rev. Lett. 92, 194301 (2004)
- 11. F. Bourrier, F. Nicot, F. Darve, Granul. Matter 10, 415 (2008)
- 12. D.I. Goldman, P. Umbanhowar, Phys. Rev. E 77, 021308 (2008)
- 13. A. Seguin, Y. Bertho, P. Gondret, J. Crassous, EPL (Europhys. Lett.) 88, 44002 (2009)
- 14. J.R. de Rruyn, A.M. Walsh, Can. J. Phys. 82, 439 (2004)
- 15. D. Lohse, R. Rauhé, R. Bergmann, D. van der Meer, Nature 432, 689 (2001)
- 16. M. Hou, Z. Peng, R. Liu, K. Lu, C.K. Chan, Phys. Rev. E 72, 062301 (2005)
- 17. H. Katsuragi, D.J. Durian, Nat. Phys. **3**, 420 (2007)
- 18. M.E. Backman, W. Goldsmith, Int. J. Eng. Sci. 16, 1 (1978)
- 19. A.H. Clark, R.P. Behringer, EPL (Europhys. Lett.) 101, 64001 (2013)
- 20. H. Katsuragi, D.J. Durian, Phys. Rev. E 87, 052208 (2013)
- 21. M. Tiwari, T.R. Krishna Mohan, S. Sen, Phys. Rev. E 90, 062202 (2014)
- 22. K. Wada, H. Senshu, T. Matsui, Icarus 180, 528 (2006)
- 23. T.A. Brzinski, P. Mayor, D.J. Durian, Phys. Rev. Lett. 111, 168002 (2013)
- 24. Y. Boguslavskii, S. Drabkin, I. Juran, A. Salman, J. Geotech. Eng. 122, 806 (1996)
- 25. Y. Boguslavskii, S. Drabkin, A. Salman, J. Phys. D 29, 905 (1996)
- 26. G. Ben-Dor, A. Dubinsky, T. Elperin, Mech. Res. Commun. 36, 625 (2009)
- 27. G. Ben-Dor, A. Dubinsky, T. Elperina, Mech. Based Design Struct. Mach. 38, 468 (2010)
- 28. N. Nordstrom, K. E. Lim, M. Harrington, W. Losert, Phys. Rev. Lett. 112, 228002 (2014)
- 29. K.E. Daniels, J.E. Coppock, R.P. Behringer, Chaos 14, S4 (2004)
- 30. A.H. Clark, L. Kondic, R.P. Behringer, Phys. Rev. Lett. 109, 238302 (2012)
- 31. A.H. Clark, A.J. Petersen, L. Kondic, R.P. Behringer, Phys. Rev. Lett. 114, 144502 (2015)
- 32. L. Kondic, X. Fang, W. Losert, C.S. O'Hern, R.P. Behringer, Phys. Rev. E 85, 011305 (2012)
- 33. A.M. Nakamura, M. Setoh, K. Wada, Y. Yamashita, K. Sangen, Icarus 223, 222 (2013)
- 34. R.A. Bagnold, Proc. R. Soc. A 225, 49 (1954)
- F. da Cruz, S. Emam, M. Prochnow, J.N. Roux, F.m.c. Chevoir, Phys. Rev. E 72, 021309 (2005)
- 36. N. Mitarai, H. Nakanishi, Phys. Rev. Lett. 94, 128001 (2005)
- 37. O. Pouliquen, Phys. Fluids **11**, 542 (1999)
- L.E. Silbert, D. Ertas, G.S. Grest, T.C. Halsey, D. Levine, S.J. Plimpton, Phys. Rev. E 64, 051302 (2001)
- 39. C.R. Wassgren, J.A. Cordova, R. Zenit, A. Karion, Phys. Fluids 15, 3318 (2003)

References 155

- 40. R. Bharadwaj, C. Wassgren, R. Zenit, Phys. Fluids 18, 043301 (2006)
- 41. T.A. Brzinski III, D.J. Durian, Soft Matter **6**, 3038 (2010)
- 42. Y. Takehara, S. Fujimoto, K. Okumura, EPL (Europhys. Lett.) 92, 44003 (2010)
- 43. A.H. Clark, A.J. Petersen, R.P. Behringer, Phys. Rev. E 89, 012201 (2014)
- N.V. Brilliantov, T. Pöschel, Kinetic Theory of Granular Gases (Oxford University Press, New York, 2004)
- 45. A.R. Abate, H. Katsuragi, D.J. Durian, Phys. Rev. E **76**, 061301 (2007)
- 46. V. Buchholtz, T. Pöschel, Granul. Matter 1, 33 (1998)
- 47. C. Clanet, Annu. Rev. Fluid Mech. 39, 469 (2007)
- 48. X. Cheng, G. Varas, D. Citron, H.M. Jaeger, S.R. Nagel, Phys. Rev. Lett. 99, 188001 (2007)
- 49. T.G. Sano, H. Hayakawa, Phys. Rev. E 86, 041308 (2012)
- 50. E.L. Nelson, H. Katsuragi, P. Mayor, D.J. Durian, Phys. Rev. Lett. 101, 068001 (2008)
- 51. A. Seguin, Y. Bertho, P. Gondret, Phys. Rev. E 78, 010301 (2008)
- 52. S. von Kann, S. Joubaud, G.A. Caballero-Robledo, D. Lohse, D. van der Meer, Phys. Rev. E 81, 041306 (2010)
- F. Pacheco-Vázquez, G.A. Caballero-Robledo, J.M. Solano-Altamirano, E. Altshuler, A.J. Batista-Leyva, J.C. Ruiz-Suárez, Phys. Rev. Lett. 106, 218001 (2011)
- E. Altshuler, H. Torres, A. González-Pita, G. Sánchez-Colina, C. Pérez-Penichet, S. Waitukaitis, R.C. Hidalgo, Geophys. Res. Lett. 41, 3032 (2014)
- 55. P. Umbanhowar, D.I. Goldman, Phys. Rev. E 82, 010301 (2010)
- 56. M. Schröter, S. Nägle, C. Radin, H.L. Swinney, EPL (Europhys. Lett.) 78, 44004 (2007)
- 57. S. Torquato, F.H. Stillinger, Rev. Mod. Phys. 82, 2633 (2010)
- 58. A.J. Liu, S.R. Nagel, Annu. Rev. Cond. Matt. Phys. 1, 347 (2010)
- 59. Y. Takehara, K. Okumura, Phys. Rev. Lett. 112, 148001 (2014)
- J.R. Royer, E.I. Corwin, A. Flior, M.L. Cordero, M.L. Rivers, P.J. Eng, H.M. Jaeger, Nat. Phys. 1, 164 (2005)
- G. Caballero, R. Bergmann, D. van der Meer, A. Prosperetti, D. Lohse, Phys. Rev. Lett. 99, 018001 (2007)
- 62. J.R. Royer, E.I. Corwin, P.J. Eng, H.M. Jaeger, Phys. Rev. Lett. 99, 038003 (2007)
- J.R. Royer, B. Conyers, E.I. Corwin, P.J. Eng, H.M. Jaeger, EPL (Europhys. Lett.) 93, 28008 (2011)
- 64. D. Lohse, R. Bergmann, R. Mikkelsen, C. Zeilstra, D. van der Meer, M. Versluis, K. van der Weele, M. van der Hoef, H. Kuipers, Phys. Rev. Lett. 93, 198003 (2004)
- 65. J.O. Marston, I.U. Vakarelski, S.T. Thoroddsen, Phys. Rev. E **86**, 020301 (2012)
- 66. N. Mitarai, F. Nori, Adv. Phys. **55**, 1 (2006)
- 67. T.A. Brzinski, J. Schug, K. Mao, D.J. Durian, Phys. Rev. E 91, 022202 (2015)
- 68. C. Ringl, E.M. Bringa, H.M. Urbassek, Phys. Rev. E 86, 061313 (2012)
- 69. D. Wang, X. Ye, X. Zheng, Eur. Phys. J. E 35, 1 (2012)
- 70. M. Nishida, M. Okumura, K. Tanaka, Granul. Matter 12, 337 (2010)
- 71. B.T. Werner, P.K. Haff, Sedimentology **35**, 189 (1988)
- 72. R.S. Anderson, P.K. Haff, Science 241, 820 (1988)
- 73. F. Rioual, A. Valance, D. Bideau, Phys. Rev. E 62, 2450 (2000)
- 74. F. Rioual, A. Valance, D. Bideau, EPL (Europhys. Lett.) **61**, 194 (2003)
- 75. D. Beladjine, M. Ammi, L. Oger, A. Valance, Phys. Rev. E 75, 061305 (2007)
- 76. M.Y. Louge, M.E. Adams, Phys. Rev. E **65**, 021303 (2002)
- 77. H. Kuninaka, H. Hayakawa, Phys. Rev. Lett. **93**, 154301 (2004)
- 78. J. Crassous, D. Beladjine, A. Valance, Phys. Rev. Lett. 99, 248001 (2007)
- 79. A. Valance, J. Crassous, Eur. Phys. J. E 30, 43 (2009)
- 80. X. Ye, D. Wang, X. Zheng, Phys. Rev. E 86, 061304 (2012)
- 81. M.B. Stone, D.P. Bernstein, R. Barry, M.D. Pelc, Y.K. Tsui, P. Schiffer, Nature 427, 503 (2004)
- M.B. Stone, R. Barry, D.P. Bernstein, M.D. Pelc, Y.K. Tsui, P. Schiffer, Phys. Rev. E 70, 041301 (2004)
- 83. G. Hill, S. Yeung, S.A. Koehler, EPL (Europhys. Lett.) 72, 137 (2005)

- 84. Z. Peng, X. Xu, K. Lu, M. Hou, Phys. Rev. E 80, 021301 (2009)
- 85. H. Katsuragi, Phys. Rev. E 85, 021301 (2012)
- 86. H. Katsuragi, Chem. Eng. Sci. **76**, 165 (2012)
- 87. F. Zhou, S.G. Advani, E.D. Wetzel, Phys. Rev. E **71**, 061304 (2005)
- 88. K. Matsuyama, H. Katsuragi, Nonlin. Process. Geophys. 21, 1 (2014)
- 89. A. Seguin, Y. Bertho, F. Martinez, J. Crassous, P. Gondret, Phys. Rev. E 87, 012201 (2013)
- 90. D. Chehata, R. Zenit, C. Wassgren, Phys. Fluids 15, 1622 (2003)
- 91. A. Seguin, Y. Bertho, P. Gondret, J. Crassous, Phys. Rev. Lett. 107, 048001 (2011)
- 92. M. Raffel, C. Willert, S. Wereley, J. Kompenhans, Particle Image Velocimetry: A Practical Guide, 2nd edn. (Springer, Heidelberg, 2007)
- 93. J.T. Jenkins, S.B. Savage, J. Fluid Mech. **130**, 187 (1983)
- 94. E. Kolb, P. Cixous, N. Gaudouen, T. Darnige, Phys. Rev. E 87, 032207 (2013)
- 95. R. Albert, M.A. Pfeifer, A.L. Barabási, P. Schiffer, Phys. Rev. Lett. 82, 205 (1999)
- 96. I. Albert, P. Tegzes, B. Kahng, R. Albert, J.G. Sample, M. Pfeifer, A.L. Barabási, T. Vicsek, P. Schiffer, Phys. Rev. Lett. **84**, 5122 (2000)
- 97. I. Albert, P. Tegzes, R. Albert, J.G. Sample, A.L. Barabási, T. Vicsek, B. Kahng, P. Schiffer, Phys. Rev. E 64, 031307 (2001)
- 98. D.J. Costantino, J. Bartell, K. Scheidler, P. Schiffer, Phys. Rev. E 83, 011305 (2011)
- 99. I. Albert, J.G. Sample, A.J. Morss, S. Rajagopalan, A.L. Barabási, P. Schiffer, Phys. Rev. E **64**, 061303 (2001)
- 100. F. Guillard, Y. Forterre, O. Pouliquen, Phys. Rev. Lett. 110, 138303 (2013)
- 101. J. Geng, R.P. Behringer, Phys. Rev. E 71, 011302 (2005)
- 102. F. Guillard, Y. Forterre, O. Pouliquen, Phys. Rev. E **91**, 022201 (2015)
- 103. N. Gravish, P.B. Umbanhowar, D.I. Goldman, Phys. Rev. Lett. 105, 128301 (2010)
- 104. Y. Ding, N. Gravish, D.I. Goldman, Phys. Rev. Lett. 106, 028001 (2011)
- 105. F.Q. Potiguar, Phys. Rev. E **84**, 061302 (2011)
- 106. F.Q. Potiguar, Y. Ding, Phys. Rev. E 88, 019905 (2013)
- 107. J.M. Solano-Altamirano, G.A. Caballero-Robledo, F. Pacheco-Vázquez, V. Kamphorst, J.C. Ruiz-Suárez, Phys. Rev. E 88, 032206 (2013)
- 108. R.D. Maladen, Y. Ding, C. Li, D.I. Goldman, Science 325, 314 (2009)
- 109. R.D. Maladen, Y. Ding, P.B. Umbanhowar, D.I. Goldman, Int. J. Robot. Res. 30, 793 (2011)
- 110. T. Shimada, D. Kadau, T. Shinbrot, H.J. Herrmann, Phys. Rev. E 80, 020301 (2009)
- 111. J.E. Avron, O. Kenneth, D.H. Oaknin, New J. Phys. **7**, 234 (2005)
- 112. R. Harich, T. Darnige, E. Kolb, E. Clément, EPL (Europhys. Lett.) 96, 54003 (2011) 113. G. Caballero-Robledo, E. Clément, Eur. Phys. J. E 30, 395 (2009)
- 114. D.A. Huerta, V. Sosa, M.C. Vargas, J.C. Ruiz-Suárez, Phys. Rev. E 72, 031307 (2005)
- 115. B. Akers, A. Belmonte, J. Non-Newton. Fluid Mech. 135, 97 (2006)
- 116. L.B. Smolka, A. Belmonte, J. Non-Newton. Fluid Mech. 115, 1 (2003)
- 117. Y. Cho, J. Hartnett, W. Lee, J. Non-Newton. Fluid Mech. 15, 61 (1984)
- 118. D. Rajagopalan, M. Arigo, G.H. McKinley, J. Non-Newton. Fluid Mech. 65, 17 (1996)
- 119. A. Belmonte, Rheol. Acta 39, 554 (2000)
- 120. A. Mollinger, E. Cornelissen, B. van den Brule, J. Non-Newton. Fluid Mech. 86, 389 (1999)
- 121. A. Jayaraman, A. Belmonte, Phys. Rev. E **67**, 065301 (2003)
- 122. H. Tabuteau, D. Sikorski, S.J. de Vet, J.R. de Bruyn, Phys. Rev. E 84, 031403 (2011)
- 123. S.R. Waitukaitis, H.M. Jaeger, Nature **487**, 205 (2012)
- 124. M. Roché, E. Myftiu, M.C. Johnston, P. Kim, H.A. Stone, Phys. Rev. Lett. 110, 148304 (2013)
- 125. S.i. Nagahiro, H. Nakanishi, N. Mitarai, EPL (Europhys. Lett.) 104, 28002 (2013)
- 126. H. Nakanishi, N. Mitarai, J. Phys. Soc. Jpn. 80, 033801 (2011)
- 127. H. Nakanishi, S.i. Nagahiro, N. Mitarai, Phys. Rev. E 85, 011401 (2012)
- 128. R. Seto, R. Mari, J.F. Morris, M.M. Denn, Phys. Rev. Lett. 111, 218301 (2013)
- 129. R. Mari, R. Seto, J.F. Morris, M.M. Denn, J. Rheol. 58, 1693 (2014)
- 130. D.A. Head, A. Ajdari, M.E. Cates, Phys. Rev. E **64**, 061509 (2001)
- 131. C.B. Holmes, M.E. Cates, M. Fuchs, P. Sollich, J. Rheol. 49, 237 (2005)
- 132. E. Brown, H.M. Jaeger, J. Rheol. 56, 875 (2012)

Chapter 5 Morphodynamics of Planetary Impact Craters

In this chapter, the shape and mechanics of impact craters are discussed. In particular, planetary-scale craters will be featured. Because crater sizes are distributed over a very wide range (over several orders of magnitude), scaling method and dimensional analysis such as Π -groups method introduced in Sect. 2.5.2 have been applied to understand the physical mechanisms of the cratering process. The crater erasure process by impact-induced seismicity will also be discussed briefly. Fundamentals of the morphological classification of various craters and the scaling-based analysis method are introduced in the following text.

5.1 Classification of Craters

As already discussed in Chap. 1, the lunar surface is covered with myriads of impact craters. Furthermore, we can find many impact craters on the surfaces of other terrestrial planets, satellites, and asteroids. Most of these craters appear somewhat circular. However, they actually have a wide variety of shapes. Characteristic features of cratering mechanics and resultant crater shapes have been partially clarified by in-depth investigations based on recent explorations, laboratory experiments, and theories. The traditional classification of crater's shape is summarized in this section based on Ref. [1].

Simple crater The simplest bowl-shaped craters are called *simple craters*. A typical example of simple craters is shown in Fig. 5.1. Simple craters are produced by relatively small-scale impacts, and the intersection of the cavity shape can be approximated by a parabolic function. The ratio between the crater's rim-to-rim diameter D_c and its rim-to-floor depth D_h in fresh craters are approximately



Fig. 5.1 Example of a simple crater on the Moon: Moltke crater photographed by Apollo 10 astronauts in 1969. The diameter is approximately 7 km. The crater cavity intersection has an approximate parabolic shape (Credit: NASA)

related as $^1D_h/D_c \simeq 1/5$ [2]. This indicates that the simple crater's diameter is proportional to the depth, $D_c \sim D_h$. Thus, the crater volume V_c can be estimated as $V_c \sim D_c^2D_h \sim D_c^3$. Simple craters are indeed the simplest remnant of small-scale impacts. Presumably this simple crater shape is most familiar and understandable as a representative crater shape. However, note that only small craters can be simple.

Complex crater When the crater's diameter exceeds a certain critical value, the crater shape exhibits a drastic change from a simple crater to a *complex crater*. The critical size of this transition is approximately 20 km on the Moon. One of the most significant difference between simple and complex craters is the aspect ratio, D_h/D_c . In complex craters, D_h/D_c is approximately 1/8 [1]. Thus, the cavity of a complex crater is more flattened than that of a simple crater. Moreover, complex craters usually have a flat floor and a steeply standing rim by angle of repose. Note that the ratio D_h/D_c remains constant, namely, $D_h \sim D_c$ is also satisfied for complex craters. Another noticeable hallmark of complex craters is a *central peak* structure. The central peak is a mound structure observed at the crater's center (Fig. 5.2a). A complex crater with a central peak can be observed in intermediate-size complex craters (e.g., $20 < D_c < 140 \,\mathrm{km}$ on the Moon). While the central peak structure reminds us of the jet made by a cavity collapse in liquid or granular impact phenomena (Sect. 6.3), its origin cannot be simply explained by the cavity collapse jet. Thus, the central peak formation problem remains unsolved. In Fig. 5.2a, one

¹For fresh craters on asteroids, this ratio reduces: 0.15 (Ida) [3], 0.14 (Gaspra) [4], 0.13 (Eros) [5], and 0.08 (Itokawa) [6].

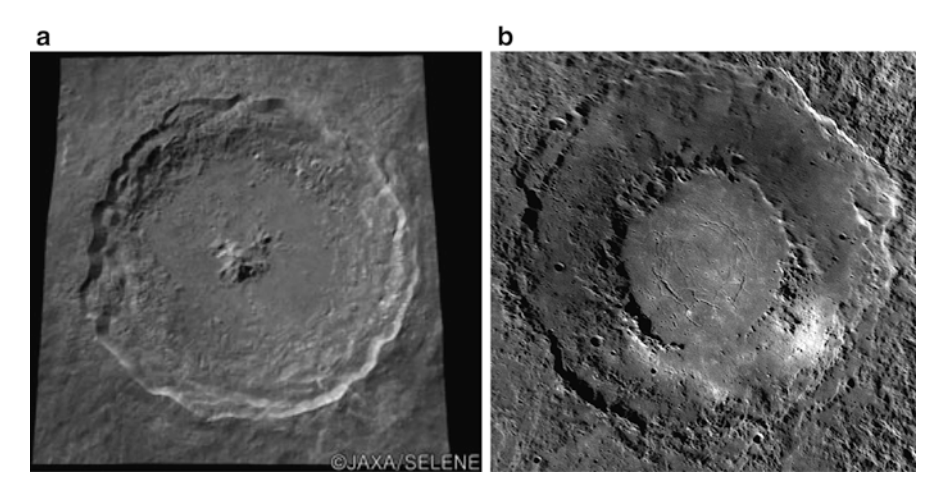


Fig. 5.2 Complex crater examples. (a) Tyco crater on the Moon taken by SELENE. The crater possesses a typical central peak and terrace wall. The diameter of the Tyco crater is approximately 85 km (Copyrighted by JAXA/SELENE). (b) Rachmaninoff peak-ring crater on Mercury. Its diameter is 290 km (Credit: NASA)

can also observe the wall terraces that are probably formed by landslides of the side wall. A *central pit* structure can sometimes be observed instead of the central peak.

Extremely large complex craters (e.g., $D_c > 140 \, \mathrm{km}$ on the Moon) have different shapes. The central peak almost vanishes in such large complex craters. Instead, an inner concentric ring with irregularly shaped mountain peaks decorates complex craters. These craters are called *peak-ring craters* and are observed on the Moon, Mars, Mercury, and Earth. An actual example of a peak-ring crater is shown in Fig. 5.2b. The diameter of the inner ring is approximately half of D_c .

The transition diameter from the simple crater to the complex crater, D_{crit} , depends on gravitational acceleration. That is, D_{crit} is different among the Moon, Mars, Mercury, and Earth. The transition diameter is inversely proportional to the gravitational acceleration, $D_{\text{crit}} \propto g^{-1}$ [7]. This tendency can be understood naturally by considering the balance between the hydrostatic pressure $\rho_t g D_h$ and the yield stress of the crater structure Y_c . If we assume that the density ρ_t and the yield stress Y_c of the craters are almost uniform, the transition point should be simply written by a dimensionless factor $Y_c/\rho_t g D_h$. The structure is stable as long as its yield stress is sufficiently large compared with the hydrostatic (gravitational) stress. The transition diameter is inversely proportional to g if we assume that ρ_t and Y_c are constant. Large craters cannot sustain their own shapes because of the large hydrostatic stress. Finally, landslide flows are also triggered by similar instabilities.

Multiring basin When the crater's size becomes even larger, a *multiring basin* is formed (Fig. 5.3). Multiple concentric ring structures can be observed in this type of crater. It is considered that the rings are formed outside the original impact crater. In contrast, the original crater rim in the peak-ring crater is seemingly the outer ring.

Fig. 5.3 Picture of a multiring basin on the Mare Orientale of the Moon taken by Lunar Reconnaissance Orbiter. The diameter is 950 km. An asteroid-scale impact approximately 3 billion years ago produced this large impact basin (Credit: NASA)

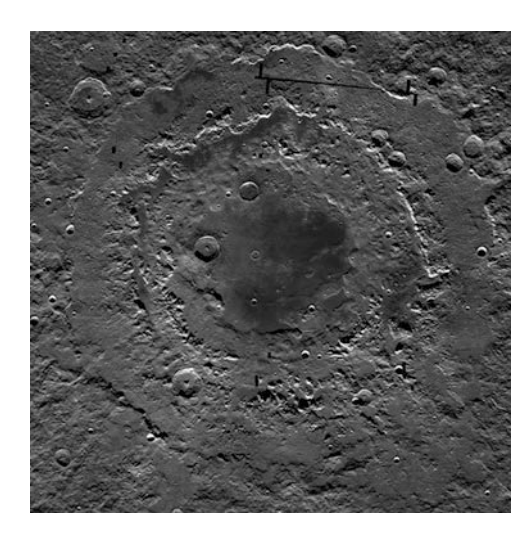
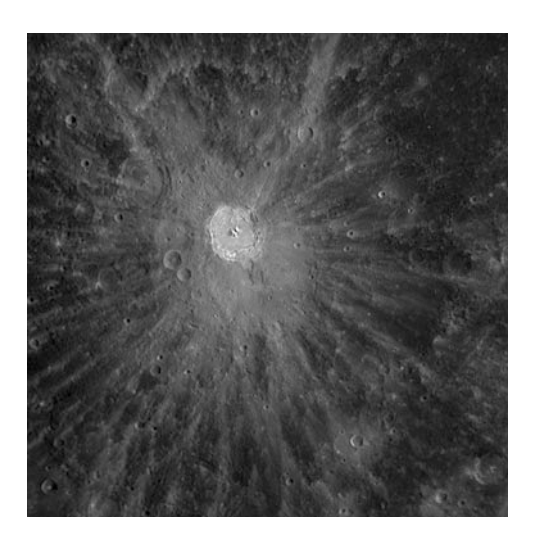


Fig. 5.4 Ray crater example: Kuiper crater on Mercury. Its diameter is approximately 62 km. Many rays can be observed in the deposited ejecta. The ray crater can mainly be observed on airless planets (Credit: NASA)



Namely, the additional rings are formed outside the original ring in the multiring basin, and the additional rings in the peak-ring crater are formed inside the original ring. The transition diameter from a complex crater to a multiring basin is not scaled by the gravitational acceleration. Thus, the origin of multiring basins cannot be simply understood by the gravitational collapse and should be distinguished from peak-ring complex craters, although these craters (peak-ring and multiring) are seemingly alike.

Ray crater Looking at the deposited ejecta shape rather than the crater cavity shape, one can observe some peculiar structures. For example, a *ray crater* is a particular type of ejecta deposition. In Fig. 5.4, a typical example of a ray

Fig. 5.5 Typical example of rampart crater observed on Mars. The diameter of the crater is approximately 27 km. The petal-like structure of the ejecta blanket is confirmed. Fluidized content due to H₂O is supposed to contribute to making this peculiar ejecta shape, although there is only limited experimental evidence for this idea (Credit: NASA)



crater is shown. Rays spreading radially from the center of the crater are clearly observed in Fig. 5.4. This structure suggests that the spreading of the ejecta is not homogeneous; there might be some sort of instability in the spreading ejecta cloud. The hydrodynamic instability of a spreading liquid such as milk-crown formation, might be recalled when examining the ray structure. To evaluate the possibility of such a naive analogy, we must discuss fluid impact splashing in detail. Fluid splashing instability will be discussed later in Sect. 6.6. The surface tension is sometimes crucial to induce hydrodynamic instability for the fluid splashing. As long as we consider the noncohesive grains as constituents of ejecta, the surface tension effect must be negligible. Additionally, the capillary length (Eq. (2.99)) is much shorter than the planetary crater's length scale. Moreover, ray crater can usually be observed on airless planets, whereas the instability of an impacting liquid drop requires a surrounding atmosphere [8] (see Sect. 6.6.4). On Mars, crater rays can only be recognized by the thermal infrared images [9]. We have not yet fully understood the mechanism of the formation of ray craters. According to the experiment by Kadono et al. [10], the ray structure may originate from the inelastic collisions between ejecta particles rather than fluid splashing instability.

Rampart crater An even stranger ejecta deposition structure called a *rampart* crater can be observed. A rampart crater is defined as a crater with petal-like ejecta deposition. A typical rampart crater is shown in Fig. 5.5. The diameter of the rampart crater is usually larger than 15 km. The origin of this strange ejecta deposition has still not been well understood. However, it is believed that the presence of water (or other volatiles) could be necessary to produce rampart craters [11]. A mixture of water and debris behaves like a slurry, which grovels on the surface rather than flies as an ejecta cloud or sheet. This idea is consistent with the fact that rampart craters can be observed on Mars, where H₂O (ice or water) has certainly existed. However, the detailed behaviors of the mixture of water and regolith grains have not yet been revealed. As discussed in Sect. 4.3.3, a dense suspension (mixture of liquid and grains) exhibits peculiar rheological properties.

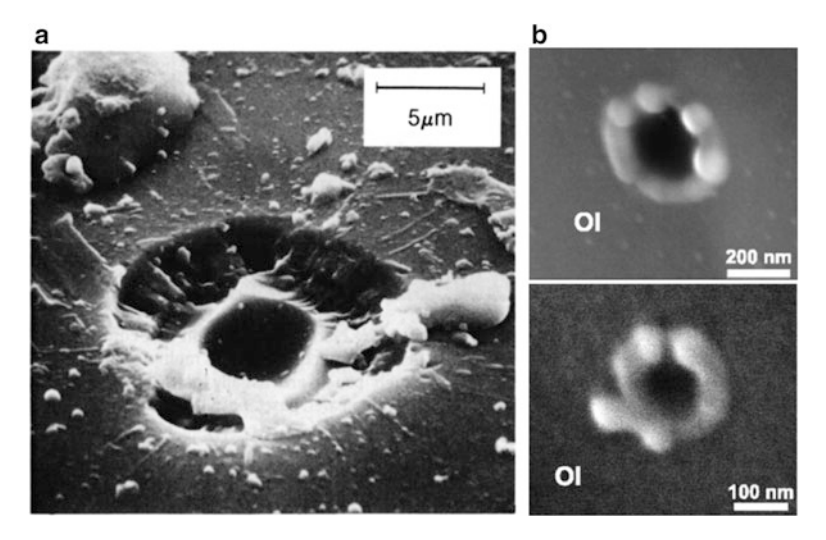


Fig. 5.6 (a) Micro crater approximately $5\,\mu m$ in diameter and surrounded by an approximately $5\,\mu m$ spall zone. This micro crater was observed on an Apollo 11 glass sphere [12] (Credit: NASA). (b) Micro craters found on the surface of Itokawa's grain. Ol means olivine substrate. The typical diameter is approximately 200 nm, and the craters are surrounded by seven or eight spherical bumps at the rim (After [13])

Micro crater Tiny craters were also observed on planetary samples as a counterpart to huge craters. All the crater shapes mentioned thus far are large-scale shapes. Because of the finite resolution limit of the exploration of planetary surfaces, we usually focus on large impact craters. Of course, large craters are important because they must be produced by high-energy impacts. Evidently, large-scale impacts affect the history of planets much more significantly than small-scale impacts. Thus, it is natural to focus on large impact craters. However, we can also examine microscopic craters. *Micro craters* were observed on samples that returned from space. The returned samples can be examined very carefully using accurate instruments such as scanning electron microscope (SEM). Then, the measurement resolution limit can be below the micrometer scale. Through such careful inspections, some micro craters have been located in the returned samples.

An example of micro craters comes from the Moon. In Fig. 5.6a, an SEM image of a micro crater ($D_c = 5 \,\mu$ m) observed on the Apollo 11 glass sphere is shown [12]. One can observe a bowl-shaped central pit surrounded by a larger depression called a spall zone.

Another example was observed on grains that returned from the small asteroid Itokawa. The Japanese spacecraft Hayabusa collected tiny grain samples from the asteroid Itokawa. On the surface of the grains, micro craters were observed [13]. Figure 5.6b shows photos of Itokawa's micro craters. The typical diameter is approximately 200 nm, and the structure is quite different from the micro craters on the Moon. The wavy structure caused by seven or eight spherical bumps can be

observed on the rim of Itokawa's micro craters. This wavy structure again recalls the milk-crown-like hydrodynamic instability similar to the ray crater case. For the ray crater structure, it was difficult to consider the surface tension effect because the ray crater is extremely large. The upper limit length scale of surface-tension-related phenomena can be estimated by the capillary length (Eq. (2.99)), which is usually on the millimeter scale on the surface of the Earth and is related to gravity as $g^{-1/2}$. This length scale is sufficiently large for the micro craters considered here. Therefore, surface tension could play a role in micro crater formation. In Sect. 6.6, the fingering instability of impact splashing will be discussed. However, the situation is not so simple. For the hydrodynamic impact, the crater rim structure will be relaxed in a short time. It is difficult to freeze the structure of the wavy rim such as in Fig. 5.6b. Moreover, the target cannot be a simple viscous fluid. Complex rheological behavior such as the Bingham model may need to be considered. A possible and naive scenario for the wavy micro crater formation is as follows. The target is molten by the impact-induced heat, and the impact causes a wavy rim structure because of hydrodynamic instability. Then, the structure is frozen by the solidification due to the cooling-down and energy dissipation of the target rim. According to this naive scenario, various rheological regimes (from hard to soft) of the target material must contribute to the structure formation, and therefore, all these regimes must be understood to fully explain this structure. In particular, the soft impact regimes are crucial. To discuss the origin of the wavy rim structure of the micro craters, systematic studies of impact cratering with various soft matters are necessary. Some seemingly relevant soft impact experiments will be introduced in the next chapter. Much more systematic and exhausted investigations for the soft impact cratering phenomena are one of the most important future problems for understanding the micro crater structure.

5.2 Population of Craters

The size of planetary craters ranges at least from 100 nm to 1,000 km. We cannot actually observe the intermediate scale craters because of the resolution limit of explorations. The usual lower limit of the length scale of exploration data is approximately 10 m in the current remote-sensing database. Sub-millimeter-scale micro craters can only be observed in samples that returned from space. Some centimeter to meter scale craters have also been observed in porous lunar regolith [1]. However, the observed number of micro- and intermediate-scale craters is very small. Even then, the scale of craters still ranges over approximately five orders of magnitude in the larger regime. Natural questions concerning such a widely ranging distribution can be raised as follows. How can we characterize the crater size-frequency distribution? Furthermore, is there a characteristic size? To answer these questions, the crater size-frequency distribution is measured by direct crater counting of the photos of planetary surfaces. In general, the measured crater size-frequency distribution is almost self-similar (power law). The cumulative

number N_{cum} of craters with diameter equal to or greater than D_c per unit area is simply approximated by

$$N_{\text{cum}} = c_c(t)D_c^{-b_c},\tag{5.1}$$

where $c_c(t)$ and b_c are parameters characterizing the crater size-frequency distribution. While the distribution can be globally approximated by a simple power-law form such as Eq. (5.1), it is slightly different from the exact power-law distribution. Note that N_{cum} denotes the cumulative number of craters per unit area. Thus, the dimension of N_{cum} is $[N_{\text{cum}}] = \mathsf{L}^{-2}$. In other words, $c_c(t)$ has a dimension of L^{b_c-2} , i.e., it becomes dimensionless only when $b_c = 2$. To analyze the population of craters, logarithmic binning is usually adopted because N_{cum} approximately obeys the power-law form. The number of craters whose diameters are in the range from D_s to $\sqrt{2}D_s$ is

$$N(D_s, \sqrt{2}D_s) = N_{\text{cum}}(D_s) - N_{\text{cum}}(\sqrt{2}D_s) = c_c(t) \left(1 - 2^{-b_c/2}\right) D_s^{-b_c}.$$
 (5.2)

In this form, b_c represents the *local* power-law exponent in the range of $(D_s, \sqrt{2}D_s)$. Local properties of the crater population statistics can be quantified by a so-called R plot, which is defined by

$$\mathsf{R} = \frac{\langle D_c \rangle_{\mathsf{geo}}^3}{D_l - D_s} N(D_s, D_l),\tag{5.3}$$

where $\langle D_c \rangle_{\rm geo}$ is the geometric mean of the crater's diameter, and D_l indicates the upper limit (maximum value) of the crater's diameter. Note that R is a dimensionless value. By substituting $D_l = \sqrt{2}D_s$ and $\langle D_c \rangle_{\rm geo} = 2^{1/4}D_s$, R in the range of $(D_s, \sqrt{2}D_s)$ is written as $\mathsf{R}(D_s) = [2^{3/4}/(\sqrt{2}-1)]D_s^2N(D_s, \sqrt{2}D_s)$. The value of R represents the degree of the surface coverage by craters. The fraction of the surface covered with craters in the diameter range $(D_s, \sqrt{2}D_s)$ can be approximately computed by $f_c(D_s) \simeq (\pi/4)\sqrt{2}D_s^2N(D_s, \sqrt{2}D_s)$. Because $N(D_s, \sqrt{2}D_s)$ is the number of craters per unit area, $f_c(D_s)$ is dimensionless and becomes unity when the surface is completely covered with craters. By comparing the coefficients, $\mathsf{R}(D_s)$ and $f_c(D_s)$ are related as

$$\mathsf{R}(D_s) \simeq 3.66 f_c(D_s). \tag{5.4}$$

Using Eq. (5.2), $R(D_s)$ becomes

$$\mathsf{R}(D_s) = \frac{2^{3/4} \left(1 - 2^{-b_c/2}\right)}{\sqrt{2} - 1} c_c(t) D_s^{2 - b_c}. \tag{5.5}$$

Therefore, if $b_c = 2$ is always satisfied, $R(D_s)$ becomes constant irrespective of D_s . The constant value is determined by the surface age t through $c_c(t)$. The concrete estimation method of the surface age is briefly discussed later.

If the planetary surface is exposed to meteor bombardments for a sufficiently long time, N_{cum} distribution may reach a geometric saturation. The saturated cumulative distribution $N_{\text{cum,sat}}$ is written as [11, 14]

$$N_{\text{cum,sat}} = c_{\text{sat}} D_c^{-2}, \tag{5.6}$$

with a dimensionless parameter $c_{\rm sat}=1.54$. Note that $N_{\rm cum,sat}$ is a function of the crater diameter D_c . This saturation is geometrically related to the two-dimensional random close packing (RCP) problem. Because the crater shape is almost circular, it is difficult to completely fill the surface with craters (circles). According to hard disc packing, the densest packing fraction achieved in a bidisperse system is 0.84 ± 0.01 [15], which suggests that the value of f_c at geometric saturation should be 0.84. The coverage factor f_c at geometric saturation is analytically calculated to be²

$$f_c = \int_{\sqrt{2}D_s}^{D_s} \frac{\pi}{4} D_c^2 \frac{dN_{\text{cum,sat}}}{dD_c} dD_c = \left[-\frac{\pi}{2} c_{\text{sat}} \ln D_c \right]_{\sqrt{2}D_s}^{D_s} = \frac{\pi \ln 2}{4} c_{\text{sat}}.$$
 (5.7)

Inputting $c_{\rm sat}=1.54$ into Eq. (5.7), we obtain the two-dimensional RCP value, $f_c=0.84$. The ideal geometric saturation coincides with the RCP of the craters circles. If we assume that all the craters have the same diameter, the maximum value of f_c is $\sqrt{3}\pi/6 \simeq 0.9069$; then, the corresponding $c_{\rm sat}$ is 1.67. However, the actual crater's cumulative distribution reaches equilibrium at a few % of the ideal $c_{\rm sat}$. That is, the actual equilibrium is attained much faster than the geometric saturation limit. At equilibrium, another relation,

$$N_{\text{cum,eq}} = c_{\text{eq}} D_c^{-2}, \tag{5.8}$$

is satisfied. According to the detailed numerical simulation, the dimensionless value of $c_{\rm eq}$ depends on the distribution of the impactor population [16]. After the equilibration, the cumulative number of craters no longer varies, and reaches a type of steady state. In this equilibrium state, the rate of newly added craters is in balance with the rate of erasure of craters. If the cratered area is resurfaced for some reason such as volcanic lava flow, that area is reset in terms of the cratered age.

The effect of equilibration can be detected from the crater counting data by the deflection of $N_{\text{cum}}(D_c)$. The ideal crater production is approximated by Eq. (5.1); however, the equilibrated distribution obeys Eq. (5.8). By equating these relations, the equilibrium crater diameter $D_{\text{eq}}(t)$ is calculated to be

$$D_{\rm eq}(t) = \left(\frac{c_c(t)}{c_{\rm eq}}\right)^{\frac{1}{b_c - 2}}.$$
 (5.9)

²More precisely, the logarithmic binning with a constant rate *B* yields $d \log_B D_c = dD_c/D_c \ln B$. However, this factor is canceled out in Eq. (5.7).

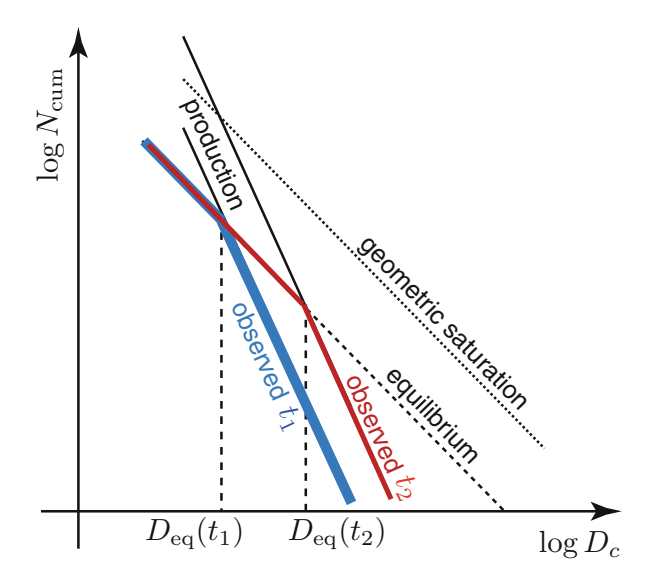


Fig. 5.7 Cumulative distribution N_{cum} of craters equal to or larger than D_c . The crater density equilibrium is attained much below the ideal geometric saturation level. At a certain time t_1 , the observed N_{cum} shows a deflection at $D_{\text{eq}}(t_1)$. This deflection point grows as time passes. Its growth manner follows Eq. (5.9). Because the case of $b_c > 2$ is considered here, the equilibration affects the number of small craters; and thus, t_2 is greater than t_1 in this plot

If we assume the constant bombardment rate $c_c(t) \propto t$, the equilibrium diameter grows as $D_{\rm eq}(t) \propto t^{1/(b_c-2)}$. The qualitative behavior of $D_{\rm eq}(t)$ varies depending on the b_c value: $b_c > 2$ or $b_c < 2$. When $b_c > 2$, the equilibration affects the number of small craters. As observed in Fig. 5.7, the distribution by real production can be directly observed only in the large crater regime, $D_c > D_{\rm eq}(t)$. Because $D_{\rm eq}(t)$ is an increasing function of time t, the equilibrated regime grows as time increases. If $b_c = 2$, the entire distribution simultaneously reaches equilibrium. Thus, no deflection is observed under this particular condition, $b_c = 2$. When b_c is less than 2, the situation is slightly complicated. The qualitative behavior becomes opposite to the case of $b_c > 2$. $D_{\rm eq}(t)$ is a decreasing function of time in this regime, and the larger craters are affected by the equilibrium. However, the large crater formation events rarely occur. Additionally, a very large crater formation causes the obliteration of many small craters. Thus, equilibrium evaluation becomes very difficult because of the large uncertainty in the $b_c < 2$ regime.

An example of the local crater counting on the Moon is shown in Fig. 5.8 [17]. In Fig. 5.8, cumulative size-frequency distributions of four different regions are indicated by the data points. While all of these data exhibit a similar trend, the crater density $c_c(t)$ depends on the region of interest. The offset due to the variation of $c_c(t)$ originates from the difference in the age at each counted region. Evidently, the younger region should be covered with less craters. Thus, $c_c(t)$ becomes small in the young region, which implies that the number density $c_c(t)$ can be a chronological

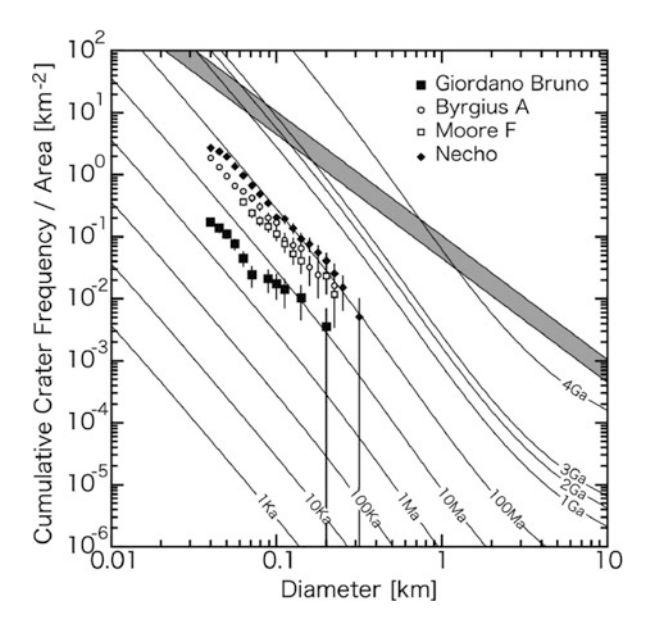


Fig. 5.8 Cumulative size-frequency distribution of craters counted on the continuous ejecta of four young craters: Giordano Bruno, Byrgius, Moore, and Necho. The isochrons are calculated from Neukum's lunar standard size-frequency distribution and cratering chronology curve [18]. The *gray zone* indicates an equilibrium level that corresponds to 3–7% of the geometric saturation (Reproduced from Ref. [17] by permission of John Wiley & Sons Ltd.)

indicator. Therefore, c_c is denoted by a function of time. Note that this "craters clock" is reset when the region is completely resurfaced by volcanic lava flood, and so on. We can estimate the relative age of the focused region by this offset, namely, by the number density of craters in the region. This method can be used as long as the number density of craters is not equilibrated. To determine the absolute age, calibrations by the actual samples, for which the absolute age is measurable, are required.

From systematic crater counting studies, the standard size-frequency distribution for lunar craters was obtained [18]. To obtain the standard distribution, numerous local distribution curves should be normalized to the $c_c(t)$ value. If the normalized curves are collapsed to a unified distribution curve, the distribution will be the standard distribution. Isochrons in Fig. 5.8 are computed from the form of the standard distribution and the calibrations with the absolute age. A key assumption to obtain the standard distribution curve is that the distribution form is independent of the era. The steady (time-independent) size-frequency distribution form for the craters production is assumed. The time dependence appears only in $c_c(t)$. Therefore, the local surface age can be estimated from the crater counting data simply from the number density of craters $c_c(t)$.

At present, the absolute age calibration has been possible only for the Moon. In the calibration process, the collision rate as a function of time can be obtained for the Moon by comparing the craters number density with the absolute age. For Mars or other astronomical objects, the crater counting isochrons must be modeled from the lunar data or other modeling. For instance, Ref. [19] addresses the crater counting chronology for Mars. The frequency of impact events can be estimated from the population of asteroids by simply assuming the Poisson process. To estimate the crater production rate, the conversion from the impactor's size-frequency distribution to the resultant crater's size-frequency distribution is necessary. The scaling and dimensional analysis provide a powerful tool for this purpose. Therefore, the crater scaling based on the Π -groups method is introduced later in Sect. 5.5.

The crater chronology is now widely used to discuss the phenomena that occurred on the planetary surfaces. The population of craters and evaluated collision history are valuable information to uncover the history of the solar system. In this book, however, we will focus mainly on the impact mechanics and crater morphology rather than the population and statistics. Thus, only the basic idea of crater chronology has been briefly reviewed here. See, e.g., Ref. [20] for more details on crater chronology.

5.3 Mechanics of Planetary Impact Cratering

Next, we continue the discussion of the hypervelocity impact cratering mechanics which is relevant to the planetary cratering. Planetary (hypervelocity) impact cratering mechanics can be classified into five stages: (i) contact and compression, (ii) excavation, (iii) modification, (iv) ejecta deposition, and (v) degradation. Because the hypervelocity impact cratering occurring on a planetary surface is a sequential event, these stages are not clearly separated and instead overlap and interact with each other. However, the cratering is too complex to be analyzed by a compact single process. In general, the event is divided into these stages for brevity. The phenomena that occur in each stage are briefly introduced in this section. The standard scenario of hypervelocity impact cratering introduced in this section is mainly based on Refs. [1, 11].

5.3.1 Contact and Compression

The first stage of impact cratering is contact and compression. When a hypervelocity impactor strikes a surface of a target planet, shock waves are induced both in the target and impactor. Using a set of governing equations called Hugoniot equations and some approximations, one can estimate the pressure and temperature (internal energy) attained by the impact. The duration of shock loading can also be estimated; this duration corresponds to a characteristic timescale of the contact and compression stage. Hugoniot equations correspond to the conservation laws of mass, momentum, and energy between the shocked and unshocked states.

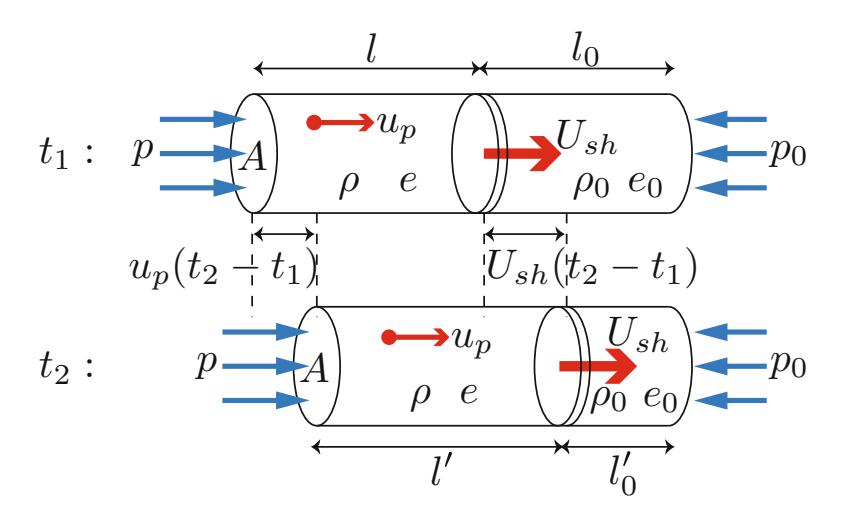


Fig. 5.9 Definitions of parameters in the Hugoniot equations. Simple one-dimensional shock wave propagation and material compression (planar shock approximation) during $t_2 - t_1$ are modeled. By considering the mass, momentum, and energy conservation laws, the Hugoniot equations can be derived as Eqs. (5.12), (5.13), and (5.20)

Let us derive the Hugoniot equations. The considered setup and notations of parameters are shown in Fig. 5.9. Let p_0 , ρ_0 , and e_0 be the pressure, density, and internal energy per unit mass in an unshocked state. These values suddenly increase to p, ρ , and e because of the shock wave propagation of the velocity $U_{\rm sh}$. The actual motion's velocity of the shocked material (particle velocity in the shocked state) is defined as u_p . Here we consider the planar wave approximation, i.e., one-dimensional propagation of the shock wave through a unit of area A is considered. At time $t = t_1$, the length of the unshocked and shocked states are denoted as l_0 and l, respectively. Because of the shock wave propagation, these lengths become l'_0 and l' at $t = t_2$. From the geometrical conditions, the lengths should satisfy

$$l_0' - l_0 = -U_{\rm sh}(t_2 - t_1), (5.10)$$

$$l' - l = (U_{\rm sh} - u_p)(t_2 - t_1). \tag{5.11}$$

In this setup, the mass conservation law is written as $A\left[\rho(l'-l) = -\rho_0(l'_0-l_0)\right]$. Using Eqs. (5.10) and (5.11), the first Hugoniot equation is obtained from the mass conservation law as

$$\rho(U_{\rm sh} - u_p) = \rho_0 U_{\rm sh}. \tag{5.12}$$

The momentum transfer is written as $A\left[\rho u_p(l'-l) = (p-p_0)(t_2-t_1)\right]$. Using Eq. (5.11), this relation is rewritten as $\rho u_p(U_{\rm sh}-u_p) = p-p_0$. Then, substituting Eq. (5.12) to this relation, one can obtain the second Hugoniot equation as follows:

$$\rho_0 u_p U_{\rm sh} = p - p_0. \tag{5.13}$$

Equations (5.12) and (5.13) can be transformed into

$$U_{\rm sh} = \frac{1}{\rho_0} \sqrt{(p - p_0) \left(\frac{\rho \rho_0}{(\rho - \rho_0)}\right)},$$
 (5.14)

$$u_p = \sqrt{(p - p_0) \left(\frac{1}{\rho_0} - \frac{1}{\rho}\right)}.$$
 (5.15)

The energy conservation is written as $E_{\text{tot}}(t_2) - E_{\text{tot}}(t_1) = pAu_p(t_2 - t_1)$, where E_{tot} is the total energy (not per unit mass) of the system. The right-hand side corresponds to the work performed during $t_2 - t_1$. The total energy is computed by the sum of the internal energy and the kinetic energy as

$$E_{\text{tot}}(t_1) = \rho_0 l_0 e_0 A + \rho l e A + \frac{1}{2} \rho l u_p^2 A, \qquad (5.16)$$

$$E_{\text{tot}}(t_2) = \rho_0 l_0' e_0 A + \rho l' e A + \frac{1}{2} \rho l' u_p^2 A.$$
 (5.17)

Using Eqs. (5.16), (5.17), (5.10), and (5.11), the energy conservation law is expressed as

$$\rho e(U_{\rm sh} - u_p) + \frac{1}{2}\rho u_p^2(U_{\rm sh} - u_p) - \rho_0 e_0 U_{\rm sh} = p u_p. \tag{5.18}$$

Applying Eq. (5.12), we obtain a relation

$$e - e_0 = \frac{pu_p}{\rho_0 U_{\rm sh}} - \frac{1}{2} u_p^2. \tag{5.19}$$

Substituting Eqs. (5.14) and (5.15) into Eq. (5.19), we finally obtain the third Hugoniot equation

$$e - e_0 = \frac{1}{2}(p + p_0)\left(\frac{1}{\rho_0} - \frac{1}{\rho}\right).$$
 (5.20)

These three equations (Eqs. (5.12), (5.13), and (5.20)) are useful for evaluating the hypervelocity impact phenomena.

However, these equations are not sufficient to derive all the required quantities. Generally, some additional equations or approximations are employed to estimate the quantities. For instance, $U_{\rm sh}$ is frequently approximated by

$$U_{\rm sh} = C_s + S_p u_p, \tag{5.21}$$

where C_s and S_p are the sound speed and a dimensionless coefficient, respectively. These values are material-dependent and can be determined by calibration experiments. In this sense, the relation (Eq. (5.21)) is an empirical approximation. In contrast, the Hugoniot equations are based on the conservation laws. Conservation laws are the very fundamental bases in physics. Note that, however, the Hugoniot equations do not include the thermodynamic principle.

Using these equations, the contact and compression stage are partially understood [1]. Both the impactor and target have a set of corresponding quantities $(p, \rho, e, u_p, U_{\rm sh})$. Because the values in the unshocked state are measurable or guessable, only the shocked state quantities are regarded as unknown variables. Thus, there are 10 unknown variables in the system. However, there are only 4 governing equations (Eqs. (5.12), (5.13), (5.20), and (5.21)) for both the impactor and the target, i.e., there are 8 equations in total. Therefore, we need 2 additional constraints to solve the problem. Usually, the relations

$$p_p = p_t \tag{5.22}$$

and

$$v_0 = u_{pp} + u_{pt} (5.23)$$

are used as additional constraints for the shocked states (impedance matching). The former equation (Eq. (5.22)) indicates the pressure equivalence between the impactor (p_p) and the target (p_t) . The latter equation (Eq. (5.23)) indicates that the impact velocity v_0 is partitioned into the particle velocity of the impactor u_{pp} and that of the target u_{pt} . We assume that v_0 is measurable. Using these relations, relevant quantities of the shocked state can be computed. In addition, one can estimate the attained temperature caused by the impact using thermodynamic relations [1, 11, 21]. The attained pressure and temperature are fundamental and necessary information to discuss the phenomena that occur because of the impact.

The contact and compression stage generated by the shock wave propagation in the impactor lasts until the impactor is unloaded. When the impact-induced compressive shock wave reaches the rear surface of the impactor's body, it is reflected back as a rarefaction wave. The impactor is unloaded by the propagation of the rarefaction wave. Thus, the duration of the contact and compression stage is estimated as

$$t_{cc} = \frac{D_i}{U_{\rm sh}} + \frac{\rho_0}{\rho} \frac{D_i}{C_r},\tag{5.24}$$

where D_i and C_r are the impactor's diameter and the rarefaction wave velocity, respectively. The rarefaction wave speed C_r is approximated by $C_r = \sqrt{[K_0 + np_p]/\rho}$ [1], where K_0 and n are the bulk modulus and material-dependent constant, respectively. The first term in Eq. (5.24) corresponds to the contact timescale, and the second term originates from the rarefaction wave propagation time.

In the near-surface zone, the reflected rarefaction wave interferes with the direct compressive shock wave. This effect may produce a spall zone, as observed in the lunar micro crater (Fig. 5.6a).

5.3.2 Excavation

After the initial contact and compression stage, the shock wave can still propagate and attenuates in the target. During this stage, the crater cavity is dug and the ejecta is released. As long as the shock wave is the principal effect for excavation, the diameter of resultant crater is considerably greater than that of the impactor, which contrasts with the low-velocity loose granular impact case, where the crater diameter is comparable to that of the impactor [22, 23] because the ejecta is driven by momentum transfer rather than the shock wave.

In this excavation stage, the shock pressure plays the most important role in the hypervelocity planetary impact cratering. The shock pressure attenuation is empirically written as

$$p \propto r_p^{-\alpha_p},\tag{5.25}$$

where r_p and α_p are the distance from the impact point and the characteristic exponent (1 $\leq \alpha_p \leq$ 3), respectively. The elastic limit corresponds to³ $\alpha_p =$ 1 (geometric attenuation), and the high pressure (large released energy) limit corresponds to⁴ $\alpha_p =$ 3.

During the excavation stage, seismicity is also induced. The seismic energy $E_{\rm seis}$ caused by the impact of the kinetic energy $E_{\rm kei}$ is approximately written as $E_{\rm seis} = \eta_{\rm seis} E_{\rm kei}$ [24], where $\eta_{\rm seis}$ is the impact seismic efficiency factor by which $E_{\rm kei}$ is ultimately converted into the seismic vibration energy $E_{\rm seis}$. The moment magnitude M_m and $E_{\rm seis}$ are related as $\log_{10} E_{\rm seis} = 4.8 + 1.5 M_m$ [25]. Combining these equations and assuming a typical value $\eta_{\rm seis} \simeq 10^{-4}$, the seismic moment magnitude induced by the impact can be estimated to be $M_m = 0.67 \log_{10} E_{\rm kei} - 5.87$.

Excavation flow is caused by the propagation of shock waves in the target and results in ejecta splashing when the flow reaches the surface of the target and its energy is sufficiently large for the departure. Note that this ejection mechanism is different from the spallation discussed previously in this section. As already discussed, the excavation flow by hypervelocity impact is not driven by the impactor's momentum in contrast with the low-velocity loose granular impact. The pressure

³The spherical wave equation is written as $\partial^2(r_p p)/\partial t^2 = (1/C_s^2)(\partial^2(r_p p)/\partial r_p^2)$. Thus, the traveling wave solution is obtained as $p \propto (1/r_p)[p(r_p - C_s t) + p(r_p + C_s t)]$. More intuitively, the wave energy on the spherical surface $(4\pi r_p^2)$ is constant, and the wave amplitude is the square root of the energy. Thus, the distance attenuation of the spherical wave is proportional to $1/r_p$.

⁴The released energy is simply distributed to the volume r_p^3 . In this case, the pressure (stress) should be regarded as the energy per unit volume (Eq. (2.129)).

gradient drives the excavation flow. Trajectories of the excavation flow have been studied mainly by kinematic methods. Assuming that the excavation flow speed u_r at r_p satisfies $u_r \propto r_p^{-Z}$, the geometry of the excavation flow can be computed analytically for an incompressible target [26]. According to this so-called Z-model, the most realistic 45° ejection angle [27–29] is explained by Z=3. The isotropic radial velocity field can be expressed by Z=2, which is a type of inverse-square law. The Z value actually depends on the phase of crater growth [30]. Moreover, the granular low-velocity impact produces 56° ejecta splashing (Sect. 6.2.2). The ejected debris forming a radial sheet-like structure is called the ejecta curtain. In the excavation stage, the transient crater depth and diameter grow as $\propto t^{0.4}$ [31].

5.3.3 Ejecta Deposition

Most of the portion of ejecta created by the released excavation flow finally sediments around the crater. A part of ejected debris whose velocity exceeds the escape velocity does not return back onto the surface of the target body but moves away from the target body. Such debris is a possible source of meteoroids. The ejecta deposition process leaves a structure called the ejecta blanket. The thickness of the ejecta blanket is empirically known to be inversely proportional to the cube of the horizontal distance from the center of the crater r, e.g., the ejecta thickness $z_{\rm eje}$ of lunar craters can be approximately modeled by the expression [32]

$$z_{\rm eje} \propto D_c^{0.74} \left(\frac{D_c}{r}\right)^{3.0}.\tag{5.26}$$

This r^{-3} profile can be understood by the volume conservation between the cavity and ejecta rim (Eq. (6.4) in Sect. 6.1.1).

The ejecta deposition process affects the surface landform around the crater. Sufficiently large or fast debris makes secondary craters when it impacts back on the target surface (Fig. 5.10a). No systematic algorithm is available to recognize the secondary craters while they often appear as clusters, streams, or chains, as observed in Fig. 5.10a. Their shape becomes peculiar if they are created far from the original crater. The structure of secondary craters might be related to the inhomogeneity of the ejecta curtain. If the ejecta include liquid content, a petal-like ejecta blanket (a rampart crater structure, Fig. 5.5) could be produced, as discussed in Sect. 5.1. The rampart crater has an irregular but somehow isotropic shape. An anisotropic ejecta blanket can also be observed as shown in Fig. 5.10b (asymmetric crater). The asymmetry of the crater and its ejecta flow is related to the angle of the oblique impact. When θ_{imp} is below 30°, asymmetric ejecta deposition can be observed; a wedge structure is formed in the up-range direction (Fig. 5.10b). At very low angle impact (θ_{imp} < 10°), even butterfly-like ejecta with an elliptic crater shape can be observed. As discussed before, the ray structure can be observed in a certain class of craters (Fig. 5.4). The ray crater is most likely formed during the ejecta

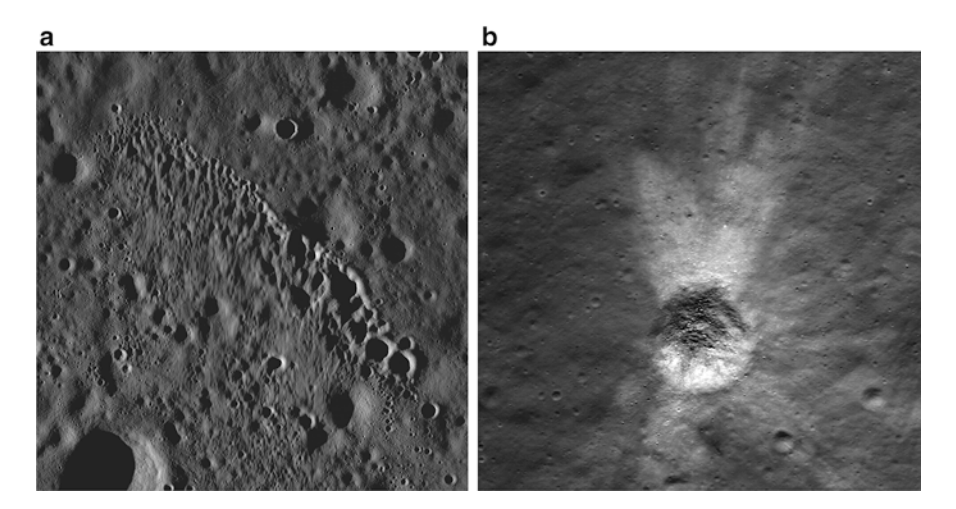


Fig. 5.10 (a) Example picture of a chain of secondary craters on the Moon taken by Lunar Reconnaissance Orbiter. The length of this chain is approximately 4.5 km and the largest crater is 340 m in diameter. The secondary craters can be recognized by this form of clustering of craters (Credit: NASA). (b) An example of an asymmetric crater on the Moon taken by Lunar Reconnaissance Orbiter. The diameter of this crater is approximately 140 m (Credit: NASA)

deposition stage. All these peculiar ejecta blanket shapes must be related to ejecta deposition dynamics. However, the understanding of the details of ejecta deposition dynamics is limited. The instability of and associated pattern formation for ejecta flow deposition processes are crucial subjects to be investigated to advance the understanding of various ejecta blanket shapes.

5.3.4 Modification

Indeed, the crater's cavity formed during the excavation stage is transient. The structure of the crater is significantly modified after the excavation. This modification is mainly driven by the gravitational force. For example, landslides could occur at the side wall of the crater. The crater shape would be modified until it becomes stable. Because of this shape relaxation, a sedimentary layer called a breccia lens is formed in the original crater's cavity (Fig. 5.11). Before the modification, the depth of the crater is considered to be approximately 1/2.7 of the crater diameter [1]. The ratio varies approaching 1/5 by modification toward the simple crater. For complex craters, more complex modifications must be considered, e.g., phase transitions could be a crucial process. The terrace wall structure is also formed by the gravitational shape relaxation. The transient crater can expand by the terrace formation. As mentioned before, some complex craters have central peaks, and others have peak-rings or central pits. The specific origins for these structures have not yet been well understood. To discuss the viscosity-induced cavity collapse for

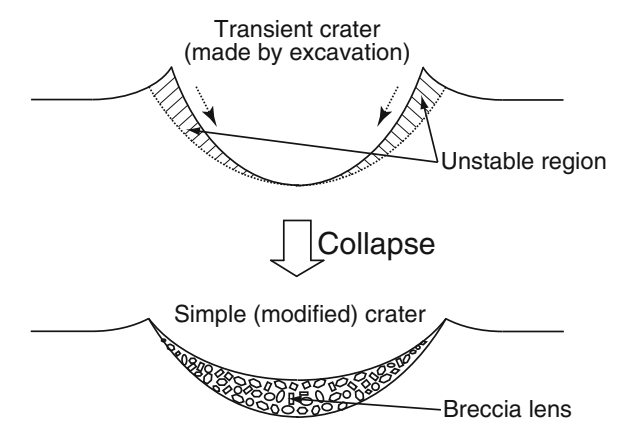


Fig. 5.11 Modification process of a simple crater. First, the transient cavity is formed by the excavation process. The crater side wall is unstable and impact-induced acoustic fluidization or another trigger causes its collapse. Finally, the modified crater shape is obtained with a breccia lens. Complex craters must also be affected by more complex modifications such as the phase transition and terrace formation

the origin of the central peak structure, the target must be well-fluidized to achieve a sufficiently low (effective) viscosity.⁵ Furthermore, a geological study of the impact crater on the Earth revealed the clear central uplift even in a relatively deep region beneath the crater [33], which indicates that the central peak originates from uplift rather than cavity collapse. Perhaps the central peak can be produced by an elastic rebound [34]. Discussion regarding the origin of the central peak structure is still controversial.

In large-scale cratering, the fluidization effect must be considered. As a result of large-scale impact, numerous impact melts and fragments would be produced. Furthermore, vibration would be induced by the impact. Thus, the crater site will consist of a mixture of grains and melt under vibration. Then, the crater site must be fluidized as discussed in Sect. 3.9. This effect is called *acoustic fluidization* (see the next section for the detail) [1, 11, 35, 36]. By means of dimensional analysis, two dimensionless numbers, $\rho_t g D_h/Y_c$ and $\rho_t g^{1/2} D_i^{3/2}/\eta$, were used to classify the impact cratering using Bingham model rheology [35]. The former represents the ratio of the hydrostatic pressure and yield stress. A similar form will be discussed later in Eq. (5.44). The latter corresponds to the balance between gravity and viscosity (see Eq. (4.31)). These numbers represent the dimensionless forms of two effects in the Bingham model: strength and viscosity. However, it is unclear whether the fluidized regolith behaves like a Bingham model fluid. A detailed rheological study of acoustically fluidized regolith layer is a necessary step to clarify the possible effect of the acoustic fluidization. Table-top granular experiments have

⁵For a viscous target, the central jet formation occurs when its viscosity is less than $\pi^{3/2} \rho_c g^{1/2} D_c^{3/2}$ [1].

revealed that the granular behavior is considerably affected by the vibration even if its amplitude is very small (Sect. 4.2.4). However, the similarity between vibrated granular matter and acoustic fluidization of regolith remains qualitative. Moreover, the complex rheological behavior of fluidized grains might also be responsible for the rampart crater formation. The experimental system should be designed with the concept of similarity modeling (Sect. 2.8) to obtain further relevant quantitative relations among them, which is a challenging future problem.

As already discussed in Sect. 3.6.3, the frictional rheology of the granular flow is partly similar to the Bingham model. However, much more detailed and quantitative assessments of this problem are necessary to draw conclusions concerning the mechanics in the crater modification stage. In the next chapter, some table-top experiments of soft impact will be introduced to discuss possible relations to various craters.

5.3.5 Degradation

Similar to all other constructions, craters cannot maintain their shape forever. After its creation, a crater must be gradually degraded by some effects, such as neighbor impacts, volcanism, and erosion. If a very large impact event occurs in the vicinity of already existing craters, the craters might be completely obliterated. At least, the crater must be degraded by ejecta, acoustic fluidization, and melt flow caused by the impact. Cosmic-ray exposure can also degrade the appearance of craters. Sharp structures such as rays and rims have been degraded step by step since a crater was formed, which suggests that we might be able to speculate how old the crater is from the degree of degradation.

It is difficult to find impact craters on the Earth. Evidently, weathering and erosion by air and water eliminates craters on the Earth much faster than on other airless (and waterless) planets. The rate of degradation strongly depends on various conditions and the surrounding environment. Thus, the environmental conditions might also be estimated from the degradation. However, actual physical properties such as surface viscosity and strength are required to quantify the degree of degradation. The obliteration of craters due to the impact-induced acoustic fluidization and global seismic shaking are examples of quantitatively assessable degradation. Thus, the effects of the local acoustic fluidization and global seismic shaking are discussed in the next section.

5.4 Acoustic Fluidization and Seismic Shaking Induced by Impact

Astronomical-scale impact induces not only cratering but also seismicity. As discussed in the previous section, some portion of the impact energy $\eta_{\text{seis}}E_{\text{kei}}$ is transmitted to the seismic energy. Although direct measurements of seismic

activities are limited only to the Earth or the Moon,⁶ we can imagine that seismicity plays an important role particularly when the target object is small. For a very small asteroid, the gravitational acceleration can be extremely small. For instance, the surface gravitational acceleration on the asteroid Itokawa is as low as $g_I \simeq 10^{-4}$ m/s² [37, 38]. In such a microgravity environment, global seismic shaking as well as local acoustic fluidization might be induced by the impact. In fact, the effect of global seismic shaking was estimated for Eros [39, 40] and Itokawa [41] by compiling the results of numerical simulations, observations, and experiments into a unified model. According to the model, impact craters are erased through regolith migrations induced by impacts. Itokawa's impact craters are very indistinct most likely because of this seismic erasure effect [6].

5.4.1 Acoustic Fluidization

The first topic discussed in this subsection is the *local* acoustic fluidization due to the rarefaction by the acoustic wave. Dry rock debris might be fluidized by strong acoustic waves. In general, debris can be agitated by acoustic waves if the rarefaction effect is sufficiently large to disable the friction support. This effect is called acoustic fluidization [1, 42]. Let ρ and μ_f be the density and static friction coefficient of a homogeneous rock debris (granular) layer. At depth h, the hydrostatic pressure $p = \rho gh$ works as an overburden. According to the Coulomb failure criterion (Eq. (3.47)), the static granular layer is stable as long as the shear stress σ_s satisfies the criterion

$$\sigma_s \le (p - S_r)\mu_f,\tag{5.27}$$

where S_r is the rarefaction peak by the acoustic wave. When S_r is greater than the critical value, $S_c = p - \sigma_s/\mu_f$, a slip (flow) can be induced.

First, the strain γ caused by the mean shear stress $\tilde{\sigma}_s$ that acts on the bulk layer is estimated. The elastic constitutive law (Eq. (2.18)) is adopted to compute the strain. In addition, a simple isothermal relation between the elastic modulus G and the bulk sound speed C_s is assumed $C_s = \sqrt{G/\rho}$. Then, the strain is computed as $\gamma = \tilde{\sigma}_s/\rho C_s^2$. In general, the acoustic field does not result in a steady rarefaction stress but one that fluctuates in time. The fluidization is induced only when S_r exceeds S_c . Therefore, by denoting the probability of $S_r \geq S_c$ as $P(S_r \geq S_c)$, the net strain $\gamma_{\rm net}$ is written as

⁶Although the seismometer mounted on the Viking landers tried to detect the seismic events on Mars, the data were too noisy.

⁷This criterion is similar to that in the liquefaction case. In the liquefaction case, S_r corresponds to the interstitial fluid pressure.

$$\gamma_{\text{net}} = \frac{\tilde{\sigma}_s}{\rho C_s^2} P(S_r \ge S_c). \tag{5.28}$$

The value of $\tilde{\sigma}_s$ is somewhat larger than the applied stress σ_s because the effective volume to support the energy density by the applied stress⁸ is reduced by the rarefaction. On average, the fraction of available volume is estimated to be $(1 - P(S_r \ge S_c))$. Therefore, the mean stress can be approximated as $\tilde{\sigma}_s \simeq \sigma_s/(1-P(S_r \ge S_c))$. Substituting this relation to Eq. (5.28), we obtain

$$\gamma_{\text{net}} = \frac{\sigma_s}{\rho C_s^2} \left[\frac{P(S_r \ge S_c)}{1 - P(S_r \ge S_c)} \right]. \tag{5.29}$$

The strain rate and corresponding viscosity can also be approximately estimated. To evaluate the net strain rate $\dot{\gamma}_{\rm net}$, a characteristic timescale is introduced by the wavelength λ divided by C_s , λ/C_s . Then, the net strain rate is computed as

$$\dot{\gamma}_{\text{net}} = \frac{\gamma_{\text{net}}}{\lambda/C_s} = \frac{\sigma_s}{\rho \lambda C_s} \left[\frac{P(S_r \ge S_c)}{1 - P(S_r \ge S_c)} \right]. \tag{5.30}$$

Using the viscous constitutive relation (Eq. (2.17)), the effective viscosity η can be calculated as

$$\eta = \rho \lambda C_s \left[\frac{1 - P(S_r \ge S_c)}{P(S_r \ge S_c)} \right]. \tag{5.31}$$

Equation (5.31) is derived only for a single wavelength λ . In general, the acoustic field could have a broad range of wavelengths. For a more precise evaluation, therefore, all the relevant wavelengths and their couplings must be considered.

Furthermore, the specific form of $P(S_r \ge S_c)$ is unclear. A plausible approximation is the Gaussian probability density, $p(S_r)dS_r = \exp(-S_r^2/2\Sigma_s^2)dS_r/\sqrt{2\pi}\Sigma_s$, where Σ_s denotes the standard deviation of the distribution. Then, $P(S_r \ge S_c)$ can be computed as

$$P(S_r \ge S_c) = \int_{S_c}^{\infty} p(S_r) dS_r = \frac{1}{2} \left[1 - \operatorname{erf}\left(\frac{S_c}{\sqrt{2}\Sigma_s}\right) \right].$$
 (5.32)

Here the definition of the error function, Eq. (3.35), was used. For further simplification, the simplest assumption that both S_c and Σ_s are proportional to the overburden pressure $\rho g h$, is employed. Then, the argument of the error function becomes a constant, $S_c / \sqrt{2} \Sigma_s \simeq f_s$, where f_s is some constant. Finally, the viscosity by the acoustic fluidization is approximated as

⁸Note that the stress can be regarded as the energy density (Eq. (2.129)).

$$\eta = \frac{\rho \lambda C_s}{2} \left[\frac{1 + \operatorname{erf}(f_s)}{1 - \operatorname{erf}(f_s)} \right]. \tag{5.33}$$

Although this formulation of the acoustic fluidization is based on many assumptions and parameters, it could be helpful to estimate how dry rock debris move and to speculate the resultant landforms.

5.4.2 Global Seismic Shaking

Next, the basic framework of *global* seismic shaking and the resultant crater erasure are discussed in this subsection. When a small astronomical object is subjected to an impact, its entire body might be shaken by the impact. The maximum acceleration a_{max} of the impact-induced global seismic shaking can be estimated by considering the energy balance. The kinetic energy of the impactor E_{kei} is

$$E_{\text{kei}} = \frac{\pi}{12} \rho_i D_i^3 v_0^2, \tag{5.34}$$

where ρ_i , D_i , and v_0 are the density, diameter, and velocity of the impactor, respectively. In contrast, the vibrational energy induced in the target object E_{vib} can be computed using the maximum acceleration a_{max} and the frequency f:

$$E_{\text{vib}} = \frac{\pi}{12} \rho_t D_t^3 v_{\text{vib}}^2 = \frac{\rho_t D_t^3 a_{\text{max}}^2}{48\pi f^2},$$
 (5.35)

where ρ_t , D_t , and $v_{\rm vib} = a_{\rm max}/2\pi f$ are the target density, diameter, and maximum vibrational speed, respectively. Here the impact seismic efficiency factor $\eta_{\rm seis}$ is used to estimate the vibrational energy $E_{\rm vib}$. Then, the relation $E_{\rm vib} = \eta_{\rm seis} E_{\rm kei}$ yields

$$a_{\text{max}} = 2\pi f v_0 \sqrt{\eta_{\text{seis}} \left(\frac{\rho_i}{\rho_t}\right) \left(\frac{D_i}{D_t}\right)^3}.$$
 (5.36)

This value is the maximum acceleration attained by the impact-induced global seismic shaking. Note that this $a_{\rm max}$ is achieved in the whole body. Thus, this effect is called the global seismic shaking. To compare $a_{\rm max}$ with the surface gravitational acceleration, we use a relation $g = 2\pi \mathcal{G}D_t\rho_t/3$, where $\mathcal{G} = 6.67 \times 10^{-11} \, \mathrm{m}^3/\mathrm{kgs}^2$ is the gravitational constant. Then, the ratio between the vibrational and gravitational accelerations Γ defined by Eq. (3.67) is calculated as

$$\Gamma = \frac{a_{\text{amx}}}{g} = \frac{3fv_0}{\mathcal{G}} \sqrt{\eta_{\text{seis}} \frac{\rho_i}{\rho_i^3} \frac{D_i^3}{D_i^5}}.$$
 (5.37)

In principle, we can estimate the maximum acceleration of the global seismic shaking using this equation. Note that both the impactor and target are assumed to be spheres to obtain the above result. Additionally, the value of $\eta_{\rm seis}$ and the dominant frequency f induced by the impact cannot be determined solely by this form. Actually, $\eta_{\rm seis}$ ranges from 10^{-1} to 10^{-6} depending on the experimental conditions ([40] and references therein). As a typical value for Eros or Itokawa, $\eta_{\rm seis} = 10^{-4}$ or 10^{-6} has been used. For the dominant frequency, Richardson et al. performed numerical simulations of the seismic wave propagating in a heterogeneously fractured object [40]. These researchers found that the dominant frequency is distributed at approximately 5–50 Hz.

The attenuating diffusion of the seismic energy density must be considered to model the realistic seismic shaking. The seismic energy density e_s is defined by the vibrational energy per unit volume⁹ as follows:

$$e_s = \frac{\rho_t a_{\text{max}}^2}{8\pi^2 f^2}. (5.38)$$

In usual continua, a seismic wave propagates as a simple elastic wave; however, the seismicity in astronomical objects might be slightly complex. The direct seismic observation is limited to the Earth and the Moon. To date, other astronomical objects have never been observed directly by seismometers. According to the lunar seismicity, the observed seismic waveforms exhibited spindle-like shapes followed by a long tail, which indicates highly diffusive propagation of the seismic energy density with low dissipation [43]. In general, astronomical objects can be very heterogeneous. Namely, there are many cracks, faults, and boundaries along the course of the wave propagation. Thus, the elastic wave is scattered many times at these boundaries, and the seismic energy density propagates similar to random walks. Then, the propagation of the seismic energy density can be modeled by the diffusion process (see the discussion near Eq. (3.29)). In such a situation, the diffusion coefficient can be roughly estimated by $K_d \simeq C_s \lambda_{\rm mfp}/3$ [40], where C_s is the elastic wave propagation rate (bulk speed of sound), and λ_{mfp} indicates the mean free path of the elastic wave. ¹⁰ That is, λ_{mfp} corresponds to the average mutual distance among inhomogeneous distributed faults and boundaries. Additionally, the dissipation of the propagating seismic energy density should be involved in the model. The attenuating oscillation equation discussed in Sect. 3.4 is helpful for this purpose.

From the aforementioned considerations, the simplest model for astronomical seismicity can be written as

$$\frac{\partial e_s}{\partial t} = K_d \nabla^2 e_s - \frac{2\pi f}{O} e_s, \tag{5.39}$$

⁹Note that this definition is different from the energy density per unit mass used in Sect. 5.3.1.

¹⁰The form of Eq. (3.28) can be obtained by assuming $t_o = \lambda_{\rm mfp}/C_s$. The factor three comes from the isotropic three-dimensionality.

where Q is the seismic quality factor (Eq. (3.20)). In this model, K_d is related to the transport rate of the seismic energy density, and $2\pi f/Q$ represents its dissipation rate. These two factors determine how the target object is shaken by the impact-based energy injection. The second term on the right-hand side of Eq. (5.39) simply introduces the exponential decay of the energy density. By neglecting the first term, we obtain a simple solution, $e_s = e_0 \exp(-2\pi f t/Q)$, where e_0 is the initial seismic energy density. Note that the attenuation factor $\exp(-2\pi f t/Q)$ is dimensionless.

Using this dimensionless attenuation factor and the relation $e_s \propto a_{\rm amx}^2$ (Eq. (5.38)), Eq. (5.37) is improved to the time-dependent form [41]

$$\Gamma(t) = \frac{3fv_0}{\mathcal{G}} \sqrt{\eta_{\text{seis}} \frac{\rho_i}{\rho_t^3} \frac{D_i^3}{D_t^5}} \exp\left(-\frac{\pi f t}{Q}\right). \tag{5.40}$$

The timescale of the diffusive transport for distance D_t can be evaluated as $\tau_{\text{diff}} = D_t^2/\pi^2 K_d$ [40]. This timescale indicates the duration for which the seismic energy density diffuses to the whole body by a half wavelength (see, e.g., n=1 in Eqs. (3.41) and (3.42)). The dissipation during this timescale can be estimated as $2\pi f \tau_{\text{diff}}/Q$. Substituting τ_{diff} into t of Eq. (5.40), the strength of global seismic shaking can be evaluated using this form. It was revealed for Itokawa that $\Gamma(\tau_{\text{diff}}) > 1$ is attained even by a small-scale impact ($D_i = 0.01$ m) under the plausible parameter values condition [41]. If $\Gamma > 1$ is satisfied all over the target object, the global regolith convection might be induced. Although it remains quite uncertain whether the global regolith convection is really possible, the criterion for the onset of granular convection, $\Gamma > 1$ (Sect. 3.9.1), is indeed easily fulfilled on the surface of Itokawa. In either case, surface regolith migration is somehow induced by global seismic shaking.

Although nobody knows the actual values of K_d , Q, and f induced by the impact to asteroids, we must estimate these quantities to model the seismicity caused by the astronomical impact. Continuous efforts have been devoted to determining the values of these parameters. For instance, hypervelocity impacts to a sand layer were experimentally measured [44]; however, the details remain unknown. Richardson et al. combined various types of observational data, experimental results, and numerical simulations to estimate these values for the asteroid Eros [39, 40]. Similar values were also used for Itokawa in Ref. [41]. The values estimated and employed in these studies were $K_d = 0.125-2.0 \,\mathrm{km}^2/\mathrm{s}$, Q = 200-2000, and $f = 5-100 \,\mathrm{Hz}$.

As a next step, the degradation of crater profiles due to global seismic shaking is considered. Because of the global seismic shaking, the crater morphology is gradually degraded. The model of this degradation can also be written using another diffusion equation. Specifically, the surface crater profile $z_{\rm cra}$ is degraded obeying the relation

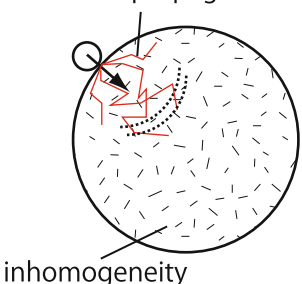
$$\frac{\partial z_{\text{cra}}}{\partial t} = K_r \nabla^2 z_{\text{cra}},\tag{5.41}$$

Fig. 5.12 Two types of diffusion models for impact-induced seismic shaking. (a) The propagation of the seismic energy density is modeled by an attenuating diffusion (Eq. (5.39)) due to the highly inhomogeneous structure of the target object. (b) The crater shape relaxation is described by a different diffusion equation (Eq. (5.41)). Note that the two diffusion coefficients K_d and K_r are basically independent

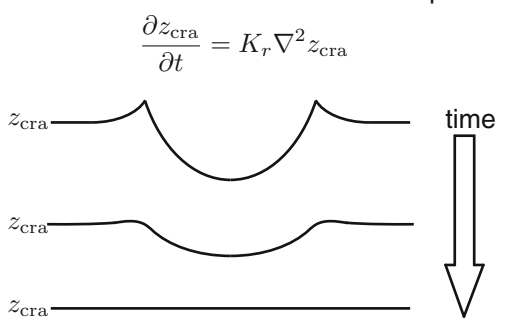
a diffusive propagation of seismicity

$$\frac{\partial e_s}{\partial t} = K_d \nabla^2 e_s - \frac{2\pi f}{Q} e_s$$

scattered propagation



b diffusive relaxation of crater shape



where K_r is a diffusion coefficient that represents the relaxation rate of the crater profile. Note that the physical meaning of K_r in Eq. (5.41) is completely different from K_d in Eq. (5.39). Equation (5.39) describes the diffusive propagation of the seismic energy density. In contrast, Eq. (5.41) is a model of the diffusive relaxation of the crater profile. This difference is schematically drawn in Fig. 5.12. The diffusive relaxation of a bumpy profile is also demonstrated in Fig. 3.4. The diffusive relaxation degrades the high-wavenumber component more efficiently than the low-wavenumber component. Such a wavenumber-dependent (and temporally attenuating) solution for the diffusion equation can be found in Eq. (3.41). By considering the general wavenumber components based on the form of Eq. (3.41), the relaxation of the crater shape in cylindrical coordinates (r, z) can be written as [40]

$$z_{\text{cra}}(r,t) = \sum_{k_n=0}^{\infty} C_{k_n} J_0(k_n r) \exp\left(-K_r k_n^2 t\right),$$
 (5.42)

where k_n , C_{k_n} , and J_0 are the wavenumber, amplitude of the k_n component, and zeroth-order Bessel function of the first kind, respectively. Here the axisymmetric crater shape is assumed to omit the azimuthal dependence.

Although Eq. (5.42) is a temporally continuous equation, the real seismic shaking events (or equivalently the corresponding impact events) occur intermittently. However, in the wavenumber space, the relaxation of the k_n component can be accumulated simply as $\exp(-K_r k_n^2 \sum_i t_i)$ because only the exponential relaxation is considered. ¹² Here t_i is the effective duration of the *i*-th seismic shaking event. The value of $K_r t_i$ was numerically evaluated and depends on the thickness of the regolith layer h_{rego} . Thus, the parameter $K_{si} = K_r t_i / h_{\text{rego}}$ is used to evaluate the relaxation of the crater profile 13 [39, 40, 46]. Note that K_{si} has a dimension of length $[K_{si}] = L$. K_{si} characterizes the sliding distance per seismic shaking event. The value of K_{si} varies depending on the impact conditions such as the impact energy and momentum. Thus, its specific value was numerically assessed in Refs. [39, 40]. By summing up K_{si} with the help of impact frequency models [47, 48], the degree of the crater's shape relaxation can be estimated by $K_{st} = \sum_{i}^{N} K_{si}$, where the number of total impact events N depends on the age of the target object. Then, the structure of the wavenumber k_n is degraded by the factor $\exp(-K_{st}k_n^2h_{rego})$. Finally, erasure of the crater shape is evaluated by putting a criterion of the crater's demise. For instance, $K_{st} \ge 3D_{cra}^2/8h_{rego}$ was used to define the complete relaxation of the crater's shape. This criterion is obtained by assuming $k_n = 4/D_{\rm cra}$ and a factor e^{-6} ($\simeq 1/403$) for the critical degradation (6 $\leq K_{st}(4D_{cra})^2 h_{rego}$) [39, 40]. To obtain a reliable result of the crater chronology, particularly for small astronomical objects such as Eros and Itokawa, crater erasures by global seismic shaking must be considered. In fact, the effect of global seismic shaking is indispensable when explaining the observed crater populations [39, 40, 46]. Furthermore, the number of very small craters on Itokawa has not yet been explained even by the global seismic shaking effect [46]. There might be additional factors to erase very small craters on the surface of small astronomical objects.

As mentioned thus far, the effect of global seismic shaking depends on various parameters such as the impact seismic efficiency factor η_{seis} , seismic quality factor Q, diffusion coefficient of seismic energy density K_d , thickness of the regolith layer h_{rego} , crater relaxation coefficients K_r or K_{st} . We must reduce the uncertainties of these values by utilizing the information from experiments, numerical simulations,

¹¹The axisymmetric diffusion equation for the polar coordinate can be written as $\partial z_{\rm cra}/\partial t = K_r[(\partial^2/\partial r^2) + (1/r)(\partial/\partial r)]z_{\rm cra}$. By assuming the exponential decay form $z_{\rm cra} = \tilde{z}_{\rm cra}(r) \exp(-\lambda_r t)$ and $k_n = \sqrt{\lambda_r/K_r}$, the diffusion equation is cast into a Bessel's differential equation $[(d^2/d\tilde{r}^2) + (1/\tilde{r})(d/d\tilde{r})]\tilde{z}_{\rm cra} + \tilde{z}_{\rm cra} = 0$, where $\tilde{r} = k_n r$.

¹²The exponential function satisfies the simple relation $\exp(a) \times \exp(b) = \exp(a+b)$.

 $^{^{13}}$ The thickness of shear banding is in the order of 10^1 grain diameters in usual granular experiments (e.g., [45]). If this value is applicable to the regolith migration, h_{rego} is determined only by the regolith size regardless of its thickness. However, its applicability is unclear.

or observations. In other words, informative experiments to estimate these values are required to increase the precision of the global seismic shaking effect.

5.5 Scaling for Planetary Impact Cratering

In the previous sections, the fundamentals of morphology and related mechanics including degradation of planetary-scale impact craters have been discussed. Natural planetary craters are extremely complicated to be fully understood. Even the formation process of simple craters is not so simple. Furthermore, our ability, particularly for observation, is very limited. What we can observe is a snapshot of the current state in which all the effects discussed in the previous section are accumulated. How can we discuss such complex phenomena with only very limited information? The dimensional analysis method, which was introduced in Chap. 2, is a powerful tool to approach little known and limited information phenomena. Therefore, the dimensional analysis method has been applied to the study of impact cratering [31, 49–52]. Moreover, the scaling method has been applied not only to the cratering regime but also to fragmentation or catastrophic disruption [53–55]. In this section, the scaling method for impact cratering is discussed in the following.

Specifically, the Π -groups method has been applied to analyze impact cratering. The crater volume, ejecta velocity, ejecta mass, target porosity, and viscosity effect can be estimated by the systematic dimensional analysis based on the Π -groups method. The obtained scaling relations are briefly reviewed in the following subsections.

While these scaling relations were developed for hypervelocity impacts, they are also applicable to low-velocity loose granular impact. Therefore, some of the scaling relations obtained in this section are also compared with the low-velocity loose granular impact experiments. Note that these scaling relations can be applied only to the transient (initial) crater formation (not to a final crater shape) particularly in complex craters.

5.5.1 Crater Volume Scaling

The volume of a crater V_c is one of the most fundamental quantities to characterize the impact crater. We would like to estimate V_c using the dimensional analysis method.

The first thing we should do is to list all the relevant parameters. Here we consider the impactor density ρ_i , its diameter D_i , the target density ρ_t , its strength Y_t , and the gravitational acceleration g. The goal of this analysis is to obtain a scale estimate of the crater volume V_c produced by the impact velocity v_0 under the abovementioned conditions. Because we consider a purely mechanical case, the number of fundamental dimensions is 3 (M, L, T). Thus, we can make 4 = 7 - 3 dimensionless numbers according to the Buckingham Π theorem (Sect. 2.5.2).

Four dimensionless numbers are probably excessive to simply understand the governing scaling relation for the impact cratering. To reduce the number of free parameters, an additional restriction can be assumed. Let us first assume that the kinetic energy of the impactor, $E_{\rm kei} \sim \rho_i D_i^3 v_0^2$, is essential. In other words, suppose that the same $E_{\rm kei}$ results in an identical cratering event. Under such an assumption, ρ_i , D_i , and v_0 can be combined into a single quantity $E_{\rm kei}$ in the dimensional analysis. Another candidate for the essential quantity is the momentum of the impactor, $P_{\rm imp} \sim \rho_i D_i^3 v_0$. Because $E_{\rm kei}$ and $P_{\rm imp}$ have similar forms, a generalized quantity called the *point source measure*, $C_{\rm psm}$, can be introduced as

$$C_{\rm psm} = D_i v_0^{\mu} \rho_i^{\nu}, \tag{5.43}$$

where μ and ν are the characteristic exponents, in which $1/3 \le \mu \le 2/3$ and $\nu = 1/3$. The limit cases $\mu = 1/3$ and $\mu = 2/3$ correspond to $C_{\rm psm} \sim P_{\rm imp}^{1/3}$ and $C_{\rm psm} \sim E_{\rm kei}^{1/3}$, respectively. The exponent μ indicates the importance of the kinetic energy relative to the momentum for the impact cratering. By utilizing $C_{\rm psm}$ as a relevant quantity instead of raw ρ_i , D_i , and v_0 , we can reduce the number of relevant dimensionless numbers. Moreover, it is difficult to separate each effect of ρ_i , D_i , and v_0 , from the actual observation data. This unification of the parameters is also reasonable in this sense.

The concept of point source measure is only valid for the late stage of the cratering. At the impact moment, complex factors such as the geometries of the impactor and target affect the cratering. However, at a location far from the impact point, the cratering events of the identical $C_{\rm psm}$ should look similar because the pressure wave induced by the impact propagates almost hemispherically. Details at the contact moment are negligible at this late stage of the cratering, which is called late stage equivalence [56].

Directly before beginning a systematic Π -groups analysis, here we introduce a dimensionless number R_{gY} , which characterizes the ratio between the gravitational stress and strength:

$$R_{gY} = \frac{\rho_t g D_i}{Y_t}. (5.44)$$

When R_{gY} is considerably greater than unity $(R_{gY} \gg 1)$, the gravitational stress dominates the cratering. This regime is called the *gravity regime*. At the other limit $(R_{gY} \ll 1)$, the strength of the target dominates the cratering mechanics. This regime corresponds to the small crater regime (small D_i), which is called the *strength regime*. The scaling will be considered separately in each regime. If we consider a specific target body, the material-dependent parameters, ρ_t , g, and Y_t , are fixed. Then, R_{gY} is a function only of D_i . In small-scale impacts $(R_{gY} \ll 1)$, the effect of gravity is negligible and the strength dominates the cratering mechanics—the strength regime. As D_i increases, the gravitational effect becomes important. In the large D_i limit, gravity dominates the cratering mechanics—the gravity regime.

Table 5.1 Dimension table	
for the crater volume scaling	

	$[V_c]$	$[C_{\mathrm{psm}}]$	$[\rho_t]$	$[Y_t]$	[g]
М	0	ν	1	1	0
L	3	$1+\mu-3\nu$	-3	-1	1
Т	0	$-\mu$	0	-2	-2

By replacing ρ_i , D_i , and v_0 with $C_{\rm psm}$, the set of relevant quantities becomes (V_c , $C_{\rm psm}$, ρ_t , Y_t , g). Now, the number of relevant dimensionless numbers is 2=5-3. This number fits the current demand when considering two limit cases: the gravity regime and the strength regime. The systematic Π -groups method is applied to this set of relevant quantities. As already learned in Sect. 2.5, a dimension table should be created, and the corresponding simultaneous equations should be computed to obtain dimensionless numbers. Table 5.1 is the dimension table for this problem. Then, Eq. (2.44) for this problem is written as

$$\Pi = V_c^{a_1} C_{\text{psm}}^{a_2} \rho_t^{a_3} Y_t^{a_4} g^{a_5}. \tag{5.45}$$

Using Table 5.1 and the definition of the dimensionless number (Eq. (5.45)), the following simultaneous equations are obtained:

$$va_2 + a_3 + a_4 = 0, (5.46)$$

$$3a_1 + (1 + \mu - 3\nu)a_2 - 3a_3 - a_4 + a_5 = 0, (5.47)$$

$$-\mu a_2 - 2a_4 - 2a_5 = 0. (5.48)$$

To compute the relevant dimensionless number in the gravity regime $(R_{gY} \gg 1)$, the strength dependence should be neglected $(a_4 = 0)$. Substituting $a_4 = 0$ into Eqs. (5.46) and (5.48), we obtain $a_3 = -\nu a_2$ and $a_5 = -\mu a_2/2$. Using these relations, Eq. (5.47) can be transformed into $a_2 = -3a_1/[1 + (\mu/2)]$. Because we only want to know the scaling of V_c , $a_1 = 1$ should be used. Then, the remaining exponents are computed as $a_2 = -6/(2 + \mu)$, $a_3 = 6\nu/(2 + \mu)$, and $a_5 = 3\mu/(2 + \mu)$. These exponents compose a dimensionless number relevant in the gravity regime Π_g :

$$\Pi_{g} = V_{c} \cdot \left(D_{i} v_{0}^{\mu} \rho_{i}^{\nu}\right)^{-\frac{6}{2+\mu}} \cdot \rho_{t}^{\frac{6\nu}{2+\mu}} \cdot g^{\frac{3\mu}{2+\mu}}$$

$$= \frac{V_{c}}{D_{i}^{3}} \left(\frac{gD_{i}}{v_{0}^{2}}\right)^{\frac{3\mu}{2+\mu}} \left(\frac{\rho_{t}}{\rho_{i}}\right)^{\frac{6\nu}{2+\mu}} \tag{5.49}$$

$$= \frac{\rho_t V_c}{m_i} \left(\frac{gD_i}{v_0^2}\right)^{\frac{3\mu}{2+\mu}} \left(\frac{\rho_t}{\rho_i}\right)^{\frac{6\nu}{2+\mu}-1}.$$
 (5.50)

Here we use the mass of the impactor, $m_i \sim \rho_i D_i^3$.

In contrast, Y_t is dominant and g is irrelevant in the strength regime. To compute the dimensionless number for the strength regime, Π_Y , the gravity effect should be neglected; $a_5 = 0$. Then, the relations $a_4 = -\mu a_2/2$, $a_3 = [(\mu/2) - \nu]a_2$, and $a_2 = -3a_1$ can be obtained from Eqs. (5.46), (5.47), and (5.48). Substituting $a_1 = 1$, the exponents for Π_Y are calculated as $a_2 = -3$, $a_3 = 3\nu - 3\mu/2$, and $a_4 = 3\mu/2$. Thus, the specific form of Π_Y is

$$\Pi_{Y} = V_{c} \cdot \left(D_{i} v_{0}^{\mu} \rho_{i}^{\nu}\right)^{-3} \cdot \rho_{t}^{3\nu - \frac{3}{2}\mu} \cdot Y_{t}^{\frac{3}{2}\mu}$$

$$= \frac{V_{c}}{D_{i}^{3}} \left(\frac{Y_{t}}{\rho_{t} v_{0}^{2}}\right)^{\frac{3}{2}\mu} \left(\frac{\rho_{t}}{\rho_{i}}\right)^{3\nu} \tag{5.51}$$

$$= \frac{\rho_t V_c}{m_i} \left(\frac{Y_t}{\rho_t v_0^2} \right)^{\frac{3}{2}\mu} \left(\frac{\rho_t}{\rho_i} \right)^{3\nu - 1}.$$
 (5.52)

According to the conventional notation in planetary science, Π_g and Π_Y are divided into four dimensionless numbers:

$$\pi_V = \frac{\rho_t V_c}{m_i}, \quad \pi_2 = \frac{gD_i}{v_0^2}, \quad \pi_3 = \frac{Y_t}{\rho_t v_0^2}, \quad \pi_4 = \frac{\rho_t}{\rho_i}.$$
 (5.53)

The normalized crater volume π_V is called the *cratering efficiency*. π_2 corresponds to the reciprocal of F_r (Eq. (2.98)). Furthermore, R_{gY} defined by Eq. (5.44) is π_2/π_3 . These four dimensionless numbers (π_V , π_2 , π_3 , π_4) compose a set of independent dimensionless numbers for the original seven quantities. In the current analysis, these numbers are not independent and are related as Π_g and Π_Y by the point source measure constraint. Although the number of relevant quantities can be reduced by introducing the point source measure, this process also yields two exponents, μ and ν . The total number of degrees of freedom is certainly unchanged. However, the physical insight can be clarified using the point source measure.

What we would like to know is the scaling relation for the volume of the impact crater, V_c . There are two dimensionless numbers, Π_g and Π_Y , as long as we assume that the point source measure is relevant. According to Eq. (2.46), these dimensionless numbers can be related by a certain function as

$$\Pi_g = \psi_g(\Pi_Y). \tag{5.54}$$

Similar to the blast wave analysis (Sect. 2.5.3), we can consider the irrelevant dimensionless number as a constant. In the gravity regime, the strength is too weak to be balanced with the impact inertia. Thus, Π_Y can be regarded as a small constant, and hence, $\psi_g(\Pi_Y)$ is constant. Consequently, the crater efficiency scaling in the gravity regime is written as

$$\Pi_g = \frac{\rho_t V_c}{m_i} \left(\frac{gD_i}{v_0^2}\right)^{\frac{3\mu}{2+\mu}} \left(\frac{\rho_t}{\rho_i}\right)^{\frac{6\nu}{2+\mu}-1} \simeq \text{const.}$$
(5.55)

Therefore, the crater volume at the gravity regime is scaled as

$$V_c \sim \frac{m_i}{\rho_t} \left(\frac{gD_i}{v_0^2}\right)^{-\frac{3\mu}{2+\mu}} \left(\frac{\rho_t}{\rho_i}\right)^{\frac{2+\mu-6\nu}{2+\mu}}.$$
 (5.56)

Similarly, a crater volume scaling in the strength regime is calculable by assuming $\Pi_Y \simeq \text{const.}$ The corresponding scaling is written as

$$V_c \sim \frac{m_i}{\rho_t} \left(\frac{Y_t}{\rho_t v_0^2}\right)^{-\frac{3}{2}\mu} \left(\frac{\rho_t}{\rho_i}\right)^{1-3\nu}.$$
 (5.57)

Further simplification of the crater volume scaling is helpful to discuss the essential factors of the scaling laws. It is natural to assume that both the impactor and target in the planetary impact consist of similar materials, which indicates that the density ratio dependence is negligible; $\pi_4 \simeq 1$. Then, the simplified scaling laws are written as

$$\pi_V \sim \pi_2^{-\frac{3\mu}{2+\mu}}$$
 $(R_{gY} \gg 1; \ \pi_2 \gg \pi_3)$ (5.58)

$$\sim \pi_3^{-\frac{3}{2}\mu}$$
 $(R_{gY} \ll 1; \ \pi_2 \ll \pi_3).$ (5.59)

The scaling behavior is schematically summarized in Fig. 5.13. In Fig. 5.13, the qualitative behaviors of $\log \pi_V$ vs. $\log \pi_2$ are shown. In the small $\pi_2 (= gD_i/v_0^2)$ region, g is irrelevant (strength regime). Thus, $\pi_V (= \rho_t V_c/m_i)$ becomes constant (independent of π_2) and this constant value is determined by Eq. (5.59). As the value of π_2 increases, π_2 becomes relevant, and the scaling instead obeys Eq. (5.58). This transition occurs near $\pi_2 \simeq \pi_3$; $(R_{gY} \simeq 1)$. In the very large π_2 region, this scaling might not be applicable. This limit corresponds to the transition scale from a simple to complex crater. The values of μ and ν for various materials have been experimentally measured. Representative values obtained by experiments are $\mu \simeq 0.41$ for dry sand, $\mu \simeq 0.55$ for nonporous materials, and $\nu \simeq 0.4$ regardless of the material type [49, 50, 57]. While the experimentally obtained μ values are consistent with the expected range $1/3 \le \mu \le 2/3$, ν is slightly different from the expected value $\nu = 1/3$.

In actual planetary craters, the impactor's properties ρ_i , D_i , and v_0 are unknown. To estimate the specific values of these quantities, in general, some more assumptions and approximations are necessary.

Crater-size scalings for the low-velocity loose granular impact cratering (Eqs. (4.1) and (4.2)) are derivable from Eqs. (5.58) and (5.59). Considering the relations $D_c \sim (V_c)^{1/3}$ and $E_{\rm kei} \propto v_0^2$, the scaling $D_c \propto E_{\rm kei}^{1/3}$ can be obtained

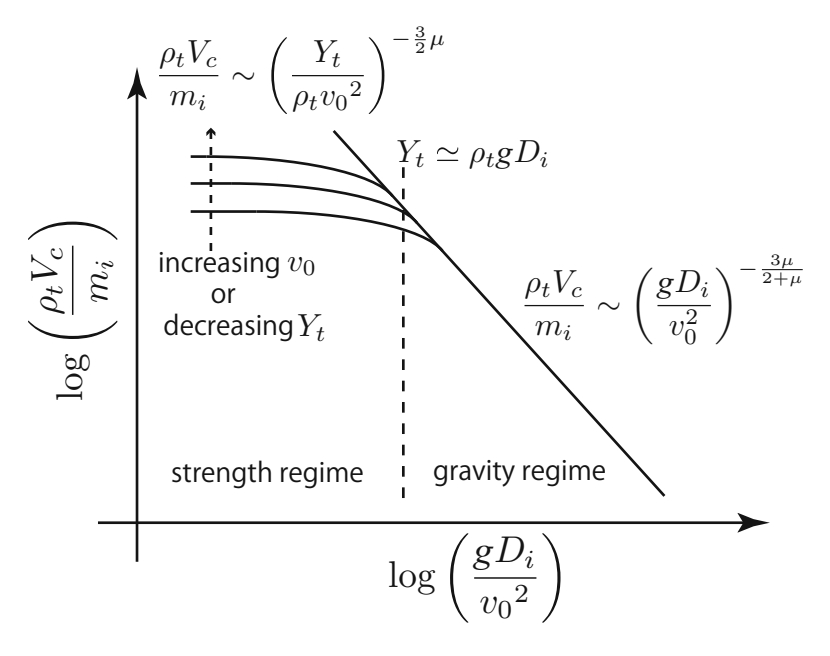


Fig. 5.13 Scaling of the crater volume. The main parameters are the cratering efficiency $\pi_V = \rho_t V_c/m_i$ and the gravity-scaled size $\pi_2 = gD_i/v_0^2 = F_r^{-1}$. In the small impactor regime (strength regime), π_V should be almost constant. The value of the constant π_V depends on π_3 (Eq. (5.59)). By increasing π_2 , the gravity regime scaling (Eq. (5.58)) is achieved

from Eq. (5.59) with $\mu = 2/3$ (energy scaling). The other scaling, $D_c \propto E_{\rm kei}^{1/4}$, corresponds to Eq. (5.58) with $\mu = 2/3$. These are the reasons why 1/4 and 1/3 scalings correspond to the gravity-dominant and strength-dominant (plasticdeformation-dominant) cases, respectively, as mentioned in Sect. 4.1.1. A planetary crater's aspect ratio D_h/D_c is independent of the crater size (Sect. 5.1). This finding implies that both the depth and diameter should be scaled similarly. Nevertheless, the granular impact experiments show different scalings for D_c and D_h (Fig. 4.3). In the granular impact, the horizontal length scale is governed by gravity, while the vertical length scale appears to be governed by strength. This behavior might be qualitatively understandable because the granular matter has apparent strength in a deep region resulting from the frictional support and hydrostatic pressure. In fact, the depth-scaling exponent depends slightly on the packing fraction of the target [58]. The exponent decreases in the looser granular target. Although it is difficult to directly compare the loose (and low-velocity) granular impact experiments and hypervelocity impact cratering, some of the characteristics, particularly for the gravity regime, might be similar because loose granular matter generally has very small Y_t . Because the kinetic energy and momentum are, of course, the crucial quantities even for the low-velocity loose granular impact, the abovementioned scaling relations based on the point source measure are presumably applicable to granular impact.

The momentum limit $\mu=1/3$ cannot provide any information about the loose granular impact craters made by a solid impactor. It appears that the kinetic energy is more relevant for the crater size scaling of loose granular impact. However, the result of hypervelocity impact on a soil target ($\mu\simeq0.41$ [50, 59]) is closer to the momentum limit case $\mu=1/3$. This experimentally obtained value $\mu\simeq0.41$ results in a simple relation, $V_c\propto v_0^{1.0}$ in the gravity regime. Assuming $V_c\sim D_c^3$ and $E_{\rm kei}\sim m_i v_0^2$, this relation corresponds to

$$D_c \propto E_{\rm kei}^{1/6}.\tag{5.60}$$

For dissipative materials such as porous targets, it has been considered that μ decreases toward 1/3. This idea is natural because the momentum conservation is more important than the energy conservation for the dissipative (inelastic) impact. Nevertheless, loose granular impact behavior, which must be very dissipative, can be explained by $\mu = 2/3$.

Even by the energy scaling ($\mu=2/3$), it is impossible to attain a perfect agreement between the scaling obtained in this section and the loose granular impact experiments. For instance, the crater diameter is proportional to $(\rho_i/\rho_t)^{1/4}$ and the depth is proportional to $(\rho_i/\rho_t)^{1/2}$ in loose granular impact (Eqs. (6.31) and (6.32)) [22]. Using energy scaling ($\mu=2/3$ and $\nu=1/3$), the corresponding exponents can be calculated from Eqs. (5.49) and (5.51) to be $6\nu/3(2+\mu)=1/4$ and $3\nu/3=1/3$, respectively. The former agrees with the experimental result, whereas the latter does not. The experimentally obtained ν value ($\nu=0.4$) provides a slightly better estimation of the low-velocity loose granular impact.

Scaling using the dimensional analysis method partially works to explain the impact experiment. The problems mentioned above are some sort of puzzle of exponents. The main assumption of the late stage equivalence (or point source measure) might not be the best assumption to obtain a fully consistent result. Because such a limitation of the capability in the scaling analysis could sometimes be serious, we should be careful not to be overconfident in its ability.

5.5.2 Ejecta Scaling

The ejecta velocity can also be discussed by scaling through dimensional analysis [52]. The crater volume scaling discussed in the previous subsection is the very first step to analyze the impact cratering phenomena by dimensional analysis. The crater volume (or equivalently its size) is one of the most important pieces of information when we observe the crater. This parameter is directly related to the crater morphology. The next parameter that we can discuss using dimensional analysis is the ejecta velocity, which is also a very crucial quantity to understand the crater morphology. In particular, the ejection velocity distribution relates to the ejecta blanket structure.

The relevant quantities for this problem are the ejecta velocity $v_{\rm ej}$ at the launch position x_e (distance from the impact point), $C_{\rm psm} = D_i v_0^\mu \rho_i^\nu$, and ρ_t . Then, the only relevant dimensionless number is immediately obtained as

$$\Pi_e = \frac{x_e}{D_i} \left(\frac{v_{\rm ej}}{v_0}\right)^{\mu} \left(\frac{\rho_t}{\rho_i}\right)^{\nu}.$$
 (5.61)

From the dimensional homogeneity, $\Pi_e \simeq \text{const.}$ can be assumed. Thus, the ejecta velocity obeys the scaling

$$\frac{v_{\rm ej}}{v_0} \sim \left(\frac{x_e}{D_i}\right)^{-\frac{1}{\mu}} \left(\frac{\rho_t}{\rho_i}\right)^{-\frac{\nu}{\mu}}.$$
 (5.62)

Similar to the crater efficiency scaling, Eq. (5.62) is very useful if we have information about the impactor's dimensions, density, and impact velocity. Because the point source measure consists of the impactor's properties, the corresponding information is required to use Eq. (5.62). Indeed, the information is available in usual laboratory experiments. However, it is difficult to speculate the proper values for actual planetary craters, in general. In contrast, the resultant crater's size is generally observable. Furthermore, the scaling of the crater's size was already obtained in the previous subsection. Therefore, we can rewrite the ejecta velocity as a function of the crater's size by incorporating the scaling relations obtained thus far. Specifically, we use the crater volume scalings (Eqs. (5.49) and (5.51)) to transform Eq. (5.62) into a more understandable form.

In the gravity regime, a relation $\Pi_g \simeq \text{const.}$ can be used. From Eq. (5.49), the relation $D_i \sim D_c \pi_4^{\nu} (\pi_2 D_c/D_i)^{\mu/2} = D_c (\rho_t/\rho_i)^{\nu} (gD_c/v_0^2)^{\mu/2}$ is obtained. Here we use the relation $V_c = D_c^3$. Substituting this relation into $\Pi_e \simeq \text{const.}$, the simple scaling,

$$\frac{v_{\rm ej}}{\sqrt{gD_c}} \sim \left(\frac{x_e}{D_c}\right)^{-\frac{1}{\mu}} \qquad (R_{gY} \gg 1; \quad \pi_2 \gg \pi_3), \tag{5.63}$$

is obtained. Similarly, the following scaling is computed using Eq. (5.51) for the strength regime:

$$\frac{v_{\rm ej}}{\sqrt{Y_{\rm e}/\rho_{\rm e}}} \sim \left(\frac{x_e}{D_c}\right)^{-\frac{1}{\mu}}$$
 $(R_{gY} \ll 1; \ \pi_2 \ll \pi_3).$ (5.64)

Equations (5.63) and (5.64) have a similar structure; the normalized ejecta velocity is scaled by the normalized launch position and the density ratio dependence is canceled out. Furthermore, the scaling exponent is identical between Eqs. (5.63) and (5.64).

The mass of ejecta M_e with velocity greater than $v_{\rm ej}$ can also be evaluated using dimensional analysis. Because $v_{\rm ej}$ should be a monotonically decreasing function

of x_e , M_e corresponds to the mass of the spherical region inside x_e ; $M_e \sim \rho_t x_e^3$. Substituting this relation into $\Pi_e^3 = \text{const.}$, the ejecta mass scaling is obtained as

$$\frac{M_e}{m_i} \sim \left(\frac{v_{\rm ej}}{v_0}\right)^{-3\mu} \left(\frac{\rho_t}{\rho_i}\right)^{1-3\nu}.$$
 (5.65)

Similar to the ejecta velocity case, this scaling can be rewritten by the target properties using Eq. (5.49) for the gravity regime and Eq. (5.51) for the strength regime. Therefore, the ejecta mass scaling in the gravity regime is written as

$$\frac{M_e}{\rho_t V_c} \sim \left(\frac{v_{\rm ej}}{\sqrt{gD_c}}\right)^{-3\mu}, \qquad (R_{gY} \gg 1; \ \pi_2 \gg \pi_3).$$
(5.66)

In the strength regime, the ejecta mass is scaled as

$$\frac{M_e}{\rho_t V_c} \sim \left(\frac{v_{\rm ej}}{\sqrt{Y_t/\rho_t}}\right)^{-3\mu}, \qquad (R_{gY} \ll 1; \ \pi_2 \ll \pi_3).$$
(5.67)

The scaling relations obtained for M_e are similar again between the gravity and strength regimes. The most important quantity is the typical velocity caused by the gravity $\sqrt{gD_c}$ or strength $\sqrt{Y_t/\rho_t}$.

A slightly different dimensionless number Π_{ed} has also been considered for the discussion of the time-dependent ejecta dynamics. Here the characteristic ejecta velocity $v_{\rm ej}$ in Eq. (5.61) is replaced by x_e/t to evaluate the ejecta dynamics:

$$\Pi_{ed} = \frac{x_e}{D_i} \left(\frac{x_e/t}{v_0}\right)^{\mu} \left(\frac{\rho_t}{\rho_i}\right)^{\nu}.$$
 (5.68)

Using this Π_{ed} , one can estimate the cavity and ejecta velocity scalings for both the gravity and strength regimes [60]. The cavity development scaling in the gravity regime can be obtained using the constraints $\Pi_{ed} = \text{const.}$ and $\Pi_g = \text{const.}$ The scaling obtained from these constraints is written as

$$\frac{x_e}{D_c} \sim \left(t\sqrt{\frac{g}{D_c}}\right)^{\frac{\mu}{1+\mu}}.$$
 (5.69)

The ejecta velocity scaling can be rewritten by substituting Eq. (5.69) into Eq. (5.63) as

$$\frac{v_{\rm ej}}{\sqrt{gD_c}} \sim \left(t\sqrt{\frac{g}{D_c}}\right)^{-\frac{1}{1+\mu}}.$$
 (5.70)

For the strength regime, the constraints, $\Pi_{ed} = \text{const.}$ and $\Pi_Y = \text{const.}$ should be used to compute the scaling relation. The obtained scaling is written as

$$\frac{x_e}{D_c} \sim \left(\frac{t}{D_c} \sqrt{\frac{Y_t}{\rho_t}}\right)^{\frac{\mu}{1+\mu}}.$$
 (5.71)

Similar to the gravity regime case, the ejecta velocity scaling can be obtained as

$$\frac{v_{\rm ej}}{\sqrt{Y_t/\rho_t}} \sim \left(\frac{t}{D_c} \sqrt{\frac{Y_t}{\rho_t}}\right)^{-\frac{1}{1+\mu}}.$$
 (5.72)

In Ref. [52], various experimental results were compiled and analyzed along the line of the ejecta scaling discussed above. We have to be careful about the region of scaling of the ejecta velocity. As long as the point source measure (late stage equivalence) is adopted, the scaling is applicable roughly to the range of $x_e > D_i/2$. In the very vicinity of the impact point $(x_e < D_i/2)$, a jetting occurs (see e.g., Ref. [61]). The jetting is different from the usual ejection process considered thus far. At $x_e \simeq D_c/2$, $v_{\rm ej}$ becomes zero because the gravity or strength arrests the excavation flow. In other words, the crater radius $D_c/2$ is determined by the limit of $v_{\rm ej} \rightarrow 0$. Thus, the upper limit of the scaling is $x_e \simeq D_c/2$. The scaling relations obtained above hold within the intermediate launch position, $D_i/2 < x_e < D_c/2$ [52]. In this regime, the experimental data can be fitted by the scaling. In future studies, some unconsidered factors such as the target porosity (or equivalently packing fraction) and viscosity should be examined.

In the very early stage of the ejection, the ejecta velocity scaling has to be improved. In the abovementioned scaling for the ejecta velocity, the late stage equivalence was generally assumed. The speed of sound in the target material C_s would be an additional relevant quantity for the early stage dynamics. Then, a possible corresponding dimensionless number Π'_{ed} can be written as

$$\Pi'_{ed} = \frac{v_{ej}t}{D_i} \left(\frac{C_s}{v_0}\right)^{\mu} \left(\frac{\rho_t}{\rho_i}\right)^{\nu}.$$
 (5.73)

Therefore, the ejecta velocity at the early stage is scaled as

$$\frac{v_{\rm ej}}{v_0} \sim \left[t \frac{v_0}{D_i} \left(\frac{\rho_t}{\rho_i} \right)^{\nu} \left(\frac{C_s}{v_0} \right)^{\mu} \right]^{-1}. \tag{5.74}$$

Using the hypervelocity impact (v_0 is in the order of 10^0 km/s) on the quartz sand target ($D_g \simeq 1$ mm), the ejecta velocity $v_{\rm ej}$ at an early stage was measured and roughly scaled by Eq. (5.74) [62, 63]. To best fit the experimental data, $\mu = 2/3$ and $\nu = 1/3$ were used. These values correspond to the energy limit of the point source measure (Eq. (5.43)). However, the ejection velocity at the late stage was scaled differently as [63]

source measure		
Gravity regime $(R_{gY} \gg 1)$	General	Strength regime $(R_{gY} \ll 1)$
	$C_{\rm psm} = D_i v_0^{\mu} \rho_i^{\nu}$	
$\Pi_g = \frac{\rho_t V_c}{m_i} \left(\frac{gD_i}{v_0^2}\right)^{\frac{3\mu}{2+\mu}} \left(\frac{\rho_t}{\rho_i}\right)^{\frac{6\nu}{2+\mu}-1}$		$\Pi_Y = \frac{\rho_t V_c}{m_i} \left(\frac{Y_t}{\rho_t v_0^2}\right)^{\frac{3}{2}\mu} \left(\frac{\rho_t}{\rho_i}\right)^{3\nu - 1}$
	$\Pi_e = rac{x_e}{D_i} \left(rac{v_{ m ej}}{v_0} ight)^{\mu} \left(rac{ ho_t}{ ho_i} ight)^{ u}$	
	$\Pi_{ed} = \frac{x_e}{D_i} \left(\frac{x_e/t}{v_0}\right)^{\mu} \left(\frac{\rho_t}{\rho_i}\right)^{\nu}$	
	$\Pi'_{ed} = \frac{v_{\rm ej}t}{D_i} \left(\frac{C_s}{v_0}\right)^{\mu} \left(\frac{\rho_t}{\rho_i}\right)^{\nu}$	
$V_c \sim rac{m_i}{ ho_t} \left(rac{gD_i}{v_0^2} ight)^{-rac{3\mu}{2+\mu}} \left(rac{ ho_t}{ ho_i} ight)^{rac{2+\mu-6v}{2+\mu}}$		$V_c \sim rac{m_i}{ ho_t} \left(rac{Y_t}{ ho_t v_0^2} ight)^{-rac{3}{2}\mu} \left(rac{ ho_t}{ ho_i} ight)^{1-3 u}$
$\frac{M_e}{\rho_I V_c} \sim \left(\frac{v_{\rm ej}}{\sqrt{gD_c}}\right)^{-3\mu}$		$\frac{M_e}{\rho_t V_c} \sim \left(\frac{v_{\rm ej}}{\sqrt{Y_t/\rho_t}}\right)^{-3\mu}$
$\frac{v_{\rm ej}}{\sqrt{gD_c}} \sim \left(\frac{x_e}{D_c}\right)^{-\frac{1}{\mu}}$		$\frac{v_{\rm ej}}{\sqrt{Y_t/ ho_t}} \sim \left(\frac{x_e}{D_c}\right)^{-\frac{1}{\mu}}$
$\frac{v_{\rm ej}}{\sqrt{gD_c}} \sim \left(t\sqrt{\frac{g}{D_c}}\right)^{-\frac{1}{1+\mu}}$		$rac{v_{ m ej}}{\sqrt{Y_t/ ho_t}} \sim \left(rac{t}{D_c}\sqrt{rac{Y_t}{ ho_t}} ight)^{-rac{1}{1+\mu}}$
$\frac{x_e}{D_c} \sim \left(t \sqrt{\frac{g}{D_c}}\right)^{\frac{\mu}{1+\mu}}$		$rac{x_e}{D_c} \sim \left(rac{t}{D_c} \sqrt{rac{Y_t}{ ho_t}} ight)^{rac{\mu}{1+\mu}}$
	$\frac{v_{\rm ej}}{v_0} \sim \left[t \frac{v_0}{D_i} \left(\frac{\rho_t}{\rho_i}\right)^{\nu} \left(\frac{C_s}{v_0}\right)^{\mu}\right]^{-1}$	

Table 5.2 Dimensionless numbers and scaling relations for the impact cratering by the point source measure

$$\frac{v_{\rm ej}}{\sqrt{gD_c}} \sim \left(t\sqrt{\frac{g}{D_c}}\right)^{-0.71},\tag{5.75}$$

where D_c is the crater diameter. In this late stage, gravity plays an essential role in the scaling. This form is consistent with the late stage scaling of Eq. (5.70). The corresponding μ is computed as $\mu = 0.41$, which is a typical value of μ in the hypervelocity impact of a dry granular target.

Standard scaling relations for hypervelocity impacts have been introduced thus far based on the concept of point source measure (late stage equivalence). In Table 5.2, the important dimensionless numbers and scaling relations are summarized.

5.5.3 Oblique Impact Scaling

As almost all meteors obliquely impact the target, an understanding of oblique impact is indispensable. Nevertheless, oblique impact is much less understood than vertical impact. Most planetary craters possess an almost circular shape; only approximately 5% of craters have elliptic shapes that correspond to the low-angle impact of $\theta_{imp} < 12^{\circ}$ (see Fig. 4.13 for the definition of θ_{imp}) [64] because the propagation of the shock wave is almost independent of the impact angle, at least in the late stage. How robust are the scaling relations discussed in this section?

Although the impact angle has not been considered as a relevant parameter in the aforementioned scaling, it may affect the scaling.

The validity of the scaling relations for the oblique impact was verified both by an experiment [65] and a numerical simulation [66]. In the numerical simulation, the effects of the impact angle and the internal friction of the target were systematically examined using a three-dimensional hydrocode. From the numerical result, the cratering efficiency scaling in the gravity regime was written as

$$\pi_V \sim \left(\frac{gD_i}{v_0^2 \sin^2 \theta_{\rm imp}}\right)^{-\frac{3\mu}{2+\mu}} = \pi_2^{-\frac{3\mu}{2+\mu}} \sin^{\frac{6\mu}{2+\mu}} \theta_{\rm imp}.$$
 (5.76)

This scaling holds at $\theta_{\rm imp} \geq 30^{\circ}$. The limit angle 30° coincides with that of the loose granular impact drag force form (Sect. 4.1.8). The modified scaling (Eq. (5.76)) indicates that only the vertical component of v_0 plays a role in the cratering efficiency. The numerical prefactor and scaling exponent in Eq. (5.76) were measured in the simulation. Then, both were slightly increasing functions of $\theta_{\rm imp}$ and decreasing functions of internal friction coefficient [66]. In addition, similar scaling is observed experimentally even in a small angle regime $\theta_{\rm imp} \leq 30^{\circ}$ [65].

The effect of the oblique impact angle has been also studied for shock wave propagation [67], ejecta deposition [68], and central peak formation [69]. However, these effects are not sufficient to fully understand the oblique impact phenomenology. Because oblique impact is the majority impact in natural impact cratering, much more detailed studies, particularly for low-angle impacts, are necessary to conclude the scaling form of the impact cratering.

5.5.4 Porous Target Impact Scaling

The target material porosity (or equivalently the packing fraction) could affect the impact cratering. The densities of asteroids have been estimated using various methods [70]. These estimates suggest that some asteroids have very small densities (below 1.5×10^3 kg/m³). Comets have also been considered to have highly porous structures. According to empirical and theoretical modeling, cometary nuclei could have very low packing fractions $\phi = 0.2$ –0.4 (e.g., [71, 72]). Such very porous astronomical objects might be *rubble-pile* objects that are supposed to be produced by the reaccumulation of disrupted fragments. Impact cratering occurring in rubble-pile objects could be different from the usual cratering discussed thus far. For example, the target compression might dominate the cratering process in porous targets. Perhaps, cohesion among constitutive grains is extremely important for discussing the impact of porous targets. Using an enhanced-gravity experiment, cratering in porous targets was examined [73]. The researchers observed that the crater shape, ejecta mass, and cratering efficiency were affected by the porosity. Although the crater shape exhibited complex behavior, the ejecta mass was generally a

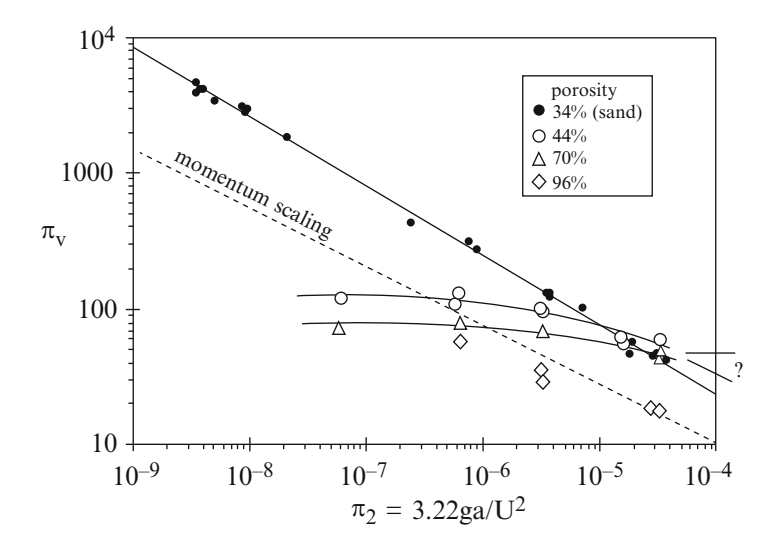
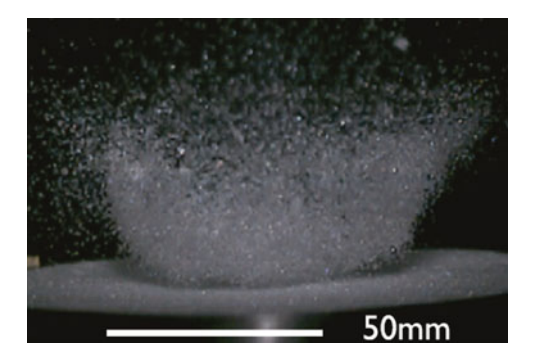


Fig. 5.14 Cratering efficiency π_v vs. gravitational scale π_2 . U and a in this plot correspond to the impact velocity v_0 and the impactor diameter D_i , respectively. Reprinted from Ref. [73] (Copyright 2003, with permission from Elsevier. Data for sand come from Refs. [57] and [59])

decreasing function of the porosity. The experimentally obtained cratering efficiency scaling is shown in Fig. 5.14. For the cratering efficiency scaling, intermediate porous targets (porosity of 44% and 70%) exhibited roughly constant cratering efficiency, which implies that cohesion (strength) governs cratering efficiency rather than gravity. In contrast, loose sand and highly porous targets (porosity 96%) exhibited momentum scaling, i.e., $\mu = 1/3$; $\pi_V \sim \pi_2^{-3/7}$. It is unclear whether a gravity-dominant regime is present in large π_2 . In general, momentum scaling appears to be more appropriate than energy scaling for porous targets including sand. This result contrasts with the scaling of crater dimensions for the low-velocity loose granular impacts, in which the energy-based scaling $\mu = 2/3$ better explains the result. The difference between porous targets and loose granular targets is not very clear. The order of impact velocity might also be an important parameter to distinguish the impact cratering state.

Sintered snow targets were also used to model small icy satellites [74]. The porous snow can be strengthened by sintering. The strength of a porous snow target (packing fraction $\phi \simeq 0.64$) varies with the sintering duration. The dynamic strength defined by the maximum value of the impact stress σ_{max} to disrupt the target is scaled by the sintering duration t_{sin} as $\sigma_{\text{max}} \propto t_{\text{sin}}^{0.28}$. This result indicates that aging by sintering is also an important factor to be considered, particularly for icy bodies. The strength of an icy body of the same packing fraction but of different age can be different. Using a systematic impact experiment, Arakawa and Yasui revealed the scaling relation for sintered porous snow targets. Specifically, a small icy impactor $(D_i = 7 \text{ mm}, m_i = 0.21 \text{ g}, \text{ and } \phi = 0.7)$ was shot into a sintered snow target.

Fig. 5.15 Ejecta curtain made by a porous snow target. An icy impactor is shot with $v_0 = 41$ m/s onto the porous ($\phi \simeq 0.64$) snow target sintered for 15 min at -10° C (Reprinted from Ref. [74]. Copyright 2011, with permission from Elsevier)



The impact velocity v_0 ranged from 31 to 150 m/s. Because the experimental range appears to correspond to the strength regime, these researchers compared π_V and π_3 . However, the direct comparison of these dimensionless numbers does not yield good data collapse. Instead, they proposed an improved strength parameter

$$\pi_3' = \frac{Y_t}{\frac{\rho_i C_{si} \rho_t C_{st}}{\rho_i C_{si} + \rho_t C_{st}}} v_0, \tag{5.77}$$

where C_{si} and C_{st} denote the sound speed for the impactor and target, respectively. To obtain π'_3 , the dynamic pressure $\rho_t v_0^2$ in the definition of π_3 (Eq. (5.53)) is improved using the idea of shock pressure (Eqs. (5.13) and (5.21)). Then, all the data are scaled by

$$\pi_V \sim \pi_3^{\prime - 1.2}$$
. (5.78)

They also observed a characteristic ejecta curtain shape in the sintered snow target impact. In Fig. 5.15, a snapshot of the ejecta curtain made by a porous snow target is shown. This ejecta curtain shape is slightly different from liquid and loose granular impacts (Figs. 6.1 and 6.4). The boundary between the ejecta and target surface is discontinuous, whereas the boundary is smooth in fluid or loose granular impact. Although the dynamics of a porous and sintered icy target must be complex, it would be a necessary piece to deeply understand the soft impact mechanics relevant to the planetary science.

5.5.5 Viscosity Scaling

Until now, we have not considered the effect of viscosity in the scaling. The viscosity has been implicitly regarded as an irrelevant property for this problem. In some class of impact cratering, however, there might be a viscous regime. The viscosity is too weak to be balanced with the impact inertia for most of the impact phenomena.

However, the complex behaviors of fluidized debris, melt, and liquid water must be considered to explain the various planetary crater shapes. Thus, here we consider the viscous scaling along the line of point source measure scaling [75]. If V_c , $C_{\rm psm}$, ρ_t , and η are employed as relevant quantities, one dimensionless number can be obtained by a similar computation performed thus far:

$$\Pi_{\eta} = \frac{V_c}{D_i^3} \left(\frac{\eta}{\rho_t D_i v_0} \right)^{\frac{3\mu}{1-\mu}} \left(\frac{\rho_t}{\rho_i} \right)^{\frac{3\nu}{1-\mu}}.$$
 (5.79)

Fink et al. performed silicon oil target experiment and assumed $\mu=1/2$ to conclude that the viscosity significantly affects the cratering efficiency in the following regime [76]:

$$\eta > \rho_t D_i^{1.2} v_0^{0.6} g^{0.2}.$$
(5.80)

In a typical case ($D_i \simeq 1 \, \mathrm{km}$, $\rho_t \simeq 10^3 \, \mathrm{kg/m^3}$, $v_0 \simeq 10 \, \mathrm{km/s}$, and $g \simeq 9.8 \, \mathrm{m/s^2}$), this value roughly corresponds to $\eta > 10^9 \, \mathrm{Pa\cdot s}$. This regime is much more viscous than that of a usual fluid but much less viscous than that estimated for the salt dome diapir structure (Sect. 2.8.4). The effect of viscosity could play a role in some regime of the impact cratering event. Fluid-like behavior might be a missing important part even in planetary-scale impact cratering.

5.6 Summary

A brief review of studies relating to large-scale natural impact cratering was provided in this chapter. Typical crater structures observed on the surfaces of planets, satellites, and other astronomical objects were first reviewed. Examples include the simple crater, central peak structure, multiring basin, ray crater, and rampart crater. The micro craters observed on returned samples from the Moon and the asteroid Itokawa were also introduced. Furthermore, the standard scenario of the processes producing such crater morphologies was briefly overviewed. In general, the planetary cratering process consists of five stages: contact and compression, excavation, modification, ejecta deposition, and degradation. What happens in each stage, such as shock wave propagation, was briefly explained. Crater erasure by impact-induced seismic shaking, which is particularly relevant to small astronomical objects, was also discussed. Finally, the scaling analysis for the cratering process was discussed on the basis of the Π -groups method. A key quantity called the point source measure was used to derive some scaling relations. The point source measure characterizes the relative importance between kinetic energy and momentum in impact cratering. Topics argued in this chapter are actually very limited and biased mainly due to the tether of my ability. For further study, Ref. [1] is the best reference to learn about general cratering mechanics. The

References 199

possible origin of some curious crater morphologies will be discussed further in the next chapter. In particular, low-velocity soft impact cratering and the resultant crater shapes will be analyzed using the scaling method. These simple mimics might be helpful to understand complex cratering events occurring in space.

References

- 1. H.J. Melosh, *Impact Cratering* (Oxford University Press, New York, 1989)
- 2. R.J. Pike, Geophys. Res. Lett. 1, 291 (1974)
- R. Sullivan, R. Greeley, R. Pappalardo, E. Asphaug, J. Moore, D. Morrison, M. Belton, M. Carr,
 C. Chapman, P. Geissler, R. Greenberg, J. Granahan, J.H. III, R. Kirk, A. McEwen, P. Lee,
 P. Thomas, J. Veverka, Icarus 120, 119 (1996)
- M. Carr, R. Kirk, A. McEwen, J. Veverka, P. Thomas, J. Head, S. Murchie, Icarus 107, 61 (1994)
- M.S. Robinson, P.C. Thomas, J. Veverka, S.L. Murchie, B.B. Wilcox, Meteorit. Planet. Sci. 37, 1651 (2002)
- N. Hirata, O.S. Barnouin-Jha, C. Honda, R. Nakamura, H. Miyamoto, S. Sasaki, H. Demura, A.M. Nakamura, T. Michikami, R.W. Gaskell, J. Saito, Icarus 200, 486 (2009)
- 7. R.J. Pike, Geomorphology of impact craters on mercury, in *Mercury* (University of Arizona Press, Tucson, 1988), pp. 165–273
- 8. L. Xu, W.W. Zhang, S.R. Nagel, Phys. Rev. Lett. 94, 184505 (2005)
- L.L. Tornabene, J.E. Moersch, H.Y. McSween, A.S. McEwen, J.L. Piatek, K.A. Milam, P.R. Christensen, J. Geophys. Res.: Planets 111(E10), E10006 (2006)
- T. Kadono, A.I. Suzuki, K. Wada, N.K. Mitani, S. Yamamoto, M. Arakawa, S. Sugita, J. Haruyama, A.M. Nakamura, Crater-ray formation by impact-induced ejecta particles. Icarus 250, 215 (2015)
- 11. H.J. Melosh, *Planetary Surface Processes* (Cambridge University Press, Cambridge, 2011)
- 12. G.H. Heiken, D.T. Vaniman, B.M. French (eds.), *LUNAR SOURCEBOOK: A User's Guide to the Moon* (Cambridge University Press, New York, 1991)
- E. Nakamura, A. Makishima, T. Moriguti, K. Kobayashi, R. Tanaka, T. Kunihiro, T. Tsujimori,
 C. Sakaguchi, H. Kitagawa, T. Ota, Y. Yachi, T. Yada, M. Abe, A. Fujimura, M. Ueno,
 T. Mukai, M. Yoshikawa, J. Kawaguchi, PNAS 109, E624 (2012)
- 14. D.E. Gault, Radio Sci. 5, 273 (1970)
- 15. D. Bideau, J.P. Troadec, J. Phys. C 17, L731 (1984)
- 16. J.E. Richardson, Icarus 204, 697 (2009)
- T. Morota, J. Haruyama, H. Miyamoto, C. Honda, M. Ohtake, Y. Yokota, T. Matsunaga,
 N. Hirata, H. Demura, H. Takeda, Y. Ogawa, J. Kimura, Meteorit. Planet. Sci. 44, 1115 (2009)
- G. Neukum, B.A. Ivanov, Cratering size distributions and impact probabilities on Earth from lunar, terrestrial planet, and asteroid cratering data, in *Hazards Due to Comets and Asteroids* (University of Arizona Press, Tucson, 1994), pp. 359–416
- 19. W.K. Hartmann, Icarus 174, 294 (2005)
- 20. G. Neukum, B. Ivanov, W. Hartmann, Space Sci. Rev. 96, 55 (2001)
- H. Mizutani, S.i. Kawakami, Y. Takagi, M. Kato, M. Kumazawa, J. Geophys. Res.: Solid Earth 88(S02), A835 (1983)
- 22. J.S. Uehara, M.A. Ambroso, R.P. Ojha, D.J. Durian, Phys. Rev. Lett. 90, 194301 (2003)
- 23. A.M. Walsh, K.E. Holloway, P. Habdas, J.R. de Bruyn, Phys. Rev. Lett. 91, 104301 (2003)
- 24. P.H. Shultz, D.E. Gault, The Moon 12, 159 (1975)
- C.H. Scholz, The mechanics of Earthquakes and Faulting, 2nd edn. (Cambridge University Press, New York, 2002)

- D.E. Maxwell, in *Impact and Explosion Cratering*, ed. by D.J. Roddy, R.O. Pepin, R.B. Merrill (Pergamon Press, New York, 1977), pp. 1003–1008
- 27. M.J. Cintala, L. Berthoud, F. Hörz, Meteorit. Planet. Sci. 34, 605 (1999)
- 28. J.L.B. Anderson, P.H. Schultz, J.T. Heineck, Meteorit. Planet. Sci. 39, 303 (2004)
- J.L.B. Anderson, P.H. Schultz, in *Thirty-Sixth Lunar and Planetary Science Conference* (Lunar and Planetary Institute, Houston, 2005), Abstract #1773
- M.G. Austin, J.M. Thomsen, S.F. Ruhl, D.L. Orphal, W.F. Borden, S.A. Larson, P.H. Schultz, Proc. Lunar Planet. Sci. 12A, 197 (1981)
- 31. K.A. Holsapple, R.M. Schmidt, J. Geophys. Res.: Solid Earth 92(B7), 6350 (1987)
- 32. T. McGetchin, M. Settle, J. Head, Earth Planet. Sci. Lett. 20, 226 (1973)
- 33. H.G. Wilshire, K.A. Howard, Science **162**, 258 (1968)
- 34. R.B. Baldwin, The Mechanics of the Moon (University of Chicago Press, Chicago, 1963)
- 35. H.J. Melosh, J. Geophys. Res.: Solid Earth 87(B1), 371 (1982)
- 36. H.J. Melosh, E.S. Gaffney, J. Geophys. Res.: Solid Earth 88(S02), A830 (1983)
- S. Abe, N. Mukai, N. Hirata, O.S. Barnouin-Jha, A.F. Cheng, H. Demura, R.W. Gaskell, T. Kubota, M. Matsuoka, T. Mizuno, R. Nakamura, D.J. Sheeres, M. Yoshikawa, Science 312, 1344 (2006)
- A. Fujiwara, J. Kawaguchi, D.K. Yeomans, M. Abe, T. Mukai, T. Okada, J. Saito, H. Yano, M. Yoshikawa, D.J. Scheeres, O. Barnouin-Jha, A.F. Cheng, H. Demura, R. Gaskell, N. Hirata, I. Ikeda, T. Kominato, A.M. Miyamoto, H. Nakamura, R. Nakamura, S. Sasaki, K. Uesugi, Science 312, 1330 (2006)
- 39. J.E. Richardson, H.J. Melosh, R. Greenberg, Science 306, 1526 (2004)
- 40. J.E. Richardson Jr, H.J. Melosh, R.J. Greenberg, D.P. O'Brien, Icarus 179, 325 (2005)
- H. Miyamoto, H. Yano, J.D. Scheeres, S. Abe, O. Barnouin-Jha, A.F. Cheng, H. Demura, R.W. Gaskell, N. Hirata, R. Ishiguro, T. Michikami, A.M. Nakamura, R. Nakamura, J. Saito, A. Sasaki, Science 316, 1011 (2007)
- 42. H.J. Melosh, J. Geophys. Res.: Solid Earth 84(B13), 7513 (1979)
- G.V. Latham, M. Ewing, F. Press, G. Sutton, J. Dorman, Y. Nakamura, N. Toksöz, R. Wiggins, J. Derr, F. Duennebier, Science 167, 455 (1970)
- 44. A. McGarr, G.V. Latham, D.E. Gault, J. Geophys. Res. 74, 5981 (1969)
- 45. H. Katsuragi, A.R. Abate, D.J. Durian, Soft Matter **6**, 3023 (2010)
- 46. P. Michel, D. O'Brien, S. Abe, N. Hirata, Icarus **200**, 503 (2009)
- W.F. Bottke Jr., D.D. Durda, D. Nesvorný, R. Jedicke, A. Morbidelli, D. Vokrouhlický, H. Levison, Icarus 175, 111 (2005)
- 48. D.P. O'Brien, R. Greenberg, Icarus 178, 179 (2005)
- 49. K.A. Holsapple, R.M. Schmidt, J. Geophys. Res.: Solid Earth 87(B3), 1849 (1982)
- 50. K.A. Holsapple, Annu. Rev. Earth Planet. Sci. 21, 333 (1993)
- 51. K.A. Holsapple, K.R. Housen, Icarus **187**, 345 (2007)
- 52. K.R. Housen, K.A. Holsapple, Icarus **211**, 856 (2011)
- 53. K.R. Housen, K.A. Holsapple, Icarus **84**, 226 (1990)
- 54. K. Holsapple, Planet. Space Sci. 42, 1067 (1994)
- 55. K.R. Housen, K.A. Holsapple, Icarus **142**, 21 (1999)
- J.K. Dienes, J.M. Walsh, in *High Velocity Impact Phenomena*, ed. by R. Kinslow (Academic, New York, 1970), pp. 45–104
- R.M. Schmidt, in *Eleventh Lunar and Planetary Science Conference* (Lunar and Planetary Institute, Houston, 1980), Abstract #1351
- 58. J.R. de Rruyn, A.M. Walsh, Can. J. Phys. **82**, 439 (2004)
- R.M. Schmidt, K.R. Housen, Int. J. Impact Eng. 5, 543 (1987). Hypervelocity Impact Proceedings of the 1986 Symposium
- K.R. Housen, R.M. Schmidt, K.A. Holsapple, J. Geophys. Res.: Solid Earth 88(B3), 2485 (1983)
- 61. W. Yang, T.J. Ahrens, Icarus **116**, 269 (1995)
- 62. B. Hermalyn, P.H. Schultz, Icarus 209, 866 (2010)
- 63. B. Hermalyn, P.H. Schultz, Icarus **216**, 269 (2011)

References 201

- 64. W.F. Bottke Jr., S.G. Love, D. Tytell, T. Glotch, Icarus 145, 108 (2000)
- 65. D.E. Gault, J.A. Wedekind, in *Ninth Lunar and Planetary Science Conference* (Lunar and Planetary Institute, Houston, 1978), Abstract #1131
- 66. D. Elbeshausen, K. Wünemann, G.S. Collins, Icarus 204, 716 (2009)
- 67. J.M. Dahl, P.H. Schultz, Int. J. Impact Eng. 26, 145 (2001)
- 68. J.L.B. Anderson, P.H. Schultz, J.T. Heineck, J. Geophys. Res.: Planets 108(E8), 5094 (2003)
- 69. K. Wünemann, D. Elbeshausen, G.S. Collins, in *Fortieth Lunar and Planetary Science Conference* (Lunar and Planetary Institute, Houston, 2009), Abstract #1593
- 70. D.T. Britt, D. Yeomans, K. Housen, G. Consolmagno, Asteroidal density, porosity, and structure, in *Asteroids III* (The University of Arizona Press, Tucson, 2002), pp. 485–500
- 71. J.M. Greenberg, in *Asteroids, Coets, Meteors II, Proceedings of the International Meeting*, ed. by C.I. Lagerkvist, B.A. Lindblad, H. Lundstedt, H. Rickman (Uppsala, 1986), pp. 221–223
- 72. S. Sirono, J. Greenberg, Icarus **145**, 230 (2000)
- 73. K.R. Housen, K.A. Holsapple, Icarus **163**, 102 (2003)
- 74. M. Arakawa, M. Yasui, Icarus **216**, 1 (2011)
- C.R. Chapman, W.B. Mckinnon, Cratering of planetary satellites, in *Satellites* (University of Arizona Press, Tucson, 1986), pp. 492–580
- 76. J. Fink, D. Gault, R. Greeley, J. Geophys. Res.: Solid Earth 89(B1), 417 (1984)

Chapter 6 Soft Impact Cratering

In this chapter, various experiments of impact cratering performed at a laboratory scale will be reviewed. As discussed in Chap. 5, natural planetary craters have a wide variety of shapes. Very high-speed and large-scale impact events must be reproduced to fully mimic the actual planetary craters, which is evidently impossible to accomplish. Instead, low-velocity soft matter impact experiments might be helpful for understanding the morphology and fundamental processes of actual cratering on the basis of scaling concept written in Chap. 2. Moreover, a basic understanding of the cratering mechanics brings crucial and primordial knowledge to soft matter physics itself. Therefore, phenomenological studies of soft matter impacts and some of their tentative relations to the actual cratering will be exemplified in this chapter.

6.1 Liquid Impact Cratering

First, we will focus on the simplest case: Newtonian fluid impact for which some analytic and approximated calculations are possible. When a liquid droplet (or solid sphere) impinges on a liquid pool, crater formation can be observed, as illustrated in Fig. 6.1. In this picture, cavity structures such as those in Fig. 2.8 cannot be observed because the moment directly after the impact is filmed. If the impact inertia is sufficiently large, the dynamics of deep cavity formation and its collapse will be the principal processes. However, if the impact inertia is insufficient, surface cavity formation including ejecta deposition mainly dominates the cratering mechanics. Low-velocity liquid droplet impact corresponds to the latter (low inertia case). In this regime, the surface tension must be considered in addition to impact inertia and cavity potential. Although the crater's shape is immediately relaxed in the fluid impact, its maximal cavity size can be estimated using a simple calculation. Let us consider this simpler case first.

Fig. 6.1 Typical side-view snapshot of a crater produced by a steel ball impact on a water pool. Cavity and splash can be clearly observed. At the edge of the splashing rim, numerous tiny droplets are produced by the capillary-based instability

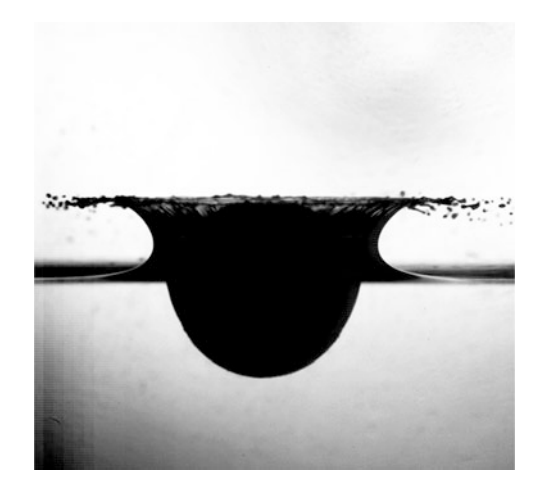
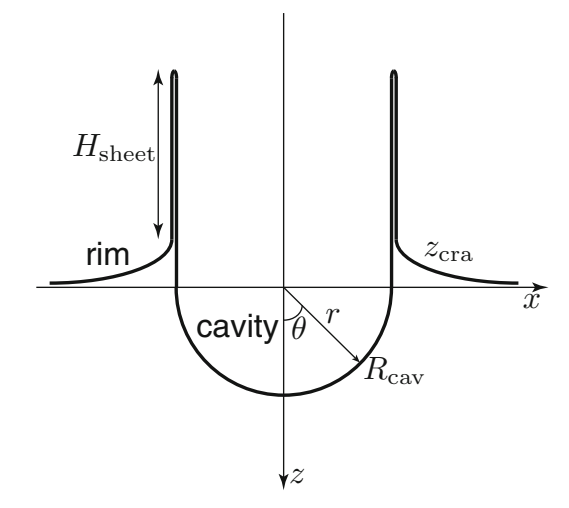


Fig. 6.2 Schematic image of the crater cavity and rim produced by a liquid-droplet impact onto a liquid pool. The crater's cross-sectional profile is denoted by $z_{\rm cra}$. The crater cavity is approximately hemispherical (with radius $R_{\rm cav}$), and the rim has a tall sheet with height $H_{\rm sheet}$ at $x = R_{\rm cav}$. The thickness of the sheet is negligibly thin



6.1.1 Geometric Energy Balance of Liquid Impact Cratering

Cavity formation by a liquid droplet (density ρ_i) impacting onto a liquid pool (density $\rho_t \simeq \rho_i$) will be considered herein. For this simple case, crater formation and its cavity shape were studied by Engel [1, 2]. The maximum cavity shape can be calculated by considering the energy balance. A schematic image of the coordinate system used in the calculation is presented in Fig. 6.2. Let $R_{\rm cav}$ be the maximal radius of the hemispherically approximated cavity, z be the vertical axis, and x be the horizontal distance from the center of the cavity. z = 0 corresponds to the surface level before the impact. We assume that the cavity has an axisymmetric shape. Then, the potential energy of the liquid cavity $E_{\rm cav}$ can be computed by considering an annular unit $z_{\rm cra} \cdot 2\pi x \cdot dx$ and its centroid height $z_{\rm cra}(x)/2$:

$$E_{\text{cav}} = \rho_t g \int_0^{R_{\text{cav}}} \frac{z_{\text{cra}}(x)}{2} \cdot z_{\text{cra}}(x) 2\pi x dx = \pi \rho_t g \int_0^{R_{\text{cav}}} z_{\text{cra}}^2(x) x dx, \tag{6.1}$$

where $z_{\text{cra}}(x)$ is the height profile of the crater at the horizontal location x. Using a relation $x^2 + z_{\text{cra}}^2(x) = R_{\text{cav}}^2$ (at $x \le R_{\text{cav}}$), E_{cav} is computed as

$$E_{\rm cav} = \pi \rho_t g \int_0^{R_{\rm cav}} \left(R_{\rm cav}^2 - x^2 \right) x dx = \frac{\pi}{4} \rho_t g R_{\rm cav}^4. \tag{6.2}$$

Here we assume that the target liquid is incompressible, i.e., the volume of the cavity is equal to the volume of the rim outside the cavity. Thus, the total volume of the crater rim should be equal to the volume of the hemisphere of radius R_{cav} :

$$\int_{R_{\text{cav}}}^{\infty} z_{\text{cra}}(x) 2\pi x dx = \frac{2}{3}\pi R_{\text{cav}}^3.$$
 (6.3)

A simple solution of z_{cra} for Eq. (6.3) is written as

$$z_{\rm cra} = \frac{R_{\rm cav}^4}{3x^3}.\tag{6.4}$$

This solution satisfies the constraint of $z_{\rm cra}(\infty) = 0$. At $x = R_{\rm cav}$, the height of the cavity becomes $z_{\rm cra} = R_{\rm cav}/3$. Moreover, Eq. (6.4) resembles the function of the ejecta thickness of lunar craters² (Eq. (5.26)). The potential energy of the rim $E_{\rm rim}$ can be obtained using Eq. (6.4) and the form of Eq. (6.1) as

$$E_{\text{rim}} = \pi \rho_t g \int_{R_{\text{cav}}}^{\infty} \frac{R_{\text{cav}}^8}{9x^6} x dx = \frac{\pi}{36} \rho_t g R_{\text{cav}}^4.$$
 (6.5)

In general, the capillary effect is not negligible in the small-scale liquid deformation. By the cratering, the generated surface area at the cavity S_{cav} is written as

$$S_{\text{cav}} = 2\pi R_{\text{cav}}^2 - \pi R_{\text{cav}}^2 = \pi R_{\text{cav}}^2.$$
 (6.6)

At $x = R_{cav}$, a vertical rim wall is generated, and its surface area S_{vw} is

$$S_{\rm vw} = 2\pi R_{\rm cav} z_{\rm cra}(R_{\rm cav}) = \frac{2}{3}\pi R_{\rm cav}^2.$$
 (6.7)

¹This assumption is called Schröter's rule.

²This is natural because the lunar craters could also roughly satisfy the volume conservation. Note that, however, the lunar crater cavity is not spherical. The relation of the rim height and the cavity radius should be different in actual lunar craters.

Outside the cavity ($x > R_{cav}$), the surface area generated by the rim S_{rim} (the area difference from the original surface) is numerically obtained as³ [1]

$$S_{\text{rim}} = 2\pi \int_0^{R_{\text{cav}}/3} x \left[1 + \left(\frac{dx}{dz_{\text{cra}}} \right)^2 \right]^{1/2} dz_{\text{cra}} - 2\pi \int_{R_{\text{cav}}}^{\infty} x dx \simeq 0.14\pi R_{\text{cav}}^2.$$
 (6.8)

Finally, the liquid sheet that produces the reverse water bell (surface closure) substantially contributes to generate the surface area S_{sheet} as⁴

$$S_{\text{sheet}} \simeq 2 \left(2\pi R_{\text{cav}} H_{\text{sheet}} \right),$$
 (6.9)

where H_{sheet} is the height of the water sheet above the rim, and the factor 2 comes from two sides of the liquid sheet. Using a typical value at the maximum cavity state $H_{\text{sheet}} \simeq 2R_{\text{cav}}$, the maximal S_{sheet} can be approximated as $8\pi R_{\text{cav}}^2$. Thus, the generated surface energy in total can be estimated by utilizing the surface tension γ_c as

$$E_{\text{surf}} = (S_{\text{cav}} + S_{\text{vw}} + S_{\text{rim}} + S_{\text{sheet}}) \gamma_c \simeq 10\pi R_{\text{cav}}^2 \gamma_c.$$
 (6.10)

On the other hand, the kinetic energy E_{kei} of an impinging liquid droplet with diameter D_i and impact velocity v_0 is expressed as

$$E_{\text{kei}} = \frac{\pi}{12} \rho_i D_i^3 v_0^2. \tag{6.11}$$

Considering that half of $E_{\rm kei}$ is used for the crater deformation, the following relation,

$$E_{\rm cav} + E_{\rm rim} + E_{\rm surf} = \frac{E_{\rm kei}}{2},\tag{6.12}$$

can be assumed at the maximal cavity state. Here we neglect other energy sinks such as sound wave emission and viscous dissipation. In fact, the sound energy radiated by the impact is considerably smaller than that radiated by an entrapped air bubble [3]. Furthermore, their acoustic energies are negligible. Moreover, the remaining half of $E_{\rm kei}$ is most likely delivered to the flow field within the target fluid by the impact (virtual mass). This factor is rather an uncertain parameter. Substituting Eqs. (6.2), (6.5), (6.10), and (6.11) into Eq. (6.12), we obtain a relation for the maximal cavity radius $R_{\rm cav,max}$,

$$\frac{5}{18}\pi\rho_t g R_{\text{cav,max}}^4 + 10\pi\gamma_c R_{\text{cav,max}}^2 - \frac{1}{24}\pi\rho_i D_i^3 v_0^2 = 0.$$
 (6.13)

³Since both terms in Eq. (6.8) diverge at $z_{\rm cra}=0$ ($x=\infty$), these values must be numerically evaluated.

⁴Note that the sheet is very thin, and its potential energy is negligible.

By solving this equation, $R_{\text{cav,max}}$ is calculated as

$$R_{\text{cav,max}} = \left[\sqrt{\left(\frac{18\gamma_c}{\rho_t g}\right)^2 + \frac{3}{20} \left(\frac{\rho_i}{\rho_t}\right) \frac{D_i^3 v_0^2}{g}} - \frac{18\gamma_c}{\rho_t g} \right]^{1/2}.$$
 (6.14)

If the impact inertia or hydrostatic force is sufficiently strong, the surface tension effect can be neglected. From Eq. (6.14), a criterion to neglect γ_c is obtained by comparing two terms in the square root:

$$\left[\left(\frac{\rho_i D_i v_0^2}{\gamma_c} \right) \left(\frac{\rho_t g D_i^2}{\gamma_c} \right) \right]^{1/4} \gg 1. \tag{6.15}$$

The first factor on the left-hand side of Eq. (6.15) corresponds to the Weber number, and the second factor indicates the balance between the hydrostatic force and surface tension. When this criterion is fulfilled, the maximal cavity size is considerably greater than $\sqrt{18\gamma_c/\rho_t g} \simeq 4.2\lambda_c$, where λ_c represents the capillary length (Eq. (2.99)). In this large inertia regime, a simple scaling relation is derived as

$$R_{\text{cav,max}} \sim \left[\left(\frac{\rho_i}{\rho_t} \right) \frac{D_i^3 v_0^2}{g} \right]^{1/4}. \tag{6.16}$$

Because the potential energy is solely considered in this limit, Eq. (6.16) has a similar form as Eq. (4.2); the crater's cavity size is scaled as $E_{\rm kei}^{1/4}$. In contrast, the capillary effect plays an important role for a small-cavity and low-inertia regime. Under such a condition, Eq. (6.14) should be used instead of Eq. (6.16) to estimate the cavity dimension.

6.1.2 Cavity Growth Dynamics of Liquid Impact Cratering

To discuss the dynamics of cavity growth, the kinetic energy and energy dissipation of the deformed target should be considered. The potential and surface energies by the cavity of R_{cav} were already computed in the previous subsection. Here we assume that the flow field in the target is irrotational and incompressible. Then, the flow velocity \boldsymbol{u} can be defined by the velocity potential Φ_f as $\boldsymbol{u} = \nabla \Phi_f$ because of the irrotational condition $\nabla \times \boldsymbol{u}$, and the velocity potential satisfies $\nabla^2 \Phi_f = 0$ (Laplace equation) because of the incompressibility (Eq. (2.26)). A well-known solution of the Laplace equation is

$$\Phi_f = \frac{A_{\text{cav}} R_{\text{cav}}}{r} \cos \theta, \tag{6.17}$$

where A_{cav} is a constant depending on the boundary conditions. The spherical coordinate is used to discuss the cavity growth dynamics (Fig. 6.2). The zenith angle

 θ is measured from the downward vertical line. The origin is defined at the impact point, and the distance from the origin is denoted as r. Thus, the x axis corresponds to r at $\theta = \pm \pi/2$. Then, the radial and angular components of the velocity are computed from $u_r = -\partial \Phi_f/\partial r$ and $u_\theta = -(1/r)(\partial \Phi_f/\partial \theta)$, respectively, as

$$u_r = \frac{A_{\text{cav}} R_{\text{cav}}}{r^2} \cos \theta, \tag{6.18}$$

$$u_{\theta} = \frac{A_{\text{cav}} R_{\text{cav}}}{r^2} \sin \theta. \tag{6.19}$$

Therefore, the absolute value of the flow velocity u = |u| is written as

$$u = \frac{A_{\text{cav}}R_{\text{cav}}}{r^2}. (6.20)$$

This *u* becomes zero at $r = \infty$, as expected. At the boundary of the cavity ($r = R_{\text{cav}}$), *u* must be dR_{cav}/dt . Then, A_{cav} is calculated using Eq. (6.20) as

$$A_{\text{cav}} = R_{\text{cav}} \frac{dR_{\text{cav}}}{dt}.$$
 (6.21)

Substituting Eq. (6.21) into Eqs. (6.17) and (6.20), we obtain

$$\Phi_f = \frac{R_{\text{cav}}^2}{r} \frac{dR_{\text{cav}}}{dt} \cos \theta, \tag{6.22}$$

and

$$u = \frac{R_{\text{cav}}^2}{r^2} \frac{dR_{\text{cav}}}{dt}.$$
 (6.23)

The kinetic energy of the target fluid E_{target} is computed using the velocity potential as follows [4]⁵:

$$E_{\text{target}} = -\frac{\rho_t}{2} \int_{S} \Phi_f \frac{\partial \Phi_f}{\partial r} dS, \qquad (6.24)$$

where $\int_S dS$ denotes the surface integral at the cavity. This form is natural because the integral can be dimensionally regarded as $\rho_t \int u l u_r dS$. Using Eq. (6.22), E_{target} at $r = R_{\text{cav}}$ is calculated as

⁵Specifically, $2E_{\text{target}}/\rho_t$ can be computed as $\int_V (\nabla \Phi_f)^2 dV = \int_V [\nabla \cdot (\Phi_f \nabla \Phi_f) - \Phi_f \nabla^2 \Phi_f] dV = \int_S \Phi_f \nabla \Phi_f \cdot n dS = \int_S \Phi_f v_n dS$, where v_n is the outward normal component of velocity at the surface S. Here, we use Gauss' theorem and irrotational condition $\nabla^2 \Phi_f = 0$.

$$E_{\text{target}} = -\frac{\rho_t}{2} \int \left[\frac{R_{\text{cav}}^2}{r} \frac{dR_{\text{cav}}}{dt} \cos \theta \right] \cdot \left[-\frac{R_{\text{cav}}^2}{r^2} \frac{dR_{\text{cav}}}{dt} \cos \theta \right] dS$$

$$= \frac{\rho_t}{2} \int_0^{2\pi} R_{\text{cav}} \left(\frac{dR_{\text{cav}}}{dt} \right)^2 \cos^2 \theta \cdot 2\pi R_{\text{cav}} \sin \theta \cdot R_{\text{cav}} d\theta$$

$$= \frac{\pi \rho_t R_{\text{cav}}^3}{3} \left(\frac{dR_{\text{cav}}}{dt} \right)^2. \tag{6.25}$$

The kinetic energy outside the crater cavity E_{out} is computed as

$$E_{\text{out}} = \frac{\rho_t}{2} \int_{R_{\text{cav}}}^{\infty} 2\pi r z_{\text{cra}} \langle u \rangle^2 dr$$
$$= \frac{\pi \rho_t R_{\text{cav}}^3}{60} \left(\frac{dR_{\text{cav}}}{dt} \right)^2. \tag{6.26}$$

Here we use Eq. (6.4) with x = r and assume $\langle u \rangle \simeq (R_{\rm cav}^2/r^2)(dR_{\rm cav}/dt)$. $E_{\rm out}$ is considerably smaller than $E_{\rm target}$; $E_{\rm out}/E_{\rm target} = 1/20$.

The total dissipation rate D_{rf} by viscosity η is given by [4]

$$D_{rf} = -\eta \int_{S} \frac{\partial u^2}{\partial r} dS. \tag{6.27}$$

Considering that $\partial u/\partial r$ corresponds to the strain rate, D_{rf} indeed becomes $\eta u \dot{\gamma} S$, which corresponds to the energy dissipation rate. Using Eq. (6.23) (and performing a calculation similar to Eq. (6.25)), Eq. (6.27) can be integrated at $r = R_{\text{cav}}$ as

$$D_{rf} = 8\pi \eta R_{\text{cav}} \left(\frac{dR_{\text{cav}}}{dt}\right)^2. \tag{6.28}$$

Thus, the dissipated energy E_{diss} is given as

$$E_{\rm diss} = 8\pi \eta \int_0^t R_{\rm cav} \left(\frac{dR_{\rm cav}}{dt'}\right)^2 dt'. \tag{6.29}$$

Finally, the cavity growth dynamics should be governed by

$$E_{\text{cav}} + E_{\text{rim}} + E_{\text{surf}} + E_{\text{target}} + E_{\text{out}} + E_{\text{diss}} = \frac{E_{\text{kei}}}{2}.$$
 (6.30)

Here the simple assumption that half of $E_{\rm kei}$ is spent on target deformation is employed again similar to the previous static calculation case. Therefore, this relation corresponds to a modification of Eq. (6.12) by considering the kinetic energy and viscous dissipation at the cavity surface. Thanks to this improvement, the time-dependent dynamics of cavity growth can be estimated. Note that, however,

the kinetic energies and dissipation considered in Eq. (6.30) are computed mainly at the surface of the cavity and rim; $r=R_{\rm cav}$ and $z_{\rm cra}(x)$. Bulky fluid motion by the impulsive momentum transfer, which may be represented by the virtual mass, was still not taken into account. The virtual mass could be responsible for the other half of $E_{\rm kei}$; $E_{\rm out}$ is insufficient to consider the impulsive virtual mass effect. Unfortunately, Eq. (6.30) is not analytically solvable. Because $E_{\rm diss}$ involves the temporal integral of $dR_{\rm cav}/dt$, Eq. (6.30) becomes an integrodifferential equation. In Ref. [2], therefore, Eq. (6.30) was numerically solved. The researcher observed that the numerical solution can explain the experimental results [2]. In the aforementioned discussion, some unobvious assumptions were used, e.g., $H_{\rm sheet} \simeq 2R_{\rm cav}$ and $E_{\rm kei}/2$ for the deformation. To analyze the various cratering events, numerical factors for such nontrivial assumptions must be tuned appropriately.

The model discussed above is based on the energy balance and some assumptions such as incompressibility and a hemispherical cavity shape. While they appear to be too simple to fully describe the actual cratering events, laboratory experiments can be roughly explained using the model [1, 2]. The detailed dynamics of the cavity growth has also been investigated using other theoretical and numerical methods [5–7]. Note that the shock wave propagation is not involved in the model. Therefore, this model is relevant to relatively low-velocity impacts. It might be difficult to compare this model directly with planetary craters. Moreover, for actual planetary craters, the final crater shape is evidently different from the maximum cavity shape created by the impact. The cavity shape is more parabolic than spherical in actual planetary craters. For the sake of simplicity, we have neglected some complex factors such as rheological properties (elasticity or plasticity), instability at the perimeter of the rim, and cavity collapse jetting. These factors might affect the crater shape as well. Some of these complex effects will be partly discussed in what follows in this chapter.

Crater formation by a solid sphere's impact on a viscoplastic target was also investigated experimentally [8]. Carbopol gels showing Herschel-Bulkley model rheology (Eq. (3.7)) were employed as the targets, and various spheres were used as impactors. The measured crater diameter does not monotonically depend on the impact inertia. The experimental results indicate that the crater diameter D_c is almost constant in the low Reynolds number regime, $R_e \leq 10$. Then, D_c slightly decreases until $R_e \simeq 40$. After that, D_c increases in the large R_e regime, $R_e > 40$. In this large R_e regime, the central peak structure can be observed. Because the Herschel-Bulkley viscoplastic fluid has a yield stress, it can sustain a complex crater shape after the dissipation of the impact inertia. The cavity pinch-off depth was also measured in this experiment and was simply scaled by R_e . Up to $R_e \simeq 10$, the cavity pinch-off depth is almost constant before beginning to increase in the large R_e regime.

6.2 Granular Impact Cratering

If the granular matter is used as a target, the crater shape clearly remains after the impact. One can readily measure the dimensions of the crater using simple experiments. However, the quantitative characterization of the crater shape is not so easy because the governing equations for dense granular deformation and flow have not yet been established. Thus, the scaling method is frequently used for the characterization of granular crater morphology. In this and following sections, such scaling-based studies for granular impact cratering are reviewed.

6.2.1 Scaling of Granular Impact Craters

The crater shape created by a solid sphere's impact onto a granular target has been studied. In Sect. 4.1, the drag force and resultant penetration depth were the main focus. In this section, the entire crater morphology including the crater diameter and rim structure will be discussed.

Vertical impact cratering Uehara et al. performed a low-velocity granular impact experiment with a free-fall solid impactor. These researchers obtained scaling relations for the crater diameter D_c and the penetration depth d [9, 10]. The obtained relations are written as

$$D_c \sim \left(\frac{1}{\mu_f}\right)^{1/2} \left(\frac{\rho_i}{\rho_t}\right)^{1/4} D_i^{3/4} H^{1/4},$$
 (6.31)

$$d \sim \frac{1}{\mu_f} \left(\frac{\rho_i}{\rho_t}\right)^{1/2} D_i^{2/3} H^{1/3},\tag{6.32}$$

where μ_f is the frictional coefficient of the target granular matter and H is the total drop distance (= free-fall distance h + penetration depth d), i.e., H is proportional to the total released potential energy. For shallow penetration ($h \gg d$), the released potential energy of the impactor $(\pi/6)\rho_iD_i^3gH$ can be approximated by its kinetic energy $E_{\rm kei} = (\pi/12)\rho_iD_i^3v_0^2$. Then, the form of Eq. (6.31) is quite similar to Eq. (6.16). However, the form of the penetration depth scaling is written differently, and this form is essentially the same as that of Eq. (4.3). In fact, Walsh et al. reported a 1/4 power-law scaling for both the crater diameter D_c and depth D_h [11]. The final crater depth D_h and penetration depth d are slightly different. The modification process might be a reason for the different scaling. In this chapter, the crater depth D_h should be emphasized rather than the penetration depth d.

Using a laser profilometry system, the crater shapes produced by the granular impact were precisely measured [12]. The parameters used in Ref. [12] are $D_i = 3.95-19.26 \,\mathrm{mm}$, $\rho_i = 2.5-15 \times 10^3 \,\mathrm{kg/m^3}$, $v_0 = 0.6-4.4 \,\mathrm{m/s}$, and $D_g = 106 \sim 212$, $180 \sim 300$, and $200 \sim 425 \,\mu\mathrm{m}$. According to the experimental result, the crater shape obeys the scaling

$$D_c \propto E_{\rm kei}^{0.226} D_i^{0.22},$$
 (6.33)

$$D_h \propto E_{\text{kei}}^{0.210} \rho_i^{-0.264}$$
. (6.34)

	D_c	D_h	Nonporous	Sand
μ	0.5	0.67	0.55	0.41
ν	0.25	-0.086	0.4	0.4

Table 6.1 Characteristic exponents μ and ν of the point source measure based on Eqs. (6.35) and (6.36) and Refs. [13–15]

These scaling relations are different from Eqs. (6.16), (6.31), and (6.32). Although the scaling exponents for $E_{\rm kei}$ are close to 1/4, nontrivial D_i or ρ_i dependences are added in the scaling relations. Put another way, D_c and D_h cannot be scaled solely by $E_{\rm kei}$, which indicates that the concept of point source measure (Sect. 5.5.1) might be useful for understanding the low-velocity granular impact cratering. The point source measure description might allow us to obtain meaningful scaling variables for D_c and D_h instead of combinations of $E_{\rm kei}$ and D_i or ρ_i . Using the relation $E_{\rm kei} \sim \rho_i D_i^3 v_0^2$, Eqs. (6.33) and (6.34) are rewritten approximately as

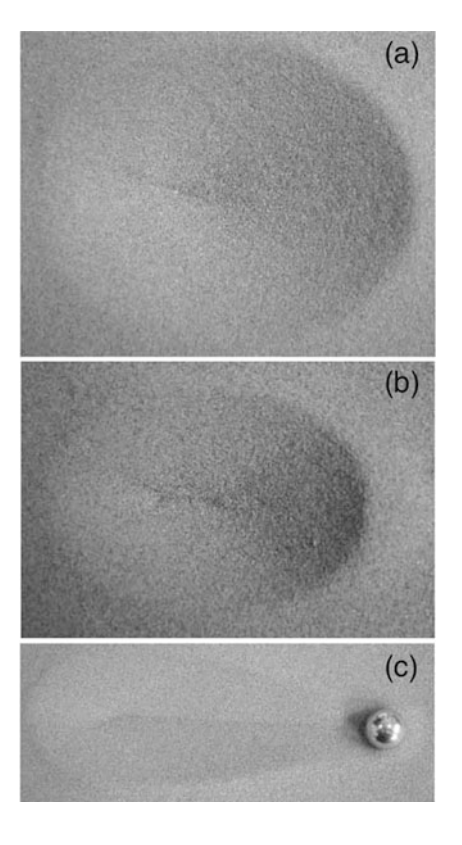
$$D_c \propto \left(\rho_i^{0.25} D_i v_0^{0.50}\right)^{0.90},$$
 (6.35)

$$D_h \propto \left(\rho_i^{-0.086} D_i v_0^{0.67}\right)^{0.63}.$$
 (6.36)

By considering a definition of the point source measure (Eq. (5.43)), the characteristic exponents μ and ν can be computed for each equation. In Table 6.1, the computed values are listed, and these values are compared with hypervelocity impact results [13–15]. Unfortunately, the values are very different from each other. In particular, the exponent ν exhibits significantly small values in D_h scaling. In fact, the definitions of D_c and D_h are slightly different among Refs. [9, 11–15]. However, the difference is very minor and would not affect the scaling result. A difference on the order of v_0 is rather significant among these studies. From the current experimental results, it is difficult to obtain quantitative relations among μ , ν , and other experimental parameters in the low-velocity granular impact cratering. Additionally, the difference in the scaling exponents between D_c and D_h is puzzling. The negative ν for D_h indicates that a shallower crater depth is caused by a denser impactor's impact. Because the absolute value of ν in D_h scaling is very small, the ρ_i effect on D_h is very weak. In the experiment of Ref. [12], only the craters in which the impactor was completely buried were measured, i.e., shallow craters were not involved in the analysis. Thus, this result might only imply that the crater depth is almost independent of ρ_i once the impactor penetrates deep into the granular target.

More importantly, for the low-velocity granular impact, the cross-sectional profile of the crater's cavity could be approximated by a hyperbola rather than a parabola [12]. The planetary-scale simple craters have nearly parabolic cross sections, and the liquid impact crater's cross sections are approximated by a spherical shape. All of these curves are different types of quadratic curves. Unfortunately, we have not yet understood what determines the type of crater's cavity cross section.

Fig. 6.3 Typical crater shapes produced by the low-velocity oblique impact of a steel sphere onto a loose granular bed [16]. (a) A simple crater is produced by a large θ_{imp} impact. (b) An elliptic crater is observed in the middle range of the impact angle: $40^{\circ} \le \theta_{\rm imp} \le 70^{\circ}$. (c) A triangle crater is created by the low-angle impact $\theta_{\rm imp} < 40^{\circ}$. With kind permission of The European Physical Journal (EPJ)



Oblique impact cratering Crater shapes created by a low-velocity oblique impact on a loose granular bed were also studied experimentally [16]. A steel sphere $(D_i = 4-18.3 \,\mathrm{mm})$ was dropped along an oblique rail groove onto a natural quartz sand bed. As a result of the nearly vertical impact $(\theta_{\mathrm{imp}} \geq 70^\circ)$; see Fig. 4.13 for the definition of θ_{imp}), a simple crater was formed (Fig. 6.3a). When the impact angle θ_{imp} was in the middle range: $40^\circ \leq \theta_{\mathrm{imp}} \leq 70^\circ$, an elliptic crater was observed (Fig. 6.3b). In the very small impact angle regime $(\theta_{\mathrm{imp}} < 40^\circ)$, the crater's shape becomes an acute triangle or a tadpole (Fig. 6.3c). The critical angle 40° is slightly larger than that for the granular drag force modeling and planetary Π -groups analysis (Sects. 4.1.8 and 5.5.3). In the drag force modeling, the critical angle, above which the simple drag force law is applicable, was $\theta_{\mathrm{imp}} \simeq 30^\circ$. The same critical angle was observed in the analysis of the crater efficiency scaling. The morphological variation in oblique granular impact cratering originates from the elongation of the cavity shape due to the horizontal momentum of the impactor. The long axis length D_l and orthogonal width D_w of the crater were measured and scaled as

$$D_l \sim D_i^{a_l} h^{1-a_l},$$
 (6.37)

$$D_{w} \sim D_{i}^{a_{w}} h^{1-a_{w}}, \tag{6.38}$$

where D_i , h, a_l , and a_w are the impactor's diameter, its traveling distance along the rail groove $(0.1 \le h \le 2 \text{ m})$, and two characteristic exponents, respectively. The exponent a_l is almost constant, $a_l \simeq 0.75$ at $\theta_{\text{imp}} \ge 40^{\circ}$. For low-angle impacts $(\theta_{\text{imp}} < 40^{\circ})$, a_l becomes an increasing function of θ_{imp} . In contrast, a_w becomes a monotonically decreasing function of θ_{imp} . In the large θ_{imp} regime, the constant value $a_l = 0.75$ is consistent with the scaling of Eq. (6.31). For the low-angle impact, the horizontal rolling motion after the impact almost determines the length of the long axis D_l . In contrast, D_w is mainly determined by the impact inertia, which corresponds to the released potential energy. By considering that h is directly related to the impact velocity as $v_0 \simeq \sqrt{2gh}$, the tendency of the abovementioned experimental result is qualitatively understandable. However, an adequately quantitative discussion for the oblique granular impact cratering remains lacking.

6.2.2 Ejecta Splashing

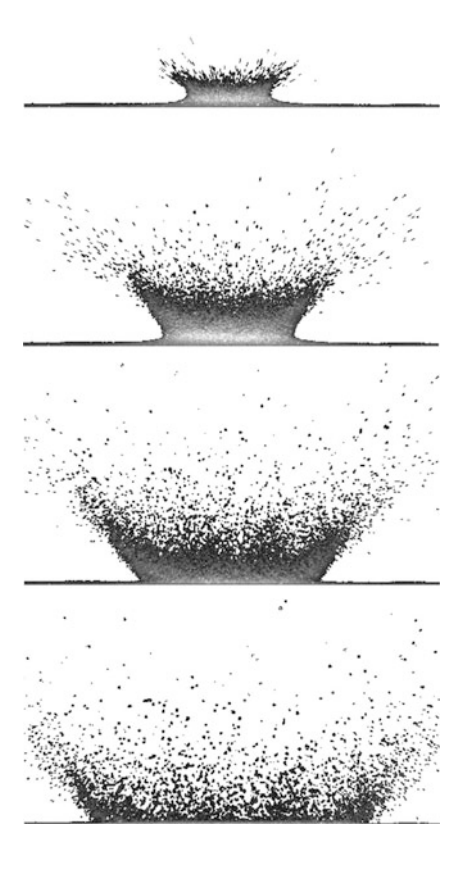
Ejecta splashing and associated corona formation were also studied in low-velocity granular impact experiment. Morphology and kinematic information of the ejecta curtain were experimentally investigated by Deboeuf et al. [17]. These researchers dropped a steel sphere ($D_i = 10.3$ –19 mm and $\rho_i = 7.8 \times 10^3 \, \text{kg/m}^3$) onto a glassbead bed ($D_g = 0.4 \pm 0.1 \,\mathrm{mm}$) with impact velocity $v_0 = 1-4 \,\mathrm{m/s}$. The acquired side-view images sequence is shown in Fig. 6.4. These researchers observed that the slope of the ejecta curtain is almost independent of the impact velocity and time; the angle is a constant of approximately 56°, which is slightly steeper than the angle generally observed in hypervelocity impacts (45°) [18–20]. Indeed, the angle of the grains' ejection depends on the ejection point, time, impact velocity, and impact angle. The precision is not sufficient to discuss the detailed parameter dependences of the ejecta curtain angle. However, the equality between the grains ejection angle and ejecta curtain angle is frequently assumed. According to the Zmodel (Sect. 5.3.2), a 56° ejecta splashing corresponds to 3 < Z < 4. The shape of the ejecta curtain can be generally explained by the ballistic free-fall motion of grains with an assumption of the equality between the ejection angle and ejecta curtain angle.

Deboeuf et al. also measured the effective restitution coefficient of the granular impact. From the experimental data, it was revealed that the average kinetic energy of each ejected grain $E_{\rm ej}=m_g v_{\rm ej}^2/2$ is scaled by the impactor's kinetic energy $E_{\rm kei}=m_i v_0^2/2$ as

$$E_{\rm ej} = 0.56 \times 10^{-7} E_{\rm kei}^{0.37 \pm 0.05},$$
 (6.39)

where m_g and $v_{\rm ej}$ are the mass and characteristic ejection velocity of each grain, and m_i is the mass of the impactor. Note that $v_{\rm ej}$ was effectively computed from the motion of the ejecta curtain under the assumption that the ejection angle and

Fig. 6.4 Side-view images of the granular ejecta curtain produced by the impact of a steel sphere ($D_i = 13.5 \text{ mm}$, $\rho_i = 7.8 \times 10^3 \text{ kg/m}^3$, and $v_0 = 2.45 \text{ m/s}$). The target granular bed consists of glass beads with $D_g = 0.4 \pm 0.1 \text{ mm}$. Images were taken every 30 ms (Reprinted with permission from Ref. [17]. Copyright 2009 by American Physical Society)



angle of ejecta curtain are identical. For the number of ejected grains, $n_{\rm ej}$, a simple relation $n_{\rm ej}=7.2\times10^5E_{\rm kei}^{0.70\pm0.05}$ was obtained by considering the grain number conservation between the crater cavity and ejecta. Note that the numerical prefactors in these scaling equations are not dimensionless. The total ejected (restituted) kinetic energy $E_{\rm ej,total}$ is approximately estimated as $E_{\rm ej,total}=n_{\rm ej}E_{\rm ej}\simeq0.031E_{\rm kei}$. Thus, the effective restitution coefficient by splashing can be computed as

$$\epsilon_{re} = \sqrt{\frac{E_{\rm ej,total}}{E_{\rm kei}}} \simeq 0.18.$$
 (6.40)

Ejecta splashing from a thin $(1-10 \,\mathrm{mm}$ thickness) glass-bead layer $(D_g = 65-600 \,\mu\mathrm{m})$ impacted by a steel sphere $(D_i = 2-14 \,\mathrm{mm}, \,v_0 \leq 1.2 \,\mathrm{m/s})$ was also studied [21]. The outer radius of the ejecta curtain was carefully measured in this experiment. The researchers observed that the radius increased rapidly to the maximal value and then slightly decreased. This partial closing of the ejecta curtain occurred at a later stage of the cratering. The timescale of this closing is considerably longer than that of the initial cavity opening. The reason for this partial closing might be a negative pressure by Bernoulli's principle. The researchers

also revealed that the shear strain rate $\dot{\gamma}$ calculated from the ejecta velocity profile can be explained by the characteristic timescale as $\dot{\gamma} = \sqrt{g/D_g}$. Although these findings are interesting, it is not clear whether these characteristics originate from the thinness of the target layer. The universality and robustness of these findings should be checked with care.

Using a very high-speed imaging technique, Marston et al. observed granular impact splashing [22]. The highest frame rate they used was 100,000 fps. These researchers focused on the very initial stage of the splashing using this very high-speed imaging. A steel sphere with $D_i = 20-50\,\mathrm{mm}$ was impinged on various grain beds with $v_0 = 0.78-16\,\mathrm{m/s}$. They observed that high-speed grains were ejected at the lowest ejection angle during the very early stage (before the development of the ejecta curtain). The grains ejection velocity $v_{\rm ej}$ was observed to be up to five times v_0 :

$$\max\{v_{\rm ej}\} \simeq 5v_0. \tag{6.41}$$

The ejection velocity $v_{\rm ej}$ was directly measured by the high-speed imaging. Perhaps, such a very high-speed jetting⁶ might be the origin of the ray crater structure (Fig. 5.4), although the number of grains ejected by the jetting is very limited. For this very fast jetting, the normalized ejection velocity $v_{\rm ej}/v_0$ was scaled by the normalized time as $v_{\rm ej}/v_0 \sim (tv_0/D_i)^{-1}$. This relation indicates that the ejecta grains released at the late stage have slower ejection velocities than those released at the early stage. The scaling relation between the kinetic energy of ejecta $E_{\rm ej}$ and that of impactor $E_{\rm kei}$ is written as

$$E_{\rm ej} \propto E_{\rm kei}^{\kappa_e},$$
 (6.42)

where κ_e is a characteristic exponent that depends on the range of $E_{\rm kei}$. The scaling shows a crossover at $E_{\rm kei} \simeq 5\,\rm J$. At $E_{\rm kei} < 5\,\rm J$, κ_e is approximately 1.3; however, it is approximately 0.4 at large $E_{\rm kei}(>5\,\rm J)$. While the scaling of Eq. (6.39) is close to κ_e in the large $E_{\rm kei}$ regime, the experimental condition for Eq. (6.39) is on the order of $E_{\rm kei} \simeq 10^{-1} - 10^{-2}\,\rm J$ [17]. This $E_{\rm kei}$ regime corresponds to the small one ($E_{\rm kei} < 5\,\rm J$) in which κ_e should be 1.3. Using microgravity experiments, Colwell et al. obtained a relation $E_{\rm ej} \sim E_{\rm kei}$ using the low-velocity impact on granular targets ($v_0 = 0.2 - 2.3\,\rm m/s$, $E_{\rm kei} \le 10^{-2}\,\rm J$). Moreover, another scaling law, $E_{\rm ej} \propto E_{\rm kei}^{1/4}$, was derived for the comparative D_i and D_g case (Eq. (4.43)). Currently, it is difficult to conclude the energy scaling form for the granular impact ejecta. The situation is, unfortunately, somewhat confusing.

For the fine-grains target case ($D_g = 31 \,\mu\text{m}$), the propagation velocity of the ejecta curtain sheet v_{curt} is approximated as $v_{\text{curt}} = 2v_0$ [22]. This behavior is somewhat similar to that of the fluid target splashing.

⁶This jetting is different from the jet induced by the cavity collapse. The jet by cavity collapse is discussed in the next section.

The ejecta radius at its neck point $r_{\rm ej}-r_{\rm em}$ is scaled by the normalized time $(t-t_{\rm em})v_0/D_i$ as

$$\frac{r_{\rm ej} - r_{\rm em}}{D_i} \sim \left[(t - t_{\rm em}) \frac{v_0}{D_i} \right]^{\beta_{\rm ej}}, \tag{6.43}$$

where $r_{\rm ej}$, $r_{\rm em}$, and $t_{\rm em}$ are the radius of the ejecta curtain, that at the emergent state, and its emergent time, respectively, i.e., $r_{\rm ej}(t_{\rm em})=r_{\rm em}$. The characteristic exponent $\beta_{\rm ej}$ lies in the range $0.45 \leq \beta_{\rm ej} \leq 0.75$ [22]. In particular, the target made of loosely packed small grains results in $\beta_{\rm ej}=0.49$ which is similar to the liquid-droplet impact onto a liquid film case [23]. Namely, the impact on the granular bed composed of loosely packed small grains is similar to the fluid impact in terms of ejecta splashing. The consistency between Eq. (6.43) and the late-stage receding of the ejecta curtain reported in Ref. [21] is unclear. The target thickness might be an important parameter for the development of the ejecta curtain.

The collapse of the surface cavity made of liquid impact can be observed as a reverse water bell (e.g., Fig. 2.8). This collapse is induced by the surface tension and negative pressure that originated from Bernoulli's principle. Such a pressure gradient causes ambient air flow and air drag to the ejecta curtain. For the granular target case, the smaller grains are affected by air drag more substantially than the larger grains. As a result, the collapse tendency of the granular ejecta curtain can be observed to be more significant in the smaller grain target than in the larger grain target [24]. If the ambient gas density is increased, this cavity collapse can be clearly observed [25]. For tiny grains, this negative pressure may affect the jet formation as well as ejecta curtain, as discussed in the next section.

6.3 Impact-Induced Granular Jet Formation

The impact-induced jet formation due to the cavity collapse can be observed even in granular impacts. For liquid impacts, Worhington performed pioneering works on this phenomenon [26–28]. Thus, the jet is called the Worthington jet. In a viscous liquid case, the morphology of the Worthington jet has been evaluated using some parameters such as density, viscosity, surface tension, and gravity [29]. Similar jet formation was observed in the granular impact [30, 31]. In Ref. [31], a lead sphere ($D_i = 13.4\,\mathrm{mm}$, $\rho_i = 11.5 \times 10^3\,\mathrm{kg/m^3}$) was dropped onto a glass-bead layer with $D_g = 0.08$, 0.118, or 0.176 mm. According to the experimental result, the jet height is an increasing function of the impact velocity and a decreasing function of the grain size D_g . The jet height $h_{\rm jet}$ was scaled as [31] $h_{\rm jet}/D_i \sim [(v_0/\sqrt{gD_i})(D_i/D_g)^2]^{1.2}$. Although this scaling can be approximately obtained by slightly improving the energy balance between the kinetic energy of the impactor $\rho_i D_i^3 v_0^2$ and the potential energy of the jet $\rho_t g D_g^2 h_{\rm jet}^2$ (and multiplying the factor D_i/D_g), it actually cannot universally explain the $h_{\rm jet}$ behaviors of various D_i [25].

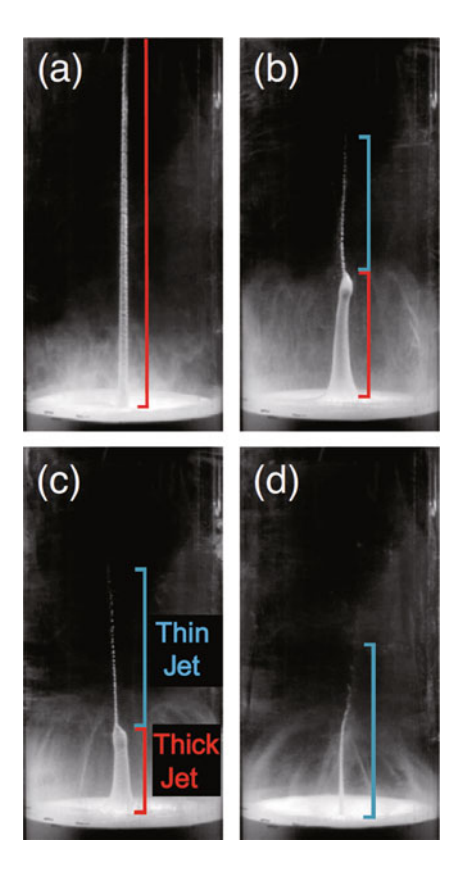
Lohse et al. observed that $h_{\rm jet}$ can exceed the release height of the impactor under some impact conditions [32, 33]. To produce such an extraordinary tall jet, the target grains must be very small. Specifically, fine sand (nonspherical grains with $D_g=40\,\mu{\rm m}$) was used in the experiment. Additionally, the grains were fluidized by the air flow before the impact. The packing fraction achieved using this procedure was approximately 0.41. This very loose sand is called dry quicksand. To make a remarkable granular jet, a very loose granular target (similar to dry quicksand) consisting of tiny grains and an air-bubble cavity formed by the impact are necessary. In particular, the grain diameter D_g should be on the order of $10^{-2}\,{\rm mm}$ to satisfy the requirements. As discussed in Sect. 3.9.2, the gravity and air drag are comparable for such small grains ($D_g=10^{-2}\,{\rm mm}$) under atmospheric conditions. Therefore, the ambient air would play a role in the granular jet formation. In the experiment, granular eruption presumably caused by an air bubble rising in the granular target was also observed. Rayleigh-type cavity development [33, 34] was applied to explain cavity pinch-off dynamics.

The granular jet height is reduced under vacuum condition [35], which is somewhat counterintuitive because the air drag is usually a source of dissipation. The higher jet can be simply expected under the vacuum condition. Nevertheless, the vacuum condition suppresses the granular jet formation. Moreover, the twostage jet structure was observed in vacuum experiments (Fig. 6.5). In the two-stage jet, the thin jet emerges at the top of a thick jet with a sharp shoulder. From Fig. 6.5, one can observe that the thick-jet height is an increasing function of the ambient pressure. The initial tip velocity of the thick jet v_{iet} depends on the ambient air pressure p as $v_{\rm iet} \propto (p - p_{\rm crit})^{1/2}$, where $p_{\rm crit}$ is approximately 5.7 kPa under which the thick jet does not appear [35]. To explain the pressure-dependent jet height, Royer et al. considered that it is difficult to compress the entire granular bed under the high ambient pressure condition, while the granular bed can be easily compressed beneath the impactor under the low-pressure condition. Then, the energy is rapidly dissipated by the friction due to the grain compaction. Therefore, the resultant jet height is reduced by this large dissipation in the low-pressure regime [25].

In addition, these researchers experimentally demonstrated that the jet formation process does not depend on the density of the interstitial gas [25]. Using a heavy interstitial gas of SF_6 , similar experiments were performed with a fixed ambient pressure. The granular jet formation did not show significant differences from the case of usual air. Although the density of SF_6 is approximately five times greater than air, this density difference does not affect the jet formation. The only difference caused by the heavy interstitial gas was the shape of the corona. Because the negative pressure due to Bernoulli's principle is pronounced by the large density of the interstitial gas, the corona tends to shrink rapidly and collapse (forming a reverse water-bell structure). Then, the jet height is interrupted by the collapsed corona. However, other behaviors in the granular jet formation were not affected by the interstitial gas density.

Another research group claims a different scenario for the granular jet formation. Using systematic experiment, the Twente group (Caballero et al. [36] and von

Fig. 6.5 Granular jets produced by the impact of a steel sphere ($D_i = 22.5 \text{ mm}$) at various ambient pressures: (a) 101 kPa, (b) 26.7 kPa, (c) 13.3 kPa, and (d) 2.6 kPa. The release (free-fall) height of the sphere is 1.1 m, and the target grains are glass beads with $D_g \simeq 53 \,\mu\text{m}$. Clear two-stage jet formation can be observed in (b) and (c) (Reprinted with permission from Ref. [25]. Copyright 2008 by American Physical Society)



Kann et al. [37]) unveiled the effects of ambient air and the container wall on granular jet formation. These researchers observed that the impactor's penetration depth was reduced under low ambient pressure. The reduced jet height and impactor's penetration depth exhibited a linear relation in the low-pressure regime: $p \le 40$ kPa. In addition, the frictional drag parameter k in Eq. (4.4) was computed from the experimental data in the low v_0 (F_r < 80) regime by neglecting the inertial term. The obtained frictional parameter k depended on the ambient pressure p as $k \propto p^{-1/2}$, which indicates that the solid-like (frictional) property of the target granular bed is reduced by the ambient air pressure effect. These researchers consider that the compressed air in front of the impactor fluidizes the granular bed. Then, the effective drag force (particularly the frictional drag) is weakened by this compressed ambient air pressure effect. Therefore, deeper penetration and vigorous jet formation are simultaneously achieved by the larger cavity collapse in a relatively high-ambient-pressure environment. Furthermore, if the air pressure is very low, the cavity shape is hardly maintained. Thus, the eruption cannot be observed in the lowpressure regime. Although this scenario is plausible for loose targets, the penetration depth in the low ambient pressure regime can be greater in an initially dense target, as described in Sect. 4.1.7 (Fig. 4.12). Although this trend is opposite to the above scenario, the jet formation cannot be observed in the impact of such a very dense target. The effect of ambient air for the granular jet formation remains a matter of debate.

This group further tested the effect of the container size (side wall). The jet height increased when a wider container was used.⁷ The reason for the enhanced jet formation in the wider container can be explained by the deeper and faster cavity closure. The cavity closure depth increases for the wider container. In addition, the cavity closure time is decreased mainly because of the larger closing speed of the cavity most likely due to the large hydrostatic pressure. Thus, the resultant jet height increases in a wider container.

Marston et al. studied the effect of the packing fraction ϕ on the granular jet formation [38]. The experimental results suggested that the jet height was a slightly decreasing function of ϕ , particularly in the small ϕ regime; however, the jet height is almost independent of ϕ in the relatively large ϕ regime. In addition, a two-stage jet was only observed in the small ϕ regime. There is a certain critical packing fraction above which the two-stage jet does not emerge. Moreover, the size of the impactor does not affect the onset of the two-stage jet formation. The important factors for the onset of the two-stage jet are the appropriate ambient pressure level and low packing fraction.

The physical mechanism of the two-stage jet formation has not yet been completely solved. The first jet structure is formed by the closure of an impact-induced cavity. For the second jet, its origin remains controversial. The second jet might originate from the deep secondary cavity closure or it may come from the pressure of the rising cavity.

Although the impressively pronounced jet is produced only by the loose granular target, a certain degree of jet formation can be observed even in the usual ($D_g \sim 10^{-1}$ mm) granular target impact, depending on its experimental conditions. The jet formation affects the final crater shape to a certain extent. For instance, Walsh et al. reported some types of crater shapes modified by the jet formation (Fig. 6.6) [11]. In Fig. 6.6a, one can observe a simple bowl-shaped crater. This crater shape appears qualitatively similar to planetary-scale simple craters (Fig. 5.1). In Fig. 6.6b, a small central peak structure can be observed at the center of the crater. Most likely, this central peak structure was produced by the jet. To obtain a clear central peak, an appropriate jet must be formed. Indeed, the impactor's free-fall height in Fig. 6.6b is slightly higher than that in Fig. 6.6a case. If the impact inertia is even stronger, the crater shape becomes more complex, as observed in Fig. 6.6c. A terrace wall structure can be observed in addition to a central mound. This crater shape might correspond to the complex craters observed on the actual planetary surface. However, the resemblance is limited only in their appearances. In general, the planetary-scale craters are formed by a shock wave rather than the impactor's penetration and associated cavity formation. According to the concept of similitude, both large and small-scale impacts could be

⁷Indeed, the range of container diameter varies within a relatively narrow regime $(D_{con} \le 6D_i)$.

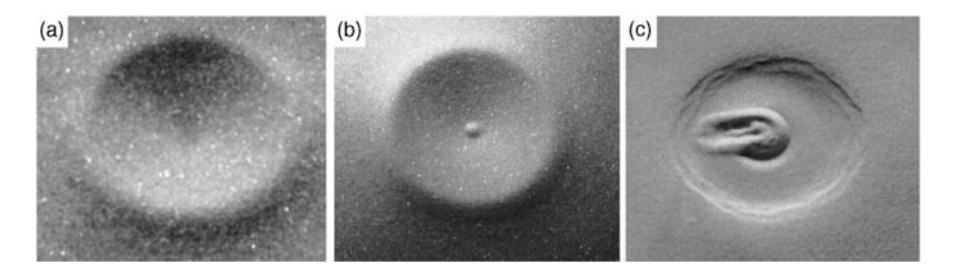


Fig. 6.6 Crater shapes formed by the impact of a steel sphere (diameter $D_i = 25.4$ mm and density $\rho_i = 7.7 \times 10^3 \, \text{kg/m}^3$) onto a glass-bead bed. (a) A simple bowl-shaped crater (grain diameter $D_g = 180 \sim 250 \, \mu\text{m}$ and free-fall height $h = 0.148 \, \text{m}$). (b) A bowl-shaped crater with a small central peak ($D_g = 180 \sim 250 \, \mu\text{m}$ and $h = 0.325 \, \text{m}$). (c) A complex crater with a central mound and terrace wall ($D_g = 45 \sim 90 \, \mu\text{m}$ and $h = 0.401 \, \text{m}$) (Reprinted with permission from Ref. [11]. Copyright 2003 by American Physical Society)

similar at least in the late stage of the cratering. Perhaps, the granular jet formation might occur on the planetary scale. The physics of the fundamental processes of the granular jet have been uncovered step by step thus far. Nonetheless, some principal questions are left unsolved. It is apparent that numerous investigations are required to understand planetary-scale phenomena. For example, the effect of gravitational acceleration must be clarified to discuss planetary-scale phenomena. All the experiments discussed in this section were performed on the surface of the Earth, i.e., $g = 9.8 \,\mathrm{m/s^2}$. Certainly, g depends on the size of the astronomical object and would affect the crater shape, as discussed in Sect. 5.1.

6.4 Granular-Granular Impact Cratering

A central peak structure can be formed by another way: impact between a granular impactor and a granular target. Thus far, most attention has been paid to the impact of an unbreakable solid impactor onto a very weak soft matter target. In this section, impact cratering caused by a fragile impactor is discussed. Specifically, some experimental results using a mud ball impactor will be introduced. In the experiments, a mud ball consisting of a mixture of grains and liquid was dropped onto a hard floor or a granular bed. Because the impactor is fragile, the resultant deformation and cratering are different from that in the solid impactor case.

6.4.1 Impact Deformation of a Mud Ball

The deformation dynamics of a mud ball impinging on a hard wall was experimentally studied [39]. A comparison of the impact-induced deformations of a mud ball and a water droplet is made in Fig. 6.7. As observed, the water droplet deforms until

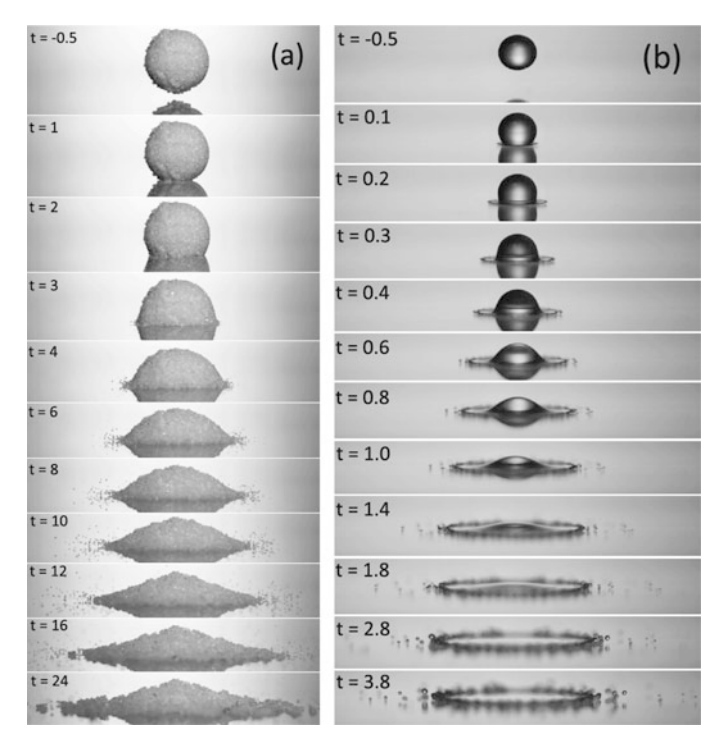


Fig. 6.7 Time sequences of deformations of (a) a mud ball ($D_i = 26 \,\mathrm{mm}$) impacting onto a thick glass plate and (b) a water droplet ($D_i = 3.6 \,\mathrm{mm}$) impacting onto a hydrophobic glass plate. In both cases, $v_0 \simeq 2.6 \,\mathrm{m/s}$. The unit of time t is milliseconds (Reprinted with permission from Ref. [39]. Copyright 2013 by American Physical Society)

it becomes a thin liquid sheet. In contrast, a mud ball cannot deform down to a thin sheet. Instead, it leaves a mound at the center. Thus, the deformation dynamics is qualitatively different between the mud ball impact and the water droplet impact. Nonetheless, these impacts share quantitative similarities. According to the experimental result [39], the spread diameter $D_{\rm spread}$ of the impacting mud ball at the impinging point can be scaled as

$$\frac{D_{\text{spread}}}{D_i} \sim \sqrt{t \frac{v_0}{D_i}},\tag{6.44}$$

where D_t , v_0 , and t are the original impactor's diameter, impact velocity, and time, respectively. Equation (6.44) can be expressed using the Strouhal number S_t as $D_{\text{spread}}/D_i \sim S_t^{-1/2}$. Actually, the same scaling has also been observed in the case of a water droplet impact [40, 41]. In the experiment of Ref. [39], the water saturation⁸

⁸Water saturation indicates the fraction of water in the pore space expressed by volume ratio (Eq. (4.36)).

in the mud ball was fixed at 0.3. Because the dynamics of wet granular matter strongly depends on the water saturation as discussed in Sect. 4.1.7, more systematic experiments with various water saturation levels are necessary to examine the reason for this similarity among mud balls and water droplets. The physics of wet granular matter itself is a very complex problem [42, 43].

The splashing condition of the impacting mud ball was also experimentally examined [44]. When a mud ball impacts a hard floor, splashing occurs because of grain detachment, particularly in the large impact velocity regime. The onset of splashing is characterized by the particle-based Weber number. The particle-based Weber number is defined as $W_{ep} = \rho_g r_g v_0^2/\gamma_c$, where ρ_g and $r_g = D_g/2$ are the true density and radius of the grains, respectively. Of course, v_0 and γ_c correspond to the impact velocity and the surface tension of liquid content, respectively. In the experiment, it was demonstrated that the onset criterion of splashing corresponds to $W_{ep} \simeq 14$ [44]. The particle-based Weber number can be regarded as a balance between the impacting kinetic energy per grain and the surface energy on each splashed grain. In this experiment, the viscosity of the interstitial liquid did not play an important role in the splashing of an impacting mud ball.

The ejected-grain velocity was also measured in the mud ball impact experiment. The grains are ejected after the deformation reaches $D_{\text{spread}} \simeq D_i$. Then, the maximal ejected-grain velocity decays linearly with time. The ejected-grain velocity v_{ej} satisfies the following relation [39]:

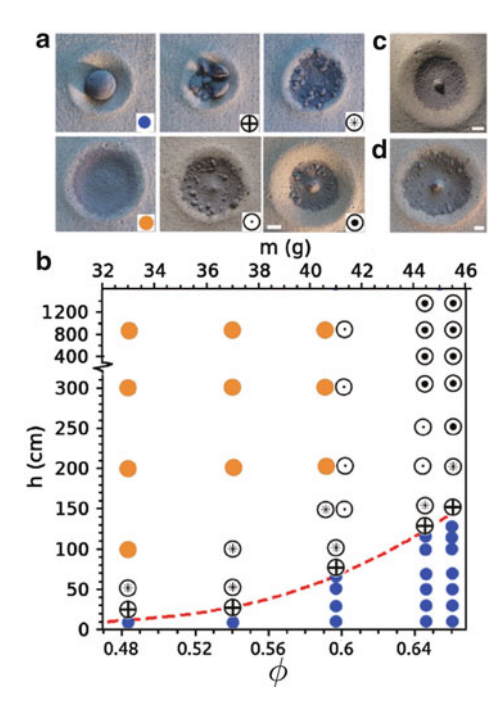
$$\frac{v_{\rm ej}}{v_0} \le 2. \tag{6.45}$$

This $v_{\rm ej}$ is smaller than the velocity of the dry grains ejected by the solid impact, where $v_{\rm ej}$ reaches $5v_0$ (Eq. (6.41)).

6.4.2 Crater Morphology by Granular-Granular Impact

The mound structure observed in Fig. 6.7a recalls the central peak of a complex crater. In fact, various complex crater shapes can be formed by the impact of a mud ball onto a granular bed. This type of impact (mud ball vs. granular bed) is called *granular-granular impact* [45, 46]. Varying the free-fall height and the packing fraction of a mud ball, diverse crater morphologies have been observed. The phase diagram of the granular-granular impact cratering obtained by experiments with a wide range of v_0 is presented in Fig. 6.8. In the experiment, a mud ball with $D_i = 36.5$ mm was made with various packing fraction, $\phi_i = 0.48$ –0.66. The mud ball impactor was dropped from a free-fall height h (up to 13.5 m). The packing fraction of the target granular bed was fixed at $\phi_t = 0.55$. The representative crater shapes corresponding to each marker in the phase diagram (Fig. 6.8b) are shown in Fig. 6.8a. In the low impact velocity and high packing fraction regime, the impactor maintains its original shape, and the crater shape is similar to that of the solid impactor case. In the high velocity and low packing fraction regime, the impactor is

Fig. 6.8 (a) Various crater morphologies and (b) a phase diagram of the granular-granular impact cratering. Representative crater shapes for each marker in (b) are shown in (a) with corresponding markers. (c) and (d) show typical complex crater shapes with a clear central peak structure. h, ϕ , and m in this figure correspond to the free-fall height, packing fraction and mass of the impactor, respectively (Reprinted with permission from Ref. [45]. Copyright 2011 by American Physical Society)



completely pulverized, and a simple crater shape remains again. In the intermediate regime, complex craters can be observed. Furthermore, the central peak structure is formed in the relatively high packing fraction and high impact velocity regime. The origin of this central peak is not a granular Worthington jet. Rather, this peak originates from the mound structure observed in Fig. 6.7a. Moreover, this mound structure is most likely related to the stagnation of the obstructed granular flow that is called a dynamic sand dune [47].

The dimensions of the crater formed by granular-granular impact were measured and analyzed [45]. The crater diameter of granular-granular impact D_{cg} is the same as that of the solid impactor as long as the impactor is not broken. Once the impactor breaks, D_{cg} becomes greater than that made by solid impactor. The diameter difference $\Delta D_c = D_{cg} - D_c$ is almost a constant in a wide range of impact velocities. Here D_c indicates the crater diameter created by a solid impact (Eq. (6.31)). Then, the scaling for the crater diameter by granular-granular impact is written as

$$D_{cg} = C_c \left(\frac{\rho_i}{\rho_t}\right)^{1/4} D_i^{3/4} h^{1/4} + \Delta D_c \Theta(h - h_f), \tag{6.46}$$

where Θ is the Heaviside step function⁹ and C_c is a dimensionless constant. The free-fall height at which the impactor starts to break is defined as h_f . The first term

 $^{{}^{9}\}Theta(x) = 0$ for (x < 0) and 1 for (x > 0).

on the right-hand side in Eq. (6.46) comes from Eq. (6.31). The experimentally observed ΔD_c is positive, which indicates that the impact kinetic energy is transferred to the horizontal direction more effectively in the granular-granular impact than in the solid-granular impact. The value of h_f and ΔD_c must relate to the cohesion-originated strength of the granular impactor (mud ball).

The behavior of the crater depth is peculiar in the granular-granular impact. In the low-velocity impact regime $(h < h_f)$, the resultant crater depth is the same as that in the solid impactor case, as expected. However, the crater depth suddenly becomes a constant in the large inertia regime $(h > h_f)$. Thus, one can conclude that a fragile impactor such as a mud ball results in a slightly wider and shallower crater compared with that in the solid impactor case. Although the modification process (Sect. 5.3.4) has been considered to be a principal factor in determining the final crater shape, complex effects such as the abovementioned granular-granular impact might also play vital roles in the cratering mechanics.

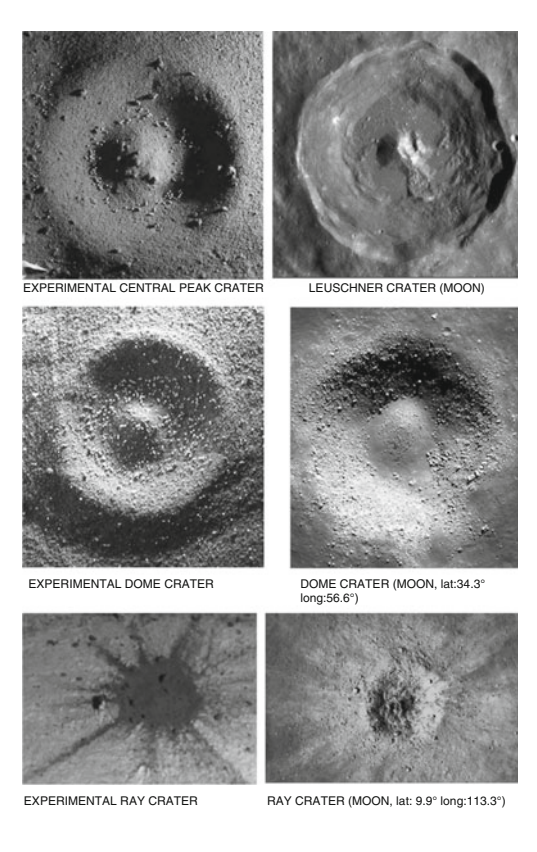
The granular-granular impact craters and actual planetary craters exhibit a similar scaling [46]. Although the high-velocity impact experiments performed on the Earth result in a simple relation between the crater volume V_c and its diameter D_c , $V_c \sim D_c^3$, the actual craters on the Moon, Ganymede, and Callisto obey slightly different scaling, $V_c \propto D_c^{2.5}$ [46]. Additionally, granular-granular impact craters are close to the latter. Note, however, that the consistency between the relation $V_c \propto D_c^{2.5}$ and the constant D_h/D_c ($D_h/D_c \simeq 1/5$ for simple craters and 1/8 for complex craters; see Sect. 5.1) is not clear. We usually expect $V_c \sim D_c^2 D_h \sim D_c^3$. Perhaps, a complex crater shape such as a central peak might affect the scaling. Moreover, the aging of craters by degradation might be crucial.

In addition to the central peak structure, granular-granular impact can produce various complex crater morphologies including a ray crater (Fig. 6.9). In Fig. 6.9, granular-granular impact craters are compared with actual craters observed on the Moon. The mud ball impactor mimics porous astronomical objects. Such porous objects are actually very ubiquitous in space. Their physical properties are determined by cohesiveness among grains [48]. The effect of the target porosity has been considered in the study of planetary impact cratering [49]. However, the effect of an impactor's porosity has not been thoroughly studied. More systematic studies are required to discuss various impact conditions.

Through direct geological field studies of terrestrial craters, clear central uplifts of the crater's floors have been observed, as mentioned in Sect. 5.3.4 [50]. Planetary explorations have also supported the idea that central peak structures come from the deep part. Thus, the origin of the central peak structure has been considered as an uplift rather than a residue of the impactor. The comparison in Fig. 6.9 might be rather eccentric. However, the general mechanism for the central peak structure might not be necessarily unique. A much more detailed study of the granular-granular impact must be performed to discuss the similarity with actual planetary impact cratering, particularly for the central peak structure.

The penetration of a mud ball into a water target was also studied experimentally [51]. Both the penetration dynamics and the cavity shape opened by the impact depends on the packing fraction of the mud ball and its impact velocity.

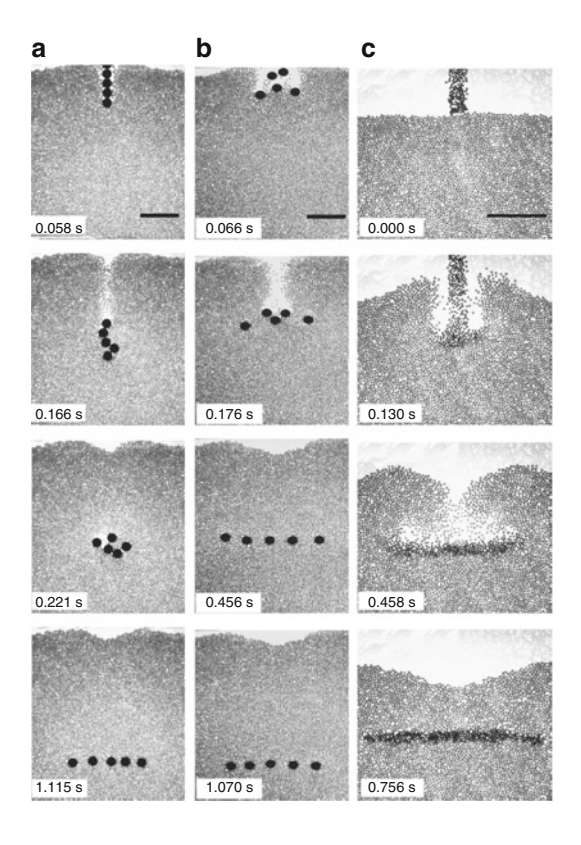
Fig. 6.9 Various crater shapes made by the granular-granular impact (*left*), and the actual craters observed on the Moon (*right*) (After [46]; Courtesy of J. C. Ruiz-Suárez)



6.4.3 Interaction of Multiple Impactors

One additional interesting experimental result relating to granular-granular impact was reported by Pacheco-Vázquez and Ruiz-Suárez using multiple impactors [52]. If the breakable impactor moves in a thick atmosphere with a very high speed, the impactor will break up into many fragments before the impact. Then, a series of successive impacts by multiple impactors might occur. In this situation, does a sequence of impacts affect the dynamics of penetration? To investigate this problem, a sequential-impact experiment with multiple impactors was performed with a very lightweight-grain bed ($D_g = 5 \, \text{mm}$ and $\rho_g = 14 \, \text{kg/m}^3$). The granular drag force by very lightweight grains is slightly different from the drag force by usual-weight grains ($\rho_g \simeq \mathcal{O}(10^3) \, \text{kg/m}^3$). Specifically, the frictional drag force in light-weight grains is readily saturated obeying the form written in Eq. (4.33) mainly due to the Janssen effect. Moreover, for the multiple impactor situation, the interaction among impactors through interstitial grains could be very complex. The impactors can experience both repulsive and attractive interactions. In such a complex system, these researchers observed a curious cooperative motion of plural

Fig. 6.10 Cooperative motion of impactors resulting in a horizontal distribution at the final state. (a) Five impactors strike the lightweight-grain bed vertically. (b) A clump of impactors. (c) Numerous small impactors (Reprinted by permission from Macmillan Publishers Ltd: Ref. [52], Copyright 2010)



impactors. Because of the complex interactions, the group of impactors finally lined up horizontally, regardless of the initial state. Representative images of this horizontal lineup are shown in Fig. 6.10. One can easily observe the horizontally ordered final state regardless of the state of impact. To understand the complex interactions in a dynamic lightweight-grain bed, systematic investigations both by experiments and simulations have been performed [53]. According to Ref. [53], the lightweight-grain bed is fluidized by the impact and fluid-like interaction similar to Bernoulli's principle might become crucial for understanding the cooperative motion of the impactors. While it is difficult to directly draw conclusions concerning the planetary-scale multi-impactor situations from this experimental result, the possible complexity of the multi-impactors penetration must be acknowledged.

As discussed in Sect. 4.1.7, when two steel spheres are dropped onto a target comprising glass beads, the interaction of the two impactors is not very significant [54]. The characteristic length scale of the interaction is considerably smaller than the impactor's size and approximately 20 times the grain diameter. A general understanding of the multiple impactors' penetration on a granular bed has not been achieved and remains a frontier of active research in this area.

6.5 Droplet-Granular Impact Cratering

A different class of complex cratering can be observed in a *droplet-granular impact*. In the preceding section, the impact of a mud ball, which consists of a mixture of grains and liquid, was discussed. In this section, the focus is on cratering by a liquid droplet impacting a granular bed. In Sect. 6.1, cratering on a liquid target layer was mainly emphasized. In this section, cratering associated with complex interactions between a liquid droplet and a granular target is specifically discussed. First, the elementary scaling theory of the deformation dynamics of a liquid droplet impacting a solid wall is reviewed. Then, the dynamics of the impact between a liquid droplet and a granular bed is discussed based on experimental observations.

6.5.1 Droplet Deformation by an Impact on a Solid Wall

First, we would like to estimate the maximal deformation of an impacting liquid droplet in preparation for the discussion of droplet-granular impact. As already discussed in the previous section, the spread diameter $D_{\rm spread}$ of an impacting mud ball is scaled by the impact velocity v_0 , original diameter D_i , and time t as $D_{\rm spread}/D_i \sim (tv_0/D_i)^{1/2}$ (Eq. (6.44)). This scaling is also valid for the deformation of an impacting liquid droplet. Because the size of an impacting droplet is finite, there must be a limit of the deformation. Then, the maximal deformation diameter $D_{\rm max}$ can be estimated by considering the energy balance or the force balance. In general, the spreading dynamics of an impacting droplet strongly depends on the target hydrophilicity. Here the super-hydrophobic case is mainly considered to concentrate on the droplet's intrinsic behavior (Fig. 6.11).

In the case of inviscid liquid droplet impact, the droplet deformation is determined by the balance between the surface energy and impact kinetic energy. The former at the maximal deformation state is scaled as $\gamma_c D_{\rm max}^2$, and the latter is scaled as $\rho_i D_i^3 v_0^2$, where γ_c and ρ_i are the surface tension and density of the liquid, respectively. Equating these two energies, a simple scaling for $D_{\rm max}$ is obtained as

$$D_{\text{max}} \sim D_i \sqrt{\frac{\rho_i v_0^2 D_i}{\gamma_c}} = D_i W_e^{1/2},$$
 (6.47)

where W_e is the Weber number. Unfortunately, this simple scaling cannot explain the experimental result. An experiment of a liquid-droplet impact onto a superhydrophobic surface exhibits different scaling, $D_{\text{max}} \propto W_e^{1/4}$ [55]. To improve the scaling, we must introduce an *impact capillary length* λ_{imp} by replacing gravity g with the characteristic acceleration v_0^2/D_i and using ρ_i for the density in the definition of the capillary length (Eq. (2.99)). Then, λ_{imp} is written as

a before impact

b maximal deformation state

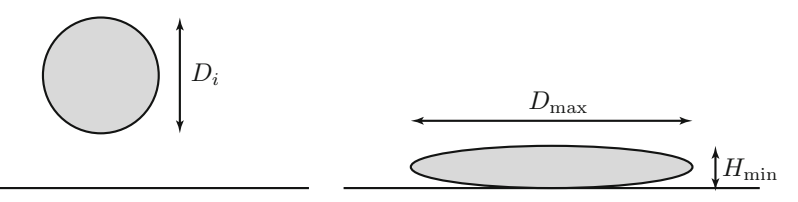


Fig. 6.11 Geometry of a droplet impact. D_i denotes the droplet diameter before the impact. D_{max} and H_{min} correspond to the diameter and height at the maximal deformation state after the impact, respectively

$$\lambda_{\rm imp} = \sqrt{\frac{\gamma_c D_i}{\rho_i v_0^2}}. (6.48)$$

Substituting this λ_{imp} into the characteristic length of the Weber number, D_{max} is rewritten as

$$D_{\text{max}} \sim D_i \left[\frac{\rho_i v_0^2}{\gamma_c} \left(\frac{\gamma_c D_i}{\rho_i v_0^2} \right)^{1/2} \right]^{1/2},$$

$$= D_i \left(\frac{\rho_i v_0^2 D_i}{\gamma_c} \right)^{1/4} = D_i W_e^{1/4}.$$
(6.49)

While this scaling explains the experimental results [55–57], one might feel that the derivation of the scaling is somewhat expedient.

This scaling can be derived in another way [58]. Force balance and geometric constraint are used in the following derivation. The geometrical notation used is illustrated in Fig. 6.11. By considering the Euler equation $\rho_i(Dv/Dt) = -\nabla p + \rho_i g$, and neglecting hydrostatic term, the balance between the inertia term and pressure gradient term should be evaluated. The inertial force per unit volume in the impacting droplet $\rho_i v_0^2/D_i$ should balance with the Laplace pressure gradient at the maximally deformed sate γ_c/H_{\min}^2 . At the same time, a geometric constraint using an incompressible approximation,

$$D_i^3 \sim D_{\text{max}}^2 H_{\text{min}},\tag{6.50}$$

must be fulfilled. Using these quantities, one can obtain a relation, $\rho_i v_0^2/D_i \sim \gamma_c D_{\rm max}^4/D_i^6$. From this relation, Eq. (6.49) can be immediately calculated. The applicability limit of this type of deformation is evaluated by a so-called splashing parameter that is defined later in Eq. (6.81).

A typical timescale created by the capillary force is also derivable from the balance between the droplet inertia and the Laplace pressure gradient. Because the dimension of γ_c is [force]/[length], it can be regarded as a type of spring constant (stiffness). Thus, an oscillatory timescale due to this spring-like effect must exist in the system. To derive this typical timescale t_γ , we must consider the balance between inertia and the capillary effect. Therefore, the droplet inertia per unit volume is dimensionally estimated as $\rho_i D_i/t_\gamma^2$. For the Laplace pressure gradient, γ_c/D_i^2 should be considered. Because we are interested in the pseudo-elastic potential of the droplet at its natural length, we employ D_i as a representative length scale. Then, by equating these quantities, we obtain a scaling relation:

$$t_{\gamma} \sim \sqrt{\frac{\rho_i D_i^3}{\gamma_c}}.$$
 (6.51)

Because this timescale is a characteristic period of the liquid spring, it must correspond to a contact time of the bouncing of an impacting droplet. Based on an impact experiment between a liquid droplet and a super-hydrophobic solid, the validity of this scaling has been confirmed [59]. Specifically, the contact time was observed to be independent of the impact velocity and clearly exhibited a $D_i^{3/2}$ dependence. This experimental result is fully consistent with the expression of Eq. (6.51). By normalizing the timescale as $t_{\gamma}^* = t_{\gamma} v_0/D_i$, one can obtain the scaling

$$t_{\nu}^* \sim W_e^{1/2}$$
. (6.52)

Indeed, the abovementioned scaling is not a unique solution. As already discussed in Sect. 2.5, there remains arbitrariness in the scaling and dimensional analysis. For instance, if we use a term $\rho_i v_0/t_\gamma$ for the droplet inertial force per unit volume instead of $\rho_i D_i/t_\gamma^2$, the timescale becomes $t_\gamma \sim \rho_i v_0 D_i^2/\gamma_c$. This form is slightly different from Eq. (6.51) but is dimensionally sound; however, this scaling cannot fit the experimental result. Put another way, the impact velocity v_0 is an irrelevant parameter to characterize the oscillation timescale t_γ . Therefore, Eqs. (6.49) and (6.51) are regarded as correct answers for the liquid-droplet impact dynamics. Validation by experimental tests (or corresponding theoretical framework) is necessary to confirm the scaling relation, in general.

Furthermore, another scaling can be obtained if we assume an elastic sphere's impact. The deformation of an elastic sphere obeys the Hertz law (Sect. 2.5.4). Because the applied force F and the deformation δ in the Hertz law are related as $F \sim E D_i^{1/2} \delta^{3/2}$ (Eq. (2.66)), the corresponding elastic potential energy E_e becomes $E_e \sim E D_i^{1/2} \delta^{5/2}$ (because $|F| = \partial E_e/\partial \delta$), where E is Young's modulus. When this potential energy balances with the impact kinetic energy $\rho_i D_i^3 v_0^2$, the maximal deformation $\delta_{\text{max}} = D_i - H_{\text{min}}$ is written as [60, 61]

$$\delta_{\text{max}} = D_i - H_{\text{min}} \sim D_i \left(\frac{\rho_i v_0^2}{E}\right)^{2/5}.$$
 (6.53)

Assuming $E \sim \gamma_c/D_i$ and $t_\gamma^* = (\delta_{\rm max}/v_0)(v_0/D_i)$, the following scaling relation is obtained: $t_\gamma^* \sim W_e^{2/5}$ [59]. However, this scaling does not work well for the droplet impact deformation. The experimental result suggests that Eqs. (6.49), (6.51) and (6.52) are suitable for the droplet impact. Hertz law is only applicable for small deformation, whereas the droplet impact deformation is not small. Thus, the Hertz law is inappropriate in this case. A liquid-droplet impact on a hydrophobic target can be modeled by a simple spring whose spring constant is γ_c . Such physical insights are always required to obtain a proper scaling law.

The temporal variation of D_{spread} can be computed using the above scaling relations. Using Eqs. (6.44) and (6.52), one can obtain

$$\frac{D_{\text{spread}}}{D_i} \sim \left(\frac{t}{t_{\nu}}\right)^{1/2} W_e^{1/4}.\tag{6.54}$$

Note that Eq. (6.54) can be used until the maximal deformation is achieved ($t \le t_{\gamma}$). If the liquid droplet is very viscous, the viscosity governs the deformation dynamics [55]. In such a situation, the balance between the kinetic energy and viscous dissipation should be considered as

$$\rho_i D_i^3 v_0^2 \sim \eta \left(\frac{v_0}{H_{\min}}\right) D_{\max}^3. \tag{6.55}$$

Here it is assumed that D_{max} is a relevant characteristic length scale for the viscous dissipation. The H_{min} dependence can be eliminated using a geometric constraint of Eq. (6.50). Then, D_{max} is scaled as

$$D_{\text{max}} \sim D_i R_{\rho}^{1/5}$$
. (6.56)

The crossover from the capillary-dominant regime to the viscosity-dominant regime occurs at $W_e^{1/4} \simeq R_e^{1/5}$. Thus, Eq. (6.49) can be generalized as

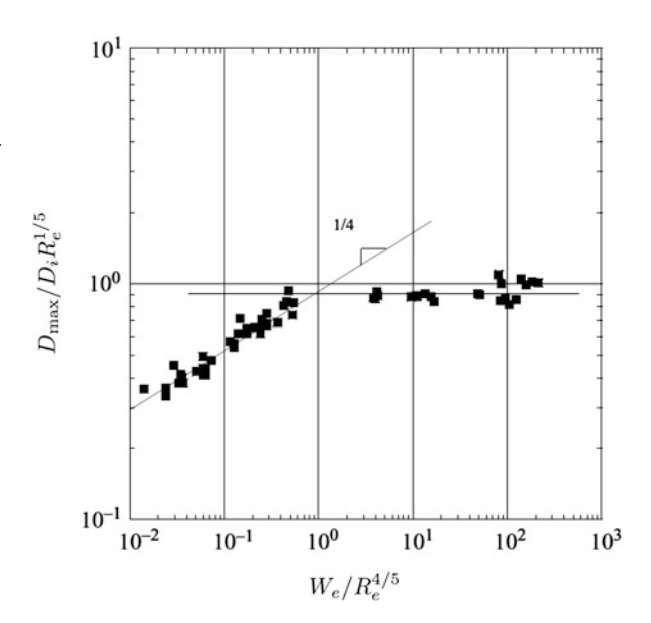
$$\frac{D_{\text{max}}}{D_i} \sim R_e^{1/5} \psi_d \left(\frac{W_e}{R_e^{4/5}} \right), \tag{6.57}$$

where the function $\psi_d(x)$ is $\psi_d(x) \sim x^{1/4}$ at $x \ll 1$ and $\psi_d(x) \sim$ const. at $x \gg 1$. This combined scaling behavior has been experimentally confirmed [55]. Experimental data that are consistent with this scaling are plotted in Fig. 6.12.

The scaling analysis of the deformation of an impacting liquid droplet has been briefly reviewed in this subsection. There are some additional interesting

¹⁰This assumption is important for the scaling. Another scaling relation can be obtained by a different definition of viscous dissipation. This point will be discussed later in the next section (see Eqs. (6.78) and (6.79)).

Fig. 6.12 Scaling of the maximal deformation of a liquid-droplet impact. The experimental data are fully consistent with the scaling of Eq. (6.57) (Reproduced with permission from Ref. [55])



phenomena concerning the impact of a liquid droplet. French researchers performed various experiments using a water droplet and a super-hydrophobic or very hot solid target. As an example, these researchers observed that an impacting droplet can deform into a staircase pyramid or a torus depending on the experimental conditions [56]. The restitution coefficient ϵ_r was also measured. In the impact between a water droplet and a super-hydrophobic solid target, the impacting droplet behaves like a spring. However, its restitution coefficient is limited to approximately 0.9 [62]. This limit likely comes from the energy partition to the internal oscillation of the droplet after the lift-off, and this internal oscillation would be finally dissipated by viscosity. In the very hot (more than 100°C) solid target experiment, the restitution coefficient depends on W_e as $\epsilon_r \sim W_e^{-1/2}$ [57]. That is, in the large W_e regime, the very hot solid target cannot behave like a simple hydrophobic target because of the thermal effect.

6.5.2 Crater Morphology by Droplet-Granular Impact

In this subsection, we consider the result of a liquid-droplet impacting a granular bed. The principal scope of this subsection is to provide an overview of the crater morphology resulting from a droplet-granular impact. In Sect. 6.4, we already surveyed the state-of-the-art of granular-granular impact cratering. The mud-ball impactor is more fragile than elastic. Because of the fragility, various crater shapes are produced as observed in Figs. 6.8 and 6.9. Thus, the following natural question arises: what happens if the impactor is more elastic but still very soft or viscous?

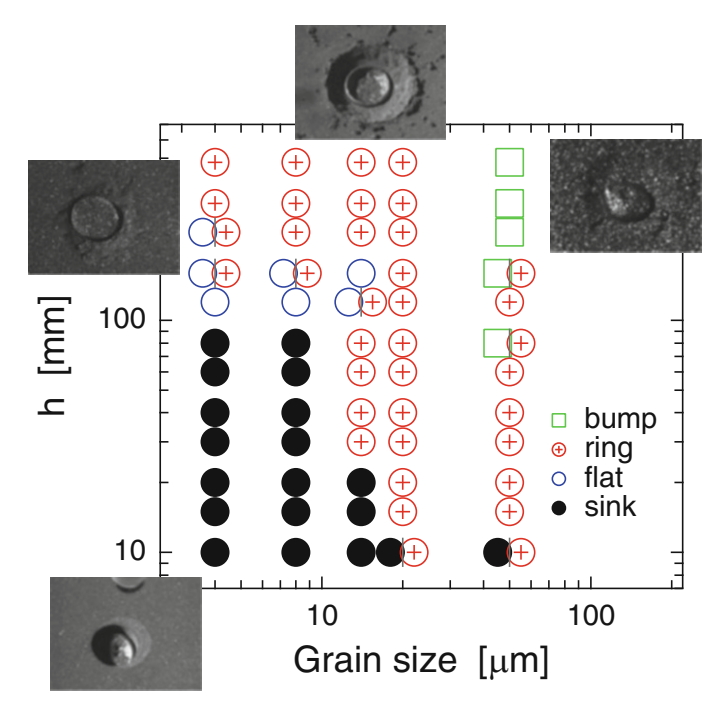


Fig. 6.13 Phase diagram of the crater shape produced by a water droplet impact onto a SiCabrasive bed. Four types of craters (sink-type, ring-type, flat-type, and bump-type) are observed, depending on the droplet free-fall height and target grain size (Reprinted with permission from Ref. [63]. Copyright 2010 by American Physical Society)

A liquid droplet is very soft and elastic as discussed in the preceding subsection. Thus, the impact between a liquid droplet and a granular bed would be intriguing. We will review the experimental studies on droplet-granular impact cratering in the following of this section.

Various crater shapes have been observed in droplet-granular impact experiments. The phase diagram of the crater shapes obtained by low-velocity ($v_0 < 4 \text{ m/s}$) free-fall impacts between a water droplet and SiC abrasive target is presented in Fig. 6.13 [63]. By varying the free-fall height h and target grain size D_g , we can observe four types of crater shapes: sink-type, flat-type, ring-type, and bump-type.

A relatively low-velocity impact on a small-grain bed produces a sink-type crater. In this slow impact regime, an impacting water droplet rebounds without deforming the target at the initial impact. Then, the droplet falls down to the surface again and exhibits attenuating oscillation on the surface. Finally, the droplet settles on the surface and slowly penetrates into the bed by a drain. During the slow penetration by the drain, a cylindrical hole structure whose wall stands vertically is produced. We call this structure a *sink-type crater*. Because SiC abrasives are not very hydrophilic, a water droplet penetrates very slowly. Additionally, the small-grain target bed has a small packing fraction, $\phi_0 \simeq 0.31$. Therefore, compaction of the target bed is

induced by the slow penetration of the liquid droplet. The combination of the slow drain and associated compaction of the target granular bed induces the sink-type cratering.

When the impacting velocity or the grain size is increased, a ring-type crater is formed. In this regime, the impinging droplet is significantly deformed by the initial impact inertia and also experiences rebound and attenuating oscillation. At the initial impact moment, some grains are immediately absorbed into the droplet. Moreover, a clear crater outer rim structure is formed by the initial impact. This outer rim diameter is greater than the initial droplet diameter. After settling by the attenuating oscillation, the droplet also penetrates into the target in this case. However, because the target bed is already compressed by the initial impact, 11 the target bed cannot be compressed further by the penetration. Instead, the ring structure persists after the drain of the droplet. The diameter of this ring is close to the diameter of the penetrating droplet because its drain is the cause of this ring structure. As a result of these processes, concentric rings are produced in this regime. This type of doublering crater is defined as a ring-type crater. The ring-type crater is the most popular crater shape in this phase diagram. 12 Although the actual dynamics of the inner ring formation is not well understood, capillary-driven ring stains formed by a dried liquid droplet [64, 65] might relate to the inner ring formation. A *flat-type crater* can be observed at the boundary of a sink-type crater and a ring-type crater. A central flat table and an outer rim are produced by the initial impact.

An additional curious shape observed in the droplet-granular impact is the *bump-type crater*. The reason we call this crater a bump-type crater is because of its particular mound-like structure. A usual impact crater has a concave structure because of the excavation and compression caused by the impact. However, the bump-type crater has a convex shape. Using precise surface profilometry, it was established that the peak height of the bump was higher than the initial target bed height [63]. Moreover, the volume of the created bump was larger than the excavated volume of the crater. This finding implies that the target bed dilates effectively by the droplet impact. Why is such a dilation possible? The reason for this dilation is actually related to the cratering dynamics, which will be discussed later in this section.

Quantitative characterization of droplet-granular impact cratering is not so easy. The phase diagram is very useful for qualitative characterization; however, it is difficult to obtain quantitative information solely from the phase diagram. The next step that should be performed is an examination of the crater dimensions. As discussed in the previous chapters as well as the current chapter, crater dimensions such as the diameter and depth are important quantities for characterizing the crater shape. For droplet-granular impact craters, the crater diameter D_c was measured and scaled as [63]

¹¹The typical initial packing fraction is $\phi_0=0.44$. Furthermore, the target is considerably compressed by the impact.

¹²Note that the axes in the phase diagram of Fig. 6.13 are on logarithmic scales.

$$\frac{D_c}{D_i} \sim \frac{\rho_t}{\rho_i} W_e^{1/4},\tag{6.58}$$

where D_i , ρ_i , and ρ_t are the diameter and density of the droplet, and the bulk density of the target granular bed, respectively. W_e is the Weber number.

The 1/4 power law for the crater diameter appears again. Equations (4.2), (6.16), and (6.31) appear similar to this scaling because W_e is proportional to the square of the impact velocity. Considering the free-fall relation ($v_0 = \sqrt{2gh}$), it is easy to show that $W_e^{1/4}$ is equivalent to $h^{1/4}$, which indicates that Eqs. (6.58), (6.31), and (4.2) have almost the same scaling tendency in terms of h dependence (at least for shallow cratering). The 1/4 power law in these equations can be explained by the energy transfer from the impactor's kinetic energy to the ejecta's gravitational potential energy (Fig. 4.2b). If we assume that this idea is also applicable to the droplet-granular impact cratering, the density ratio dependence in Eq. (6.58) is quite contradictory. The density dependence of the crater diameter is completely opposite between Eqs. (6.16) and (6.58). Equation (6.58) suggests that a denser target granular bed results in a larger crater diameter. However, a denser target must result in a smaller crater if the ejecta's potential energy is the principal carrier of the impact energy. Therefore, the scaling of Eq. (6.58) is qualitatively different from that of Eqs. (4.2) and (6.31).

Droplet deformation is the crucial factor to understand the scaling of Eq. (6.58). According to Eq. (6.49), the maximal deformation of the impacting droplet obeys the $W_e^{1/4}$ power law. This scaling is a possible origin of Eq. (6.58). In the droplet-granular impact, it is difficult to directly deform the target granular bed by the impact inertia when the target granular bed is dense. Instead, the impacting droplet deforms itself, and this spreading (deformed) droplet scoops the shallower but wider granular surface layer. This phenomenon implies that the wider and shallower crater is formed mainly because of the shearing by an expanding droplet rather than the normal compression or the excavation. This deformation-based process determines the outer rim diameter (and depth) of the craters. To consider this deformability effect, the momentum transfer between the droplet and target should be considered. The starting point is a simple momentum transfer, $\rho_i D_i^3 v^2/d_1 \sim \rho_i A v^2$ (Sects. 2.6.2 and 4.1.4). Here we assume that the characteristic length scale d_1 is written as $d_1 \sim D_i^3/D_{\rm max}^2$ and effective area A is proportional to $D_i D_{\rm max}$. Then, we obtain a simple relation:

$$\frac{D_{\text{max}}}{D_i} \sim \frac{\rho_t}{\rho_i}.\tag{6.59}$$

Combining Eqs. (6.49) and (6.59), the scaling of Eq. (6.58) can be understood.

The dilation of the bump-type crater is consistent with the abovementioned droplet deformation scenario. The bump-type crater is observed only in the large v_0 impact onto a large-grain bed. Because the large-grain bed is relatively dense ($\phi_0 \simeq 0.5$), the impacting droplet has to deform significantly. This deformation results in a shallower but wider crater. Furthermore, in the initial impact stage, the deformed

droplet collects surface grains. During the draining stage, grains accumulate on the surface. These slowly sedimented grains leave a bump made by the relatively porous grain structure. Slow penetration makes this porous sedimentation possible.

The size ratio of inner and outer rings was examined experimentally [66]. The outer ring diameter D_c (crater diameter) is determined by the droplet deformation while the inner ring is a footprint of the drained droplet, and the inner ring diameter $D_{\rm in}$ is not precisely the same as the initial droplet diameter D_i . The ratio $D_c/D_{\rm in}$ is affected by the competition of timescales between the oscillation (spreading and recession) and penetration of the droplet. In particular, these two timescales become comparative when hydrophilic grains such as glass beads are used. The measured ratio $D_c/D_{\rm in}$ has a maximum value at $W_e \simeq 200$ for a glass-bead target [66].

Various time sequences of the droplet-granular impact cratering are shown in Fig. 6.14 [67]. In the experiment of Ref. [67], the liquid viscosity and surface tension were varied by blending water and glycerol or ethanol. Furthermore, the target grain materials and their sizes were varied; glass beads ($D_g = 5{\text -}100\,\mu\text{m}$) were used in addition to SiC abrasives. As observed in Fig. 6.14, typical crater shapes such as sink-type, ring-type, and bump-type shapes were observed for some experimental conditions. Some other interesting shapes were also observed in Fig. 6.14.

First, no cratering (perfect wetting) can be observed in Fig. 6.14f. In this case, small glass beads ($D_g \simeq 5 \, \mu \text{m}$) were used as constituents of the target. Because glass is hydrophilic, it is difficult to completely eliminate the capillary bridge effect in such a small-bead bed. If the capillary effect strengthens the structure of the glass-bead bed. In addition, hydrophilicity emphasizes the permeability of water that prefers wetting rather than moving to respond to the impact inertia. Therefore, impacting droplet inertia cannot form a crater. Immediately, a liquid droplet expands and wets the surface.

Second, one can find secondary crater formation in a low surface tension droplet impact, which is quite natural because the low surface tension droplet is unstable. The droplet is easily fragmented into small droplets, as observed in rows (h) and (i) of Fig. 6.14. In this low surface tension regime, the resultant crater shape and size are significantly affected by this shattering process.

Third, petal-like rim structures can be observed, e.g., in Fig. 6.14e, g. This structure appears to originate from the fingering instability of the deformed droplet. A similar petal-like structure was also observed in other experiments [68]. Fingering instability and satellite droplet formation are observed in the large W_e regime. When the impact inertia is considerably greater than the surface tension effect, the droplet is fragmented by the impact and satellite droplets are produced. According to the experimental result of the droplet splashing [69], although the number of satellite droplets grows as v_0 increases, their characteristic sizes decrease as v_0 increases. This result is reasonable if we consider that the droplet shattering originates from the fingering instability of the impacting droplet. As v_0 increases, the deformation

¹³Because the capillary effect becomes dominant in the small-scale regime (Sect. 2.8.5), its effect is pronounced in a small-bead bed.

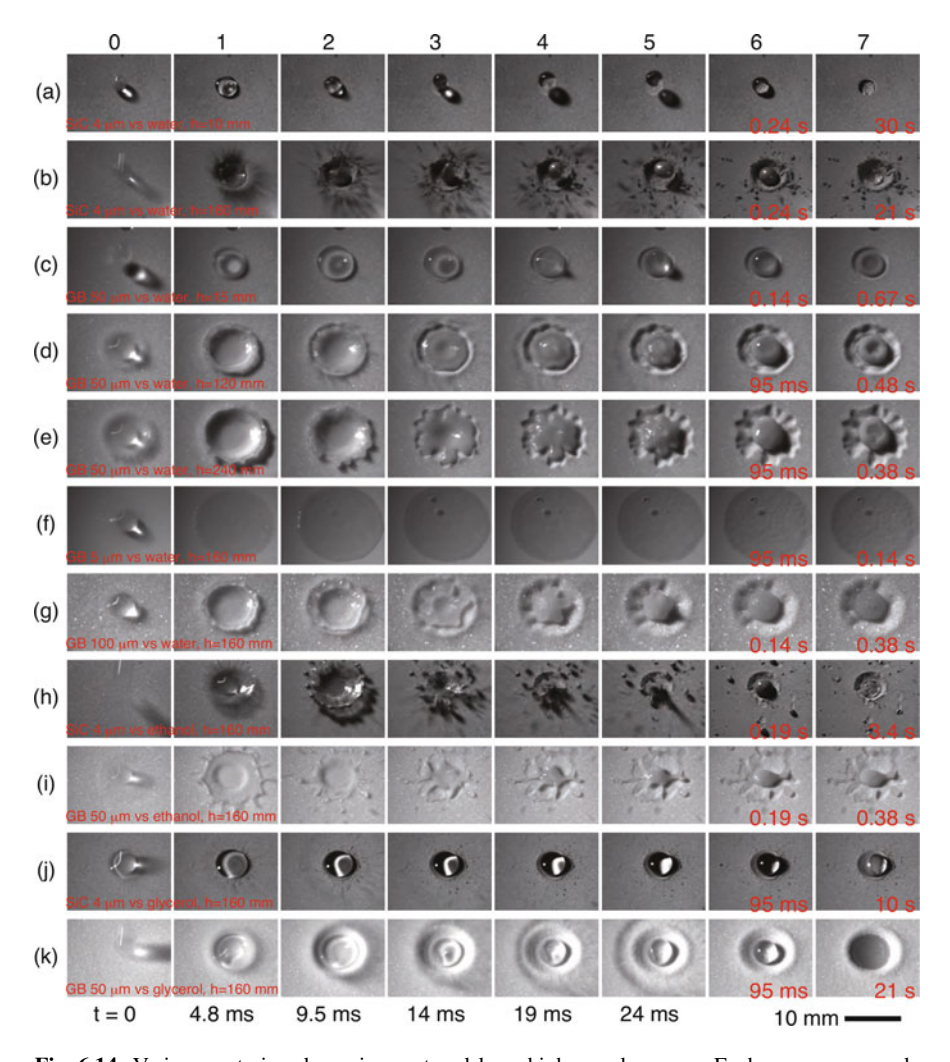


Fig. 6.14 Various cratering dynamics captured by a high-speed camera. Each row corresponds to an experimental condition, as cited at *left bottom* part of each row. Column 0 corresponds to the instant of impact (t=0) identified by 210 fps video data. Columns 1–5 present successive images directly after the impact (1/210 s interval). Columns 6 and 7 show the later stages of penetration. The scale bar (10 mm) is shown at the *right bottom*. Various droplet deformations and crater morphologies are observed. The specific experimental conditions are as follows: (**a**) SiC with $D_g = 4 \,\mu\text{m}$ vs. water droplet with $D_i = 2.6 \,\text{mm}$ and free-fall height $h = 10 \,\text{mm}$; (**b**) same as (**a**) except $h = 160 \,\text{mm}$; (**c**) glass beads with $D_g = 50 \,\mu\text{m}$ vs. water droplet with $D_i = 4.4 \,\text{mm}$ and $h = 15 \,\text{mm}$; (**d**) same as (**c**) except $h = 120 \,\text{mm}$; (**e**) same as (**c**) except $h = 240 \,\text{mm}$; (**f**) glass beads with $D_g = 5 \,\mu\text{m}$ vs. water droplet with $D_i = 4.4 \,\text{mm}$ and $h = 160 \,\text{mm}$; (**g**) glass beads with $D_g = 100 \,\mu\text{m}$ vs. water droplet with $D_i = 4.4 \,\text{mm}$ and $h = 160 \,\text{mm}$; (**h**) SiC with $D_g = 4 \,\mu\text{m}$ vs. ethanol droplet with $D_i = 3.0 \,\text{mm}$ and $h = 160 \,\text{mm}$; (**j**) glass beads with $D_g = 50 \,\mu\text{m}$ vs. ethanol droplet with $D_i = 3.0 \,\text{mm}$ and $h = 160 \,\text{mm}$; (**j**) SiC with $D_g = 4 \,\mu\text{m}$ vs. glycerol droplet with $D_i = 3.8 \,\text{mm}$ and $h = 160 \,\text{mm}$; (a) glass beads with $D_g = 50 \,\mu\text{m}$ vs. glycerol droplet with $D_i = 3.8 \,\text{mm}$ and $h = 160 \,\text{mm}$; (a) glass beads with $D_g = 50 \,\mu\text{m}$ vs. glycerol droplet with $D_i = 3.8 \,\text{mm}$ and $h = 160 \,\text{mm}$; (a) glass beads with $D_g = 50 \,\mu\text{m}$ vs. glycerol droplet with $D_i = 3.8 \,\text{mm}$ and $h = 160 \,\text{mm}$; and (b) glass beads with $D_g = 50 \,\mu\text{m}$ vs. glycerol droplet with $D_i = 3.8 \,\text{mm}$ and $h = 160 \,\text{mm}$; and (c) glass beads with $D_g = 50 \,\mu\text{m}$ vs. glycerol droplet with $D_i = 3.8 \,\text{mm}$ and $h = 160 \,\text{mm}$; and (d) glass beads with $D_g = 50 \,\mu\text{m}$ vs. glycerol droplet with D_i

of the impacting droplet is enhanced, which results in several small fingers at the perimeter of the deformed droplet. In fact, the fingering instability and resultant satellite droplet formations can be clearly confirmed in Fig. 6.14e, i. In another experiment, the onset condition of fingering instability in a droplet-granular impact was studied [68]. These researchers observed that the fingering instability occurs at

$$W_e^{1/2} R_e^{1/4} \ge 120. (6.60)$$

The fingering instability of an impacting droplet might be crucial when discussing the complex crater morphologies (e.g., micro crater rim structure and rampart crater). Because the fingering-like instability of the impacting liquid droplet is also an interesting problem in soft matter physics, an in-depth discussion of the fingering structure will be provided in the next section.

According to Ref. [69], the Bond number $B_o = \rho_i g D_i^2/\gamma_c$ (Eq. (2.104)) is an important dimensionless number to classify the dynamics of droplet-granular impact. In the large $B_o(>1)$ regime, the maximal droplet diameter $D_{\rm max}$ is linearly related to the impact velocity v_0 . In the small $B_o(<1)$ regime, $D_{\rm max}$ is scaled as $D_{\rm max}/D_i \sim W_e^{1/5}$. Note that the estimated scaling exponent is slightly smaller than 1/4. Furthermore, viscosity scaling, $D_{\rm max}$ (or D_c) $\propto R_e^{1/5}$ (Eq. (6.56)) could not be clearly confirmed in the droplet-granular impact experiment [67, 68]. Instead, the simple W_e scaling or v_0 dependence has been robustly observed. As observed in Fig. 6.14j, k, very viscous liquid droplets cannot be deformed significantly. Thus, the cratering by a very viscous droplet resembles the solid impactor case. If the impact inertia is dissipated by viscosity, R_e -dependent scaling must be observed in principle. In the very viscous droplet impact, however, the impact inertia would be dissipated mainly by the deformation of the granular target rather than the droplet viscosity. The target granular bed is weaker than the very viscous droplet.

The hydrophilicity of target grains affects the deformation dynamics. Some differences among SiC and glass-bead targets were already introduced above. In addition, if the target glass beads are coated by a hydrophobic suspension, the droplet deformation by the impact becomes completely different. Specifically, the maximal droplet diameter is scaled as $D_{\rm max} \propto W_e^{2/5}$ [70]. Moreover, the shape of the rebounding droplet can be frozen into a very irregular shape in this very hydrophobic grain case. The scaling exponent 2/5 is different from 1/4 and 1/5. Indeed, the scaling exponent for the relation between D_{max}/D_i (or D_c/D_i) and W_e is distributed from 1/6 to 2/5 [63, 66–71]. The relation $D_c \propto (\rho_i v_0^2 D_i^3)^{1/6}$ was observed in the droplet-granular impact experiment [71]. The scaling exponent 1/6 is quite different from 1/4; this 1/6 scaling is similar to a certain class of hypervelocity impacts [14, 72] and the 1/6 scaling exponent corresponds to the case of $\mu = 2/5$ in Eq. (5.58) scaling (Eq. (5.60)). This μ value is closer to the momentum scaling ($\mu = 1/3$) than the energy scaling ($\mu = 2/3$) (see Sect. 5.5.1 for the detail). In addition, the depth-diameter ratio $D_h/D_c \simeq 1/5$ was confirmed by this experiment. This result is consistent with the observed planetary-scale simple craters (Sect. 5.1). The similarity among hypervelocity impacts and very soft impacts is

suggestive of a simple physical mechanism. Perhaps, this result might indicate that the droplet-granular impact and hypervelocity solid-granular impact are very dissipative, whereas the low-velocity solid-granular impact is energy dominated.

Characteristic timescales of droplet-granular impact There are some characteristic timescales in this phenomenon. The first timescale is the droplet oscillation period governed by the surface tension, t_{γ} (Eq. (6.51)). The measured oscillation period for the droplet-granular impact is indeed independent of v_0 [63, 67]. This result is consistent with Eq. (6.51), which was originally computed for the droplet impact onto a hard wall.

Another important timescale is the penetration time, t_{pen} , which is defined by the duration from the impact instant to the complete drain. The measured t_{pen} shows a nontrivial dependence on the viscosity as [67]

$$t_{\rm pen} \propto \sqrt{\frac{\eta}{\rho_i}}$$
. (6.61)

Classical theory of liquid penetration into a porous medium predicts a simple relation called the Washburn law: $t_{\rm pen} \propto \eta/\gamma_c$ [73]. Using very slow droplet-granular penetration experiments, $t_{\rm pen}$ was measured and characterized by a simple relation which is consistent with the Washburn law [74, 75]. This result is contrary to Eq. (6.61). The reason for this discrepancy is the effect of the impact itself. When the impact velocity is sufficiently large, the granular target is significantly deformed and compacted by the initial impact. The physical property of such a deformed and compacted granular target could be different from the usual (unloaded) porous media.

The timescale of jet formation resulting from the droplet retractive collapse, $t_{\rm jet}$, was also measured and scaled as $t_{\rm jet}v_0/D_i \sim W_e^{1/2}$ [69]. This scaling is consistent with Eq. (6.52), which is not so surprising because the timescale of collapse of the receding droplet is determined by the droplet oscillation timescale. As mentioned above, the contact time, which represents the duration from the impact to the detachment by rebound, is almost independent of the impact velocity v_0 . This result is also consistent with Eq. (6.51). Thus, the contact time is also governed by the surface tension of the impacting droplet. Note that Eqs. (6.51) and (6.52) are consistent with each other; thus, all the timescales discussed in this subsection except $t_{\rm pen}$ are intrinsically identical.

Ejecta splashing by droplet-granular impact Granular ejecta splashed by liquid-droplet impact were investigated by Marston et al. [69]. Typical snapshots of the splashing and final crater shape are presented in the top left and right panels in Fig. 6.15, respectively. In general, the global structure of the splashing (ejecta curtain) is similar to that made by a solid sphere's impact (cf. Fig. 6.4). The difference between Figs. 6.4 and 6.15 is the degree of clustering in the ejecta curtain. One can observe the clustering of ejected grains in Fig. 6.15, which might be granulation due to the capillary bridge effect. Namely, the clustering can be caused by the liquid-droplet impact that mixes liquid and grains. This clustering structure is also confirmed in the top right panel of Fig. 6.15, in which a top view of the

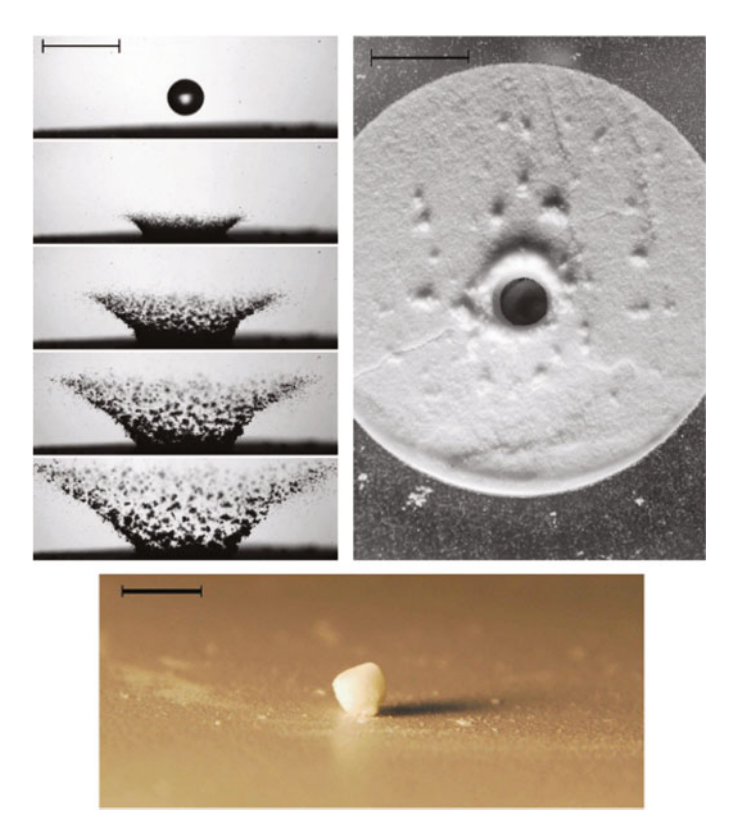


Fig. 6.15 Top left images: side-view snapshots of a droplet impact ($D_i = 2.4 \,\mathrm{mm}$ and 50% glycerol) captured by a high-speed camera. The target and impact conditions are $\phi_0 \sim 0.41$, $W_e = 188$, and $O_h = 0.019$. Top-right image: top view of the final crater and the deposited ejecta. Bottom image: granule nucleus structure after removal from the target granular bed. The scale bars are 5 mm (top left, bottom) and 10 mm (top right) (Reprinted from Ref. [69]. Copyright 2010, with permission from Elsevier)

final crater shape and ejected grains is shown. Several clustered ejecta fragments are distributed around the crater cavity. By precise tracking of ejecta fragments, the ejecta grains were classified into two types: the ejecta of water-encapsulated grains and the dry grains ejected from the periphery of the impact crater [76]. Distributions of the ejection velocity, angle, and travel distance were also measured in the experiment. However, the physical characterization of these distributions is not yet sufficient. Much more detailed studies are required to reveal what happens in the ejecta curtain created by the droplet-granular impact.

Granule nucleation and chemical engineering application The capillary-based cohesive effect can be observed directly by the granule nucleation as observed in the bottom plate of Fig. 6.15. The granular nucleus bound by the liquid capillary bridge is formed by the droplet-granular impact at its center. Such a nucleation process is very crucial in a wide range of chemical engineering processes. There are many

chemical engineering processes that require the efficient mixing of granular matter and liquid. Thus, the droplet-granular impact and the associated penetration have also been studied extensively in the chemical engineering field [74, 75, 77–80]. To control the mixture of grains and liquid, we must obtain the phase diagram of the mixing.

A spray of droplets on a granular bed is used to make granule or a general mixture of liquid and grains. In chemical engineering processes, the granular target layer is usually showered by numerous tiny droplets with a constant rate. By adjusting the spray rate per unit surface area, the granulation process is controlled. In such a situation, the dimensionless spray flux Ψ_{sp} is useful for characterizing its behavior [78]. Ψ_{sp} is defined as $\Psi_{sp} = 3\dot{V}/2\dot{A}D_i$, where \dot{V} , \dot{A} , and D_i are the spray (liquid) volume rate, area flux of the spray zone, and average diameter of the sprayed droplets, respectively.

In Refs. [79, 80], the crater morphologies are classified into three regimes: tunneling, spreading, and crater formation. The tunneling phase represents slow penetration with granule formation. Most likely, the sink-type crater (e.g., Fig. 6.14a) corresponds to this tunneling phase. In this capillary-dominated regime, a capillary force binds the granule structure. Thus, the capillary force must be stronger than the gravitational force. In contrast, if the capillary effect is not strong enough, the granular layer cannot be deformed by the penetrating droplet, and the produced nucleus cannot be stabilized. In this gravity-dominated regime, the impact inertia must be utilized to characterize the behavior. Cratering and spreading are observed in this regime. Thus, the balance between the capillary effect and gravity effect could be an essential factor to categorize the boundary between the tunneling and cratering (or spreading) phases. The granular Bond number B_{og} is introduced to characterize this balance:

$$B_{og} = \frac{\gamma_c}{D_o^2 \rho_g g},\tag{6.62}$$

where γ_c , D_g , and ρ_g are the surface tension of the droplet, diameter of grains, and density of each particle (not bulk density), respectively. When B_{og} is less than 60,000, spreading and cratering occurs whereas tunneling dominates at $B_{og} > 60,000$ [80]. In the small B_{og} regime, cratering or spreading occurs depending on impact inertia and target strength. The spreading phase corresponds to a rapid spreading of the droplet that results in surface wetting. This phase can be observed in Fig. 6.14f. To attain the spreading without cratering, grains must be very hydrophilic. Of course, B_{og} is not a unique quantity to classify the droplet-granular impact phases. Other factors such as impact inertia and viscosity could affect the phase boundary. Because the sprayed droplets are tiny and their impact velocities are not large in usual chemical engineering processes, B_{og} is the most important parameter.

Ring crater morphology At the end of this section, the morphologies of an actual lunar crater and droplet-granular impact crater are compared. In Fig. 6.16, the actual complex crater on the Moon and the ring-type crater created by the droplet-granular impact are displayed. Both craters have similar concentric double-ring

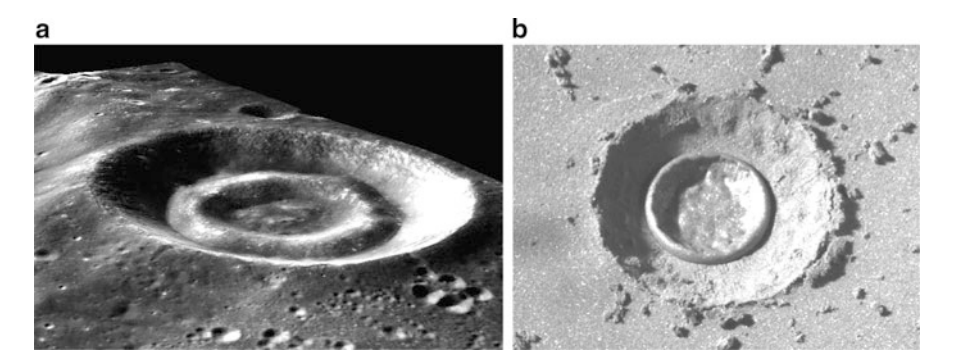


Fig. 6.16 (a) Actual lunar crater (Hesiodus A) with a concentric double-ring structure. Its diameter is approximately 15 km. The image was taken by SELENE and is provided courtesy of T. Morota. (b) Ring-type crater produced by a droplet-granular impact [63]. Its diameter is approximately 10 mm. Although their crater shapes are similar, the similarity of the underlying physical mechanisms is not clear. Rather, at present, this similarity is a coincidence

structures. However, their diameters are quite distinct. The diameters of the lunar crater and droplet-granular impact crater are approximately 15 km and 10 mm, respectively. The difference is over six orders of magnitude! Thus, the governing physical mechanisms must be different. For the droplet-granular impact cratering, surface tension of the droplet plays an essential role as discussed in this section. However, surface tension is completely negligible on a large scale. Although the surface gravity on the Moon is approximately 1/6 of that on the Earth, it remains sufficiently large to overwhelm the surface tension effect on the kilometer scale. Nevertheless, the actual crater's inner ring exhibits good circularity. The origin of this ring-type crater has not yet been understood. Whereas thermal effects, such as phase transitions, have been neglected in almost all the discussions thus far, these complex effects might be indispensable to rationalize the origin of various crater shapes. Currently, it is difficult to conclude the similarity between actual and laboratory-experimented craters. Most likely, these craters appeared similar by chance. Perhaps it is inappropriate to present these two crater shapes in the same figure. The similarity of the underlying physical mechanisms is necessary to discuss the correspondence of these shapes. However, such a morphological coincidence is sufficiently interesting to invoke curiosity. Much more detailed and systematic studies of soft impact cratering might provide some useful information to discuss the origin of various complex craters.

6.6 Instability of Soft Impact Cratering Rim

Instability on the expanding droplet's rim can be observed in the droplet-granular impact (e.g., Fig. 6.14e, i). The evidence of instability remains in the form of petal-like rim structures or secondary craters made by satellite droplets. This type of

instability induced in the impacted liquids (droplet or target) is related to the socalled milk-crown structure. Because the morphology of the milk-crown structure is very impressive, many research efforts have been devoted to the study of instability on expanding liquid film. Both the impacting droplet [81] and impacted waterbell structure [82] have been investigated as entities exhibiting the instability. Furthermore, a similar instability-like pattern was observed at the micro crater's rim observed on a sample that returned from the asteroid Itokawa (Fig. 5.6b). If the wavy crater rim structure observed in Fig. 5.6b originates from the instability, it will be possible to compare its rim structure with laboratory experiments. Using this comparison, the useful information from Itokawa's sample might be extracted from the morphology of the crater. For this purpose, the relation among the impact conditions (e.g., v_0 and D_i) and the number of fingers created by the impact-induced instability is particularly emphasized in this section. The former is what we want to know, and the latter is what we can observe directly. Here we introduce two contrasting scaling analyses. One is based on the impact Reynolds number and the other is associated with the Rayleigh-Taylor instability. Although these two ideas are not very consistent with each other, both are introduced and discussed through this section. The latter will be applied to estimate the impact velocity for the asteroid Itokawa's micro craters. However, some serious problems need to be overcome to reach a fully convincing estimate. Perhaps, we have not merely reached the unified principle behind this phenomenon. Thus, various understandings are possible and remain controversial; these understandings may only be empirical approximations. This situation is very similar to the former controversy concerning the various scaling laws for the granular impact drag force (Sect. 4.1.2). In the granular drag force case, the laws were finally unified by the empirical drag force law, Eq. (4.4). In contrast, our knowledge of the fingering and complex crater morphology remains very limited.

6.6.1 Impact Reynolds Number Scaling

From the viewpoint of dimensional analysis, the number of fingers induced by the splashing instability can be scaled by a relevant dimensionless number. The simplest starting point is the Reynolds number, R_e . Although R_e denotes the balance between inertia and viscosity, the surface tension must also be crucial for the fingering instability. Thus, we must involve the surface tension effect in the dimensionless number. To consider the surface tension effect, the characteristic timescale of the liquid spring t_{γ} (Eq. (6.51)) is considered here. A characteristic length scale l_{η} (diffusion length), which is made by viscosity-driven momentum diffusion during t_{γ} , is scaled as 14

¹⁴See Eq. (3.28). Note that the kinematic viscosity η/ρ_i corresponds to the diffusion coefficient K_d .

$$l_{\eta} \sim \left(\frac{\eta}{\rho_i} t_{\gamma}\right)^{1/2} = \left(\eta D_i \sqrt{\frac{D_i}{\rho_i \gamma_c}}\right)^{1/2}.$$
 (6.63)

Using l_{η} for the length scale of R_e , the impact Reynolds number, R_{eI} , is defined as

$$R_{eI} = \frac{\rho_i v_0 l_\eta}{\eta} = \left(\frac{\rho_i v_0^2 D_i}{\gamma_c}\right)^{1/4} \left(\frac{\rho_i v_0 D_i}{\eta}\right)^{1/2} = W_e^{1/4} R_e^{1/2}.$$
 (6.64)

In Refs. [83, 84], R_{el} was introduced and used for the analysis of the fingering instability induced by the liquid-droplet impact. The number of fingers N_f induced by the droplet impact on a hard floor is scaled as

$$N_f \sim R_{eI}^{3/4}$$
. (6.65)

The scaling exponent 3/4 was obtained by experimental data fitting [83]. However, the specific origin and physical meaning of the obtained exponent value remains unrevealed. Moreover, another dimensionless number $W_e^{5/4}R_e^{-1/2}$ can be obtained from the W_e form $\rho_i v_0^2 l_\eta / \gamma_c$. However, it appears to be inappropriate for characterizing the fingering. Because the validity of the scaling of Eq. (6.65) is demonstrated by the experiment, it is an empirical law.

6.6.2 Rayleigh-Taylor Instability

As introduced in Chap. 1, a type of instability is induced if a denser fluid layer is horizontally superposed on a lighter fluid layer under the uniform gravity condition. Because this initial state is gravitationally unstable, an overturning of these layers will occur. At the very initial stage of this overturn, a fingering structure called the Rayleigh-Taylor instability is observed. In general, if an acceleration a is applied normally to the interface of two fluids of densities ρ_h and ρ_l ($\rho_h > \rho_l$), the Rayleigh-Taylor instability is induced on the surface. Here the direction of a must be from the heavier fluid toward the lighter fluid. Otherwise, the layered structure is stable. By considering the capillary effect, the perturbation of a characteristic (angular) wavenumber k_f is selectively pronounced by the Rayleigh-Taylor instability.

The characteristic wavenumber k_f for an inviscid fluid layer is analytically calculable [85]. Here we derive k_f using an intuitive approach developed by Refs. [86, 87]. Let us consider the situation shown in Fig. 6.17. The heavier fluid is superposed above the lighter fluid. The initial (equilibrium) interface is taken as the x direction, and the acceleration is applied in the perpendicular direction from the heavier fluid to the lighter fluid. The depth dimension of the interface is denoted by D. Thus, the intersectional area of the interface is written as $A = D/k_f$. We focus on the case that the depth D is much less than $1/k_f$, namely, the quasi-two-dimensional

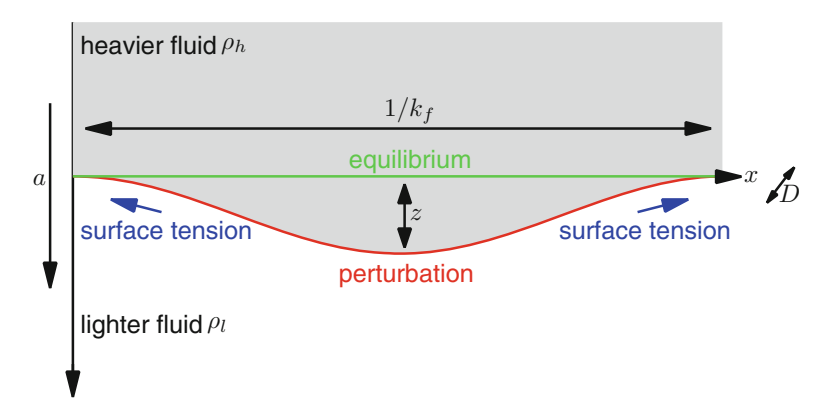


Fig. 6.17 Schematic drawing of the perturbation induced by the Rayleigh-Taylor instability. At the initial (equilibrium) state, the pressure is balanced. Any perturbation written by $z \exp(ik_F x)$ is always unstable if there is no surface tension. By considering the surface tension effect, the maximum growth rate is determined at a certain wavenumber written in Eq. (6.75)

situation is mainly considered. In other words, we neglect the perturbation structure in the depth direction. Both fluids are supposed to be incompressible, inviscid, and immiscible. At the initial equilibrium state, the pressure on the interface is balanced although it is unstable.

Here we consider a situation in which the equilibrium interface is disturbed by a perturbation. The scale of the perturbation to the acceleration direction is denoted by z, and its wavelength is written as $1/k_f$. The very early stage of the instability $(z \ll 1/k_f)$ is emphasized in this analysis. The force made by this perturbation F_p acting on the intersectional area A is written as

$$F_p = (\rho_h - \rho_l)azA = (\rho_h - \rho_l)az\frac{D}{k_f}.$$
 (6.66)

Fluids must be moved to develop this perturbation. The mass (inertia) of fluids relating to this perturbation motion can be estimated as

$$m_p = \rho_h \frac{A}{k_f} + \rho_l \frac{A}{k_f} = (\rho_h + \rho_l) \frac{D}{k_f^2}.$$
 (6.67)

Here we assume that the related volume is proportional to A/k_f rather than Az, which indicates that z is not a relevant length scale for the motion-relating volume estimation. The perturbation scale z only relates to the force as written in Eq. (6.66). Because the fluid motion evidently affects its neighborhood, it is impossible to move only the volume Az without any other fluid motion. Therefore, the length scale $1/k_f$ becomes relevant instead of z. This relating mass form is a key assumption in determining the appropriate characteristic wavenumber for the Rayleigh-Taylor instability.

Although the surface tension effect is necessary to obtain a meaningful characteristic wavenumber, we initially neglect its effect. Then, from Newton's equation of motion $(m_p(d^2z/dt^2) = F_p)$ and Eqs. (6.66) and (6.67), we obtain the following relation:

$$\frac{d^2z}{dt^2} = \frac{\rho_h - \rho_l}{\rho_h + \rho_l} ak_f z. \tag{6.68}$$

The solution of this ordinary differential equation (ODE) is

$$z = z_0 \exp\left(t\sqrt{\frac{\rho_h - \rho_l}{\rho_h + \rho_l}ak_f}\right),\tag{6.69}$$

where z_0 is the initial value of the perturbation. This solution suggests that any perturbation exponentially grows with time. This result is reasonable because the initial superposed structure $(\rho_h - \rho_l > 0)$ is absolutely unstable, and there is no resistance to it. The Atwood number $A_t = (\rho_h - \rho_l)/(\rho_h + \rho_l)$ (Eq. (2.108)) indicates the strength of this instability. The growth rate of this instability is denoted as $\delta_R = \sqrt{A_t a k_f}$. If $\rho_l > \rho_h$, Eq. (6.69) represents the oscillation. By considering the viscous dissipation, the perturbation vanishes because of the attenuating oscillation, namely, the setup can be stable due to the viscosity.

Next, we consider the role of surface tension for the instability. The surface tension at the interface works to stabilize (straighten) the interface of two fluids. The competition between the acceleration-driven instability and the capillary-driven stabilization determines the characteristic wavenumber of the Rayleigh-Taylor instability. The surface tension force acting at the interface can be calculated as

$$F_{\gamma} = \frac{\gamma_c}{R_c} A,\tag{6.70}$$

where γ_c is the surface tension of the interface and R_c is the radius of curvature of the perturbation, i.e., γ_c/R_c corresponds to the Laplace pressure (two-dimensional version of Eq. (2.100) with $R_1 = R_c$ and $R_2 = \infty$). The definition of the radius of curvature is given as ¹⁵

$$R_c = \frac{\left[1 + (dz/dx)^2\right]^{3/2}}{d^2z/dx^2}.$$
 (6.71)

¹⁵The radius of curvature is defined by $R_c = ds/d\theta$, where $ds = \sqrt{(dx)^2 + (dz)^2}$ is an arc length and $d\theta$ is the corresponding arc angle. The relation $d\theta = (d^2z/dx^2)dx/[1 + (dz/dx)^2]$ is obtained from the geometrical condition $\tan(\theta + d\theta) = dz/dx + (d/dx)(dz/dx)dx$ (using $d\theta \ll 1$, $\tan\theta = dz/dx$ and $\tan(\theta + d\theta) = (\tan\theta + \tan d\theta)/(1 - \tan\theta \tan d\theta)$). Equation (6.71) is computed from these relations.

Although the form of Eq. (6.71) is slightly complicated, the radius of curvature of the considered perturbation is approximated as

$$R_c \simeq -\frac{1}{zk_f^2}. ag{6.72}$$

Here a form of $z(x) = z \exp(ik_f x)$ is used and the conditions $k_f z \ll 1$ and $k_f x \ll 1$ are assumed because we focus on the vicinity of the perturbation tip, i.e., the Taylor expansion is applicable. From the equation of motion $m_p(d^2z/dt^2) = F_p + F_\gamma$ and Eqs. (6.66), (6.67), (6.70), and (6.72), one can obtain

$$\frac{d^2z}{dt^2} = \left[\frac{\rho_h - \rho_l}{\rho_h + \rho_l} a k_f - \frac{\gamma_c k_f^3}{\rho_h + \rho_l}\right] z. \tag{6.73}$$

The corresponding growth rate becomes

$$\delta_{Rs} = \sqrt{\frac{\rho_h - \rho_l}{\rho_h + \rho_l} ak_f - \frac{\gamma_c k_f^3}{\rho_h + \rho_l}}.$$
(6.74)

In contrast to the no surface tension case, this growth rate can be either a real number or an imaginary number depending on k_f even if ρ_h and ρ_l are fixed. The maximum growth rate is achieved when $\partial \delta_{\rm Rs}/\partial k_f=0$. Thus, the maximum-growth wavenumber is obtained as

$$k_f = \sqrt{\frac{(\rho_h - \rho_l)a}{3\gamma_c}}. (6.75)$$

This form is quite natural because it can be expressed by the inverse of the capillary length. Using $(\rho_h - \rho_l)a$ instead of ρg in Eq. (2.99), a simple relation $k_f = (\sqrt{3}\lambda_c)^{-1}$ is obtained. As long as the competition between the inertia and capillary effect governs the instability, ¹⁶ the corresponding capillary length must be a characteristic length scale.

6.6.3 Instability-Based Scaling and Splashing Parameter

The relation among the fingering number and impact conditions can be evaluated by assuming that the fingering structure on the splashing rim originates from the Rayleigh-Taylor instability. Because the impact of a droplet of diameter D_i and velocity v_0 is considered, the characteristic acceleration a can be estimated as

¹⁶This criterion is equivalent to the condition that the viscosity is negligible.

 $a \simeq v_0^2/D_i$. Furthermore, let us consider the situation that the density difference is very large, $\rho_i \simeq \rho_h \gg \rho_l$. Applying these approximations, Eq. (6.75) is rewritten as

$$k_f \simeq \frac{1}{\sqrt{3}D_i} W_e^{1/2}.$$
 (6.76)

To compute the number of fingers N_f , the total length of the accelerated interface is required. This value can be approximated by the perimeter length of the droplet at the maximally deformed state, $\pi D_{\rm max}$. Because the wavelength is written as $2\pi/k_f$, $N_f = \pi D_{\rm max}/(2\pi/k_f)$ is calculated as [88]

$$N_f \simeq \frac{1}{2\sqrt{3}} \frac{D_{\text{max}}}{D_i} W_e^{1/2}.$$
 (6.77)

When the droplet deformation obeys spring-like behavior, Eq. (6.49) can be used to estimate $D_{\rm max}$. Then, a simple scaling $N_f \sim W_e^{3/4}$ is obtained. The number of fingers is purely determined by W_e in this form. However, it is empirically known that the viscosity also affects the fingering; then, $D_{\rm max}$ should be related to the viscosity. This necessity of viscosity is a slightly tricky assumption to obtain the general relation among N_f , W_e , and R_e . Moreover, the mode obtained by Eq. (6.75) is based on the inviscid assumption. Thus, the following derivation of the relevant dimensionless number is very empirical. The relation between $D_{\rm max}$ and R_e can be computed in the viscosity-dominant regime. Although such a relation was already estimated in Eq. (6.57), another scaling has been used in the literatures for the fingering instability [89–91]. Concretely, the energy dissipation due to the viscosity is estimated by the method slightly different from Eq. (6.55). The viscous energy dissipation W_η is estimated as

$$W_{\eta} \sim \eta \left(\frac{v_0}{H_{\min}}\right)^2 D_{\max}^2 H_{\min} t_{\text{def}},\tag{6.78}$$

where $t_{\rm def}$ is the time taken to achieve the maximal deformation, $t_{\rm def} \sim D_i/v_0$. If the kinetic energy $E_{\rm kei} \sim \rho_i D_i^3 v_0^2$ is mainly dissipated by W_{η} , $D_{\rm max}$ is scaled by D_i and R_e as

$$D_{\text{max}} \sim D_i R_e^{1/4}$$
. (6.79)

Here the geometrical relation $H_{\rm min}D_{\rm max}^2 \sim D_i^3$ is used to obtain Eq. (6.79). The obtained scaling exponent 1/4 is slightly different from the previously calculated value 1/5 in Eq. (6.56). In the literature, the energy balance was considered with numerical factors and the relation $D_{\rm max} \simeq (1/2)D_iR_e^{1/4}$ was obtained for the case $W_e \gg R_e$ (viscosity-dominant regime) [89–91]. Substituting this relation into Eq. (6.77), N_f is evaluated as

$$N_f \simeq \frac{1}{4\sqrt{3}} W_e^{1/2} R_e^{1/4}. \tag{6.80}$$

The dimensionless number K_s defined by

$$K_s = W_e^{1/2} R_e^{1/4} (6.81)$$

is called the *splashing parameter* and is often used to characterize the phase boundary between the no-splashing (stable) and splashing (unstable) phases. Actually, Eq. (6.60) (onset criterion for the splashing) is an example of such characterizations. The critical splashing parameter was obtained for a smooth surface target case as 57.7 [89], and for a 5 μ m fiber bed as 87 [92]. According to Eq. (6.56), $W_e^{1/2}R_e^{1/5}$ might also be possible for the splashing parameter. Because the difference between $R_e^{1/4}$ and $R_e^{1/5}$ is not remarkable in the studied regime, it is difficult to definitely conclude which one is better than the other. This type of ambiguity is a typical limitation of the dimensional analysis, especially when the considered range of parameters is limited. However, the splashing parameter is usually denoted by $W_e^{1/2}R_e^{1/4}$.

There is another serious conflict in the scaling of N_f . Whereas the splashing parameter is denoted as $K_s = W_e^{1/2} R_e^{1/4}$, the impact Reynolds number is expressed as $R_{el} = W_e^{1/4} R_e^{1/2}$. This difference originates from the derivation approach of the relevant dimensionless numbers (Eqs. (6.65) and (6.80)). For the derivation of the impact Reynolds number, a capillary-based timescale t_{ν} and the length scale of momentum diffusion due to the viscosity were considered. However, capillaryinduced instability and viscous dissipation were considered in the derivation of the splashing parameter K_s . That is, the origins of the instability are supposed to be the viscosity-capillary-related momentum diffusion and the capillary-based Rayleigh-Taylor instability for R_{el} and K_s , respectively. Note that Eq. (6.65) cannot predict the absolute number of the induced fingers because it is derived solely on the basis of dimensional analysis. In contrast, because Eqs. (6.80) and (6.77) include the numerical factor, the concrete value of N_f can be directly calculated using these forms. Although Eq. (6.77) is based on the instability theory, the numerical coefficient in Eq. (6.80) is somehow obtained empirically. Thus, the use of Eq. (6.77) might be safer than the use of Eq. (6.80) as long as it is useful.

The abovementioned computation has concerned the liquid droplet deformation. To consider the cratering, the scaling of cratering should be employed instead of the droplet deformation scaling. By considering the gravity regime for the liquid cratering, another scaling of N_f is obtained. Here the energy balance between the crater cavity potential $E_{\rm cav} = \pi \rho_t g (D_{\rm max}/2)^4/4$ (Eq. (6.2)) and the kinetic energy $E_{\rm kei} = \pi \rho_i D_i^3 v_0^2/12$ is assumed. Then, $D_{\rm max}$ is calculated as

$$D_{\text{max}} = \left(\frac{16}{3} \frac{\rho_i}{\rho_t} \frac{D_i^3 v_0^2}{g}\right)^{1/4} = 2D_i \left(\frac{\rho_i}{3\rho_t} F_r\right)^{1/4}.$$
 (6.82)

Essentially, this form is identical to Eq. (6.16). Substituting Eq. (6.82) into Eq. (6.77), N_f in the gravity regime is obtained as

$$N_f \simeq \left(\frac{1}{27} \frac{\rho_i}{\rho_t} F_r\right)^{1/4} W_e^{1/2}.$$
 (6.83)

This form might better explain the fingering by cratering of a fluid (gravity regime), although capillary- and viscosity-based scalings are relevant to the droplet impact situation.

6.6.4 Instability in Various Cratering and Impact Phenomena

Using Eq. (6.77), one can roughly evaluate the impact velocity causing the wavy rim structure observed on Itokawa's micro crater (Fig. 5.6b). The impact velocity v_0 is calculated from Eq. (6.77) as

$$v_0 \simeq \frac{2N_f}{D_c} \sqrt{\frac{3D_i \gamma_c}{\rho_i}},\tag{6.84}$$

where D_c is the crater diameter. Of course, Eq. (6.84) provides a reasonable estimate for the fingering states observed in Fig. 6.14d, e. Substituting typical values ($N_f = 10$, $D_c = 2D_i = 10$ mm, $\gamma_c = 72 \times 10^{-3}$ J/m², and $\rho_i = 10^3$ kg/m³) into Eq. (6.84), one can obtain $v_0 \simeq 2$ m/s which is consistent with the actual experimental condition.

To compute v_0 of Itokawa's micro crater, the characteristic properties of both the impacting and impacted materials (supposed to be silicate) are assumed to be $\rho_i=2\times 10^3\,\mathrm{kg/m^3},\ \gamma_c=0.014\,\mathrm{J/m^2}$ [93], and $D_c\simeq 2D_i\simeq 200\,\mathrm{nm}$. Then, from $N_f\simeq 7,\ v_0=1.0\times 10^2\,\mathrm{m/s}$ is obtained. If the target is molten, γ_c becomes approximately one order of magnitude larger. Although this difference certainly affects the v_0 estimation, the order of v_0 is $10^2\,\mathrm{m/s}$ as long as Eq. (6.84) is relevant. The assumption $D_c\simeq 2D_i$ roughly corresponds to $F_r\simeq 1$ in the gravity regime (Eq. (6.82)). However, it is actually difficult to satisfy this condition under the microgravity condition. Instead, the finite strength of the target Y_t should be considered. From the simple energy balance with a hemispherical cavity approximation, $\pi D_c^3 Y_t/12 = \pi \rho_i D_i^3 v_0^2/12$, one can modify Eq. (6.84) as [94]

$$v_0 = \left(\frac{12N^2 \gamma_c}{\rho_t D_i}\right)^{3/10} \left(\frac{Y_t}{\rho_i}\right)^{1/5}.$$
 (6.85)

The strength of the target can be estimated as $Y_t = 2.5$ MPa using Eq. (6.85) and the abovementioned parameters. The number of fingers N_f in this strength regime can be written as

¹⁷The assumption $D_c \simeq 2D_i$ is not actually very evident in astronomical impacts. While we assume this approximation herein, another constraint is necessary to obtain the truly closed form.

$$N_f \simeq \frac{1}{2\sqrt{3}} \left(\frac{\rho_i v_0^2}{Y_t}\right)^{1/3} W_e^{1/2}.$$
 (6.86)

This form is useful for the rough estimate of the impact conditions particularly in the microgravity environment. Equations (6.83) and (6.86) represent the number of fingers in the gravity and strength regimes, respectively.

However, this estimate is far from perfect. First, the impactor and target must be sufficiently soft to induce the instability. However, the deformed target must be rapidly solidified directly after the fingering; otherwise, the induced fingering structure is relaxed by viscosity. It is not apparent whether such a fortunate impact event is possible. The next problem may be more fatal. We have assumed the Rayleigh-Taylor instability for the origin of the fingering instability. The Rayleigh-Taylor instability requires the existence of a boundary interface of two fluids. However, the space environment is ultra-high vacuum. The existence of ambient air is essential for splashing instability, although we often forget its presence. In fact, it turns out that the splashing instability is inhibited under the vacuum condition [95]. To evaluate the boundary between the splashing (fingering) state and the nonsplashing state, the stress balance was considered in Ref. [95]. The shock stress of the surrounding gas σ_G can be estimated as $\sigma_G = \rho_G C_G v_G$, where ρ_G , C_G , and v_G are the gas density, its speed of sound, and the expanding velocity of the interface, respectively. And, the stress caused by the capillary and viscosity effects of the liquid impactor, $\sigma_L = \gamma_c/l_{\eta} = \gamma_c/\sqrt{\eta t/\rho_L}$, works as a counterpart. Here η , ρ_L and t denote the liquid viscosity, its density, and the time measured from the instant of impact, respectively. Considering the ideal gas, $\rho_G C_G v_G$ can be written as $\rho_G C_G v_G = (pm_m/k_B T) \sqrt{\gamma_a k_B T/m_m} \sqrt{D_i v_0/4t}$, where m_m , γ_a , k_B , and T are the molecular weight of the gas, adiabatic constant, Boltzmann constant, and temperature, respectively. According to the experimental result, the unstable splashing (fingering) occurs when σ_G/σ_L exceeds approximately 0.5 [95]. From this experimental result, one can evaluate the required impact velocity v_{0r} to induce the instability as

$$v_{0r} \propto \frac{\gamma_c^2}{\eta} \frac{T}{p^2}.\tag{6.87}$$

Because the pressure in space is extremely low (less than 10^{-10} atm), it is impossible to attain the fingering instability using a practical impact velocity range.

To overcome these difficulties, melting and vaporization caused by the impact must be considered. Then, liquid and ambient gaseous phases might be simultaneously created. The rheological and thermodynamic properties of molten and vaporized silicate would be needed for a complete consistency check of this concept. Perhaps, some other factors such as viscoelasticity might be helpful to induce the fingering-like instability in space. Whereas the impact onto a viscoelastic target has been studied [96–98], details specific to the fingering instability have not yet been

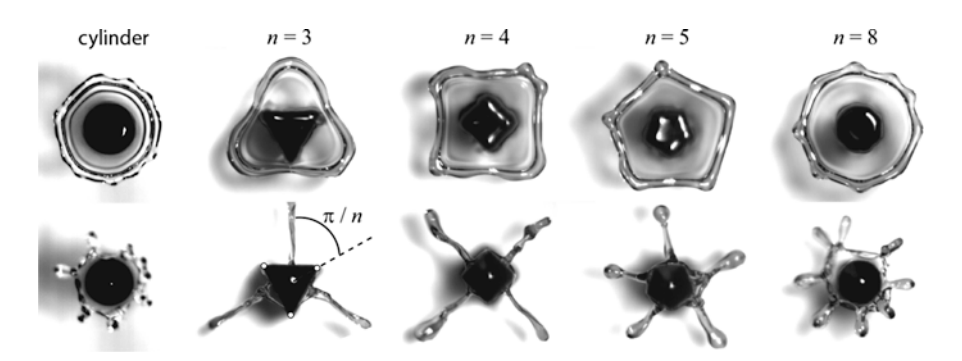


Fig. 6.18 Top-view images of the liquid lamella created by the impact of a liquid droplet consisting of a mixture of water and glycerol. The droplets are vertically impinged onto geometric target posts with $R_e = 550$ and $W_e = 250$. The number of vertices of the post is denoted by n. The *top row* and *bottom row* correspond to the snapshots at $t = 2D_i/v_0$ and $4D_i/v_0$, respectively (Reprinted with permission from Ref. [100]. Copyright 2012 by American Physical Society)

revealed. In-depth analyses including the thermodynamic effect, phase transitions, and complex rheology are necessary to assess the possible fingering instability occurring in space.

Moreover, the splashing instability depends on other factors. For example, the hydrophilicity of the impactor or target surface significantly affects the splashing state. When a very hydrophilic impactor impinges on a liquid pool, a quiet (no-splashing) penetration can be observed [99]. The roughness of the surface further enhances the instability, and the target shape can also affect the number of fingers induced by the droplet impact [100]. In Fig. 6.18, geometry-dependent lamella shapes created by a liquid-droplet impact onto various geometric target posts are shown. The liquid-droplet impactor comprises a mixture of water and glycerol. The impact condition for all the impacts in Fig. 6.18 is $R_e = 550$ and $W_e = 250$. The top and bottom rows in Fig. 6.18 correspond to two characteristic times: $t = 2D_i/v_0$ and $4D_i/v_0$, respectively, and n denotes the number of vertices of the target post. One can clearly observe that the number of fingers induced by the impact is determined by n. If n is sufficiently large (n > 7), however, the situation is similar to the cylindrical target posts. In this large n regime, the fingering instability is presumably determined by the intrinsic fluid property.

In this section, we have overviewed the fingering instability occurring in soft matter impact. In particular, the liquid-droplet impact and the associated fingering instability have been emphasized. Two possibly relevant dimensionless parameters, the impact Reynolds number $R_{eI} = W_e^{1/4} R_e^{1/2}$ and the splashing parameter $K_s = W_e^{1/2} R_e^{1/4}$, were introduced. While the former is based on the liquid spring mechanism and viscosity-based momentum diffusion length scale, the latter is derived from the Rayleigh-Taylor instability (or equivalently the corresponding capillary length) and the viscous dissipation. Additionally, $(\rho_i/\rho_t)^{1/4} F_r^{1/4} W_e^{1/2}$ and $(\rho_i v_0^2/Y_t)^{1/3} W_e^{1/2}$ were introduced to model the fingering of craters in the gravity and strength regime, respectively. The number of fingers induced by the droplet-granular

impact can be estimated using the Rayleigh-Taylor (capillary-based) instability. However, it is not easy to apply that instability to the fingering (wavy structure) observed on the asteroid Itokawa's nano-crater rim. Thermodynamic effects and complex rheological properties must be involved for a more accurate estimate. Because various effects such as the surface property and target shape can affect the fingering instability, several additional studies should be performed to discuss the origin of the fingering structure observed in the space environment.

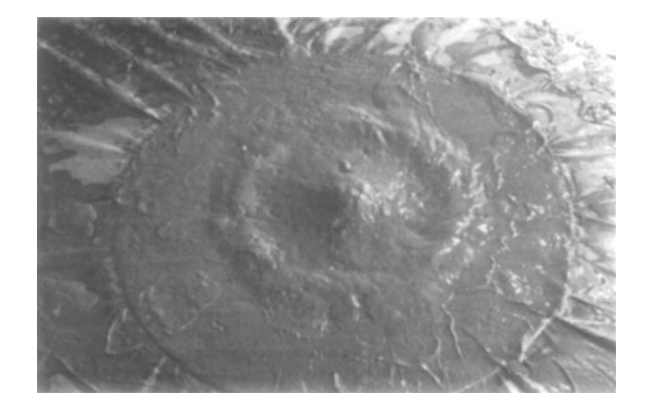
6.7 Wet Granular Impact Cratering

How does the target property (e.g., cohesiveness of grains) affect the impact crater morphology? More specifically, what occurs when the target granular layer is wet and cohesive? In Sect. 4.1.7, we have already reviewed the effect of the interstitial liquid content on the impact drag force. However, the effect of the interstitial liquid on crater morphology has not been discussed. In fact, there are very few investigations that address wet granular impact cratering. Some studies on crater morphology produced by the wet granular target will be introduced in this section.

Soupy mud impact In 1978, a high-velocity impact experiment on a "soupy" mud target was performed to mimic rampart crater formation [101]. A Pyrex glass sphere with diameter $D_i = 3.175-6.35\,\mathrm{mm}$ was shot into a soupy mud target with an impact velocity of $v_0 = 1.6\,\mathrm{km/s}$. The soupy mud target consisted of homogeneous mixtures of potter's clay and water. A typical resultant crater is shown in Fig. 6.19. As observed in Fig. 6.19, ejected mud layers compose a petal-like structure, which indeed resembles the rampart crater morphology. However, the similarity is limited only in the morphological style. The underlying physical mechanisms causing such structures have not yet been revealed.

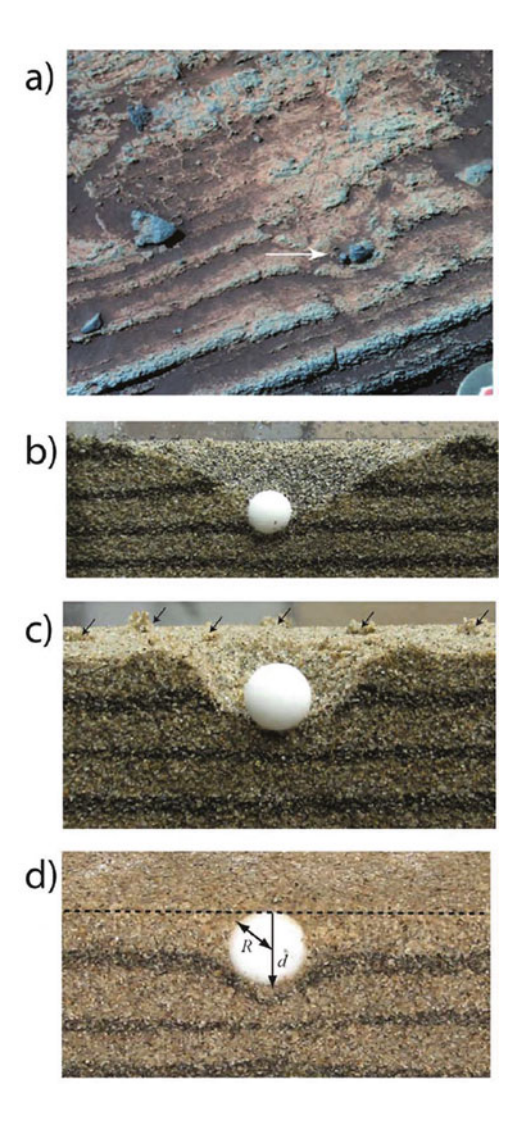
Over 30 years have passed since this pioneering work on wet granular impact cratering [101]. Nevertheless, only very few studies have tackled wet granular impact cratering since then.

Fig. 6.19 Crater shape produced by a hypervelocity impact ($v_0 = 1.6 \text{ km/s}$) of a Pyrex sphere ($D_i = 3.175 \text{ mm}$) on a soupy mud target. A typical ejecta deposition pattern and a central peak structure can be observed (Reprinted from Ref. [101], with permission from Elsevier)



Bomb sag The next study was performed to discuss the bomb sag structures observed on the surface of Mars [102]. Although this study did not focus on the rampart crater, it is also motivated by the possible cohesiveness-related terrain observed on Mars. By the Mars exploration rover Spirit, a bomb sag on Mars was found. Its structure is shown in Fig. 6.20a [103]. The size of the bomb (clast) is approximately 4cm. Thus, this structure is not a large-scale structure such as rampart craters. Bomb sags are usually associated with volcaniclastic deposits. When a clast exploded by eruption is emplaced onto an ash (fine grains) bed, such a typical bomb sag is formed, at least on the Earth. Manga et al. performed a low-velocity impact experiment on the dry or wet granular target (using sand in diameter

Fig. 6.20 (a) Bomb sag discovered by the Mars exploration rover Spirit. The bomb is approximately 4 cm across. One can confirm the deflected layer, which provides evidence of soft impact. Vertical slices of the wet granular impact experiments are shown in (b)-(d): (b) Dry sand, (c) damp sand, and (d) water-saturated sand were used as targets (Reproduced from Ref. [102] by permission of John Wiley & Sons Ltd)



 $D_g \simeq 0.5$ mm) to reproduce the bomb sag structure [102]. The impactors that they used are spheres and natural scoria particles of $\rho_i = 1.0$ –7.7 \times 10³ kg/m³ and $D_i \simeq 13$ –130 mm. The bomb sag structure differs from the usual impact cratering because the impacting clast deforms the layers beneath it. Such deformation cannot be observed if the target granular bed is cohesionless. The target bed is simply excavated in usual impact cratering, and the layered structure is never deflected by the impact (Fig. 6.20b). If the target is wet but its water content is insufficient, no bomb sag structure is confirmed, whereas the clustered ejecta is observed (Fig. 6.20c). Although the quantitative characterization of the degree of water-grain mixing was not conducted in this study, these researchers observed that low-angle oblique impact onto a water-saturated granular bed is necessary to mimic the bomb sag structure (Fig. 6.20d). This finding indicates that abundant liquid content and gentle impact are necessary to form a bomb-sag-like structure. These researchers also observed that the penetration depth depends on the constituent grain's size in the water-saturated granular impact [104].

Crater morphology for wet granular impact A low-velocity impact cratering experiment using various wet granular beds was systematically performed by Takita and Sumita [105]. These researchers employed beach sand ($D_g \simeq 0.2$ mm and $\rho_g \simeq$ 2.6×10^3 kg/m³) as a target and methodically varied the water saturation parameter S_{at} (Eq. (4.36)). A steel sphere ($D_i = 10.0 - 22.2 \,\mathrm{mm}$ and $\rho_i = 7.7 \times 10^3 \,\mathrm{kg/m^3}$) was dropped onto the wet granular target with $v_0 = 1.2-5.8$ m/s. The crater morphology and its classification were examined in this study. When the water saturation S_{at} is less than 0.02, a simple crater is created, i.e., the crater shape is the same as the dry granular target case. At $0.02 < S_{at} < 0.04$, a transitional crater is formed. In this regime, the angle of the crater's wall is steeper than that of the simple crater because of the stabilization by the water content. In the transitional crater, a corrugated wall structure can also be observed. This corrugation most likely originates from the yielding of the wet granular target. When S_{at} is greater than 0.04 (but less than 0.6), the side wall of the crater stands vertically against gravity. Thus, the resultant crater left in this regime has a cylindrical shape. In Ref. [105], the very high saturation regime ($S_{at} > 0.6$) was not tested. In this high saturation regime, the yield stress of the wet granular matter becomes a decreasing function of S_{at} [105]. This regime corresponds to the soupy mud state rather than the wet sand state.

6.8 Fluid Flow Impact Cratering

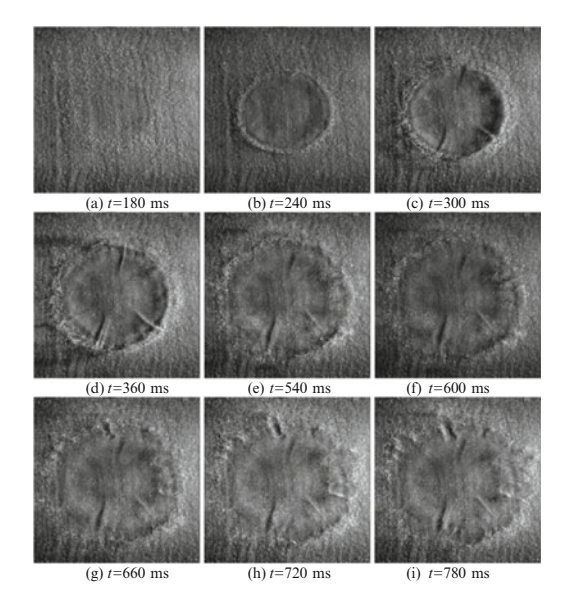
At the limit of $S_{at} = 1$, the granular layer is completely submerged in a liquid layer, i.e., all the void space is filled by liquid content. In this situation, the interstitial liquid effect would play a vital role in the cratering dynamics. This completely saturated state almost corresponds to soupy mud or a dense suspension. In fact, even in dry granular matter under 1 atm ambient pressure condition, the void space is filled with air. Therefore the usual dry granular matter is surrounded by

gas. However, its effect is negligible because of the small $R_{\eta g}$ as long as we use macroscopic grains of $D_g > 0.1$ mm (see Sect. 3.9.2). In this case, because the density of solid grains is much greater than that of interstitial air, only the viscosity is considered. However, the density of the liquid can be comparable (becomes the same order) with that of solid grains. Thus, we may need to consider the inertia of the interstitial fluid as well as that of the grains to analyze the bulk motion of granular matter submerged in water. The Shields number S_h (Eq. (2.113)) would be a relevant dimensionless number.

Successive impacts of a train of droplets onto a water-covered sand bed were experimentally investigated [106]. Specifically, water droplets with diameters of $D_i \simeq 2$ mm were successively dropped from a free-fall height of approximately 0.1 m onto a water-covered sand bed. Then, the crater shape created by the successive impacts were analyzed. According to Ref. [106], if the impact rate exceeds a certain critical value (roughly $\mathcal{O}(10^0)$ drops/s), the crater shape becomes asymmetric. Although the physical mechanism of this symmetry breaking has not yet been revealed, this experimental result typically shows the complex interaction between the interstitial fluid and grains in the crater formation event.

Vortex ring impact cratering If the inertia of the interstitial fluid is sufficiently strong, fluid flow can directly form a crater-like structure. For instance, a vortex ring impacting onto a granular layer in a water pool was experimentally studied [107–109]. A typical temporal sequence of cratering by the vortex ring impact is shown in Fig. 6.21. Directly after the impact, a symmetric shallow crater is produced. After a while, radial structures are engraved by the secondary vortex rings. Although this cratering may be a type of complex cratering, its relevance to planetary-scale phenomena remains uncertain. If a meteor impactor strikes the

Fig. 6.21 Temporal sequence of a vortex ring impact onto a granular surface in water ($R_e = 4,100$). At the very initial stage, a symmetric circular crater is produced. Then, secondary vortex rings engrave complex patterns around the crater rim (Reproduced by permission of IOP Publishing: [109], Copyright: The Japan Society of Fluid Mechanics)



6.9 Summary 257

ocean, this type of crater can be formed on the seabed. R_e and S_h are considered to be the relevant dimensionless numbers in characterizing this phenomenon. However, the quantitative description of the phenomena, such as scaling analysis, has not yet been completely established.

Gas jet impact cratering Even a gas jet flow can produce a crater. Although the density of gas is small, its inertia is not negligible if the jet speed is sufficiently high. When a spacecraft leaves or lands on the surface of planets, the surface regolith layer is exposed to the jet flow from the spacecraft. To appropriately handle the spacecraft, we must know the cratering dynamics induced by the gas jet impinging onto a granular bed. This problem has been studied by space engineers since the 1960s. From these pioneering works, three mechanisms in the jet-induced cratering were proposed [110, 111]. The first mechanism is viscous erosion, in which the surface layer of the grain bed is eroded by shear. Thus, this mechanism works tangentially to the surface. The second mechanism is called bearing capacity failure. This mechanism dominates the phenomenon when the dynamic pressure of the jet exceeds the bearing capacity of the target granular bed. By this mechanism, the jet applies mechanical loading and forms a depression; it corresponds to the normal stress loaded on the surface by the localized source of the gas jet. The third mechanism is diffused gas eruption, which is an eruption of grains caused by immersed gas pressure in the granular bed. As previously mentioned, the cratering by a vortex ring impact appears to be driven mainly by viscous erosion. Viscous erosion was also studied using the direct gas jet impact on loose granular matter [112]. According to various experimental results, the depth of the crater formed by the gas jet logarithmically increases with time [110, 112].

6.9 Summary

Cratering phenomena induced by a relatively low-velocity impact on a soft matter target have been discussed in this section. Various types of complex crater shapes were experimentally produced by oblique impact, jet formation, granular-granular impact, and droplet-granular impact. In particular, the complex interaction among liquid and granular matter induces various intriguing crater shapes through the granular-granular and droplet-granular impacts. Some characteristic structures such as rampart craters, fingering instability, and bomb sag, were also discussed mainly on the basis of the results of laboratory experiments. Although some of these structures might be relevant to planetary-scale impact cratering, a large gap between the low-velocity impact experiments and actual planetary cratering still persists. Nevertheless, both sometimes exhibit similar morphologies and scaling relations. The usual laboratory experiment is strongly constrained by gravity. On the other hand, the space environment is ultimate: microgravity, vacuum, and low temperature. Additionally, the impact velocity could be very high in astronomical impact events. It is difficult to reproduce impact cratering with such an ultimate environment.

Instead, various laboratory analogue experiments have been performed. Although simple analogue experiments could be helpful in understanding the nature of impact cratering, much further details are required to compare these soft impact results with actual planetary cratering. For further reading, Ref. [113] is an evocative review article concerning granular impact cratering phenomena. Soft impact cratering itself is actually interesting enough for the fundamental physics of soft matter. The cratering is a result of the complex rheological property of the impactor and target. In-depth investigations of soft impact cratering are crucial for both planetary science and fundamental physics.

References

- 1. O.G. Engel, J. Appl. Phys. 37, 1798 (1966)
- 2. O.G. Engel, J. Appl. Phys. 38, 3935 (1967)
- 3. A. Prosperetti, H.N. Oguz, Ann. Rev. Fluid Mech. 25, 577 (1993)
- 4. H. Lamb, Hydrodynamics, 6th edn. (Cambridge University Press, New York, 1993)
- 5. I.V. Roisman, E. Berberovic, C. Tropea, Phys. Fluids **21**, 052103 (2009)
- E. Berberović, N.P. van Hinsberg, S. Jakirlić, I.V. Roisman, C. Tropea, Phys. Rev. E 79, 036306 (2009)
- 7. A. Bisighini, G.E. Cossali, C. Tropea, I.V. Roisman, Phys. Rev. E 82, 036319 (2010)
- 8. H. Tabuteau, D. Sikorski, S.J. de Vet, J.R. de Bruyn, Phys. Rev. E 84, 031403 (2011)
- 9. J.S. Uehara, M.A. Ambroso, R.P. Ojha, D.J. Durian, Phys. Rev. Lett. 90, 194301 (2003)
- 10. J.S. Uehara, M.A. Ambroso, R.P. Ojha, D.J. Durian, Phys. Rev. Lett. 91, 149902 (2003)
- 11. A.M. Walsh, K.E. Holloway, P. Habdas, J.R. de Bruyn, Phys. Rev. Lett. 91, 104301 (2003)
- 12. S.J. de Vet, J.R. de Bruyn, Phys. Rev. E 76, 041306 (2007)
- 13. K.A. Holsapple, R.M. Schmidt, J. Geophys. Res. Solid Earth 87(B3), 1849 (1982)
- 14. K.A. Holsapple, Annu. Rev. Earth Planet. Sci. 21, 333 (1993)
- R.M. Schmidt, in Eleventh Lunar and Planetary Science Conference (Lunar and Planetary Institute, Houston, 1980), Abstract #1351
- 16. X.J. Zheng, Z.T. Wang, Z.G. Qiu, Eur. Phys. J. E 13, 321 (2004)
- 17. S. Deboeuf, P. Gondret, M. Rabaud, Phys. Rev. E 79, 041306 (2009)
- 18. M.J. Cintala, L. Berthoud, F. Hörz, Meteorit. Planet. Sci. 34, 605 (1999)
- 19. J.L.B. Anderson, P.H. Schultz, J.T. Heineck, Meteorit. Planet. Sci. 39, 303 (2004)
- J.L.B. Anderson, P.H. Schultz, in *Thirty-sixth Lunar and Planetary Science Conference* (Lunar and Planetary Institute, Houston, 2005), Abstract #1773
- 21. J.F. Boudet, Y. Amarouchene, H. Kellay, Phys. Rev. Lett. 96, 158001 (2006)
- 22. J.O. Marston, E.Q. Li, S.T. Thoroddsen, J. Fluid Mech. 704, 5 (2012)
- 23. D.A. Weiss, A.L. Yarin, J. Fluid Mech. 385, 229 (1999)
- G. Caballero-Robledo, K. Kelly, T. Homan, J. Weijs, D. Meer, D. Lohse, Granul. Matter 14, 179 (2012)
- J.R. Royer, E.I. Corwin, B. Conyers, A. Flior, M.L. Rivers, P.J. Eng, H.M. Jaeger, Phys. Rev. E 78, 011305 (2008)
- 26. A.M. Worthington, R.S. Cole, Philos. Trans. R. Soc. A 189, 137 (1897)
- 27. A.M. Worthington, R.S. Cole, Philos. Trans. R. Soc. A 194, 175 (1900)
- 28. A.M. Worthington, A Study of Splashes (Longman and Green, London, 1908)
- A. Ogawa, K. Utsuno, M. Mutou, S. Kouzen, Y. Shimotake, Y. Satou, Part. Sci. Technol. 24, 181 (2006)
- 30. M.A. Cook, K.S. Mortensen, J. Appl. Phys. 38, 5125 (1967)
- 31. S.T. Thoroddsen, A.Q. Shen, Phys. Fluids 13, 4 (2001)

References 259

- 32. D. Lohse, R. Rauhé, R. Bergmann, D. van der Meer, Nature 432, 689 (2001)
- D. Lohse, R. Bergmann, R. Mikkelsen, C. Zeilstra, D. van der Meer, M. Versluis, K. van der Weele, M. van der Hoef, H. Kuipers, Phys. Rev. Lett. 93, 198003 (2004)
- 34. H.N. Oğuz, A. Prosperetti, J. Fluid Mech. 257, 111 (1993)
- J.R. Royer, E.I. Corwin, A. Flior, M.L. Cordero, M.L. Rivers, P.J. Eng, H.M. Jaeger, Nat. Phys. 1, 164 (2005)
- G. Caballero, R. Bergmann, D. van der Meer, A. Prosperetti, D. Lohse, Phys. Rev. Lett. 99, 018001 (2007)
- 37. S. von Kann, S. Joubaud, G.A. Caballero-Robledo, D. Lohse, D. van der Meer, Phys. Rev. E 81, 041306 (2010)
- J.O. Marston, J.P.K. Seville, Y.V. Cheun, A. Ingram, S.P. Decent, M.J.H. Simmons, Phys. Fluids 20, 023301 (2008)
- 39. J.O. Marston, M.M. Mansoor, S.T. Thoroddsen, Phys. Rev. E 88, 010201 (2013)
- 40. R. Rioboo, M. Marengo, C. Tropea, Exp. Fluids 33, 112 (2002)
- 41. J. Eggers, M.A. Fontelos, C. Josserand, S. Zaleski, Phys. Fluids 22, 062101 (2010)
- 42. N. Mitarai, F. Nori, Adv. Phys. 55, 1 (2006)
- 43. S. Herminghaus, Wet Granular Matter (World Scientific, Singapore, 2013)
- 44. I.R. Peters, Q. Xu, H.M. Jaeger, Phys. Rev. Lett. 111, 028301 (2013)
- 45. F. Pacheco-Vázquez, J.C. Ruiz-Suárez, Phys. Rev. Lett. **107**, 218001 (2011)
- R. Bartali, G.M. Rodríguez-Liñán, Y. Nahmad-Molinari, D. Sarocchi, J.C. Ruiz-Suárez, arXiv:1302.0259v2 (2013)
- 47. Y. Amarouchene, J.F. Boudet, H. Kellay, Phys. Rev. Lett. 86, 4286 (2001)
- 48. D. Scheeres, C. Hartzell, P. Sánchez, M. Swift, Icarus **210**, 968 (2010)
- 49. K.R. Housen, K.A. Holsapple, Icarus 163, 102 (2003)
- 50. H.G. Wilshire, K.A. Howard, Science 162, 258 (1968)
- 51. J. González-Gutiérrez, J.L. Carrillo-Estrada, J.C. Ruiz-Suárez, Sci. Rep. 4, 6762 (2014)
- 52. F. Pacheco-Vázquez, J.C. Ruiz-Suárez, Nat. Commun. 1, 123 (2010)
- J.M. Solano-Altamirano, G.A. Caballero-Robledo, F. Pacheco-Vázquez, V. Kamphorst, J.C. Ruiz-Suárez, Phys. Rev. E 88, 032206 (2013)
- 54. E.L. Nelson, H. Katsuragi, P. Mayor, D.J. Durian, Phys. Rev. Lett. 101, 068001 (2008)
- 55. C. Clanet, C. Béguin, D. Richard, D. Quéré, J. Fluid Mech. 517, 199 (2004)
- Y. Renardy, S. Popinet, L. Duchmin, M. Renardy, S. Zaleski, C. Josserand, M.A. Drumright-Clarke, D. Richard, C. Clanet, D. Quéré, J. Fluid Mech. 484, 69 (2003)
- 57. A.L. Biance, F. Chevy, C. Clanet, G. Lagubeau, D. Quéré, J. Fluid Mech. 554, 47 (2006)
- 58. K. Okumura, F. Chevy, D. Richard, D. Quéré, C. Clanet, EPL (Europhys. Lett.) 62, 237 (2003)
- 59. D. Richard, C. Clanet, D. Quere, Nature 417, 811 (2002)
- 60. J. Duran, Sands, Powders, and Grains: An Introduction to the Physics of Granular Materials (Springer, New York, 2000)
- 61. L.D. Landau, E.M. Lifshitz, *Theory of Elasticity* (Pergamon, New York, 1986)
- 62. D. Richard, D. Quéré, EPL (Europhys. Lett.) 50, 769 (2000)
- 63. H. Katsuragi, Phys. Rev. Lett. 104, 218001 (2010)
- R.D. Deegan, O. Bakajin, T.F. Dupont, G. Huber, S.R. Nagel, T.A. Witten, Nature 389, 827 (1997)
- R.D. Deegan, O. Bakajin, T.F. Dupont, G. Huber, S.R. Nagel, T.A. Witten, Phys. Rev. E 62, 756 (2000)
- 66. G. Delon, D. Terwagne, S. Dorbolo, N. Vandewalle, H. Caps, Phys. Rev. E 84, 046320 (2011)
- 67. H. Katsuragi, J. Fluid Mech. 675, 552 (2011)
- 68. E. Nefzaoui, O. Skurtys, Exp. Therm. Fluid Sci. 41, 43 (2012)
- 69. J.O. Marston, S.T. Thoroddsen, W.K. Ng, R.B.H. Tan, Powder Tech. 203, 223 (2010)
- 70. J.O. Marston, Y. Zhu, I.U. Vakarelski, S.T. Thoroddsen, Powder Tech. 228, 424 (2012)
- 71. R. Zhao, Q. Zhang, H. Tjugito, X. Cheng, PNAS 112, 342 (2015)
- 72. R.M. Schmidt, K.R. Housen, Int. J. Impact Eng. 5, 543 (1987). Hypervelocity Impact Proceedings of the 1986 Symposium
- 73. E.W. Washburn, Phys. Rev. 17, 273 (1921)

- 74. K.P. Hapgood, J.D. Litster, S.R. Biggs, T. Howes, J. Colloid Interface Sci. 253, 353 (2002)
- 75. K.P. Hapgood, J.D. Litster, R. Smith, AIChE J. 49, 350 (2003)
- E.J. Long, G.K. Hargrave, J.R. Cooper, B.G.B. Kitchener, A.J. Parsons, C.J.M. Hewett, J. Wainwright, Phys. Rev. E 89, 032201 (2014)
- 77. S.M. Iveson, J.D. Litster, AIChE J. 44, 1510 (1998)
- J. Litster, K. Hapgood, J. Michaels, A. Sims, M. Roberts, S. Kameneni, T. Hsu, Powder Tech. 114, 32 (2001)
- 79. H.N. Emady, D. Kayrak-Talay, W.C. Schwerin, J.D. Litster, Powder Tech. 212, 69 (2011)
- 80. H.N. Emady, D. Kayrak-Talay, J.D. Litster, AIChE J. 59, 96 (2013)
- 81. A.L. Yarin, Ann. Rev. Fluid Mech. 38, 159 (2006)
- 82. C. Clanet, Ann. Rev. Fluid Mech. **39**, 469 (2007)
- 83. H. Marmanis, S.T. Thoroddsen, Phys. Fluids **8**, 1344 (1996)
- 84. S.T. Thoroddsen, J. Sakakibara, Phys. Fluids 10, 1359 (1998)
- 85. S. Chandrasekhar, *Hydrodynamic and Hydromagnetic Stability* (Oxford University Press, New York, 1961)
- 86. A.R. Piriz, O.D. Cortázar, J.J. López Cela, N.A. Tahir, Am. J. Phys. 74, 1095 (2006)
- 87. A. Bret, Laser Part. Beams 29, 255 (2011)
- 88. R.F. Allen, J. Colloid Interface Sci. 51, 350 (1975)
- 89. C. Mundo, M. Sommerfeld, C. Tropea, Int. J. Multiphase Flow 21, 151 (1995)
- 90. M. Pasandideh-Fard, Y.M. Qiao, S. Chandra, J. Mostaghimi, Phys. Fluids 8, 650 (1996)
- 91. R. Bhola, S. Chandra, J. Mater. Sci. 34, 4883 (1999)
- 92. A.N. Lembach, H.B. Tan, I.V. Roisman, T. Gambaryan-Roisman, Y. Zhang, C. Tropea, A.L. Yarin, Langmuir **26**, 9516 (2010)
- 93. J. Blum, R. Schräpler, Phys. Rev. Lett. 93, 115503 (2004)
- 94. H. Katsuragi, EPJ Web of Conferences 92, 02032 (2015)
- 95. L. Xu, W.W. Zhang, S.R. Nagel, Phys. Rev. Lett. 94, 184505 (2005)
- 96. J. Lampe, R. DiLalla, J. Grimaldi, J.P. Rothstein, J. Non-Newton. Fluid Mech. 125, 11 (2005)
- 97. S. Pregent, S. Adams, M.F. Butler, T.A. Waigh, J. Colloid Interface Sci. 331, 163 (2009)
- 98. M. Tomé, S. McKee, K. Walters, J. Non-Newton. Fluid Mech. 165, 1258 (2010)
- 99. C. Duez, C. Ybert, C. Clanet, L. Bocquet, Nat. Phys. 3, 180 (2007)
- G. Juarez, T. Gastopoulos, Y. Zhang, M.L. Siegel, P.E. Arratia, Phys. Rev. E 85, 026319 (2012)
- 101. D.E. Gault, R. Greeley, Icarus 34, 486 (1978)
- 102. M. Manga, A. Patel, J. Dufek, E.S. Kite, Geophys. Res. Lett. 39, L01202 (2012)
- 103. S.W. Squyres, O. Aharonson, B. Clark, B.A. Cohen, L. Crumpler, P.A. de Souza, W.H. Farrand, R. Gellert, J. Grant, J.P. Grotzinger, A.F.C. Haldemann, J.R. Johnson, G. Klingelhöfer, K.W. Lewis, R. Li, T. McCoy, A.S. McEwen, H.Y. McSween, D.W. Ming, J.M. Moore, R.V. Morris, T.J. Parker, J.W. Rice, S. Ruff, M. Schmidt, C. Schröder, L.A. Soderblom, A. Yen, Science 316, 738 (2007)
- 104. S.P.D. Birch, M. Manga, B. Delbridge, M. Chamberlain, Phys. Rev. E 90, 032208 (2014)
- 105. H. Takita, I. Sumita, Phys. Rev. E 88, 022203 (2013)
- 106. H. Kellay, EPL (Europhys. Lett.) 71, 400 (2005)
- 107. R.J. Munro, N. Bethke, S.B. Dalziel, Phys. Fluids 21, 046601 (2009)
- 108. N. Masuda, J. Yoshida, B. Ito, T. Furuya, O. Sano, Fluid Dyn. Res. 44, 015501 (2012)
- 109. J. Yoshida, N. Masuda, B. Ito, T. Furuya, O. Sano, Fluid Dyn. Res. 44, 015502 (2012)
- P. Metzger, C. Immer, C. Donahue, B. Vu, R. Latta, M. Deyo-Svendsen, J. Aerosp. Eng. 22, 24 (2009)
- 111. P.T. Metzger, R.C.L. III, J.M. Schuler, C.D. Immer, arXiv:0905.4851 (2009). Powders and Grains 2009, Golden, Colorado, USA
- 112. A.H. Clark, R.P. Behringer, Granul. Matter 16, 433 (2014)
- 113. J.C. Ruiz-Suárez, Rep. Prog. Phys. 76, 066601 (2013)

Chapter 7 Grains and Dust Dynamics

We have studied impact drag force and impact cratering mechanics thus far in this book. As a target material, dense granular beds have been principally considered. Soft impact with a loose granular target causes many intriguing phenomena, as described in the previous chapters. In this chapter, we will focus on other types of soft impact phenomena that are also related to planetary science. First, the impact of dust aggregates in a protoplanetary disk will be discussed. Dust grains coagulate to become fluffy dust aggregates. The physical properties of the aggregates are key quantities to understanding the history of planetesimal formation. Next, we will return to the discussion of dense macroscopic grains called regolith that cover the surface of various astronomical objects. Some interesting physical properties relating to the impact of dust aggregates and regolith migration will be briefly discussed in this chapter.

7.1 Soft Impact of Dust Aggregates

The principal ingredients for forming planets in a protoplanetary disk (PPD) are most likely very small dust grains. PPD is a rotating disc comprising a mixture of gas and dust grains. The main components of the solid (dust) materials are silicate and ice. It is considered that tiny dust grains stick to each other by collisions and finally form planetesimals with diameters of approximately 1–10 km. Then, planets are formed by the gravitational accretion of planetesimals. Although this standard scenario is sufficiently plausible to explain the history of planetary formation, some difficulties remain with regard to the completion of the solar system biography. Because the entire story is a long tale, we will not discuss the details of this story. A comprehensive review of the astrophysics of planetary formation can be found in e.g. Ref. [1]. Here we only focus on the soft impact among fluffy dust aggregates that is a leading player in the planetesimal formation process.

The starting materials that we consider are interstellar particles whose size is approximately $0.1\,\mu m$ [2, 3]. These dusts can coagulate through their mutual collisions and grow to a macroscopic size. This naive idea, however, presents some nontrivial doubts. For example, it is not clear for large aggregates to be able to continue growth while avoiding shattering. Furthermore, it is unclear how long the formation of planetesimals takes. The planetesimal formation timescale must be in the practical range. These issues actually relate to the known difficulties in planetesimal formation. Additionally, a proper understanding of soft impact mechanics could be a key factor to overcome the difficulties. In this section, the theory for the impact velocity among dust aggregates is briefly reviewed. Then, collision outcomes resulting from the impact among various dust aggregates are discussed on the basis of soft impact experiments and simulations.

7.1.1 Relative (Impact) Velocity of Dust Aggregates

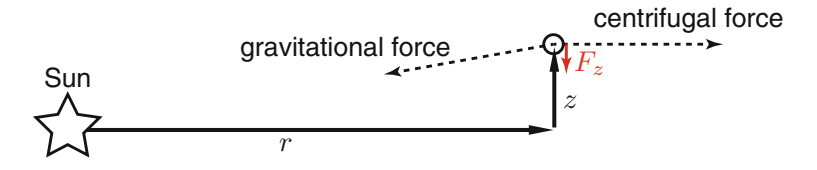
In a PPD, the relative impact velocity among dust aggregates is determined by the aerodynamic effects rather than the gravitational effect when the size of aggregates is very small. As the dust aggregates grow, they are decoupled from the gas flow. Therefore, the gravitational effect mainly determines their relative impact velocity for large bodies. In this chapter, we will focus on the very first stage of the agglomeration during which the dust aggregates are very fluffy, and their mutual collision velocity is dominated by aerodynamic effects. To compute a realistic relative velocity among dust aggregates, various factors must be considered [1, 4–6]. In this aerodynamic regime, the relative impact velocity Δv can be expressed by the root sum square of various components:

$$\Delta v \simeq \sqrt{(\Delta v_B)^2 + (\Delta v_z)^2 + (\Delta v_r)^2 + (\Delta v_{\varphi})^2 + (\Delta v_{\text{edd}})^2},$$
 (7.1)

where Δv_B , Δv_z , Δv_r , Δv_{φ} , and $\Delta v_{\rm edd}$ are the relative velocities due to Brownian motion, vertical settling, radial drift, azimuthal drift, and turbulence, respectively. Theoretically derived forms for these terms are briefly reviewed in the following text. The definition of the directions of v_z , v_r , and v_{φ} are provided in Fig. 7.1. As already mentioned, the gravitational effect is neglected in Eq. (7.1) because tiny grains are considered. For sufficiently large bodies (large S_{tk} regime), aerodynamic drag is less important and the gravitational effect becomes predominant. In this case, the escape velocity $v_{\rm esc}$ should be a characteristic velocity scale:

$$v_{\rm esc} = \sqrt{\frac{4\mathcal{G}m_t}{D_t}},\tag{7.2}$$

a side view



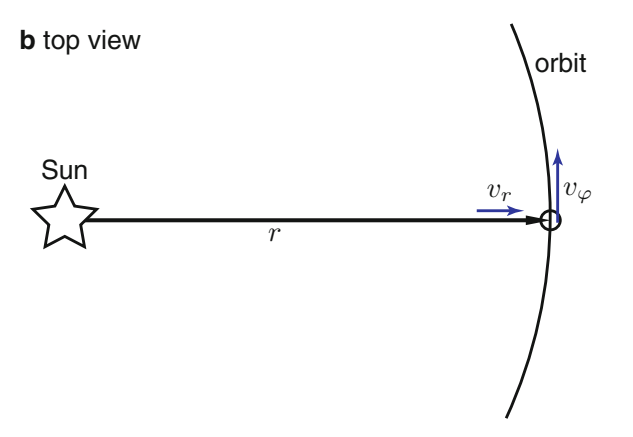


Fig. 7.1 Schematic image of the dust motion in a PPD. Panel (**a**) represents the side view (vertical slice) and panel (**b**) shows the top view (horizontal slice at the central plane) of the PPD. In panel (**a**), the settling force F_z as a net force of the gravitational and the centrifugal forces is shown. A dust particle at (r, z) settles by the settling velocity v_z made by F_z and the Epstein drag F_E , as written in Eq. (7.6). In panel (**b**), the coordinate system of the azimuthal motion and the radial drift is shown

where \mathcal{G} is the gravitational constant and m_t and D_t are the mass and diameter of the (large) body, respectively. The order of the impact velocity of the crater formation discussed in Chap. 5 is rather close to $v_{\rm esc}$. The aerodynamic-based relative velocity Δv is only relevant to the small-scale grains.

Brownian motion The relative velocity due to the Brownian motion is usually modeled by

$$\Delta v_B = \sqrt{\frac{8(m_1 + m_2)k_B T}{\pi m_1 m_2}},\tag{7.3}$$

where m_1 and m_2 are the masses of two colliding aggregates. This form originates from the mean velocity of the Maxwell-Boltzmann distribution (refer to Eq. (2.87)) and the reduced mass $m_1m_2/(m_1 + m_2)$.

Settling The next simplest motion for dust aggregates is the settling to the central plane. Let us consider the PPD that has a finite thickness and rotates approximately by the circular Keplerian motion. The Keplerian motion speed v_K can be obtained from the force balance between the centrifugal and gravitational forces, $v_K^2/r = \mathcal{G}M_*/r^2$. Thus, v_K is written as $v_K = \sqrt{\mathcal{G}M_*/r}$, where M_* is the solar mass and r is the distance from the Sun (central star) on the central plane. The angular frequency of the Keplerian motion Ω_K is computed from the relation, $2\pi/\Omega_K = 2\pi r/v_K$. Specifically, Ω_K is written as

$$\Omega_K = \frac{v_K}{r} = \sqrt{\frac{\mathcal{G}M_*}{r^3}}. (7.4)$$

If a dust aggregate is at a height z from the central plane, it experiences the vertical force to the central plane because of the net force created by the gravitational and centrifugal forces. In Fig. 7.1a, the setup considered here is schematically shown. The vertical force F_z can be computed by assuming $z/r \ll 1$:

$$F_z \simeq \frac{\mathcal{G}M_*}{r^2} \frac{z}{r} m_i = \Omega_K^2 z m_i, \tag{7.5}$$

where m_i is the mass of the dust aggregate. In the PPD, the gas is very tenuous, and the dust aggregate considered here is very small. The molecular mean free path in the PPD may be on the order of $\lambda_{\rm mfp} \simeq 0.1$ m at 1 AU [7]. Thus, the Epstein drag rather than the Stokes drag should be adopted. By equating Eqs. (7.5) and (2.89), the settling velocity v_z can be obtained as

$$v_z = \frac{1}{2\delta_E} \frac{\rho_i}{\rho_t} \frac{\Omega_K^2 z D_i}{\langle u_t \rangle} = \Omega_K^2 z t_b, \tag{7.6}$$

where δ_E , ρ_t , ρ_i , and D_i are the efficiency factor of the Epstein drag, density of gas, density of the dust aggregate, and its diameter, respectively. Here we use a simple spherical approximation $m_i = (\pi/6)\rho_i D_i^3$, and t_b is the braking time of the Epstein drag (Eq. (2.90)). Although we assume the Epstein drag law to derive Eq. (7.6), the obtained form $v_z = \Omega_K^2 z t_b$ is also valid for viscous drag as well, which can be readily examined using Eq. (2.69) instead of Eq. (2.89). The notable thing in Eq. (7.6) is that the vertical settling velocity v_z principally depends on the diameter of the dust aggregate D_i . If the viscous drag is adopted, v_z depends on D_i^2 . In either case, v_z varies mainly depending on a certain power of D_i . Other parameters can be assumed as almost constants.

Here we define a dimensionless number τ_b to characterize the competition between the drag relaxation and Keplerian motion:

$$\tau_b = t_b \Omega_K. \tag{7.7}$$

Because τ_b represents the balance between the settling time and the motion timescale, it can be regarded as a type of Stokes number (or maybe Deborah number). This Stokes-like number τ_b represents the competition between the drag timescale and the period of Keplerian motion, which indicates that the Epstein (or Stokes) drag relaxation takes longer time than a Keplerian rotation if $\tau_b \geq 1$. In contrast, when $\tau_b < 1$, the steady settling velocity is attained faster than a Keplerian rotation. The most important factor determining v_z is the size of the dust aggregates D_i . The relative velocity of two settling dust aggregates Δv_z can be modeled by the difference in v_z . Then, from Eq. (7.6), the relative velocity of aggregates 1 and 2 is written as

$$\Delta v_z = \Omega_K z |\tau_{h,1} - \tau_{h,2}|,\tag{7.8}$$

where the subscripts $_{,1}$ and $_{,2}$ denote the values for aggregates 1 and 2, respectively. As mentioned previously, the size difference is the principal factor to produce a relative (collision) velocity Δv_z because t_b mainly depends on D_i .

Radial and azimuthal drift Next, the radial and azimuthal (orbital) drift components are evaluated. For this purpose, the force balance for gas in the PPD must be considered, which is slightly different from the force balance for dust aggregates. In the PPD, dust aggregates rotate simply by the balance of the gravitational and centrifugal forces, i.e., Keplerian motion. However, a gas has its own pressure p, which affects the force balance. Specifically, the azimuthal velocity of gas $v_{\varphi,g}$ should satisfy the following relation:

$$\frac{v_{\varphi,g}^2}{r} = \frac{\mathcal{G}M_*}{r^2} + \frac{1}{\rho_t} \frac{dp}{dr}.$$
 (7.9)

The last term represents the force by the pressure gradient and that is specific for a gas. Namely, this pressure gradient term is absent in the dust force balance. To estimate the pressure gradient, a simple power-law form of the gas pressure is usually assumed as $p \propto r^{-n}$. Additionally, a locally isothermal equation of state $p = \rho_t C_s^2$, where C_s is the speed of sound, is assumed. Then, the pressure gradient term can be written as

$$\frac{1}{\rho_t} \frac{dp}{dr} = -n \frac{C_s^2}{r}.\tag{7.10}$$

Inserting Eq. (7.10) into Eq. (7.9) and considering the Keplerian speed $v_K = \sqrt{\mathcal{G}M_*/r}$, we find

$$v_{\varphi,g} = v_K \sqrt{1 - \eta_g},\tag{7.11}$$

where $\eta_g = nC_s^2/v_K^2$ indicates the degree of gas velocity deviation from the Keplerian motion due to the pressure gradient. Although the typical order of η_g is approximately 10^{-3} , it significantly affects the fate of dust aggregates, as discussed below.

To compute velocities, we consider the equation of motion for dust aggregates. Dust aggregates do not have a pressure gradient, which indicates that dust motion is slightly faster than the gas motion. Thus, they are dragged by the headwind due to the reduced gas velocity written in Eq. (7.11). Then, the dust aggregates are decelerated and lose their angular momenta. Consequently, dust aggregates drift inward by the slight excess of the gravitational force against the centrifugal force.

This drift motion can be evaluated by considering the equation of motions below. The radial velocity v_r and azimuthal (orbital) velocity v_{φ} for dust aggregates (Fig. 7.1b) obey the following equation of motions:

$$\frac{dv_r}{dt} = \frac{v_{\varphi}^2}{r} - \frac{v_K^2}{r} - \frac{1}{t_b} \left(v_r - v_{r,g} \right), \tag{7.12}$$

$$\frac{d}{dt}\left(rv_{\varphi}\right) = -\frac{r}{t_{b}}\left(v_{\varphi} - v_{\varphi,g}\right),\tag{7.13}$$

where $v_{r,g}$ denotes the radial velocity of the gas. The first and second terms on the right-hand side of Eq. (7.12) come from the centrifugal and gravitational forces, respectively. The last term in Eq. (7.12) and the right-hand side of Eq. (7.13) come from the drag force by the headwind. Here we use the relation $t_b = m_i |v/F_D|$ for the drag force F_D . Furthermore, the m_i dependence is dropped because it is arbitrary in Eqs. (7.12) and (7.13). By assuming $v_{\varphi} \simeq v_K$, the left-hand side of the azimuthal equation (Eq. (7.13)) can be simplified as

$$\frac{d}{dt}(rv_{\varphi}) \simeq v_r \frac{d}{dr}(rv_K) = \frac{1}{2}v_r v_K. \tag{7.14}$$

Here the relation $dv_k/dr = -(1/2)v_k/r$, which can be derived from the definition of v_k , is used. Then, from Eqs. (7.4), (7.7), (7.13), and (7.14), we obtain

$$v_{\varphi} - v_{\varphi,g} \simeq -\frac{1}{2} \frac{t_b v_K}{r} v_r = -\frac{1}{2} \tau_b v_r.$$
 (7.15)

For the radial equation of motion, by replacing v_{φ}^2 with $[v_{\varphi,g} + (v_{\varphi} - v_{\varphi,g})]^2$ and using Eq. (7.11), Eq. (7.12) is transformed into

$$\frac{dv_r}{dt} = \frac{1}{r} \left[\left\{ v_{\varphi,g} + \left(v_{\varphi} - v_{\varphi,g} \right) \right\}^2 - v_K^2 - \frac{r}{t_b} \left(v_r - v_{r,g} \right) \right]
\simeq \frac{1}{r} \left[-\eta_g v_K^2 + 2v_K \left(v_{\varphi} - v_{\varphi,g} \right) - \frac{r}{t_b} \left(v_r - v_{r,g} \right) \right].$$
(7.16)

In this calculation, only the lowest order term remains, i.e., $\eta_{\rm g}(v_{\varphi}-v_{\varphi,\rm g})$ and $(v_{\varphi}-v_{\varphi,\rm g})^2$ are neglected. In a steady state $(dv_r/dt=0)$, the radial drift of dust aggregates relative to gas motion is written as

$$v_r - v_{r,g} = 2\tau_b \left(v_\varphi - v_{\varphi,g} \right) - \eta_g \tau_b v_K. \tag{7.17}$$

Again, the radial drift velocity simply depends on the braking time τ_b . Thus, the radial component of the relative velocity of dust impact is also determined mainly by the size difference of aggregates.

Radial drift yields a crucial constraint to the timescale of planetesimal formation. Using Eqs. (7.15) and (7.17), v_r is computed as

$$v_r = \frac{v_{r,g} - \tau_b \eta_g v_K}{\tau_b^2 + 1}. (7.18)$$

This v_r exhibits an extreme value at $dv_r/d\tau_b=0$. From Eq. (7.18), this condition corresponds to $\tau_b^2-1-2(v_{r,g}/\eta_gv_K)\tau_b=0$. By assuming $|v_{r,g}/\eta_gv_K|\ll 1$ [1], it is easy to deduce that $|v_r|$ exhibits a peak value at $\tau_b\simeq 1$. Therefore, substituting $\tau_b=1$ into Eq. (7.18), the peak drift velocity can be approximated by $v_{r,\text{peak}}\simeq -\eta_gv_K/2$. Here we neglect the $v_{r,g}$ term because it is considerably smaller than η_gv_K as mentioned above. The minimum timescale for the radial drift is computed as $t_{\text{drift}}=r/|v_{r,\text{peak}}|=2/\eta_g\Omega_K$. Because η_g is on the order of 10^{-3} , its timescale is approximately 10^3 years at several AU. This timescale is considerably shorter than the usual planetesimal growth timescale [1]. This issue is called the *radial drift barrier* for planetesimal formation.

The relative impact velocities Δv_r and Δv_{φ} can be computed using Eqs. (7.18) and (7.15). The most important fact is that the velocities are determined by the braking time τ_b similar to the case of the settling component v_z . Additionally, τ_b mainly depends on the aggregates size D_i . This tendency is valid both for Stokes (viscous) and Epstein drags.

Turbulence The motion of dust aggregates is further affected by the turbulence in the PPD. In general, the turbulent nature of gas motion is not so simple. A simple model called the astronomical α model (see, e.g., [8]) has been used to evaluate the turbulent effect in the PPD. The α model defines the turbulent kinematic viscosity as

$$v_t = \alpha_v C_s H_{\text{scale}},\tag{7.19}$$

where α_{ν} is a parameter characterizing the strength of the turbulence, C_s is the speed of sound, and H_{scale} is the scale height (roughly corresponding to the thickness) of the PPD. The turbulent viscosity ν_t can also be expressed by $\nu_t = L_{\text{edd}} v_{\text{edd}}$, where L_{edd} and v_{edd} are the largest eddy scale and representative velocity scale,

respectively. By introducing the angular frequency of the turnover along the largest eddies $\Omega_t = v_{\rm edd}/L_{\rm edd}$ and the relation 1 $H_{\rm scale} = C_s/\Omega_K$, one can obtain a relation

$$v_{\rm edd} = C_s \left(\alpha_v\right)^{1/2} \left(\frac{\Omega_t}{\Omega_K}\right)^{1/2}.$$
 (7.20)

The value of α_{ν} determines the typical turbulent flow velocity. Although the typical order of α_{ν} in the PPD is considered $\alpha_{\nu} \simeq 10^{-3}$, its origin has not yet been completely clarified. One of the possible origins of the strong turbulence is magnetorotational instability (MRI) [9]. Note that the actual turbulent velocity is rather random, whereas Eq. (7.20) provides the characteristic velocity scale given by turbulence. Furthermore, the aerodynamic coupling among dust aggregates and turbulent flow determines the relative velocity of dust aggregates $\Delta v_{\rm edd}$ in the turbulent case.

Summary of the relative impact velocity of dust aggregates These aerodynamic effects are coupled with the dust aggregate motion through their dimensionless braking timescale τ_b . In addition, the most important parameter in the braking timescale is the size of the dust aggregates D_i . When the size of the dust aggregates is sufficiently large, the motion is decoupled from the gas flow. The fidelity of the dust aggregates in a gas flow determines the timescale. Because the main concern in planetary science is the history of the solar system, appropriate determination of the timescale for each phenomenon is crucial.

In Fig. 7.2, the contour diagram of impact velocity (unit: m/s) as a function of two colliding aggregates size is shown. The dashed contours are drawn on the basis of the calculations discussed thus far² [5]. The colors in Fig. 7.2 represent the corresponding collision outcomes and will be discussed later. From Fig. 7.2, we can confirm that the relatively large ($D_i > 1$ m) aggregates experience an impact velocity of up to 75 m/s. However, it is not evident whether the dust aggregates can sustain their growth without shattering until such a relatively large impact velocity regime. Numerical and experimental evaluations on this issue are discussed below.

7.1.2 Dust Growth

The dust aggregates must grow to form planetesimals. In the last subsection, the relative impact velocity among different-size aggregates was estimated. However, the effect of the growth of aggregates was not considered. Here a simple model of

¹The scale height H_{scale} is computed from the balance between the vertical force F_z in Eq. (7.5) and the pressure gradient force as $\Omega_K^2 z + (1/\rho_t) dp/dz = 0$. Assuming the isothermal condition $p = \rho_t C_s^2$, the vertical density profile is computed as $\rho_t \sim \exp[-(z/H_{\text{scale}})^2]$.

 $^{^{2}\}alpha_{\nu} = 10^{-3}$ is used to calculate the collision velocity.

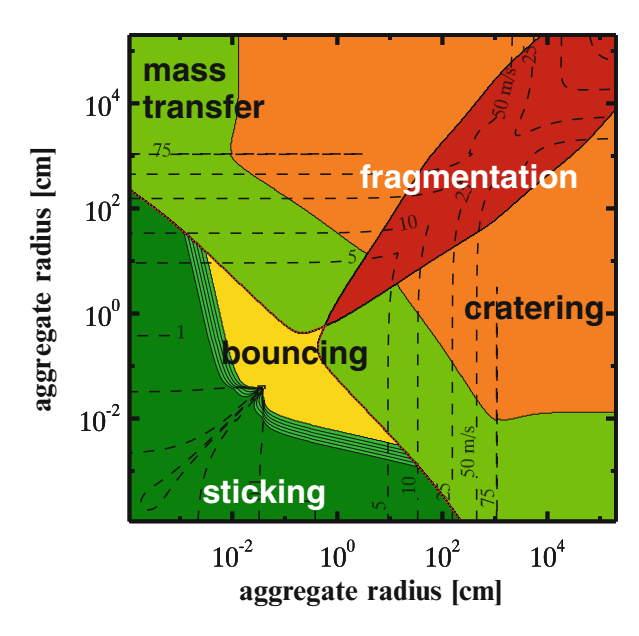


Fig. 7.2 Phase diagram of the impact velocities and the corresponding collision outcomes. Relative impact velocities for two colliding dust aggregates are represented by the *dashed contours* with units of m/s. The colored regions indicate the corresponding collision outcomes (Courtesy of Stefan Kothe and Jürgen Blum)

dust growth is considered. The simplest starting point to discuss dust coagulation is perfect sticking. If every collision results in sticking, the mass growth rate of a dust aggregate, dm_i/dt , can be computed from the amount of solid material in the volume swept by the dust aggregate's motion per unit time:

$$\frac{dm_i}{dt} = \frac{\pi}{4} D_i^2 \Delta v_{dg} \rho_{\text{dust}},\tag{7.21}$$

where Δv_{dg} and $\rho_{\rm dust}$ indicate the relative velocity (among a dust aggregate and gas) and the bulk (not true) density of solid materials in the PPD. Such a growth model must be coupled with the aforementioned relative impact velocity models to consider the temporal development of dust aggregate size. The most serious problem on dust coagulation is imperfect sticking. If sticking always occurs, the growth model is indeed very simple. However, perfect sticking is an extreme simplification of the growth process; there must be various collision outcomes.

To verify the feasibility of dust growth, various experimental studies were performed by Blum and his coworkers³ [10–13]. These researchers performed system-

³Since the handling of tiny grains under a microgravity environment demands sophisticated experimental techniques, only this group has been able to perform this type of experiment.

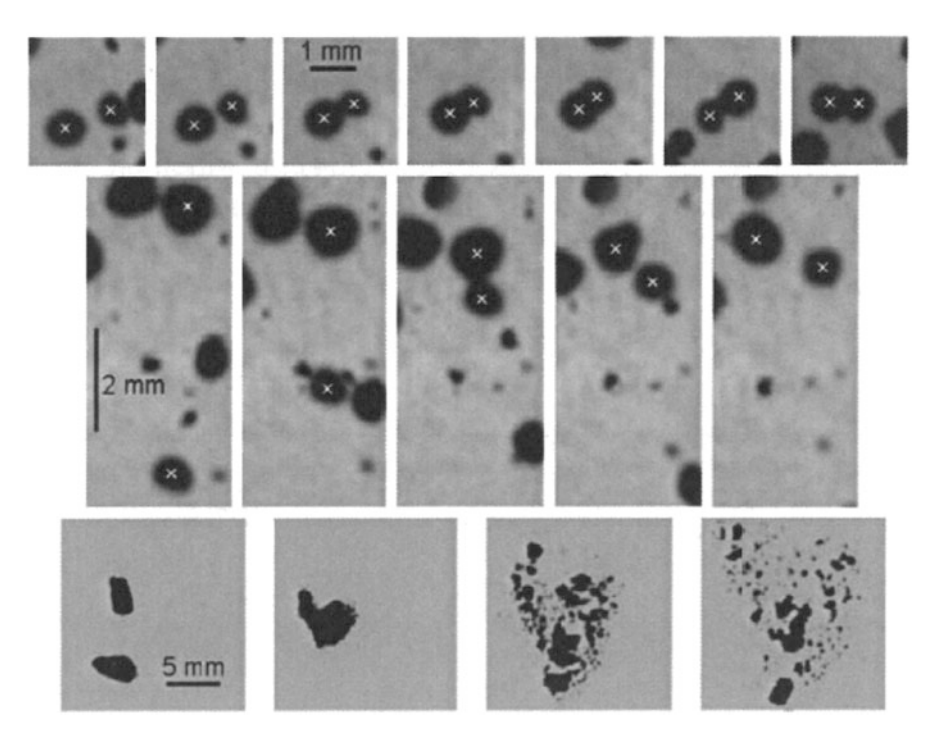


Fig. 7.3 Typical examples of laboratory impact experiments of two SiO₂ aggregates. The *top row* images represent sticking by impact velocity $v_0 = 0.004 \, \text{m/s}$. In the *middle row*, bouncing by $v_0 = 0.16 \, \text{m/s}$ is displayed. The *bottom row* corresponds to fragmentation by $v_0 = 5.1 \, \text{m/s}$. Colliding aggregates are marked by × in the top and middle rows. The experiments were performed under a microgravity condition. Note that the time intervals among the pictures are not identical (Reproduced by permission of the RAA, from Ref. [12])

atic experiments and directly confirmed various representative phases of collision outcomes. Examples of their experimental results are presented in Fig. 7.3 [12]. In the low-velocity impact regime, sticking is observed. However, as the impact velocity increases, bouncing and fragmentation occur. The bouncing and fragmentation may prevent the dust aggregates from further coagulation. That is, these phases are barriers to be overcome in the formation of planetesimals from dust aggregates. In the following subsections, experimental and numerical works related to how these barriers can be evaluated and overcome by soft impact effects are reviewed.

7.1.3 Static Structure of Dust Aggregates

The first thing we should consider is the static structure of dust aggregates. In the theoretical framework discussed thus far, only two parameters ρ_i and D_i characterize dust aggregates. We have implicitly assumed that dust aggregates are spheres having

a homogeneous structure. However, the aggregates could have complex structures in reality. When submicron-sized particles collide and stick randomly, the resultant aggregates may become porous. The structures of such aggregates were extensively studied by numerical simulations [14–16] and experiments [17–19].

The structure of aggregates can be characterized by the fractal dimension d_f . The gyration radius $R_{\rm gy}$ is frequently used to measure d_f . $R_{\rm gy}$ of an aggregate is defined by

$$R_{\rm gy} = \sqrt{\frac{1}{N} \sum_{i}^{N} |\mathbf{x}_i - \mathbf{x}_M|^2}, \tag{7.22}$$

where x_i is the position vector of the *i*-th monomer particle, 4x_M corresponds to the center of mass, and N is the total number of monomer particles constructing the aggregate. Then, d_f , R_{gy} , and N are related as follows:

$$N \propto R_{\rm gv}^{d_f}$$
. (7.23)

Evidently, the compact structure in three-dimensional space corresponds to $d_f = 3$ because N represents the mass or equivalently the volume of the aggregate. In general, d_f can be a noninteger. The value of d_f indicates the sparseness of the aggregate. The smaller the d_f , the sparser the structure of the aggregate becomes.

The value of d_f of fluffy dust aggregates depends on the recipe for forming the aggregates. The simplest hit-and-sticking phase can be classified into two extreme cases [20, 21]. When a single monomer particle ballistically hits and sticks to the aggregate step by step, the aggregate becomes relatively dense. Then, the resultant aggregate shows $d_f \simeq 3$. This type of aggregate is called the ballistic particle cluster aggregate (BPCA). In contrast, if two identical-mass aggregates hit and stick to each other, the resultant aggregate becomes very sparse, and the corresponding fractal dimension will be $d_f \simeq 2$. Such an aggregate is called the ballistic cluster cluster aggregate (BCCA). The algorithms to form BPCA and BCCA are schematically drawn in Fig. 7.4. In various experiments and simulations, BCCA is assumed as a candidate of the dust aggregate in the PPD. Moreover, the aggregates with $d_f < 2$ are commonly observed in experiments [17–19].

7.1.4 Restructuring and Fragmentation of Dust Aggregates

Next, the restructuring of the aggregate induced by the impact should be discussed. When the fluffy aggregates collide, the restructuring of aggregates may

⁴The word *monomer* represents individual submicron-sized particle that compose the dust aggregate.

Fig. 7.4 Recipes to form the ballistic particle cluster aggregate (*BPCA*) and ballistic cluster cluster aggregate (*BCCA*)

occur simultaneously with sticking, bouncing, and fragmentation. Dominik and Tielens are pioneers who developed a method to simulate the impacting of dust aggregates [22–24]. These researchers built a model of aggregates consisting of spherical monomers. The key point of their aggregate modeling is the realistic quantification of contact mechanics. When two spheres are in contact, there are four modes for contact mechanics: normal (push or pull), rolling, sliding, and twist. Because rolling and sliding have two independent degrees of freedom, there are six degrees of freedom in total. The modeling of the contact mechanics is based on the JKR theory [25]. In Sect. 2.5.4, the scaling of JKR theory was briefly introduced. To discuss the deformation at the contact point, the critical values by which the yielding of the contact modes occurs are essential quantities. The most important mode is rolling because it is the easiest motion for spherical-monomers contact. The energy associated with the yielding of the rolling mode $e_{\rm roll}$ can be computed as [22, 24]

$$e_{\rm roll} \sim \gamma_c \xi_{\rm crit}^2,$$
 (7.24)

where γ_c and $\xi_{\rm crit}$ are the surface tension of two contacting monomers and the critical distance for the rolling elasticity, respectively. Namely, if the rolling distance is less than $\xi_{\rm crit}$, the energy is stored elastically in the rolling mode contact. In contrast, when the rolling distance exceeds $\xi_{\rm crit}$, the energy is dissipated and the restructuring of the aggregate due to the yielding (plastic deformation) occurs. In other words, the elastoplastic constitutive law is assumed in the contact mechanics. Although a more detailed analytical calculation is necessary to obtain the numerical prefactor in Eq. (7.24), the dimensional relation is natural in terms of the surface energy that governs the contact mechanics. Note that $e_{\rm roll}$ is independent of the monomer's diameter D_i , i.e., the yielding criterion is determined only by the local condition. To characterize the restructuring, a unit of dissipated energy $E_{\rm roll}$ is defined by $90^{\circ} = \pi/4$ rotation. Using this definition, $E_{\rm roll} \sim \gamma_c D_i \xi_{\rm crit}$ is obtained. In contrast to $e_{\rm roll}$, $E_{\rm roll}$ depends on the monomer diameter D_i .

⁵If two monomer sizes are different (D_1 and D_2), D_i corresponds to the reduced diameter $D_i = D_1D_2/(D_1 + D_2)$.

The effective impact energy by two spheres of masses m_1 and m_2 and of the relative impact velocity v_0 is written as

$$E_{\text{kei}} = \frac{1}{2} \frac{m_1 m_2}{m_1 + m_2} v_0^2. \tag{7.25}$$

Numerical simulations have been performed to reveal the details of the soft impact among fluffy dust aggregates [14–16]. BPCA and BCCA are extreme cases, and actual aggregates are in between them. Restructuring and compaction are also caused by the impact. Therefore, d_f would range between 2 (BCCA) and 3 (BPCA). The deformable BCCA is the most plausible modeling. According to the numerical simulation, the global restructuring phases can be classified using E_{roll} and E_{kei} . When E_{kei} is small, no restructuring is induced. Sticking or bouncing without visible restructuring is the major outcome in this regime. As $E_{\rm kei}$ increases, the visible restructuring begins to occur at $E_{\rm kei} \simeq 5E_{\rm roll}$. Because the rolling is the easiest deformation mode for the aggregate restructuring, it is reasonable that the restructuring threshold is related to E_{roll} . By further increasing E_{kei} , the maximum compression is attained at $E_{\text{kei}} \simeq n_c E_{\text{roll}}$, where n_c is the total number of contacts in the aggregate. This result indicates that the aggregate has to be compressed by the impact within the range of $5E_{\text{roll}} < E_{\text{kei}} < n_c E_{\text{roll}}$. By the energy injection of $n_c E_{\text{roll}}$, all the contacts can rotate to find the better-compacted structure. Thus, this criterion is reasonable again.

According to the numerical result [16], the degree of compression of the impacted aggregate depends on the impact energy $E_{\rm kei}$. The resultant gyration radius $R_{\rm gy}$ is scaled by the number of constituent monomers N and the normalized impact energy $E_{\rm kei}/NE_{\rm roll}$ as

$$R_{\rm gy} \propto N^{\frac{1}{2.5}} \left(\frac{E_{\rm kei}}{NE_{\rm roll}}\right)^{-0.1}$$
 (7.26)

This form indicates that the aggregates are fractal with $d_f = 2.5$. This compression exhibits a saturation at a certain impact energy, and the maximally compressed aggregates do not exceed $d_f \simeq 2.5$ [16]. Therefore, even the fully compressed aggregates still have fluffy structures. It is difficult to compress the aggregate to the truly compact ($d_f \simeq 3$) state. Moreover, the scaling exponent 0.1 is very small, which indicates that the drastic compaction by $E_{\rm kei}$ is not so easy. Examples of the numerical simulations are presented in Fig. 7.5. Figure 7.5a shows the low-velocity impact resulting in sticking without restructuring. Furthermore, the maximum compression is attained at $E_{\rm kei} \simeq 0.19 n_c E_{\rm roll}$, as observed in Fig. 7.5b.

When E_{kei} exceeds a certain threshold, the aggregate will be shattered. A unit of the breaking energy E_{break} is defined as [15, 26]

$$E_{\text{break}} \sim \left(\frac{\gamma_c^5 D_i^4}{E^2}\right)^{1/3}.\tag{7.27}$$

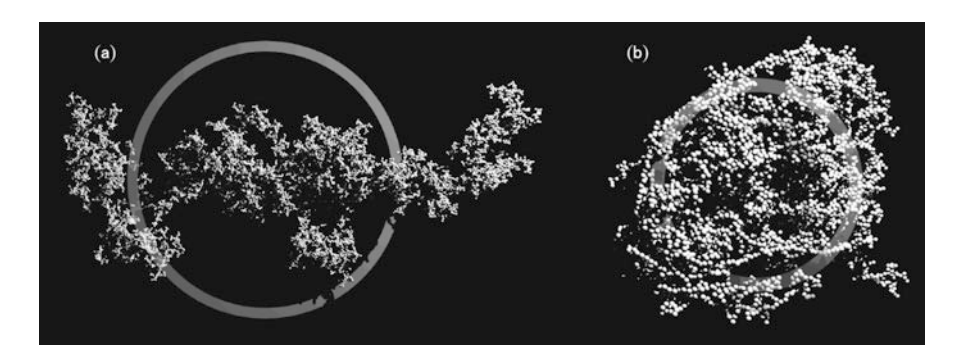


Fig. 7.5 Examples of collision outcomes of the two deformable BCCA impacts. The final outcomes by two identical BCCA cluster impacts are shown. (a) No restructuring is observed in the very low $E_{\rm kei}$ regime, $E_{\rm kei}=0.01E_{\rm roll}$. (b) The maximum compression is attained in the large $E_{\rm kei}$ regime, $E_{\rm kei}=0.19n_cE_{\rm roll}$. Both aggregates consist of 16,384 monomers with radius $0.1~\mu$ m and $\xi_{\rm crit}=0.8~\rm nm$. *Gray circles* correspond to the gyration radii $R_{\rm gy}$ (Reproduced with permission from Ref. [16]. Copyright: AAS)

Here a simple relation $E_{\text{break}} \sim F_{\text{break}} \delta_{\text{break}}$ is assumed. In addition, a relation $F_{\text{break}} \sim \gamma_c D_i$ and the JKR scaling (Eq. (2.68)) for δ_{break} are also used to derive Eq. (7.27). Thus, E in Eq. (7.27) represents the Young's modulus. To be more precise, $E_{\text{break}} \simeq 1.54 F_{\text{break}} \delta_{\text{break}}$ was obtained by the numerical simulation [15]. Using this E_{break} , the fragmentation phase can be classified in more detail. Specifically, one monomer particle starts to detach from the aggregate at $E_{\text{kei}} \simeq 3n_c E_{\text{break}}$. When E_{kei} becomes greater than $10n_c E_{\text{break}}$, catastrophic disruption occurs [15, 24].

7.1.5 Experiments of Dust Aggregate Collisions

As already mentioned, the collision outcomes were also studied by various experiments. Comprehensive reviews of relevant experimental works are summarized in Refs. [10–13]. All three phases [mass gain (sticking), mass conservation (bouncing), and mass loss (fragmentation)] were experimentally reproduced. Compressive restructuring can be associated with some of these phases. Kothe and Blum compiled the experimental and numerical results into a phase diagram, as shown by the color map in Fig. 7.2. In the phase diagram, the cratering and mass transfer regimes can be observed in addition to three basic outcomes. These two phases correspond to intermediate states between mass gain (sticking) and mass loss (fragmentation) phases. The important fact is that mass gain (sticking) is possible only in a relatively small-scale regime. Bouncing, mass transfer, cratering, and fragmentation become predominant in the larger aggregate regime. Thus, it is not easy to continue the growth for meter-sized aggregates. According to the phase diagram (Fig. 7.2), bouncing or fragmentation starts to occur at the aggregate size $D_i = 0.1$ –1 m.

Although the dust aggregates must grow through these regions to form planetesimals, bouncing and fragmentation clearly prevent aggregates from growing further.

The difference in compactness between the impactor and target is also a crucial factor to evaluate the collision outcomes [13]. As discussed in Sect. 7.1.1, the size ratio is the most important parameter to estimate the relative impact velocity. The ratio of compactness (or equivalently the porosity ratio) between the impactor and target also significantly affects the collision outcomes. If a small compact impactor collides against a large porous target, sticking by penetration can be observed. Furthermore, the mass transfer between two colliding aggregates might be naturally possible by considering the porosity ratio effect. Therefore, the collision outcomes appear to depend on the ratios of both size and porosity between the impactor and target. In Ref. [13], the phase diagrams of collision outcomes were drawn for each combination of size and porosity ratios, e.g., small compact aggregate vs. large porous aggregate and small porous aggregate vs. large porous aggregate, etc. Using the phase diagrams, a numerical simulation of dust coagulation was performed and the feasibility of dust growth was assessed [27]. According to the numerical evaluation, the growth is stopped by bouncing rather than fragmentation, which indicates that direct dust growth by collision is difficult. This is the bouncing barrier of the growth of dust aggregates. If dust aggregates pass over the bouncing barrier, they are subjected to the next hurdle of shattering called the fragmentation barrier.

7.1.6 Soft Impact of Dust Aggregates

As discussed thus far, it is not so easy for dust aggregates to grow to the planetesimal scale. There are some barriers that must be overcome: radial drift, bouncing, and fragmentation barriers. In addition, the electric charge of dust aggregates might also affect their growth scenario [28]. The dust aggregates are very porous and have a fractal structure as long as they are sufficiently small, which implies that the target dust aggregates can deform and be restructured by the impact. In numerical simulations, this restructuring effect was quantified using $E_{\rm roll}$ and $E_{\rm break}$, as discussed above. However, such a simple characterization is not sufficient to model realistic collision outcomes. There might be some soft impact effects that are helpful to overcome the barriers. For example, the numerical results introduced thus far are based on the head-on collision whereas most of the natural impacts undergo offset collisions. The effect of offset collisions might affect the growth scenario of dust aggregates. In this subsection, some of the soft impact effects relating to fluffy dust aggregates are discussed.

Offset collision effect The effect of offset collision was systematically examined by numerical simulations [29, 30]. To evaluate the degree of offset collision, the impact parameter b_{imp} is usually utilized. The impact parameter b_{imp} is defined

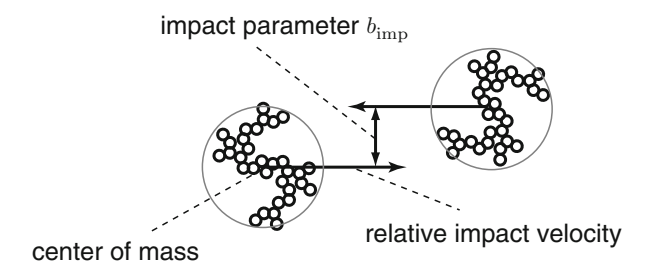


Fig. 7.6 The definition of impact parameter b_{imp} , which characterizes the offset collision

by the distance of the centers of mass in the plane perpendicular to the impact velocity. A schematic image of b_{imp} is presented in Fig. 7.6. By the energetic head-on collision among equal-mass dust aggregates, the aggregates are strongly compressed until they exhibit a pancake-like structure. As a result of the offset collision, however, the elongation of aggregates can be observed. With the offset impact having very large $E_{\rm kei}$, the fragmentation indeed occurs. In some fragmentation cases, however, the largest fragment mass could be greater than the initial aggregate mass. Namely, dust aggregates can grow by partial sticking even in such a fragmentation phase. The condition of this effective growth was numerically examined for the offset collision among icy BCCA aggregates. Using numerical simulation, the critical velocity below which the effective growth is possible was observed to be approximately 35–70 m/s [29]. This value is close to the typical largest impact velocity in the PPD (Fig. 7.2). Therefore, the fragmentation barrier could be overcome by considering the offset collision of icy dust aggregates. The numerical simulation also revealed that the critical E_{kei} for BCCA in a head-on collision is smaller than that for BPCA, i.e., BCCA is disrupted more easily than BPCA. Note that, these researchers assumed icy dust rather than silicate dust. For silicate grains, the critical velocity is reduced by roughly one order of magnitude because the surface tension of silicate is also roughly one order of magnitude smaller than that of ice. Thus, the fragmentation barrier might still be serious issue for silicate dust aggregates.

Coordination number effect The soft impact of fluffy aggregates might be able to surmount the bouncing barrier as well. Using numerical simulations, Wada et al. investigated the coordination number dependence of the collision outcomes [31]. The coordination number $n_{\rm co}$ indicates the average number of contacts per monomer in the aggregate network structure. These researchers observed that bouncing is suppressed when $n_{\rm co}$ is less than 6. Notably, this criterion is independent of material properties. Both ice and silicate aggregates exhibit almost the same behavior. For very fluffy aggregates with $n_{\rm co} < 6$, the sticking phase is predominant until fragmentation occurs by very large $E_{\rm kei}$. The critical value $n_{\rm co} = 6$ roughly corresponds to the packing fraction $\phi \simeq 0.3$ in three-dimensional packing. Although some experiments with $\phi \simeq 0.15$ exhibit bouncing [10, 32], sticking behavior can also be

experimentally observed by the impact of highly porous ($\phi \leq 0.3$) snow balls [33]. By considering these numerical and experimental results, very porous icy aggregates might be able to overcome the bouncing barrier. However, the effect of coordination number for dust aggregate growth remains a matter of debate. More controlled experiments are necessary to confirm this effect.

Fluffy structure effect The radial drift barrier again appears to be related to the structure of dust aggregates. Assuming icy dust aggregates, the breakthrough possibility of the radial drift barrier was numerically assessed [34]. Because the fractal dimension of dust aggregates cannot exceed a certain threshold $d_f \simeq 2.5$ (Eq. (7.26) [16]), the effect of the internal structure on the dust growth scenario is not trivial. In particular, when the dimensionless braking time τ_b becomes larger than unity, the growth rate of dust aggregates is drastically accelerated because the dominant drag force switches from Epstein to Stokes. The fractal nature of aggregates and the switch of drag force laws appear to be important factors in the numerical simulation. This rapid growth effect is sufficiently large to overcome the radial drift barrier [34]. It should be noted, however, that these researchers also used icy dust aggregates to neglect the fragmentation effect.

Role of ice and its sintering As discussed above, the presence of ice or snow might be very important to explain planetesimal formation. Our planet Earth is covered with plenty of water. The existence of water enables us to live on the surface of the Earth. Furthermore, water plays a crucial role in terrestrial tectonics. In contrast, the ambient gas pressure is extremely low for water to be liquid in space; water would be in the form of vapor or solid ice. The location in the PPD at which the ice condensation (sublimation) starts to occur and water-rich mineral formation is possible is called the snow line.

Around the snow line, icy dust aggregates experience sintering [35]. As a result of the sintering, the thickness of the neck between connecting monomers grows. The driving force of sintering is the redistribution of surface molecules induced by the Laplace pressure, i.e., surface tension. The Laplace pressure is inversely proportional to the radius of curvature (Eq. (2.100)), and the thin neck has a small radius of curvature. Thus, the neck thickness grows to minimize the Laplace pressure (or equivalently maximize the radius of curvature) by sintering.

The Laplace pressure also affects the size-frequency distribution of constituent monomers. Let us consider a dust aggregate composed of various-sized icy monomers. The largest monomer has the smallest Laplace pressure, and vice versa. Then, the transport of ice molecules from small monomers to large monomers occurs to minimize the total Laplace pressure. Because of this effect, the size difference among monomers is enhanced. According to the numerical investigations, this ripening effect may affect the planetesimal formation [36, 37]. In particular, the fragmentation of aggregates might be

caused by the ripening effect [36]. However, because sintering can increase the strength of the monomer contact by thickening the contacting neck, it may also affect the mechanical properties of dust aggregates. Both effects proceed simultaneously. Although some impact experiments with sintered porous ices were carried out [33, 38], it is not easy to directly compare the numerical and experimental results, particularly for microscopic aggregate growth. The sintering of ice occurs very rapidly in laboratory experiments. Thus, its precise control is very difficult.

Outlook of the soft impact of dust aggregates In short, the detailed processes of planetesimal formation are still controversial. It appears that there is a possibility to overcome some barriers by considering the fluffy ice dust aggregates. Although the numerical investigations have an advantage to model the motion of tiny grains under a microgravity environment, the numerical methods are not almighty. For instance, the effect of a nonspherical monomer shape has hardly been considered and may significantly affect the $E_{\rm roll}$. Then, the entire story might be rewritten again.

There must be a way to form our solar system because the Earth undoubtedly exists. Additionally, many exoplanets have been located in space. It is an exciting challenge to build a universal story to produce various planetary systems. It is impossible for me to provide an exhaustive review of planetary formation. Rather, I am a learner in this field. For example, the details of the effects of turbulence, electrostatic, radiation pressure, among others, have not been considered here. The dynamics of natural dust aggregates would be very complex. However, we must concentrate on the predominant dynamics to build a physically meaningful model. I can definitely say that the fundamental processes of microscopic *soft impact* are necessary bricks for building the planetary system's history.

7.2 Regolith Grains

In this section, we will return to the discussion of macroscopic-scale grains. As mentioned in Chap. 1, surfaces of terrestrial (solid) planets and asteroids are usually covered with grains called regolith. A part of the surface of the Earth is also covered with sand. However, the origins and dynamics of the Earth's soil and planetary regolith are quite different. On the Earth, an abundance of atmosphere, water, and biological activities evidently affect surface dynamics and resultant landforms. In contrast, most of the small astronomical objects have airless and waterless surfaces that are free from biological activity. In fact, the Earth is a rather peculiar planet. The origin and dynamics of planetary regolith will be discussed in the following of this subsections.

7.2 Regolith Grains 279

7.2.1 Regolith Formation by Impacts

First, why are planetary surfaces covered with regolith? The original material of the solar system is most likely tiny grains, as discussed in the last section. Is the regolith a direct remnant of such commencing materials? The answer is "no". Rather, gardening by impacts is considered to be the main source of regolith formation [39]. Namely, ejecta grains splashed by impacts and finally falling back onto the planetary surface are deposited and form the regolith layer.

Lunar regolith has been more intensively investigated than other objects because the Moon is our nearest neighbor. The typical thickness of the lunar regolith layer is on the order of 10^0 – 10^1 m. Its depth distribution is highly inhomogeneous. Because the elementary process of regolith formation is supposed to be impacts, a regolith layer's thickness must be related to the craters abundance. Impact cratering cultivates the surface of the target object, and ejecta grains are splashed on its circumference. The planetary surface is iteratively exposed to various-scale impacts. Because the frequency of a large-scale impact event is rarer than that of a small-scale event, the surface layer is cultivated many times in a shallow region. Impact cratering frequency is roughly expressed by a power-law form, as discussed in Sect. 5.2.

By assuming that the floor of regolith layer is composed of the bottom of the crater's cavities, we can estimate the distribution of the regolith depth using the crater population. The cavity opened by impact cratering would be deposited by ejecta grains (regolith) splashed by subsequent nearby impacts. Sooner or later, the cavity might be filled with grains and the regolith layer is finally formed. In this case, the local crater population density should be related to the local thickness of the regolith layer.

A simple model was proposed for the relation between the crater's size-frequency distribution and the regolith thickness [39, 40]. First, the coverage factor by craters in the diameter range from D_s to D_{eq} is computed as

$$f_c(D_s, D_{eq}) = \int_{D_{eq}}^{D_s} \frac{\pi}{4} D_c^2 \frac{dN_{\text{cum}}(D_c)}{dD_c} dD_c = \frac{\pi b_c c_{eq}}{4(b_c - 2)} \left[\left(\frac{D_{eq}}{D_s} \right)^{b_c - 2} - 1 \right].$$
(7.28)

Here we use Eqs. (5.1) and (5.9) to obtain this form. $D_{\rm eq}$ indicates the equilibrium crater diameter. At $b_c=2$, it is impossible to use this form because $D_{\rm eq}$ becomes arbitrary and Eq. (5.9) is not applicable. Note that $f_c=1$ means that the accumulated cratered area is simply equal to the considered area. Because the crater depth is proportional to its diameter (Sect. 5.1), the thickness of the regolith layer (floor depth) can also be proportional to the crater diameter. If the proportional constant is independent of crater size, $D_{\rm eq}/D_s$ on the right-hand side of Eq. (7.28) can be simply replaced by $h_{\rm eq}/h_s$. Here the thicknesses (crater depth) of the regoliths made by craters with diameters D_s and $D_{\rm eq}$ are denoted by h_s and $h_{\rm eq}$, respectively. Defining

the constant proportionality as $D_s = Qh_s$ (and $D_{eq} = Qh_{eq})^6$, Eq. (7.28) can be rewritten as

$$h_s = \frac{D_{\text{eq}}}{Q} \left[\frac{4(b_c - 2)f_c(Qh_s, D_{\text{eq}})}{\pi b_c c_{\text{eq}}} + 1 \right]^{\frac{1}{2-b_c}}.$$
 (7.29)

From the crater counting, the values of b_c , $c_{\rm eq}$, and $D_{\rm eq}$ are directly measurable. Next, we assume that the planetary surface is sufficiently covered by regolith when the coverage factor f_c reaches 2. Roughly speaking, the open cavities can completely cover the surface at $f_c \simeq 1$. Then, these cavities can be filled with ejected grains at $f_c \simeq 2$. By this coverage factor $f_c = f_{\rm min} = 2$, the considered surface is fully mantled by the regolith layer of the corresponding thickness $h_{\rm min}$ which can be estimated using Eq. (7.29). The thickness of the regolith layer must be greater than $h_{\rm min}$ everywhere in the considered area because $f_c = 2$ is assumed on the D_s scale. At the time, the portion of the thicker regolith layers can be estimated using the corresponding f_c value. A deeper regolith layer of thickness $h_1 = D_c/Q$ is formed by the cratering in diameter $D_c(>D_s)$. Because the corresponding coverage factor $f_c(Qh_1, D_{\rm eq})$ at the moment of $f_c(D_s, D_{\rm eq}) = 2$ is less than 2, the regions of regolith thickness h_1 become patchy. Assuming that the probability $P(h_1)$ to find the regolith layer with thickness h_1 is proportional to the corresponding coverage factor $f_c(Qh_1, D_{\rm eq})$, one obtains the form of $P(h_1)$ as

$$P(h_1) = \frac{f_c(Qh_1, Qh_{eq})}{f_{\min}} = \frac{(h_{eq}/h_1)^{b_c-2} - 1}{(h_{eq}/h_{\min})^{b_c-2} - 1}.$$
 (7.30)

Note that the maximum value of h_1 is $h_{eq} = D_{eq}/Q$. Finally, the median value $\bar{h_1}$ can be computed from the relation $P(\bar{h_1}) = 1/2$. Thus, $\bar{h_1}$ is obtained as

$$\bar{h_1} = 2^{\frac{1}{b_c - 2}} h_{\text{eq}} \left[\left(\frac{h_{\text{eq}}}{h_{\text{min}}} \right)^{b_c - 2} + 1 \right]^{\frac{1}{2 - b_c}}.$$
 (7.31)

This simple model roughly agrees with the lunar observation results [39]. Moreover, using Eq. (5.9), the rate of regolith formation can be evaluated as

$$h_{\rm eq} = \frac{1}{\mathcal{Q}} \left(\frac{c_c(t)}{c_{\rm eq}} \right)^{\frac{1}{b_c - 2}}.$$
 (7.32)

However, this model has some limitations. First, the selection of $f_{\min}=2$ is arbitrary. $P(h_1)$ and therefore $\bar{h_1}$ depends on its value. Second, the maximum value $h_{\rm eq}=D_{\rm eq}/\mathcal{Q}$ is unclear. In addition, the validity of this model in the regime of small $b_c(<2)$ remains uncertain.

⁶Note that this factor Q and the quality factor Q are different.

7.2.2 Compaction by Thermal Cycling

The next topic is the thermal behavior of bulk regolith layers. The regolith layer can be heated by solar radiation. If the surface facing the Sun varies with time just like the Earth, its surface is exposed to thermal cycling. As mentioned in Sect. 3.9.2, the effect of temperature variation is almost negligible for granular behaviors as long as the grain size is macroscopic. However, small but cyclic temperature perturbation is actually capable of affecting the structure of granular matter. The gradual compaction of a granular column can be induced by the thermal cycling [41, 42]. Its compaction rate depends on the amplitude and frequency of the thermal cycling. Although the compaction proceeds very slowly on the timescale of laboratory experiments, it may be sufficiently fast for planetary phenomena. Thus, this type of thermal-driven compaction would take place on every planetary surface covered with regolith. At a final steady state, the packing fraction should be approximately $\phi = 0.64$ in three-dimensional space (random close packing (RCP)). With the thermal cycling, the packing fraction increases in a logarithmic manner [43]:

$$\phi_{\rm ss} - \phi_{n_{\rm cyc}} \propto \frac{1}{\ln n_{\rm cyc}},\tag{7.33}$$

where ϕ_{ss} , n_{cyc} , and $\phi_{n_{cyc}}$ are the packing fraction at the finally achieved steady state, cycle number, and packing fraction at the n_{cyc} -th cycle, respectively. Because of the logarithmic functional form, the truly steady state might not be attained even in the astronomical timescale.

Even with weak mechanical vibration, compaction is induced. The compaction by weak mechanical vibration obeys the stretched exponential relaxation form [44],

$$\phi_{\rm ss} - \phi_{n_{\rm cyc}} \propto \exp\left[-\left(\frac{n_{\rm cyc}}{n_{\rm char}}\right)^{\beta_{\rm char}}\right],$$
 (7.34)

where n_{char} and β_{char} are two fitting parameters characterizing the relaxation. The reason for different functional forms for the thermal cycling (Eq. (7.33)) and weak mechanical vibration (Eq. (7.34)) is not yet unveiled; both forms are only empirical forms.

The thermal property of granular matter is not negligible particularly for quasistatic deformation. It proceeds slowly but gradually in the regolith behaviors. Slow and weak mechanical vibration can further affect the packing structure. Such slow but long timescale effects are ubiquitous in geological and planetary phenomena. It is not obvious whether granular compaction due to the thermal cycling is sufficiently fast or not in terms of geological timescale. In either case, the planetary surface regolith layer is usually subjected to thermal cycling, which results in compaction. This compacted structure might be strongly disturbed by impact events. The impact causes regolith splashing, migration, among others. Slow compactions and intermittent but intense impacts are very contrastive. Regolith migration and convection possibly induced by impacts are addressed later in Sects. 7.2.4 and 7.2.5.

Moreover, thermal cycling might be able to cause the weathering-based regolith formation. When rocks are subjected to thermal cycling, internal cracks are created by the inhomogeneity of the thermal expansion rate. Because of the thermal cycling, the cracks grow and the rocks might be fragmented by these cracks. According to Ref. [45], this thermal fatigue effect could be more efficient than the impact-based regolith formation. However, the thermal fatigue weathering rate must depend on various environmental conditions. While it is difficult to conclude that the thermal fatigue is definitely the main process of regolith formation, it must not be neglected, at least under some environmental conditions.

7.2.3 Thermal Conduction and Thermal Inertia

In this subsection, the thermal conduction on the surface of regolith layer is discussed. In general, heat transmits through bulk granular matter mainly by thermal diffusion. Radiation and convection effects are usually negligible for granular heat transfer. Thus, we can use the diffusion equation to model the thermal conduction in bulk granular matter. Here we consider thermal diffusion under the thermal cyclic condition. For the diffusion equation, a solution that is convenient to discuss thermal cycling was already introduced in Eqs. (3.39) and (3.40). Because we consider thermal conduction, the general physical quantity Ψ in Eq. (3.39) should be replaced by temperature T. Then, the equations are rewritten as

$$T = T_0 \exp(-k_n x) \sin(\omega_n t - k_n x), \tag{7.35}$$

$$k_n = \sqrt{\frac{\omega_n}{2K_d}},\tag{7.36}$$

where T_0 corresponds to the amplitude of sinusoidally oscillating temperature (thermal cycling). Let us consider the planetary surface heated up and cooled down by cyclic (diurnal) irradiation. Then, Eq. (7.35) models the temperature variation in time t and depth x. This model is a simple one-dimensional model, and x = 0 corresponds to the surface. The penetration depth of the thermal cycling depends on the frequency of the cycle because the decay factor in Eq. (7.35) is written as $\exp(-k_n x)$. The thermal penetration depth (or thermal skin depth) δ_{th} is defined by the reciprocal of the wavenumber k_n as

$$\delta_{\rm th} = 2\pi \sqrt{\frac{2K_d}{\omega_n}} = \sqrt{\frac{4\pi\kappa_h P_{\rm cyc}}{\rho C_{\rm th}}}.$$
 (7.37)

⁷This situation is the same as that in the case of thermal conduction in rocks.

Here we use bulk regolith properties such as density ρ , thermal conductivity κ_h , thermal capacity $C_{\rm th}$, and period of the cycle $P_{\rm cyc}$. By definition, these properties are related as $K_d = \kappa_h/\rho C_{\rm th}$. At the depth $x = \delta_{\rm th}$, the amplitude of the temperature oscillation decays to 1/e. According to Eq. (7.37), thermal penetration depth is proportional to the square root of the cycle period. Therefore, thermal cycling with longer period penetrates deeper in the regolith layer.

Thermal inertia is frequently used to characterize the thermal property of the heated boundary. At the surface boundary x = 0, the length scale in the heat flux can be nondimensionalized using δ_{th} as

$$\kappa_h \left. \frac{\partial T}{\partial x} \right|_{x=0} = \left. \sqrt{\frac{\kappa_h \rho C_{\text{th}}}{4\pi P_{\text{cyc}}}} \left. \frac{\partial T}{\partial x^*} \right|_{x^*=0},$$
 (7.38)

where $x^* = x/\delta_{th}$ is the dimensionless depth. The thermal inertia I_{th} is defined by

$$I_{\rm th} = \sqrt{\kappa_h \rho C_{\rm th}}. (7.39)$$

Thermal inertia is one of the most important properties to characterize planetary surface. It is necessary information to estimate the heat budget in planets. For example, a detailed evaluation of thermal inertia on the Martian surface is reported in Ref. [46]. However, an adequate understanding of the thermal properties of granular matter is still far from complete. The very slow dynamics of thermally oscillated granular matter must be investigated in further detail.

7.2.4 Regolith Migration

Regolith migration may be induced by impact-based seismic shaking. As discussed in Sect. 5.4.2, the meteors impacting onto a small asteroid can play a significant role in the development of its surface terrain. In Sect. 5.4.2, obliteration of craters by global seismic shaking was discussed. In the model of obliteration of craters, the diffusion-type relaxation of the crater's shape was assumed. It is apparent that the surface regolith must migrate to relax the crater's shape.

In fact, the small asteroid Itokawa shows some evidence of the regolith migration. An image of Itokawa taken by the spacecraft Hayabusa is shown in Fig. 7.7. One can categorize its surface into two phases: smooth and rough terrains. As observed in Fig. 7.7, the smooth terrain is localized at the central neck part of the Itokawa. The smooth terrains are covered with relatively small (sub-centimeter- or centimeter-sized) grains and pebbles. In contrast, the rough terrains are covered with a mixture of pebbles, gravels, and boulders of various sizes. Such localization reminds us of segregation by the Brazil nut effect (BNE) (Sect. 3.9.4). The BNE is vibration-driven size segregation in a polydisperse granular matter. Such segregation may also be induced by impact-induced seismic shaking.

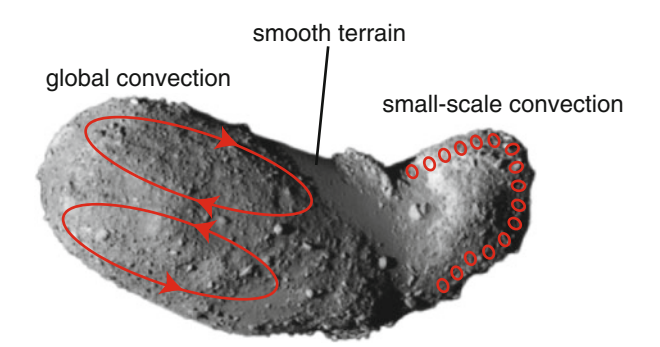
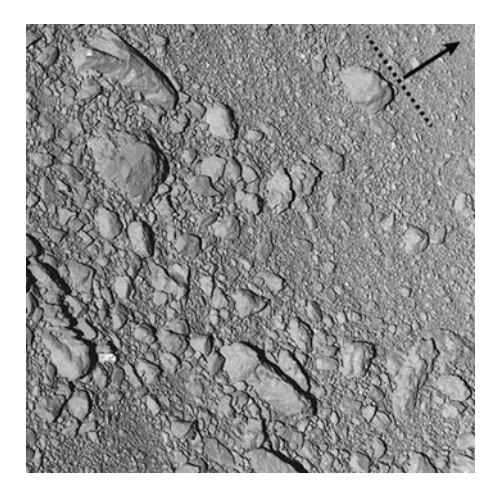


Fig. 7.7 Image of the asteroid Itokawa taken by the spacecraft Hayabusa. A smooth terrain can be observed on the central part. Schematic image of large-scale (global) convection and small-scale surface convection are shown on the left and right sides of the image, respectively. Note that this image does not indicate the actual difference between the left and right sides. This image shows only the uncertainty of the possible convection size and structure on Itokawa. Moreover, the convection probably occurs in the underground region, whereas the rolls in the figure look like surface migration (Modified from the original image of JAXA Digital Archives)

Fig. 7.8 Close examination of a boundary of rough and smooth terrains on the asteroid Itokawa. Alignment of the longest axis of pebbles (gravels) can be observed. The direction of this alignment (indicated by the dotted line) is vertical to the possible landslide slope direction (arrowed direction) [47] (Modified from the original image of JAXA Digital Archives)



Direct evidence for the regolith migration can be observed in the high-resolution image of Itokawa, as shown in Fig. 7.8 [47]. In this image, the longest axis of pebbles and gravels (dotted line in Fig. 7.8) is lined up in the direction perpendicular to the gravitational gradient (arrow direction in Fig. 7.8). This alignment is a natural consequence of landslides occurring at the slope. On the surface of landslides flow, the longest axis of pebbles should be vertical to the slope direction to minimize the moment of inertia of rotating pebbles. This alignment is observed at the boundary area of smooth and rough terrains on the Itokawa. Based on these observational facts, it is plausible to consider that regolith migration has occurred on the surface of the Itokawa and may result in the segregation.

7.2.5 Regolith Convection

The main issue that we would like to consider here is whether regolith migration occurs as a part of global regolith convection. Global seismic shaking is necessary to induce global regolith convection. Granular convection can be easily observed in a laboratory experiment of a vibrated granular bed (Sect. 3.9). Because granular convection can convey the large grains upward, BNE can be simultaneously induced in the vibrated granular bed. Although reverse BNE (RBNE) can also be induced under particular vibration conditions, the onset of segregation is important here; the direction is not the problem. Segregation can result in the localization of rough and smooth terrains in any case. Miyamoto et al. assessed the possibility of global seismic shaking using the model discussed in Sect. 5.4.2 [47]. A necessary condition to induce the granular convection is approximately $\Gamma > 1$, where Γ is the ratio of vibrational and gravitational accelerations (Eq. (3.67)). Substituting the characteristic timescale (diffusion time in the body with size D_t) $\tau_{\rm diff} = D_t^2/\pi^2 K_d$ into t of Eq. (5.40), one can estimate the globally attained vibrational acceleration that is induced by the impact (of the impactor's diameter D_i , its density ρ_i , and impact velocity v_0) as

$$\Gamma(\tau_{\text{diff}}) = \frac{3fv_0}{\mathcal{G}} \sqrt{\eta_{\text{seis}} \frac{\rho_i}{\rho_t^3} \frac{D_i^3}{D_t^5}} \exp\left(-\frac{fD_t^2}{\pi K_d Q}\right). \tag{7.40}$$

Assuming the values of some parameters ($K_d=0.25\,\mathrm{km^2/s}$, Q=200, $\eta_\mathrm{seis}=10^{-4}$, $f=10\,\mathrm{Hz}$, $\rho_t=1.9\times10^3\,\mathrm{kg/m^3}$, $\rho_i=2.5\times10^3\,\mathrm{kg/m^3}$, $v_0=4\,\mathrm{km/s}$, and $D_t=400\,\mathrm{m}$), these researchers confirmed that the condition $\Gamma(\tau_\mathrm{diff})>1$ is satisfied even by a small impactor with $D_i=10\,\mathrm{mm}$ for the asteroid Itokawa [47]. This finding indicates that small asteroids such as Itokawa can be readily fluidized by the small-scale impact. However, this estimate is based only on the criterion $\Gamma>1$. It is difficult to estimate the rapidity of the rate of migration and convection. The possibility of regolith convection should be evaluated more quantitatively.

Some experiments aiming to study granular convection or BNE under the microgravity condition were performed. In these experiments, parabolic flights were used to produce the microgravity condition. For example, the granular convective velocity in a Taylor-Couette shear cell was measured under the microgravity condition [48–50]. In the sheared cell, a shear banding structure, in which rapidly moving grains are localized near the shearing wall, can be observed toward the sheared (primary) direction. This shear banding structure is formed regardless of the strength of gravity. The secondary flow perpendicular to the primary flow (i.e., the radial direction in the Taylor-Couette cell) was also induced by the shearing. According to the experimental result, this secondary flow velocity is strongly affected by the gravitational acceleration g. The convective velocity drastically decreased under the microgravity condition, which indicates that gravity is indispensable in producing the shear-induced granular convection.

Another example is on the BNE. The rise velocity of large intruders in a vibrated granular bed was measured [51]. These researchers simulated the gravitational accelerations on Mars ($g_{\text{Mars}} = 3.71 \,\text{m/s}^2$) and the Moon ($g_{\text{Moon}} = 1.62 \,\text{m/s}^2$) by parabolic flights and measured the rise velocity of large intruders. The obtained result was compared with the result under $g_{\text{Earth}} = 9.8 \,\text{m/s}^2$. They observed that the rise velocity v_{rise} can be roughly scaled by Γ as $v_{\text{rise}} \propto (\Gamma - 1)^{1.3}$. More importantly, they observed that the rise velocity is approximately proportional to the gravitational acceleration as

$$v_{\rm rise} \propto g.$$
 (7.41)

Only three gravitational accelerations (g_{Mars} , g_{Moon} , and g_{Earth}) were examined in this experiment. Thus, it is difficult to determine the precise g dependence of v_{rise} only on the basis of this experiment although a qualitatively consistent result was obtained by the numerical simulation as well [52].

Scaling of granular (regolith) convective velocity It is not easy to control g in experiments on the ground. Therefore, parabolic flights were frequently used to directly control gravitational acceleration. However, it might be possible to speculate the gravity effect using laboratory experiments through the scaling concept. If we can build an appropriate scaling relation among the dimensionless numbers that include the gravitational acceleration, the gravity dependence can be estimated from the scaling form. In fact, the scaling for the granular convective velocity was obtained by a laboratory experiment [53]. In the experiment, some relevant parameters were systematically varied and the granular convective velocity was measured. The maximum convective velocity $v_{\rm max}$ for the vertically vibrated granular bed is scaled as

$$v_{\text{max}} = C_{\text{con}} S_{\Gamma}^{\alpha} D_{\text{sys}}^{\beta}, \tag{7.42}$$

where $C_{\rm con}$ and S_{Γ} are a dimensionless coefficient and the shaking parameter (Eq. (3.70)), respectively. Additionally, the dimensionless system size $D_{\rm sys}$ is defined by the container radius $R_{\rm s}$, bed height $H_{\rm s}$, and grain diameter D_g as $D_{\rm sys} = \sqrt{R_{\rm s}H_{\rm s}}/D_g$. The values $\alpha = 0.47$, $\beta = 0.82$, and $C_{\rm con} = 3.6 \times 10^{-3}$ were computed from the fitting of the experimental data. In Eq. (7.42), S_{Γ} is used instead of Γ to characterize the convective velocity.

The shaking parameter S_{Γ} can be obtained by a nondimensionalization of the Navier-Stokes-type equation. First, the Navier-Stokes equation (Eq. (2.30)) is rewritten with the gravitational body force term a = g as

$$\frac{\partial \mathbf{u}}{\partial t} + \mathbf{u} \cdot \nabla \mathbf{u} = -\frac{1}{\rho} \nabla p + \frac{\eta}{\rho} \nabla^2 \mathbf{u} + \mathbf{g}. \tag{7.43}$$

While this equation is originally derived for viscous fluid flow, it might also be useful for granular flow. Here we assume that all the quantities in Eq. (7.43) denote the properties of bulk granular convective motion. For instance, ρ in this equation

corresponds to the bulk density of the convecting granular matter. To simplify the equation, we consider the steady flow, i.e., $\partial u/\partial t = 0$. To nondimensionalize Eq. (7.43), we define the representative velocity $(2\pi f A_0)$ using the vibration amplitude A_0 and its frequency f. For the representative length scale, the grain diameter D_g can be used. Furthermore, we assume that the pressure term is decomposed into hydrostatic and dynamic pressures: $p = p_{\rm hyd} + p_{\rm dyn}$. These pressures are supposed to be expressed as $p_{\rm hyd} \sim \rho g D_g$ and $p_{\rm dyn} \sim \rho (2\pi f A_0)^2$. Using these assumptions, Eq. (7.43) is transformed into

$$\frac{(2\pi f A_0)^2}{gD_g} \left[\boldsymbol{u}^* \cdot \nabla^* \boldsymbol{u}^* + \nabla^* p_{\rm dyn}^* - \frac{\eta}{2\pi f A_0 \rho D_g} \nabla^{*2} \boldsymbol{u}^* \right] = \hat{\boldsymbol{g}}^* - \nabla^* p_{\rm hyd}^*, \quad (7.44)$$

where $u^* = u/2\pi f A_0$, $\nabla^* = D_g \nabla$, and $\hat{g}^* = g/g$ are the nondimensionalized velocity, nondimensionalized ∇ operator, and unit vector to the gravitational direction, respectively. One can confirm that $S_{\Gamma} = (2\pi f A_0)^2/gD_g$ is the principal dimensionless number in Eq. (7.44). It can be naturally derived by the nondimensionalization of the continuum-based Navier-Stokes-type equation. In fact, S_{Γ} can be obtained solely by the balance between the advection term $u \cdot \nabla u$ and gravity g. The key point is the definition of the characteristic length and velocity scales.

Another dimensionless number $\Gamma_B = S_{\Gamma} \eta / 2\pi f A_0 \rho D_g$ is simultaneously obtained by the nondimensionalization (Eq. (7.44)). In the viscosity-dominant regime, Γ_B should be on the order of unity, which indicates that the granular viscosity in the vibrated system is written as $\eta \sim 2\pi f A_0 \rho D_g / S_\Gamma \sim \rho g^{1/2} D_g^{3/2} / S_\Gamma^{1/2}$. The last form is similar to Eq. (4.31). As discussed in Sect. 4.1.6, a relevant timescale is required to define the granular viscosity. For the vibrated granular matter, the vibration frequency f brings an independent timescale. In addition, the gravitational acceleration g participates in the determination of the granular viscosity. Thus, the effective granular viscosity can be evaluated using f and g. However, the concrete physical meaning of this viscosity in a vibrated granular matter remains unclear. There remain some uncertainties, e.g., $\eta \propto S_{\Gamma}^{-1}$ or $\eta \propto S_{\Gamma}^{-1/2}$ and the role of D_{ϱ} and A_0 for the characteristic length scale. Experimental tests are necessary to resolve these uncertainties. For the strongly shaken system, convective transport of the granular temperature is modeled in addition to the above mentioned momentum balance equation. Then, the onset criterion of the strongly shaken granular convection can be calculated using linear stability analysis [54]. In the theoretical framework, another dimensionless number corresponding to N/D_{svs}^2 is also used to characterize the onset criterion. Here N denotes the total grain number in the system. This fact is consistent with the existence of two dimensionless numbers S_{Γ} and $D_{\text{sys}} = (\sqrt{R_s H_s}/D_g)$. Moreover, note that the model discussed in Ref. [54] is proposed for the strongly shaken regime ($\Gamma \simeq 50$). However, Eq. (7.42) was obtained by the experiment of mildly shaken granular convection ($\Gamma \simeq 3$). The coincidence of the essential dimensionless numbers (S_{Γ} and D_{sys}) is nontrivial.

We can estimate the specific value of the convective velocity using the scaling of Eq. (7.42). This scaling can be rewritten as

$$v_{\text{max}} \sim g^{\alpha + \frac{1}{2}} \left(\frac{\Gamma'}{2\pi f} \right)^{2\alpha} D_g^{-\alpha - \beta + \frac{1}{2}} \left(\sqrt{R_s H_s} \right)^{\beta}. \tag{7.45}$$

Here the dimensionless acceleration $\Gamma' = \Gamma - \Gamma_c$ is used to involve the onset criterion of the granular (regolith) convection, e.g., $\Gamma(\tau_{\text{diff}}) > \Gamma_c \simeq 1$. Here Γ_c is the critical acceleration strength below which the granular convection cannot be induced. Γ' has also been employed to determine the g dependence of the convective (and segregative) velocity in the related experiment obtaining Eq. (7.41) [51]. The possibility of regolith convection on the asteroid Itokawa was also discussed on the basis of the criterion $\Gamma > 1$ [47]. However, this onset criterion ($\Gamma_c = 1$) might not be universal. Indeed, it clearly varies depending on the experimental conditions [55]. It is difficult to scale all the data (in particular, various f data) by the fixed Γ_c . Thus, $\Gamma_c=0$ ($\Gamma'=\Gamma$) was employed to approximately obtain the simple scaling relation in Eq. (7.42) [53]. Substituting the experimentally obtained value $\alpha = 0.47$ into Eq. (7.45), one obtains a relation between convective velocity and gravitational acceleration, $v_{\rm max} \propto g^{0.97}$. This relation is similar to Eq. (7.41). Thus, the scaling obtained by the laboratory experiment is consistent with the result of parabolic flights. Furthermore, Eq. (7.45) simultaneously revealed various parameter dependences, which is an advantage of the scaling analysis.

The obtained scaling is consistent with other laboratory experiments for granular convection. In two-dimensional granular convection, the convective velocity is almost proportional to the maximum vibration speed [55]. This result is consistent with the scaling of Eq. (7.42). Specifically, Eq. (7.42) can be transformed into another form $v_{\rm max} \sim (2\pi f A_0)^{2\alpha} (\sqrt{gd})^{1-2} D_{\rm sys}^{\beta}$, and the scaling exponent $2\alpha = 0.94$ is close to unity.

However, g was not directly varied in the laboratory experiment [53]. Thus, it is difficult to conclude the g dependence solely from this experimental result. Fortunately, the obtained scaling is consistent with the experimental results obtained by parabolic-flights [51] in which the gravity was directly controlled.

There are some limitations and weak points in the experimentally obtained scaling. First, this experiment was performed within a small-scale container. In contrast, small asteroids are not supported by any wall. Their shapes are sustained by their own gravities. This is the biggest difference between laboratory experiments and actual phenomena occurring in space. However, it is impossible to remove the container wall in any granular convection experiment even under the microgravity condition. Second, the system size is usually limited to the centimeter scale for laboratory experiments. In general, the scaling validity is not guaranteed for largescale phenomena. Of course, if the governing physical mechanism is identical, the scaling form would be invariant. However, some other effects not considered in the experiment might dominate the dynamics in extremely large-scale phenomena. In particular, for the granular convection, there might be a characteristic length scale that determines the convective roll size. In fact, a multiple-roll phase was observed in a laboratory experiment of the two-dimensional granular convection [56]. If the convective roll size is spontaneously determined by the characteristic length scale, regolith convection on the asteroid should be localized. This uncertainty is graphically illustrated in Fig. 7.7. Large-scale and small-scale convection structures are

schematically drawn on the left and right sides of the Itokawa picture, respectively. It should be noted that the regolith convection occurs in the vertical direction, although the image in Fig. 7.7 appears to be surface convection. The thickness of the regolith layer could also affect the size of the convection roll. Figure 7.7 is nothing but a conceptual diagram for the uncertainty of the regolith convection. It is difficult to discern which case (large-scale or small-scale) is correct only from the current velocity scaling result. As long as the scaling is written in the power-law form, it does not contain any characteristic length scale. Thus, a different type of analysis is necessary to clarify the effect of the characteristic length scale.

In any case, the granular (regolith) convective velocity can be estimated using Eq. (7.45) as a first order approximation. Using this scaling, we can verify the feasibility of the regolith convection hypothesis. The constraints to be satisfied are (i) the convective velocity must be lower than the escape velocity, (ii) the impact energy must be below the catastrophic disruption criterion, and (iii) the endurance of vibration and resultant migration length per impact must be sufficiently large. For the asteroid Itokawa, an additional constraint was obtained from the returned sample. The cosmic-ray exposure duration of Itokawa's surface grain was estimated to be approximately 1.5-8 Myr [57, 58]. This timescale could approximately correspond to a half cycle of the regolith convection, i.e., the surface traveling time. A feasibility assessment of the regolith convection hypothesis using all the constraints and velocity scaling (Eq. (7.45)) was performed for the target asteroid of diameter D_a , using the impactors' population of Ref. [59]. According to that study, the convective resurfacing timescale T_{resurf} can be sufficiently shorter than the mean collisional lifetime of the body in the range of 8 $10^2 \le D_a \le 10^4$ m [60]. This estimate indicates that the resurfacing of the asteroid regolith layer is indeed possible, as predicted by Ref. [47]. Moreover, the order of T_{resurf} is consistent with the cosmic-ray exposure duration.

7.2.6 Wind Transport of Regolith

Friction velocity Regolith grains can be transported by wind as well as mechanical vibration. Wind transport of sand (regolith) produces ripples, dunes, and other geomorphologies that are ubiquitously observed on the Earth. Because the Earth has a thick atmosphere, its flow can deliver sand grains efficiently. To estimate its ability, the friction velocity v_f is usually employed. v_f is defined by

$$v_f = \sqrt{\frac{\sigma_s}{\rho}},\tag{7.46}$$

⁸The mean collisional lifetime $T_{\rm life}$ is determined by the average period of the large impact which results in the catastrophic disruption of the body. This upper limit of the impact energy relates to the constraint (ii). Additionally, the convective velocity by the largest impact cannot exceed the escape velocity. Thus, the constraint (i) is automatically fulfilled. For the convective roll size, we temporarily assume the small roll size ($\simeq 100D_g$) on the basis of preliminary experimental observation.

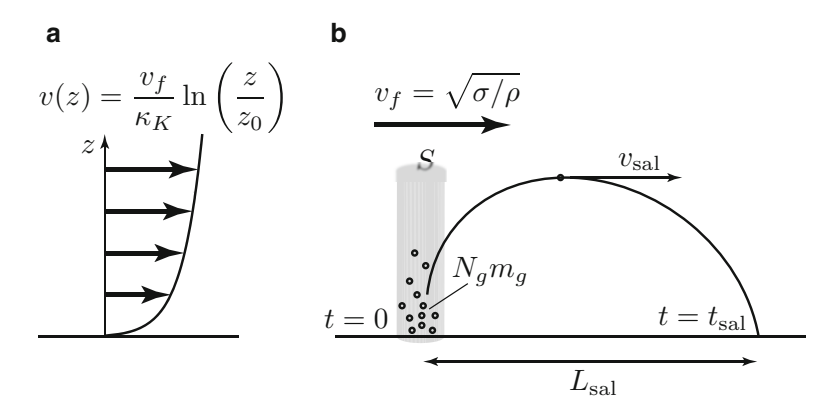


Fig. 7.9 Schematic images of the (a) vertical wind velocity profile and (b) saltation of sand grains. The wind velocity profile is characterized by the friction velocity v_f defined in Eq. (7.46). In panel (b), sand is blown by the wind flow characterized by the friction velocity. The grain mass per unit area Nm_g/S is transported to the distance $L_{\rm sal}$ during the time $t_{\rm sal}$. The form of flux per unit area is given in Eq. (7.51). Note that the vertical scales are quite different between (a) and (b)

where σ_s and ρ are the shear stress exerted on the surface of the sand layer and the density of air, respectively. In many cases, the measurement of wind velocity is considerably more practical than the stress measurement. The friction velocity v_f corresponds to a characteristic value of the wind velocity. The height dependence of the wind velocity can be estimated by assuming a simple relation $v(z) = \kappa_p z \dot{\gamma}$ based on Prandtl's mixing length theory [61]. Here v(z) is the wind velocity at height (from the surface) z, $\kappa_p \simeq 0.37$ is a constant called the Kármán constant, and $\dot{\gamma} = dv/dz$ corresponds to the shear strain rate. By integrating the approximated relation $v_f = \kappa_p z (dv/dz)$, one can obtain the velocity profile:

$$v(z) = \frac{v_f}{\kappa_p} \ln \left(\frac{z}{z_0}\right),\tag{7.47}$$

where the roughness factor z_0 is a constant representing the roughness of the blown surface. The image of the vertical wind velocity profile is illustrated in Fig. 7.9a. This profile is relevant in the relatively high velocity (or large Reynolds number) regime. Because κ_p is considered a universal constant and z_0 is determined by the surface roughness, the characteristic wind velocity is mainly characterized by the friction velocity v_f . The roughness factor z_0 is empirically known to be approximately 1/30 of the surface grains diameter [62].

Saltation threshold The frictional velocity must be sufficiently large to lift up sand grains. The force exerted on a grain by the wind flow can be estimated as $f_f \sim \rho v_f^2 D_g^2$, where D_g is the gain diameter. This force must be greater than the gravitational force $f_g \sim (\rho_g - \rho)D_g^3 g$, where ρ_g is the true density of the grain. Note that the factor $\rho_g - \rho$ indicates the buoyancy effect. Equating f_f and f_g , the threshold velocity v_{ft} is calculated to be [39, 62]

$$v_{fi} \sim \sqrt{\frac{\rho_g - \rho}{\rho} g D_g}. \tag{7.48}$$

When the friction velocity exceeds v_{ft} , the surface sand is blown, and saltation is triggered. The form of Eq. (7.48) is similar to the Shields number S_h (Eq. (2.113)). The numerical coefficient in Eq. (7.48) is determined by various factors such as the grain shape, surface friction, and cohesion effect among grains. For macroscopic grains, the coefficient is approximately on the order of 10^{-1} , which indicates that the kinetic energy to kick up a grain is approximately ten percent of the grain's potential energy. The coefficient value drastically increases upon decreasing the grain size. This finding is not surprising because surface effects, such as cohesive force, become dominant in small grains (Sect. 2.8.5). Then, the force required to lift up a grain will be considerably larger than the scaling expectation (Eq. (7.48)), in which only the gravity effect is considered. The friction Reynolds number $R_{ef} = \rho v_f D_g / \eta$ is employed to classify the dominant effect. In the large R_{ef} (> 3.5) regime, the coefficient in Eq. (7.48) is roughly constant at approximately 0.1. At $R_{ef} \simeq 3.5$, the value begins to deviate from the constant value and grows significantly [39].

Bagnold flux The flux of transported sand grains can also be scaled by the friction velocity [62]. Let us consider the saltation over distance $L_{\rm sal}$ during the time $t_{\rm sal}$ (Fig. 7.9b). Considering the surface area S above which there are N grains of mean mass m_g , the stress σ_S applied to these grains can be estimated as

$$\sigma_s = \frac{Nm_g}{S} \frac{L_{\text{sal}}}{t_{\text{col}}^2}.$$
 (7.49)

The flux of sand grains J_s is written as

$$J_s = \frac{Nm_g}{S} \frac{L_{\text{sal}}}{t_{\text{sal}}}. (7.50)$$

It should be noted that J_s represents the mass flux per unit area S (from the surface to infinite height), and $L_{\rm sal}/t_{\rm sal} (=v_{\rm sal})$ corresponds to the mean saltation velocity (Fig. 7.9b). By incorporating Eqs. (7.49) and (7.50), the flux is written as $J_s = \sigma_s t_{\rm sal}$. The saltation time $t_{\rm sal}$ can be estimated by assuming free fall in the vertical direction. Then, $t_{\rm sal}$ can be scaled as $t_{\rm sal} \sim v_f/g$. From this relation and the ram pressure form $t_{\rm sal} = t_{\rm sal} t_{\rm sal} = t_{\rm sal} t_{\rm sal} t_{\rm sal} = t_{\rm sal} t_{\rm s$

$$J_s = C_{\text{sal}} \frac{\rho}{g} v_f^3. \tag{7.51}$$

⁹To obtain this relation, we assume that the initial vertical velocity is proportional to the friction velocity.

This Bagnold flux form is widely accepted as a first order approximation for the wind transport of sand grains. Furthermore, Bagnold empirically revealed that the dimensionless prefactor $C_{\rm sal}$ is proportional to grains size [62].

Sand ripples Sand ripples are rapidly engraved by the wind flowing over a sandy surface. Its length scale (spacing) is usually less than $10\,\mathrm{cm}$ on the Earth. Thus, its pattern is easily recognized and familiar to us. The orientation of ripples is perpendicular to the wind direction, and the ripple pattern slowly moves leeward. The spacing among ripples is regular, and its range is close to the typical saltation length scale. Therefore, it is natural to consider that the spacing of ripples is mainly determined by the saltation length scale. However, such a naive idea is denied by Martian ripples. The typical regolith grain size is larger and the gravitational acceleration is smaller on Mars than those on the Earth. Therefore, the threshold friction velocity v_{fi} and saltation length $L_{\rm sal}$ should increase on Mars compared with those on the Earth. Nevertheless, the ripples spacing on Mars is similar to that on the Earth [39].

Washboard road patterns The wavy pattern might not necessarily originate only from the wind-blown ripples. A similar ripple pattern can be produced on the surface of the granular layer under a rolling wheel. This so-called washboard road [63] appears when the horizontal velocity of the rolling wheel exceeds a certain critical value. From this experimental result, Taberlet et al. proposed that the Froude-number-like dimensionless number could be an essential parameter for characterizing ripple formation [63]. Although the wind-blown ripples and washboard road are completely different in terms of their origins, the resultant patterns are partly similar. As long as the sand grains are transported along the surface, the flat leveled surface is unstable; its instability is clearly visible. Nonetheless, we do not fully understand what controls the length scale of the instability. Although the relevance of the washboard road pattern to planetary terrains is unclear, ¹⁰ the important point to note is the fact that the partly similar patterns can be produced in various different ways. Because the planetary environment is extreme, the planet's surface terrains might be better examples to verify the universality of the underlying physical mechanism of various phenomena.

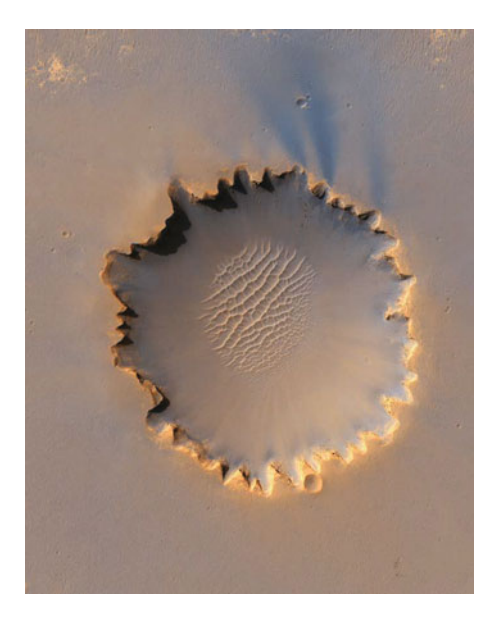
Sand dunes Sand dunes are common on Mars as well as on the Earth. Sand dunes may be initiated by a rock or other obstacle on a sandy surface. The wind streamline is separated by the obstacle. Then, a wind shadow is formed leeward of the obstacle. As a result, mobile sand grains accumulate on the windward side of the obstacle (when R_e is sufficiently high); finally, the obstacle is submerged by sand. Then, the formed sand-dune seed grows by itself. Again, the flat sandy surface is destabilized by the windy horizontal transport and the perturbation made by an obstacle. Various sand dune shapes are produced depending on environmental

 $^{^{10}}$ To make the two-dimensionally spreading washboard road pattern, an extensively wide wheel is necessary. It is difficult to imagine such a situation.

conditions such as the wind direction, supply rate of sand, and temporal changes. One of the simplest and popular dune forms is barchan. Barchans have a crescent-like shape and the horns of the crescent point leeward. Barchans are formed under conditions of a unidirectional wind and a limited sand supply. There are some other dune shapes such as blowout, transverse, linear, and star shapes. Sand dunes move slowly to the leeward side, and their velocity depends on the size. The larger dunes move more slowly than the smaller dunes with intrinsic traveling velocity $v_{\rm travel}$. $v_{\rm travel}$ is approximately proportional to the reciprocal of the dune height. Because of this size-dependent traveling velocity, sand dunes exhibit various interactions: collision, coalescence, splitting, and passing through. In particular, the passing-through interaction of barchans was demonstrated by numerical simulations [64–66] and laboratory experiments [67]. This passing-through behavior is very similar to the dynamics of solitary waves. This interesting feature was also confirmed in actual barchans by a long-term observation [68].

Aeolian processes might be a crucial factor to form various types of geomorphologies on planetary surfaces [69]. It is not so trivial because the atmospheres on planetary surfaces can be very different from that on the Earth. Terrestrial sand dunes have been extensively examined by many researches [70]. However, these structures are not fully consistent with planetary sand dunes. Detailed comparisons among the Earth and other planets might provide novel insight of surface pattern formation due to regolith transport mainly by the aeolian effect, and would also improve the understanding of sand dune dynamics on the Earth. In Fig. 7.10, sand

Fig. 7.10 Sand dunes in the Victoria crater on Mars. The sharp crater rim structure as well as the sand dunes in the crater are impressive. The diameter is approximately 730 m (Credit: NASA)



¹¹To model the large-scale dune migration in a laboratory, water flow was used in the experiment. This is a type of similar modeling for geological-scale phenomena (Sect. 2.8).

dunes developed in the Victoria crater on Mars are shown. This image was taken by the High Resolution Imaging Science Experiment (HiRISE) camera on NASA's Mars Reconnaissance Orbiter. It is not clear how the Martian surface produces such beautiful art on its surface. This landscape might be made by a collaboration of impact and aeolian processes.

7.3 Summary

Some topics relating to soft impact and planetary science have been reviewed in this chapter. In particular, the collision outcomes resulting from the impact of tiny dust aggregates and the impact-originated regolith behaviors are emphasized.

For the former, the structure and contact mechanics of dust aggregates are key factors to be considered when examining the growth history of dust aggregates. While there are some barriers in the model of aggregate growth, these barriers might be overcome by considering soft impact effects such as the fluffiness (coordination number) of the aggregates and offset collision. However, the aggregate growth scenario remains far from being completely understood. For example, the porosity dependence of the collision outcomes is not sufficiently quantitative. Only two states (porous and compact) have been considered to make the phase diagrams [13]. A systematic investigation with continuously varying porosity might be required. Then, the porosity effect can be precisely included in the dust aggregate growth model. Moreover, there might be other hidden parameters that are essential for determining the collision outcomes of dust aggregates. However, the scenario should be as simple as possible. Although it is easy to add new factors into the model, such addition makes the model complicated. Thus, we must select essential but minimal factors to model the impact of dust aggregates.

The latter part addressed regolith behavior. The principal process of regolith formation is most likely the impact events that occur intermittently on the surface of astronomical objects. Although the impact frequency and regolith thickness are related by a simple model, the universality of this model is not yet concrete. The effect of thermal cycling and migration of the regolith are also modeled on the basis of simple granular experiments. However, these considerations are still very rough. There are many things to be solved with regard to regolith behaviors. Additionally, the relevance of these models must be tested by comparison with appropriate observational data. Such interdisciplinary studies among planetary observation, laboratory experiment, and theoretical modeling are crucial next steps.

There are many other granular-related or impact-related phenomena in geophysical or planetary sciences. For further reading, Refs. [10–13] provide comprehensive reviews of the growth of dust aggregates. For geomorphological topics, detailed discussions can be found in Refs. [39, 71, 72].

References 295

References

 P.J. Armitage, Astrophysics of Planet Formation (Cambridge University Press, Cambridge, 2010)

- 2. A. Li, J.M. Greenberg, Astron. Astrophys. 323, 556 (1997)
- 3. G. Wurm, M. Schnaiter, Astrophys. J. 567, 370 (2002)
- 4. S.V.W. Beckwith, T. Henning, Y. Nakagawa, Dust properties and assembly of large particles in protoplanetary disks, in *Protostars and Planets IV* (University of Arizona Press, Tucson, 2000), pp. 533–558
- S.J. Weidenschilling, J.N. Cuzzi, Formation of planetesimals in the solar nebula, in *Protostars and Planets III* (University of Arizona Press, Tucson, 1993), pp. 1031–1060
- 6. S.J. Weidenschilling, Mon. Not. R. Astron. Soc. 180, 57 (1977)
- 7. G. Wurm, J. Blum, J.E. Colwell, Icarus 151, 318 (2001)
- 8. J.N. Cuzzi, R.C. Hogan, J.M. Paque, A.R. Dobrovolskis, Astrophys. J. 546, 496 (2001)
- 9. S.A. Balbus, J.F. Hawley, Rev. Mod. Phys. 70, 1 (1998)
- 10. J. Blum, G. Wurm, Annu. Rev. Astron. Astrophys. 46, 21 (2008)
- 11. J. Blum, Microgravity Sci. Technol. 22, 517 (2010)
- 12. J. Blum, Res. Astron. Astrophys. 10, 1199 (2010)
- C. Güttler, J. Blum, A. Zsom, C.W. Ormel, C.P. Dullemond, Astron. Astrophys. 513, A56 (2010)
- 14. D. Paszun, C. Dominik, Icarus **182**, 274 (2006)
- 15. K. Wada, H. Tanaka, T. Suyama, H. Kimura, T. Yamamoto, Astrophys. J. 661, 320 (2007)
- 16. K. Wada, H. Tanaka, T. Suyama, H. Kimura, T. Yamamoto, Astrophys. J. 677, 1296 (2008)
- 17. G. Wurm, J. Blum, Icarus 132, 125 (1998)
- 18. J. Blum, G. Wurm, Icarus 143, 138 (2000)
- 19. M. Krause, J. Blum, Phys. Rev. Lett. 93, 021103 (2004)
- 20. P. Meakin, Rev. Geophys. **29**, 317 (1991)
- 21. T. Mukai, H. Ishimoto, T. Kozasa, J. Blum, J.M. Greenberg, Astron. Astrophys. 262, 315 (1992)
- 22. C. Dominik, A.G.G.M. Tielens, Philos. Mag. A **72**, 783 (1995)
- 23. C. Dominik, A.G.G.M. Tielens, Philos. Mag. A 73, 1279 (1996)
- 24. C. Dominik, A.G.G.M. Tielens, Astrophys. J. **480**, 647 (1997)
- 25. K.L. Johnson, K. Kendall, A.D. Roberts, Proc. R. Soc. A 324, 301 (1971)
- 26. A. Chokshi, A.G.G.M. Tielens, D. Hollenbach, Astrophys. J. **407**, 806 (1993)
- A. Zsom, C.W. Ormel, C. Güttler, J. Blum, C.P. Dullemond, Astron. Astrophys. 513, A57 (2010)
- 28. S. Okuzumi, Astrophys. J. 698, 1122 (2009)
- 29. K. Wada, H. Tanaka, T. Suyama, H. Kimura, T. Yamamoto, Astrophys. J. 702, 1490 (2009)
- 30. D. Paszun, C. Dominik, Astron. Astrophys. 507, 1023 (2009)
- 31. K. Wada, H. Tanaka, T. Suyama, H. Kimura, T. Yamamoto, Astrophys. J. 737, 36 (2011)
- 32. D. Langkowski, J. Teiser, J. Blum, Astrophys. J. 675, 764 (2008)
- 33. Y. Shimaki, M. Arakawa, Icarus **221**, 310 (2012)
- 34. S. Okuzumi, H. Tanaka, H. Kobayashi, K. Wada, Astrophys. J. 752, 106 (2012)
- 35. S. Sirono, Astrophys. J. 735, 131 (2011)
- 36. S. Sirono, Astrophys. J. Lett. **733**, L41 (2011)
- 37. T. Kuroiwa, S. Sirono, Astrophys. J. **739**, 18 (2011)
- 38. Y. Shimaki, M. Arakawa, Icarus 218, 737 (2012)
- 39. H.J. Melosh, *Planetary Surface Processes* (Cambridge University Press, Cambridge, 2011)
- E.M. Shoemaker, R.M. Batson, H.E. Holt, E.C. Morris, J.J. Rennilson, E.A. Whitaker, J. Geophys. Res. 74, 6081 (1969)
- K. Chen, J. Cole, C. Conger, J. Draskovic, M. Lohr, K. Klein, T. Scheidemantel, P. Schiffer, Nature 442, 257 (2006)
- 42. T. Divoux, H. Gayvallet, J.C. Géminard, Phys. Rev. Lett. 101, 148303 (2008)
- 43. T. Divoux, Pap. Phys. **2**, 020006 (2010)

- 44. P. Philippe, D. Bideau, EPL (Europhys. Lett.) 60, 677 (2002)
- M. Delbo, G. Libourel, J. Wilkerson, N. Murdoch, P. Michel, K.T. Ramesh, C. Ganino, C. Verati, S. Marchi, Nature 508, 233 (2014)
- M.T. Mellon, R.L. Fergason, N.E. Putzig, The thermal intertia of the surface of Mars, in *The Martian Surface: Composition, Mineralogy, and Physical Properties* (Cambridge University Press, Cambridge, 2008), pp. 399–427
- H. Miyamoto, H. Yano, J.D. Scheeres, S. Abe, O. Barnouin-Jha, A.F. Cheng, H. Demura, R.W. Gaskell, N. Hirata, R. Ishiguro, T. Michikami, A.M. Nakamura, R. Nakamura, J. Saito, A. Sasaki, Science 316, 1011 (2007)
- 48. N. Murdoch, B. Rozitis, K. Nordstrom, S.F. Green, P. Michel, T.L. de Lophem, W. Losert, Phys. Rev. Lett. 110, 018307 (2013)
- 49. N. Murdoch, B. Rozitis, K. Nordstrom, S.F. Green, P. Michel, T.L. de Lophem, W. Losert, Granul. Matter 15, 129 (2013)
- N. Murdoch, B. Rozitis, S.F. Green, P. Michel, T.L. de Lophem, W. Losert, Mon. Not. R. Astron. Soc. 433, 506 (2013)
- 51. C. Güttler, I. von Borstel, R. Schräpler, J. Blum, Phys. Rev. E **87**, 044201 (2013)
- G. Tancredi, A. Maciel, L. Heredia, P. Richeri, S. Nesmachnow, Mon. Not. R. Astron. Soc. 420, 3368 (2012)
- 53. T.M. Yamada, H. Katsuragi, Planet. Space Sci. 100, 79 (2014)
- P. Eshuis, D. van der Meer, M. Alam, H.J. van Gerner, K. van der Weele, D. Lohse, Phys. Rev. Lett. 104, 038001 (2010)
- 55. P. Hejmady, R. Bandyopadhyay, S. Sabhapandit, A. Dhar, Phys. Rev. E 86, 050301 (2012)
- 56. K.M. Aoki, T. Akiyama, Y. Maki, T. Watanabe, Phys. Rev. E **54**, 874 (1996)
- 57. K. Nagao, R. Okazaki, T. Nakamura, N.Y. Miura, T. Osawa, K. Bajo, S. Matsuda, M. Ebihara, T. Noguchi, A. Tsuchiyama, H. Yurimoto, M.E. Zolensky, M. Uesugi, K. Shirai, M. Abe, T. Yada, Y. Ishibashi, A. Fujimura, T. Mukai, M. Ueno, T. Okada, J. Yoshikawa, M. Kawaguchi, Science 333, 1128 (2011)
- 58. M.M.M. Meier, C. Alwmark, S. Bajt, U. Böttger, H. Busemann, W. Fujiya, J. Gilmour, U. Heitmann, P. Hoppe, H.W. Hübers, F. Marone, U. Ott, S. Pavlov, U. Schade, N. Spring, M. Stampanoni, I. Weber, Forty-Fifth Lunar and Planetary Science Conference (Lunar and Planetary Institute, Houston, 2014), Abstract #1247
- 59. D.P. O'Brien, R. Greenberg, Icarus **178**, 179 (2005)
- 60. T.M. Yamada, K. Ando, T. Morota, H. Katsuragi, Forty-Sixth Lunar and Planetary Science Conference (Lunar and Planetary Institute, Houston, 2015), Abstract #1215
- 61. P.K. Kundu, I.M. Cohen, D.R. Dowling, Fluid Mechanics, 5th edn. (Academic, Waltham, 2011)
- 62. R.A. Bagnold, *The Physics of Blown Sand and Desert Dunes* (Methuen and Co., London, 1941)
- 63. N. Taberlet, S.W. Morris, J.N. McElwaine, Phys. Rev. Lett. 99, 068003 (2007)
- 64. V. Schwämmle, H.J. Herrmann, Nature **426**, 619 (2003)
- 65. A. Katsuki, H. Nishimori, N. Endo, K. Taniguchi, J. Phys. Soc. Jpn. 74, 538 (2005)
- 66. O. Durán, V. Schwämmle, H. Herrmann, Phys. Rev. E 72, 021308 (2005)
- 67. N. Endo, K. Taniguchi, A. Katsuki, Geophys. Res. Lett. 31, L12503 (2004)
- 68. P. Vermeesch, Geophys. Res. Lett. 38, L22402 (2011)
- 69. R. Greeley, J.D. Iversen, Wind as a Geological Process on Earth, Mars, Venus, and Titan (Cambridge University Press, Cambridge, 1985)
- 70. N. Lancaster, Geomorphology of Desert Dunes (Routledge, London/New York, 1995)
- 71. J.D. Pelletier, *Quantitative Modeling of Earth Surface Processes* (Cambridge University Press, Cambridge, 2008)
- B. Andreotti, Y. Forterre, O. Pouliquen, Granular Media (Cambridge University Press, Cambridge, 2013)

Chapter 8 Perspectives

In this book, dimensional analysis and the scaling method were mainly employed to reveal the physics of soft impact phenomena. The scaling approach is very helpful to observe the essence of the underlying physical mechanisms of the considered phenomena. In particular, scaling is very powerful for the order estimate of phenomena whose scale is widely spreading. To conduct assessments with accurate detail, however, we need a complete modeling, including numerical factors. Therefore, the ability of an order estimate based on the scaling should not be overvalued. However, the order estimate is usually appropriate for geophysical or planetary phenomena because the observable information for these phenomena is very limited in most cases. Moreover, most of the geophysical or planetary phenomena occur on an extremely large scale and over a very long time. Scaling is a unique method to discuss such phenomena. Furthermore, scaling and dimensional analysis are important methods in various fields including fluid engineering and astrophysics. These methods are based only on the concept of dimensional homogeneity. Although this concept is very simple, its applicability is extensive. The dimensional homogeneity is only one constraint. In general, it is difficult to obtain a complete physical formulation solely from the dimensional perspective. Thus, additional (real or numerical) experiments are necessary to attain useful scaling expressions, which suggests that dimensional analysis possesses an affinity for experiments. Therefore, we first studied the fundamentals of dimensional analysis and the scaling method. Then, the method was applied to various soft impacts mainly based on experimental results. One of the most important procedures in dimensional analysis and scaling is to find relevant dimensionless numbers. The relevant dimensionless numbers can be obtained using a few methods: nondimensionalization of governing equations, Π -groups method, and intuitive derivation by considering the underlying physical mechanics. These methods are important and have been utilized in various discussions in this book.

The dimensionless numbers used in this book but not listed in Table 2.5 are tabulated in Table 8.1. These dimensionless numbers are very useful tools to

298 8 Perspectives

Table 8.1 Dimensionless numbers used in this book but not listed in Table 2.5. Although some of these numbers are not named in the text, temporal names are assigned to them

Name	Form	Physical meaning	Equation
Quality factor	$\frac{1}{Q} = \frac{\eta D_i}{\sqrt{m_i k}}$	Dimensionless dissipation	(3.20)
Friction criticality	$S_{\text{fric}} = \frac{ F_t }{\mu_0 F_n}$	Tangential vs. frictional forces	(3.66)
Normalized acceleration	$\Gamma = \frac{(2\pi f)^2 A_0}{g}$	Vibration vs. gravity (acceleration)	(3.67)
Viscous efficiency	$R_{\eta g} = \frac{18\eta v}{\rho_g g D_g^2}$	Viscosity vs. gravity	(3.68)
Temperature efficiency	$R_{Tg} = \frac{6k_BT}{\pi\rho_g g D_g^4},$	Thermal fluctuation vs. gravity	(3.69)
Normalized velocity	$S_{\Gamma} = \frac{(2\pi f A_0)^2}{g D_g}$	Vibration vs. gravity (velocity)	(3.70)
Improved Froude number	$D_r = \frac{v^2}{gz} \left(\frac{\rho_t}{\rho_i}\right)^{1/2}$	Inertia vs. gravity	(4.25)
Elastic Froude number	$F_r \Lambda = \frac{(\rho_i - \rho_t) v_0^2}{G}$	Inertia vs. elasticity	(4.57)
Gravity strength ratio	$R_{gY} = \frac{\rho_t g D_i}{Y_t}$	Gravity vs. strength	(5.44)
Cratering efficiency	$\pi_V = \frac{\rho_t V_c}{m_i}$	Cratered vs. impactor masses	(5.53)
Newton number	$\pi_3 = \frac{Y_t}{\rho_t v_0^2}$	Strength vs. inertia	(5.53)
Impact Reynolds number	$R_{eI} = W_e^{1/4} R_e^{1/2}$	R_e with visco-capillary length scale	(6.64)
Splashing parameter	$K_s = We^{1/2}R_e^{1/4}$	Splashing strength	(6.81)

characterize various soft-matter or planetary phenomena. The principal goals of this book were to correctly introduce these dimensionless numbers and provide a physical rationale about their use.

In continuum mechanics, some macroscopic variables such as stress, strain, and strain rate are used to model the behaviors of solids and fluids. It is apparent that general continuous media consist of many molecules. Because the constituent molecular number is very large ($\geq 10^{23}$), we can forget the details of microscopic motions in continuous media. The microscopic particularities are averaged out. Because this strategy works well at least in small (linear) strain (or strain rate) regime, continuum mechanics can be used to evaluate and predict the macroscopic behaviors of solids and fluids. For continuum mechanics, governing equations such as the Navier-Stokes equation have been established. The relevant dimensionless parameters for this system can be directly derived by the nondimensionalization of the governing equations. Thus, the theoretical framework of dimensional analysis has been extensively developed in the field of continuum mechanics. Chapter 2 was

8 Perspectives 299

mainly devoted to explaining the usefulness and limitations of dimensional analysis and scaling.

This nondimensionalization method is not always applicable to various materials. There are many phenomena for which the governing equations are not found. Granular matter, which is the main target material in this book, is a typical example. For granular matter, the number of grains is generally much smaller than the order of Avogadro's constant. That is, we can count the number of constituent grains. In this situation, one might suppose that the microscopic approach is better to understand the behaviors of granular matter. Nevertheless, in this book, the macroscopic approach has been applied to understand the physics of granular matter because the macroscopic approach is advantageous for understanding the complex behaviors by scaling experimental data. We consider the granular matter as a type of continua that exhibits both solid-like and fluid-like behaviors. Furthermore, granular matter exhibits peculiar behaviors that are quite different from solids and fluids. To model granular behaviors in the context of continuum mechanics, appropriate constitutive relations are required. Some of the relevant constitutive relations were introduced in Chaps. 3 and 4. Unfortunately, the universal governing equation has not been found for granular behaviors. Thus, the relevant dimensionless numbers cannot be automatically obtained from the nondimensionalization of the governing equation. Even in such a difficult situation, the Π -groups method enables us to derive the relevant dimensionless numbers by considering the physical mechanism for the phenomena of interest. To derive meaningful dimensionless numbers, appropriate physical intuitions are necessary, which implies that the weak point of the dimensional analysis is its arbitrariness.

Hopefully, the central idea and its specific applications of the dimensional analysis and scaling were clarified throughout the various discussions on soft impact in this book. The dimensional analysis and scaling method have been applied both for soft matter physics and planetary science. Despite this similarity, these two fields have developed almost independently. One of the main goals of this book was to highlight this similarity and search in the direction of their possible unification.

The similarity among soft and planetary impacts is not limited to the methodology. Another point of similarity between soft and planetary impacts is the subject matter. Planetary surfaces are covered by granular matter called regolith. To reveal the origins of various planetary surface terrains, in-depth understandings of granular behaviors (under many conditions such as impact, vibration, and thermal cycling) are necessary. The commencing materials of solid planets—tiny dust aggregates—can also be regarded as a type of granular matter. While there are many other subjects in soft matter physics and planetary science, granular matter is the requisite ingredient both for soft matter physics and planetary science. Therefore, granular matter is the main focus of this book. Indeed, the comparison between soft matter physics and planetary science discussed in this book was not exhaustive. Only some of the characteristic intersections among soft matter impact and planetary-related phenomena were covered. There are many other phenomena concerning both fields, e.g., landslides, volcanic lava flow, and Saturn's ring formation, that were not discussed in this book.

300 8 Perspectives

As mentioned thus far, because soft impact physics and planetary science share methodologies and subject materials, these fields can coevolve in principle. Impact cratering can be a good entity to link soft matter physics with planetary science. Thus, the impact mechanics and cratering were reviewed from both sides in Chaps. 4, 5, and 6. These chapters compose the main content of this book. Unfortunately, the complete unification remains difficult at present. Although the current cutting edges of soft and planetary impacts were surveyed, the conceptual identification and classification of these phenomena have not yet been achieved. Successive interactions among soft matter physics and planetary science are required to make crucial progress in both fields.

The communication between the fields of soft and planetary impacts is a small first step. Natural phenomena are too complex to be understood only by a physical approach. Furthermore, chemical effects must be considered to discuss actual planetary-related phenomena, although the chemistry is completely omitted in this book. For example, chemical effects such as surface cohesion can drastically affect the behavior of small grains. As explained in Sect. 2.8.5, the surface tension effect becomes predominant for small grains, particularly when the gravity effect is weak such as in the planetary environment. In addition, the value of surface tension (cohesion) strongly depends on the surface chemical state. The oxidation degree of the grains' surface significantly affects the cohesion. On the Earth, grain surfaces undergo oxidation in a relatively short time. However, the oxidation rate must be drastically reduced in space because its gas pressure is extremely low. Moreover, the grain surface is exposed to cosmic-ray irradiation in space. We do not know what happens to tiny grains under such extreme conditions in terms of surface chemistry. Of course, physical approaches such as dimensional analysis are quite useful to consider the comprehensive framework. However, if we need an accurate assessment, chemical approaches are also needed to elaborate the precise model. In some cases, the chemical effects could be more important than the scaling. Geophysics and planetary science are very interdisciplinary fields. We must compile a considerable amount of information to build a plausible scenario of geophysical or planetary phenomena. The necessity of such an interdisciplinary approach has been actually long propounded. However, achieving an adequate incorporation of physics, chemistry, and geology has not been very easy. In fact, collaborations between the fields of soft matter and planetary impacts have not been sufficient even though these fields share a similar basis of physical approaches.

Recently, the database of planetary observation has grown increasingly larger, particularly for our neighbors such as the Moon and Mars. Today, we can see high-resolution surface images of their surfaces. However, the information about relatively far objects remains very limited. Although the small asteroid Itokawa was explored in detail, this asteroid is only one example of small asteroids from which samples have been returned. In this book, we have discussed some interesting topics concerning Itokawa: the wavy-rimmed nano crater, regolith migration, among others. These phenomena are intriguing enough to be studied and can be important features in general asteroids. However, we should keep in mind that Itokawa is only one example. We know that granular-related phenomena exhibit a strong history

8 Perspectives 301

dependence. Thus, Itokawa's surface features might also be very unique. In fact, asteroids are not uniform but are rather diverse and exhibit quite different characters depending on their histories.

Each astronomical object has its own individual history and characteristics. Similarly, each regolith grain has its own peculiar history. If the regolith grains behave like an ideal gas, microscopic individuality does not matter; the collective dynamics would be simple. However, the behaviors of granular matter such as those of regolith cannot be simply understood using such an orthodox approach. The individuality and history may be essential for granular collective behaviors, which is one of the most difficult points in the investigation of granular matter. The wide variety of planetary terrains is analogous to this complex history dependence of the behavior of the constituent grains.

In this book, various recent investigations concerning soft impact have been surveyed. I would be very pleased if someone developed an interest in the intersectional field between soft matter physics and planetary science by reading this book. The ultimate unification of soft impact physics and planetary science has not yet been achieved. This problem is extremely advanced for me, and I hope that someone who reads this book begins striving to solve this problem.

Symbols

Z-model, 173

 Π -groups, 29

α model, 267 Bingham drag model, 47 Bingham model, 66, 109 body force, 15 A Boltzmann constant, 45, 94, 251 acoustic fluidization, 175, 177 bomb sag, 254 added mass, 42 Bond number, 50, 238 adiabatic index, 34 bouncing barrier, 275 advection, 71 braking time, 42, 264 advection equation, 76 Brazil nut effect (BNE), 96, 283 Brownian motion, 263 advection-diffusion equation, 71 advective transport rate, 51 Buckingham Π theorem, 29 aeolian grain transport, 134 bulk modulus, 22 Amontons' law, 81 bump-type crater, 233 angle of repose, 79 angular frequency, 75 antisymmetric deformation, 18 \mathbf{C} capillary bridge, 236 apparent mass, 42 Archimedes' principle, 148 capillary force, 49 capillary length, 49, 207 aspect ratio of crater, 158 asymmetric crater, 173 capillary number, 50 attenuating oscillation, 70 central peak, 158, 210, 220 Atwood machine, 128 central pit, 159 Atwood number, 51, 246 clogging, 5 complex crater, 158, 220 complex modulus, 67 B conservation law, 23 Bagnold, 52, 122 contact and compression, 168 Bagnold flux, 292 continuum mechanics, 4 Bagnold number, 52 convective derivative, 24 Bagnold scaling, 122 coordination number, 276 Coulomb failure criterion, 78, 90, 177 ballistic cluster cluster aggregate (BCCA), 271 ballistic particle cluster aggregate (BPCA), 271 Coulomb friction, 78, 109

barchan, 293

bearing capacity failure, 257 Bernoulli's principle, 26, 145

Coulomb number, 53 coverage factor, 165, 279 cratering efficiency, 187 creep motion, 65 critical packing state, 129 crossover packing fraction, 130

D

Deborah number, 51, 150 deep cavity, 141 deep closure, 43 degradation, 168 delta function, 75 diffused gas eruption, 257 diffusion, 71 diffusion coefficient, 51, 73 diffusion equation, 72 diffusion length, 243 diffusive transport rate, 51 diffusivity, 73 dilatancy, 84 dimensional analysis, 8 dimensionless acceleration, 92 dimensionless number, 8 dimensionless spray flux, 241 discontinuous shear thickening, 153 discrete element method (DEM), 70 drag coefficient, 39 droplet-granular impact, 228 dust aggregate, 264 dynamic friction coefficient, 79 dynamic peak, 117 dynamic pressure, 27 dynamic sand dune, 224 dynamic viscosity, 20 dynamical similarity, 56

\mathbf{E}

ejecta blanket, 173
ejecta curtain, 173, 214, 239
ejecta deposition, 168
elastic collision, 69
elastic rroude number, 150
elastic modulus, 22, 64, 150
energy density, 60
Epstein drag, 46, 263
equation of continuity, 24, 72
Eros, 177
error function, 74, 178
escape velocity, 262
Euler equation, 25, 229

Eulerian derivative, 24 excavation, 168 excavation flow, 172

F

Faraday wave instability, 6 filling factor, 52 filat-type crater, 233 fluid particle, 23 force chain, 89, 120 fractal dimension, 271 fragmentation barrier, 275 free molecule flow, 45 friction coefficient, 79 friction velocity, 289 Froude number, 48

G

Gauss' theorem, 24, 72
Gaussian integral formula, 74
geometric attenuation, 172
geometric saturation, 165
geometric similarity, 55
granular avalanches, 123
granular Bond number, 241
granular buoyancy, 99
granular temperature, 95, 122
granular-granular impact, 223
gravitational constant, 179, 263
gravity regime, 185, 249
gyration radius, 271

Н

harmonic oscillation, 70 Hayabusa, 3, 162, 284 Heaviside step function, 224 Herschel-Bulkley model, 67, 210 Hertz law, 36, 230 Hooke's law, 19, 22 Hugoniot equations, 168 hydrostatic pressure, 116

I

impact capillary length, 228 impact parameter, 275 impact Reynolds number, 244 impact seismic efficiency factor, 172, 179 impedance matching, 171 inelastic bouncing ball model (IBBM), 92 inelastic collision, 69, 84

inertial drag force, 39 inertial number, 53 inertial stress, 49 initial packing fraction, 128 internal friction angle, 79 internal stress relaxation, 64 interstitial air, 130 Itokawa (asteroid), 3, 162, 243, 283 Itokawa's micro craters, 162, 243

J

jamming, 129 Janssen effect, 84 jetting, 8 JKR theory, 37

K

Kaguya, 2
Kelvin-Helmholtz instability, 6
Kelvin-Voigt model, 63
Keplerian motion, 264
Keplerian speed, 265
kinematic similarity, 55
kinematic viscosity, 20, 51
kinetic theory, 122
Knudsen number, 46
Kronecker's delta, 19, 71
Kármán constant, 290

\mathbf{L}

Lagrange derivative, 24
Lame's elastic constants, 19
Laplace equation, 207
Laplace pressure, 49, 246, 277
Leidenfrost, 96
liquid spring, 230
liquifaction, 5, 177
lithostatic, 110
loss angle, 68
loss modulus, 68

M

Mach number, 50 magnetorotational instability (MRI), 268 Maxwell model, 63 Maxwell time, 65, 150 Maxwell-Boltzmann distribution, 45, 263 mean free path, 45 micro crater, 162 micro rebound, 121

milk-crown, 243 modification, 168 moment magnitude, 172 momentum transfer, 39 multiring basin, 159

N

Navier-Stokes equation, 23, 71, 286 near-surface zone, 172 Newton's equation of motion, 14 Newton's second law, 7 Newtonian fluid, 21, 39

o

Ohnesorge number, 50 overdamped, 69

P

packing factor, 52 packing fraction, 52, 128 Particle Image Velocimetry (PIV), 139 particle-based Weber number, 223 peak-ring crater, 159 percolation, 97 perfect fluid, 21, 124 period-doubling, 92 phenomenological mechanics, 5 plastic deformation, 107 point source measure, 185, 212 Poisson's ratio, 22 polydispersity, 3 Poncelet drag model, 47 porosiy, 52 Prandtl's mixing length theory, 290 principle of superposition, 75 probability distribution, 120 push-me-pull-you, 146 Péclet number, 51

\mathbf{c}

quality factor, 70, 181 quicksand, 109, 218

R

R plot, 164 radial drift barrier, 267 radius of curvature, 246 ram pressure, 27 rampart crater, 161

random close packing (RCP), 165, 281	sonofluidization, 148	
random walk, 73	splashing, 8	
rate- and state-dependent friction (RSF), 80,	splashing parameter, 249	
149	spring constant, 230	
ray crater, 160	static friction coefficient, 78	
Rayleigh-Plateau instability, 6	static peak, 117	
Rayleigh-Taylor instability, 5, 244	Stokes drag, 38, 264	
Rayleigh-type cavity development, 218	Stokes dynamics, 38	
reduced diameter, 272	Stokes number, 41	
reduced mass, 263	Stokes' law, 38	
regolith convection, 285	Stokeslet, 38	
restitution coefficient, 68, 135, 214	stopping time, 42, 109	
reverse Brazil nut effect (RBNE), 97, 148	storage modulus, 68	
reverse buoyancy, 99	stratification, 5	
Reynolds number, 28	stream function, 38	
ricochet angle, 134	strength regime, 185, 250	
ring-type crater, 233	stress dip, 87	
ripening, 277	stretched exponential relaxation, 281	
Robins-Euler drag model, 46	Strouhal number, 28, 51, 222	
rotating drum, 5	sub-diffusion, 73	
roughness factor, 290	super rebound, 69	
rubble-pile, 195	super-diffusion, 73	
	surface closure, 43, 206	
	surface energy, 60	
S	surface force, 15	
saltaion, 291	surface tension, 36, 49	
sand dune, 134, 292	symmetric deformation, 18	
saturation parameter, 255	symmetry breaking, 256	
Savage number, 53		
scale transformation, 48	Т	
scaling law, 8	-	
Schröter's rule, 205	Taylor vortex instability, 6 Taylor-Couette shear cell, 285	
segregation, 5 seismic erasure, 177	terminal velocity, 40	
	thermal capacity, 283	
seismic quality factor, 181 seismic shaking, 177	thermal conduction, 282	
SELENE, 2, 159	thermal conductivity, 283	
settling velocity, 264	thermal cycling, 281	
shaking parameter, 95	thermal fatigue, 282	
shaking strength, 95	thermal inertia, 283	
shear banding, 5, 285	thermal penetration depth, 282	
shear modulus, 22	thermal skin depth, 282	
shear strain rate, 39	Torricelli's law, 89	
shear stress, 39	transitional crater, 255	
Shields number, 52	transport coefficient, 71, 72	
shock wave, 145	transport phenomena, 24, 51	
simple crater, 157, 220	traveling wave solution, 77	
simple shear, 18	tunneling, 241	
sink-type crater, 233	<u>.</u>	
sintering, 277		
slope of the ejecta curtain, 214	V	
snow line, 277	virtual mass, 42, 118, 151	
soil pressure, 110	viscoelastic relaxation time, 65	
solid fraction, 52	viscous drag force, 38	

viscous erosion, 257 viscous fingering instability, 6 void fraction, 52 volume fraction, 52 volume strain, 23

W

washboard road, 292 Washburn law, 239 water saturation, 222 water-bell, 124 wavenumber, 75 Weber number, 49, 207 wind shadow, 292 Worthington jet, 217

Y vield stres

yield stress, 66, 107, 109 Young's modulus, 22, 274